DEVELOPMENT OF THE SETUP AND PERFORMANCE OPTIMIZATION OF ELECTRO-CHEMICAL HONING PROCESS

A THESIS

Submitted in partial fulfilment of the requirements for the award of the degree of

DOCTOR OF PHILOSOPHY

in

MECHANICAL ENGINEERING

By

ABHAY KUMAR DUBEY

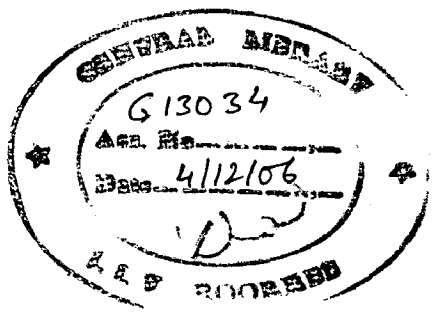

DEPARTMENT OF MECHANICAL AND INDUSTRIAL ENGINEERING
INDIAN INSTITUTE OF TECHNOLOGY ROORKEE
ROORKEE-247 667 (INDIA)

AUGUST, 2006

© INDIAN INSTITUTE OF TECHNOLOGY ROORKEE 2006
ALL RIGHTS RESERVED

6th Annual Convocation- 2006
Degree conferred on 11.11.2006

Supdt. (PGS&R)

INDIAN INSTITUTE OF TECHNOLOGY ROORKEE
ROORKEE

CANDIDATE'S DECLARATION

I hereby certify that the work which is being presented in the thesis entitled **DEVELOPMENT OF THE SETUP AND PERFORMANCE OPTIMIZATION OF ELECTRO-CHEMICAL HONING PROCESS** in partial fulfilment of the requirements for the award of the Degree of **Doctor of Philosophy** and submitted in the **Department of Mechanical and Industrial Engineering** of the Indian Institute of Technology Roorkee, Roorkee is an authentic record of my own work carried out during the period from July 2004 to August 2006 under the supervision of **Dr. H. S. Shan**, Professor and **Dr. N. K. Jain**, Lecturer in the Department of Mechanical and Industrial Engineering.

The matter presented in this thesis has not been submitted by me for the award of any other degree of this or any other Institute.

(ABHAY KUMAR DUBEY)

This is to certify that the above statement made by the candidate is correct to the best of our knowledge.

Date: 02/08/06

(N. K. JAIN)
M.I.E.D
I.I.T. Roorkee
Roorkee – 247 667

(H. S. SHAN)
M.I.E.D
I.I.T. Roorkee
Roorkee- 247 667

The Ph.D. Viva-Voce Examination of **Mr. Abhay Kumar Dubey**, Research Scholar, has been held on 31.10.06

Signature of Supervisor(s) 31/10/06

Signature of External Examiner
31/10/06

ABSTRACT

The surface quality and shape deviations play a crucial role in determining the functional performance of critical engineering components during service. Hybrid electrolytic machining processes are gaining considerable attention from the manufacturing community in order to meet the challenges of stringent surface quality and size tolerance requirements, often coupled with high part production rates. Electro-chemical honing (ECH) is a hybrid electrolytic micro-finishing technology characterized by a distinct coupling of electro-chemical machining and conventional honing processes to provide controlled functional surface generation and fast material removal capabilities in a single operation. ECH can offer a unique range of benefits to the machined surfaces not obtainable by either of the processes when applied independently. In ECH, a low DC potential is applied across the electrolyte flooded inter electrode gap (IEG) between a cathode stainless steel tool and anode workpiece for anodic dissolution while the ECH tool, which also contains non-conductive honing sticks, is stroked through the work bore with a controlled generating motion of simultaneous rotation and reciprocation. Major part of the material removal occurs through electrolytic action while the mechanical abrasion by honing sticks is controlled to a minimum, just enough to remove preferentially the metal oxide microfilm from the higher spots protruding from the ideal configuration and resulting surface non-uniformity due to electrolytic action. The process has a flexi- feature with regard to the control of machined surface characteristics. A surface having a distinct cross-hatch lay pattern, required for oil retention, alongwith compressive residual stress desirable for the components that are subject to cyclic loading can be produced. A surface completely free from stresses can also be generated. ECH possesses the ability to improve surface finish as well as to correct form deviations and smooth off ripples. Surface roughness value Ra of the order of 0.05 μm and tolerances of ± 0.002 mm can be achieved. The ability of ECH to apply these benefits productively, has led to its widespread use in many industries, especially in aerospace, auto, petrochemical reactor, roller, and gear manufacturing industries.

ECH process, however, is still in its infancy in many respects. The relationships between process parameters and performance characteristics are not completely known. The exact mechanism of material removal is only partially understood. The surface quality and part macro-geometrical aspects have not been effectively evaluated. No attempt seems to

have been made towards modeling and optimization of ECH process. Little information is available about the ECHed work surface characteristics.

The present research work makes an attempt in this direction based on a total surface quality approach, with the following objectives:

1. Design and develop an experimental setup for ECH process.
2. Explore time-dependent behaviour of ECH process.
3. Investigate the effects of key ECH parameters on the process performance characteristics.
4. Identify the material removal mechanism of ECH.
5. Evaluate ECHed work surface quality.
6. Evaluate ECHed surface macro-geometrical aspects.
7. Examine important ECHed work surface integrity aspects.
8. Multi-performance modeling of ECH process.
9. Multi-performance optimization of ECH process.

An electro-chemical honing setup was designed and developed indigenously. This setup incorporates several unique features that help to exercise a precise control over the operational kinematics and process input parameters over a good range. The setup consists of five major sub-systems: power supply, ECH tool and drives, electrolyte supply and cleaning system, work holding and positioning system, and frame and housing. A power supply with an output DC potential in the range of 3-30 V (adjustable) and current adjustable upto 200A with digital displays was used. The power supply can be operated either as a constant current source or as a constant voltage source. The positive terminal of power supply is connected to the workpiece while the negative terminal of the power supply is connected to the SS tool body through a copper-carbon brush and slip ring assembly designed to move in synchronism for achieving a shorter tool length yielding a better operational stiffness of the tool. ECH tool, designed with several unique features, is stroked through the work bore with a precisely controlled generating motion of simultaneous rotation and reciprocation. A variable speed DC servomotor for rotation and a microprocessor controlled programmable stepper motor unit for reciprocatory motion are employed. Four expandable honing sticks controlled by spring-mechanism protrude from around the circumference of the ECH tool. These sticks maintain a uniform tool-work gap and act to remove surface metal oxide microfilm preferentially from higher spots to correct geometrical inaccuracies. The electrolyte supply and cleaning system has been designed to provide a fine control of electrolytic parameters and maintain electrolyte purity. Electrolyte temperature is controlled by the heating and

cooling systems fitted with high accuracy temperature controllers. A stainless steel pump capable of developing a wide range of pressure and flow rate is installed for electrolyte supply to the IEG. Electrolyte pressure and flow controls are employed at the pump discharge. To maintain a uniform electrolytic condition in the IEG, direct electrolyte flushing has been combined with electrolyte supply through tool body at several locations in the IEG. Filtration is achieved by using two double-stage magnetic-cum-mechanical filters provided in electrolyte circuit and by settling. The machining chamber has been designed to incorporate work holding and positioning system with provisions for work loading/unloading, alignment and positioning; three-stage sealing at tool inlet to the machining chamber; mist collection, and free-float condition to workpiece for enhanced working efficiency of the setup.

For the present experimental studies the identification of process performance characteristics and key process input parameters and the determination of parameter range and levels were based on literature review, recent practices, pilot-experiments, work material characteristics and kinematics of the developed set-up. Process performance characteristics considered were the surface micro-geometry, macro-geometry, surface integrity and diametral increase rate. Measurements of the performance characteristics were carried out with precision instruments by following the standard practices. ASTM 35 cast iron cylindrical blocks were selected as workpiece specimen on consideration of the common commercial applications of the process.

Experimental investigations were planned using suitable experiment design techniques and conducted in a phased manner. In order to get insight into the time dependent behaviour of ECH, variation patterns of percent improvements in surface roughness value R_a (PIR_a); surface roughness value R_{max} (PIR_{max}); out-of-roundness (PIOR); cylindricity (PICyl); axis-straightness (PIAS); and diametral increase rate (DIR) were studied with the change in processing time (PT) employing a fully randomized one-factor-at-a-time experimental design. The R_a and R_{max} values were measured by using Mahr Perthometer and the measurements of out-of-roundness, cylindricity, axis-straightness and bore diameter were made on a 3D CMM. Results were analyzed using ANOVA; F-ratio; Fisher LSD and Duncun's multiple range tests. The variation patterns of PIR_a, PIR_{max}, PIOR and PICyl with PT are found to follow a quadratic trend. Major improvements occur in the first few minutes of ECH operation and subsequently the rate of successive improvements diminishes. The processing time effect for improvement in axis-straightness is not significant. Axis-straightness improves very rapidly and beyond a certain value there is little improvement with increase in the processing time. Diametral increase rate remains almost constant at various processing time levels. Empirical

models for the variation in PIR_a, PIR_{max}, PIOR, PICyl and DIR with the processing time have been developed using regression analysis.

Comprehensive experimental investigations using a Taguchi matrix experimental design were planned in the next phase to examine the influence of key process parameters on the performance characteristics and to identify mechanism of material removal of ECH. The effects of current intensity (C); electrolyte concentration (EC); rotary to reciprocating speed ratio (SR); electrolyte flow rate (F); electrolyte inlet temperature (T); stick-out pressure (SOP); stick grit size (G) and three prospective interactions C-EC; C-SR; EC-SR have been analyzed on PIR_a, PIR_{max}, PIOR, PICyl and DIR using ANOM, ANOVA and F-ratio on raw as well as S/N data.

Results indicate that current intensity, electrolyte concentration, speed ratio, stick-out pressure and grit size are the major players influencing the ECH performance. The improved electrolytic conditions in IEG due to the dual mode electrolyte supply and action of honing sticks are the probable cause of the lower electrolyte flow rate effect in the process as against that noticed in ECM. ECH process seems to be highly interactive in nature. The interactions amongst electrolytic and mechanical parameters play a vital role in the process. A good coordination of electro-chemical dissolution and selective mechanical abrading is vital for better results. The nature of electrolyte also has a tremendous bearing on the process performance. Therefore, selection of composition as well as concentration of electrolyte is crucial in the process. A unique behaviour of ECH is a simultaneous improvement in diametral increase rate and surface micro- as well as macro-geometrical profiles with increased current intensity. Phenomena of increased differential dissolution, viscous layer theory, anodic smoothing, highly reactive chemical attack (electrolyte dependent) and conventional honing operating simultaneously are responsible for the impressive behaviour of ECH process. In contrast to the conventional machining processes, the coarse grit sizes in ECH provide both the increased DIR and improved process micro- and macro-geometrical performance characteristics. The fine grit size is found to be less effective in all respects. Therefore, a proper selection of grit size is seen to be crucial for a better process performance. The individual effects of electrolytic parameters become less influential while at the same time the mechanical parameters and the interactions assume greater importance for macro-geometrical error correction in ECH. The process can rectify a work surface having considerable initial form deviations in roundness and cylindricity (ISO Tolerance Grade 11). The final out-of-roundness and cylindricity are within ISO Tolerance Grade 7/8 and 4/7 respectively. Multi variable regression models have been developed for PIR_a and

PIR_{max}. The optimal results for different process performance characteristics have been reported and validated through confirmation experiments.

Work surface characteristics were studied in the next stage of the study. The results on characteristic parameters such as bearing ratio, maximum peak-to-valley height of surface roughness value within the assessment length (Rt), core roughness depth (Rk), reduced peak height (Rpk) and the associated percent length of the top portion of the profile that gets worn away in the running-in-period (Mr1), reduced valley depth (Rvk) and the associated percent length of the bottom part of the profile that retains lubricant (Mr2) indicate that an ECHed surface can have superior resulting bearing and lubricant retaining capabilities. ECHed surfaces are characterized by a fine finished surface profile with a very narrow spread of surface roughness value. A uniform nano-finished plateau honed surface with much improved characteristic parameters R_a, Rt, Rk, Rpk and Mr1 coupled with a crosshatch lay pattern can be produced by ECH. Thus, very less proportion of the ECHed surface profile is susceptible to initial rapid wear. The ECH processed components can, therefore, have better wear and tribological performance. SEM photographs indicate that an effective planishing effect of ECH can remove all the traces of loosely held material as well as initial surface defects.

The ECH process, if properly operated, would leave no significant adverse impact on the surface integrity. Results of stage three studies on three main surface integrity aspects viz. the microstructural altration, microhardness change and surface residual stress change show that microhardness alterations are confined to within a narrow surface depth which is normally noticed in manufacturing processes when operated with a gentle touch. Effects similar to those obtained with 'electro-chemical machining followed by shot peening with glass beads' on the surface compressive residual stresses and sub-surface microhardness can be realized on ECHed surface. Higher speed ratio and stick-out pressure provide higher surface compressive residual stresses as well as sub-surface microhardness values. Therefore, the ECHed components produced under such conditions can be expected to provide a better fatigue endurance. The surface microhardness changes, however, were found significant at low significance levels with ANOVA, Tukey test and K-W test due to the non-uniform work material matrix.

Process modeling and multi-response optimization is necessary for utilizing the full potential of the process to meet the challenges of stringent requirements on surface quality, tolerances and production rates being demanded in globally competitive scenario. Three most effective approaches used by researchers in the recent years have been utilized for multi-performance modeling and optimization of ECH process in the present work

The Utility based Taguchi approach maximizes overall utility of the product (measuring the usefulness of various performance characteristics in meeting desired functional requirements), utilizing the Taguchi loss function methodology. Five cases of multiple ECH process performance characteristics were modeled and optimized using the approach. Results have been validated by conducting the confirmation experiments.

The artificial intelligence techniques were employed for multi-performance modeling and optimization of ECH. Seven cases of ECH multiple performance characteristics were modeled and optimized using a Taguchi-NN-GA multi-performance optimization control strategy. Radial basis function neural network (RBFNN) was used to develop the process models owing to its distinct advantages. However, the backpropagation network with steepest gradient descent learning algorithm and Levenberg-Marquardt backpropagation (an accelerated learning algorithm based on a simplified Newton's Method) models have also been developed for illustrative cases indicating that these networks can also be used. After validating the models, the multi-response outputs of RBFNN were combined into a single index using the desirability function approach to provide a fitness function to GA for multi-performance optimization. The results were also obtained using the modified desirability function approach. The modified desirability function incorporates the user's preference for flexibility. The results have been validated with actual experiments. The knowledge of many Pareto-optimal solutions can be very useful for the process user in deciding the optimal machining strategies, particularly when the current setting has changed and a new solution is required to be implemented. Therefore, non-dominated Pareto-optimal solutions have also been obtained for the various cases using an NSGA multi-objective optimization.

The real world problems are quite complex owing to uncertainty. Fuzzy set theory is an excellent mathematical tool to handle uncertainty arising due to vagueness. A Fuzzy Taguchi Inference application to ECH process has been attempted for a multi-performance optimization case study. Several fuzzy rules were derived based on the process experimental knowledge. A multi-response performance index (MRPI) was obtained based on the fuzzified loss functions of the various performance characteristics and fuzzy inference. GA and NN tuning was performed to optimize the FIS performance. Results of multi-performance modeling and optimization of ECH process obtained through various approaches are in good close agreement with the actual results. A set of guidelines formulated on the basis of results from the present research work are given at the end of the thesis to help the process user.

ACKNOWLEDGEMENTS

I express my deep sense of gratitude and indebtedness from the inner core of my heart to Dr. H.S. Shan, Emeritus Professor, Mechanical and Industrial Engineering Department, Indian Institute of Technology, Roorkee for his inspiring guidance, constant encouragement, critical reviews and invaluable help provided during the course of this research work without which this work would not have been possible. The guardianship and care provided by him and Mrs. Harpreet Shan to me as well as to my family cannot be forgotten.

I also convey my deep and sincere gratitude from the core of my heart to Dr. N.K. Jain, Lecturer, Mechanical and Industrial Engineering Department, Indian Institute of Technology, Roorkee for his invaluable supervision, constructive suggestions, motivation and support provided during the course of this study to complete it in time.

I wish to express my gratitude towards Dr. N.K. Mehta, Professor and Chairman DRC (Mechanical and Industrial Engineering Department), Dr. Dinesh Kumar, Professor (Mechanical and Industrial Engineering Department), Dr. Satya Prakash, Professor (Materials & Metallurgical Engineering Department) and Dr. P.K. Ghosh, Professor (Materials & Metallurgical Engineering Department) for their invaluable suggestions during the SRC meetings. I am also indebted to Dr. K.M. Singh, Assistant Professor (Mechanical and Industrial Engineering Department) and Dr. D.B. Goel, Professor (Materials & Metallurgical Engineering Department) who taught me the credit courses.

I acknowledge with gratitude the facilities provided by QC-T, Bharat Heavy Electricals Limited, Hardwar (INDIA) for the macro-geometrical measurements of workpieces on 3D CMM. I will remain grateful to Shri T.S. Kainth, DGM, Shri A.K. Saxena, AGM and Shri Dinesh Saxena, Dy. Manager for their invaluable support and Shri Arvind Bahukhandi for his months-long painstaking help in the measurement of such a large number of workpieces both before and after the ECH processing.

I wish to acknowledge the cooperation and help rendered by the staff of Machine Tool Laboratory, Mechanical and Industrial Engineering Department. My sincere thanks are due to Shri Jasbir Singh (Foreman) and Shri Hari Shankar (Mechanic) for their technical assistance during the setup development and experimental work.

I also acknowledge the services rendered by the staff of Welding Shop, Fitting Shop, Carpentry Shop, Machine Shop, Welding Metallurgy Laboratory, and Metrology Laboratory (Mechanical and Industrial Engineering Department), Metallography Laboratory (Materials & Metallurgical Engineering Department), Environmental Engineering Laboratory (Civil Engineering Department), and Institute Instrumentation Center IIT Roorkee. My special thanks are reserved for Shri Kalyan Singh (Microprocessor Laboratory), Electrical Engineering Department and Shri J.B. Rana, Foreman (Welding Shop), Mechanical and Industrial Engineering Department for providing help during the setup development and experimentation.

I am thankful to my employer, National Thermal Power Corporation Limited, INDIA for facilitating me by sanctioning study leave without pay to pursue this Ph.D. research. I acknowledge with gratitude the support and help provided by Shri A.N. Verma, DGM (HR) and Shri Mohan Rao, DGM (TS) NTPC Unchahar. I cannot forget the motivation given by Shri Basu Thakur, Manager (HR-ED), NTPC Unchahar to undertake the course.

I also express my heartful gratitude to my parents for their blessings, moral support and encouragement during this research work. My special thanks from core of my heart are due to my wife Mrs. Kiran Dubey for her sacrifice and providing me the much needed motivation and moral support during these two grueling years. I am also thankful to my children Master Ankit and Ms. Priyanshi for bearing painstaking inconvenience during this period.

I also extend my thanks to my colleague research scholars Mr. R.K. Gautam, Mr. Rajiv Kumar Chauhan, Mechanical and Industrial Engineering Department, and Mr. Sidhartha Panda, Electrical Engineering Department for their support during the research work. My special thanks are due to Mr. P.K. Jamwal, Sr. Lecturer, Mechanical Engineering Department, Engineering College, Kota (INDIA) for his suggestions during FIS modeling. I am also thankful to my friends for their cooperation and encouragement.

Last but not the least, the author wishes to express his gratitude to all those who generously helped him in coloring the mosaic of his thesis with the tiles of their knowledge, expertise and experience.

*Above all the great blessings and care of **ALMIGHTY** in no way can be evaluated.*

(ABHAY KUMAR DUBEY)

CONTENTS

		Page No.
CANDIDATE'S DECLARATION		i
ABSTRACT		ii
ACKNOWLEDGEMENTS		viii
CONTENTS		xi
LIST OF FIGURES		xx
LIST OF TABLES		xxviii
NOMENCLATURE		xxxix
Chapter-I:	**INTRODUCTION**	1
1.1	ADVANCED MANUFACTURING PROCESSES - AN OVERVIEW	3
1.2	PRINCIPLES OF ELECTRO-CHEMICAL MACHINING	7
1.3	PRINCIPLES AND PRACTICES OF CONVENTIONAL HONING	10
1.4	HYBRID MANUFACTURING PROCESSES: *an emerging trend*	12
1.5	ELECRO-CHEMICAL HONING PROCESS: *a prospective productive precision micro-finishing technology*	14
Chapter -II:	**LITERATURE REVIEW**	18
2.1	BASIC PRINCIPLES OF ECH	19
	2.1.1 Flexi-Features of ECH	22
	2.1.1.1 Controlling electrolytic dissolution	23
	2.1.1.2 Controlling mechanical abrasion	24
2.2	REVIEW OF PAST RESEARCH WORK ON ECH	25
Chapter-III:	**PROBLEM FORMULATION**	31
3.1	GAPS IN PAST RESEARCH WORK ON ECH PROCESS	32
3.2	OBJECTIVES OF PRESENT Ph.D. RESEARCH WORK	33

Chapter-IV: DEVELOPMENT OF ECH SETUP 34

4.1 POWER SUPPLY 40

4.2 ELECTROLYTE SUPPLY AND CLEANING SYSTEM 44

4.2.1 Electrolyte Storage and Settling Tanks 45

4.2.2 Temperature Control System 45

4.2.3 Filtration 48

4.2.4 Electrolyte Recirculation Pump 48

4.2.5 Electrolyte Supply Pump 52

4.2.6 Pressure and Flow Controls 52

4.2.7 Piping 53

4.2.8 Pressure, Flow and Temperature Measurements 53

4.2.9 Mist Collector 53

4.3 ECH TOOL AND DRIVES 54

4.3.1 ECH Tool 54

4.3.1.1 Teflon body 56

4.3.1.2 Stainless steel tool body 58

4.3.1.3 Spring controlled honing sticks 58

4.3.1.4 Tool coupling 59

4.3.1.5 Slip ring and copper connectors 59

4.3.2 Tool Drives 60

4.3.2.1 Rotary drive 60

4.3.2.2 Reciprocating drive 63

4.3.2.3 Driving head 64

4.4 WORK HOLDING AND POSITIONING SYSTEM 65

4.4.1 Work Chamber 65

4.4.2 Worktable 68

4.4.3 Work Positioning System 71

4.5 FRAME AND HOUSING 72

Chapter-V: PARAMETRIC ANALYSIS 75

5.1 WORKPIECE SELECTION 77

5.2 ECH PROCESS PARAMETERS 79

5.2.1 Current Intensity 79

5.2.2 Type and Composition of Electrolyte 80

5.2.3 Electrolyte Inlet Temperature 81

	9.1.3 Material Removal Mechanism And Effects of Key Process Parameters on ECH Performance	445
	9.1.4 Work Surface Characterization	447
	9.1.5 Work Surface Integrity Aspects	448
	9.1.6 Multi-Performance Modeling and Optimization of ECH Process	448
9.2	GUIDELINES FOR BETTER ECH RESULTS	451
9.3	SCOPE OF FUTURE RESEARCH ON ECH	452
REFERENCES		453
APPENDIX-A	SPECIFICATIONS / TECHNICAL DATA OF SETUP COMPONENTS	469
APPENDIX-B	SPECIFICATIONS OF MEASURING INSTRUMENTS / EQUIPMENT	474
APPENDIX-C	WORK MATERIAL AND ELECTROLYTE PROPERTIES	477
APPENDIX-D	FLOW CHARTS	478

8.2 TAGUCHI-NN-GA MULTI-PERFORMANCE OPTIMIZATION CONTROL STRATEGY 355
8.2.1 Artificial Neural Networks (ANN) 357
8.2.1.1 Back Propagation Neural Network (BPNN) 359
8.2.1.2 Levenberg-Marquardt (LMBP) Algorithm 362
8.2.1.3 Radial Basis Function Neural Networks (RBF NN) 363
8.2.2 Desirability Function 368
8.2.3 Non-dominating Pareto Optimal Solutions 369
8.2.4 Genetic Algorithms 370
8.2.5 Taguchi-NN-GA Multi-Performance Optimization Algorithm 376
8.2.6 Optimization of ECH using Taguchi-NN-DF-GA Multi-Performance Optimization Control Strategy 377
8.2.6 Confirmation Experiments 414
8.3 FUZZY-TAGUCHI INFERENCE APPLICATION TO ECH 416
8.3.1 Fuzzy Inference System 416
8.3.2 Fuzzy-Taguchi Inference Application to ECH 422
8.3.2.1 Fuzzy Inference Modeling 422
8.3.2.2 GA tuned FIS 425
8.3.2.3 ANFIS Modeling of ECH 428
8.3.2.4 Analysis of ECH FIS Results 434
8.3.2.5 Confirmation Experiments 438
8.4 A COMPARISON OF "UTILITY BASED TAGUCHI APPROACH", "TAGUCHI-NN-GA MULTI-PERFORMANCE OPTIMIZATION CONTROL STRATEGY" AND "TAGUCHI-FUZZY INFERENCE APPLICATION" APPLIED TO ECH 439
Chapter-IX: CONCLUSIONS, GUIDELINES AND SCOPE OF FUTURE RESEARCH 443
9.1 CONCLUSIONS 443
9.1.1 Development of Electro-Chemical Honing Setup 443
9.1.2 Time Dependent Behaviour of ECH 443

7.2.5.9 Estimation of optimal value of performance characteristic 240

7.3 PHASE-IV CONFIRMATION EXPERIMENTS 242

7.4 PHASE-III STAGE-II STUDIES 244

7.5 PHASE-III STAGE-III STUDIES 273

7.5.1 Microstructural Examination 273

7.5.2 Microhardness Examination 279

7.5.3 Residual Stress Evaluation 291

Chapter-VIII: MULTI-PERFORMANCE MODELING AND OPTIMIZATION STUDIES 298

8.1 UTILITY BASED TAGUCHI APPROACH TO MULTI-PERFORMANCE OPTIMIZATION 303

8.1.1 Algorithm of 'Utility based Taguchi Approach' for Multi-Performance Optimization 305

8.1.2 Multi-Performance Optimization of ECH Process using Utility Based Taguchi Approach 306

8.1.3 Model 1: PIR_a-PIOR 308

8.1.3.1 Selection of Optimal Levels 314

8.1.3.2 Estimation of Optimal Values of Performance Characteristics 315

8.1.4 Model 2: PIR_a-PICyl 320

8.1.4.1 Selection of Optimal Levels 326

8.1.4.2 Estimation of Optimal Values of Performance Characteristics 327

8.1.5 Model 3: PIR_a-DIR 329

8.1.5.1 Selection of Optimal Levels 334

8.1.5.2 Estimation of Optimal of Performance Characteristic Values 335

8.1.6 Model 4: PIR_a-PIOR-DIR 339

8.1.6.1 Prediction of Optimal Values of Performance Characteristics 343

8.1.7 Model 5: PIR_a-PICyl-DIR 347

8.1.7.1 Prediction of Optimal Values of Performance Characteristics 351

8.1.8 Confirmation Experiments 353

7.2.2.9 Selection of optimal levels 201
7.2.2.10Estimation of optimal value of performance characteristic 203
7.2.3 Percent Improvement in Out-of-Roundness 206
7.2.3.1 Effect of current intensity 210
7.2.3.2 Effect of electrolyte concentration 211
7.2.3.3 Effect of rotary to reciprocating speed ratio 212
7.2.3.4 Effect of electrolyte flow rate 213
7.2.3.5 Effect of electrolyte inlet temperature 213
7.2.3.6 Effect of stick-out pressure 213
7.2.3.7 Effect of stick grit size 214
7.2.3.8 Selection of optimal levels 214
7.2.3.9 Estimation of optimal performance characteristic value 216
7.2.4 Percent Improvement in Cylindricity 218
7.2.4.1 Effect of current intensity 222
7.2.4.2 Effect of electrolyte concentration 224
7.2.4.3 Effect of rotary to reciprocating speed ratio 225
7.2.4.4 Effect of electrolyte flow rate 226
7.2.4.5 Effect of electrolyte inlet temperature 226
7.2.4.6 Effect of stick-out pressure 226
7.2.4.7 Effect of stick grit size 226
7.2.4.8 Selection of optimal levels 227
7.2.4.9 Estimation of optimal value of performance characteristic 228
7.2.5 Diametral Increase Rate 230
7.2.5.1 Effect of current intensity 234
7.2.5.2 Effect of electrolyte concentration 236
7.2.5.3 Effect of rotary to reciprocating speed ratio 237
7.2.5.4 Effect of electrolyte flow rate 237
7.2.5.5 Effect of electrolyte inlet temperature 237
7.2.5.6 Effect of stick-out pressure 238
7.2.5.7 Effect of stick grit size 238
7.2.5.8 Selection of optimal levels 238

6.3.2.1 Stage-I studies 140
6.3.2.2 Stage-II and III studies 152
Chapter-VII: ANALYSIS AND DISCUSSION OF RESULTS 156
7.1 PHASE-II EXPERIMENTAL STUDIES 156
7.1.1 Effects on Percent Improvement in R_a 157
7.1.2 Effects on Percent Improvement in R_{max} 161
7.1.3 Effects on Percent Improvement in Out-of-Roundness 164
7.1.4 Effects on Percent Improvement in Cylindricity 167
7.1.5 Effects on Percent Improvement in Axis-straightness 169
7.1.6 Effects on Diametral Increase Rate 171
7.2 PHASE-III EXPERIMENTAL STUDIES 174
7.2.1 Percent Improvement in R_a 177
7.2.1.1 Effect of current intensity 181
7.2.1.2 Effect of electrolyte concentration 183
7.2.1.3 Effect of rotary to reciprocating speed ratio 184
7.2.1.4 Effect of electrolyte flow rate 185
7.2.1.5 Effect of electrolyte inlet temperature 185
7.2.1.6 Effect of stick-out pressure 186
7.2.1.7 Effect of stick grit size 186
7.2.1.8 Multi variable regression analysis 187
7.2.1.9 Selection of optimal levels 188
7.2.1.10Estimation of optimal value of performance characteristic 189
7.2.2 Percent Improvement in R_{max} 192
7.2.2.1 Effect of current intensity 196
7.2.2.2 Effect of electrolyte concentration 197
7.2.2.3 Effect of rotary to reciprocating speed ratio 197
7.2.2.4 Effect of electrolyte flow rate 198
7.2.2.5 Effect of electrolyte inlet temperature 198
7.2.2.6 Effect of stick-out pressure 199
7.2.2.7 Effect of stick grit size 199
7.2.2.8 Multi variable regression analysis 200

Chapter-VI: EXPERIMENTAL STUDIES 106

6.1 EXPERIMENTAL STUDY PLAN 106

6.1.1 Phase-I Pilot Experiments 106

6.1.2 Phase-II Time Dependent Behaviour of ECH 107

6.1.3 Phase-III Evaluating Effects of Key Process Parameters on ECH Performance, Material Removal Mechanism and Work Surface Characteristics 108

6.1.3.1 Stage-I: Examining material removal mechanism and parametric relationships 110

6.1.3.2 Stage-II: Examining work surface characteristics 110

6.1.3.3 Stage-III: Examining surface integrity aspects 110

6.1.3.3.1 *Group-I: Microstructural examination* 110

6.1.3.3.2 *Group-II: Microhardness examination* 110

6.1.3.3.3 *Group-III: Residual stress evaluation* 110

6.1.4 Phase-V Confirmation Experiments 110

6.2 DESIGN OF EXPERIMENTS AND ANALYSIS PROCEDURE 111

6.2.1 DOE for Phase-II Experimentation 112

6.2.2 Analysis Procedure for Phase-II Experiments 112

6.2.3 DOE for Phase-III Experimentation 113

6.2.4 Analysis Procedure of the Selected L_{27} Orthogonal Array (Stage-I) 118

6.2.4.1 Raw Data Analysis (Standard Analysis) 118

6.2.4.2 S/N Data Analysis 127

6.2.4.3 Parameter Classification and Selection of Optimal Levels 130

6.2.4.4 Determination of Control Limits 131

6.2.4.5 Prediction of Mean 131

6.2.4.6 Determination of Confidence Intervals 132

6.3 EXPERIMENTATION 134

6.3.1 Phases-II Experimentation 135

6.3.2 Phases-III Experimental Studies 139

5.2.4 Electrolyte Concentration 81
5.2.5 Electrolyte Contamination 83
5.2.6 Initial Inter-Electrode Gap 83
5.2.7 Electrolyte Flow Rate and Pressure 84
5.2.8 Honing Sticks 85
5.2.9 Stick-out Pressure 86
5.2.10 Honing Speeds and Speed Ratio 87
5.2.11 ECH Tool and Operation Mode of ECH 88
5.3 SELECTED PROCESS INPUT PARAMETERS 89
5.3.1 Variable Parameters 89
5.3.2 Fixed Parameters 89
5.4 ECH PERFORMANCE CHARACTERISTICS 90
5.4.1 Surface Micro-Geometrical Aspects 91
5.4.1.1 Percent improvement in R_a 92
5.4.1.2 Percent improvement in R_{max} 93
5.4.1.3 Surface micro-profile 93
5.4.1.3.1 *Standard display* 94
5.4.1.3.2 *2D analysis* 94
5.4.1.3.3 *3D interactive plot* 94
5.4.1.3.4 *3D plot* 94
5.4.1.3.5 *Filtered histogram* 94
5.4.1.3.6 *Bearing ratio* 94
5.4.1.4 Surface morphology 95
5.4.2 Macro-Geometrical Aspects 96
5.4.2.1 Percent improvement in Out-of-roundness 97
5.4.2.2 Percent improvement in Cylindricity 98
5.4.2.3 Percent improvement in Axis-straightness 99
5.4.2 Surface Integrity Aspects 100
5.4.2.1 Microstructural examination 100
5.4.2.2 Microhardness 101
5.4.2.3 Residual stress 103
5.4.3 Material Removal Aspects 104
5.5 SELECTED ECH PERFORMANCE CHARACTERISTICS 105

LIST OF FIGURES

Fig.No.	Title	Page No.
Fig.1.1	Possible chemical reactions in IEG	7
Fig.1.2	Typical crosshatch lay pattern obtained in honing	10
Fig.1.3	Geometrical inaccuracies can be corrected by ECH	15
Fig.1.4	Some specific application examples of ECH	17
Fig.2.1	Schematic of ECH process	19
Fig.2.2	Geometric-error correction in ECH	20
Fig.2.3	ECH: an interaction process	21
Fig.2.4	Working principle of ECH of gears	25
Fig.2.5	Behaviour of a better ECH electrolyte	28
Fig.2.6	Effect of stick-out pressure on material removal rate in ECH	29
Fig.2.7	Effect of process parameters on surface roughness value R_a in ECH	30
Fig.4.1	Schematic of electro-chemical honing setup	35
Fig.4.2	DC power supply	42
Fig.4.3	Copper-carbon brush assembly	42
Fig.4.4	Electrolyte heating system elements	47
Fig.4.5	Electrolyte cooling system	47
Fig.4.6	Magnetic separator-cum-mechanical filter	49
Fig.4.7	1^{st} stage magnetic separator-cum-mechanical filter details	49-50
Fig.4.8	2^{nd} stage magnetic separator-cum-mechanical filter details	50-51
Fig.4.9	ECH tool	55
Fig.4.10	ECH tool details	56
Fig.4.11	Schematic of ECH tool drives	61
Fig.4.12	Photographic view of ECH tool drives	62
Fig.4.13	Details of rotary drive coupling	62

Fig.4.14	Reciprocating drive gearing	64
Fig.4.15	Work holding and positioning system	66
Fig.4.16	Details of work chamber	67
Fig.4.17	Work fixture-cum-inlet sleeve details	69
Fig.4.18	Stainless steel connectors	69
Fig.4.19a)	Constructional details of seal body assembly	70
Fig.4.19b)	Photographic view of seal body assembly	70
Fig.4.20	Work positioning system details	71
Fig.4.21	Photographic view of ECH setup	73
Fig.4.22	Close-up view of machining chamber	74
Fig.5.1	Ishikawa cause-and-effect diagram of ECH	76
Fig.5.2	Workpiece specimen	77
Fig.5.3	Microstructure of the work material	78
Fig.5.4	Variation of electrolyte conductivity and pH with temperature	82
Fig.5.5	Surface effects produced by manufacturing processes	90
Fig.5.6	Interaction of process with material	90
Fig.5.7	Material ratio	95
Fig.5.8	Out-of-roundness	97
Fig.5.9	Cylindicity	98
Fig.5.10	Axis-straightness	99
Fig.5.11	Vickers hardness	102
Fig.6.1	L_{27} linear graph for parameter assignment in Phase-III	115
Fig.6.2	Taguchi quadratic loss and traditional step functions	128
Fig.6.3	Loss functions for lower-the better and higher-the-better type performance characteristics	130
Fig.7.1	Effect of processing time on percent improvement in R_a	159
Fig.7.2	Passivating metal oxide film covering a geometrical error	160

Fig.7.3	Effect of processing time on percent improvement in R_{max}	163
Fig.7.4	Effect of processing time on percent improvement in out-of-roundness	166
Fig.7.5	Effect of processing time on percent improvement in cylindricity	169
Fig.7.6	Effect of processing time on percent improvement in AS	170
Fig.7.7	Effect of processing time on diametral increase rate	172
Fig.7.8	Effect of process parameters on percent improvement in R_a and S/N ratio (Main Effects)	179
Fig.7.9	Relation between current intensity and percent improvement in R_a and S/N ratio at different electrolyte concentration levels	184
Fig.7.10	Relation between current intensity and percent improvement in R_a and S/N ratio at different speed ratio levels	185
Fig.7.11	Effect of process parameters on percent improvement in R_{max} and S/N ratio (Main Effects)	194
Fig.7.12	Relation between current intensity and percent improvement in R_{max} and S/N ratio at different electrolyte concentration levels	197
Fig.7.13	Relation between current intensity and percent improvement in R_{max} and S/N ratio at different speed ratio levels	198
Fig.7.14	Effect of process parameters on percent improvement in out-of roundness (PIOR) and its S/N Ratio (Main Effects)	208
Fig.7.15	Relation between current intensity and percent improvement in OR and S/N ratio at different electrolyte concentration levels	211
Fig.7.16	Relation between electrolyte concentration and percent improvement in OR and S/N ratio at different speed ratio levels	212
Fig.7.17	Effects of process parameters on percent improvement in cylindricity (PICyl) and its S/N ratio (Main Effects)	220
Fig.7.18	Relation between current intensity and percent improvement in cylindricity and S/N ratio at different electrolyte concentration levels	223
Fig.7.19	Relation between current intensity and percent improvement in cylindricity and S/N ratio at different speed ratio levels	224
Fig.7.20	Relation between electrolyte concentration and percent improvement in cylindricity and S/N ratio at different speed ratio levels	225

Fig.7.21	Effect of process parameters on diametral increase rate (DIR) and its S/N ratio (Main Effects)	232
Fig.7.22	Relation between current intensity and diametral increase rate and S/N ratio at different speed ratio levels	235
Fig.7.23	Relation between electrolyte concentration and diametral increase rate and S/N ratio at different speed ratio levels	236
Fig.7.24	Characteristics of the worksurface prior to ECH	245-248
Fig.7.25	Characteristics of ECHed worksurface (ECH Trial Condition: $C_3EC_3SR_2F_3T_2SOP_2G_1$)	249-252
Fig.7.26	Characteristics of ECHed work surface (ECH Trial Condition: $C_1EC_1SR_1F_1T_1SOP_1G_1$)	256-258
Fig.7.27	Characteristics of ECHed work surface (ECH Trial Condition: $C_1EC_1SR_2F_2T_2SOP_2G_2$)	259-261
Fig.7.28	Characteristics of ECHed worksurface (ECH Trial Condition: $C_1EC_1SR_3F_3T_3SOP_3G_3$)	262-264
Fig.7.29	Characteristics of ECHed worksurface (ECH Trial Condition: $C_2EC_2SR_2F_1T_2SOP_2G_3$)	266-268
Fig.7.30	Characteristics of ECHed worksurface (ECH Trial Condition: $C_3EC_3SR_3F_1T_3SOP_3G_2$)	269-272
Fig.7.31	Microstructure of the work material (Work sample: 32, Machining condition: $C_3EC_3SR_1F_2T_1SOP_1G_3$)	274
Fig.7.32	Microstructure of the work material (Work sample: 49, Machining condition: $C_1EC_3SR_1F_3T_3SOP_2G_2$)	275
Fig.7.33	Microstructure of the work material (Work sample: 50, Machining condition: $C_3EC_1SR_2F_1T_3SOP_1G_3$)	276
Fig.7.34	Microstructure of the work material (Work sample: 34, Machining condition: $C_3EC_3SR_2F_3T_2SOP_2G_1$)	277
Fig.7.35	Microstructure of the work material (Work sample: 9, Machining condition: $C_2EC_1SR_2F_3T_1SOP_3G_1$),	278
Fig.7.36	Microhardness variation as a function of distance from the machined surface (Work sample: 32, Machining condition: $C_3EC_3SR_1F_2T_1SOP_1G_3$)	281
Fig.7.37	Microhardness variation as a function of distance from the machined surface (Work sample: 49, Machining condition: $C_1EC_3SR_1F_3T_3SOP_2G_2$)	281

Fig.7.38	Microhardness variation as a function of distance from the machined surface (Work sample: 50, Machining condition: $C_3EC_1SR_2F_1T_3SOP_1G_3$)	282
Fig.7.39	Microhardness variation as a function of distance from the machined surface (Work sample: 34, Machining condition: $C_3EC_3SR_2F_3T_2SOP_2G_1$)	282
Fig.7.40	Microhardness variation as a function of distance from the machined surface (Work sample: 9, Machining condition: $C_2EC_1SR_2F_3T_1SOP_3G_1$)	283
Fig.7.41	Microhardness variation as a function of distance from the machined surface (Work sample: R, Machining condition: before ECH)	283
Fig.7.42	Average microhardness values in PAMZ and base material of different work samples	286
Fig.7.43	Difference between the average microhardness values in PAMZ and base material for different SR-SOP combinations	287
Fig.7.44	X-ray diffraction pattern of ECHed work sample "32" (Machining condition: $C_3EC_3SR_1F_2T_1SOP_1G_3$)	293
Fig.7.45	X-ray diffraction pattern of ECHed work sample "34" (Machining condition: $C_3EC_3SR_2F_3T_2SOP_2G_1$)	294
Fig.7.46	X-ray diffraction pattern of ECHed work sample "9" (Machining condition: $C_2EC_1SR_2F_3T_1SOP_3G_1$)	295
Fig.7.47	X-ray diffraction pattern of work sample "R" (Machining condition: before ECH)	296
Fig.7.48	Residual stress change in the work surface processed with different test conditions	297
Fig.8.1	Effects of process parameters on Utility: PIR_a-PIOR and S/N Ratio (Main Effects)	311
Fig.8.2	Interaction plots (Utility: PIR_a-PIOR)	311
Fig.8.3	Effects of process parameters on Utility: PIR_a-PICyl and S/N ratio (Main Effects)	323
Fig.8.4	Interaction plots (Utility: PIR_a-PICyl)	323
Fig. 8.5	Effects of process parameters on Utility: PIRa-DIR and S/N ratio (Main Effects)	332
Fig.8.6	Interaction plots (Utility: PIR_a-DIR)	332

Fig.8.7	Effects of process parameters on Utility: PIR_a-PIOR-DIR and S/N ratio (Main Effects)	341
Fig.8.8	Interaction Plots (Utility: PIR_a-PIOR-DIR)	341
Fig.8.9	Effects of process parameters on Utility: PIR_a-PICyl-DIR and S/N ratio (Main Effects)	349
Fig.8.10	Interaction plots (Utility: PIR_a-PICyl-DIR and S/N Ratio)	349
Fig.8.11	Architecture of a three-layer MLP NN	360
Fig.8.12	The RBF NN architecture	363
Fig.8.13	General scheme of GAs	373
Fig.8.14	SSE training and maximum test error with different spreads of RBF (Model: PIR_a-PIOR)	378
Fig.8.15	SSE training and maximum test error with different spreads of RBF (Model: PIR_a-PICyl)	379
Fig.8.16	SSE training and maximum test error with different spreads of RBF (Model: PIR_a-DIR)	379
Fig.8.17	SSE training and maximum test error with different spreads of RBF (Model: PIR_a-PIOR-DIR)	380
Fig.8.18	SSE training and maximum test error with different spreads of RBF (Model: PIR_a-PICyl-DIR)	380
Fig.8.19	SSE training and maximum test error with different spreads of RBF (Model: PIR_a-PIOR-PICyl-DIR)	381
Fig.8.20	Variation of total error with number of epochs of BPNN (Model: PIR_a-PICyl)	386
Fig.8.21	Variation of total error with number of epochs of LM algorithm (Model: PIR_a-PICyl)	386
Fig.8.22	Variation of total error with number of epochs of LM algorithm (Model: PIR_a-PIOR)	387
Fig.8.23	Variation of total error with number of epochs of LM algorithm (Model: PIR_a-PIOR-PICyl-DIR)	387
Fig.8.24	Improvement in maximum fitness of composite desirability with GA generations (DF/mod. DF approach, Model: PIR_a-PIOR)	394
Fig.8.25	Improvement in maximum fitness of composite desirability with GA generations (DF/mod. DF approach, Model: PIR_a-PICyl)	394

Fig.8.26	Improvement in maximum fitness of composite desirability with GA generations (DF approach, Model: PIR_a-DIR)	395
Fig.8.27	Improvement in maximum fitness of composite desirability with GA generations (mod. DF approach, Model: PIR_a-DIR)	395
Fig.8.28	Improvement in maximum fitness of composite desirability with GA generations (DF approach, Model: PIR_a-PIOR-DIR)	396
Fig.8.29	Improvement in maximum fitness of composite desirability with GA generations (mod. DF approach, Model: PIR_a-PIOR-DIR)	396
Fig.8.30	Improvement in maximum fitness of composite desirability with GA generations (DF approach, Model: PIR_a-PICyl-DIR)	397
Fig.8.31	Improvement in maximum fitness of composite desirability with GA generations (mod. DF approach, Model: PIR_a-PICyl-DIR)	397
Fig.8.32	Improvement in maximum fitness of composite desirability with GA generations (DF approach, Model: PIR_a-PIOR-PICyl-DIR)	398
Fig.8.33	Improvement in maximum fitness of composite desirability with GA generations (mod. DF approach, Model: PIR_a-PIOR-PICyl-DIR)	398
Fig.8.34	Improvement in maximum fitness of different performance characteristics with NSGA generations (Model: PIRa-PIOR)	407
Fig.8.35	Improvement in maximum fitness of different performance characteristics with NSGA generations (Model: PIR_a-PICyl)	407
Fig.8.36	Improvement in maximum fitness of different performance characteristics with NSGA generations (Model: PIR_a-DIR)	408
Fig.8.37	Improvement in maximum fitness of different performance characteristics with NSGA generations (Model: PIR_a-PIOR-DIR)	408
Fig.8.38	Improvement in maximum fitness of different performance characteristics with NSGA generations (Model: PIR_a-PICyl-DIR)	409
Fig.8.39	Improvement in maximum fitness of different performance characteristics with NSGA generations (Model: PIR_a-PIOR-PICyl-DIR)	409
Fig.8.40	Improvement in maximum fitness of composite desirability with GA generations (DF approach, Model: PIR_{max}-PIOR-PICyl-DIR)	412
Fig.8.41	Improvement in maximum fitness of composite desirability with GA generations (Mod.DF approach, Model: PIR_{max}-PIOR-PICyl-DIR)	412

Fig.8.42	Improvement in maximum fitness of different performance characteristics with NSGA generations (Model: PIR_{max}-PIOR-PICyl-DIR)	413
Fig.8.43	Schematic diagram of the fuzzy inference system	417
Fig.8.44	Schematic diagram of a genetic fuzzy system	419
Fig.8.45	ANFIS architecture of a two-input, two-rule first-order Sugeno model	420
Fig.8.46	Structure of three-input-one-output fuzzy inference system	422
Fig.8.47	Flow chart for optimization of FIS using GA	427
Fig.8.48	GA tuned membership functions of FIS	429
Fig.8.49	ANFIS membership function plots	431
Fig.8.50	GA tuned-FIS control surface plots	432
Fig.8.51	Control surfaces generated by ANFIS	433
Fig.8.52	Response plots (GA tuned FIS and ANFIS: PIR_a-PICyl-DIR)	436
Fig.8.53	Interaction plots (GA tuned FIS and ANFIS: PIR_a-PICyl-DIR)	436
Fig.8.54	Multi-performance predicted optimal results based on two approaches	441
Fig.8.55	Multi-performance experimental optimal results based on three approaches	442
Fig.A.D.1	Flow chart of Taguchi experimental design and analysis	478
Fig.A.D.2	RBFNN-DF/Mod DF-GA and RBFNN-NSGA flow chart	479

LIST OF TABLES

Table No.	Title	Page No.
Table1.1	Classification of AMPs	4
Table 4.1a	Materials used in power supply system	37
Table 4.1b	Materials used in ECH tool and drive system	37
Table 4.1c	Materials used in electrolyte supply and cleaning system	38
Table 4.1d	Materials used in work holding and positioning system	39
Table 4.1e	Materials used in frame and housing components	39
Table 5.1	ECH process parameters and their nature of influence	75
Table 5.2	Range of variable parameters	89
Table 5.3	Levels of fixed process parameters	89
Table 5.4	Process performance characteristics	105
Table 6.1	Levels of independent parameter (Phase-II)	107
Table 6.2	Levels of fixed parameters (Phase-II)	108
Table 6.3	Process parameters and their levels (Phase-III)	109
Table 6.4	Experimental data sheet (Phase-II)	112
Table 6.5	Experiment design matrix with L_{27} (3^{13}) OA (process parameters assigned) with responses (Raw Data and S/N Ratio) (Phase-III)	117
Table 6.6	Surface roughness (R_a) of workpieces (Phase-II)	135
Table 6.7	Results of surface micro-geometry, PIR_a (Phase-II)	136
Table 6.8	Surface roughness (R_{max}) of workpieces (Phase-II)	136
Table 6.9	Results of surface micro-geometry, PIR_{max} Phase-II)	136
Table 6.10	Out-of-roundness (OR) of workpieces (Phase-II)	137
Table 6.11	Results of part macro-geometry, PIOR (Phase-II)	137
Table 6.12	Cylindricity (Cyl) of workpieces (Phase-II)	137

Table 6.13	Results of part macro-geometry, PICyl (Phase-II)	138
Table 6.14	Axis-straightness (AS) of workpieces (Phase-II)	138
Table 6.15	Results of part macro-geometry, PIAS (Phase-II)	138
Table 6.16	Diameter (D) of workpieces (Phase-II)	139
Table 6.17	Results of diametral increase rate, DIR (Phase-II)	139
Table 6.18	Surface roughness (R_a) of workpieces (Phase-III)	141
Table 6.19	Experimental results of surface micro-geometry, PIR_a (Phase-III)	142
Table 6.20	Surface roughness (R_{max}) of workpieces (Phase-III)	143
Table 6.21	Experimental results of surface micro-geometry, PIR_{max} (Phase-III)	144
Table 6.22	Out-of-roundness (OR) of workpieces (Phase-III)	146
Table 6.23	Experimental results of part macro-geometry, PIOR (Phase-III)	147
Table 6.24	Cylindricity (Cyl) of workpieces (Phase-III)	148
Table 6.25	Experimental results of part macro-geometry, PICyl (Phase-III)	149
Table 6.26	Diameter (D) of workpieces (Phase-III)	150
Table 6.27	Experimental results of diametral increase rate, DIR (Phase-III)	151
Table 6.28	Work samples and their trial conditions used for microhardness examination	152
Table 6.29	Microhardness values of work sample 32	153
Table 6.30	Microhardness values of work sample 49	153
Table 6.31	Microhardness values of work sample 50	154
Table 6.32	Microhardness values of work sample 34	154
Table 6.33	Microhardness values of work sample 9	155
Table 6.34	Microhardness values of work sample R	155
Table 7.1	ANOVA results for percent improvement in R_a data	157

Table 7.2	Results of Duncan's multiple range test (PIR_a) (Phase-II)	158
Table 7.3	Polynomial regression for PIR_a	159
Table 7.4	ANOVA results for percent improvement in R_{max} data	161
Table 7.5	Results of Duncan's multiple range test (PIR_{max}) (Phase-II)	162
Table 7.6	Polynomial regression for PIR_{max}	163
Table 7.7	ANOVA results for percent improvement in OR data	164
Table 7.8	Results of Duncan's multiple range test (PIOR) (Phase-II)	165
Table 7.9	Polynomial regression for PIOR	166
Table 7.10	ANOVA results for percent improvement in cylindricity data	167
Table 7.11	Results of Duncan's multiple range test (PICyl) (Phase-II)	168
Table 7.12	ANOVA results for percent improvement in axis-straightness data	169
Table 7.13	The mean PIAS at different processing time levels (Phase-II)	170
Table 7.14	ANOVA results for diametral increase rate data	171
Table 7.15	The mean DIR at different processing time levels (Phase-II)	171
Table 7.16	Linear regression for DIR	173
Table 7.17	Average and Main Effects – PIR_a Raw Data (Phase-III)	178
Table 7.18	Average and Main Effects – PIR_a S/N Data (Phase-III)	178
Table 7.19	Pooled ANOVA– PIR_a Raw Data (Phase-III)	180
Table 7.20	Pooled ANOVA– PIR_a S/N Data (Phase-III)	180
Table 7.21	Average Effects of C-EC Interaction - PIR_a Raw & S/N Data (Phase-III)	181
Table 7.22	Average Effects of C-SR Interaction – PIR_a Raw & S/N Data (Phase-III)	181
Table 7.23	MVRA: PIR_a versus C, EC, T, SOP and G	187
Table 7.24	Optimal level of process parameters for mean PIR_a and S/N ratio (with interactions) (Phase-III)	189
Table 7.25	Average values of PIR_a at optimal level of process input parameters (with interactions) (Phase-III)	190

Table 7.26	Average S/N values of PIR_a at optimal level of process parameters (with interactions) (Phase-III)	191
Table 7.27	Average and Main Effects – PIR_{max} Raw Data (Phase-III)	193
Table 7.28	Average and Main Effects – PIR_{max} S/N Data (Phase-III)	193
Table 7.29	Pooled ANOVA– PIR_{max} Raw Data (Phase-III)	195
Table 7.30	Pooled ANOVA– PIR_{max} S/N Data (Phase-III)	195
Table 7.31	Average Effects of C-EC Interaction -PIR_{max} Raw and S/N Data (Phase-III)	196
Table 7.32	Average Effects of C-SR Interaction - PIR_{max} Raw and S/N Data (Phase-III)	196
Table 7.33	MVRA: PIR_{max} versus C, EC, T, SOP and G	201
Table 7.34	Optimal level of process parameters for mean PIR_{max} and S/N ratio (with interactions) (Phase-III)	203
Table 7.35	Average values of PIR_{max} at optimal level of process input parameters (with interactions) (Phase-III)	203
Table 7.36	Average S/N values of PIR_{max} at optimal level of process parameters (with interactions) (Phase-III)	204
Table 7.37	Average and Main Effects – PIOR Raw Data (Phase-III)	207
Table 7.38	Average and Main Effects – PIOR S/N Data (Phase-III)	207
Table 7.39	Pooled ANOVA– PIOR Raw Data (Phase-III)	209
Table 7.40	Pooled ANOVA– PIOR S/N Data (Phase-III)	209
Table 7.41	Average Effects of C-EC Interaction – PIOR Raw and S/N data (Phase-III)	210
Table 7.42	Average Effects of EC-SR Interaction – PIOR Raw & S/N Data (Phase-III)	210
Table 7.43	Optimal level of process parameters for mean PIOR and S/N ratio (with interactions) (Phase-III)	215
Table 7.44	Average values of PIOR at optimal level of process input parameters (Phase-III)	216
Table 7.45	Average S/N values of PIOR at optimal level of process parameters (with interactions) (Phase-III)	217
Table 7.46	Average and Main Effects – PICyl Raw Data (Phase-III)	219

Table 7.47	Average and Main Effects – PICyl S/N Data (Phase-III)	219
Table 7.48	Pooled ANOVA– PICyl Raw Data (Phase-III)	221
Table 7.49	Pooled ANOVA– PICyl S/N Data (Phase-III)	221
Table 7.50	Average Effects of C-EC Interaction – PICyl Raw & S/N Data (Phase-III)	222
Table 7.51	Average Effects of C-SR Interaction – PICyl Raw & S/N Data (Phase-III)	222
Table 7.52	Average Effects of EC-SR Interaction – PICyl Raw & S/N Data (Phase-III)	222
Table 7.53	Optimal level of process parameters for mean PICyl and S/N ratio (Phase-III)	228
Table 7.54	Average values of PICyl at optimal level of process input parameters (with interactions) (Phase-III)	228
Table 7.55	Average S/N values of PICyl at optimal level of process parameters (with interactions) (Phase-III)	229
Table 7.56	Average and Main Effects – DIR Raw Data (Phase-III)	231
Table 7.57	Average and Main Effects – DIR S/N Data (Phase-III)	231
Table 7.58	Pooled ANOVA– DIR Raw Data (Phase-III)	233
Table 7.59	Pooled ANOVA– DIR S/N Data (Phase-III)	233
Table 7.60	Average Effects of C-SR Interaction – DIR Raw and S/N Data (Phase-III)	234
Table 7.61	Average Effects of EC-SR Interaction – DIR Raw and S/N Data (Phase-III)	234
Table 7.62	Optimal level of process parameters for mean DIR (with interactions) (Phase-III)	239
Table 7.63	Optimal level of process parameters for S/N DIR (Phase-III)	239
Table 7.64	Average values of DIR at optimal level of process input parameters (with interactions) (Phase-III)	240
Table 7.65	Average S/N values of DIR at optimal level of process parameters (Phase-III)	241
Table 7.66	Confirmation experiment results (Phase-III)	243
Table 7.67	ANOVA results for work sample 32	287

Table 7.68	ANOVA results for work sample 49	288
Table 7.69	ANOVA results for work sample 50	288
Table 7.70	ANOVA results for work sample 34	288
Table 7.71	ANOVA results for work sample 9	288
Table 7.72	ANOVA results for work sample R	288
Table 7.73	Results of Tukey's method for microhardeness data	289
Table 7.74	Results of K-W test for microhardeness data	290
Table 8.1	Optimal results of ECH process performance characteristics (Phase-III)	307
Table 8.2	Preference scales for ECH process performance characteristics (Raw Data-Phase-III)	307
Table 8.3	Utility values (PIR_a-PIOR)	309
Table 8.4	Average and Main Effects (Utility: PIR_a-PIOR: Raw Data)	310
Table 8.5	Average and Main Effects (Utility: PIR_a-PIOR: S/N Data)	310
Table 8.6	Pooled ANOVA (Utility: PIR_a-PIOR: Raw Data)	312
Table 8.7	Pooled ANOVA (Utility: PIR_a-PIOR: S/N Data)	312
Table 8.8	Average Effects of C-EC Interaction (Utility: PIR_a-PIOR: Raw & S/N Data)	313
Table 8.9	Average Effects of C-SR Interaction (Utility: PIR_a-PIOR: Raw & S/N Data)	313
Table 8.10	Average Effects of EC-SR Interaction (Utility: PIR_a-PIOR: Raw & S/N Data)	313
Table 8.11	Optimal level of process parameters for mean utility: PIR_a-PIOR	314
Table 8.12	Optimal level of process parameters for S/N utility: PIR_a-PIOR	315
Table 8.13	Average values of PIR_a at optimal level of process input parameters	315
Table 8.14	Average S/N values of PIR_a at optimal level of process parameters	316

Table 8.15	Average values of PIOR at optimal level of process input parameters	317
Table 8.16	Average S/N values of PIOR optimal level of process parameters	318
Table 8.17	Utility values (PIR_a-PICyl)	321
Table 8.18	Average and Main Effects (Utility: PIR_a- PICyl: Raw Data)	322
Table 8.19	Average and Main Effects(Utility: PIR_a-PICyl: S/N Data)	322
Table 8.20	Pooled ANOVA (Utility: PIR_a-PICyl: Raw Data)	324
Table 8.21	Pooled ANOVA (Utility: PIR_a-PICyl: S/N Data)	324
Table 8.22	Average Effects of C-EC Interaction (Utility: PIR_a-PICyl: Raw & S/N Data)	325
Table 8.23	Average Effects of C-SR Interaction (Utility: PIR_a-PICyl: Raw & S/N Data)	325
Table 8.24	Average Effects of EC-SR Interaction (Utility: PIR_a-PICyl: Raw & S/N Data)	325
Table 8.25	Optimal level of process parameters for mean utility: PIR_a-PICyl	326
Table 8.26	Optimal level of process parameters for S/N utility: PIR_a-PICyl	326
Table 8.27	Average values of PICyl at optimal level of process input parameters	327
Table 8.28	Average S/N values of PICyl optimal level of process parameters	327
Table 8.29	Utility values (PIR_a-DIR)	330
Table 8.30	Average and Main Effects (Utility: PIR_a-DIR: Raw Data)	331
Table 8.31	Average and Main Effects (Utility: PIR_a- DIR: S/N Data)	331
Table 8.32	Pooled ANOVA (Utility: PIR_a-DIR: Raw Data)	333
Table 8.33	Pooled ANOVA (Utility: PIR_a-DIR: S/N Data)	333
Table 8.34	Average Effects of C-EC Interaction (Utility: PIR_a-DIR: Raw & S/N Data)	334
Table 8.35	Average Effects of C-SR Interaction (Utility: PIR_a-DIR: Raw & S/N Data)	334

Table 8.36	Optimal level of process parameters for mean utility: PIR_a-DIR	334
Table 8.37	Optimal level of process parameters for S/N utility: PIR_a-DIR	335
Table 8.38	Average values of PIR_a at optimal level of process input parameters	335
Table 8.39	Average S/N values of PIR_a at optimal level of process parameters	336
Table 8.40	Average values of DIR at optimal level of process input parameters	337
Table 8.41	Average S/N values of DIR optimal level of process parameters	337
Table 8.42	Utility values (PIR_a-PIOR-DIR)	339
Table 8.43	Average and Main Effects (Utility: PIR_a-PIOR-DIR: Raw Data)	340
Table 8.44	Average and Main Effects (Utility: PIR_a-PIOR-DIR: S/N Data)	340
Table 8.45	Pooled ANOVA (Utility: PIR_a-PIOR-DIR: Raw Data)	342
Table 8.46	Pooled ANOVA (Utility: PIR_a-PIOR-DIR: S/N Data)	342
Table 8.47	Average Effects of C-SR Interaction (Utility: PIR_a-PIOR-DIR: Raw & S/N Data)	343
Table 8.48	Average Effects of EC-SR Interaction (Utility: PIR_a-PIOR-DIR: Raw & S/N Data)	343
Table 8.49	Optimal level of process parameters for Utility: PIR_a-PIOR-DIR	343
Table 8.50	Average PIR_a at optimal level of process input parameters	344
Table 8.51	Average S/N PIR_a at optimal level of process parameters	344
Table 8.52	Average PIOR at optimal level of process input parameters	344
Table 8.53	Average S/N PIOR optimal level of process parameters	344
Table 8.54	Average DIR at optimal level of process input parameters	345
Table 8.55	Average S/N DIR optimal level of process parameters	345
Table 8.56	Utility values (PIRa-PICyl-DIR)	347

Table 8.57	Average and Main Effects (Utility: PIR_a-PICyl-DIR: Raw Data)	348
Table 8.58	Average and Main Effects (Utility: PIR_a-PICyl-DIR: S/N Data)	348
Table 8.59	Pooled ANOVA (Utility: PIR_a-PICyl-DIR: Raw Data)	350
Table 8.60	Pooled ANOVA (Utility: PIR_a-PICyl-DIR: S/N Data)	350
Table 8.61	Average Effects of C-SR Interaction (Utility: PIR_a-PICyl-DIR: Raw & S/N Data)	351
Table 8.62	Average Effects of EC-SR Interaction (Utility: PIR_a-PICyl-DIR: Raw & S/N Data)	351
Table 8.63	Optimal level of process parameters for Utility: PIR_a-PICyl-DIR	351
Table 8.64	Average PICyl at optimal level of process input parameters	352
Table 8.65	Average S/N PICyl optimal level of process parameters	352
Table.8.66	Confirmation experiment results (Utility based Taguchi Approach Multi Performance Optimization Models)	354
Table 8.67	Selected RBF NN for different Models	381
Table 8.68	RBF NN multi-performance modeling results (PIR_a-PIOR)	383
Table 8.69	RBF NN multi-performance modeling results (PIR_a-PICyl)	383
Table 8.70	RBF NN multi-performance modeling results (PIR_a-DIR)	384
Table 8.71	RBF NN multi-performance modeling results (PIR_a-PIOR-DIR)	384
Table 8.72	RBF NN multi-performance modeling results (PIRa-PICyl-DIR)	385
Table 8.73	RBF NN multi-performance modeling results (PIR_a-PIOR-PICyl-DIR)	385
Table 8.74	BPN NN multi-performance modeling results (PIR_a-PICyl)	388
Table 8.75	LM algorithm results (PIR_a-PICyl)	388
Table 8.76	LM algorithm results (PIR_a-PIOR)	389
Table 8.77	LM algorithm results (PIR_a-PICyl-DIR)	389
Table 8.78	LM algorithm results (PIR_a-PIOR-PICyl-DIR)	390

Table 8.79	Taguchi-RBF NN-DF/Mod.DF-GA Multi-Performance Optimization Results (PIR_a-PIOR)	399
Table 8.80	Taguchi-RBF NN-DF/Mod.DF-GA Multi-Performance Optimization Results (PIR_a-PICyl)	399
Table 8.81	Taguchi-RBF NN-DF-GA Multi-Performance Optimization Results (PIR_a-DIR)	400
Table 8.82	Taguchi-RBF NN-Mod.DF-GA Multi-Performance Optimization Results (PIR_a-DIR)	400
Table 8.83	Taguchi-RBF NN-DF-GA Multi-Performance Optimization Results (PIR_a-PIOR-DIR)	400
Table 8.84	Taguchi-RBF NN-Mod.DF-GA Multi-Performance Optimization Results (PIR_a-PIOR-DIR)	401
Table 8.85	Taguchi-RBF NN-DF-GA Multi-Performance Optimization Results (PIR_a-PICyl-DIR)	401
Table 8.86	Taguchi-RBF NN-Mod.DF-GA Multi-Performance Optimization Results (PIR_a-PICyl-DIR)	402
Table 8.87	Taguchi-RBF NN-DF-GA Multi-Performance Optimization Results (PIR_a-PIOR-PICyl-DIR)	402
Table 8.88	Taguchi-RBF NN-Mod.DF-GA Multi-Performance Optimization Results (PIR_a-PIOR-PICyl-DIR)	403
Table 8.89	Taguchi-RBF NN-NSGA Pareto-Optimal Results (PIR_a-PIOR)	403
Table 8.90	Taguchi-RBF NN-NSGA Pareto-Optimal Results (PIR_a-PCyl)	404
Table 8.91	Taguchi-RBF NN-NSGA Pareto-Optimal Results (PIR_a-DIR)	404
Table 8.92	Taguchi-RBF NN-NSGA Pareto-Optimal Results (PIR_a-PIOR-DIR)	405
Table 8.93	Taguchi-RBF NN-NSGA Pareto-Optimal Results (PIR_a-PICyl-DIR)	405
Table 8.94	Taguchi-RBF NN-NSGA Pareto-Optimal Results (PIR_a-PIOR-PICyl-DIR)	406
Table 8.95	RBF NN Modeling Results (PIR_{max}-PIOR-PICyl-DIR)	410
Table 8.96	Taguchi-RBF NN-DF-GA Multi-Performance Optimization Results (PIR_{max}-PIOR-PICyl-DIR)	410

Table 8.97	Taguchi-RBF NN-Mod.DF-GA Multi-Performance Optimization Results (PIR_{max}-PIOR-PICyl-DIR)	410
Table 8.98	Taguchi-RBF NN-NSGA Pareto-Optimal Results (PIR_{max}-PIOR-PICyl-DIR)	411
Table 8.99	Confirmation experiment results ("Taguchi-RBF NN-GA Multi-Performance Optimization Control Strategy")	415
Table 8.100	Universe of discourse of various FIS variables	423
Table 8.101a)	Linguistic variables for the input parameters	423
Table 8.101b)	Linguistic variables for the output parameter	423
Table 8.102	Initial rule base of ECH FIS	424-425
Table 8.103	GA optimized rule base of ECH FIS	430
Table 8.104	FIS modeling results (PIR_a-PICyl-DIR)	430
Table 8.105	Multi-Response Performance Index: PIR_a-PICyl-DIR (GA tuned FIS)	435
Table 8.106	Multi-Response Performance Index: PIR_a-PICyl-DIR (ANFIS)	435
Table 8.107	Pooled ANOVA MRPI: PIR_a-PICyl-DIR (GA tuned FIS)	437
Table 8.108	Pooled ANOVA MRPI: PIR_a-PICyl-DIR (ANFIS)	437
Table 8.109	Confirmation Experiment	438
Table 8.110	Experimental results ("Utility based Taguchi Approach", "Taguchi-RBF NN-DF-GA Multi-Performance Optimization Control Strategy" and "Fuzzy Inference Application" to ECH)	442
Table A1	Stepper motor program (20 kg-cm, 10 kg-cm and 10 kg-cm Stepper Motor unit- tandom compounded)	473

NOMENCLATURE

$\bar{T}$	Overall mean
Total	Sum of all results
W_i	Weightage assigned to the i^{th} performance characteristic
P_i	Preference number
x_i'	Minimum acceptable value of i^{th} performance characteristic
x_i^*	Optimum value of the i^{th} performance characteristic
φ_k (r)	Radial basis function
AMP	Advanced manufacturing process
ANFIS	Adaptive-Network-based Fuzzy Inference System
ANOM	Analysis of means
ANOVA	Analysis of variance
AS	Axis-straightness
C	Current intensity (A)
C.F.	Correction factor
CI_{CE}	Confidence interval for the confirmation experiments
CI_{POP}	Confidence interval for the population mean
CI_l	Confidence limit for level average
Cyl	Cylindricity
D	Diameter of workpiece (mm)
d	Interplanar spacing
D.F.	Degree of freedom
DF	Desirability function
DIR	Diametral increase rate (μm/min)
Dnet	Overall desirability
E	Young's modulus
EC	Electrolyte concentration (g/L)
ECH	Electro-chemical honing
ECHed	Electro-chemically honed
ECM	Electro-chemical machining
F	Electrolyte flow rate (lpm)

f_e	Error degree of freedom
FIS	Fuzzy inference system
G	Stick grit size
HMP	Hybrid manufacturing process
HV	Vickers hardness
IEG	Inter-electrode gap
LMBP	Levenberg-Marquardt backpropagation
LSD	Least significant difference
M. Dnet	Modified overall desirability
Mod. DF	Modified desirability function
Mr1	Percent length of top portion of the surface profile susceptible to initial rapid wear
Mr2	Percent length of the bottom part of the profile that functions to retain lubricant
MRPI	Multi-response performance index
MRR	Material removal rate
MS	Mean square or variance
MSD	Mean square deviation
MVRA	Multi variable regression analysis
NSGA	Non dominated sorting genetic algorithm
OA	Orthogonal array
OR	Out-of-roundness
PAMZ	Probable altered material zone
PIAS	Percentage improvement in axis-straightness
PICyl	Percentage improvement in cylindricity
PIOR	Percent improvement in out-of-roundness
PIR_a	Percent improvement in R_a
PIR_{max}	Percentage improvement in R_{max}
PT	Processing time (min)
R_a	Average surface roughness value (μm)
RBF NN	Radial Basis Function Neural Networks
Rk	Core roughness depth
R_{max}	Maximum roughness height (μm)
Rpk	Reduced peak height
Rt	Maximum peak-to-valley height within assessment length

R_{tm}	Average of peak-to-valley roughness heights
Rvk	Reduced valley depth
S/N	Signal-to-noise
SiC	Silicon carbide
smpm	Surface meter per minute
SOP	Stick-out pressure (kPa)
SR	Rotary to reciprocating speed ratio
SS	Sum of squares
T	Electrolyte inlet temperature (°C)
t_p	Bearing ratio or material ratio
TR	Ton of refrigeration
μ	Predicted optimal mean
v_e	Error variance
yij	ijth observation
εij	Error term
θ	Diffract angle
θ_o	Standard Bragg's angle
μ	Mean of response
ν	Poisson's ratio
σ_R	Surface residual stress
τi	ith treatment effect
ψ	Angle between sample normal and diffraction plane normal.

Note: All the dimensions indicated on Figures are in mm.

Chapter-I
INTRODUCTION

Insurgence in rapid technological advancement during last few decades has led to the development of ultra hard, high strength and difficult-to-machine materials and alloys such as stainless steel, titanium, nimonics, ceramics, stellites, metal-matrix composites, super alloys and other high strength temperature resistant (HSTR) alloys having high strength to weight ratio. These materials are being increasingly demanded for the products used in technologically advanced industries like aerospace, nuclear, automobile, missiles and turbine industries due to the unusual critical service requirements demanding increased safety, reliability and service life of the components. Emphasis on the design criteria that employ these materials much closer to their full potential, the stringent requirements being placed on surface quality, tolerances and production rates, coupled with the production of complex shapes and contours (such as aerofoil section of a turbine blade, complex cavities in dies and molds, non-circular, small, and curved holes), low rigidity structures, and micromechanical components have imposed severe limitations on the economic and effective application of the conventional edged-tool machining on these materials due to their lower economic cutting speeds, demand for improved cutting tool materials and poor attainable accuracy and surface finish. The conventional machining techniques employing the edged-tool to remove the material by plastic deformation and formation of chips turned out to be either highly uneconomical or infeasible for such challenging applications. Keeping in view the severity of the problem, the need for the development of newer concepts in metal machining was emphasized by Merchant (1962) and extensive basic and applied research during last few decades led to the evolution of an advanced class of manufacturing processes, often called

the 'modern machining processes' or 'nontraditional machining methods' (NTM) or 'advanced manufacturing processes' (AMPs), to meet such challenges (Shan, 2006)

These processes are unconventional in the sense that conventional edged-tools are not employed, instead they mostly utilize the energy in its direct form, such as electro-chemical, spark erosion, ultrasonic waves, high speed ions and electrons, photons, high temperature plasma, kinetic energy of water and abrasives, and deformable special polymers mixed with abrasive. The AMPs possess the necessary capabilities that simply cannot be met with conventional techniques. AMPs are increasingly assuming greater significance in precision machining and ultraprecision machining being demanded by the manufacturing community due to the stringent conditions placed on the surface quality, and shape deviations produced by the manufacturing process to fulfill the critical functional requirements including the high tribological performance of components during service. Taniguchi (1983) concluded that such accuracies cannot simply be achieved employing the conventional machining techniques. However, such capabilities can be provided by the suitable AMPs whereby the material is removed in the form of atoms or molecules individually or in groups. Some of these processes can also machine the conventionally inaccessible areas in the workpiece. Micro-hole drilling with stiff requirements and miniaturization are the other areas requiring specialized processes (Jain, 2002). Emphasis on productivity with possibility of effective automation, flexibility and control are some of the other relevant aspects of the scenario leading to the ever-increasing applications of AMPs in this globally competitive era.

1.1 ADVANCED MANUFACTURING PROCESSES - AN OVERVIEW

Advanced manufacturing processes can be classified into four basic categories: mechanical, electro-chemical, chemical, and thermoelectric (Pandey and Shan, 2005; Benedict, 1987), depending upon the fundamental energy mode employed as given in Table1.1. AMPs have their own distinct characteristic features and limitations. A particular process found suitable under a given condition may not be equally efficient under other conditions. Hence, selection of an appropriate manufacturing process for given application requires a careful assessment of several aspects including the physical parameters, properties of work material, shape to be machined, process capabilities and economic considerations (Pandey and Shan, 2005).

The mechanical AMPs involve erosion or abrasion of work material by utilizing the kinetic energy of either the abrasive particles (**AJM**) or water particles (**WJM**) or both (**AWJM**). MAF utilizes a magnetic abrasive brush based on the Lorentz effect of the magnetic field to finish the work surface. In USM, material is removed by the abrasive grains which are driven into the work surface by a tool oscillating normal to the work surface. Another promis ing advanced mechanical microfinishing process is abrasive flow machining (**AFM**). AFM is the controlled removal of workpiece material by flowing, under pressure, a firm but conformable, abrasive-laden, polymer-based, special compound called the media through or across the work surface (Dubey, 1996). Organic materials, composites and ceramics are, particularly, good candidates for mechanical AMPs as the workpiece is not required to be electrically conductive for these processes. However, these processes find a limited application as their performance depends upon the hardness, strength and other physical and mechanical properties of the work material as well as the workpiece geometry.

Table 1.1 Classification of AMPs [Shan, 2006; Jain, 2002]

Type of Energy	Material Removal Mechanism	Transfer Media	Energy Source	Process
Mechanical	Erosion / abrasion	High velocity particles	Pneumatic/ hydraulic pressure	Abrasive Jet Machining (**AJM**) Ultra Sonic Machining (**USM**) Water Jet Machining (**WJM**) Abrasive Water Jet Machining (**AWJM**) Abrasive Flow Machining (**AFM**) Magnetic Abrasive Finishing (**MAF**)
Chemical	Ablative relation	Reactive environment	Corrosive agent	Chemical Machining (**ChM**) Photo Chemical Machining (**PCM**)
Thermoelectric	Fusion	Hot gases	Ionized material	Ion Beam Machining (**IBM**) Plasma Arc Machining (**PAM**)
		Electrons	High voltage	Electron Beam Machining (**EBM**)
		Spark erosion	High voltage	Electric Discharge Machining (**EDM**)
	Vaporization	Radiation	Amplified light	LASER Beam Machining (**LBM**)
		Ion stream	Ionized material	PAM
Electro-Chemical	Ionic displacement	Electrolyte	High current	Electro-Chemical Machining (**ECM**) Electro-Chemical Honing (**ECH**) Electro-Chemical Grinding (**ECG**) Electro-Chemical Drilling (**ECD**)

Chemical Machining (**ChM**) involves the application of a chemically resistant material (acidic or alkaline in nature) called maskant or resist to cover the work surfaces which are not required to be machined and the desired amount of the work material is removed by chemical dissolution by the subsequent application of an etchant. ChM is, thus, basically a controlled etching process which has very narrow range of applications mainly because of very low material removal rates (MRR) and difficulty in finding a suitable maskant for the given material. ChM and **PCM** are the notable processes which fall under the chemical AMPs.

In thermoelectric AMPs, the material removal is achieved by fusion and vaporization of a small work area subject to a concentrated energy in the form of heat (**PAM**), light (**LBM**), high speed ions (**IBM**), high speed electron bombardment (**EBM**) or electric spark (**EDM**). PAM has been identified as a rough machining technique. LBM and EBM are good enough for making extremely fine cuts and holes. However, EBM is not economically viable when only a few number of holes are to be made or when holes have high aspect ratio (L/D>10). However, electric discharge machining (EDM) is a process capable of machining the materials economically and accurately. Thus, EDM is widely used for machining hard and tough electrically conductive work materials. But the process is unsuitable for many applications where very good surface finish, low damage to the work surface and high MRR is required. Most of the thermal AMPs are not generally able to satisfy the stringent requirements on either the geometrical characteristics (viz. radial overcut, hole taper, aspect ratio) or the metallurgical characteristics (viz. heat affected zones, recast layer, micro cracking) or both.

Thus, the mechanical, chemical and thermoelectric AMPs do not offer a satisfactory solution to some of the problems of machining difficult-to-machine materials, stringent surface quality and tolerance requirements and productivity. What is really needed are the

manufacturing processes whose performance is unaffected by constraints like work material properties. Elecro-chemical (EC) based processes, owing to their capability of machining materials irrespective of their physical and mechanical properties are finding ever increasing applications. Electro-Chemical Machining (**ECM**) is a controlled anodic dissolution process based on the Faraday's law of electrolysis. The only requirement is that the work material needs to be electrically conductive. The EC based processes have seen a resurgence of industrial interest in the last few decades and hence, have a very wide field of applications due to their distinct capabilities particularly the micro-finishing with high productivity. The advantages include the absence of recast layer on the processed work surface, no tool wear, stress free and burr free surface, no thermal damage to work surface, bright surface finish and the ability to machine complex shapes and contours in materials of any hardness. The EC based potential processes are the electro-chemical machining (**ECM**), electro-chemical honing (**ECH**), electro-chemical grinding (**ECG**), electro-chemical drilling (**ECD**) and shaped tube electrolytic machining (**STEM**) (Shan, 2006; Benedict, 1987). However, a large number of EC based manufacturing applications are being explored to utilize the process potential: **ECB** (electro-chemical boring), **ECB_r** (electro-chemical broaching), **ECB_z** (electro-chemical ballizing), **ECD_e** (electro-chemical deburring), **ECDS** (electro-chemical die sinking), **ECM_i** (electro-chemical milling), **ECMM** (electro-chemical micromachining), **ECS** (electro-chemical sawing), **ECT** (electro-chemical turning), **ECT_r** (electro-chemical trepanning), **ECWC** (electro-chemical wire cutting), **ESD** (electrostream drilling) (Jain, 2002).

1.2 PRINCIPLES OF ELECTRO-CHEMICAL MACHINING

Electro-chemical machining is based on the principle in which electrical energy is used to produce chemical reactions for controlled anodic dissolution of the workpiece in an electrolytic cell. When a small electric DC potential (5-25 V) is applied across the two electrodes, i.e. cathode (tool) and anode (work) immersed in an electrolyte, metal is detached, atom by atom, from the anode surface by transfer of electrons between the ions and the electrodes. As opposed to metallic conduction, where only electrons are the charge carriers, salt solutions conduct electrical energy by migration of ions in the medium (Jain, 2002). The application of direct current through a solution of electrolyte results in REDOX reactions, as given in Fig.1.1. In the process no electrolyte is consumed except losses and vaporization. Insoluble metal hydroxides appear as solid precipitates. In actual practice, two electrodes are kept in proximity but never touch, as a result, the work surface takes on a mirror image of the tool.

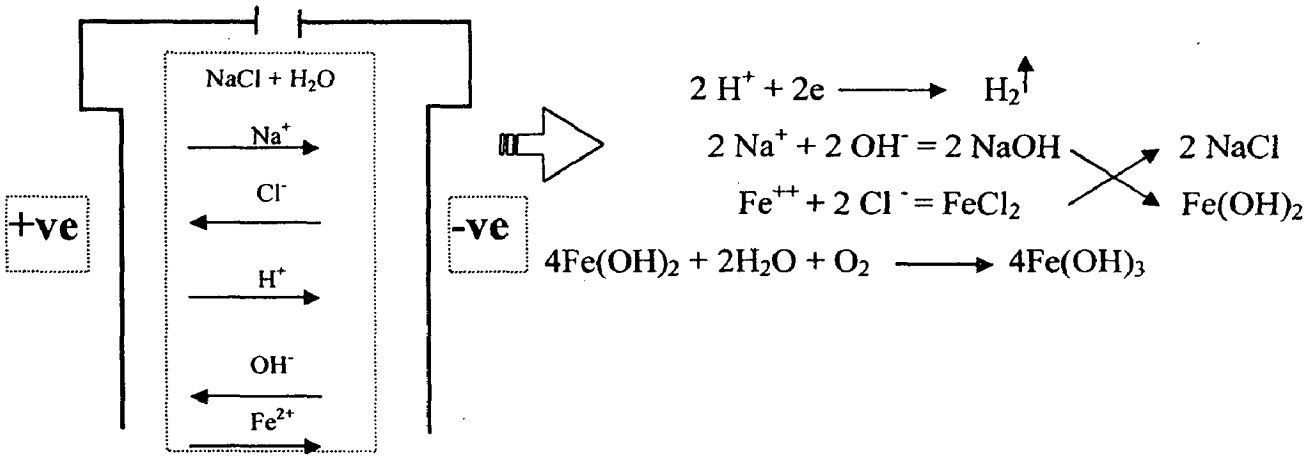

Fig. 1.1 Possible chemical reactions in IEG [Kuhn, 1971]

According to Faraday's laws of electrolysis,

1) The amount of chemical change (or the amount of substance deposited or dissolved) produced by an electric current is proportional to the amount of electricity passed.

2) The amounts of different substances deposited or dissolved by the same quantity of electricity are proportional to their chemical equivalent weights.

The laws can be expressed in the mathematical form as:

$$m = \frac{ItE}{F} \text{ or } \left(MRR = \frac{IE}{F} \right) \tag{1.1}$$

where, m is the mass in gram, I is the current in ampere, t is the time in seconds, E is the gram chemical equivalent weight of material $\left(E = \frac{\text{Atomic weight}}{\text{Valency}} \right)$, F is the Faraday's constant = 96500 ampere-seconds and MRR is the theoretical material removal rate. ECM is characterized with higher material removal capabilities. The above theoretical MRR is based on a number of simplifying assumptions and in practice, the material removal rates are often higher. ECM process possesses a self-regulating feature. If the tool advances at a faster rate than that of material removal, the IEG becomes narrower, current density increases and consequently the machining rate increases to attain a steady state condition. The converse is also true (Pandey and Shan, 2005). However, the process is highly complex and intensity and uniformity of electrolytic dissolution is dependent on many process variables: change in valency of dissolution and preferential valency mode of EC dissolution during process; gas evolution and bubble formation; electrolyte's electrical conductivity and temperature variation along the electrolyte flow path; overpotential; effect of passivity due to metal oxide film etc. For example, the dissolution of iron in NaCl electrolyte, may be either in the form of ferrous hydroxide (Fe^{2+}) or ferric oxide (Fe^{3+}), depending upon the machining conditions. Mode of EC dissolution of alloys is still more difficult to know. The preferential valency mode of dissolution has been reported to depend upon the electrolyte flow rate, IEG and

length of electrolyte flow path. The change in electrolyte's electrical conductivity and hence the anodic dissolution along the flow path has been reported to be the function of temperature change, size and distribution of hydrogen bubbles besides the contamination of electrolyte by sludge and the presence of evolving gases and water vapor, etc. (Jain, 2002). The rate of hydrogen gas bubble generation at the cathode surface is governed by the current density. The net effect of the presence of hydrogen gas bubbles is to decrease the electrolyte's electrical conductivity and thus, local anodic dissolution rate. Landolt et al. (1970) have reported that the increase in the bubble layer thickness in downstream is low in case of increased electrolyte flow rate and the size of the bubbles decreases with decrease in the current density and increase in electrolyte pressure or velocity or both. Thus, a higher electrolyte pressure in the range of 0.2-3.5 MPa, leading to the electrolyte flow velocity in IEG as high as 20-30 m/s are desirable in ECM (Jain, 2002).

1.3 PRINCIPLES AND PRACTICES OF CONVENTIONAL HONING

Honing is a controlled abrasive super-finishing process used primarily to generate the final functional characteristics of geometry, diametral size and surface typically on load-bearing or sealing surfaces. Honing consists of simultaneous rotation and reciprocation of bonded abrasive sticks, mounted around the periphery of the honing tool, to finish the work surface. The sticks are forced-out radially with equal pressure by a cone shaped wedge in the center of the tool. To ensure equal pressure on all sticks, either the tool or the workpiece is usually allowed to float. Thus, the geometric axes of the tool and the bore align themselves automatically during the operation (Bralla, 1986). The action of a honing tool is based on the definition of a cylinder, i.e. a form generated by rotating a rectangle about one of its sides. Thus, the simultaneous rotation and reciprocation of the cutting surfaces of the sticks generate a geometrically true cylinder (Randlett and Ellis, 1967, 1968). Honing is employed not only to produce high surface finish, but also to correct out-of-roundness (OR) and cylindricity, and remove taper, boring tool marks, and bell mouth, barrel and axial-distortion in the workpiece. However, it cannot correct location of the hole or its perpendicularity. In honing, the simultaneous rotating and reciprocating motions of honing sticks result in a characteristic crosshatch lay pattern (Fig.1.2) which has tremendous impact on the functional properties of the surface (Bolz, 1981).

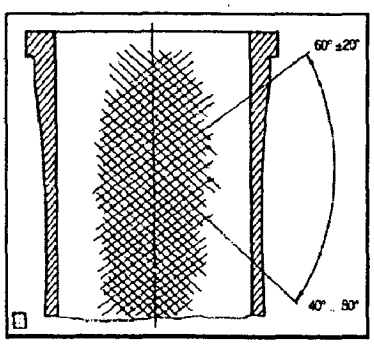

Fig. 1.2 Typical crosshatch lay pattern obtained in honing

Cross-hatch angle (2α) can be estimated from the following relation.

$$\tan\alpha = \frac{\textit{reciprocating speed in surface meter per minute}}{\textit{Rotary speed in surface meter per minute}} \qquad (1.2)$$

In majority of the applications a cross-hatch angle of 30° is common, but in practice it varies from 20 to 45°. The stroke is set such that stick travels nearly 1/3 of its total length or a minimum 20 mm out on either end of the bore (Production Technology, 1980). The commonly used abrasives are aluminum oxide, silicon carbide, cubic boron nitride (CBN), and diamond. Aluminum oxide is commonly used to rough-hone steel; silicon carbide works well on cast iron, bronze, beryllium, some nonmetallics, and to fine-finish steel. CBN is used on most steels and their alloys as well as cast iron. Diamond, the hardest abrasive, is used on cast iron and tungsten carbide. Abrasive grit size can range from 70 to 1200 (Schnitzler, 2001). Careful selection of abrasive type and bond hardness is required to satisfy both self-sharpening and free cutting economically. Honing speed in rotation mainly depends on the diameter of the bore to be honed. The choice of spindle speed is influenced by material being honed, its hardness, surface roughness, number and width of the sticks in the tool and finish requirement, while the reciprocating speed depends mainly on the desired cross hatch angle (Metals Handbook, 1980). Honing speeds for cast iron range from 60 to 75 smpm in rotation and 15 to 25 smpm in reciprocation. For steel, honing speeds range from 45 to 60 smpm in rotation and upto 15 smpm in reciprocation (Bolz, 1981). A wide range of honing pressure is required to yield acceptable efficiency and results. In some of the equipment the hydraulic pressure for stick-out is varied from 1 to 3 MPa. However, honing is more often controlled by stick-out than by gauge pressure. Insufficient pressure leads to a low rate of material removal. When pressure is excessive, a rougher finish will result as the abrasives break down very fast. Surface finish of 0.25 to 0.4 μm can be obtained easily and finish of less than 0.05 μm can be achieved and reproduced while tolerances on roundness, straightness and size can be controlled to within 0.008 mm (Bralla, 1986).

1.4 HYBRID MANUFACTURING PROCESSES: *an emerging trend*

Hybrid manufacturing processes (HMPs), particularly the EC based hybrid processes owing to their distinct capabilities, are gaining considerable attention from the manufacturing community to meet the challenges of stringent surface quality, tolerances, high productivity requirements, particularly with the critical and tribologically significant components made of difficult-to-machine advanced materials. The technological improvement of manufacturing processes is being achieved by combining different physico-chemical action on the processed work material. In particular, the mechanical action of suitable conventional machining processes are being integrated with advanced manufacturing processes to make use of the combined or mutually enhanced advantages, and to avoid or reduce some adverse effects the constituent processes produce when they are individually applied (Rajurkar, et. al, 1999). There is a long fairish of the hybrid machining processes that are under development worldwide to achieve specific benefits on the machined surfaces:

Electro-Chemical Grinding (**ECG**): (U.K., Russia, China, Japan)
Electro-Chemical Honing (**ECH**): (Russia, China, Germany, Poland)
Electro-Chemical Arc Machining (**ECAM**): (U.K, Russia, Poland)
Electro-Chemical Discharge Machining (**ECDM**): (Russia, U.K)
Electrolytic Magnetic Abrasive Finishing (**EMAF**): (Japan)
Ultrasonic Machining with Electro-Chemical assistance (**USMEC**): (Russia)
Laser assistance Electro-Chemical Machining (**LECM**) (U.S.A., Russia, U.K., Poland)
Laser Assistance Etching (**LAE**): (U.S.A., Germany)
Mechano-Chemical Polishing (**MCP**): (Japan, U.S.A.)
Electrical Discharge Grinding (**EDG**): (U.K., U.S.A., Russia, Japan)
Abrasive Electrical Discharge Machining (Sinking) (**AEDM**): (Japan)
Magnetic Abrasive Finishing (**MAF**): (Japan, Russia, U.S.A.)
Ultrasonic Assistance Electrical Discharge Machining (**UAEDM**): (France, Japan, U.S.A., Russia, China)
Turning with thermal assistance (hot machining) such as Laser Assistance Turning (**LAT**), and Plasma Assistance Turning (**PAT**): (U.S.A., Russia)
Elastic Emission Machining (**EEM**): (Japan)

A detailed treatment of the above process has been given by Kozak and Rajurkar (2001). HMPs can be classified into two major categories: 'Processes in which all

constituent processes are directly involved in the material removal' and 'Processes in which only one of the participating processes directly removes the material while the others only assist in removal by changing the conditions of machining in a "positive" direction from the point of view of improving capabilities of machining'. In both the categories, electro-chemical, thermal, chemical, and mechanical interactions can occur. Most of the HMPs are in their inception and developmental phase and a sustained research is required to transform them into matured technologies for their successful induction into the industries. Some of the HMPs like ECH, ECG and ECDG have shown to be very effective in machining new and advanced materials and manufacturing of machine parts and tools.

Electro-chemical honing (ECH) is a promising hybrid manufacturing technology which, in spite of being used in some industrial plants, is still not fully described and researched. ECH can be seen to belonging to the second category.

1.5 ELECRO-CHEMICAL HONING PROCESS: a prospective productive precision micro-finishing technology

Electro-chemical honing (ECH) is a hybrid electrolytic micro-finishing technology characterized by a distinct coupling of electro-chemical machining and honing actions to provide controlled functional surface generation and fast material removal capabilities in a single operation. ECH can offer a unique range of benefits to the machined surfaces not obtainable by either of the processes when applied independently (Shan, 2006).

ECH has a flexi- feature with regard to the control of machined surface characteristics. A surface having a distinct cross-hatch lay pattern to enhance the resultant lubricating oil retention capabilities of the work surface functionally required in parts such as connecting rods and fluid power cylinders, alongwith compressive residual stresses desirable for the components that are subject to cyclic loading can be produced. A surface completely free from stresses, required for some critical applications, can also be generated. Surface finishes of 0.1 to 0.8 μm can be easily obtained on material of any hardness as long as it is electrically conductive. Surface roughness value R_a of the order of 0.05 μm and tolerances of ± 0.002 mm can be achieved (Benedict, 1987). Roundness and straightness can be maintained at less than 0.005 mm and can be duplicated on each part. The process can be used to remove materials at rates up to 5-10 times faster than conventional honing and upto 4 times faster than internal grinding (Tool and Manufacturing Engineers Handbook, 1983). Besides the capability to provide fine surface finish, ECH can correct form deviations such as out-of-roundness, cylindricity, axis-distortion, taper, waviness, barrel and bell- mouth and smooth off ripples [Fig. 1.3] (Randlett and Ellis, 1968; Guoqiang et. al., 1986).

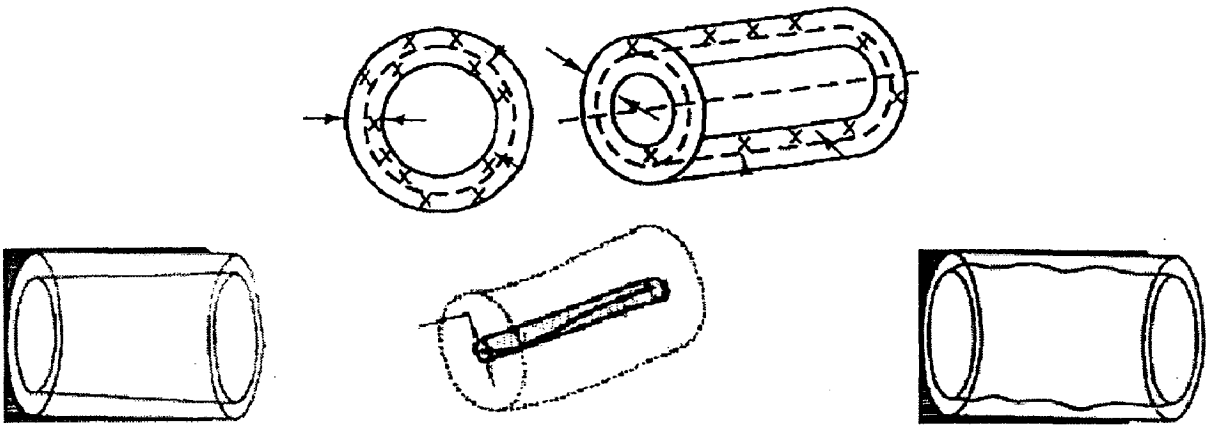

Fig. 1.3 Geometrical inaccuracies can be corrected by ECH

Size of the work that can be processed is limited only by the amount of current and electrolyte that can be supplied and by practical limits on ECH tool size.

Some of the advantages of the electro-chemical honing process as against the constituent processes can be summarized as:

Advantages of ECH process:

1. Improved productivity (reduced processing time) as compared to ECM and conventional honing processes. The gain is more pronounced when used to hone hard and tough metals (Shan, 2006).
2. Capability to provide fine finishes with precise control over the size and geometrical tolerances. Hardness of the material is no limitation.
3. Increased accuracy and less material damage due to very little heat built up and low temperature involved in ECH. The process is well suited for processing the parts which are susceptible to heat distortion (Tool and Manufacturing Engineers Handbook, 1983).
4. Distinct capability to generate a surface with characteristic crosshatch lay pattern and compressive residual stresses, as well as a surface completely free from stresses.
5. Life of abrasive sticks is much extended (Metal Handbook, 1980).

6. Thin-walled tubes can be finished with much reduced noise and distortions due to the less pressure involved between work surface and abrasive sticks (Shan, 2006).

7. Automatically deburrs the work surface, sharp or burred edges of cross holes or other intersections which break into the bore [Randlett and Ellis, 1968].

Thus, ECH can become an ideal choice for improving the surface integrity (and consequently the service life) of critical components made of hard and tough metals and the parts which are susceptible to heat distortions. However, the workpiece is required to be conductive. ECH is more suitable for longer production runs than for tool-room and job-shop because of its electrical and fluid handling elements and the need for corrosion protection and the costlier nature of ECH tooling.

Due to its distinct capabilities, ECH has great potential as an effective micro-finishing technology in several industries, especially in aerospace, auto, petrochemical reactor, roller and gear manufacturing (HE, et.al., 2000). Its material applications include the processing of a wide range of materials like cast tool steels, high-alloy steels, carbides, titanium alloys, incoloy 901, 17-7 PH stainless steel, inconel, and gun steels. Internal cylindrical honing is the most common commercial application of ECH. Recently the process has been applied for finishing gear teeth profile. Parts processed include, typically, the piston pump body, pinion and transmission gears, carbide bushings, sleeves and cylinders (Randlett and Ellis, 1968; Machining Data Handbook, 1980). Fig. 1.4 presents some specific application examples of ECH.

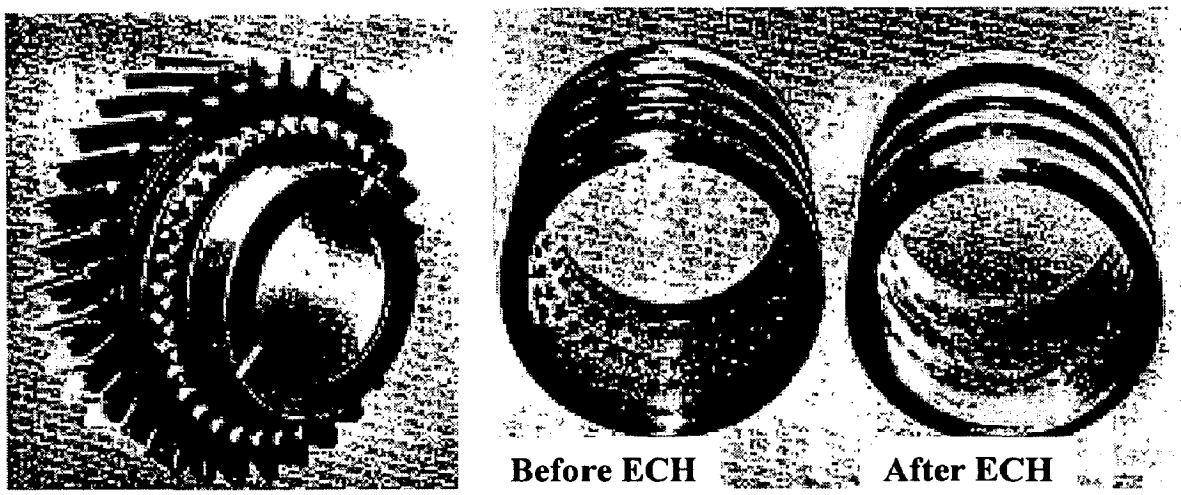

Fig. 1.4 Some specific application examples of ECH

A review of principles and practices of the electro-chemical honing process followed by the past research work on ECH is presented in the next Chapter.

Chapter-II
LITERATURE REVIEW

General principle of anodic metal removal was one of the discoveries of Michael Faraday (1791-1867) from which stemmed the development of electro-chemical processes. The first proposal for the application of anodic material removal principles as a machining technique was given by a Russian W. Gusseff in 1929 and again much later by C.F. Burgess in a paper submitted to the Electrochemical Society (USA) in 1941. But, it was not until 1959 that the phenomenon of controlled anodic metal removal, a basis for all electro-chemical processes, was put forward in the form of a commercial apparatus for the regular industrial application of electro-chemical machining (ECM) by Anocut Engineering Company of Chicago (Wilson, 1971). However, it is only during the last couple of decades that this method has been used extensively and a number of hybrid electrochemical processes including electro-chemical honing (ECH) have been developed to provide distinct benefits to the machined surfaces (Jain, 2002). Electrolytic applications to conventional honing started in 1962 -1963 (Horgan, 1962; Eshelman, 1963). Initially the purpose of electrolytic aid to conventional honing was just to improve the process productivity owing to the higher material removal capabilities of ECM process while the functional surface generation was primarily achieved by the conventional honing process itself. In the later stages, the role of mechanical action got reduced down, just enough to a preferential scrubbing of the resulting metal oxides, produced due to electro-chemical (EC) action, from the work surface in a controlled manner to modify the nature of electrolytic process to achieve the functional capabilities of conventional honing alongwith improved productivity. Most of the material removal occurs through EC action (Metals Handbook, 1980).

The following sections give the basic principles of ECH process followed by a review of the past research work on this.

2.1 BASIC PRINCIPLES OF ECH

The working principle of electro-chemical honing process is shown in Fig.2.1. ECH is a hybrid process of ECM and conventional honing. In ECH, metal is removed when a small DC electric potential is applied across the cathode tool-anode workpiece gap filled with suitable electrolyte. The ECH tool, having nonconductive honing sticks around its periphery, is stroked through the bore with a controlled generating motion of simultaneous rotation and reciprocation as in conventional honing (Tool and Manufacturing Engineers Handbook, 1983).

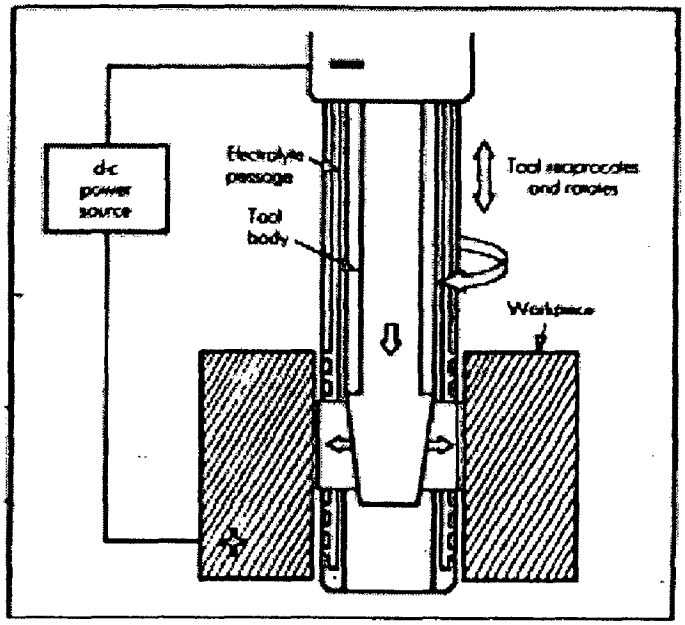

Fig. 2.1 Schematic of ECH process

[Tool and Manufacturing Engineers Handbook, 1983]

Abrasive sticks remove metal oxides produced by electrolytic action preferentially from the higher spots protruding from the ideal configuration as well as any high spots resulting from non-uniform electrolytic action as illustated in Fig. 2.2.

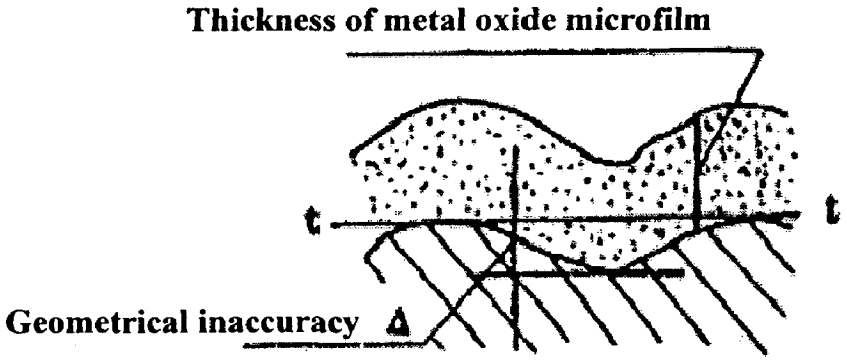

Fig.2.2 Geometric-error correction in ECH

Removal of metal oxide film from the higher spots leads to a heavier electro-chemical action at these spots because these are made more receptive for EC attack, while the lower valleys, present due to macro-geometrical as well as macro-geometrical errors in the surface micro-profile, will remain still covered by protective metal oxide microfilm. Consequently, the lower areas will have weaker EC dissolution. Due to this working principle, ECH process possesses the ability to improve the surface finish as well as to correct geometrical inaccuracies in form and smooth ripples (Guoqiang et. al., 1986). Conventional honing mechanism, where the honing sticks cut most aggressively on the high or tight areas to remove the geometric errors, also aids to the process depending on the tool design. Electro-chemical honing mechanism can be described as given in Fig.2.3. ECH is an interaction process of ECM and conventional honing and it is the nature and efficiency of the interacting processes as well as their coordination that determines the unique ECH capabilities.

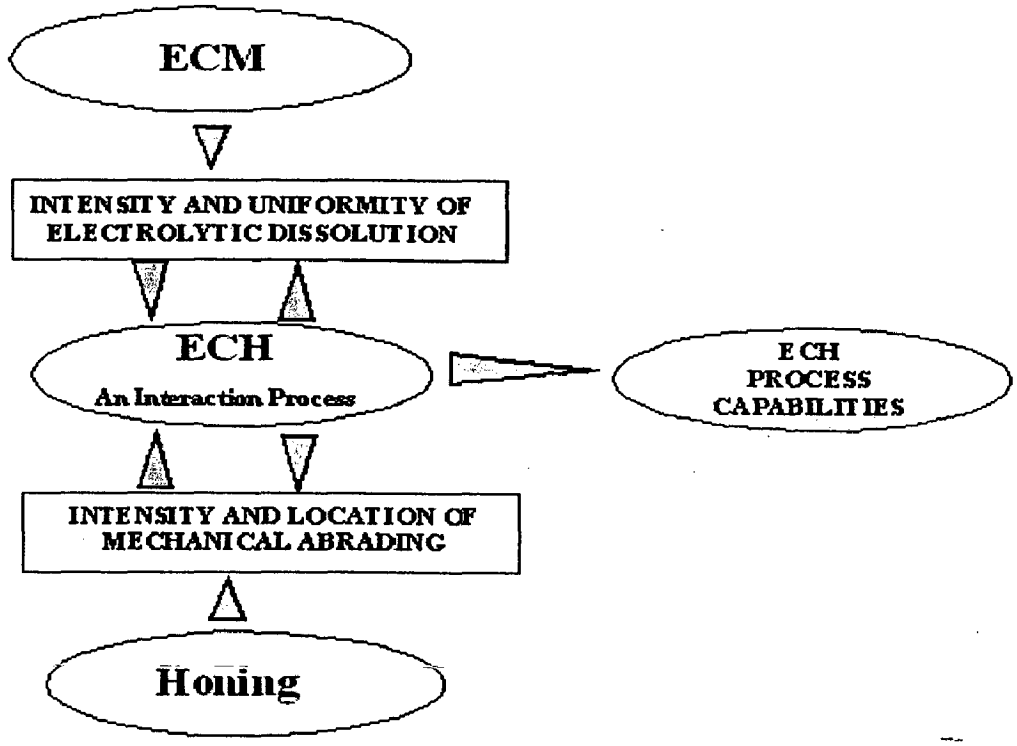

Fig. 2.3 ECH: an interaction process

In ECH, the action of honing sticks keeps the surface receptive and tends to correct the surface irregularities resulting from non-uniform electrochemical dissolution, the electrolyte does not have to be so much corrosive as in ECM. Sodium Chloride and Sodium Nitrate are the most commonly used electrolytes in ECH. Also the control of electrolyte pH and its composition, as well as sludge control becomes less critical (Benedict, 1987; Sharma, 2004).

In ECH, more than ninety percent of the material removal occurs through electrolytic action (Tool and Manufacturing Engineers Handbook, 1983). The mechanical action is controlled to a minimum. Therefore, only a light unit surface pressure is desired which could be achieved using a light spring system for automatic feed-out of sticks (Benedict, 1987). As against the conventional honing, speeds in ECH, depend on the intensity and uniformity of electrolytic dissolution as the mechanical abrading must be coordinated with electrolytic

dissolution. Typically, the rotational speeds range upto 250 smpm and reciprocating speeds upto 18 smpm in ECH (Kitaev et. al., 1985).

2.1.1 Flexi-Features of ECH

The electro-chemical honing process has got a flexi- feature with regard to the control of machined surface characteristics. ECH can generate a surface having a distinct crosshatch lay pattern as in conventional honing that is particularly beneficial for the lubricating oil retention and thus, the resulting frictional properties and wear of the work surface is much improved. The end cycle conventional honing action for few seconds without the electric supply can provide compressive residual stresses on the processed surface which are desirable for the parts that are subject to cyclic loading to improve the fatigue endurance properties of the work surface. The process can provide a completely stress free surface required for some critical applications using a few seconds end cycle operation in the pure ECM mode with retracted / removed honing sticks (Tool and Manufacturing Engineers Handbook, 1983; Benedict, 1987).

ECH possesses another flexi feature with the mechanism of geometrical error correction. This can be achieved using two approaches: by achieving a suitable ratio between the electro-chemical dissolution and mechanical abrasion rates such that the process assumes a convergent character in which the protective ability of resulting metal oxide microfilm is utilized effectively to correct the geometrical inaccuracies. The ratio of metal removal rates with and without mechanical abrasion has been suggested to be used as a characteristic parameter for geometric-error correction in ECH (Guoqiang et. al., 1986). In the other approach observed earlier, the ECH tool can be designed to correct geometrical inaccuracies similar to the conventional honing (Budzynski, 1983). It is the tool design aspects which limit the application of this precision machining process mostly for internal cylindrical honing.

Another flexi-feature is with regard to control of the process: the coordination between the electrolytic dissolution and mechanical abrasion can be exercised either by adjusting the EC based parameters or by honing based parameters. With a fine control over the EC parameters and suitable kinematics for the control of honing sticks motion, this control mode seems to have great prospects for applying ECH benefits to external flat as well as contoured surfaces. Another approach uses an ECH tool designed for achieving a required match (Budzynski, 1983, 1995).

2.1.1.1 Controlling electrolytic dissolution

Electrolyte flow conditions in inter electrode gap have been reported to have significant influence on the intensity and uniformity of electrolytic material removal. Temperature variation and hydrogen layer formation have been reported to be the main cause of variation in electrolyte's electrical conductivity and consequently uniformity of electrolytic dissolution. In ECM process, hydrogen generated at the cathode surface appears as a layer of bubbles mixed in the electrolyte and this layer thickens along the direction of flow of the electrolyte. Void fraction of the bubble layer is approximately 0.5 on an average. The layer moves towards the anode surface at a speed of 0.05-0.1 m/s (Rajurkar et. al., 1993). Electrolyte pressure and flow velocity are important parameters in determining the size and distribution of hydrogen bubbles. Density of current and duration of current application are also critical for size and generation rate of hydrogen bubbles. In this regard, higher values of electrolytic pressure and flow velocity and lower current density and duration are desirable for improving uniformity of the material removal. Minimum temperature variation and higher electrolyte velocity in the cutting zone are preferable to minimize the non-uniform electrolytic dissolution (Jain, 2002). Pulsed DC power supply provides an attractive alternative for improving electrolyte flow conditions in inter electrode gap leading to higher

dimensional accuracy and simpler tool design. Recent works report that shorter pulse duration (< 1 ms) is preferable for improving dimensional control in ECM (Rajurkar et.al., 1993). With the proper control and coordination of power supply and electrolyte based parameters, a fine control over the intensity and uniformity of electrolytic dissolution rate can be achieved.

2.1.1.2 Controlling mechanical abrasion

A control over the intensity of mechanical abrasion can be exercised by speed variation using variable speed drives and changing, to some extent, the stick-out pressure. Location of abrasion can be controlled by employing a suitable kinematics for the motion of the tool. A proper coordination of these two would lead to a fine control over the intensity and location of mechanical abrading.

2.2 REVIEW OF PAST RESEARCH WORK ON ECH

Randlett and Ellis (1967, 1968) compared the conventional honing with electro-chemical honing process and suggested the electrolytes for different materials. A comparison of stock removal rates on various materials for conventional and electro-chemical processes revealed that the electro-chemical honing process is much faster than the conventional honing.

The application of electro-chemical honing for gear teeth finishing was reported by **Chen Chi-Pin et al. (1981).** The working principle of electro-chemical honing of gear teeth is explained in Fig. 2.4. The workpiece gear, while rotating in mesh with a gear cathode and a gear hone, is reciprocated axially. Electro-chemical action takes place between the shaped cathode and workpiece gear teeth. The cross-axis gear hone, which is mounted on a floating stock to maintain dual flank contact with work gear, scraps the protective oxide film from high spots leading to heavier EC action when they come into EC zone. In this way the geometrical error in the work gear tooth profile is rapidly improved.

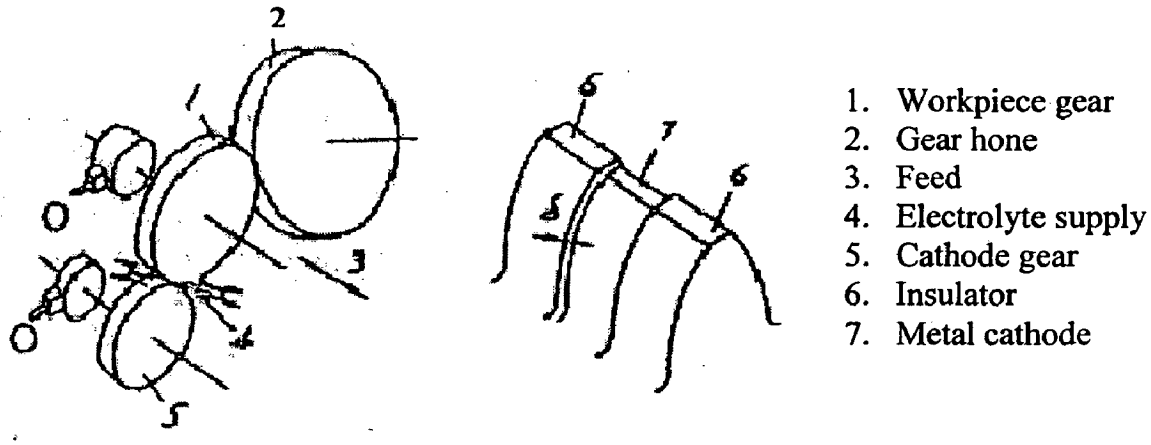

a) b)

Fig. 2.4 Working principle of ECH of gears
[Chen Chi-Pin et al., 1981]

This method was reported (Chen Chi-Pin et al., 1981) to improve the productivity, accuracy, and life of finished gears. An accuracy of 0.01 mm in tooth profile alongwith the crowning in tooth width was obtained by photo-electric control of DC supply. The surface finish was slightly better than that obtained with honing and noise level of gears in operation reduced by 5-8 dB after ECH. Three aspects have been highlighted: (i) the ability of correcting geometrical-errors in gear teeth by ECH, (ii) dynamic behavior of dual-flank meshing process in ECH of gears, (iii) false tooth profile derived from dual-flank meshing process and methods of prevention.

Budzynski (1983) attempted the optimization of ECH of cylindrical holes that were considerably deformed by heat treatment using NH_4NO_3 electrolyte. Influence of the current intensity, machining rate, hone unit pressure and machining time were examined. Effect of cathode reaction time, initial gap and electrolyte passivity on shape deviations was also analyzed. The results indicated significant effects of the current density, hone unit pressure and machining time on material removal but these parameters could not influence the shape deviations and surface finish. He pointed that this could have happened due to the last few seconds pure honing cycle employed in experiments. Results highlighted that the electrolytic reaction time should be maintained constant for every elemental work surface for better accuracy. It was noted that a radially motionless cathode with strongly passivating electrolyte provided a fast decrease of shape deviations in the form. Further, resulting wear of honed surface was found dependent on the way the components are honed.

Kitaev et al. (1985) highlighted technical specifications of semi-automatic vertical electro-chemical honing machines that were used for electrochemical honing of holes in the components manufactured under batch and small quantity production. Description of the devices for equipment protection from electrolyte, unit for securing the tool, and supply of current to the tool was also given.

Guoqiang et al. (1986) indicated that if the protective ability of metal oxide film on the work surface formed due to electro-chemical action is utilized fully and a distinct mechanical scrubbing on the work surface is achieved, ECH can become a means to correct geometrical inaccuracies too. They proposed the ratio of material removal with and without mechanical scrubbing (i.e. $\lambda = V_{with} / V_{without}$, where V is diametral change rate) to be used as a characteristic parameter indicating the ability of correcting error (ACE) in ECH. They found that many electrolytes which may provide good surface finish and productivity have poor ACE. They pointed out the following interesting characteristics with regard to different electrolytes and their λ value and nature:

- Resulting metal oxide film sticks too fast on the surface and its strength is so high that usual mechanical scrubbing action can hardly remove it.
- Metal oxide film has strong power to reduce EC dissolution, but the electric charge needed to build-up the film is too small. Thus, a very rapid alternation of EC dissolution and mechanical scrubbing is needed but it can hardly be achieved.
- Some electrolytes possess high λ values, but its rate of EC dissolution is too low which makes the process impracticable.

Fig. 2.5 presents the behaviour of a better electrolyte in ECH. Its λ value drops with increasing current density but even with this λ value, error in gear teeth profile was much improved.

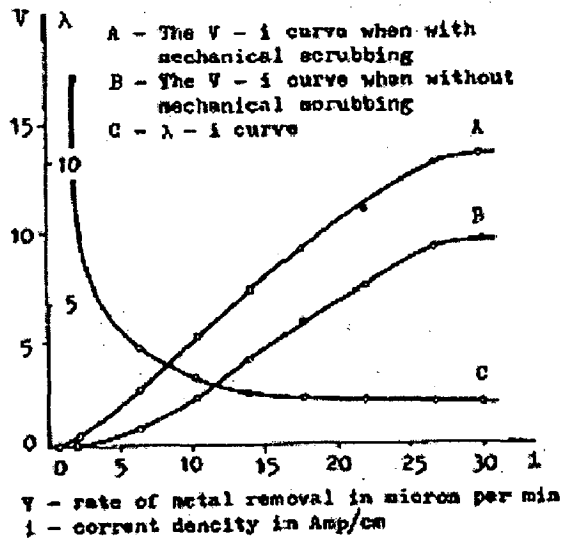

Fig. 2.5 Behaviour of a better ECH electrolyte
[*Guoqiang et. al., 1986*]

The key points to realize a good ACE in ECH requires the high protective ability of the metal oxide film, correct movement of honing sticks on work surface for the preferential removal of the film only from the higher spots, and a good coordination of EC and mechanical actions. The effect of the intensity of mechanical scrubbing i.e. the stick-out pressure on the material removal rate is shown in Fig.2.6. It is apparent that a low stick-out pressure in a narrow range could only provide a significant improvement in material removal rate in ECH due to proper match achieved between electrolytic dissolution rate and mechanical scrubbing. Further, any under-scrubbing as well as over-scrubbing would not result in significant improvements. Thus, ACE in ECH is closely related to electrolyte composition and match between mechanical scrubbing and EC dissolution rate.

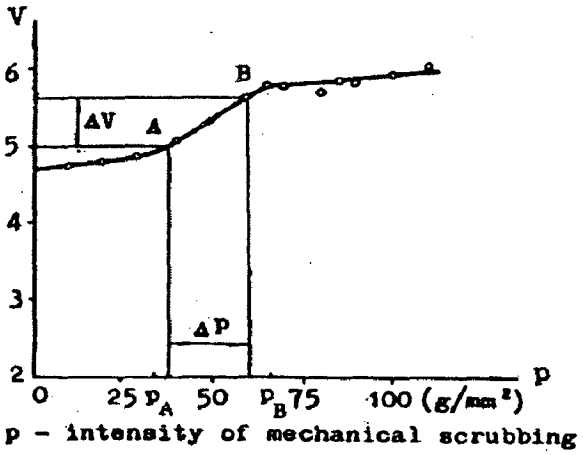

Fig. 2.6 Effect of stick-out pressure on material removal rate in ECH
[Guoqiang et. al., 1986]

Guoqiang et al. (1987) presented field controlled electro-chemical honing of gear teeth. Key to the process is indicated to be a gear-shaped cathode with the provisions of adjusting the intensity of electrochemical dissolution steplessly along the full profile of gear tooth by varying the electric supply voltage during process. The method was reported to produce any type of tip or root relief easily. It was pointed out that the accuracy of tooth profile can also be improved provided the error in tooth profile of all the teeth is nearly same.

HE et al. (2000) presented the slow scanning field controlled ECH of gear teeth. Key to the process is a gear-shaped cathode which is exposed as cathode pole strip on the work gear tooth flank. Based on the existing error in tooth profile, dwelling of the pole at different spots was controlled by varying the center distance between the cathode and work gear with the help of a programmable stepper motor. The method was reported to cancel the error in gear teeth profile very efficiently. With 2.6 min discharging time, error reduced to 2.5 μm from 6 μm in a work gear having 59 teeth, module = 2.5. It is pointed that the method can also step up tooth profile accuracy if the general accuracy is guaranteed by preceding operation.

Fasil (2004) studied the effect of electric voltage, electrolyte pressure, electrolyte concentration and speed of rotation on the resulting surface roughness value R_a in ECH.

Results revealed that the electric voltage and electrolyte concentration have significant effect on surface roughness obtained as shown in Fig. 2.7. However, the experiments were performed with a very low current intensity (max. 500mA) with $NaNO_3$ electrolyte and a fixed ratio of the rotational and reciprocating speeds.

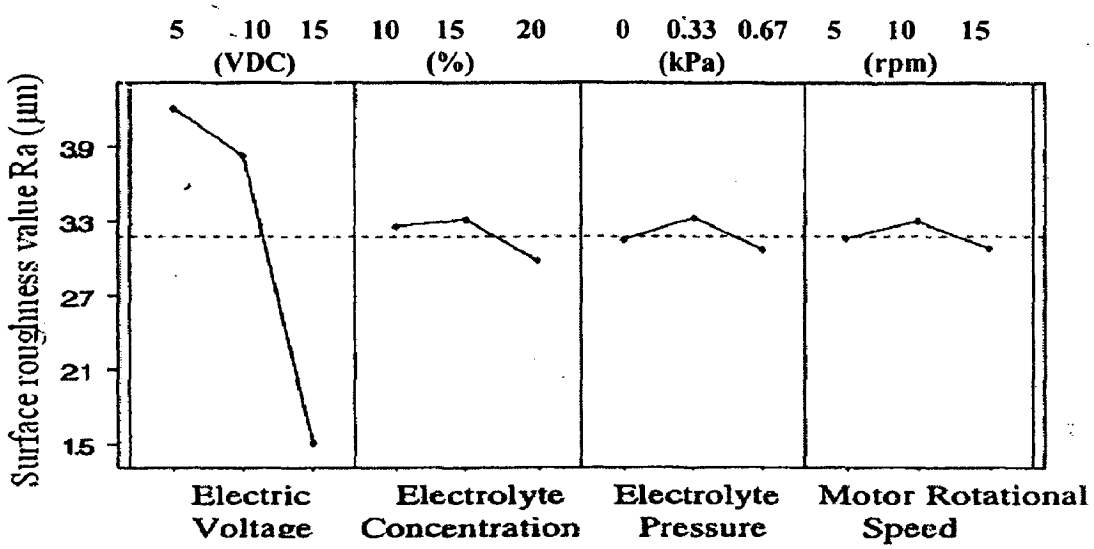

Fig. 2.7 Effect of process parameters on surface roughness value R_a in ECH

[Fasil, 2004]

Chapter-III

PROBLEM FORMULATION

In recent past, demand for increased safety, reliability and service life has led to the considerable attention directed towards the functional requirements of engineering components. Severe service conditions, development and use of more difficult to fabricate newer materials and emphasis on design criteria to employ these materials much closer to their full potential are imposing stringent requirements on functional characteristics of components. Surface conditions produced by manufacturing methods have pronounced influence on the resulting properties and performance of the component during service. Direct relationships are widely assumed to exist between the surface roughness and fatigue strength as well as other properties. Metallurgical and other alterations below the surface also have a major influence on material performance. Many potential failures have originated within the first few hundredth mm below the geometrical surface. This becomes particularly more important where high stress or severe service conditions are encountered by the component. Stringent requirements are being placed on surface quality and shape deviations produced by the manufacturing processes. Therefore, considerations must include a thorough review of the surface alterations resulting from specific machining operations. The historical emphasis on surface texture and material removal rate; is only a part of the consideration and it must be extended to include the assessment of the effects of manufacturing operations on surface integrity (microstructural alterations, microhardness changes and surface residual stress changes), size and macro-geometrical inaccuracies in form such as out-of-roundness, cylindricity tolerance and axis-straightness.

3.1 GAPS IN PAST RESEARCH WORK ON ECH PROCESS

ECH is still in its infancy in many respects. Recently some research work has been directed towards the application of this process for finishing gear teeth. The internal cylindrical honing the most potential commercial application of ECH has mostly remained unexplored. Existing literature deals mainly with qualitative description of the process and its applications. Therefore, a sustained research on ECH is required in order to utilize the full capabilities of the process. A review of the past research work reveals that there exists a lack of systematic investigation of ECH on the following aspects:

1. Process parametric influences on the process performance characteristics are not completely investigated.
2. Process parametric relationships are not established.
3. Material removal mechanism in ECH process is only partially understood.
4. Complete information on surface micro-geometrical aspects and characteristics of ECHed parts is not available.
5. Macro-geometrical aspects of ECHed parts have not been examined objectively.
6. Surface integrity aspects of ECHed parts have not been evaluated effectively.
7. Process effects on work surface residual stress are not known.
8. No effort seems to have been made towards process modeling.
9. There is little information available on process performance optimization.

3.2 OBJECTIVES OF PRESENT Ph.D. RESEARCH WORK

As a manufacturing process can influence the machined work surface in several ways, the present research work, therefore, makes an attempt in this direction based on a total surface quality approach, with the following objectives:

1. Design and develop an experimental setup for ECH process.
2. Explore time-dependent behaviour of ECH process.
3. Investigate the effects of key ECH parameters on the process performance characteristics.
4. Identify the material removal mechanism of ECH.
5. Evaluate ECHed work surface quality.
6. Evaluate ECHed surface macro-geometrical aspects.
7. Examine important ECHed work surface integrity aspects.
8. Multi-performance modeling of ECH process.
9. Multi-performance optimization of ECH process.

Chapter-IV

DEVELOPMENT OF ECH SET UP

The important features, design aspects and operational kinematics of the electro-chemical honing setup that was designed and developed indigenously for the present experimental studies are described in this chapter. The design and development of the ECH set up is based on the problem objectives; various relevant design considerations applicable to different system elements; operational efficiency and flexibility as well as manufacturing and cost considerations. Most of the setup components have been fabricated and assembled indigenously in the Machine Tool Laboratory of the Institute. Some relevant technical data and specifications of the setup elements are also embodied in Appendix-A.

Figure 4.1 shows the schematic of the developed ECH setup. The setup has the following five major sub-systems:

1. Power Supply
2. Electrolyte Supply and Cleaning System
3. ECH Tool and Drives
4. Work Holding and Positioning System
5. Frame and Housing

A low DC potential in the range of 3-30 V (adjustable) with current adjustable upto 200 A is applied across the inter-electrode gap between a cathode stainless steel tool body and anode workpiece. An ECH tool, designed with certain unique features, is stroked through the workpiece bore with a controlled generating motion of simultaneous rotation and reciprocation, employing precision speed controlled drives.

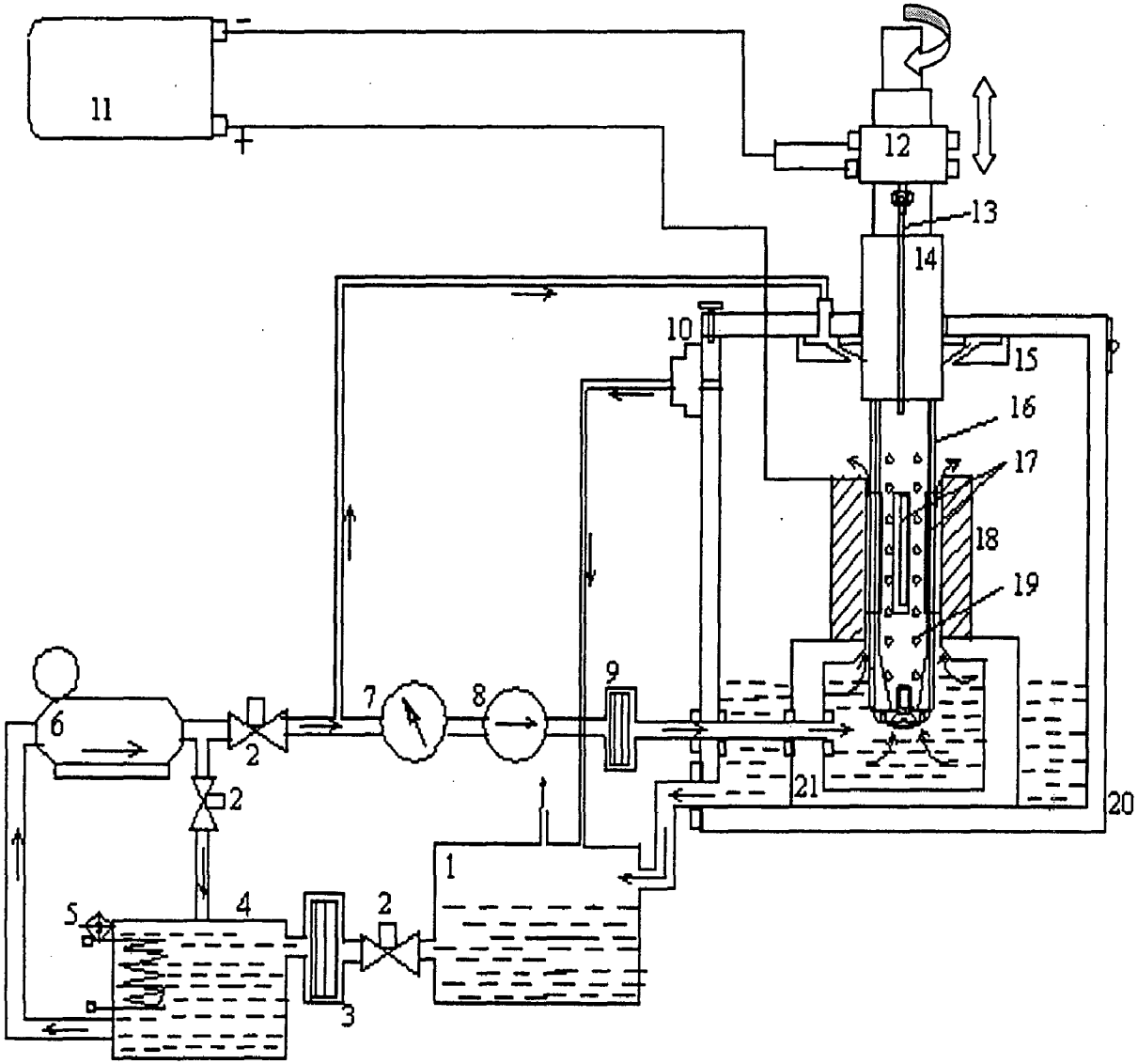

1. Electrolyte settling tank
2. Flow control valve
3. 1st stage filter-cum-magnetic separator
4. Electrolyte storage tank
5. Temperature control system
6. Stainless steel pump
7. Pressure gauge
8. Flow meter
9. 2nd stage filter-cum-magnetic separator
10. Mist collector
11. DC power source
12. Carbon brush and slip ring assembly
13. Copper connector
14. Seal hub
15. Hydraulic-cum-mechanical seal
16. Tool body
17. Honing sticks
18. Workpiece
19. Electrolyte exit holes
20. Work chamber
21. Fixture-cum-electrolyte inlet sleeve.

Fig. 4.1 Schematic of electro-chemical honing setup

different modes of supply have been uniquely combined. A part of electrolyte from the inlet sleeve directly flushes through IEG while remaining portion passes through the tool and is supplied at different locations in IEG through a number of holes drilled in the tool body. Electrolyte collected in the work chamber drains in a tank, which serves as the settling tank. Electrolyte from settling tank is returned to the electrolyte storage tank after the magnetic separation and double stage filtration. To remove salt laden vapors and gases, a mist collector is installed in the work chamber.

4.2.1 Electrolyte Storage and Settling Tanks

Two properly insulated 200 litre capacity PVC tanks have been utilized as electrolyte storage and settling tanks. Capacity and shape of the tanks are selected based on several considerations such as electrolyte flow requirements, processing time, and functional requirement for settling and temperature control system configuration. The elevation of settling tank placement is so as to obtain a natural head for free return of electrolyte from the machining chamber to settling tank as well as from settling tank to the storage tank. Recirculation of electrolyte from the pump discharge is delivered through nozzles fitted at three different locations in electrolyte storage tank to provide stirring effects for maintaining a uniform electrolyte temperature and enhancing temperature control system response by improving heat transfer coefficient of heating and cooling coils. Drain valves are provided in settling and storage tanks for emptying the tanks when cleaning is required.

4.2.2 Temperature Control System

The electrolyte storage tank is fitted with heating and cooling systems for electrolyte temperature control. Heating system (Fig. 4.4) contains a 2 kW copper sleeved heating element (Escorts) controlled by a sensitive thermocouple (Type EM-1, JUMO, Germany). It provides a rapid initial heating to raise the electrolyte temperature to a higher set value and

compensates for heat losses in the electrolyte circuitry during operation to maintain a constant electrolyte temperature as set.

Design of the cooling system is based on the heat exchange requirements during processing. Cooling system functions to provide a rapid initial cooling to lower the electrolyte temperature to a low set value and extracts heat generated due to process and heat filtrated into the electrolyte circuitry during operation in order to maintain the electrolyte temperature constant at the set point. It is composed of a copper cooling coil (25 m) fitted in the electrolyte storage tank and a ¾ TR compressor (Kirloskar Copeland, Model 2425), a condenser with cooling fan, capillary and relays (Fig. 4.5).

The cooling system is fitted with a high accuracy (± 1°C) digital temperature controller cum indicator having non-volatile EEPROM memory (SZ-7510-E, sub-zero^{TM}). The SZ-7510-E is a single set point controller specifically designed for refrigeration application wherein the compressor cuts off at set point and is restarted at a temperature of set point plus a differential. The controller incorporates several functions and protection features suitable for desirable operation. These functions include: set cut out point (±50°C), set maximum allowable high temperature limit (upto 50°C), minimum allowable low temperature set point, set differential (1-20°C), set probe calibration (±10°C), set time delay between relay restart time (0-20 min), key pad lock as well as the relay status on probe failure and end programming functions. Other technical data of temperature controller are given in Appendix-A.

With a proper control and coordination of pulsed power supply parameters (current, voltage, pulse on-time and off-time) and electrolytic parameters, a fine control over the intensity and uniformity of electrolytic dissolution can be achieved.

Therefore, a pulsed power supply suitable for use in ECH process has also been designed. The pulsed power supply is, however, under the process of procurement and thus, may be useful for future research works on electro-chemical honing process, employing the developed setup. The pulsed power supply designed for ECH has the following specifications:

---

1) 0-30 V DC power supply with current range of 10 A to 110 A, in the steps of 10 A, scaled on current selector switch.
2) Additional fine current settings of 0.5 A to 10 A in six steps with a current selection switch on front panel.
3) The voltage fully adjustable within 0-30 V with the help of voltage up and down switch. The selected voltage to be maintained constant during operation.
4) T-ON: 5 μs to 2000 μs in 12 steps.
5) Pulse OFF: 1 ms to 100 ms in 12 steps.
6) Pulse ON and Pulse OFF provision so that the power supply can be used as a continuous supply source without pulsing for the selected output voltage and current settings.
7) Audiovisual alarm for fault indication.
8) Time totalizer for T-ON.
9) SCR controlled with overload, short- circuit and other relevant protections employed in ECM.

4.2 ELECTROLYTE SUPPLY AND CLEANING SYSTEM

A good electrolyte supply and cleaning system primarily serves to control the electrolytic parameters and supply electrolytic to the inter-electrode gap while maintaining high electrolyte purity. An electrolyte supply and cleaning system with the following key features has been designed and developed for the ECH setup:

1. Precisely controlled electrolyte temperature: due to the rapid response of the temperature control system, temperature of electrolyte supplied to IEG can be maintained within ±1 °C.
2. Wide range of electrolyte pressure and flow rate: the selected stainless steel electrolyte supply pump is capable of developing 1 MPa pressure with flow rates upto100 lpm.
3. Uniquely combined two different modes of electrolyte supply to the IEG: it ensures better uniformity of electrolytic conditions in IEG.
4. Combined use of various ways of cleaning such as settling, mechanical filtration and magnetic separation: it ensures high electrolyte purity during processing.

The electrolyte supply and cleaning system consists of: (i) electrolyte storage and settling tanks, (ii) temperature control system, (iii) 1^{st} and 2^{nd} stage filter-cum- magnetic separators, (iv) electrolyte recirculation pump, (v) electrolyte supply pump, (vi) flow control valves, (vii) piping, (viii) pressure gauge, flow meter and temperature indicators, and (ix) mist collector as shown in Fig. 4.1. Electrolyte is stored in a storage tank which is fitted with heating and cooling systems for a precise control of the electrolyte temperature. A stainless steel pump has been employed to pump the electrolyte from the electrolyte storage tank. Pressure and flow controls are employed at the pump discharge and the electrolyte is supplied to the inlet sleeve of the work chamber through a magnetic separator-cum-mechanical filter ensuring high electrolyte purity. In order to achieve a uniform electrolytic condition throughout the inter-electrode gap between the cathode tool body and anode workpiece, two

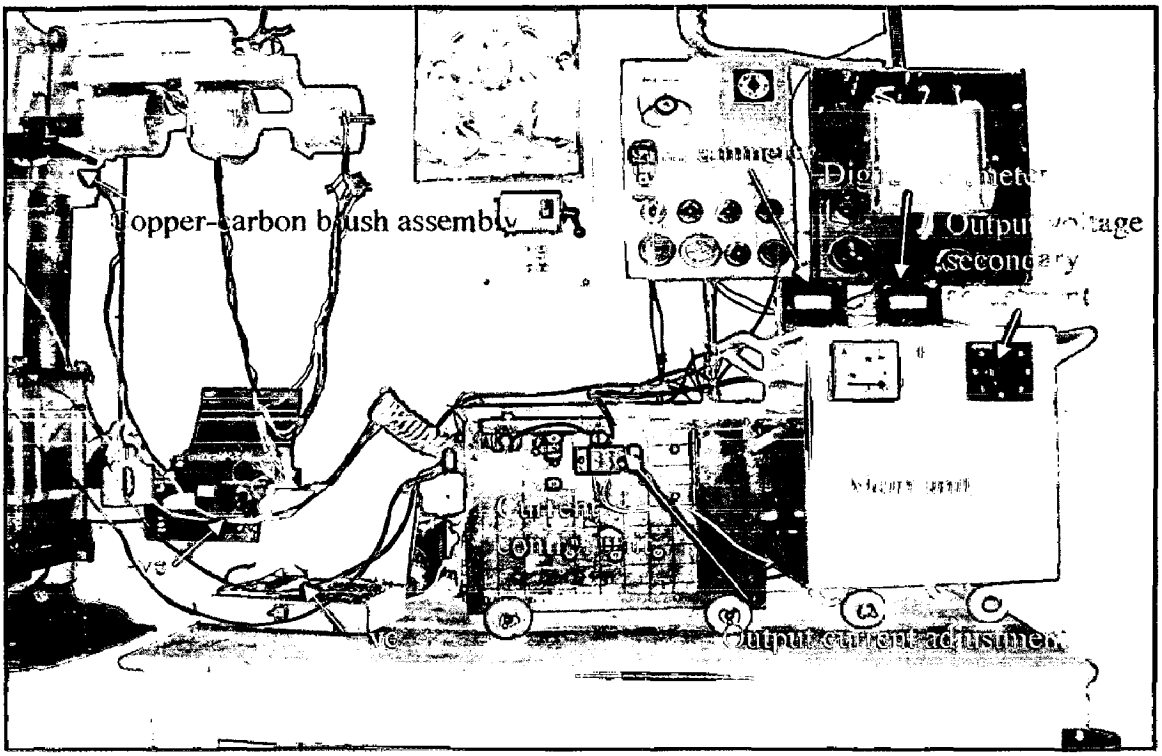

Fig. 4.2 DC power supply

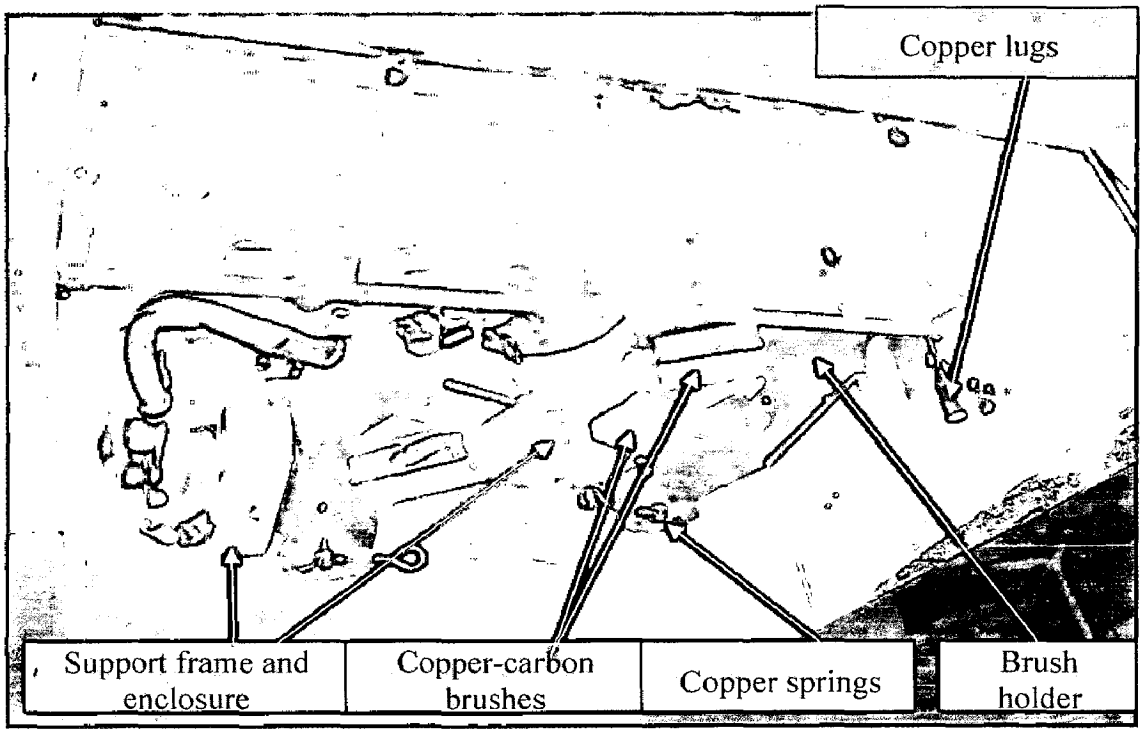

Fig. 4.3 Copper-carbon brush assembly

4.1 POWER SUPPLY

The power supply functions to provide a controlled DC potential across the inter-electrode gap which is flooded with an electrolyte. A DC power supply with the following features has been selected and procured for use in the ECH setup (Fig. 4.2):

1. Input supply: 220V 1 φ AC.
2. Output voltage: 3-30 VDC (adjustable) in 8 primary steps and 8 secondary steps. Voltage can be regulated to ±1V.
3. Output current: upto 200 A (adjustable).
4. Fitted with accurate digital ammeter and voltmeter for accurate supply output measurements.
5. Provisions for short circuit and overload protections.

The power supply is comprised of the following main elements:

1. Main Unit,
2. Current Control Unit,
3. Displays and Protections,
4. Brush Assembly.

Power supply can be operated in two different modes: as a constant current power source or as a constant voltage power source. Negative terminal of the power supply is connected to the tool through a copper-carbon brushes and slip ring assembly and the positive terminal is directly connected to the workpiece using copper lugs (Fig. 4.1).

The main unit transforms and rectifies 1 phase 220V AC electrical input to provide a 3-30V DC output. Output is obtained from its output terminals in 8 primary steps of equal increment. A fine adjustment of the selected output terminal voltage can be made using a voltage regulation knob adjustable in 8 steps. In constant voltage power source operation mode of the power supply, output from the main unit is directly supplied to inter-electrode gap. The current control unit consists of the necessary resistance circuitry and a controller

card. When a constant current power source mode of operation is desired, the power supplied to the IEG is controlled by the current control unit. The output current can be adjusted using the current control knob. In this case output voltage is automatically adjusted corresponding to the selected output current. A precise digital DC voltmeter (0-50V, Creative Control, Mumbai) and a DC ammeter (0-200 A, Creative Control, Mumbai) have been used to measure the voltage and current supplied to the IEG. The short circuit and overload protections are achieved by MCBs installed in the power supply input mains.

The brush assembly (Fig. 4.3) contains two Bakelite brush holders holding four intruding spring-loaded copper-carbon brushes connected to the negative terminal of the power supply. The brushes maintain a constant contact with slip ring mounted on a coupling that connects the ECH tool with the machine spindle. Brush holders are rigidly held in position by supports fixed on a brush assembly frame. The frame including the brush supports have been designed and proportioned for the slip ring configuration. The assembly is enclosed with a transparent insulating enclosure for operational safety, clear visibility and protection of the brush assembly from any electrolyte splashes.

Both the copper-carbon brush assembly and the slip ring are mounted on machine spindle with proper insulating arrangements and reciprocate as an integral unit alongwith ECH tool during stroking. This design provided a reduced overall length of tool giving a high rotational accuracy of the tool as a result of better tool stiffness.

A pulsed DC power supply provides an attractive alternative for achieving higher dimensional accuracy of processed components and a simpler tool design in electro-chemical based machining processes. Recent works on electro-chemical machining and electro-chemical grinding processes indicate that the use of shorter pulses (< 1 ms) results in better dimensional control of parts (Rajurkar et. al., 1993; Banerjee and Nandi, 1988).

Table 4.1c Materials used in electrolyte supply and cleaning system

System element	Constituents	Material (s)	Selection criteria
Electrolyte storage and settling tanks	Tanks	PVC	Corrosion resistance and thermal stability for temperature range employed in ECH.
	Insulation	Thermocol	Thermal insulation.
	Thermocouple pockets	Perspex	Strength, corrosion resistance and formability.
	Heating element and cooling coils	Copper	High thermal conductivity with corrosion resistance.
	Tank stand	Mild steel angle	Load bearing capability and ease of fabrication.
Flexible piping		Reinforced PVC	Stiffness, flexibility, corrosion resistance, thermal stability for temperature range employed in ECH.
Connectors and nipples, pipework and fittings		Stainless steel and brass	Strength, corrosion resistance and formability.
Valves		Gun metal	
Pump		Stainless steel	
Filter-cum-magnetic separator	Filter plates	Perspex	
	Wire mesh	Stainless steel	
	Screws	Brass	

Table 4.1d Materials used in work holding and positioning system

System element	Constituents	Material (s)	Selection criteria
Work holding system	Work chamber	Perspex	Good electrical, corrosion, and heat resistance with strength and formability.
	Fixture cum inlet sleeve	Perspex	
	Electrolyte inlet connector	Stainless steel	Strength and corrosion resistance.
	Mist collector	Brass	Corrosion resistance.
Hydraulic-cum -mechanical seal body		Perspex	Strength, formability and electrical; corrosion, and thermal resistance.
	Mechanical seal	Nylon	Sealing ability and low friction.
	Work table	Cast iron and bakelite	Damping, Electrical insulation
	Work positioning system	Mild steel and cast iron	Strength, damping and low friction.

Table 4.1e Materials used in frame and housing components

System element	Constituents	Material (s)	Selection criteria
Machine frame	Housing	Cast iron	Damping capacity
	Machine column	Mild steel	Strength and ease of fabrication.
Stepper motor frame		Mild steel angle	
Rotary motor pedestal		Mild steel angle	

The four expandable non-conducting honing sticks, controlled with the help of a light spring-mechanism, protrude from around the circumference of the cathode body of ECH tool. Besides maintaining a uniform tool-work gap, these sticks act to remove passivating metal oxide microfilm generated due to the electro-chemical action, preferentially from high spots to correct geometrical inaccuracies. The electrolyte supply and cleaning system serves to precisely control the quantity of the electrolyte supplied to IEG and maintains the electrolyte purity. In order to ensure a high uniformity of electrolytic conditions in the IEG, the electrolyte is supplied at several locations through the holes drilled in the tool body and also directly flushed through the inter-electrode gap. Filtration is achieved through settling and by using two double-stage magnetic-cum-mechanical filters. The work holding and positioning system including the machining chamber (referred as work chamber) has been designed with several unique features incorporating the provisions for loading/unloading, alignment and positioning of workpiece; a three-stage sealing at tool inlet to the work chamber; and mist collection. An appropriate frame and housing has been used to accommodate the various system elements together for proper functioning of the setup.

Since an electro-chemical operation involves both the electrolytic and electrical elements, material selection for the setup components was based on various relevant considerations such as, electrical conductivity, anti-corrosiveness, manufacturability, economics, etc. The materials used for the fabrication of various setup components alongwith their prime selection criteria are given in Tables 4.1a through 4.1e.

Table 4.1a Materials used in power supply system

System element	Constituents	Material (s)	Selection criteria
Brush assembly	Brushes	Copper impregnated carbon	Good electrical conductivity.
	Brush assembly	Bakelite and Perspex	Strength, formability and electrical resistance.
Wiring	Leads	Silver impregnated Copper with Teflon covering	High electrical conductivity with good insulation and heat resistance.
Connectors	Lugs	Copper	High electrical conductivity.

Table 4.1b Materials used in ECH tool and drive system

System element	Constituents	Material (s)	Selection criteria
ECH tool	Tool body	Stainless steel	Good electrical conductivity, strength, finish, form stability and corrosion resistance.
		Teflon	High electrical, heat and corrosion resistance with strength and formability.
	Connectors	Copper	High electrical conductivity.
	Coupling	Mild steel	Strength and ease in fabrication.
	Slip ring	Copper with ceramic insulation	Electrical conductivity, strength, and insulation.
	Honing stick feed-out springs	Brass	Corrosion resistance and stiffness.
Drives	Couplings and frame	Mild steel	Strength and ease in fabrication.

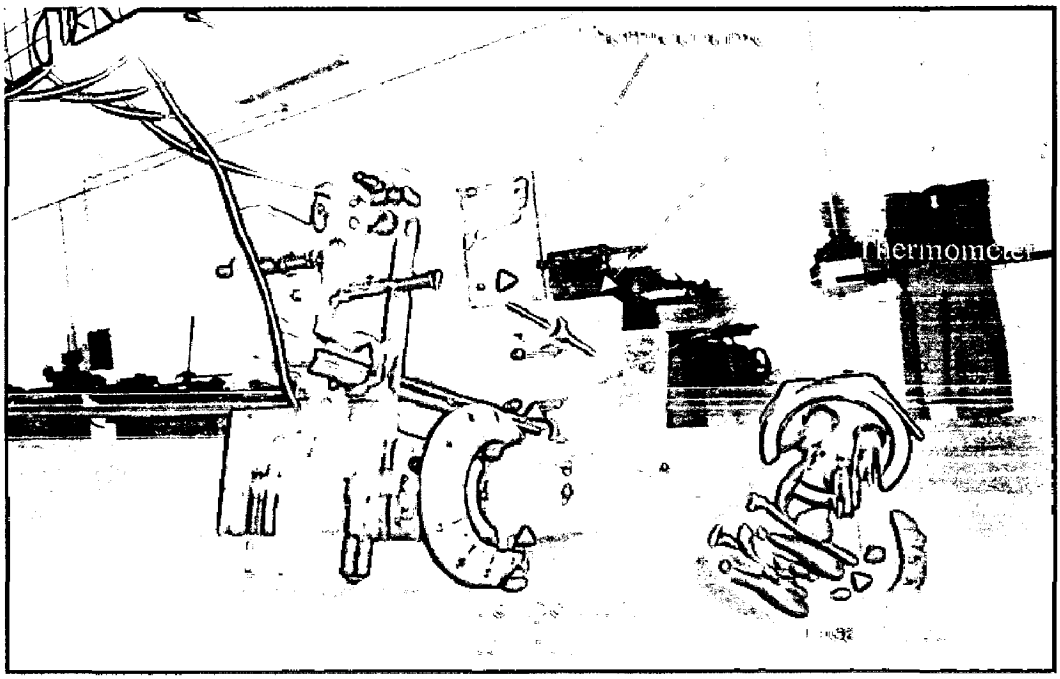

Fig. 4.4 Electrolyte heating system elements

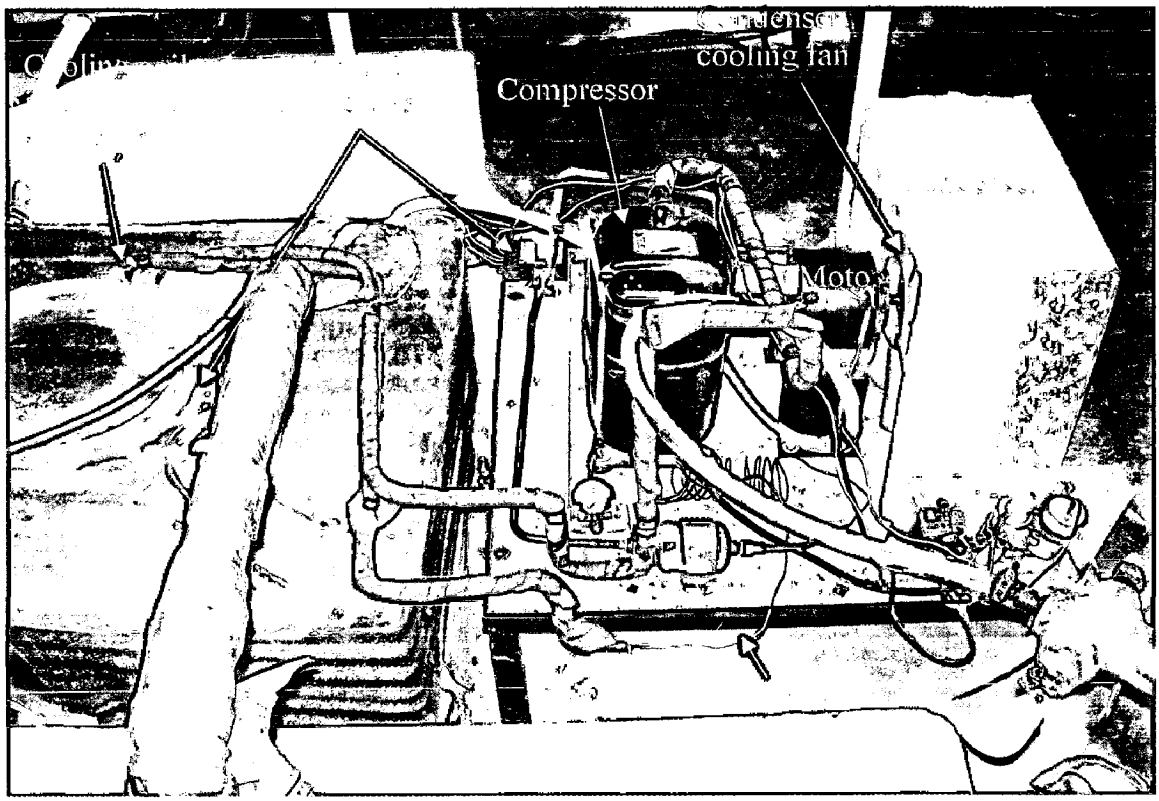

Fig. 4.5 Electrolyte cooling system

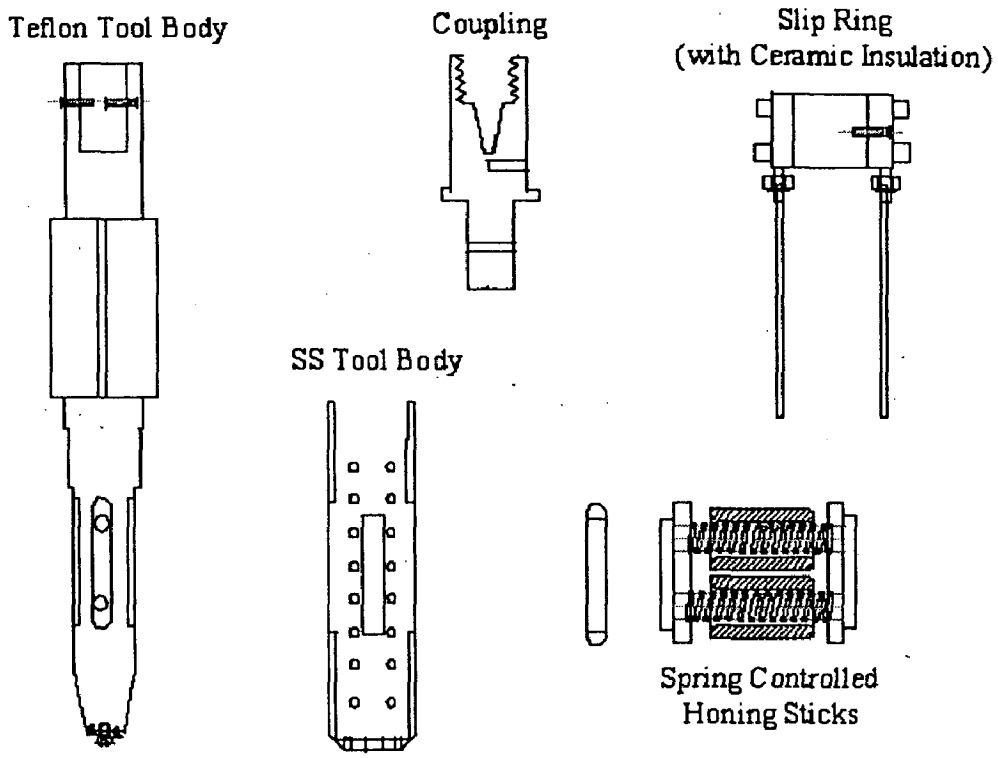

Fig. 4.10 ECH tool details

4.3.1.1 Teflon body

Teflon body forms the basic structure of tool upon which other elements are mounted. It has been proportioned optimizing several aspects such as work size consideration, machine clear span, available machining stroke, and sealing effectiveness. It is machined from a single piece of Teflon to achieve high stiffness and rotational accuracy of ECH tool.

The stainless steel tool body is slide fitted at the top with lower portion of Teflon body and screwed firmly at bottom using three brass screws. Central base screw and top slide-fit portion of Teflon body together ensure the location accuracy of the SS tool body while torsional effects are taken care of by two other base screws positioned at appropriate radial distance and the screws used to fix copper connector to SS body. The copper connector screws are screwed 25 mm deep in brass sleeves fitted in the slide-fit portion of Teflon body. The slide-fit portion also ensures proper sealing at the juncture of SS and Teflon bodies. The clearance between SS and Teflon body provides electrolyte flow path for distributing

4.2.5 Electrolyte Supply Pump

Requirements- the limiting current that can be used in the process depends on boiling point of electrolyte which, inturn, is governed by electrolyte pressure. It also controls the condition of electrolyte in the machining gap. Similarly, electrolyte flow rate affects heat removal from the gap and provides desired electrolyte velocity in cutting zone and hence, it is another critical factor determining electrolyte condition in the gap. These two parameters, in turn, determine the uniformity of electrolytic metal removal. The pump is required to be made of an anti-corrosive material. Keeping in view the range of electrolyte pressure and flow rate employed in ECH, a stainless steel pump was selected and procured. The pump (ROTO PUMPS Ltd., Model RDAA 532 R7CF3E), is capable of developing pressures upto 1.0 Mpa and flow rate upto 100 lpm. The outlet pressure of the pump is automatically adjusted depending upon the selected electrolyte flow rate and flow path resistance. Pump has been designed specifically for the intended application by the manufacturer. The electrolyte pump unit consists of a 3.7 kW electric motor, a flexible bushed-pin coupling and a pump. Technical data of the pump unit is given in Appendix-A.

4.2.6 Pressure and Flow Controls

Electrolyte from the pump discharge is directly supplied to the hydraulic seal provided at tool inlet to the work chamber. Required sealing pressure can be achieved by adjusting a flow-regulating valve provided in the sealing line. Since, the flow resistance of the hydraulic seal depends upon electrolyte flow rate through it, seal chamber pressure is automatically regulated by the pump.

Pressure and flow of electrolyte supplied to the work chamber is exercised at the pump discharge by adjusting the flow-regulating valves provided in electrolyte supply to work chamber and recirculation to electrolyte storage tank as shown in Fig. 4.1.

Regulating valves are provided in the return lines from settling tank to electrolyte storage tank that can be regulated keeping in view the selected electrolyte flow rate for processing to achieve better settling effects during operation. Further, between the two subsequent operations, they can be closed so that electrolyte can be stored in the setting tank for a proper settling of suspended machining products.

4.2.7 Piping

The piping used in the electrolyte supply and cleaning system is of both the rigid and flexible type, and made of anti-corrosive materials as given in Table 4.1b. The sizes of pipes have been decided on the basis of pressure and flow conditions in the line, and these are given in Appendix-A.

4.2.8 Pressure, Flow and Temperature Measurements

Inlet electrolyte pressure and flow rate to the work chamber is measured using a pressure gauge and ROTA meter (Rotomech) installed in chamber inlet line. ROTA meter has all its components made of stainless steel and fitted in a Perspex body. The temperature of electrolyte inlet to work chamber is measured by a thermometer (Immersion Zeal, England) as well as by digital temperature controller (SZ-7510-E, sub-zero^{TM}) installed in electrolyte storage tank and the outlet temperature is measured using a digital temperature indicator (Model 1550, Digitech) fitted in the settling tank.

4.2.9 Mist Collector

For continuous removal of generated gases and electrolyte mist from the work chamber, a brass nipple with stainless steel mesh is fitted in work chamber top zone at a location having minimum influence of electrolyte splashes. While passing through the mesh electrolyte vapors in the mist are removed in form of droplets. In order to take care of any

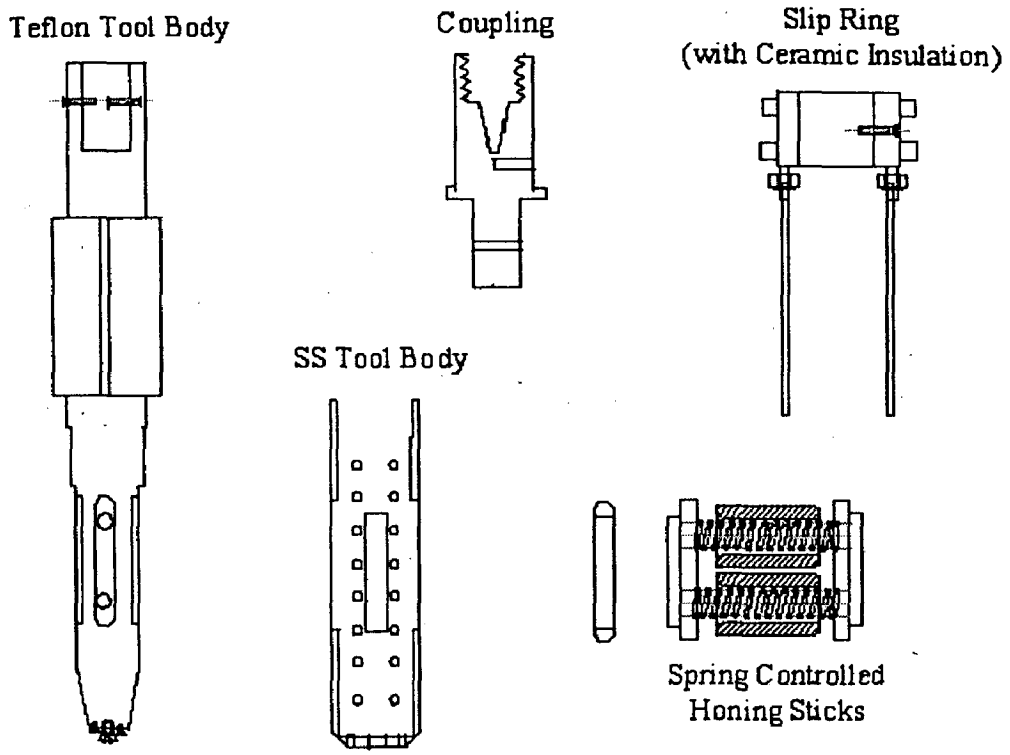

Fig. 4.10 ECH tool details

4.3.1.1 Teflon body

Teflon body forms the basic structure of tool upon which other elements are mounted. It has been proportioned optimizing several aspects such as work size consideration, machine clear span, available machining stroke, and sealing effectiveness. It is machined from a single piece of Teflon to achieve high stiffness and rotational accuracy of ECH tool.

The stainless steel tool body is slide fitted at the top with lower portion of Teflon body and screwed firmly at bottom using three brass screws. Central base screw and top slide-fit portion of Teflon body together ensure the location accuracy of the SS tool body while torsional effects are taken care of by two other base screws positioned at appropriate radial distance and the screws used to fix copper connector to SS body. The copper connector screws are screwed 25 mm deep in brass sleeves fitted in the slide-fit portion of Teflon body. The slide-fit portion also ensures proper sealing at the juncture of SS and Teflon bodies. The clearance between SS and Teflon body provides electrolyte flow path for distributing

4.3.1.4 Tool coupling

Tool body is attached to the machine spindle with the help of a precisely machined coupling to ensure a high rotational accuracy of the tool. The taper pin fitting arrangement ensures an accurate centering while coupling is screwed to the machine spindle. Coupling remains insulated from the current carrying parts of the tool.

4.3.1.5 Slip ring and copper connectors

Slip ring contains two copper rings with ceramic insulation. It is press fitted to the coupling. Slip ring is connected to the negative of the power supply though a copper-carbon brush assembly. Outlet terminals of slip ring are connected to the stainless steel tool body using two rigid copper connectors. These connectors are press fitted in the slots made in seal hub. Connectors have been shaped-flushed with seal hub surface and SS tool body. Their ends connecting SS body have been shaped in a manner to provide proper seating with sufficient bearing area to avoid any localized heating due to contact resistance. Connectors are held rigidly with SS tool body using counter sunk screws into the brass sleeves fitted in Teflon body. Additional rigidity of connectors against centrifugal force at higher rotational speeds is also ensured by the both- end fastening restraint of connectors.

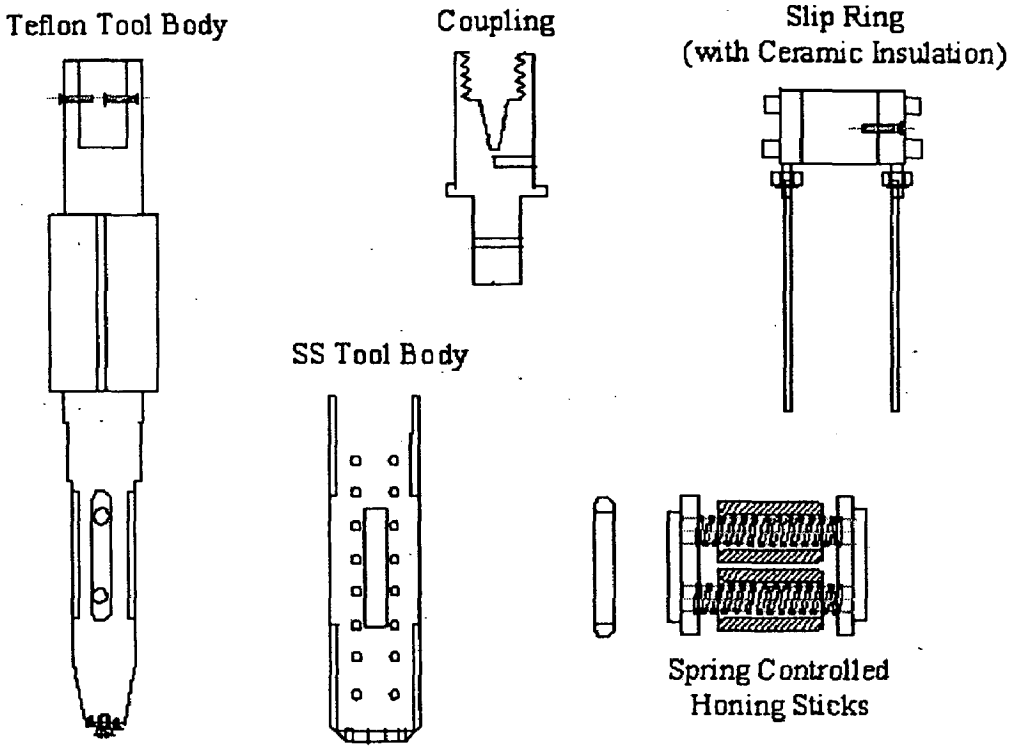

Fig. 4.10 ECH tool details

4.3.1.1 Teflon body

Teflon body forms the basic structure of tool upon which other elements are mounted. It has been proportioned optimizing several aspects such as work size consideration, machine clear span, available machining stroke, and sealing effectiveness. It is machined from a single piece of Teflon to achieve high stiffness and rotational accuracy of ECH tool.

The stainless steel tool body is slide fitted at the top with lower portion of Teflon body and screwed firmly at bottom using three brass screws. Central base screw and top slide-fit portion of Teflon body together ensure the location accuracy of the SS tool body while torsional effects are taken care of by two other base screws positioned at appropriate radial distance and the screws used to fix copper connector to SS body. The copper connector screws are screwed 25 mm deep in brass sleeves fitted in the slide-fit portion of Teflon body. The slide-fit portion also ensures proper sealing at the juncture of SS and Teflon bodies. The clearance between SS and Teflon body provides electrolyte flow path for distributing

electrolyte in IEG through several holes drilled in SS tool body. The clearance is so chosen as to achieve a low electrolyte flow resistance, proper operation of honing stick spring mechanism and ease of assembly. The bottom portion has been machined taper for smooth entry of electrolyte into the tool. The spring mechanism for controlling honing stick-out is accommodated in four through holes drilled in the Teflon body. To avoid crossing of control springs, holes of the two sets are drilled with an offset of 10 mm. Copper sleeves are press fitted in holes to ensure a smooth operation of springs. Four shaped slots are machined covering two hole ends to contain and guide the honing sticks during operation. Depth of slots has been kept slightly greater than thickness of stick so that they can be fully pressed into Teflon body for easy dismantling.

Middle portion of Teflon body is designed to serve as the sealing hub for hydraulic and mechanical seals and also to provide 1st stage sealing to deflect exiting electrolyte jet from the work-bore. Accordingly, its diameter is kept more than that of stainless steel tool body outer diameter. Length of sealing hub is kept sufficient enough to provide full coverage of seals during entire stroking.

The upper portion of Teflon body is press fitted to a coupling, especially machined to connect the tool with machine spindle, and locked with two screws. It has been designed in such a way so as to avoid any contact between the metallic coupling and current carrying copper conductors of the slip ring.

4.3.1.2 Stainless steel tool body

ECH tool consists of a hollow stainless steel body with several rows of holes drilled in it to allow fairly uniform distribution of electrolyte in IEG. Several ports have been machined in its bottom plate for electrolyte entry into the clearance between SS and Teflon bodies. SS tool body acts as a non-expanding cathode in the process and therefore, is accurately dimensioned for the bore of the selected workpiece. Length of SS body has been decided such that it maintains full coverage of work-bore during entire stoking. Expandable, non-conducting honing sticks protrude from four locations around the tool's circumference.

4.3.1.3 Spring controlled honing sticks

The honing stick control mechanism consists of two sets of 90° cross-placed spring controlled honing sticks. Each set comprises of two springs placed at 50 mm distance and two honing sticks as shown in Fig. 4.10. These honing sticks are identical to those used in conventional honing operation, except that they must resist corrosiveness of electrolyte and should be non-conductive. Sticks are especially shaped for their proper operation. Length of honing sticks is slightly more than half the length of work-bore. Silicon carbide honing sticks of different grit sizes have been used keeping in view the work material properties. Springs are made of brass coils of stiffness 0.47kN/m. Length of springs is precisely controlled so as to provide equal desired stick-out pressure to honing sticks. Springs of different stiffness can be employed to have a range of stick-out pressure. As machining proceeds the tool-workpiece gap increases and honing sticks expand to maintain constant contact with the machined surface.

4.3.1.4 Tool coupling

Tool body is attached to the machine spindle with the help of a precisely machined coupling to ensure a high rotational accuracy of the tool. The taper pin fitting arrangement ensures an accurate centering while coupling is screwed to the machine spindle. Coupling remains insulated from the current carrying parts of the tool.

4.3.1.5 Slip ring and copper connectors

Slip ring contains two copper rings with ceramic insulation. It is press fitted to the coupling. Slip ring is connected to the negative of the power supply though a copper-carbon brush assembly. Outlet terminals of slip ring are connected to the stainless steel tool body using two rigid copper connectors. These connectors are press fitted in the slots made in seal hub. Connectors have been shaped-flushed with seal hub surface and SS tool body. Their ends connecting SS body have been shaped in a manner to provide proper seating with sufficient bearing area to avoid any localized heating due to contact resistance. Connectors are held rigidly with SS tool body using counter sunk screws into the brass sleeves fitted in Teflon body. Additional rigidity of connectors against centrifugal force at higher rotational speeds is also ensured by the both- end fastening restraint of connectors.

4.3.2 Tool Drives

The primary function of drives is to impart the tool a controlled generating motion of simultaneous rotation and reciprocation. Drives have been selected keeping in view the various aspects including a precise speed control, desired speed range and torque characteristics of drives. Tool driving system comprises of a rotary drive, a reciprocating drive and the driving head (Fig. 4.11).

4.3.2.1 Rotary drive

Rotary drive consists of a DC motor, speed controller, voltage stabilizer, coupling and bevel gearing as shown in Fig. 4.12. A 1 K.W. speed controlled DC servomotor, with speeds adjustable up to 1500 rpm, has been selected. DC motor besides offering fine control over speeds, is characterized by a stable torque over a range of speeds.

Rotational speed of motor can be controlled by adjusting a knob provided with the speed controller. Speed is measured using a digital tachometer (Model HTM 590, Systems & Controls, Bangalore). Power input to the speed controller is supplied through a 2 KVA voltage stabilizer (Spectrum Power Control, New Delhi) to take care of even a minor variation in the input supply voltage. Motor is mounted on a separate pedestal to avoid any vibrational influence to the machining zone. Motor shaft is connected to the machine spindle using 1:1 bevel gearing through a coupling. Coupling is supported on motor pedestal using a ball bearing. Coupling details are given in Fig. 4.13.

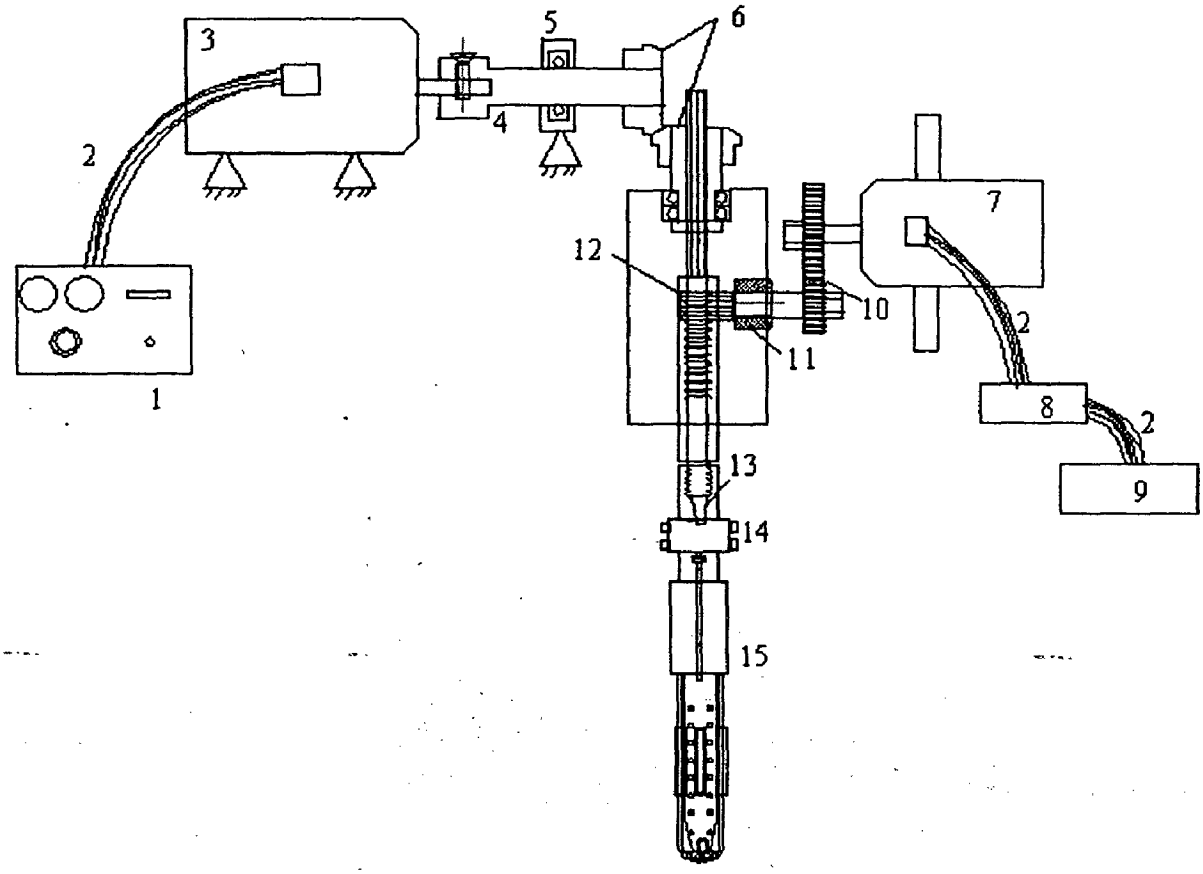

(1) Speed controller (2) Wire cable (3) Speed controlled DC motor (4) Coupling (5) Bearing (6) 1:1 Bevel gearing (7) Programmable speed controlled stepper motors (8) Interface card (9) Microprocessor (10) 1:2 Gearing (11) Bushing (12) Rack and pinion drive (13) Taper pin (14) Slip ring and carbon brush assembly (15) ECH tool

Fig. 4.11 Schematic of ECH tool drives

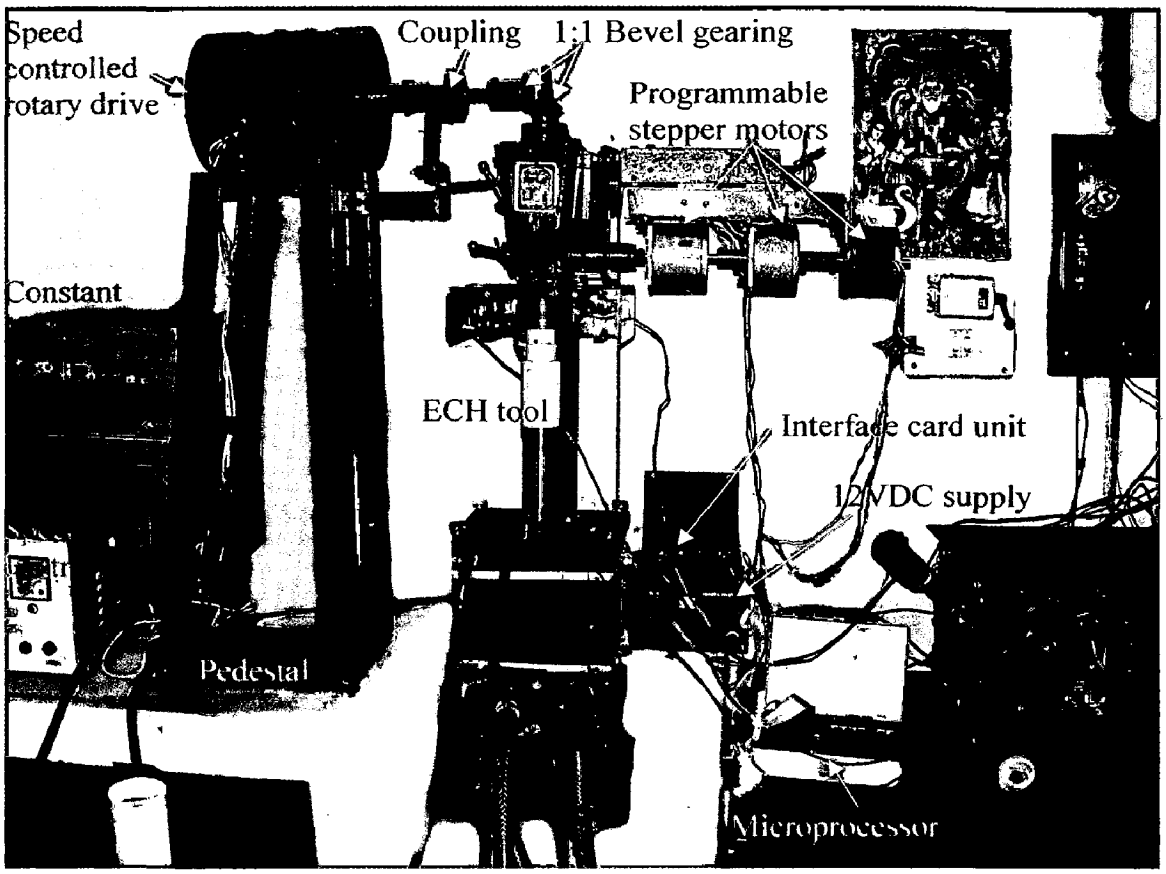

Fig. 4.12 Photographic view of ECH tool drives

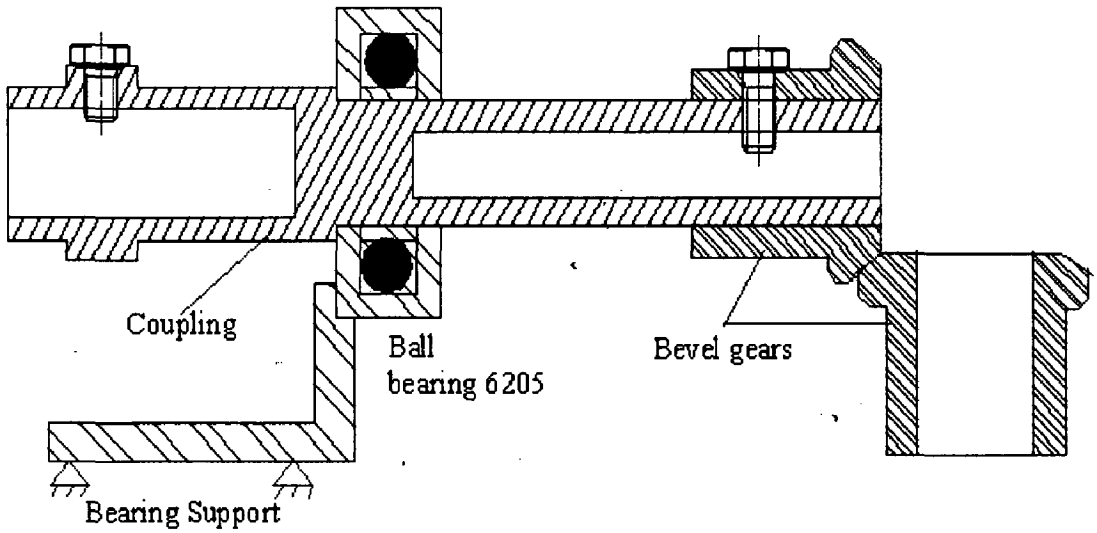

Fig. 4.13 Details of rotary drive coupling

4.2.5 Electrolyte Supply Pump

Requirements- the limiting current that can be used in the process depends on boiling point of electrolyte which, inturn, is governed by electrolyte pressure. It also controls the condition of electrolyte in the machining gap. Similarly, electrolyte flow rate affects heat removal from the gap and provides desired electrolyte velocity in cutting zone and hence, it is another critical factor determining electrolyte condition in the gap. These two parameters, in turn, determine the uniformity of electrolytic metal removal. The pump is required to be made of an anti-corrosive material. Keeping in view the range of electrolyte pressure and flow rate employed in ECH, a stainless steel pump was selected and procured. The pump (ROTO PUMPS Ltd., Model RDAA 532 R7CF3E), is capable of developing pressures upto 1.0 Mpa and flow rate upto 100 lpm. The outlet pressure of the pump is automatically adjusted depending upon the selected electrolyte flow rate and flow path resistance. Pump has been designed specifically for the intended application by the manufacturer. The electrolyte pump unit consists of a 3.7 kW electric motor, a flexible bushed-pin coupling and a pump. Technical data of the pump unit is given in Appendix-A.

4.2.6 Pressure and Flow Controls

Electrolyte from the pump discharge is directly supplied to the hydraulic seal provided at tool inlet to the work chamber. Required sealing pressure can be achieved by adjusting a flow-regulating valve provided in the sealing line. Since, the flow resistance of the hydraulic seal depends upon electrolyte flow rate through it, seal chamber pressure is automatically regulated by the pump.

Pressure and flow of electrolyte supplied to the work chamber is exercised at the pump discharge by adjusting the flow-regulating valves provided in electrolyte supply to work chamber and recirculation to electrolyte storage tank as shown in Fig. 4.1.

Regulating valves are provided in the return lines from settling tank to electrolyte storage tank that can be regulated keeping in view the selected electrolyte flow rate for processing to achieve better settling effects during operation. Further, between the two subsequent operations, they can be closed so that electrolyte can be stored in the setting tank for a proper settling of suspended machining products.

4.2.7 Piping

The piping used in the electrolyte supply and cleaning system is of both the rigid and flexible type, and made of anti-corrosive materials as given in Table 4.1b. The sizes of pipes have been decided on the basis of pressure and flow conditions in the line, and these are given in Appendix-A.

4.2.8 Pressure, Flow and Temperature Measurements

Inlet electrolyte pressure and flow rate to the work chamber is measured using a pressure gauge and ROTA meter (Rotomech) installed in chamber inlet line. ROTA meter has all its components made of stainless steel and fitted in a Perspex body. The temperature of electrolyte inlet to work chamber is measured by a thermometer (Immersion Zeal, England) as well as by digital temperature controller (SZ-7510-E, sub-zero^{TM}) installed in electrolyte storage tank and the outlet temperature is measured using a digital temperature indicator (Model 1550, Digitech) fitted in the settling tank.

4.2.9 Mist Collector

For continuous removal of generated gases and electrolyte mist from the work chamber, a brass nipple with stainless steel mesh is fitted in work chamber top zone at a location having minimum influence of electrolyte splashes. While passing through the mesh electrolyte vapors in the mist are removed in form of droplets. In order to take care of any

carry-over of electrolyte, mist is first delivered to the settling tank from where it is ventilated outside the machining area into the atmosphere.

4.3 ECH TOOL AND DRIVES

4.3.1 ECH Tool

ECH tool is the most crucial element of electro-chemical honing process. It performs multi-functions: acting as the cathode tool for electrolytic dissolution, accommodating honing sticks with their control mechanism and regulating their action to provide a selective abrasion of metal oxide microfilm, providing a good coordination of these two actions, directing and distributing electrolyte in IEG so as to achieve maximum uniformity of electrolyte condition in the gap, and providing desired generating motion of simultaneous rotation and translation to honing sticks. Effective realization of these functions, coupled with precise fabrication of tool for the work sizes, high rotational and reciprocating accuracy, and stability under high electrolyte flow thrusts, makes the tool design highly complex.

The ECH tool, shown in Fig. 4.9, has been designed and fabricated considering all the above requirements as well as incorporating several other impressive features uniquely. Tool provides 1st stage sealing, at tool inlet to work chamber, in that electrolyte exiting from IEG is deflected sideways by seal hub of the tool. Thus, the direct electrolytic flow impact in the sealing zone is reduced to a minimum and hence, the hydraulic seal load is much reduced. The tool has been designed to permit both the modes of electrolyte supply to IEG: direct through flushing and distribution to different locations in IEG via tool itself: leading to greater uniformity of electrolytic condition in gap.

Fig.4.10 gives constructional details of the ECH tool. The tool is comprised of (i) a Teflon body, (ii) stainless steel tool body, (iii) spring controlled honing sticks, (iv) coupling, and (v) slip ring and connectors. The material selection aspects for various components of ECH tool have been already described in Table 4.2b.

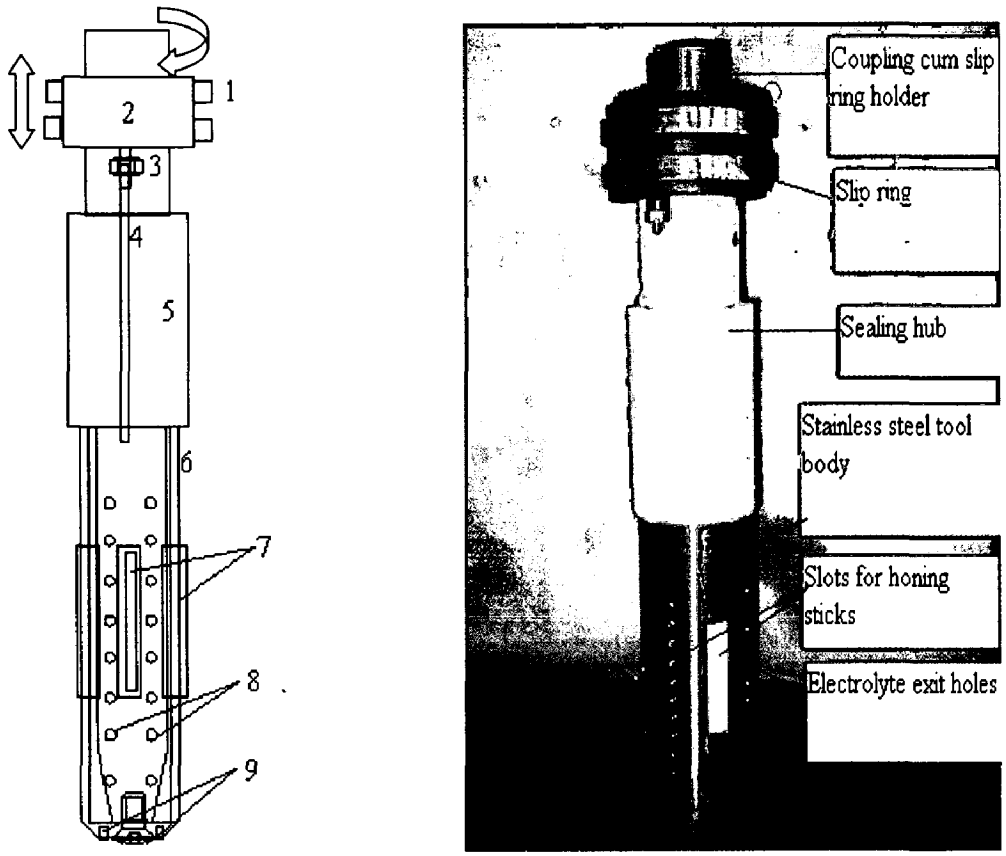

(1) Carbon brush assembly (2) Slip ring (with ceramic insulation) (3) Copper lug (4) Copper connector (5) Seal hub (6) Stainless steel tool body (7) Spring controlled honing sticks (8) Electrolyte exit holes (9) Electrolyte inlet ports

Fig. 4.9 ECH tool

4.2.3 Filtration

Besides the settling, effective filtration is achieved using magnetic separator- cum-mechanical filters provided at two distinct locations in the electrolyte circuitry. First stage filtration is done at the outlet of the settling tank and the second stage filtration is performed at the work chamber inlet. Filters are composed of a coarse stainless steel wire mesh (mesh size 450μm), a permanent magnet and a fine stainless steel wire mesh (mesh size 150μm) clamped between two fixture plates for achieving an effective filtration in sequential stages as shown in Fig. 4.6. Fixture plates are clamped using four brass fasteners to provide ease of assembly and dismantling for cleaning purposes. The constructional and assembly details of the 1^{st} stage and 2^{nd} stage magnetic separator-cum-mechanical filters are given in the Fig. 4.7 and Fig. 4.8 respectively.

4.2.4 Electrolyte Recirculation Pump

A small electrolyte recirculation pump fitted in electrolyte storage tank is used for stirring the electrolyte to achieve a quick initial temperature built-up of electrolyte.

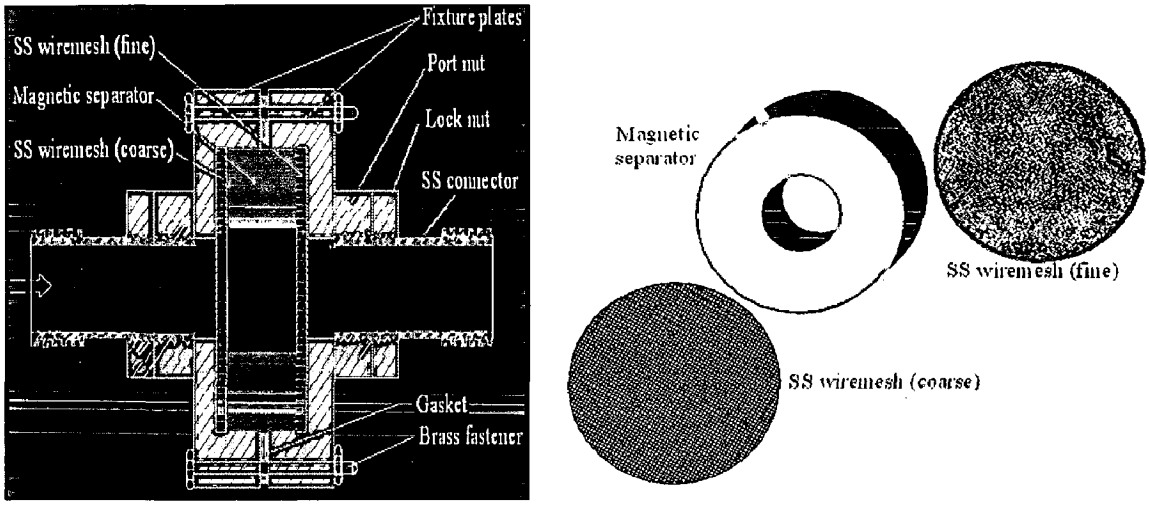

Fig. 4.6 Magnetic separator-cum-mechanical filter

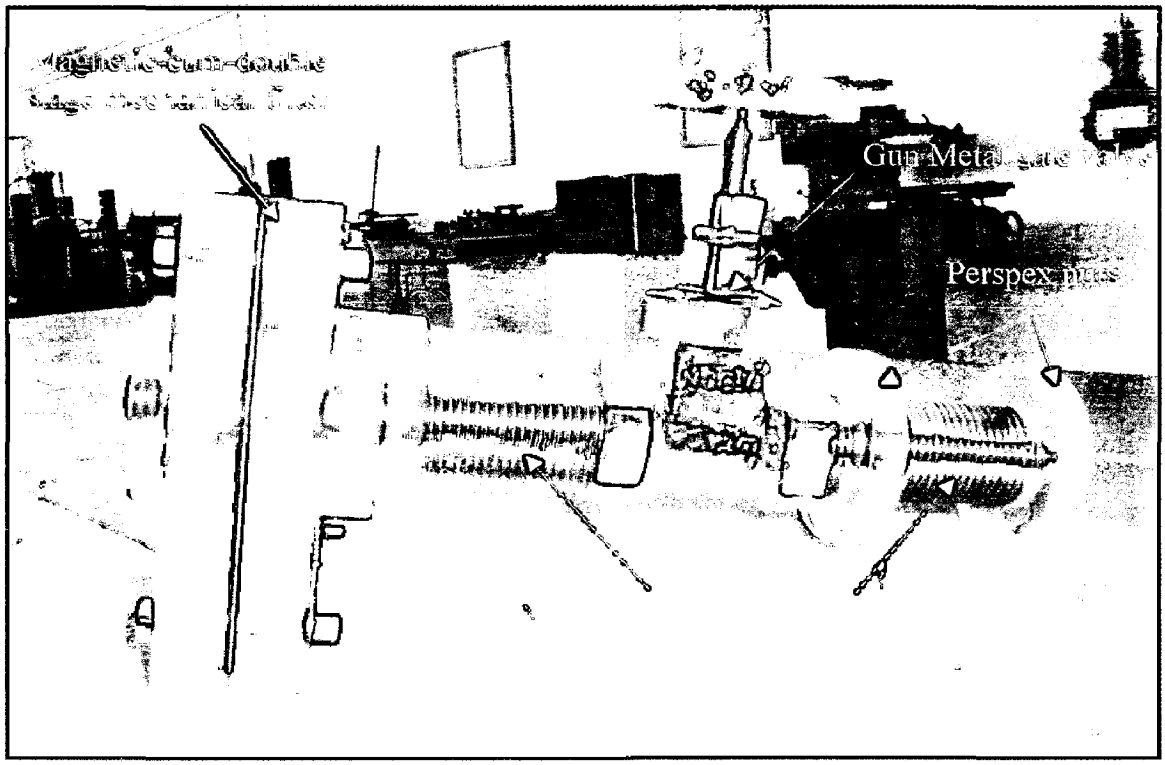

Fig. 4.7a) Filter assembly

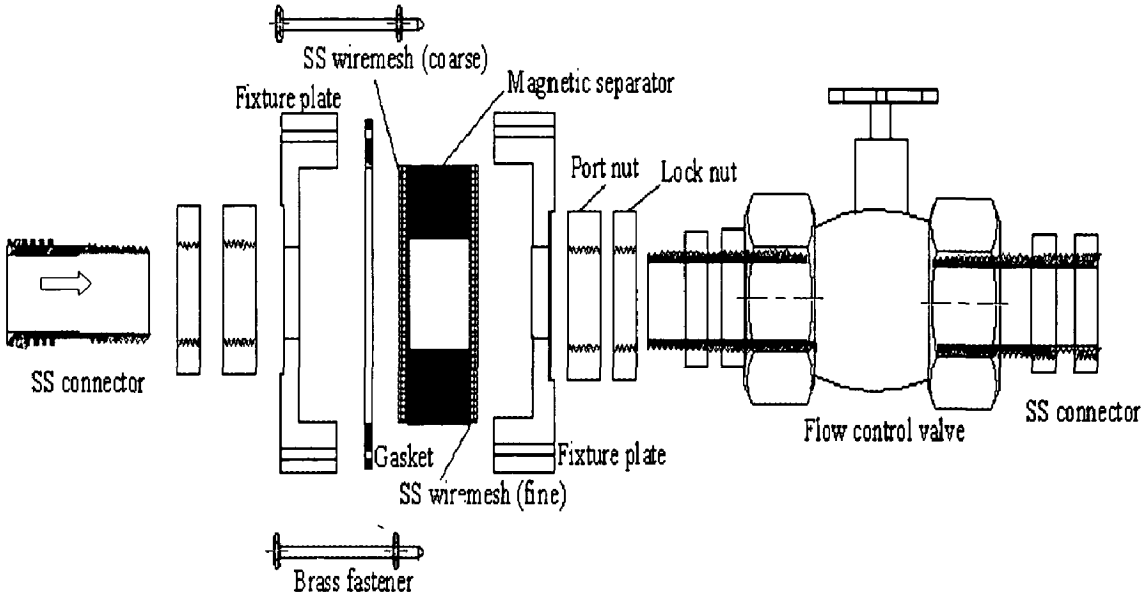

Fig. 4.7b) Constructional detail

Fig. 4.7 1st stage magnetic separator-cum-mechanical filter details

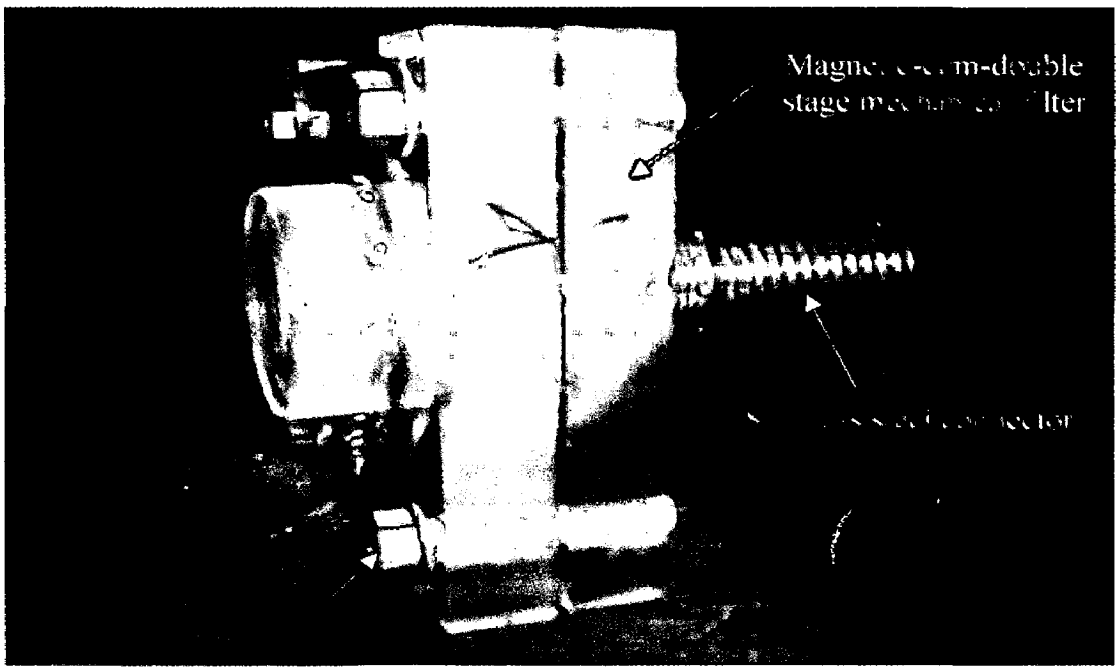

Fig. 4.8a) Filter assembly

G13034

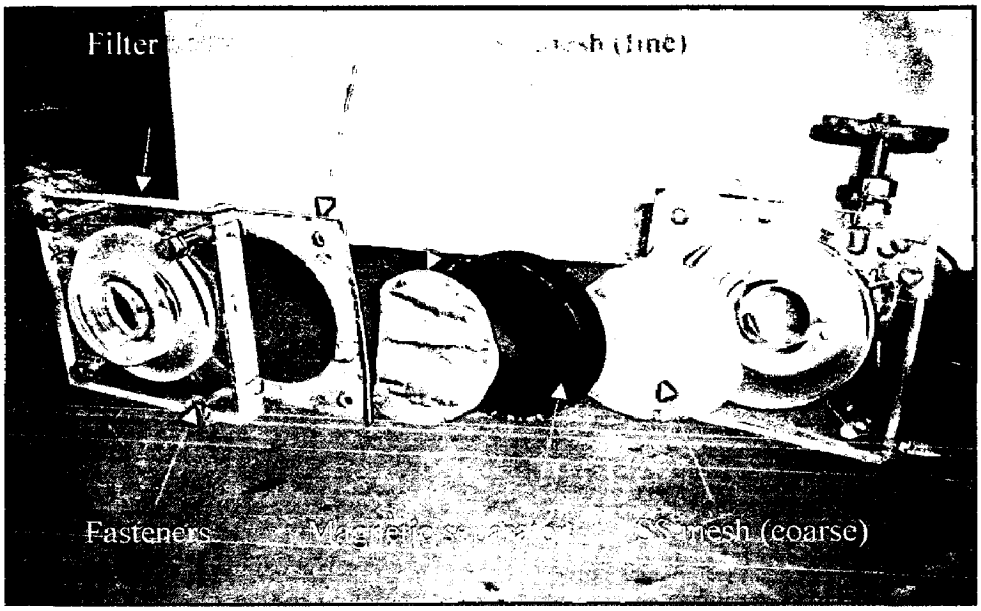

Fig. 4.8b) Assembly details

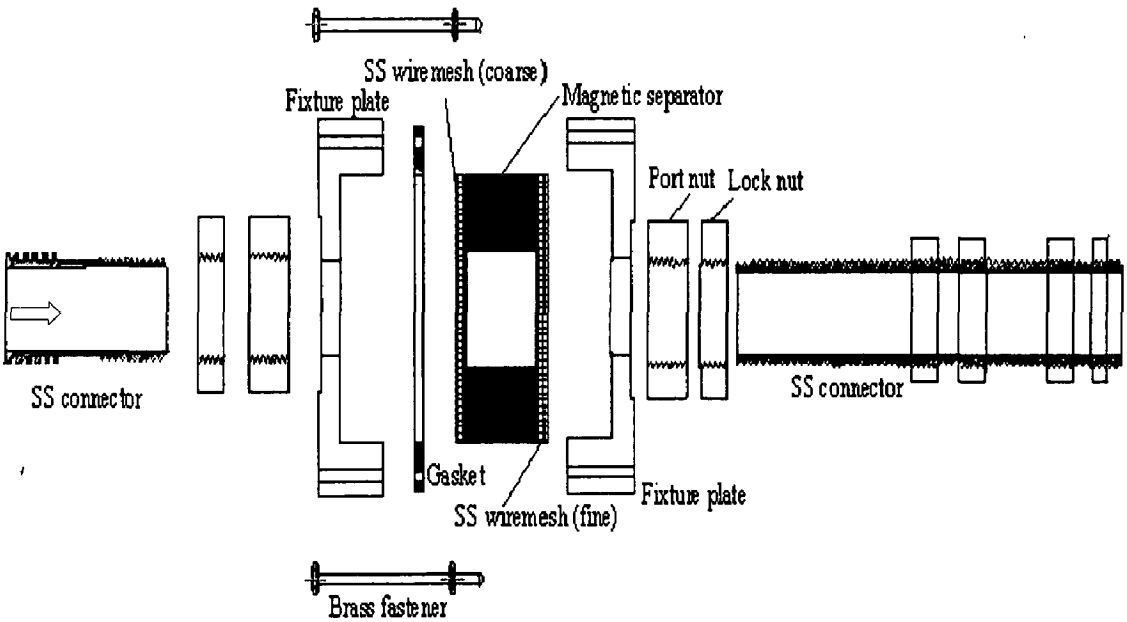

Fig.4.8c) Constructional details

Fig. 4.8 2nd stage magnetic separator-cum-mechanical filter details

4.3.2.2 Reciprocating drive

Reciprocating speed influences the finish and characteristic crosshatch angle of the machined surface. Therefore, a programmable stepper motor unit consisting of 3 tandom-compounded stepper motors, controlled by a Vinytics 8501 microprocessor training kit through interface cards, has been utilized for the reciprocation of the tool (Fig. 4.12). Stepper motors are characterized by their high holding toque, rotation accuracy, precise speed control and instant reversal as desired in ECH process for reciprocating the tool. Three stepper motors are coupled in series for obtaining a sufficiently high torque required for reciprocation. Motors are housed in a fabricated bracket attached to the driving head. Programming was done to achieve a proper synchronized operation of stepper motors. Stroke length and speed of translation of tool is adjustable as per the program.

Assembly language programs (given in Appendix-A) were stored in microprocessor kit for forward and backward movements of stepper motors for the selected speed and stroke length of tool. The Vynitics microprocessor training kit is powered by a 12V DC supply. The program and necessary commands can be entered through the keyboard connected to the microprocessor unit. The output of the executing program is sent to the interface cards through input/output port of the microprocessor. The interface card unit supplies 12V power to the stepper motors depending upon the signal it receives from the i/o port of microprocessor. Stepper motors are directly coupled to a spindle which in turn is connected to the reciprocating unit through a rack and pinion mechanism. Motors can also be fitted using a 2:1 gearing (Fig. 4.14) in case a higher speed range is desired.

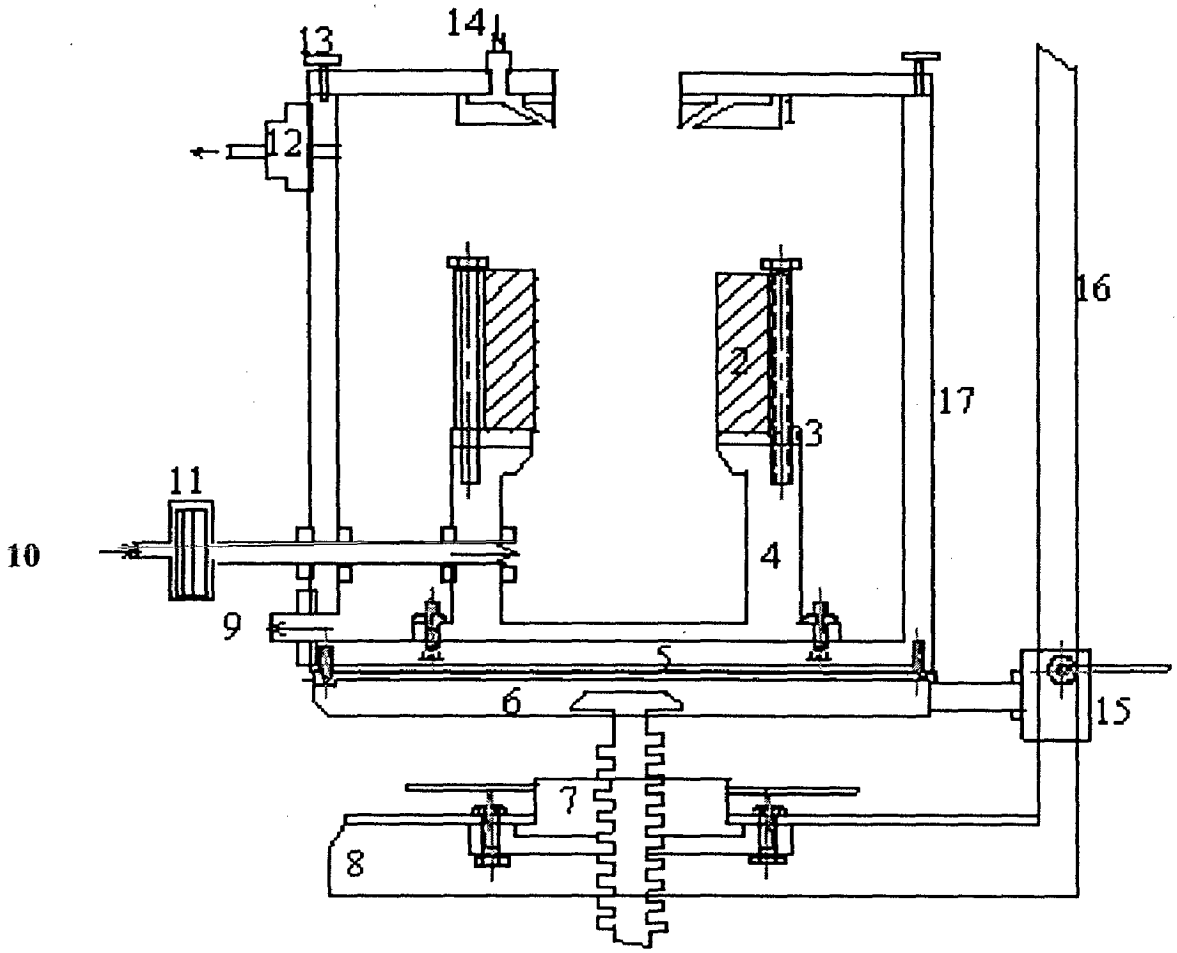

(1) Hydraulic-cum-mechanical seal body (2) Workpiece (3) Rubber plate (4) Fixture-cum-electrolyte inlet sleeve (5) Insulator (6) Work table (7) Work positioning system (8) Machine base (9) Electrolyte outlet (10) Electrolyte inlet (11) Filter-cum-magnetic separator (12) Mist collector (13) Fly screw (14) Hydraulic seal inlet (15) Swivel system (16) Machine column (17) Work chamber

Fig. 4.15 Work holding and positioning system

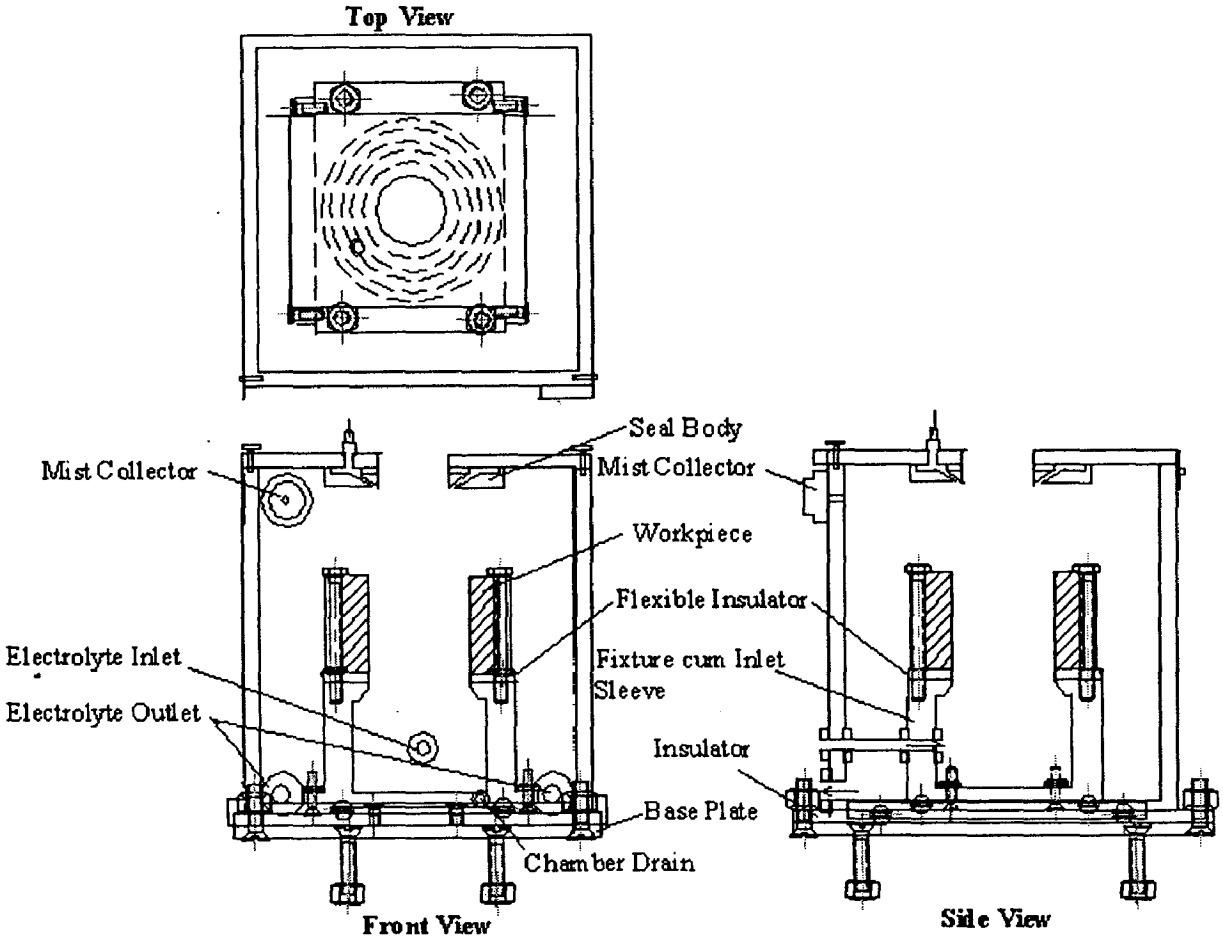

Fig. 4.16 Details of work chamber

Electrolyte is supplied to the work fixture using a stainless steel connector, which after being screwed through in work chamber and fixture, is locked and sealed using Perspex locknuts and rubber gaskets. Inlet end of the connector contains the 2nd stage filter-cum-magnetic separator. Workpiece is mounted using four sleeved bolts, which are screwed in fixture top plate with a rubber gasket interposed in between to achieve free float condition to work during machining. Detachable top cover of the work chamber, fitted with fly bolts and C clamps can be lifted up for measuring the work-tool gap. Work chamber is fitted with stainless steel connectors (Fig. 4.18) for providing two regular and one chamber drains. A mist collector is located in the top portion of the chamber for removing salt laden vapors and gases generated during the process.

4.2.3 Filtration

Besides the settling, effective filtration is achieved using magnetic separator- cum-mechanical filters provided at two distinct locations in the electrolyte circuitry. First stage filtration is done at the outlet of the settling tank and the second stage filtration is performed at the work chamber inlet. Filters are composed of a coarse stainless steel wire mesh (mesh size 450μm), a permanent magnet and a fine stainless steel wire mesh (mesh size 150μm) clamped between two fixture plates for achieving an effective filtration in sequential stages as shown in Fig. 4.6. Fixture plates are clamped using four brass fasteners to provide ease of assembly and dismantling for cleaning purposes. The constructional and assembly details of the 1st stage and 2nd stage magnetic separator-cum-mechanical filters are given in the Fig. 4.7 and Fig. 4.8 respectively.

4.2.4 Electrolyte Recirculation Pump

A small electrolyte recirculation pump fitted in electrolyte storage tank is used for stirring the electrolyte to achieve a quick initial temperature built-up of electrolyte.

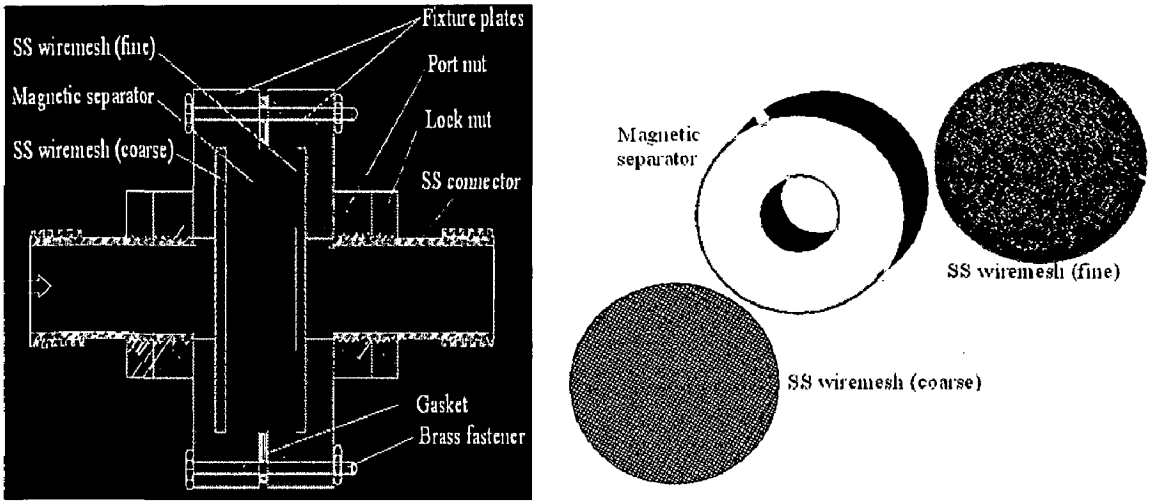

Fig. 4.6 Magnetic separator-cum-mechanical filter

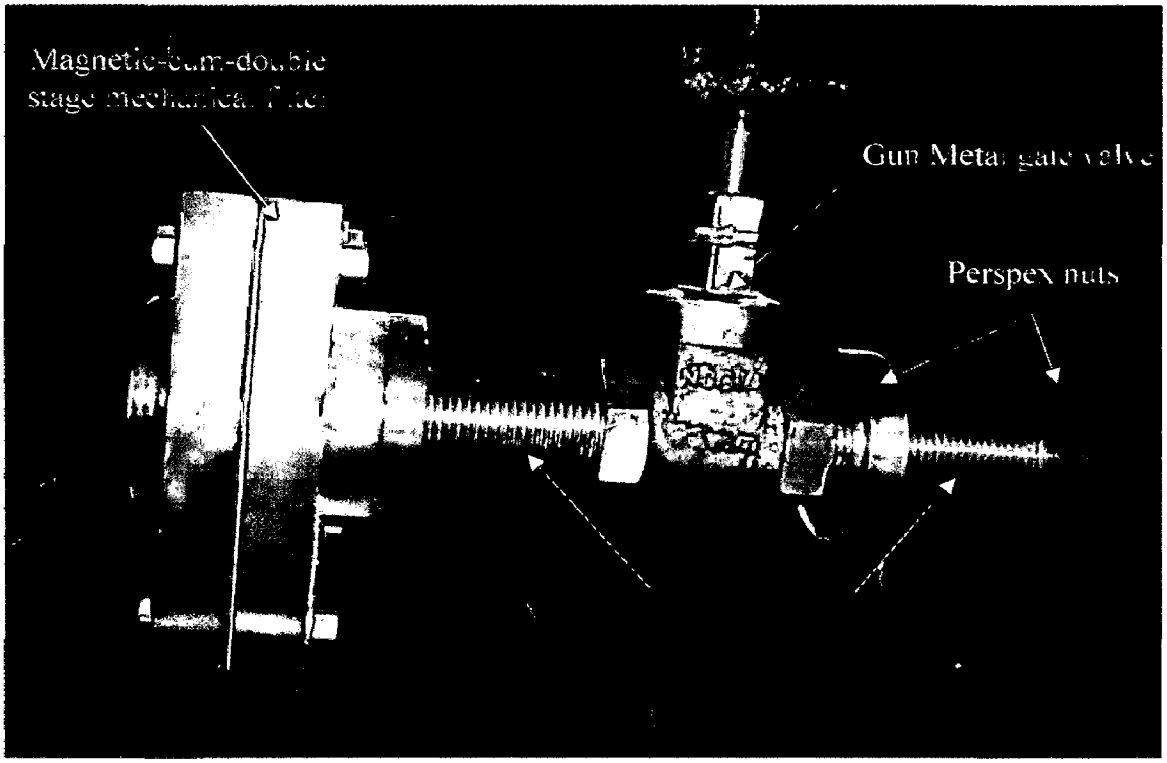

Fig. 4.7a) Filter assembly

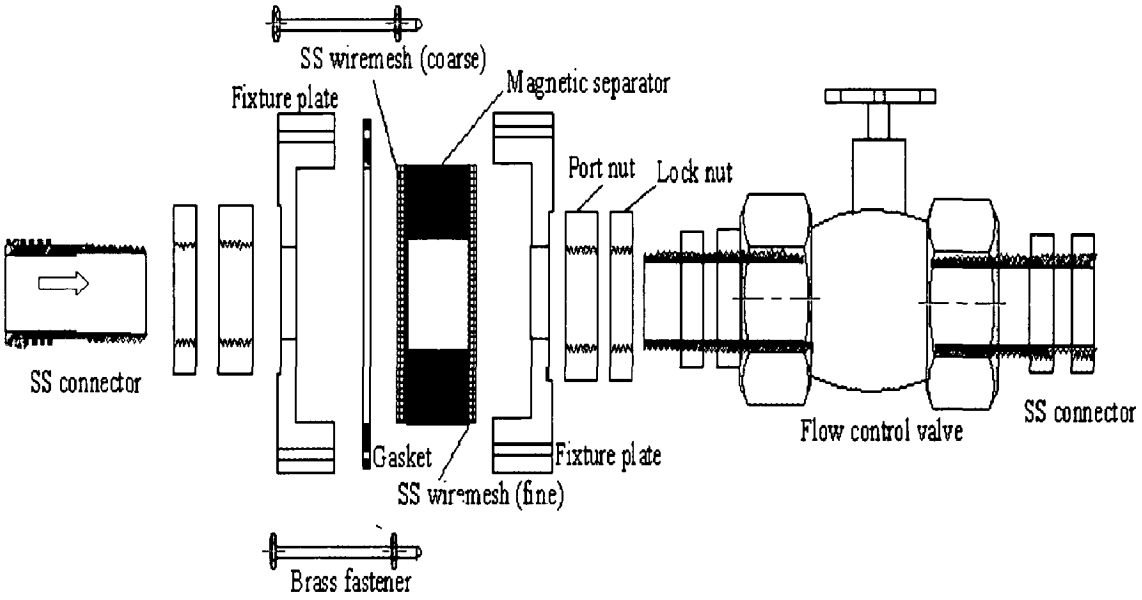

Fig. 4.7b) Constructional detail

Fig. 4.7 1st stage magnetic separator-cum-mechanical filter details

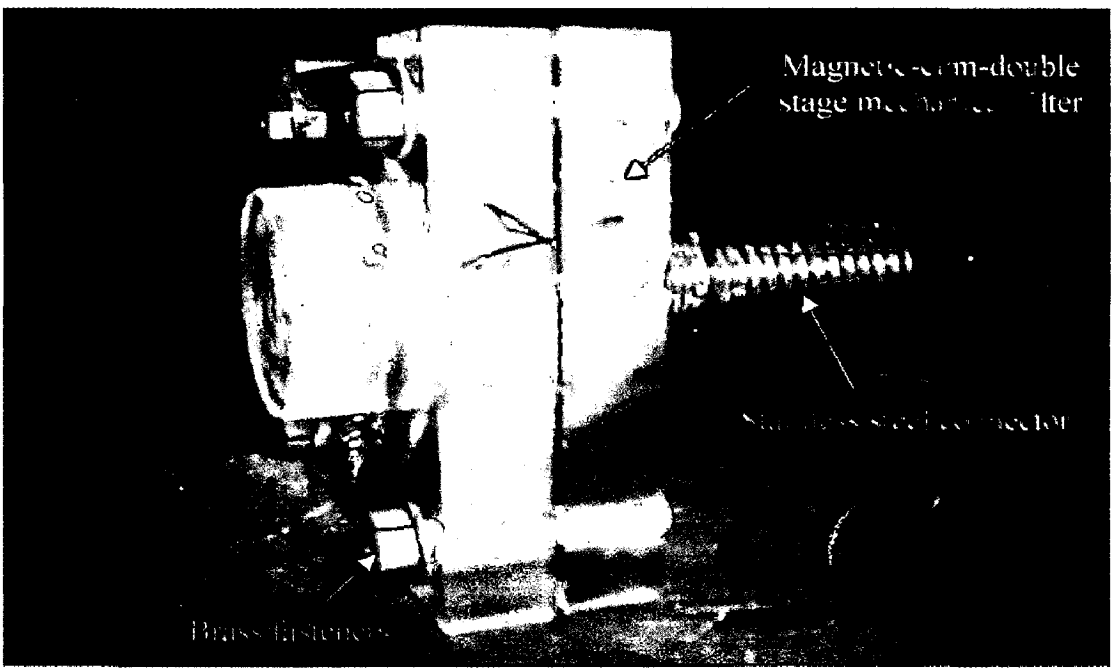

Fig. 4.8a) Filter assembly

G13034

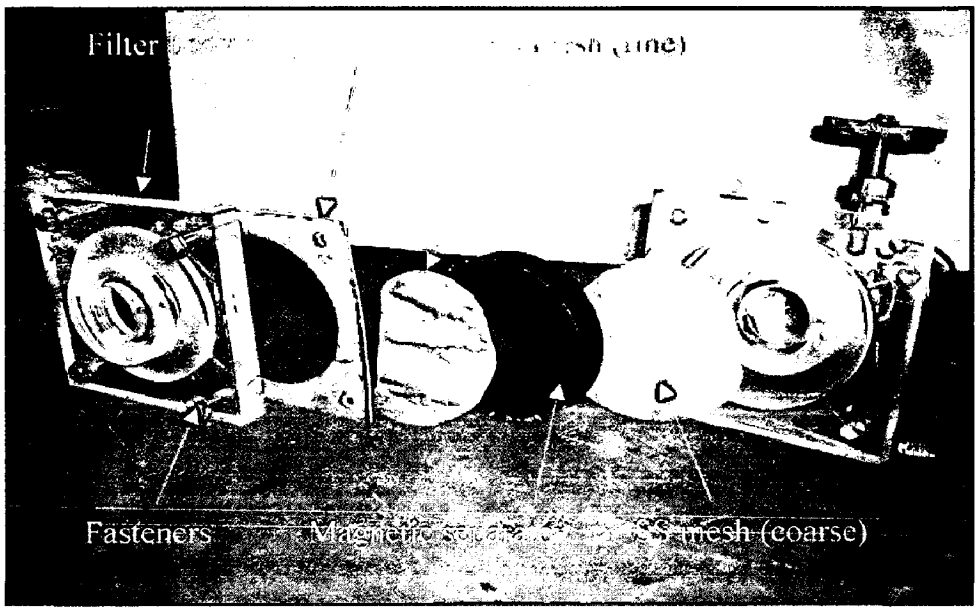

Fig. 4.8b) Assembly details

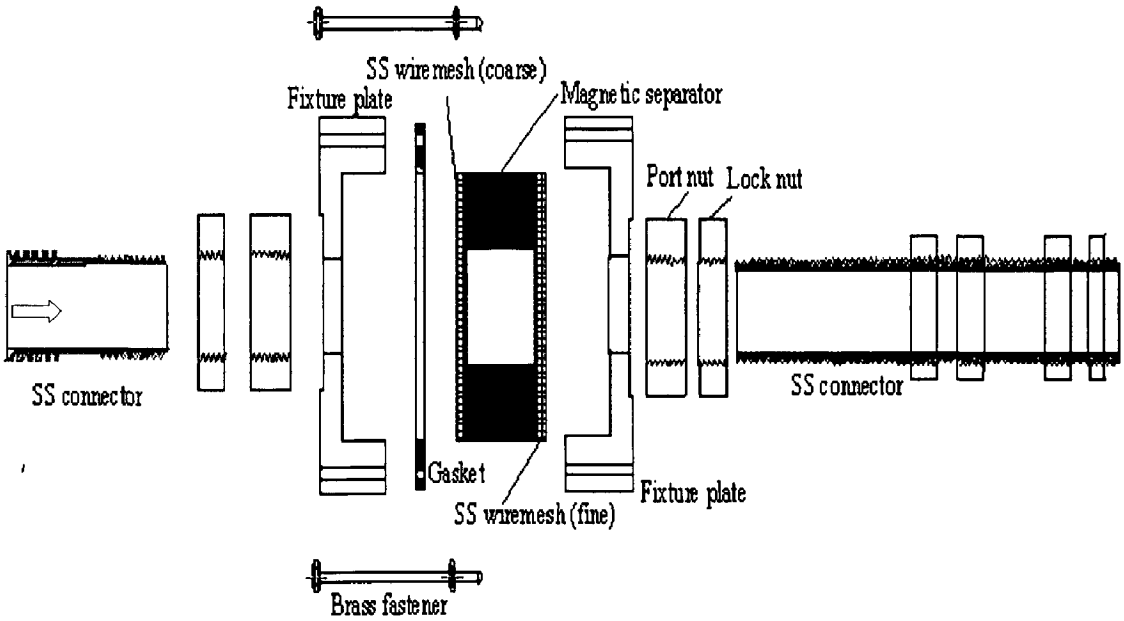

Fig.4.8c) Constructional details

Fig. 4.8 2nd stage magnetic separator-cum-mechanical filter details

4.3.2.2 Reciprocating drive

Reciprocating speed influences the finish and characteristic crosshatch angle of the machined surface. Therefore, a programmable stepper motor unit consisting of 3 tandom-compounded stepper motors, controlled by a Vinytics 8501 microprocessor training kit through interface cards, has been utilized for the reciprocation of the tool (Fig. 4.12). Stepper motors are characterized by their high holding toque, rotation accuracy, precise speed control and instant reversal as desired in ECH process for reciprocating the tool. Three stepper motors are coupled in series for obtaining a sufficiently high torque required for reciprocation. Motors are housed in a fabricated bracket attached to the driving head. Programming was done to achieve a proper synchronized operation of stepper motors. Stroke length and speed of translation of tool is adjustable as per the program.

Assembly language programs (given in Appendix-A) were stored in microprocessor kit for forward and backward movements of stepper motors for the selected speed and stroke length of tool. The Vynitics microprocessor training kit is powered by a 12V DC supply. The program and necessary commands can be entered through the keyboard connected to the microprocessor unit. The output of the executing program is sent to the interface cards through input/output port of the microprocessor. The interface card unit supplies 12V power to the stepper motors depending upon the signal it receives from the i/o port of microprocessor. Stepper motors are directly coupled to a spindle which in turn is connected to the reciprocating unit through a rack and pinion mechanism. Motors can also be fitted using a 2:1 gearing (Fig. 4.14) in case a higher speed range is desired.

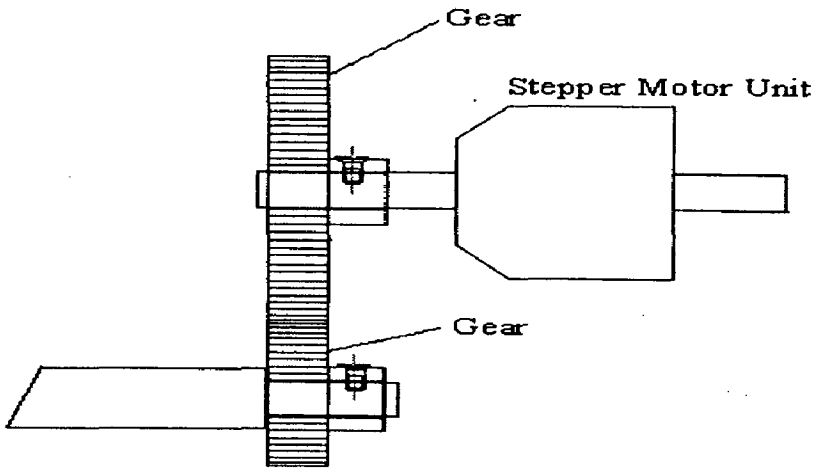

Fig. 4.14 Reciprocating drive gearing

4.3.2.3 Driving head

To accommodate the rotary and reciprocating drives together and apply both the motions simultaneously to the machine spindle holding the ECH tool, the mechanism used in a drill machine was used. For this purpose, a bench drill machine head with suitable modifications has been utilized.

4.4 WORK HOLDING AND POSITIONING SYSTEM

The work holding and positioning system (Fig. 4.15) containing the work chamber (machining chamber), worktable and work positioning system has been designed to perform several crucial functions including an accurate positioning of workpiece in relation to ECH tool, holding the workpiece in a way to provide it a state of floating condition, minimum work distortion due to machining torque, containing electrolyte splashes, effective sealing at tool inlet to the work chamber, mist collection, easy loading/unloading of workpiece and optimum utilization of available machine stroke length. Work chamber remains insulated from the other elements of the setup. This helps avoiding any resulting anodic corrosion of the metallic parts of the setup. The material selection aspects for the components of the work holding and positioning system are given in Table 4.1d.

4.4.1 Work Chamber

The details of the work chamber are given in Fig. 4.16. The rectangular chamber is made of Perspex. It is mounted on a mild steel base plate with a 10 mm bakelite sheet interposed in between and clamped together using counter sunk brass screws and bolts in a ways to achieve the perfect insulation of work chamber from work table and its rigidity against the machining torque and forces.

A work fixture, especially designed for the selected workpiece, is fixed to the bottom plate of the chamber using four counter sunk brass bolts. Details of the fixture are given in Fig. 4.17. It is designed to withstand hydrostatic and hydrodynamic forces besides having sufficient rigidity against machining torque, provide proper space to facilitate full down stroking of tool through work and accommodate and guide the inlet electrolyte flow. Work fixture also works as inlet sleeve for electrolyte supply to the IEG and therefore, it is sealed properly from the remaining work chamber.

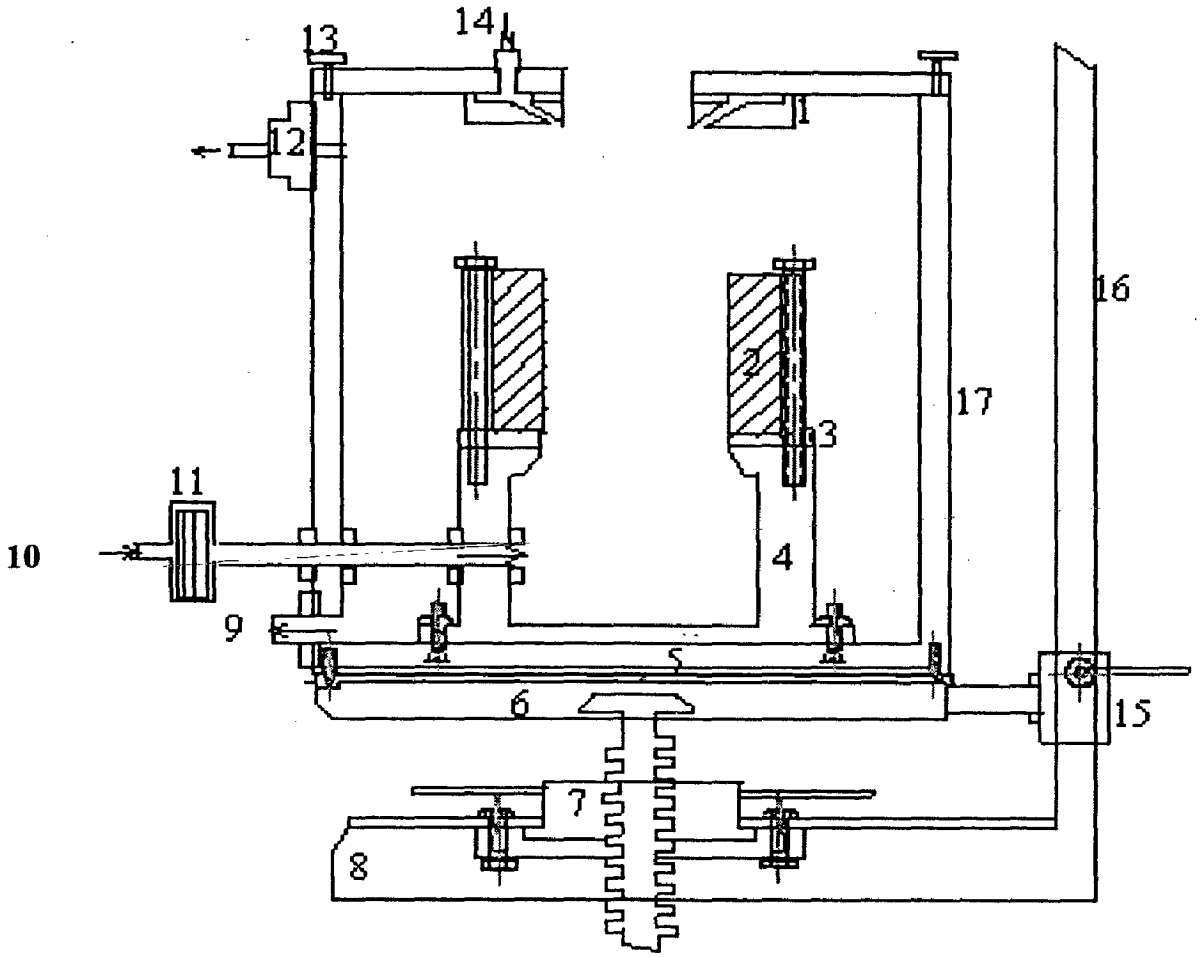

(1) Hydraulic-cum-mechanical seal body (2) Workpiece (3) Rubber plate (4) Fixture-cum-electrolyte inlet sleeve (5) Insulator (6) Work table (7) Work positioning system (8) Machine base (9) Electrolyte outlet (10) Electrolyte inlet (11) Filter-cum-magnetic separator (12) Mist collector (13) Fly screw (14) Hydraulic seal inlet (15) Swivel system (16) Machine column (17) Work chamber

Fig. 4.15 Work holding and positioning system

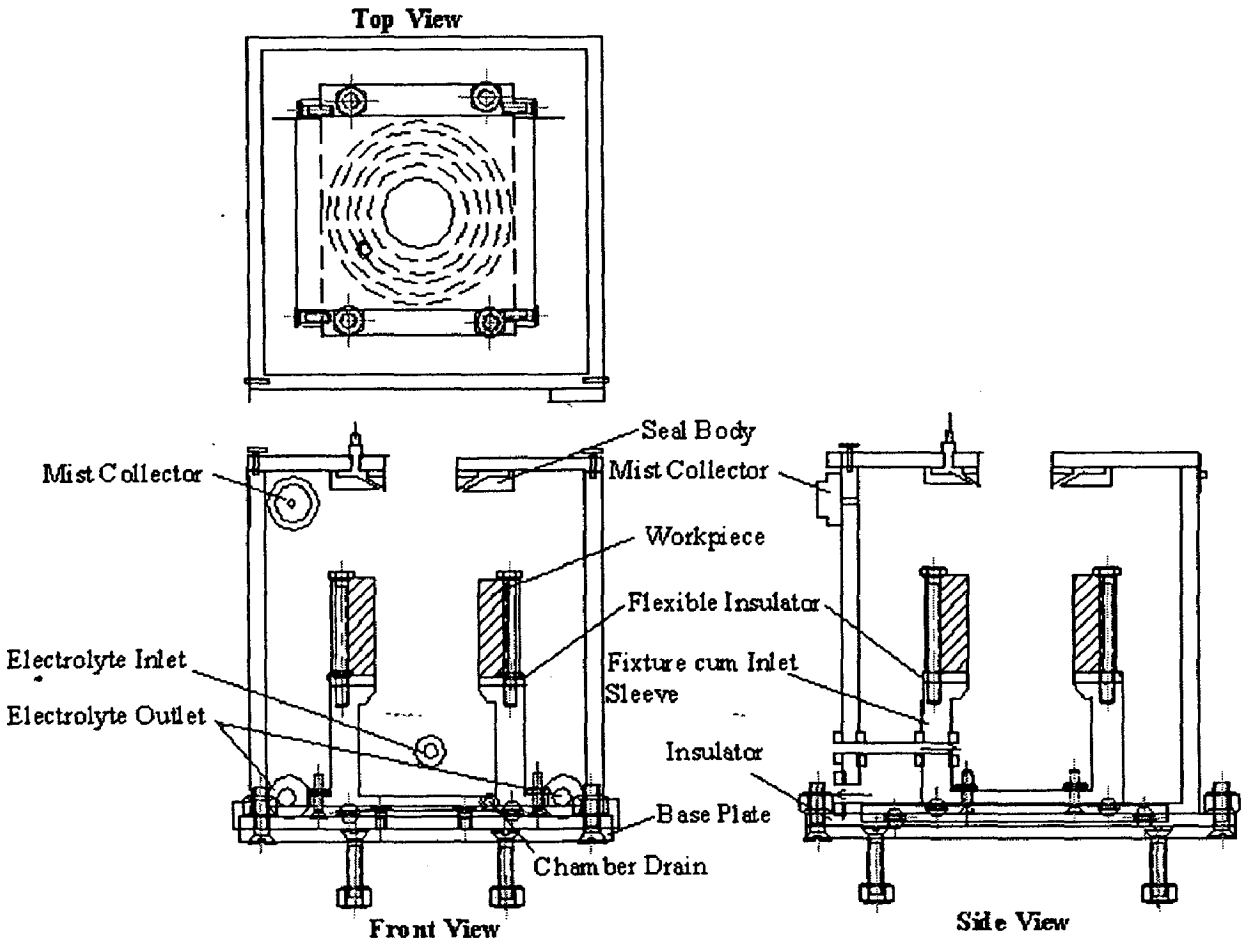

Fig. 4.16 Details of work chamber

Electrolyte is supplied to the work fixture using a stainless steel connector, which after being screwed through in work chamber and fixture, is locked and sealed using Perspex locknuts and rubber gaskets. Inlet end of the connector contains the 2nd stage filter-cum-magnetic separator. Workpiece is mounted using four sleeved bolts, which are screwed in fixture top plate with a rubber gasket interposed in between to achieve free float condition to work during machining. Detachable top cover of the work chamber, fitted with fly bolts and C clamps can be lifted up for measuring the work-tool gap. Work chamber is fitted with stainless steel connectors (Fig. 4.18) for providing two regular and one chamber drains. A mist collector is located in the top portion of the chamber for removing salt laden vapors and gases generated during the process.

Sealing at tool inlet to the work chamber is achieved in three stages. 1st stage sealing is via deflecting the exiting electrolyte jet from work-bore by the sealing hub of the ECH tool. Any further sweeping electrolyte is sealed using a hydraulic seal in 2nd stage while a final 3rd stage sealing is done using a mechanical seal. The hydraulic-cum-mechanical seal body is fixed with the top cover plate of the work chamber as shown in Fig. 4.19.

The seal body consists of two hydraulic channel rings; upper and lower seal body plates; and a nylon mechanical seal. Electrolyte from the pump discharge enters the hydraulic channel formed by the hydraulic channel rings through a nipple fixed in the chamber top plate. The converging conical passage formed between the upper and lower seal body plates provides a circumferential jet, flowing at 127° against the exit electrolyte from the work bore, to achieve hydraulic sealing. A nylon seal contained between upper seal body and top plate is used for a subsequent mechanical sealing.

4.4.2 Worktable

A rigid cast iron worktable supports the work chamber. The work chamber base plate is fixed using four bolts with the radial slots in workable for accurate radial posioning of work and tool. As shown in Fig. 4.20, worktable is attached to the machine column using a swivel arrangement for ease in loading/unloading and alignment of the workpiece. The swivel system can also slide on the cylindrical machine column to achieve axial positioning of workpiece with respect to ECH tool. After the proper alignment and positioning of the work, worktable can be locked in position using a lever provided in the swivel system.

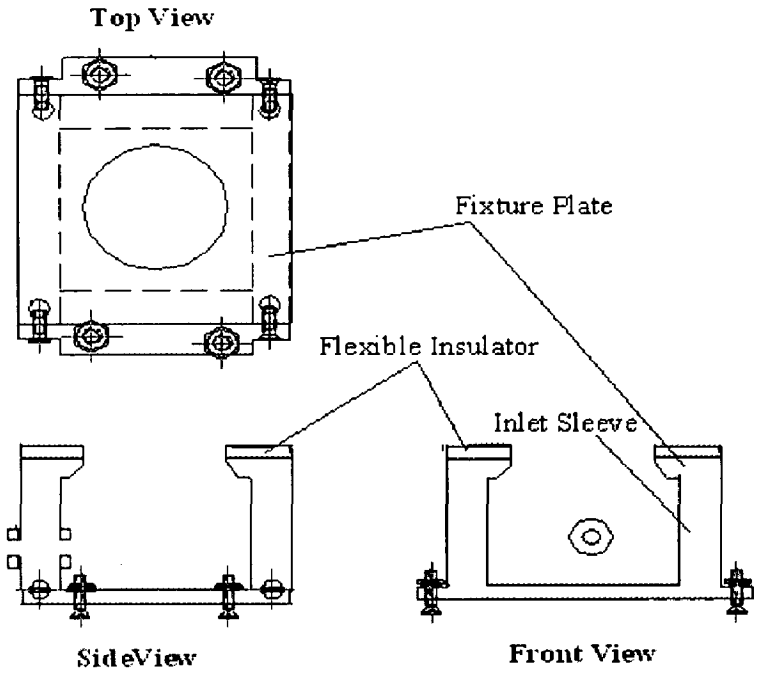

Fig. 4.17 Work fixture-cum-inlet sleeve details

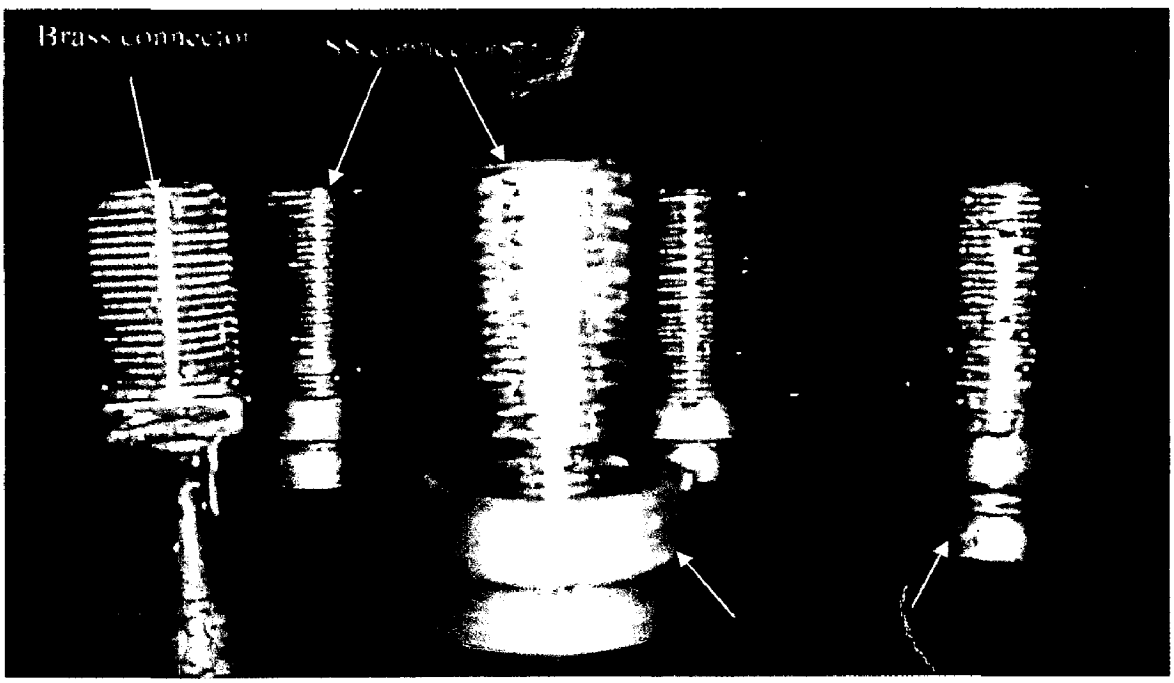

Fig. 4.18 Stainless steel connectors

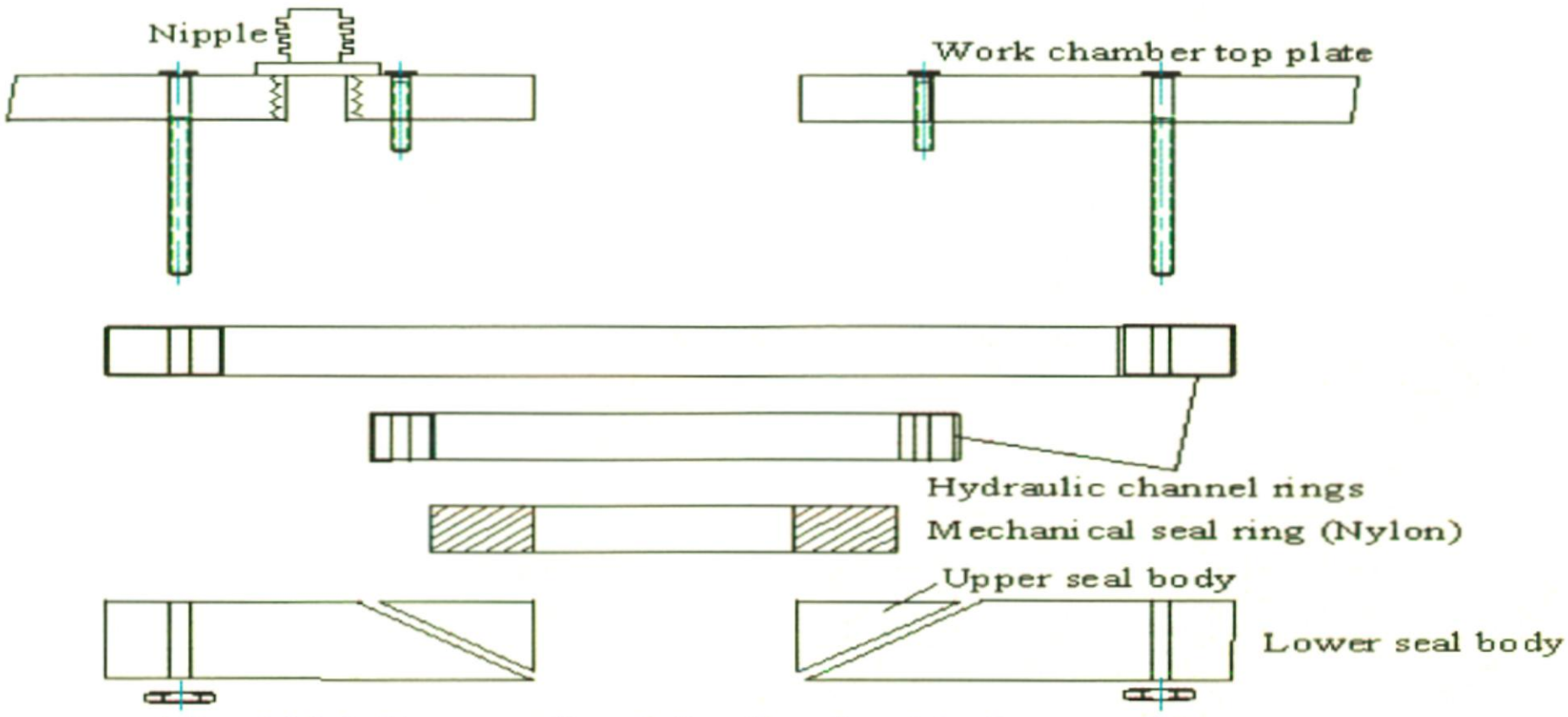

Fig. 4.19a) Constructional details of seal body assembly

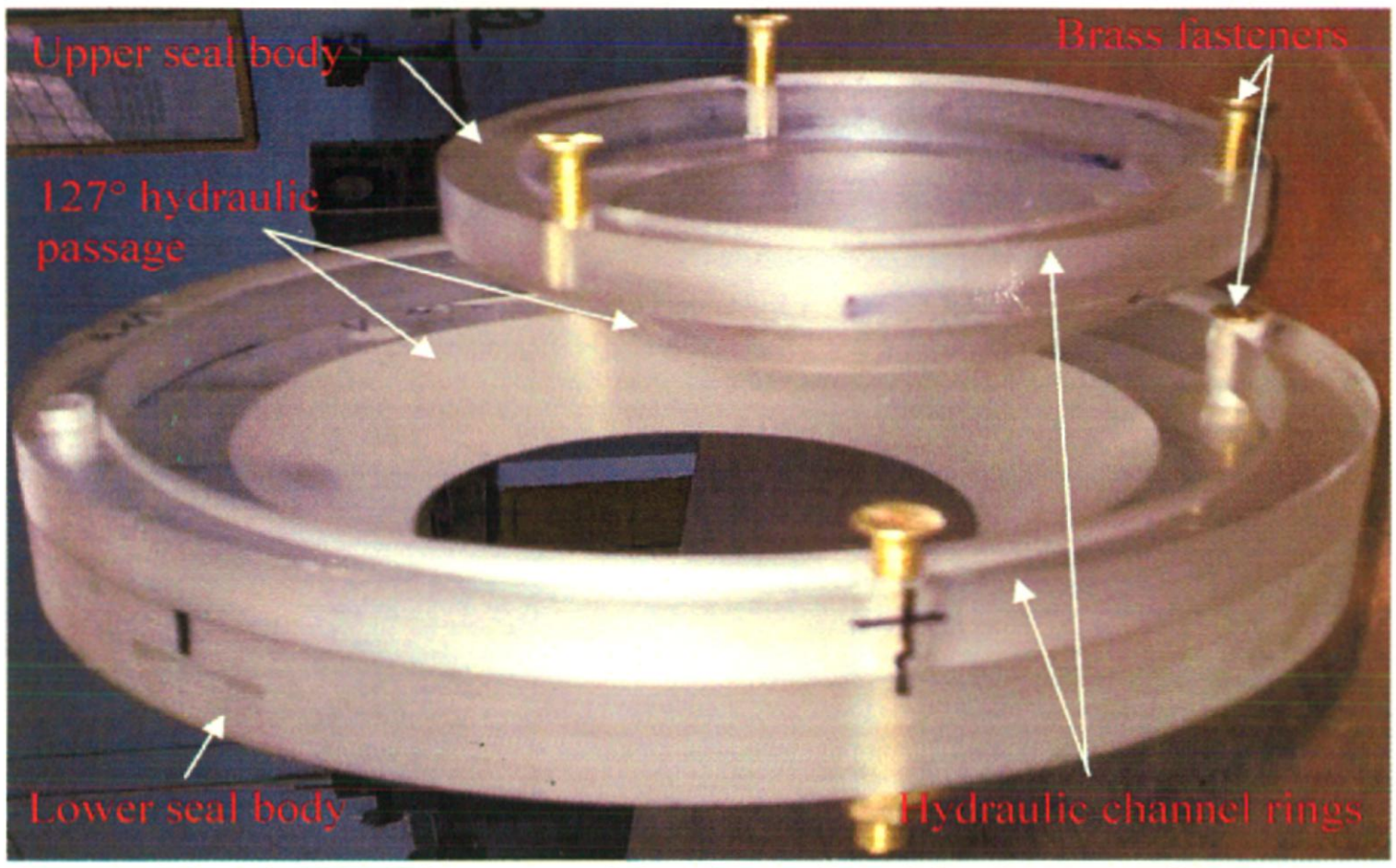

Fig. 4.19b) Photographic view of seal body assembly

4.4.3 Work Positioning System

Work positioning system is used for proper axial positioning of workpiece in relation to tool for optimum utilization of the available machine stroke and to facilitate loading and unloading of the workpiece. A screw jacking system, designed and fabricated for the required travel of the work holding system, is attached to the machine base as given in Fig. 4.20. A support bracket fastened to the machine base provides bearing surface for the cast iron load nut. Any upward movement of load nut is checked by its collared projection at bottom. Two handles are fitted to the load nut for moving the jacking screw used for axial positioning of the worktable. During processing, the work positioning system serves as an additional support to the worktable. For loading / unloading of workpiece, jacking screw is unscrewed down in a sleeve grouted in the foundation.

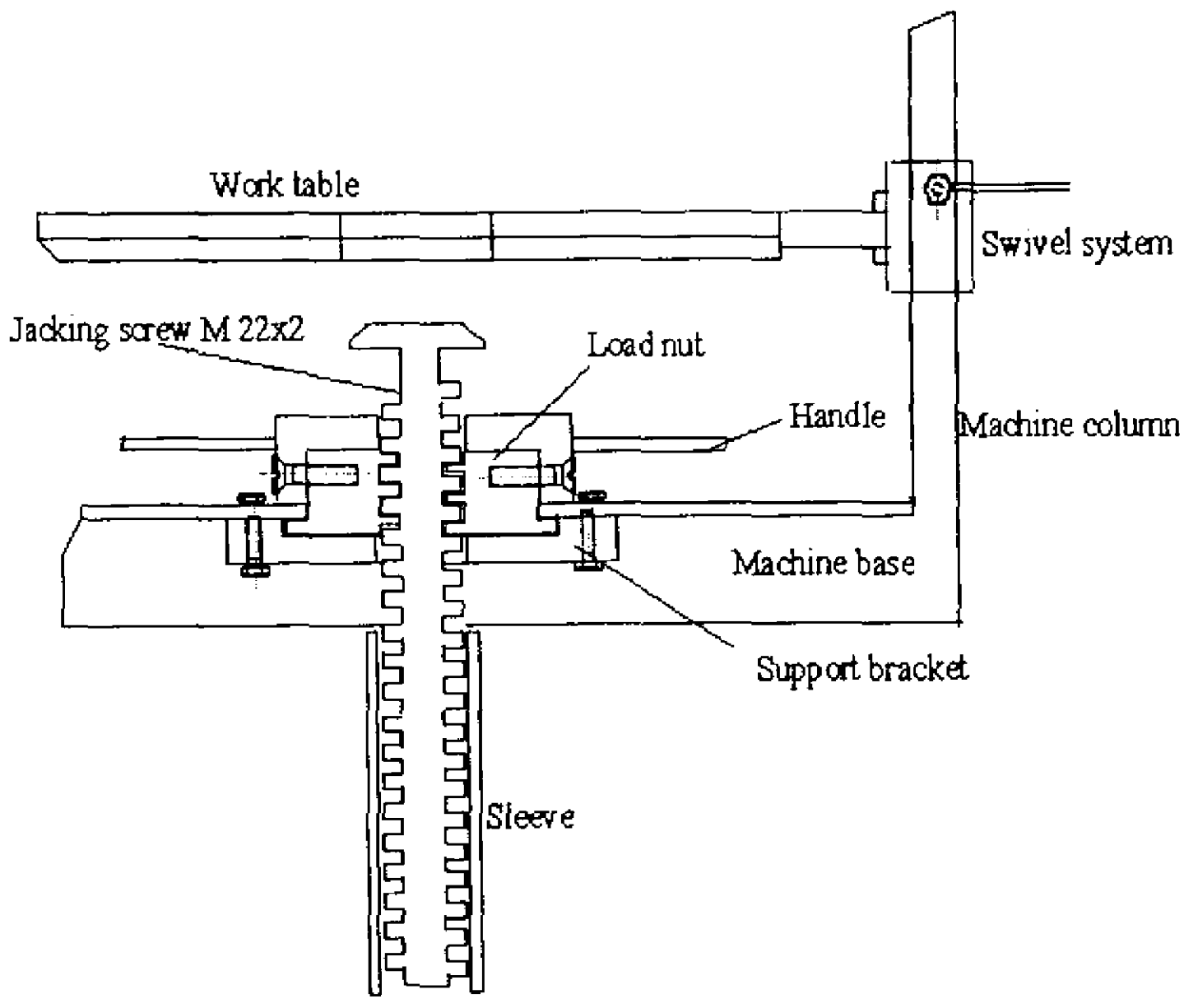

Fig. 4.20 Work positioning system details

4.5 FRAME AND HOUSING

The purpose of the frame and housing is to accommodate the ECH tool, drives, and work holding and positioning systems for operation as a unit. The functional requirements include a suitable shape and size to provide the safe operation and maintenance and high stiffness. It was found suitable to use the column with base and driving head of a bench drill machine as the frame and housing for the setup.

The photographic view of the developed ECH setup is given in Fig. 4.21, and Fig. 4.22 presents a close-up of the machining chamber.

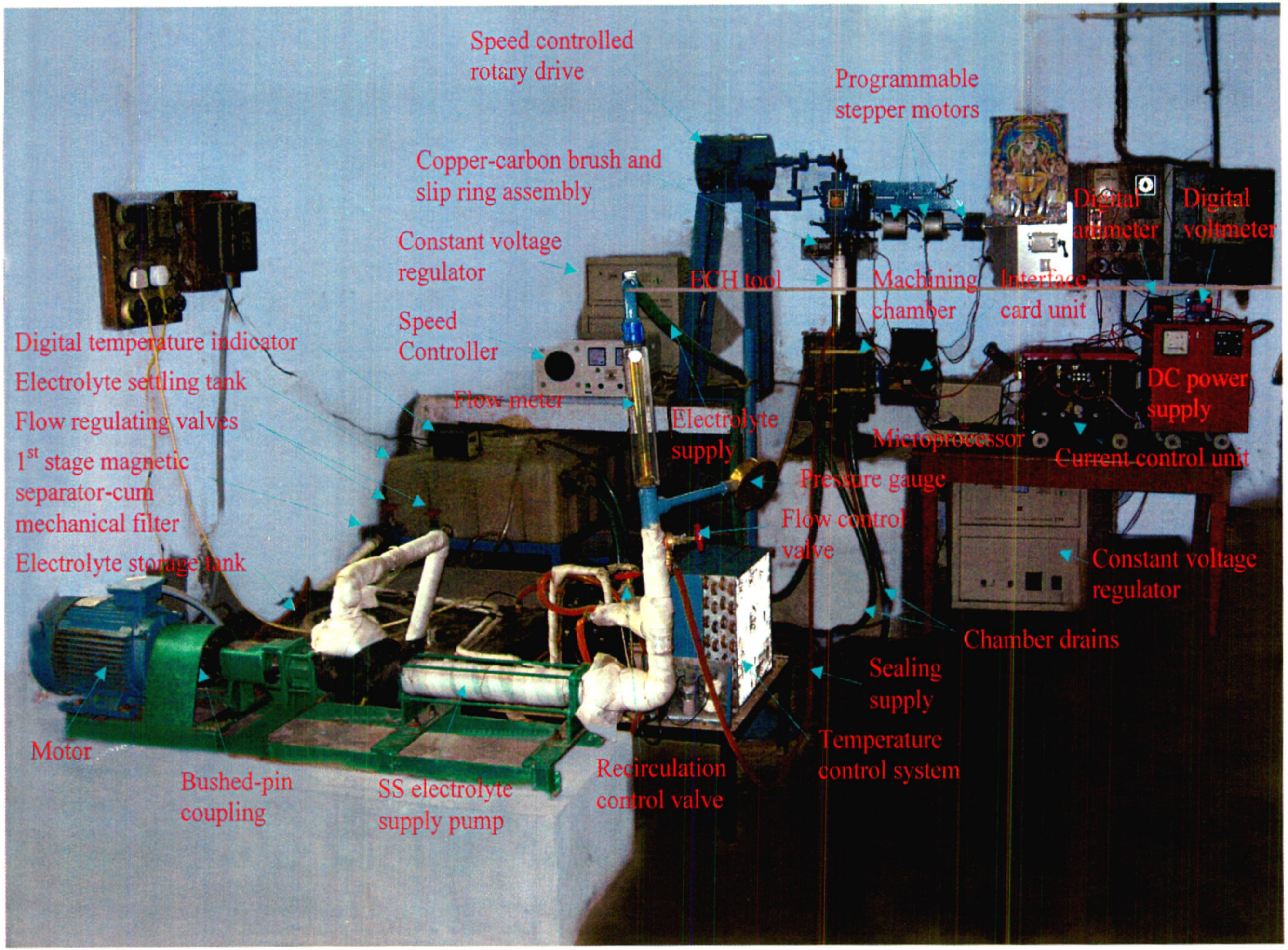

Fig. 4.21 Photographic view of ECH setup

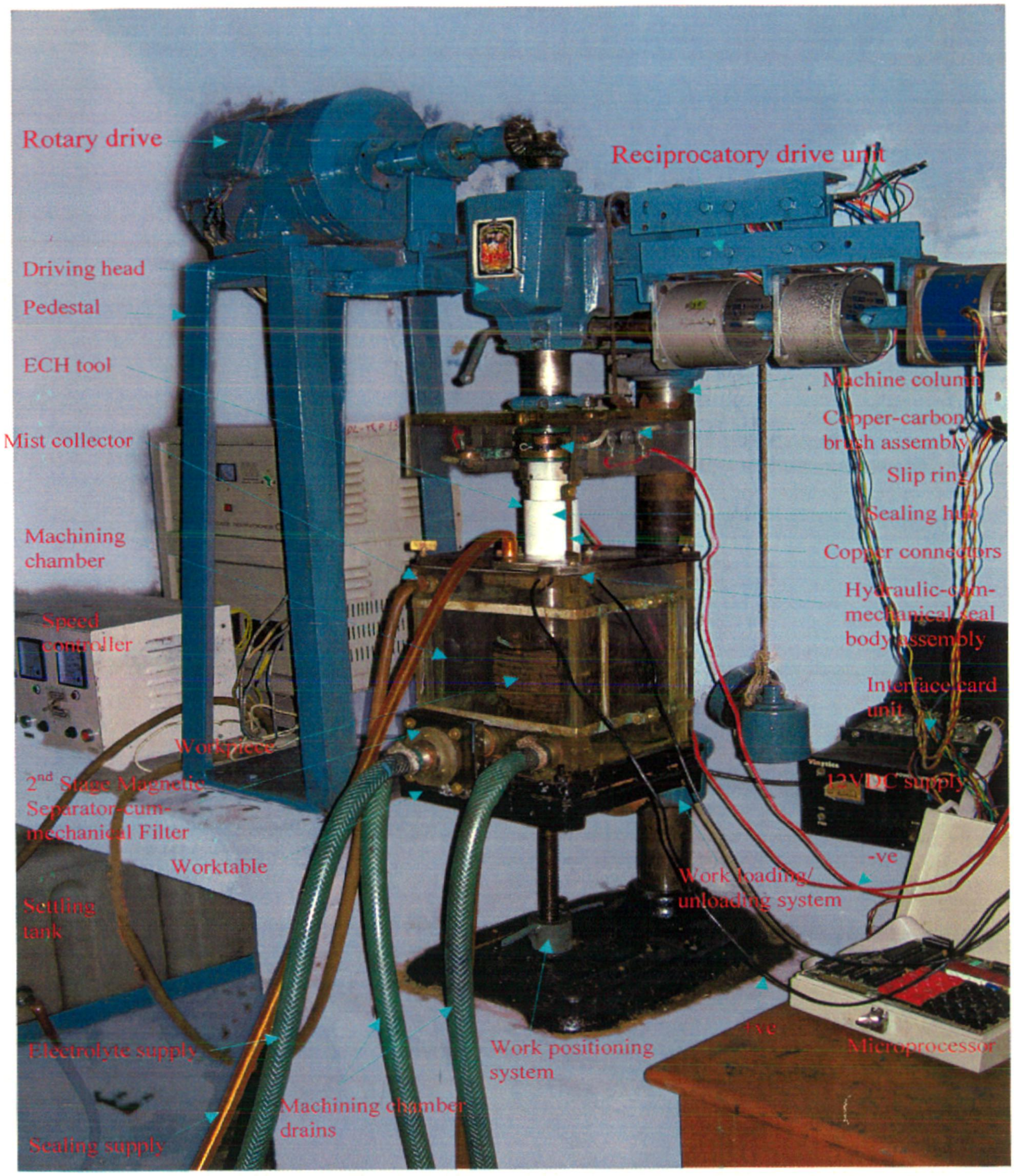

Fig. 4.22 Close-up view of machining chamber

Chapter-V

PARAMETRIC ANALYSIS

The parametric analysis presented in this chapter deals with the selection of Electro-Chemical Honing response characteristics (output/quality/performance) and the choice of process input parameters, their levels and ranges. A brief description of measuring instruments utilized for measuring the various process parameters and the response characteristics is also included, while detailed specifications are given in Appendix-B.

ECH process parameters can be divided into three main categories, depending upon the nature of influence of the parameter in the process as shown in Table 5.1. The electro-chemical (EC) based parameters influence the electrolytic dissolution in the process in terms of both intensity and uniformity. Intensity and location of mechanical abrading is decided mainly by honing based parameters. The selection and coordination of both categories of these parameters is, in turn, also dependent on the workpiece and tooling parameters.

Table 5.1 ECH process parameters and their nature of influence

EC based parameters	Honing based parameters	Workpiece and Tooling based parameters
(i) Power supply parameters	(i) Honing stick (ii) Honing speeds	(i) Workpiece parameters
(ii) Electrolytic parameters	(iii) Stick-out pressure	(ii) Tooling parameters (iii) Inter-electrode gap

In order to identify process parameters that may affect the quality characteristics of electro-chemical honing process, an Ishikawa Cause-and-Effect diagram has been constructed as given in Fig. 5.1.

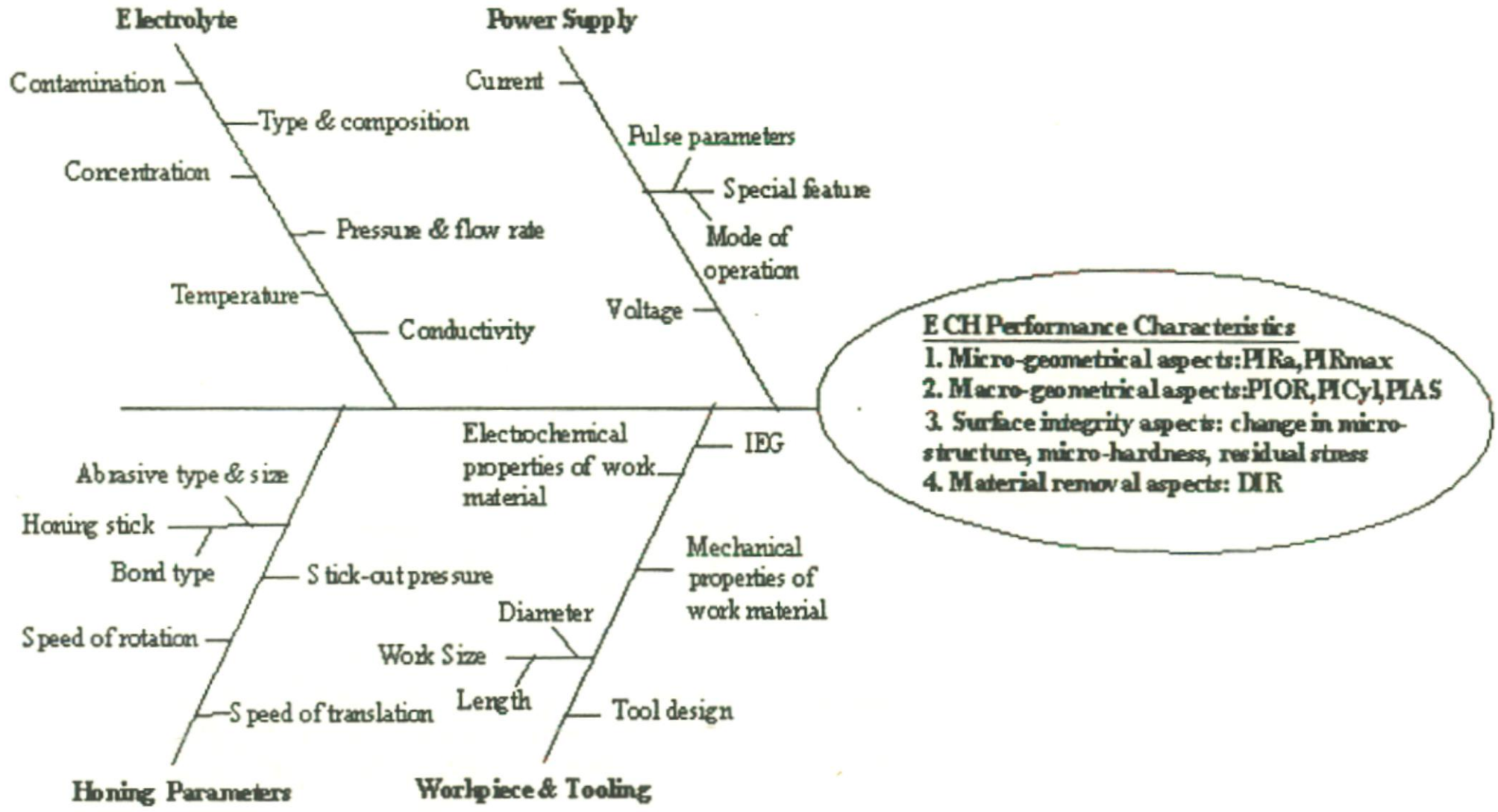

Fig. 5.1 Ishikawa cause-and-effect diagram of ECH

ECH process parameters, depending upon the system elements that control them, can be grouped as:

a) DC power supply based parameters:

Current, voltage, and special features: pulse on time and off time; mode of operation such as constant voltage or constant current

b) Electrolyte based parameters:

Type, composition, concentration, pressure, flow rate, temperature, conductivity, contamination

c) Honing based parameters:

Type of abrasive, grit-size, type of bond, speed of rotation, speed of reciprocation, stick-out pressure

d) Workpiece and tooling based parameters:

Electro-chemical and mechanical properties of work material, size of workpiece, tool design, and inter-electrode gap (IEG)

5.1 WORKPIECE SELECTION

Electro-Chemical Honing has great prospects of its applications in automobile, petrochemical reactors, valve/die polishing, and power-cylinder processing industries. Internal cylindrical honing represents, typically, the most common commercial application of the process. Therefore, ASTM 35 cast iron cylindrical blocks, as shown in Fig. 5.2, were selected as the workpiece specimens in the present study. The material is most commonly used for automobile cylinders.

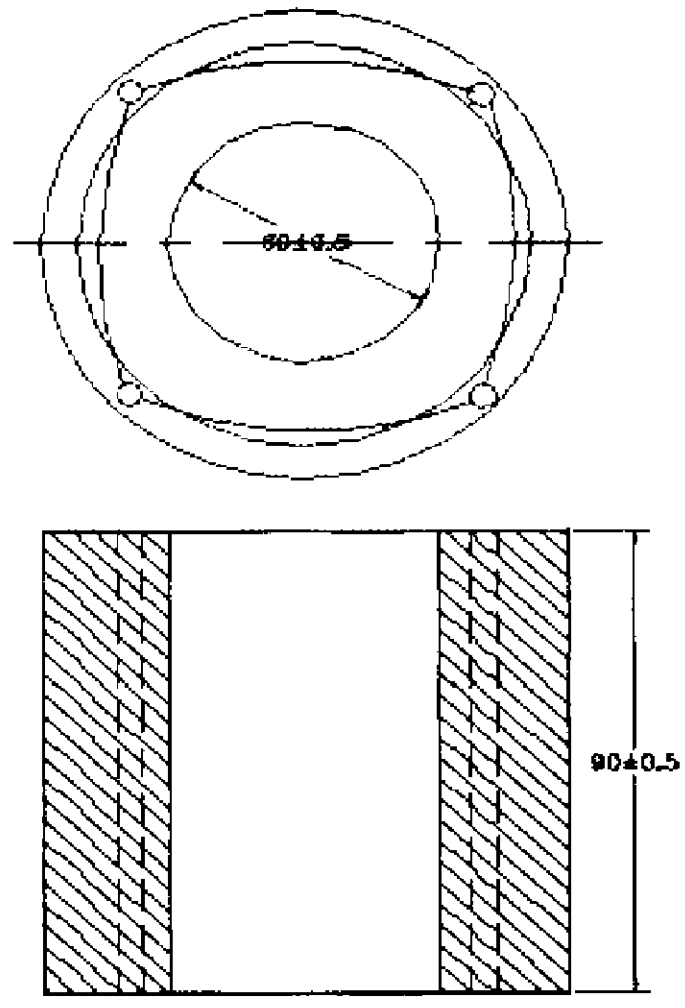

Fig. 5.2 Workpiece specimen

The work pieces were prepared by boring operation on a precision center lathe to initial bore diameter 60±0.5 mm and bore length 90±0.5 mm. The workpices were 45° taper turned for a 5 mm depth from top to provide a smooth entry of ECH tool into the workpiece bore during processing.

The microstructure of the work material was taken using the procedure described in § 5.4.3.1§ (Fig. 5.3). It consists of a gray cast iron matrix having ferrite with graphite flakes dispersed through out (ASTM A 48, grade G35). The form of graphite can be categorized as

Type A flake graphite - random orientation (ASTM A 247). The material has an average hardness value of 212 BHN, as tested on Hardness Testing Machine (HPO 250, WPM, Germany).

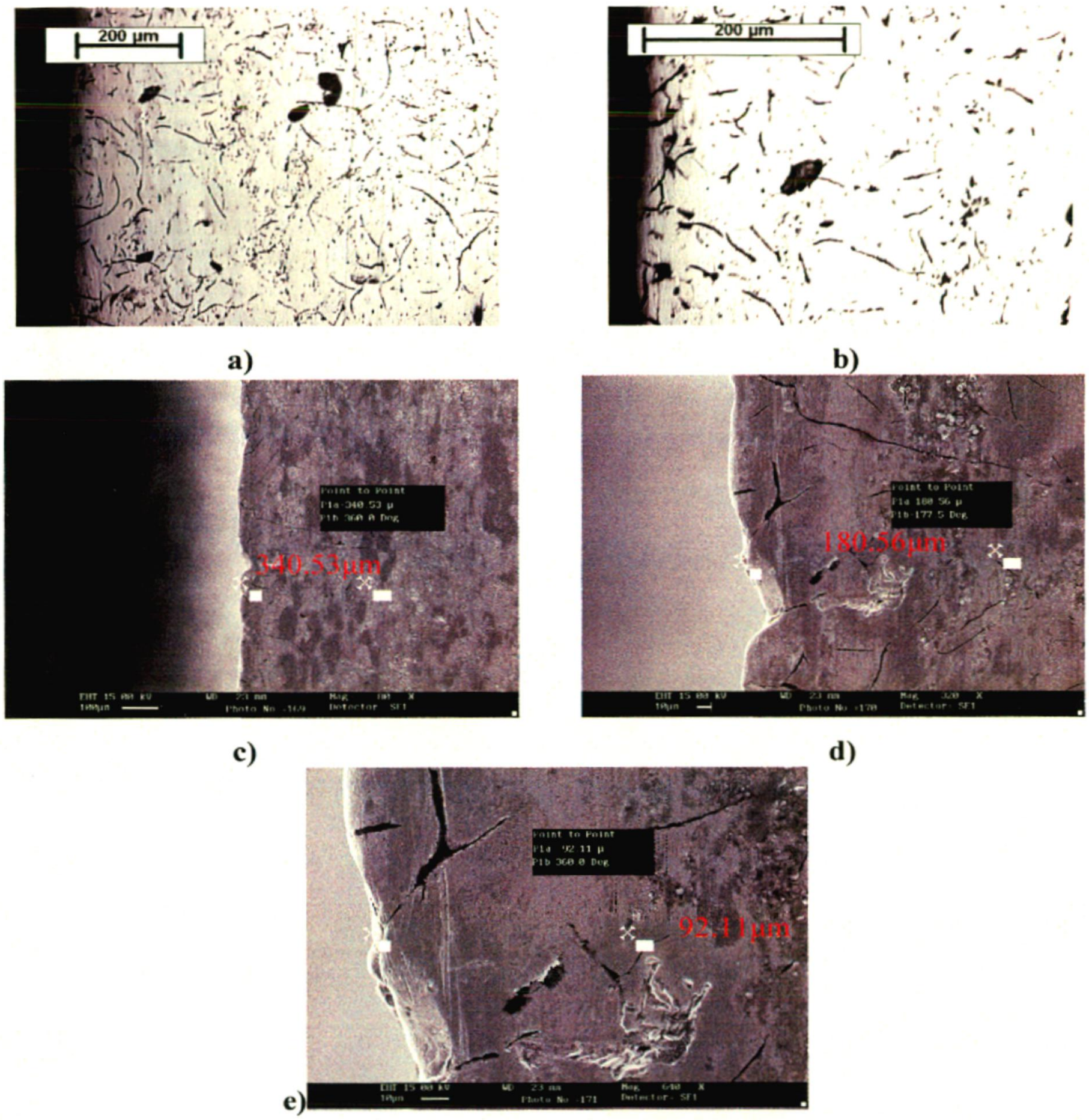

Fig. 5.3 Microstructure of the work material a) 160X, scale 0.5, b) 320 X, scale 0.5, c) SEM micrograph 80X, scale 0.25, d) SEM micrograph 320X, scale 0.25 e) SEM micrograph 640X, scale 0.25

5.2 ECH PROCESS PARAMETERS

The range and levels of process input parameters used in the experimental study have been decided based on literature review, pilot-studies and constraints of the developed set-up. Pilot experimentation was done using one-factor-at-a-time approach.

5.2.1 Current Intensity

In electro-chemical honing, a low DC potential of 6-30 V is desirable across the inter-electrode gap. A current intensity of 100-300A is normally used in various applications (Tool and Manufacturing Engineers Handbook, 1983). Current densities usually range from 0.5 to 2 A/cm^2 depending upon the workpiece material and sizes (Kitaev et al, 1985). However, higher current intensities (12-47 A/cm^2) are also employed (Benedict, 1987). This particularly helps avoiding the preferential intergranular attack (IGA) observed in certain materials like tungsten carbide.

Pilot experiments were conducted to decide upon a suitable range of current intensity to be used for gray cast iron workpieces. Results revealed that current in the range of 50-180 A was suitable for the selected workpiece both in terms of processing time and improvements in response characteristics. Also, within this range there was no indication of any IGA. Further advantages in the selected range as compared to very high current density were expected to be realized in terms of smaller temperature variation and lesser hydrogen bubble formation, which are reported to have an adverse effect on uniformity of electrolytic dissolution (Jain, 2002).

The power supply is operated as a constant current source during different experimental studies. Output voltage is automatically adjusted depending upon the selected level of the current intensity. Current is controllable to within ±5% at the different selected levels. DC output current from power supply was measured by a digital ammeter (Creative

Control, Mumbai). DC potential across the IEG was recorded using a digital voltmeter (Model 96x96, Creative Control, Mumbai).

5.2.2 Type and Composition of Electrolyte

The electrolyte, besides facilitating electrochemical functions, carries away the heat and generated products of reaction from the machining zone. High electrical conductivity, low viscosity, high specific heat, high chemical stability, non-corrosiveness and non-toxicity, low cost and ready availability are the desirable properties of the electrolyte (Shan, 2006). It has been reported (Guoqiang et al, 1986) that the protective ability of metal oxide microfilm plays a vital role in the process which, in turn, depends upon the type and composition of the electrolyte. The selection of proper electrolyte and its composition is therefore crucial in ECH process.

The most commonly used electrolytes are sodium chloride and sodium nitrate. Ammonium nitrate has also been tried for certain applications (Budzynski, 1983). It is also recommended that sodium chloride and sodium nitrate produce good surface finish on a gray cast iron work material (Pandey and Shan, 2005).

Therefore, pilot studies were separately conducted using sodium chloride and sodium nitrate electrolytes. NaCl provided a rapid improvement in surface roughness as compared to $NaNO_3$. However, owing to its passivating nature, $NaNO_3$ produced a better uniformity of surface roughness values. Accordingly, electrolytes having different proportions of sodium chloride and sodium nitrate were tried. An electrolyte having a composition of "¾ part NaCl and ¼ part $NaNO_3$" was found highly suitable for the ECH application and therefore, selected for the present study. The electrolyte is also cost-effective. The weight of electrolyte was taken using a precision electronic balance (Sartorius type 1518).

5.2.3 Electrolyte Inlet Temperature

In ECH, the electrolyte temperature is maintained typically at about 38°C through the use of temperature control system (Tool and Manufacturing Engineers Handbook, 1983; Machining Data Handbook, 1980).

In order to investigate the effects of considerably lower as well as higher electrolyte inlet temperatures on the process performance, the electrolyte inlet temperature variation from 10 to 50°C was selected for the present study. While deciding the range of electrolyte inlet temperature a due consideration was given to the free flowing characteristics of electrolyte at very low temperature as well as associated effects on electrolyte conductivity particularly with lower concentrations and boiling of electrolyte at very high temperatures. Therefore, sufficient margins were taken.

Electrolyte inlet temperature is controlled by the temperature control system, comprising of heating and cooling coils fitted with high quality temperature controllers (sub-zero^{TM} Model SZ-7510-E) in the electrolyte tank. It was possible to maintain the temperature within ± 1°C.

5.2.4 Electrolyte Concentration

The commonly used concentrations are 120 g/L for sodium chloride and 240 g/L for sodium nitrate (Tool and Manufacturing Engineers Handbook, 1983; Machining Data Handbook, 1980).

A lower limit of 100g/L electrolyte concentration was decided based on the pilot-experiments that showed inappropriate improvements in the responses, particularly at lower electrolyte inlet temperature. The maximum electrolyte concentration was decided to keep as 200g/L keeping in view the corrosive nature of sodium chloride.

Electrolyte properties were determined for the selected range of temperature for three electrolyte concentration levels used in the study: 100g/L, 150g/L and 200g/L of electrolyte

prepared with tap water. Electrolyte conductivity was recorded using a digital conductivity meter (Testronix 15, Agrawal Electronics, Mumbai) fitted with a CD-06 conductivity cell. Electrolyte pH was measured by a digital pH meter (CAT. No. CL46, Toshniwal). The conductivity and pH of the electrolytes at different electrolyte temperature are shown in Fig. 5.4.

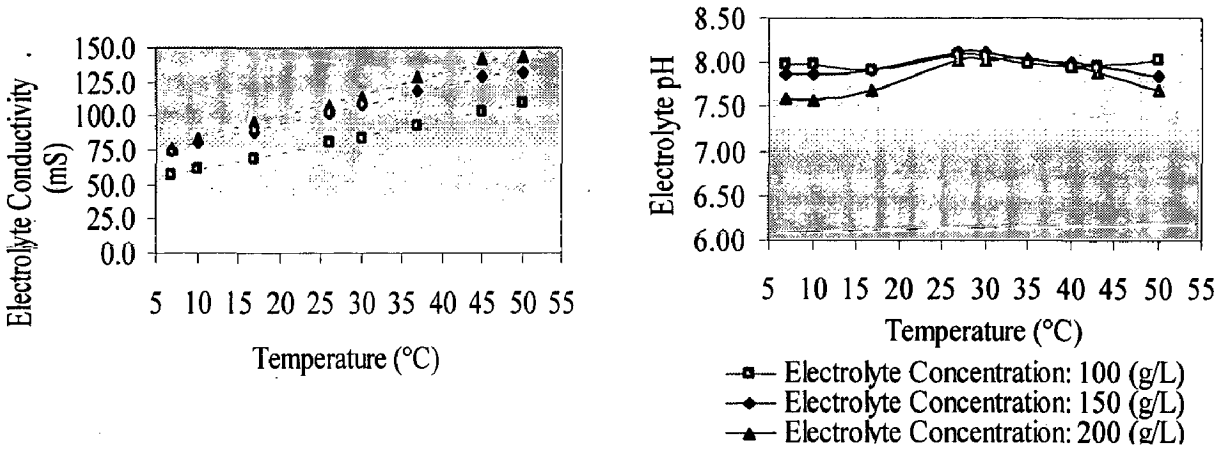

a) b)

Fig. 5.4 Variation of electrolyte conductivity and pH with temperature: a) electrolyte conductity vs temperature plot, b) electrolyte pH vs temperature plot

Fig. 5.4 reveals that the electrical conductivity of electrolyte is directly related to temperature. Electrolyte conductivity increases almost linearly with increase in electrolyte temperature at all the three concentration levels. As apparent from the slope coefficients of the trend lines, the change is higher at increased electrolyte concentrations. Electrolyte at different concentrations has a different nature as reflected in pH-temperature plot. pH, being maximum at room temperature for all the three concentrations, decreases as the temperature is changed from room temperature. A larger variation in pH is observed with change in temperature at increased electrolyte concentrations. However, maximum variation in pH with 200g/L electrolyte concentration is only less than 0.5.

5.2.5 Electrolyte Contamination

In ECH, the abrasive action of honing sticks keep the surface receptive and tends to correct the surface irregularities resulting from non-uniform electrochemical dissolution, the control of pH, composition, and sludge becomes less critical (Tool & Manufacturing Engineers Handbook, 1983; Benedict, 1987; Sharma, 2004).

In spite of this underlying fact, the electrolyte purity and sludge control during experimentation was achieved using a double stage magnetic-cum-mechanical filtration and settling. Monitoring of electrolyte conductivity and pH was done off-line based on the results obtained in Fig. 5.4.

5.2.6 Initial Inter-Electrode Gap

An inter-electrode gap is usually kept between 0.075 to 0.25 mm at the beginning of ECH operation. As the metal is removed, IEG increase. It has been reported (Randlett and Ellis, 1968; Tool and Manufacturing Engineers Handbook, 1983) that even a gap of 1 mm does not materially affect the stock removal rate when a constant current supply is used.

While selecting an initial IEG, a due consideration needs also to be given to the composition and properties of the work material. The gray cast iron work material used in the study is composed of a large quantum of free graphite flakes in iron. It has been recommended to use the larger machining gaps ranging between 0.5-0.8 mm, so as to allow the graphite particles to be swept clear (Shan, 2006).

Experiments were conducted with different initial IEG ranging from 0.35 –0.70 mm. No appreciable influence on diametral increase rates of workpieces was observed with the change in gap. Nurai et al. (1967) also noted that the effect of inter-electrode gap is not so predominant in the case of electro-chemical honing.

Therefore, a nominal initial IEG of 0.5 mm was selected for the present study. Initial IEG for different workpieces used in the experimental studies varied from 0.40-0.60 mm due the inherent variation in workpiece bore sizes obtained from the boring operation.

5.2.7 Electrolyte Flow Rate and Pressure

Electrolyte flow condition in inter electrode gap has tremendous influence on the intensity and uniformity of electrolytic dissolution. Temperature variation and hydrogen layer effects have been reported to be the main cause of variation in electrolyte conductivity and thus the uniformity of electrolytic dissolution is affected. Electrolytic pressure and flow velocity are crucial parameters in determining the size and distribution of hydrogen bubbles and temperature variation in IEG. In ECM the hydrogen generated on the cathode surface appears as a layer of bubbles mixed in the electrolyte, and this layer thickens as it flows downstream with the electrolyte. However, its thickness decreases if the electrolyte flow rate is increased. The size of individual bubbles decreases as the electrolyte velocity or pressure or both are increased. This effect is minimized by supplying the electrolyte at a pressure of 0.2-3.5 MPa, leading to the electrolyte flow velocity as high as 20-30 m/s in ECM (Jain, 2002). A typical electrolyte flow rate of 15 L/min was found suitable in ECH of cylindrical workpieces of 50 mm bore diameter and 100 mm bore length (Budzynski, 1983).

Keeping in view the above considerations, electrolyte flow rate in the range of 10-30 L/min was selected for the investigations. The lower limit was decided in view of ensuring sufficient flooding of the gap while the upper limit was based on the avoidance of problems of flow dynamics and sealing associated with higher flow rates. The selected range besides maintaining a proper electrolyte velocity in IEG desirable for better results, provided a wide range of 1 to 7 m/s (estimated for initial IEG involved) electrolyte velocity in IEG enabling an effective determination of influence of the electrolyte flow rate on process responses. A

ROTA meter (Rotomech) was used to measure the flow rate of electrolyte entering the work chamber. Since, the electrolyte pressure and flow are related in ECH, depending upon the selected level of flow rate the pressure is automatically adjusted by the pump as decided by the flow resistance of the circuit. The electrolyte pressure at the chamber inlet is recorded using a sensitive pressure gauge.

5.2.8 Honing Sticks

The abrasive honing sticks for use in ECH are identical to conventional honing sticks, except that they have to resist the electrolytic corrosion and are nonconductive (Benedict, 1987). As in conventional honing, the abrasive should be selfdressing (Shan, 2006).

Silicon carbide, besides being nonconductive, has been reported to perform well on cast iron in conventional honing (Schnitzler, 2001). Silicon carbide crystals are very hard (Knoop hardness 2200-2800), friable, and rather brittle with irregular grit shapes having every possible rake angle and are commonly used for grinding of low tensile strength materials like gray cast iron where high surface finish is required. Friability refers to the fracture of grits and is opposite to toughness, providing a re-sharpening ability. Vitrified bonds are porous, strong, rigid, and unaffected by oils, water, or temperature over the ranges usually encountered in metal cutting (Hajra Choudhury et. al., 1991; DeGarmo et. al., 1997). Vitrified bonded abrasive sticks can be used for high stock removal while maintaining smooth surface finishes (Production Technology, 1980).

SiC abrasives have also been successfully employed to have good results with a high process efficiency (electrolytic material removal/total material removal) in electro-chemical grinding (Kuppuswamy,1977; Kuppuswamy and Venkatesh,1979).

Therefore, vitrified bonded silicon carbide honing sticks of different grit sizes were employed in the present study keeping in view the conventional honing practices of gray cast iron, honing stick characteristics and ECH requirements. Stick grit sizes in conventional

5.2.11 ECH Tool and Operation Mode of ECH

During pilot experimentation it was observed that the introduction of end-cycle-conventional honing (with power supply switched off) had no appreciable impact on the process responses. This is obvious as the stick-out pressure employed in ECH is too low to produce any appreciable mechanical material removal. Therefore, the experimental studies were conducted with a pure electro-chemical honing mode of operation by using the ECH tool developed (discussed in Chapter-IV). No mechanical honing was done at the end of ECH cycle.

5.3 SELECTED PROCESS INPUT PARAMETERS

5.3.1 Variable Parameters

The selected process parameters and their ranges are given in Table 5.2.

Table 5.2 Range of variable parameters

Sl. No.	Parameter	Range
1.	Current intensity (ADC)	50-180
2.	Electrolyte flow rate (lpm)	10-30
3.	Electrolyte concentration (g/L)	100-200
4.	Electrolyte inlet temperature (°C)	10-50
5.	Rotary to reciprocating speed ratio	50-250
6.	Stick-out pressure (kPa)	10-30
7.	Stick grit-size	360- 1200

5.3.2 Fixed Parameters

Table 5.3 gives parameters kept fixed during the entire experimentation.

Table 5.3 Level of fixed process parameters

Sl. No.	Parameter	Level	Criteria
1.	Reciprocating speed (smpm)	0.4	• Pilot-studies • Literature review
2.	Machining time (s)	300	• Single factor experiments
3.	Initial IEG (mm)	0.5	• Pilot-studies • Work material consideration
4.	Electrolyte composition (by weight)	¾ Part NaCl + ¼ Part $NaNO_3$	• Pilot-studies • Literature review
5.	Honing stick	SiC (Vitrified bonded)	• Literature review.
6.	Mode of process operation	ECH	
7.	Work specimen	ASTM 35 CI cylindrical blocks	• Industrial applications

5.4 ECH PERFORMANCE CHARACTERISTICS

The application of manufacturing process to the work surface may produce several surface effects as shown in Fig.5.5.

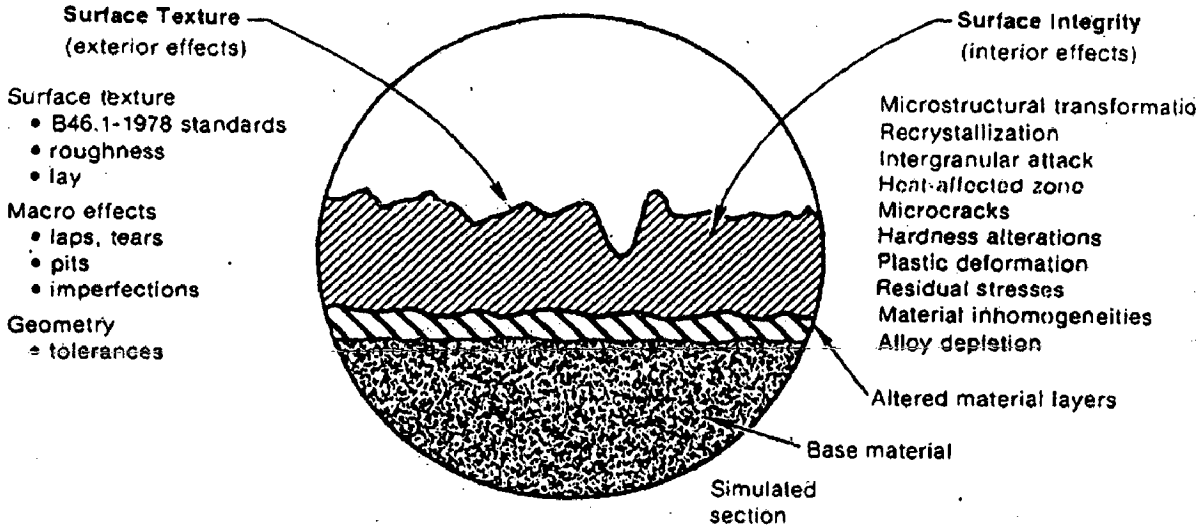

Fig. 5.5 Surface effects produced by manufacturing processes
(Machining Data Handbook, 1980)

During machining, the process energies blend with the work material properties to produce a variety of these effects. Surface effects produced during a manufacturing process affect the properties of the work material and in turn the component performance as well as reliability as given in Fig. 5.6.

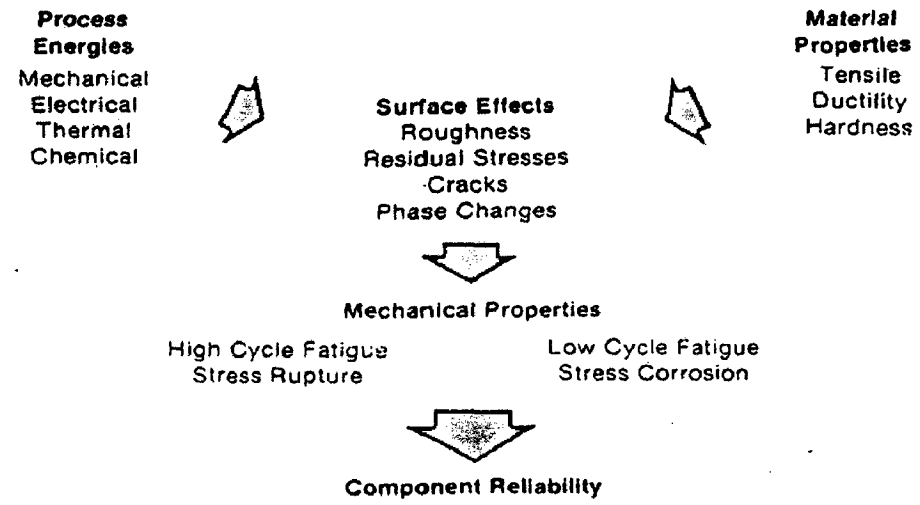

Fig. 5.6 Interaction of process with material
(Machining Data Handbook, 1980)

ECH is a micro-finishing process and surface quality assumes a prime significance. The surface quality includes both the surface texture and the surface integrity. Therefore, following a 'total surface quality approach', the response characteristics included in the present research study were determined covering all the following aspects of ECH response:

a) Surface micro-geometry,

b) Part macro-geometry,

c) Surface integrity,

d) Diametral increase rate.

In the following sections the selection and determination of various objective as well as subjective ECH response characteristics will be discussed.

5.4.1 Surface Micro-Geometrical Aspects

Surface texture, i.e. the regular and irregular spacings that tend to form a pattern or texture on the surface, is generated by a combination of factors that are either due to the manufacturing process or due to the material being finished. The reasons to measure the surface roughness are both to predict the performance of the component during service and also to control the manufacturing process. Too rough surfaces are prone to fast wear. Therefore, the surface should be smooth enough to provide sufficient bearing area to improve the wear properties and hence, the resulting tribological performance of the component. At the same time it should also allow the lubricant to be retained in small pockets to provide minimum friction so as to improve the efficiency.

Historically, the surface roughness has been the prime criterion for surface quality and resulting service life of the engineering components. Arithmetic average roughness (R_a) is by far the most commonly used response parameter in surface finish measurement and for general surface quality. Despite its limitations, it is easy to measure and offers a good overall

description of the height characteristics of the surface micro profile (Srinivasulu et. al., 1999; De Chiffre et. al., 2000). The surface roughness value R_a has a significant drawback in that many differing profiles can have same R_a and yet have very different performance behaviour. Therefore, not only the average value but also the peak intrusions of surface irregularities have a pronounced bearing on the fatigue endurance performance and fracture strength of the component material. A surface micro intrusion or crack of a depth C will have an impact similar to an internal crack of length 2C in reducing the fracture strength of the material (Reed-Hill and Abbaschian, 2003). Thus for surfaces subject to high stresses it is desirable to measure the maximum roughness height R_{max}, or average of peak-to-valley roughness heights R_{tm}. The R_{max} parameter measures the highest and lowest points of the profile and is particularly valuable as large peak-to-valley heights are prone to crack propagation (ASM Handbook, 1994).

The surface micro-geometrical process characteristics, therefore, include the dominant machining criteria, i.e., surface roughness improvement in order to evaluate the effect of the key ECH process parameters on the process performance. The percent improvements in both the R_a and R_{max} values have been analyzed. Further analyses with the aid of surface micro-profiles and scanning electron microscopy are also performed for a more detailed examination of physical character of the electrochemically honed surfaces.

5.4.1.1 Percent improvement in R_a

R_a is the universally recognized parameter of roughness. It is the arithmetic mean of the departures of the surface micro profile from the mean line. It is normally determined as the mean results of several consecutive sampling lengths (Machining Data Handbook, 1980). The commonly used sampling length, referred also as cutoff, for the calculation of R_a is 0.8mm (DeGarmo et al., 1997).

The workpieces were cleaned with acetone. Surface roughness before and after ECH was measured by Mahr Perthometer (Mahr Perthometer 4615) with a cut-off length of 0.8 mm. The change in surface roughness value R_a expressed as percentage of R_a before ECH, termed as percent improvement in R_a (PIR_a), has been taken as a response characteristic so as to negate the effect of initial surface roughness variation. Five separate measurements at top, middle and bottom were taken perpendicular to the lay obtained by boring and ECH operations and the average value used.

$$PIR_a = 100^* (Ra_{\text{before ECH}} - Ra_{\text{after ECH}}) / Ra_{\text{before ECH}} \quad (5.1)$$

5.4.1.2 Percent improvement in R_{max}

R_{max} is the maximum peak-to-valley height of the surface micro irregularities within the sampling length. R_{max} values of the work surface before and after ECH were recorded using the procedure similar to that used for R_a and percent improvement in R_{max} has been taken as a response characteristic.

Percentage improvement in R_{max} (PIR_{max}) is defined as:

$$PIR_{max} = 100^* (Rmax_{\text{before ECH}} - Rmax_{\text{after ECH}}) / Rmax_{\text{before ECH}} \quad (5.2)$$

5.4.1.3 Surface micro-profile

In an endeavor to gain more understanding of surface quality generated by ECH, the machined surfaces were further examined for their micro-profiles. Effective surface profile evaluations have been done with the help of internationally recognized parameters (ASM Handbook, 1994) such as bearing ratio, R_t, R_k, R_{pk}, M_r1, R_{vk}, and M_r2, besides the R_a and R_{max} in order to minimize the subjective assessment of the surface character. Surface micro-profile studies were done using especially prepared work samples. For this purpose, the workpices were carefully cut along their cross-section to prepare the work samples. Surface

topography was examined on optical profiler (Wyko NT 1100) interfaced with Vision® 32 software. All the work samples were examined using the VSI (vertical scanning interferometery) mode of operation with speed set 3 for a scan length of 100μm and scan width of 50μm. Some of the graphical tools (Technical Reference Manual, Wyko NT 1100) used for explaining the findings have been briefly described in the following sections:

5.4.1.3.1 Standard display

Standard display is a contour plot, a color-coded topographical map of the surface, which includes the basic statistics from the measurement.

5.4.1.3.2 2D analysis

2D analysis displays histograms taken from the surface data. It has wide variety of uses.

5.4.1.3.3 3D interactive plot

This display presents a 3-dimentional contour map of the surface.

5.4.1.3.4 3D plot

3D plot is a 3-dimentional rendering of the surface data.

5.4.1.3.5 *Filtered histogram*

The histogram plot shows the distribution of individual surface height values in histogram form, indicating how often various heights occur in the data array. The horizontal axis indicates the individual height values, while the vertical axis shows the number of data points contained within equally spaced intervals.

5.4.1.3.6 *Bearing ratio*

Bearing area is defined as the area of a surface intercepted by a plane parallel to the mean plane of the surface. Bearing Area ratio t_p, also known as the material ratio, is the ratio of the bearing area to the total evolution area. Material ratio can also be calculated as the ratio

of the length of the surface to the evaluation length at the specified depth in the profile (Fig. 5.7).

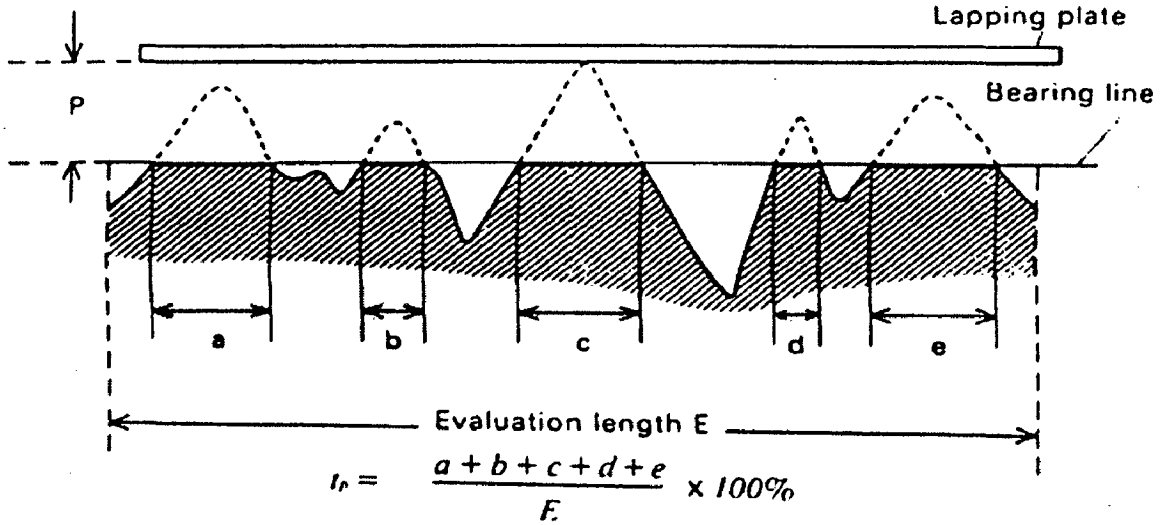

Fig. 5.7 Material ratio, tp [ASM Handbook, 1994]

The bearing ratio curve, also known as the material ratio curve, is a graphical representation of t_p parameter in relation to the surface level. The bearing ratio curve shows how the bearing ratio varies with level. The bearing ratio curve is the curve generated by running a plane, extending parallel to the mean surface plane, down through the surface, and is defined as the percentage of the plane that intercepts material, versus the depth of the plane into the surface. This curve contains all of the amplitude information of a surface.

5.4.1.4 Surface morphology

A more detailed examination of processed surface was carried out using the scanning electron micrographs. For this purpose, the workpices were carefully cut along their cross-section to prepare the work samples. A series of SEM photographs of ECHed surfaces at various increasing magnifications were taken to analyze the nature of the surface character

and resulting surface defects, if any, like laps, tears, pits or imperfections that might result due to the application of the ECH process.

5.4.2 Macro-Geometrical Aspects

Part macro-geometrical aspects include the size and geometric tolerances. These tolerances specify the diameter or the width of the tolerance zone necessary for a part to meet its required accuracy. When applying geometric tolerances a modifier is used to modify the limit of the size of a part. The maximum material condition (MMC) indicates that a part is made with the largest amount of material allowable. The least material condition (LMC) is the converse of the MMC. Regardless of feature size (RFS) indicates that tolerances apply to a geometric feature for any size it may be. Many geometric tolerances or feature control symbols are stated with respect to a particular or reference surface. There are four tolerances that specify the permitted variability of forms: flatness, straightness, out-of-roundness and cylindricity. Form tolerances describe how an actual feature may vary from a geometrical ideal feature (DeGarmo et. al., 1997).

Out-of-roundness, cylindricity and axis-straightness are the most common shape deviations that characterize the internal cylindrical electro-chemical honing. Therefore, to explore the capability of ECH in controlling form deviations and to gain better understanding of the macro-geometrical characteristics of the components processed by electro-chemical honing, Percent improvement in out-of-roundness (PIOR), Percentage improvement in cylindricity (PICyl) and Percentage improvement in axis-straightness (PIAS) were taken as macro-geometrical response characteristics. Percentage improvement of responses with reference to their pre-ECH values were taken in order to minimize the effect of any small random initial variations resulting from the precision lathe boring operation.

Out-of-roundness, cylindricity, axis-straightness and diameter were measured on a 3D Co-ordinate Measuring Machine (MOUSER KMZ 201210, ZEISS, Germany) interfaced with

Universal Measuring Software UMESS 300. Minimum 400 points in scanning mode were taken each at top, middle and bottom of the workpiece for the out-of-roundness and diameter measurements and the average value used, while a minimum 16 points were considered for cylindricity measurements.

5.4.2.1 Percent improvement in Out-of-Roundness

The polar distances (radii) between the calculated 'best fit circle' mid point and the nearest (min) and most distant (max) probing points form the circular rings of actual out-of-roundness. The form routine establishes these two reference circles which are concentric with the 'best fit circle' and which contain all of the measured points. Out-of-roundness (OR) is defined as the difference in the radii of these two reference circles (Fig. 5.8) (Operating Instructions, UMESS 300, ZEISS; DeGarmo et. al, 1997).

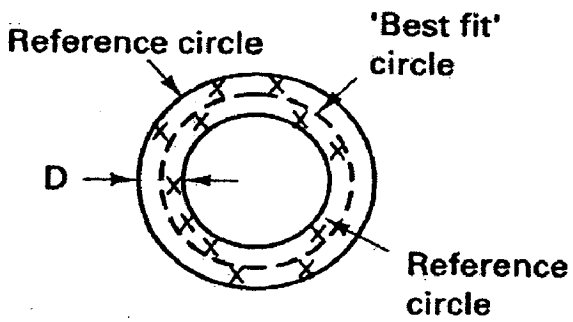

Fig. 5.8 Out-of-roundness

Percentage improvement in out-of-roundness (PIOR) is defined as:

$$PIOR = 100^* (OR_{\text{before ECH}} - OR_{\text{after ECH}}) / OR_{\text{before ECH}} \quad (5.3)$$

5.4.2.2 Percent improvement in Cylindricity

The polar distances between the calculated axis and the nearest (min) and most distant (max) probing points form the radii of two concentric cylinders. The form routine establishes these two reference cylinders which are co-axial to the 'best fit cylinder', and which just contain all of the measured points. Cylindricity (Cyl) is defined as the difference in the radius of these two reference cylinders (Fig. 5.9) (Operating Instructions, UMESS 300, ZEISS; DeGarmo et. al., 1997).

As per *ANSI Y14.5 National Standard on Dimensioning and Tolerancing,* ASME 1982 (known as the GD&T Y14.5 Standard), cylindricity is defined as (Carr and Ferreira, 1995):

"Cylindricity is a condition of a surface of revolution in which all points of the surface are equidistant from a common axis. A cylindricity tolerance specifies a tolerance zone bounded by two co-axial cylinders within which the surface must lie".

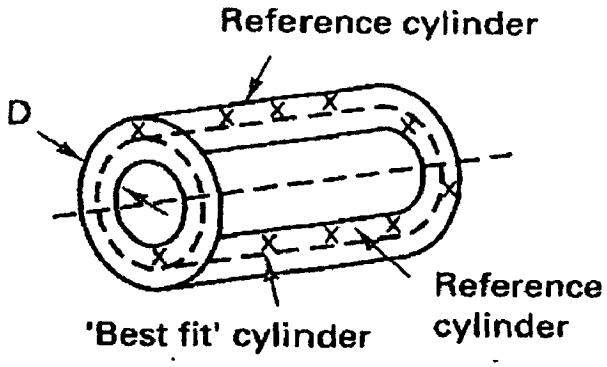

Fig. 5.9 Cylindicity

Percentage improvement in cylindricity (PICyl) is defined as:

$$PICyl = 100^* (Cylindricity_{before\ ECH} - Cylindricity_{after\ ECH}) / Cylindricity_{before\ ECH} \quad (5.4)$$

5.4.2.3 Percent improvement in Axis-straightness

Measured or previously calculated points may be used to determine a 'best fit line'. Straightness is the difference between two reference lines which are parallel to 'the best fit line' and which just contain all the measured or calculated points (DeGarmo et al., 1997). As per GD&T Y14.5 Standard, axis-straightness is defined as (Carr and Ferreira, 1995):

"Straightness is a condition where an axis is a straight line. A straightness tolerance for the derived median line of a feature specifies that the derived median line must lie within some cylindrical zone whose diameter is the specified tolerance" (Fig. 5.10).

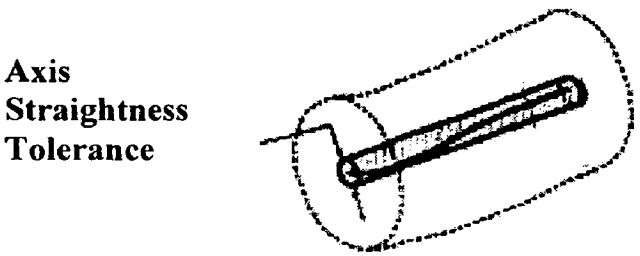

Fig. 5.10 Axis-straightness

The coordinates of 'best fit circles' mid points with reference to 'best-fit- cylinder' axis provided by machine routine were used to calculate the axis-straightness.

Percentage improvement in axis-straightness (PIAS) is defined as:

$$PIAS = 100^{*} (\text{Axis-straightness}_{\text{before ECH}} - \text{Axis-straightness}_{\text{after ECH}}) / \text{Axis-straightness}_{\text{beforeECH}} \quad (5.5)$$

5.4.3 Surface Integrity Aspects

Surface integrity aspects include a thorough examination of the probable sub-surface effect of ECH process (if any), including:

a) Microstructural changes like microcracks, microdefects (laps, inclusions, etc.), pits or selective etching, metallurgical transformations, intergranular attack.

b) Microhardness alterations,

c) Surface residual stress changes.

5.4.3.1 Microstructural examination

Microscopic examination is an important and inexpensive means of rapid initial surface integrity evaluation to examine microstructural identification such as microcracks, selective etching, IGA, inclusions, phase change, and crevice-like defects. Surface microstructural alterations, microcracks, or flaws are generally very shallow, usually of order of 0.025 to 0.075 mm. Under very abusive conditions, alterations as deep as 0.125 to 0.40 mm are reported to have been noticed. Therefore, special metallographic techniques are necessary. Optical microscopy and scanning electron microscopy are commonly used to evaluate surface metallurgy.

Cross-sectional microstructural examination was done using optical and scanning electron microscopy for identifying any sub-surface material alterations due to electro-chemical honing, in the probable altered material zone (PAMZ), such as microcracks, plastic deformations, metallurgical transformations, intergranular attack, and micro defects (laps, inclusion). To get the microstructure of work samples, the work specimens were cut along their cross-section. This was followed by polishing of the specimens on a belt-sanding machine having 180 grit emery belt. The specimens were then polished manually down to 1000 grit SiC emery paper. Final polishing was carried out on a cloth polishing wheel

machine by using red ferric oxide powder suspension. The polished specimens were mild etched by swabbing using Nital (5 mL HNO_3 and 95mL ethanol) solution. Specimens were washed and dried before being examined on a ZEISS Axiovert 200 MAI Inverted Optical Microscope interfaced with imaging software ZEISS AxioVision Release 4.1, Germany. Work samples were also examined on LEO 435 VP scanning electron microscope at various magnifications for microstructural identifications.

5.4.3.2 Microhardness

Microhardness studies are important for identifying the possible overall effects in PAMZ caused by material removal processes: hardening/softening due to metallurgical alterations, chemical softening, plastic deformation or work hardened zones. Microhardness of work samples was measured with an automatic Leitz Microhardness tester. This serves for non-destructive hardness testing (Vickers and Knoop hardness) with small test loads from 19.62×10^{-3} N to 3924.0×10^{-3} N (2 to 400 p). An automatic mechanism controls the periods of load, adjustable within wide limits. Indentations are observed and measured through the eyepiece with internal measurement readings at 400 or 500X final magnifications. The spotting accuracy is $\pm$ 2 μm.

Keeping in view the work material properties, Vickers hardness readings were taken using a 100g load at various successive incremental points from the machined surface in the probable altered material zone. It is well accepted in case of materials like gray cast iron, the individual point estimates of microhardness readings has no relevance because of the resulting uneven microhardness properties of matrix due to the presence of graphite flakes. Only the average readings should be compared. Therefore, the average of the microhardness values in PAMZ was compared with the average of microhardness values taken at

considerable distance from the edge to identify any significant changes due to application of ECH.

For the determination of Vickers hardness (Operating Instructions, Leitz) an indentation is produced by means of a diamond pyramid and optically measured. The base of the Vickers pyramid is square. The apical angle between the opposite pyramid faces is always 136°. The depth of indentation corresponds to 1/7 of the indentation diagonal. Vickers hardness (HV) is determined as:

$$HV = (1854.4 / 9.81 \times 10^{-3}) \left(\frac{F}{d^2}\right) \quad (5.6a)$$

$$= (189.03 \times 10^{3}) \left(\frac{F}{d^2}\right) \quad (5.6b)$$

where, F is load in N, d is length of the indentation diagonal in μm. The HV at the selected load for the optically measured d value can be directly obtained from the tables. While taking Vickers hardness, the glazing must be atleast 10 times t, and mutual influence of the indentations must be avoided (Fig. 5.11).

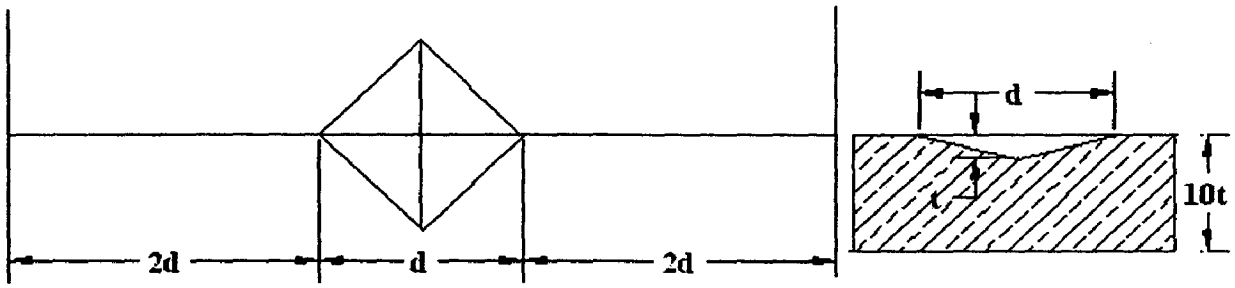

Fig. 5.11 Vickers hardness

5.4.3.3 Residual stress

Distortion may occur in the manufacturing of components as a result of application of material removal processes, which can leave substantial residual stresses in the surface layers. The nature and intensity of the residual stresses affect the functional characteristics of the component. It is established that the components are more prone to fatigue failures in case they possess tensile stresses (Reed-Hill and Abbaschian, 2003). The intensity of residual stresses is also known to have a pronounce impact on fatigue endurance strength of material. It has been reported (Machining Data Handbook, 1980) that the fatigue endurance strength decreases very sharply with fairly linear relationship when peak residual stress value increases from negative to positive (compressive to tensile). There are several ways of determining the residual stress profile. The two most common are X-ray diffraction and layer removal deflection techniques. Most of the machining-induced residual stress occurs in first 0.0125 to 0.25mm below the surface. The use of X-ray diffraction for measuring residual stress has by and large superseded the deflection test strip method. In the present study, therefore, the work samples were analyzed for residual stresses using X-ray diffraction technique.

5.4.4 Material Removal Aspects

Diametral increase rate, a most appropriate variant of material removal rate for internal cylindrical honing, was also included as a response parameter in the study from the perspective of stock allowance requirement and process productivity. This may be very useful particularly in deciding the stock allowances for a given processing time required in achieving a targeted improvement of surface micro- or macro-geometrical response characteristics as well as for exercising a better control over the part size. Workpiece diameter was measured at top, middle and bottom of the workpiece on the 3D CMM considering a minimum of 400 points in scanning mode at each location and the average value was used. The diametral increase rate (DIR) is defined as:

$$DIR = (Diameter_{after\ ECH} - Diameter_{before\ ECH}) / \text{Processing time} \quad (5.7)$$

5.5 SELECTED ECH PERFORMANCE CHARACTERISTICS

The selected ECH process performance characteristics are given in Table 5.4.

Table 5.4 Process performance characteristics

Performance measure	Performance characteristics	
	Objective (Measurable)	**Subjective cum Objective**
Surface micro-geometrical aspects	• Percent improvement in surface roughness R_a • Percent improvement in surface roughness R_{max}	• Surface profile • Scanning electron micrography (a series of SEM photographs at increasing X
Part macro-geometrical aspects	• Percent improvement in out-of-roundness • Percent improvement in cylindricity • Percent improvement in axis-straightness	
Surface integrity aspects	• Sub-surface microhardness alteration • Surface residual stress alteration	• Microstructure • Scanning electron micrography
Material removal aspects	• Diametral increase rate	

Chapter-VI
EXPERIMENTAL STUDIES

Comprehensive experimental investigations have been carried to establish process input and performance parametric relationships, material removal mechanism, machined surface characteristics, and surface integrity aspects of electro-chemical honing process. Experimentation has also been carried out for process performance optimization including the confirmation experiments conducted for verifying the results of experimental and analytical findings. Experimentation was planned based on the problem objectives and parametric analysis, keeping in view the best utilization of time and other resources as well as the availability of measuring facilities.

A series of experiments were conducted in a phased manner using the developed ECH setup and following suitable design of experiment techniques. The selection of experiment design and corresponding analysis are discussed in the subsequent sections. Experimental results of various experiments as well as the methodology adopted to analyze them are also presented in this chapter.

6.1 EXPERIMENTAL STUDY PLAN

The present work was planned in the following four phases:

6.1.1 Phase-I Pilot Experiments

The main purpose of conducting pilot experimentation was to complement the parametric analysis, as discussed in Chapter-V, for deciding suitable range and levels of process input parameters and identifying the key prospective parameters to be varied in the successive planned experiments for in-depth exploration of electro-chemical honing process performance.

6.1.2 Phase-II Time Dependent Behaviour of ECH

This phase of experimentation was planned to visualize the pattern of variation of key response characteristics of electro-chemical honing in relation with processing time. Besides giving insight into the nature of the process, this experimentation helped deciding an optimal setting of processing time so that the effect of other prominent parameters could effectively be investigated in successive phases of experimentation.

This phase of experiments were conducted at the mid position conditions of the selected experimental domain keeping all the other parameters constant except the successive processing time variation as given in Table 6.1.

Surface micro-geometrical aspects were analyzed using the percentage improvement in R_a (PIR_a) as well as percent improvement in R_{max} (PIR_{max}). The percent improvement in Out-of-roundness (PIOR), percent improvement in Cylindricity (PICyl), and percent improvement in Axis-straightness (PIAS) were taken as the response characteristics for examining the part macro-geometrical aspects. Diametral increase rate was used to evaluate the material removal aspects of electro-chemical honing process.

Table 6.1 Levels of independent parameter (Phase-II)

Process Input Parameter	Parameter Designation	Levels			
		L_1	L_2	L_3	L_4
Processing Time (min)	PT	1.5	3.0	4.5	6.0

Table.6.2 shows the levels of the parameters held fixed during experimentation.

Table 6.2 Levels of fixed parameters (Phase-II)

Sl. No.	Parameter	Level
1.	Mode of the Process Operation	ECH
2.	Work Specimen	ASTM 35 CI cylindrical blocks with initial bore = Φ60mm and length 90mm.
3.	Honing Sticks	SiC
4.	Stick Grit Size	600
5.	Electrolyte Concentration (g/L)	150
6.	Electrolyte Composition (by weight)	¾ Part NaCl + ¼ Part $NaNO_3$
7.	Initial IEG (mm)	0.5
8.	Current Intensity (ADC)	115
9.	Reciprocating Speed (surface meter per minute)	0.4
10.	Rotary to Reciprocating Speed Ratio	150
11.	Electrolyte Flow Rate (lpm)	20
12.	Electrolyte Inlet Temperature (°C)	30
13.	Stick-out Pressure (kPa)	20

6.1.3 Phase-III Evaluating Effects of Key Process Parameters on ECH Performance, Material Removal Mechanism and Work Surface Characteristics

This phase of comprehensive experimentation was planned to examine the overall influence of most of the key process input parameters in electro-chemical honing process. Process performance was evaluated considering various aspects as discussed in Chapter-V to investigate thoroughly the process parametric relationships, mechanism of material removal and work surface integrity issues.

All the seven main process parameters, as identified through parametric analysis, namely current intensity, electrolyte concentration, rotary to reciprocating speed ratio, electrolyte flow rate, electrolyte inlet temperature, stick-out pressure and grit size were

included as input process variables in this study. Each process variable was decided to be varied at three levels in order to identify any curvature present in the response pattern. To explore the interactive behavior of certain prospective parameters, the following interactions were also included for examination:

1. Current Intensity – Electrolyte Concentration (C-EC),
2. Current Intensity – Speed Ratio (C-SR), and
3. Electrolyte Concentration – Speed Ratio (EC-SR)

The levels of the process input parameters are given in Table 6.3.

Table 6.3 Process parameters and their levels (Phase-III)

Process input parameters	**Parameter Designation**	**Levels**		
		L_1	L_2	L_3
Current Intensity (ADC)	C	50	115	180
Electrolyte Concentration (g/L)	EC	100	150	200
Rotary to Reciprocating Speed Ratio	SR	50	150	250
Electrolyte Flow Rate (lpm)	F	10	20	30
Electrolyte Inlet Temperature (°C)	T	10	30	50
Stick-out Pressure (kPa)	SOP	10	20	30
Stick Grit Size	G	360	600	1200
Fixed Parameters:				
Mode of Process Operation	: ECH			
Work Specimen	: ASTM 35 CI cylindrical blocks with initial bore = Φ60mm and length 90mm.			
Honing Sticks	: SiC			
Reciprocating Speed	: 0.4 smpm			
Electrolyte Composition (by weight)	: ¾ Part NaCl + ¼ Part $NaNO_3$			
Initial IEG	: 0.5 mm			
Processing Time	: 300s			

The studies were planned to be carried out in three distinct stages:

6.1.3.1 Stage-I: Examining material removal mechanism and parametric relationships

Process input and performance parametric-analysis was selected in this stage for in-depth investigations into identification of the underlying mechanism of material removal in ECH process and examination of the effects of process input parameters on the process performance characteristics, PIR_a, PIR_{max}, PIOR, PICyl, and DIR.

6.1.3.2 Stage-II: Examining work surface characteristics

Work surface was analyzed for micro profiles using optical profilometry. Nature of the surface characteristics and any other resulting surface defects / alterations due to the application of the ECH process was also examined with the help of SEM photographs of ECHed surface taken at increasing magnifications.

6.1.3.3. Stage-III: Examining surface integrity aspects

Surface integrity investigations included three main groups of studies:

6.1.3.3.1 *Group-I: Microstructural examination* - to identify any microstructural changes due to the process application.

6.1.3.3.2 *Group-II: Microhardness examination* - to identify any microhardness alterations in PAMZ due to the process application.

6.1.3.3.3 *Group-III: Residual stress evaluation* – to identify any changes in surface residual stresses.

6.1.4 Phase-V Confirmation Experiments

These experiments were designed to validate the findings of the analytical studies.

6.2 DESIGN OF EXPERIMENTS AND ANALYSIS PROCEDURE

Experimentation and analysis of results are two essential components of scientific methodology for any investigations of product or process. In case of process, experiments are performed by investigators to discover or learn something about its performance. An experiment is a test or series of tests in which purposeful changes are made to the input parameters (variables) of a process to observe and identify the reasons for changes that may occur in the process performance characteristics. Statistical design of experiments refers to the process of planning the experiment so that appropriate data that can be analyzed by statistical methods can be collected, resulting in valid and objective conclusions (Montgomery, 2004). The primary goals of a designed experiment are to:

- Determine the variables that influence the response.
- Determine the levels of these variables.
- Determine how to manipulate these variables to control the response.

There are several advantages of experimental design (Adler et. al., 1975; Peterson, 1985):

- Number of trials is significantly reduced.
- Identification of important decision variables, which control and improve the performance of the product or the process.
- Optimal setting of parameters can be estimated.
- Experimental error can be determined.
- Inference regarding the effect of parameters on the product characteristics or process performance characteristics can be made.

The selected experimental designs for various experimental studies and their analysis procedures have been describes in the following sections:

6.2.1 DOE for Phase-II Experimentation

Phase-II experiments were conducted using one-factor-at-a-time approach, with completely randomized experimental design, with the processing time considered as the independent parameter keeping all the other parameters constant as mentioned in Table 6.2. Three replicates were taken for each of the trial conditions. The experimental data sheet for this set of experiments is given in Table 6.4.

Table 6.4 Experimental data sheet (Phase-II)

Trial No.	Processing Time (min)	Response		
		Y_{R1}	Y_{R2}	Y_{R3}
1	1.5			
2	3.0			
3	4.5			
4	6.0			

6.2.2 Analysis Procedure for Phase-II Experiments

Experimental results were analyzed in three steps:

i) Statistical analysis using standard "one-way ANOVA" and F-ratio was performed with the experimental data to test for the significance of processing time in the process performance.

ii) Paired comparison of treatment means was done using the two most powerful tests the "Fisher Least Significant Difference (LSD) Method" and "Duncan's multiple range test" to identify the most suitable processing time level. The LSD method is a very effective test for detecting true differences in means if it is applied only after the F test in analysis of variance is significant at 5 percent. Duncan's multiple range test is also

known to be very good performer in detecting true differences in means (Montgomery, 2004).

iii) Experimental data of phase-II experiments were examined with the help of average effects plots to visualize the trends of variation of the various response characteristics with the processing time. Regression analysis was performed to obtain an orthogonal polynomial best fitting the data.

6.2.3 DOE for Phase-III Experimentation

Robust design is a central component of the modern approach to the quality improvement and is a phrase used to describe any engineering activity whose objective is to develop high quality products (or processes) at low cost. A key characteristic of the robust design is the use of statistically planned (designed) experiments to identify those process variables that describe product quality. Robust design was developed in Japan by G. Taguchi in early 1950s and its wide spread use throughout Japanese industry is one of the main reasons Japan has emerged as a major producer of relatively cheap high quality products, especially in the automobile, home electronics and microprocessor sectors. The realization that quality is a vital ingredient required for success in today's globally competitive markets has prompted many engineering companies around the world to embrace the robust design concept (Evans, 2003).

Taguchi has espoused an excellent philosophy for quality control in the manufacturing industries. His philosophy has far reaching consequences, yet it is founded on three very simple and fundamental concepts. These concepts are (Roy, 1990):

1. Quality should be designed into the product and not inspected into it.

2. Quality is best achieved by minimizing the deviation from the target. The product/process should be so designed that it is immune to uncontrollable environmental factors.

3. The cost of quality should be measured as a function of deviation from the standard and losses should be measured system-wide.

Taguchi has built upon W.E. Deming's observation (Roy, 1990) that 85 % of poor quality is attributed to the manufacturing processes and only 15% to the worker. Hence, his attempt has been to develop manufacturing systems that are "robust" or insensitive to daily and seasonal variations of environment, machine wear, and other external factors.

Robust designs utilize matrix experiments using special matrices, called orthogonal arrays that allow the effects of several parameters to be determined efficiently. The orthogonality implies the statistical independence of columns enabling an efficient determination of the effects of several process parameters. Further, orthogonal arrays can be used with continuous as well as discrete factors in contrast to central composite designs commonly used in classical experiment design, especially in conjunction with the response surface methodology for estimating the curvature effects of the factors, which are useful for only continuous factors (Phadke, 1989). Another important feature of OA is that it minimizes the number of experiments.

Therefore, to study the effects of seven process input parameters and three interactions, Taguchi experiment design technique, being the most appropriate for the present research problem, was selected for phase-III experimental studies. It was decided to vary each process input parameter at three levels because any non-linear behaviour of the process parameters can only be determined if more then two levels are used (Byrne and Taguchi, 1987).

The selection of appropriate orthogonal array is based on the condition that the selected OA must satisfy the following inequality (Ross, 1988):

Total Degree of Freedom of the OA ≥ Total Degree of Freedom required for the experiment.

Since a three level parameter has 2 degree of freedom (number of levels –1), the total D.F. required for seven process input parameters, each at three levels is 14 [= 7x(3-1)]. Each second-order interaction has 4 D.F. (=2x2) and accordingly, the required total D.F. for 3 two-parameter interactions is 12 [=3x(2x2]. Hence, with seven process input parameters each at three levels and three second-order interactions, the total degree of freedom required for experiment is 26 (=14+12).

Therefore, an L_{27} (3^{13}) OA (a standard 3-level OA) was selected for the present work. Experiment design matrix for phase-III experimental studies is given in Table 6.5. The seven three level process input parameters and three two-parameter interactions were assigned to different columns of L_{27} OA using the linear graph as shown in Fig. 6.1 to achieve the maximum information out of the experimentation.

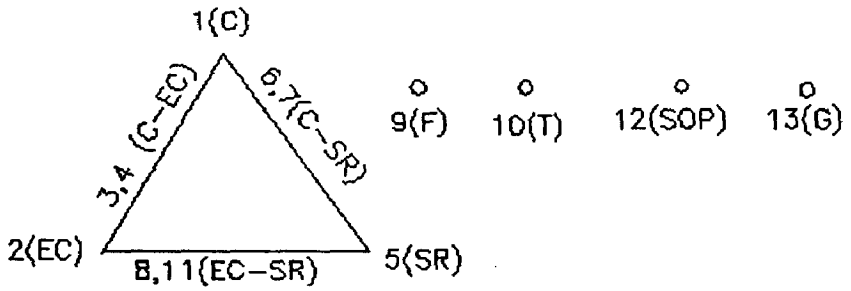

Fig. 6.1 L_{27} linear graph for parameter assignment in Phase-III

The experimental trials have been repeated twice. Trial repetitions are desirable as they increase the sensitivity of the experiment in detecting any small change due to noise variation and permit determination of the variance index called the S/N ratio. A minimum of two runs per trial is necessary to perform S/N ratio analysis. Any additional runs per trial for

expensive and time consuming tests, however, should be determined by means of expected payoff for the added cost (Ross, 1988; Roy, 1990). Higher order OAs provide increased sensitivity with comparatively lesser number of trials. For example, an L_{16} OA with two repetitions per trial provides 90% confidence in detecting a change of about one standard deviation in average. This is a fairly sensitive experiment, and sample sizes larger than this do not add much to the sensitivity (Ross, 1988).

Table 6.5 Experiment design matrix with L_{27} (3^{13}) OA (process parameters assigned) with responses (Raw Data and S/N Ratio) (Phase-III)

Trial No.	Run Order	C	EC	C-EC	C-EC	SR	C-SR	C-SR	EC-SR	F	T	EC-SR	SOP	G	Response (Raw Data)		S/N Ratio (dB)
		1	2	3	4	5	6	7	8	9	10	11	12	13	Y_{R1}	Y_{R2}	
1	27	1	1	1	1	1	1	1	1	1	1	1	1	1			
2	1	1	1	1	1	2	2	2	2	2	2	2	2	2			
3	7	1	1	1	1	3	3	3	3	3	3	3	3	3			
4	8	1	2	2	2	1	1	1	2	2	2	3	3	3			
5	15	1	2	2	2	2	2	2	3	3	3	1	1	1			
6	17	1	2	2	2	3	3	3	1	1	1	2	2	2			
7	22	1	3	3	3	1	1	1	3	3	3	2	2	2			
8	14	1	3	3	3	2	2	2	1	1	1	3	3	3			
9	24	1	3	3	3	3	3	3	2	2	2	1	1	1			
10	2	2	1	2	3	1	2	3	1	2	3	1	2	3			
11	19	2	1	2	3	2	3	1	2	3	1	2	3	1			
12	26	2	1	2	3	3	1	2	3	1	2	3	1	2			
13	23	2	2	3	1	1	2	3	2	3	1	3	1	2			
14	25	2	2	3	1	2	3	1	3	1	2	1	2	3			
15	10	2	2	3	1	3	1	2	1	2	3	2	3	1			
16	6	2	3	1	2	1	2	3	3	1	2	2	3	1			
17	12	2	3	1	2	2	3	1	1	2	3	3	1	2			
18	13	2	3	1	2	3	1	2	2	3	1	1	2	3			
19	5	3	1	3	2	1	3	2	1	3	2	1	3	2			
20	11	3	1	3	2	2	1	3	2	1	3	2	1	3			
21	3	3	1	3	2	3	2	1	3	2	1	3	2	1			
22	4	3	2	1	3	1	3	2	2	1	3	3	2	1			
23	9	3	2	1	3	2	1	3	3	2	1	1	3	2			
24	20	3	2	1	3	3	2	1	1	3	2	2	1	3			
25	18	3	3	2	1	1	3	2	3	2	1	2	1	3			
26	16	3	3	2	1	2	1	3	1	3	2	3	2	1			
27	21	3	3	2	1	3	2	1	2	1	3	1	3	2			

6.2.4 Analysis Procedure of the Selected L_{27} Orthogonal Array (Stage-I)

In Taguchi methodology, two different approaches have been recommended to be adopted for analyzing the experimental results. In the first approach, called the standard approach, the results of single run or the average of repetitive runs are processed through main effect also called analysis of means (ANOM) and analysis of variance (ANOVA). Second approach, which is strongly recommended for multiple runs, is to use the Signal-to-Noise (S/N) ratio. The S/N ratio measures the sensitivity of the quality characteristics being investigated in a controlled manner to those external influencing factors (noise factors) not under control.

The analysis of the selected L_{27} OA is discussed using the parameters C assigned to column 1 of the L_{27} OA (Table 6.5). Therefore, two responses called raw data have been recorded under the columns Y_{R1} and Y_{R2} for 27 trial conditions. The higher-the-better S/N ratio calculated using equation 6.5 §6.2.4.2§ is also recorded for each trial. Accordingly, there are total 54 raw data and 27 S/N data for each response characteristics investigated.

6.2.4.1 Raw Data Analysis (Standard Analysis)

Level totals and their averages:

The average value of the response characteristic at each parameter level is obtained by adding the results of all trial conditions at the level considered, and then dividing by the number of data points added. Thus, for parameter C, the level totals of the response at L_1, L_2 and L_3 are calculated as (Roy, 1990):

C (1) = Level total for parameter C at level L_1

$= (y_{11}+y_{12}) + (y_{21}+y_{22}) + \ldots\ldots\ldots + (y_{91}+y_{92})$

where yij = response of trial i and repetition j,

i.e. y_{12} = response of trial 1 and repetition 2.

Similarly, the other level totals C (2), and C (3) are calculated. The same procedure is followed to calculate the level totals for parameters EC, SR, F, T, SOP, and G.

The interactions C-EC, C-SR and EC-SR appear in two columns as: C-EC in columns 3 and 4, C-SR in columns 6 and 7, and EC-SR in columns 8 and 11. Therefore, both the columns are considered to calculate the level totals of interaction terms. The level total C-EC (1) for C-EC, for example, is calculated as follows (Roy, 1990):

C-EC (1) = sum of level totals due to interaction C-EC at level L_1 in columns 3 and 4. In this calculation accordingly 36 raw data points (9x2 data points for each column) are added. Following the same procedure, other level totals for interaction terms are calculated.

The average response values due to parameters and interactions are calculated as (Roy, 1990):

$\bar{C}(1)$ = Average effect due to parameter C at level L_1

$$= \frac{C(1)}{18}, \text{ [since 18 data points are added to get C (1)]}$$

Similarly, $\bar{C}(2), \bar{C}(3)$ and average effect due to other parameters are calculated.

The average effect due to the interaction C-EC at level 1 is calculated as:

$$\overline{C\text{-}EC}(1) = \frac{C\text{-}EC(1)}{36}, \text{ [since 36 data points are added to get C-EC (1)]}$$

Similar approach is used to find the average effects at other levels and for other interactions.

i) Main effects due to parameters and interactions:

The main effects of parameter C when its level changes from L_1 to L_2 and L_2 to L_3 are given as (Roy, 1990):

Main effect of parameter C when it changes from level L_1 to L_2 (L_2-L_1)

= Difference in average effects at L_2 and L_1 of parameter C = $\bar{C}(2) - \bar{C}(1)$

Main effect of parameter C when it changes from level L_2 to L_3 (L_3-L_2)

= Difference in average effects at L_3 and L_2 of parameter C = $\bar{C}$ (3) - $\bar{C}$ (2)

The main effects of other parameters and interactions are calculated accordingly.

ii) Analysis of Variance (ANOVA) (Roy, 1990)

Step 1. Total of all results (Total)

$$\text{Total} = \sum_{i=1}^{n} \sum_{j=1}^{R} y_{ij}$$

where n = Total number of trials = 27, R= Total number of repetitions = 2.

Step 2. Correction factor (C.F.)

$$\text{C.F.} = \frac{\text{Total}^2}{\text{N}}$$

where N = Total number of experiments = 27 x 2 = 54

Step 3. Total sum of squares (SS_{Total})

$$SS_{Total} = \sum_{i=1}^{n} \sum_{j=1}^{R} y_{ij}^2 - \text{C.F.}$$

Step 4. Sum of squares due to a parameter

$$SS_C = \frac{C^2(1)}{N_{C1}} + \frac{C^2(2)}{N_{C2}} + \frac{C^2(3)}{N_{C3}} - \text{C.F.}$$

where N_{C1}, N_{C2} and N_{C3} are the total number of trials with parameter C at level 1, 2, and 3 respectively. Sum of squares due to the other parameters are calculated following the same approach.

Step 5. Sum of squares due to an interaction

Since the interaction terms appear in two columns, the sum of squares due to interaction is calculated using both the columns (Roy, 1990).

$SS_{C\text{-}EC}$ = $SS_{C\text{-}EC}$ due to column 3 + $SS_{C\text{-}EC}$ due to column 4

$SS_{C\text{-}SR}$ = $SS_{C\text{-}SR}$ due to column 6 + $SS_{C\text{-}SR}$ due to column 7

$SS_{EC\text{-}SR}$ = $SS_{EC\text{-}SR}$ due to column 8 + $SS_{EC\text{-}SR}$ due to column 11

Step 6. Error sum of squares (SS_e)

$$SS_e = SS_{Total} - (SS_C + SS_{EC} + SS_{SR} + SS_F + SS_T + SS_{SOP} + SS_G + SS_{C\text{-}EC} + SS_{C\text{-}SR} + SS_{EC\text{-}SR})$$

Step 7. Degree of freedom (D.F.)

f_{Total} = Total D.F. = (Total number of trials – 1) = (R x n – 1) = (2 x 27 – 1) = 53

f_C = D.F. for parameter C = (Number of levels of parameter C -1) = 3- 1 = 2

Similarly, $f_{EC} = 2$, $f_{SR} = 2$, $f_F = 2$, $f_T = 2$, $f_{SOP} = 2$ and $f_G = 2$.

$f_{C\text{-}EC}$ = D.F. for interaction C-EC = (Product of D.F. of interacting parameters) (Ross, 1988)

$= f_C \times f_{EC} = 2 \times 2 = 4$

Similarly, $f_{C\text{-}SR} = 4$ and $f_{EC\text{-}SR} = 4$

D.F. for error = $f_e = f_{Total} - (f_C + f_{EC} + f_{SR} + f_F + f_T + f_{SOP} + f_G + f_{C\text{-}EC} + f_{C\text{-}SR} + f_{EC\text{-}SR})$

$= 53 - 26 = 27$

Step 8. Mean square or variance (MS)

$$MS_C = \text{variance due to parameter C} = \frac{SS_C}{fc}$$

$$MS_{EC} = \frac{SS_{EC}}{f_{EC}}$$

$$MS_{SR} = \frac{SS_{SR}}{f_{SR}}$$

$$MS_F = \frac{SS_F}{f_F}$$

$$MS_T = \frac{SS_T}{f_T}$$

$$MS_{SOP} = \frac{SS_{SOP}}{f_{SOP}}$$

$$MS_G = \frac{SS_G}{f_G}$$

MS_e = Variance due to error

$$= \frac{SS_e}{f_e}$$

Step 9..Percentage contribution (P)

P_C = % contribution of parameter C in total variation.

$$= \frac{SS_C}{SS_{Total}} x100$$

Similarly,

$$P_{EC} = \frac{SS_{EC}}{SS_{Total}} x100$$

$$P_{SR} = \frac{SS_{SR}}{SS_{Total}} x100$$

$$P_F = \frac{SS_F}{SS_{Total}} x100$$

$$P_T = \frac{SS_T}{SS_{Total}} x100$$

$$P_{SOP} = \frac{SS_{SOP}}{SS_{Total}} x100$$

$$P_G = \frac{SS_G}{SS_{Total}} x100$$

$P_{C\text{-}EC}$ = % contribution of interaction C-EC in total variation

$$= \frac{SS_{C\text{-}EC}}{SS_{Total}} x100$$

Similarly,

$$P_{C\text{-}SR} = \frac{SS_{C\text{-}SR}}{SS_{Total}} x100$$

$$P_{EC\text{-}SR} = \frac{SS_{EC\text{-}SR}}{SS_{Total}} x100$$

Step 10. F-ratio

$$F_C = \frac{MS_C}{SS_e}$$

$$F_{EC} = \frac{MS_{EC}}{MS_e}$$

$$F_{SR} = \frac{MS_{SR}}{MS_e}$$

$$F_F = \frac{MS_F}{MS_e}$$

$$F_T = \frac{MS_T}{MS_e}$$

$$F_{SOP} = \frac{MS_{SOP}}{MS_e}$$

$$F_G = \frac{MS_G}{MS_e}$$

$$F_{C\text{-}EC} = \frac{MS_{C\text{-}EC}}{MS_e}$$

$$F_{C\text{-}SR} = \frac{MS_{C\text{-}SR}}{MS_e}$$

$$F_{EC\text{-}SR} = \frac{MS_{EC\text{-}SR}}{MS_e}$$

Step 11..Pooling

The combining the column effects for a better estimate of error variance is referred to as "pooling". When the contribution of a parameter or interaction term is small, the sum of square for that factor is combined with the error sum of square. This process of disregarding the contribution of a selected factor and subsequently adjusting the contribution of other parameters and interactions is known as pooling. Contributions below 5% are generally not considered significant (Roy, 1990). In certain cases, pooling process may significantly affect the results. But a larger error D.F., as a result of pooling, increases the confidence level of the significant parameters. Therefore, it is recommended (Roy, 1990) that no matter the effect on the result, insignificant parameters should always be pooled.

Two pooling strategies exist (Ross, 1988):

1. Pooling up (Taguchi):

Pooling up strategy entails F-testing the smallest column effect against the next larger one to see if significance exists. If no significant F ratio exists, then these two effects are pooled to test the next larger column effect until some significant F ratio exists. No clear guidelines are established regarding confidence level. However, if the confidence level is below 90%, then it is common practice to pool the factor (Roy, 1990).

Taguchi's guideline for pooling (Taguchi, 1987) requires a start with the smallest main effect and successively includes larger effects until the total pooled D.F. equals approximately half of the total D.F. in experiment.

Phadke (1989) recommended that the sum of squares corresponding to the bottom half of the factors (as defined by lower mean square) corresponding to about half of the total degree of freedom to be used to estimate the error mean square or error variance. This rule is similar to considering the bottom half harmonics in a Fourier expansion as error and using the rest to explain the function being investigated. This is particularly useful, when error D.F. is small or zero, which is the case when all columns of OA are occupied and trials are not repeated or when analyzing S/N data.

2. Pooling down (Box and Hunter, 1978)

Pooling down strategy entails pooling all but the largest column effect and F testing the largest against the remaining factors pooled together. If the column effect is significant, then the next largest is removed from the pool and these two column effects are F-tested against all the other pooled until some insignificant F ratio is obtained.

Pooling up strategy tends to maximize the number of columns judged to be significant, and the pooling down strategy tends to minimize the number of significant columns. Pooling up strategy is preferred, as it tends to avoid beta mistakes of ignoring helpful factors (Ross, 1988; Roy, 1990).

If a parameter is pooled, the sum of square of the parameter is added to the error sum of square and the other ANOVA terms are modified. For instance, if parameter C is pooled,

$SS_{e(pooled)} = SS_e + SS_C$

$f_{e(pooled)} = f_e + f_C$

$$MS_{e(pooled)} = \frac{SS_{e(pooled)}}{f_{e(pooled)}}$$

Step 12. Pure sum of squares (SS')

If parameter C is significant,

$SS'_C = SS_C - [MS_{e(pooled)} \times f_C]$

Similarly, pure sum of squares for other significant parameters and interactions is calculated. The subtracted amount of SS must be added to the error sum of squares so that SS_{Total} remains unchanged.

$SS'_{e(pooled)} = SS_{e(pooled)} + [MS_{e(pooled)} \times f_C]$

Step 13. Modified percentage contribution

After the pooling of insignificant parameters and interactions, the percentage contribution of significant parameters and interactions are calculated. If parameter C is significant, the modified percent contribution is calculated as:

$$P'_C = \frac{SS'_C}{SS_{Total}} \times 100$$

Similarly for other significant parameters or interactions and error term, the modified percentage contribution is calculated.

P_{Total} = sum of P' for all significant parameters and interactions + $P'_{e(pooled)}$

Ross, 1988). The S/N ratio consolidates several repetitions (at least two data points are required) into one value. A high value of S/N ratio indicates optimum value of quality with minimum variation. The S/N ratio developed by Taguchi is a performance measure to choose control levels that best cope with noise (Byrne and Taguchi, 1987; Phadke, 1989).

Depending upon the type of response the following three types of S/N ratios are employed in practice (Byrne and Taguchi, 1987).

1. Lower-the-better (LB)

$$(S/N)_{LB} = -10 \log (MSD)_{LB} \quad (6.4)$$

where $(MSD)_{LB} = \frac{1}{R}\sum_{j=1}^{R} y_i^2$

2. Higher-the-better (HB)

$$(S/N)_{HB} = -10 \log (MSD)_{HB} \quad (6.5)$$

where $(MSD)_{HB} = \frac{1}{R}\sum_{j=1}^{R} \frac{1}{y_i^2}$

2. Nominal-the-best (NB)

$$(S/N)_{NB} = -10 \log (MSD)_{NB} \quad (6.6)$$

where $(MSD)_{NB} = \frac{1}{R}\sum_{j=1}^{R} (y_i - 1)^2$, R is number of repetitions=R and y_i denotes the value of the quality characteristic.

For nominal-the-best characteristic, the standard definition of MSD is used. For lower-the-better characteristic, the unstated target value is zero. For higher-the-better characteristic, the inverse of each large value becomes a small value and again the unstated target is zero. Thus for all the three MSD expressions, the smallest magnitude of MSD is being sought (Roy, 1990). The purpose of using constant 10 in the calculation is to magnify the S/N number for easier analysis and negative sign is used to set S/N ratio of the higher-the-better relative to the square deviation of the lower-the-better (Jiang and Komanduri, 1997).

The loss function for the lower-the-better and the higher-the-better product characteristics is shown in Fig. 6.3. A standard ANOVA can be done on S/N ratio, which will identify factors significant to increasing the average value of S/N ratio and subsequently reducing variation. The use of S/N ratio of the results, instead of the average values, introduces some minor changes in the analysis. Degree of freedom of the entire experiment is reduced (Roy, 1990):

D.F. with S/N ratio = number of trial conditions-1 (i.e., number of repetitions is reduced to 1)

For L_{27} OA with S/N ratio as response, the total D.F. = 27-1 = 26

The rest of the analysis follows the standard procedure.

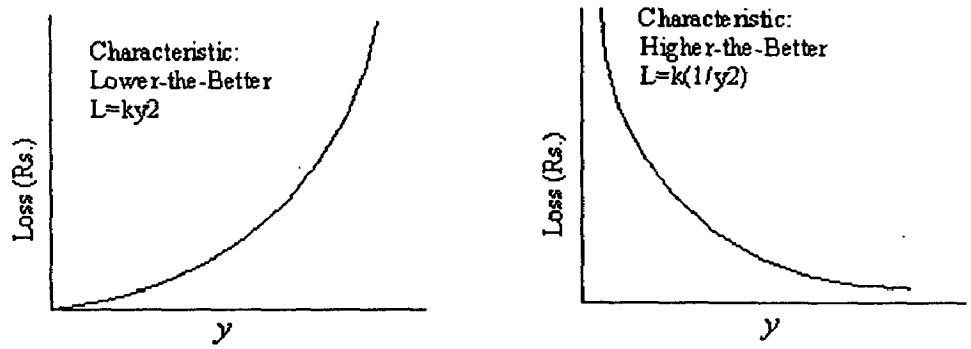

Fig. 6.3 Loss functions for lower-the better and higher-the-better type performance characteristics

6.2.4.3 Parameter Classification and Selection of Optimal Levels

ANOVA of raw data and S/N ratio identifies the control parameter (factors), which affect the average response and variation in the response respectively. The control parameters are classified into four categories:

Class I: Parameters, which affect both average and variation

Class II: Parameters, which affect variation only

Class III: Parameters, which affect average only

Class IV: Parameters, which affect nothing

The parameter design strategy is to select the appropriate levels of Class I and II parameters so as to reduce variation and Class III parameters to adjust the average value to the target value. Class IV parameters may be set at the most economical levels since nothing is affected.

6.2.4.4 Determination of Control Limits

The estimate of a parameter level mean is only a point estimate based on the average of experimental results for that level. For a better interpretation of results, a confidence interval (CI) is estimated within which the parameter level mean is likely to fall at a given statistical level of confidence. The method of calculating a CI which defines the control limits of an existing experimental mean is given as (Ross, 1988):

$$CI_1 = \sqrt{\frac{F_{\alpha,1,f_e} v_e}{n}} \tag{6.7}$$

where $F_\alpha(1,f_e)$ = F ratio at a confidence level of (1-α) against D.F. one and error D.F. f_e, v_e = error variance and n = number of trials under that condition.

6.2.4.5 Prediction of Mean

Once the optimum condition is decided, the next step involves the prediction of the mean of performance characteristic (μ) at the optimum condition. This mean is estimated only from the significant parameters as suggested by ANOVA. Suppose parameters C, EC and SR are significant and C_2, EC_1, SR_2 (second level of both C and SR and first level of EC) is optimal trial condition. Then, the mean at the optimal condition (optimal value of performance characteristic) is estimated as (Ross, 1988):

$$\mu = \overline{T} + (\overline{C_2} - \overline{T}) + (\overline{EC_1} - \overline{T}) + (\overline{SR_2} - \overline{T}) \tag{6.8}$$

$$\mu = \overline{C_2} + \overline{EC_1} + \overline{SR_2} - 2\overline{T}$$

$$F_{C\text{-}EC} = \frac{MS_{C\text{-}EC}}{MS_e}$$

$$F_{C\text{-}SR} = \frac{MS_{C\text{-}SR}}{MS_e}$$

$$F_{EC\text{-}SR} = \frac{MS_{EC\text{-}SR}}{MS_e}$$

Step 11..Pooling

The combining the column effects for a better estimate of error variance is referred to as "pooling". When the contribution of a parameter or interaction term is small, the sum of square for that factor is combined with the error sum of square. This process of disregarding the contribution of a selected factor and subsequently adjusting the contribution of other parameters and interactions is known as pooling. Contributions below 5% are generally not considered significant (Roy, 1990). In certain cases, pooling process may significantly affect the results. But a larger error D.F., as a result of pooling, increases the confidence level of the significant parameters. Therefore, it is recommended (Roy, 1990) that no matter the effect on the result, insignificant parameters should always be pooled.

Two pooling strategies exist (Ross, 1988):

1. Pooling up (Taguchi):

Pooling up strategy entails F-testing the smallest column effect against the next larger one to see if significance exists. If no significant F ratio exists, then these two effects are pooled to test the next larger column effect until some significant F ratio exists. No clear guidelines are established regarding confidence level. However, if the confidence level is below 90%, then it is common practice to pool the factor (Roy, 1990).

Taguchi's guideline for pooling (Taguchi, 1987) requires a start with the smallest main effect and successively includes larger effects until the total pooled D.F. equals approximately half of the total D.F. in experiment.

Phadke (1989) recommended that the sum of squares corresponding to the bottom half of the factors (as defined by lower mean square) corresponding to about half of the total degree of freedom to be used to estimate the error mean square or error variance. This rule is similar to considering the bottom half harmonics in a Fourier expansion as error and using the rest to explain the function being investigated. This is particularly useful, when error D.F. is small or zero, which is the case when all columns of OA are occupied and trials are not repeated or when analyzing S/N data.

2. Pooling down (Box and Hunter, 1978)

Pooling down strategy entails pooling all but the largest column effect and F testing the largest against the remaining factors pooled together. If the column effect is significant, then the next largest is removed from the pool and these two column effects are F-tested against all the other pooled until some insignificant F ratio is obtained.

Pooling up strategy tends to maximize the number of columns judged to be significant, and the pooling down strategy tends to minimize the number of significant columns. Pooling up strategy is preferred, as it tends to avoid beta mistakes of ignoring helpful factors (Ross, 1988; Roy, 1990).

If a parameter is pooled, the sum of square of the parameter is added to the error sum of square and the other ANOVA terms are modified. For instance, if parameter C is pooled,

$SS_{e(pooled)} = SS_e + SS_C$

$f_{e(pooled)} = f_e + f_C$

$$MS_{e(pooled)} = \frac{SS_{e(pooled)}}{f_{e(pooled)}}$$

Step 12. Pure sum of squares (SS')

If parameter C is significant,

$SS'_C = SS_C - [MS_{e(pooled)} \times f_C]$

Similarly, pure sum of squares for other significant parameters and interactions is calculated. The subtracted amount of SS must be added to the error sum of squares so that SS_{Total} remains unchanged.

$SS'_{e(pooled)} = SS_{e(pooled)} + [MS_{e(pooled)} \times f_C]$

Step 13. Modified percentage contribution

After the pooling of insignificant parameters and interactions, the percentage contribution of significant parameters and interactions are calculated. If parameter C is significant, the modified percent contribution is calculated as:

$$P'_C = \frac{SS'_C}{SS_{Total}} \times 100$$

Similarly for other significant parameters or interactions and error term, the modified percentage contribution is calculated.

P_{Total} = sum of P' for all significant parameters and interactions + $P'_{e(pooled)}$

6.2.4.2 S/N Data Analysis

Taguchi defines quality in terms of the loss incurred to society from the moment a product is shipped. Taguchi defines quality loss by the loss function. He unites the financial loss with the functional specification through a quadratic relationship that comes from a Taylor theorem expansion about the target value (Kackar, 1985). The quadratic loss function is described by equation 6.1.

$$L(y) = k(y-\tau)^2 \qquad if\ y-\tau \geq 0 \qquad (6.1)$$

where L = Loss in monetary unit

τ = Target value at which characteristic should be set

y = Quality characteristics

k = A constant which is dependent upon the cost structure of a process

Fig. 6.2 shows the difference between the traditional step function and the Taguchi loss function concept. The following observations can be made:

1. The farther the product/process characteristic from the target value, the greater is the loss. This loss must be zero when the quality characteristic of a product/process meets its target value.
2. The magnitude of the loss increases rapidly as the quality characteristic deviates from the target value.
3. The loss function is a continuous function and not a sudden step as in the case of traditional step function approach. This consequence of the continuous loss function illustrates the point that merely making a product within the specification limits does not necessarily mean that the product is of good quality.

The loss function has two practical applications:

(i) The primary application is for estimating the potential cost savings resulting from the improvements achieved by optimizing a product or process design.

(ii) The second application is to determine manufacturer and supplier tolerances based on the customer's perception of the quality range.

The loss function for a mass production process is expressed by

$$L(y)=k\{(y_1-\tau)^2+(y_2-\tau)^2+(y_3-\tau)^2+\ldots\ldots\ldots\ldots\ldots+(y_n-\tau)^2\}/n \quad (6.2)$$

where $y_1, y_2, \ldots\ldots, y_n$ are actual values of the characteristic for units 1, 2, 3...n respectively

n = Number of units in a given sample

k = Constant depending upon the magnitude of the characteristic and the monetary unit involved

τ = Target value at which characteristic should be set

The equation (6.2) can also be expressed as:

$$L(y)=k(MSD) \quad (6.3)$$

where MSD is mean square deviation which reflects the deviation from the target value rather than around the average value.

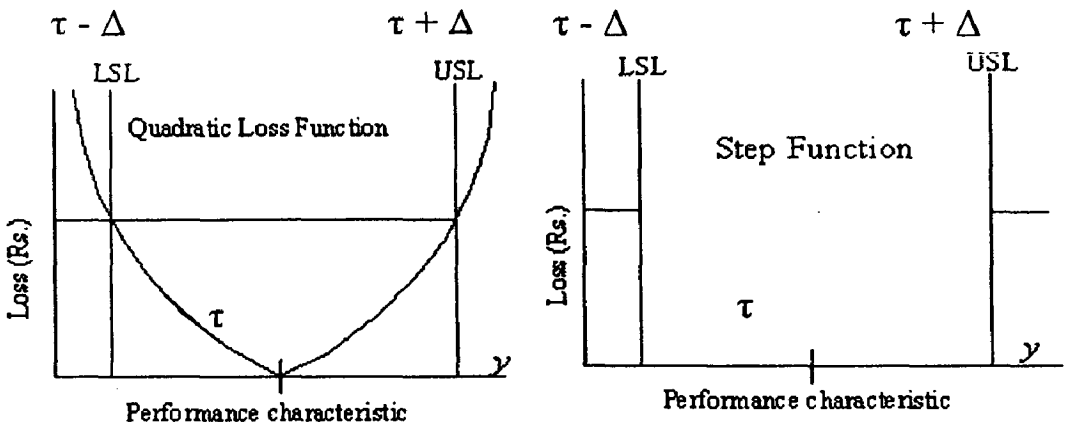

Fig. 6.2 Taguchi quadratic loss and traditional step functions

Taguchi transformed the loss function into a concurrent statistic called S/N ratio borrowed from electrical control theory (Phadke, 1989), which combines both the mean level of quality characteristic and variance around this mean into a single metric (Barker, 1990;

Ross, 1988). The S/N ratio consolidates several repetitions (at least two data points are required) into one value. A high value of S/N ratio indicates optimum value of quality with minimum variation. The S/N ratio developed by Taguchi is a performance measure to choose control levels that best cope with noise (Byrne and Taguchi, 1987; Phadke, 1989).

Depending upon the type of response the following three types of S/N ratios are employed in practice (Byrne and Taguchi, 1987).

1. Lower-the-better (LB)

$$(S/N)_{LB} = -10 \log (MSD)_{LB} \quad (6.4)$$

where $(MSD)_{LB} = \frac{1}{R}\sum_{j=1}^{R} y_i^2$

2. Higher-the-better (HB)

$$(S/N)_{HB} = -10 \log (MSD)_{HB} \quad (6.5)$$

where $(MSD)_{HB} = \frac{1}{R}\sum_{j=1}^{R} \frac{1}{y_i^2}$

2. Nominal-the-best (NB)

$$(S/N)_{NB} = -10 \log (MSD)_{NB} \quad (6.6)$$

where $(MSD)_{NB} = \frac{1}{R}\sum_{j=1}^{R} (y_i - 1)^2$, R is number of repetitions=R and y_i denotes the value of the quality characteristic.

For nominal-the-best characteristic, the standard definition of MSD is used. For lower-the-better characteristic, the unstated target value is zero. For higher-the-better characteristic, the inverse of each large value becomes a small value and again the unstated target is zero. Thus for all the three MSD expressions, the smallest magnitude of MSD is being sought (Roy, 1990). The purpose of using constant 10 in the calculation is to magnify the S/N number for easier analysis and negative sign is used to set S/N ratio of the higher-the-better relative to the square deviation of the lower-the-better (Jiang and Komanduri, 1997).

The loss function for the lower-the-better and the higher-the-better product characteristics is shown in Fig. 6.3. A standard ANOVA can be done on S/N ratio, which will identify factors significant to increasing the average value of S/N ratio and subsequently reducing variation. The use of S/N ratio of the results, instead of the average values, introduces some minor changes in the analysis. Degree of freedom of the entire experiment is reduced (Roy, 1990):

D.F. with S/N ratio = number of trial conditions-1 (i.e., number of repetitions is reduced to 1)

For L_{27} OA with S/N ratio as response, the total D.F. = 27-1 = 26

The rest of the analysis follows the standard procedure.

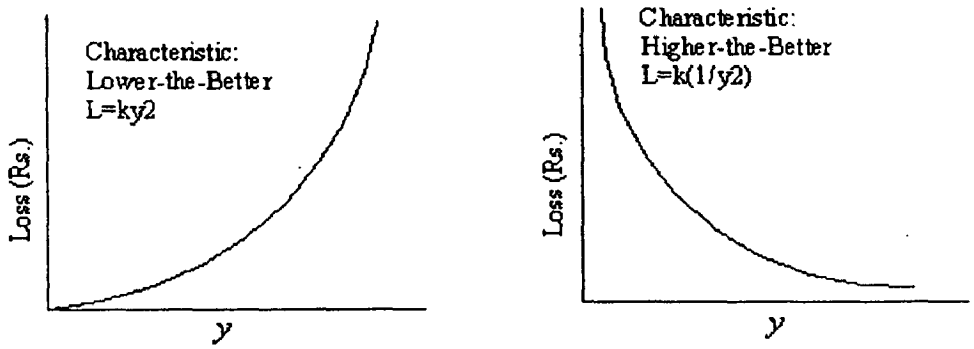

Fig. 6.3 Loss functions for lower-the better and higher-the-better type performance characteristics

6.2.4.3 Parameter Classification and Selection of Optimal Levels

ANOVA of raw data and S/N ratio identifies the control parameter (factors), which affect the average response and variation in the response respectively. The control parameters are classified into four categories:

Class I: Parameters, which affect both average and variation

Class II: Parameters, which affect variation only

Class III: Parameters, which affect average only

Class IV: Parameters, which affect nothing

The parameter design strategy is to select the appropriate levels of Class I and II parameters so as to reduce variation and Class III parameters to adjust the average value to the target value. Class IV parameters may be set at the most economical levels since nothing is affected.

6.2.4.4 Determination of Control Limits

The estimate of a parameter level mean is only a point estimate based on the average of experimental results for that level. For a better interpretation of results, a confidence interval (CI) is estimated within which the parameter level mean is likely to fall at a given statistical level of confidence. The method of calculating a CI which defines the control limits of an existing experimental mean is given as (Ross, 1988):

$$CI_1 = \sqrt{\frac{F_{\alpha,1,f_e} v_e}{n}} \tag{6.7}$$

where $F_\alpha(1,f_e)$ = F ratio at a confidence level of (1-α) against D.F. one and error D.F. f_e, v_e = error variance and n = number of trials under that condition.

6.2.4.5 Prediction of Mean

Once the optimum condition is decided, the next step involves the prediction of the mean of performance characteristic (μ) at the optimum condition. This mean is estimated only from the significant parameters as suggested by ANOVA. Suppose parameters C, EC and SR are significant and C_2, EC_1, SR_2 (second level of both C and SR and first level of EC) is optimal trial condition. Then, the mean at the optimal condition (optimal value of performance characteristic) is estimated as (Ross, 1988):

$$\mu = \bar{T} + (\overline{C_2} - \bar{T}) + (\overline{EC_1} - \bar{T}) + (\overline{SR_2} - \bar{T}) \tag{6.8}$$

$$\mu = \overline{C_2} + \overline{EC_1} + \overline{SR_2} - 2\bar{T}$$

where $\overline{C_2}$, $\overline{EC_1}$, and $\overline{SR_2}$ = average values of performance characteristic at the second level of parameter C; first level of parameter EC; and second level of parameter SR respectively and $\overline{T}$ = overall mean of the performance characteristic.

It may sometimes be possible that the predicted combination of parameters (optimal trial condition) may not be identical to those available in the experiment. In that case, the mean for that treatment condition can be obtained by averaging all the results for the trials, which are set at those particular levels (Ross, 1988).

6.2.4.6 Determination of Confidence Intervals

The estimate of mean (μ) is only a point estimate based on the average of experimental results. It is a statistical requirement that the value of parameter should be predicted along with a range within which it is likely to fall at a given level of confidence. This range is called confidence interval. The confidence interval gives maximum and minimum values between which the true average should fall at some stated confidence (Roy, 1990). Taguchi has suggested two types of confidence intervals for estimated mean of optimal treatment conditions.

(i) CI_{CE}: Around the estimated average of the treatment condition used in confirmation experiment to verify predictions. CI_{CE} is for only a small group made under the specified conditions.

(ii) CI_{POP}: Around the estimated average of a treatment condition predicted from the experiment. This is for the entire population i.e. all parts ever made under the specified conditions.

The following equations are used for calculating CI_{CE} and CI_{POP} (Roy 1990):

$$CI_{CE} = \sqrt{F_{\alpha(1,f_e)} v_e \left[\frac{1}{n_{eff}} + \frac{1}{R}\right]} \tag{6.9a}$$

$$CI_{POP} = \sqrt{\frac{F_{\alpha(1,f_e)} v_e}{n_{eff}}} \tag{6.9b}$$

where $F_{\alpha\,(1,fe)}$ = the F ratio at a confidence level of (1-α) against D.F. one and error D.F. f_e, v_e = error variance

$n_{eff} = \dfrac{N}{1 + [D.F.\ associated\ in\ the\ estimate\ of\ mean\ response]}$, N = number of trials, R = number of repetitions.

The average values of response characteristics obtained through the confirmation experiments should lie within the specified confidence interval (usual choice is 95% CI_{CE}). However, these may or may not lie within 95% CI_{POP} (Ross, 1988; Roy, 1990).

The flow chart of Taguchi methodology for experimental design and analysis is given in Appendix-D (Fig.A.D.1).

6.3 EXPERIMENTATION

Experiments were conducted under the following conditions and precautionary measures:

i) The order and replications of the trials was randomized to reduce the time error variability, if any.

ii) Each trial was performed with the pure ECH mode of operation of the process, without any post processing mechanical honing at the end of the cycle. This avoided the possibility of shading-off of even a minor parametric influence that could arise due to end cycle mechanical honing application. For this purpose, both the mechanical and the electro-chemical action were stopped simultaneously at the end of the processing time.

iii) The processing time was recorded using a stop watch set through a timer (Least count=1s).

iv) Although the control of electrolyte pH, composition, and sludge is less critical in ECH, the electrolyte purity and sludge control during experimentation was ensured using a double stage magnetic-cum-mechanical filtration, settling, and monitoring of electrolyte conductivity and pH as discussed in §5.2.4. Overnight settling was allowed between two trials and a portion of the used electrolyte was replaced with the fresh electrolyte to ensure high electrolyte purity.

v) The electrolyte composition was precisely controlled.

vi) The workpieces were thoroughly washed in tap water, dried and preserved using a thin layer of lubricating oil.

Experiments were performed on the work specimens prepared using the procedure described in §5.1. Prior to taking any measurement, the workpieces were cleaned with acetone.

Experimental Results of Macro-Geometrical Aspects

Table 6.10 Out-of-roundness (OR) of workpieces (Phase-II)

Trial No.	R1		R2		R3	
	OR (μm) before ECH	OR (μm) after ECH	OR (μm) before ECH	OR (μm) after ECH	OR (μm) before ECH	OR (μm) after ECH
1	96.96	54.50	91.53	50.00	78.69	44.60
2	61.11	28.20	73.75	34.40	49.49	22.10
3	62.71	21.30	61.62	24.20	60.38	26.20
4	54.54	18.03	56.34	19.30	41.89	15.70

*R1, R2, R3 represent repetitions.

Table 6.11 Results of part macro-geometry, PIOR (Phase-II)

Trial No.	Percent Improvement in OR (PIOR)		
	Y_{R1}	Y_{R2}	Y_{R3}
1	43.79	45.37	43.32
2	53.85	53.36	55.35
3	66.03	60.72	56.61
4	66.94	65.74	62.52

*R1, R2, R3 represent repetitions.

Table 6.12 Cylindricity (Cyl) of workpieces (Phase-II)

Trial No.	R1		R2		R3	
	Cyl (μm) before ECH	Cyl (μm) after ECH	Cyl (μm) before ECH	Cyl (μm) after ECH	Cyl (μm) before ECH	Cyl (μm) after ECH
1	57.00	22.80	53.93	20.70	37.06	16.60
2	55.53	19.00	44.39	14.20	47.03	15.60
3	51.24	13.10	59.40	17.30	75.44	16.20
4	75.09	17.00	42.98	12.30	42.99	10.65

*R1, R2, R3 represent repetitions.

Table 6.13 Results of part macro-geometry, PICyl (Phase-II)

Trial No.	Percent Improvement in Cyl (PICyl)		
	Y_{R1}	Y_{R2}	Y_{R3}
1	60.00	61.62	55.21
2	65.78	68.01	66.83
3	74.43	70.88	78.53
4	77.36	71.38	75.23

*R1, R2, R3 represent repetitions.

Table 6.14 Axis-straightness (AS) of workpieces (Phase-II)

Trial No.	R1		R2		R3	
	AS (μm) before ECH	AS (μm) after ECH	AS (μm) before ECH	AS (μm) after ECH	AS (μm) before ECH	AS (μm) after ECH
1	107.69	47.50	118.28	40.15	61.90	28.80
2	68.66	26.95	134.20	42.20	63.65	25.70
3	63.76	24.00	93.79	25.80	88.90	28.90
4	69.95	25.80	95.59	27.01	69.83	22.20

*R1, R2, R3 represent repetitions.

Table 6.15 Results of part macro-geometry, PIAS (Phase-II)

Trial No.	Percent Improvement in AS (PIAS)		
	Y_{R1}	Y_{R2}	Y_{R3}
1	55.89	66.05	53.47
2	60.75	68.55	59.62
3	62.36	72.49	67.49
4	63.12	71.74	68.21

*R1, R2, R3 represent repetitions.

Experimental Results of Material Removal Aspects

Table 6.16 Diameter (D) of workpieces (Phase-II)

Trial No.	R1		R2		R3	
	D (mm) before ECH	D (mm) after ECH	D (mm) before ECH	D (mm) after ECH	D (mm) before ECH	D (mm) after ECH
1	60.285	60.350	59.639	59.689	60.048	60.093
2	60.332	60.415	60.112	60.218	59.868	59.939
3	60.436	60.539	60.156	60.283	60.272	60.403
4	60.219	60.354	59.790	59.947	60.432	60.507

*R1, R2, R3 represent repetitions.

Table 6.17 Results of diametral increase rate, DIR (Phase-II)

Trial No.	Diametral Increase Rate (DIR) (μm/min)		
	Y_{R1}	Y_{R2}	Y_{R3}
1	43.44	33.47	30.33
2	27.77	35.23	23.70
3	22.99	28.20	29.10
4	22.55	26.20	12.50

*First reading is being termed as first repetition.

6.3.2 Phases III Experimental Studies

In this phase of comprehensive experimental studies, effects of seven process input parameters viz. current intensity, electrolyte concentration, rotary to reciprocating speed ratio, electrolyte flow rate, electrolyte inlet temperature, stick-out pressure and stick grit size, and three second-order interactions (current intensity-electrolyte concentration, current intensity-speed ratio and electrolyte concentration-speed ratio) were investigated. The levels of independent and fixed process parameters are shown in Table 6.3. Experiments were

where $\overline{C_2}$, $\overline{EC_1}$, and $\overline{SR_2}$ = average values of performance characteristic at the second level of parameter C; first level of parameter EC; and second level of parameter SR respectively and $\overline{T}$ = overall mean of the performance characteristic.

It may sometimes be possible that the predicted combination of parameters (optimal trial condition) may not be identical to those available in the experiment. In that case, the mean for that treatment condition can be obtained by averaging all the results for the trials, which are set at those particular levels (Ross, 1988).

6.2.4.6 Determination of Confidence Intervals

The estimate of mean (μ) is only a point estimate based on the average of experimental results. It is a statistical requirement that the value of parameter should be predicted along with a range within which it is likely to fall at a given level of confidence. This range is called confidence interval. The confidence interval gives maximum and minimum values between which the true average should fall at some stated confidence (Roy, 1990). Taguchi has suggested two types of confidence intervals for estimated mean of optimal treatment conditions.

(i) CI_{CE}: Around the estimated average of the treatment condition used in confirmation experiment to verify predictions. CI_{CE} is for only a small group made under the specified conditions.

(ii) CI_{POP}: Around the estimated average of a treatment condition predicted from the experiment. This is for the entire population i.e. all parts ever made under the specified conditions.

The following equations are used for calculating CI_{CE} and CI_{POP} (Roy 1990):

$$CI_{CE} = \sqrt{F_{\alpha(1,f_e)} v_e \left[\frac{1}{n_{eff}} + \frac{1}{R}\right]} \tag{6.9a}$$

$$CI_{POP} = \sqrt{\frac{F_{\alpha(1,f_e)} v_e}{n_{eff}}} \tag{6.9b}$$

where $F_{\alpha(1,fe)}$ = the F ratio at a confidence level of (1-α) against D.F. one and error D.F. f_e, v_e = error variance

$n_{eff} = \dfrac{N}{1 + [D.F.\ associated\ in\ the\ estimate\ of\ mean\ response]}$, N = number of trials, R = number of repetitions.

The average values of response characteristics obtained through the confirmation experiments should lie within the specified confidence interval (usual choice is 95% CI_{CE}). However, these may or may not lie within 95% CI_{POP} (Ross, 1988; Roy, 1990).

The flow chart of Taguchi methodology for experimental design and analysis is given in Appendix-D (Fig.A.D.1).

6.3 EXPERIMENTATION

Experiments were conducted under the following conditions and precautionary measures:

i) The order and replications of the trials was randomized to reduce the time error variability, if any.

ii) Each trial was performed with the pure ECH mode of operation of the process, without any post processing mechanical honing at the end of the cycle. This avoided the possibility of shading-off of even a minor parametric influence that could arise due to end cycle mechanical honing application. For this purpose, both the mechanical and the electro-chemical action were stopped simultaneously at the end of the processing time.

iii) The processing time was recorded using a stop watch set through a timer (Least count=1s).

iv) Although the control of electrolyte pH, composition, and sludge is less critical in ECH, the electrolyte purity and sludge control during experimentation was ensured using a double stage magnetic-cum-mechanical filtration, settling, and monitoring of electrolyte conductivity and pH as discussed in §5.2.4. Overnight settling was allowed between two trials and a portion of the used electrolyte was replaced with the fresh electrolyte to ensure high electrolyte purity.

v) The electrolyte composition was precisely controlled.

vi) The workpieces were thoroughly washed in tap water, dried and preserved using a thin layer of lubricating oil.

Experiments were performed on the work specimens prepared using the procedure described in §5.1. Prior to taking any measurement, the workpieces were cleaned with acetone.

6.3.1 Phases-II Experimentation

In this phase of experimentation, effect of the processing time was studied on the six key process response characteristics covering the micro-geometrical, macro-geometrical and material removal aspects viz. PIR_a, PIR_{max}, PIOR, PICyl, PIAS and DIR. The levels of processing time are given in Table 6.1. The values of process parameters that were held constant during experimentation are shown in Table 6.2. Total 12 test runs were performed (Table 6.4) in a completely randomized sequence to prevent the effects of unknown nuisance variables, perhaps varying out of control during the experiment, from contaminating the results. Pre and post ECH work bore properties were measured using the methods and equipment described in Chapter-V to determine the response characteristics.

The experimental results of Phase-II studies for different trail conditions are presented in Tables 6.6 through 6.17.

Experimental Results of Surface Micro-Geometrical Aspects

Table 6.6 Surface roughness (R_a) of workpieces (Phase-II)

Trial No.	R1		R2		R3	
	R_a (μm) before ECH	R_a (μm) after ECH	R_a (μm) before ECH	R_a (μm) after ECH	R_a (μm) before ECH	R_a (μm) after ECH
1	12.24	5.17	10.43	5.10	8.54	4.08
2	9.79	1.65	10.71	2.48	10.67	2.07
3	12.01	1.54	12.98	1.60	12.17	1.92
4	9.08	1.01	7.03	0.80	12.62	1.21

*R1, R2, R3 represent repetitions.

Table 6.7 Results of surface micro-geometry, PIR_a (Phase-II)

Trial No.	Percent Improvement in R_a (PIR_a)		
	Y_{R1}	Y_{R2}	Y_{R3}
1	57.77	51.16	52.30
2	83.11	76.84	80.63
3	87.13	87.67	84.21
4	88.92	88.56	90.44

*R1, R2, R3 represent repetitions.

Table 6.8 Surface roughness (R_{max}) of workpieces (Phase-II)

Trial No.	R1		R2		R3	
	R_{max} (μm) before ECH	R_{max} (μm) after ECH	R_{max} (μm) before ECH	R_{max} (μm) after ECH	R_{max} (μm) before ECH	R_{max} (μm) after ECH
1	69.56	36.08	63.50	30.75	46.51	24.60
2	55.65	9.83	68.74	14.74	66.93	12.28
3	58.57	8.86	76.93	10.76	80.51	12.91
4	45.77	6.16	28.08	4.93	57.08	7.40

*R1, R2, R3 represent repetitions.

Table 6.9 Results of surface micro-geometry, PIR_{max} (Phase-II)

Trial No.	Percent Improvement in R_{max} (PIR_{max})		
	Y_{R1}	Y_{R2}	Y_{R3}
1	48.13	51.59	47.11
2	82.34	78.56	81.65
3	84.87	86.02	83.97
4	86.53	82.443	87.04

*R1, R2, R3 represent repetitions.

Experimental Results of Macro-Geometrical Aspects

Table 6.10 Out-of-roundness (OR) of workpieces (Phase-II)

Trial No.	R1		R2		R3	
	OR (μm) before ECH	OR (μm) after ECH	OR (μm) before ECH	OR (μm) after ECH	OR (μm) before ECH	OR (μm) after ECH
1	96.96	54.50	91.53	50.00	78.69	44.60
2	61.11	28.20	73.75	34.40	49.49	22.10
3	62.71	21.30	61.62	24.20	60.38	26.20
4	54.54	18.03	56.34	19.30	41.89	15.70

*R1, R2, R3 represent repetitions.

Table 6.11 Results of part macro-geometry, PIOR (Phase-II)

Trial No.	Percent Improvement in OR (PIOR)		
	Y_{R1}	Y_{R2}	Y_{R3}
1	43.79	45.37	43.32
2	53.85	53.36	55.35
3	66.03	60.72	56.61
4	66.94	65.74	62.52

*R1, R2, R3 represent repetitions.

Table 6.12 Cylindricity (Cyl) of workpieces (Phase-II)

Trial No.	R1		R2		R3	
	Cyl (μm) before ECH	Cyl (μm) after ECH	Cyl (μm) before ECH	Cyl (μm) after ECH	Cyl (μm) before ECH	Cyl (μm) after ECH
1	57.00	22.80	53.93	20.70	37.06	16.60
2	55.53	19.00	44.39	14.20	47.03	15.60
3	51.24	13.10	59.40	17.30	75.44	16.20
4	75.09	17.00	42.98	12.30	42.99	10.65

*R1, R2, R3 represent repetitions.

Table 6.13 Results of part macro-geometry, PICyl (Phase-II)

Trial No.	Percent Improvement in Cyl (PICyl)		
	Y_{R1}	Y_{R2}	Y_{R3}
1	60.00	61.62	55.21
2	65.78	68.01	66.83
3	74.43	70.88	78.53
4	77.36	71.38	75.23

*R1, R2, R3 represent repetitions.

Table 6.14 Axis-straightness (AS) of workpieces (Phase-II)

Trial No.	R1		R2		R3	
	AS (μm) before ECH	AS (μm) after ECH	AS (μm) before ECH	AS (μm) after ECH	AS (μm) before ECH	AS (μm) after ECH
1	107.69	47.50	118.28	40.15	61.90	28.80
2	68.66	26.95	134.20	42.20	63.65	25.70
3	63.76	24.00	93.79	25.80	88.90	28.90
4	69.95	25.80	95.59	27.01	69.83	22.20

*R1, R2, R3 represent repetitions.

Table 6.15 Results of part macro-geometry, PIAS (Phase-II)

Trial No.	Percent Improvement in AS (PIAS)		
	Y_{R1}	Y_{R2}	Y_{R3}
1	55.89	66.05	53.47
2	60.75	68.55	59.62
3	62.36	72.49	67.49
4	63.12	71.74	68.21

*R1, R2, R3 represent repetitions.

Experimental Results of Material Removal Aspects

Table 6.16 Diameter (D) of workpieces (Phase-II)

Trial No.	R1		R2		R3	
	D (mm) before ECH	D (mm) after ECH	D (mm) before ECH	D (mm) after ECH	D (mm) before ECH	D (mm) after ECH
1	60.285	60.350	59.639	59.689	60.048	60.093
2	60.332	60.415	60.112	60.218	59.868	59.939
3	60.436	60.539	60.156	60.283	60.272	60.403
4	60.219	60.354	59.790	59.947	60.432	60.507

*R1, R2, R3 represent repetitions.

Table 6.17 Results of diametral increase rate, DIR (Phase-II)

Trial No.	Diametral Increase Rate (DIR) (μm/min)		
	Y_{R1}	Y_{R2}	Y_{R3}
1	43.44	33.47	30.33
2	27.77	35.23	23.70
3	22.99	28.20	29.10
4	22.55	26.20	12.50

*First reading is being termed as first repetition.

6.3.2 Phases III Experimental Studies

In this phase of comprehensive experimental studies, effects of seven process input parameters viz. current intensity, electrolyte concentration, rotary to reciprocating speed ratio, electrolyte flow rate, electrolyte inlet temperature, stick-out pressure and stick grit size, and three second-order interactions (current intensity-electrolyte concentration, current intensity-speed ratio and electrolyte concentration-speed ratio) were investigated. The levels of independent and fixed process parameters are shown in Table 6.3. Experiments were

conducted according to the trial conditions mentioned in L_{27} OA (Table 6.5). Each trial was repeated twice. The random order sequence of the trial is also given in Table 6.5.

6.3.2.1 Stage-I studies

The following properties of work bore were measured, before and after ECH, using the methods and equipment described in Chapter-V to determine the response characteristics of the process:

i) Surface roughness value R_a

ii) Surface roughness value R_{max}

iii) Out-of-roundness

iv) Cylindricity

v) Bore diameter

Experimental Results of Surface Micro-geometrical Aspects

Surface roughness R_a values of workpieces, obtained in various trial condition and their replications, are recorded in Table 6.18. The raw and S/N data of the process performance characteristic, the percent improvement in R_a (PIR_a), derived using the equation 5.1, are given in Table 6.19. The R_{max} values of surface roughness of the workpieces are presented in Table 6.20 and Table 6.21 gives the raw and S/N data of percent improvement in R_{max} (PIR_{max}), derived using the Eq. 5.2.

Table 6.18 Surface roughness (R_a) of workpieces (Phase-III)

Trial No.	R1		R2	
	R_a (μm) before ECH	R_a (μm) after ECH	R_a (μm) before ECH	R_a (μm) after ECH
1	4.71	1.87	5.06	1.87
2	6.64	2.31	5.96	1.98
3	5.86	1.83	4.95	1.63
4	5.60	1.74	5.13	1.65
5	8.01	2.45	5.33	1.79
6	9.96	2.73	4.88	1.23
7	7.23	1.18	6.34	1.28
8	5.03	1.21	4.81	1.50
9	5.33	1.13	6.52	1.45
10	4.63	1.75	5.52	1.98
11	5.58	1.56	5.38	1.45
12	5.92	1.92	5.65	1.85
13	6.58	2.00	5.72	1.82
14	3.94	1.27	6.88	2.10
15	4.51	1.17	4.89	1.14
16	5.42	0.97	6.55	1.40
17	6.00	1.32	5.99	1.10
18	6.30	1.93	5.37	1.56
19	7.26	1.19	6.08	1.06
20	4.73	1.40	6.19	1.89
21	6.15	1.32	4.36	0.83
22	4.63	0.99	4.78	1.06
23	6.33	1.73	6.25	1.55
24	4.95	1.70	4.31	1.42
25	4.51	1.26	6.27	1.48
26	4.63	0.94	6.14	1.04
27	5.93	0.82	7.54	0.85

*R1, R2 represent repetitions.

Table 6.19 Experimental results of surface micro-geometry, PIR_a (Phase-III)

Trial No.	Percent Improvement in R_a (PIR_a)		S/N Ratio (dB)
	Y_{R1}	Y_{R2}	
1	60.27	63.08	35.80
2	65.22	66.78	36.39
3	68.87	67.09	36.65
4	68.99	67.74	36.70
5	69.45	66.48	36.64
6	72.55	74.80	37.34
7	83.74	79.74	38.24
8	75.92	68.80	37.16
9	78.87	77.75	37.88
10	62.20	64.05	36.00
11	72.04	73.09	37.21
12	67.54	67.19	36.57
13	69.65	68.18	36.77
14	67.78	69.40	36.72
15	74.06	76.63	37.54
16	82.02	78.62	38.09
17	78.07	81.65	38.04
18	69.30	70.91	36.91
19	83.62	82.58	38.39
20	70.31	69.43	36.89
21	78.47	80.89	38.02
22	78.56	77.79	37.86
23	72.68	75.12	37.37
24	65.55	67.03	36.43
25	72.02	76.36	37.40
26	79.73	83.03	38.21
27	86.17	88.78	38.83
	$\overline{T}_{PIRa}$ = Overall Mean of PIR_a		
	= 73.27 %		=37.26 dB

*R1, R2 represent repetitions.

Table 6.20 Surface roughness (R_{max}) of workpieces (Phase-III)

Trial No.	R1		R2	
	R_{max} (μm) before ECH	R_{max} (μm) after ECH	R_{max} (μm) before ECH	R_{max} (μm) after ECH
1	32.38	18.21	37.90	21.61
2	43.08	22.77	42.22	21.94
3	39.82	17.53	34.37	16.43
4	37.68	15.49	33.41	13.68
5	56.19	20.90	38.31	13.40
6	59.03	22.40	36.80	14.05
7	44.91	10.98	42.58	10.33
8	36.96	17.63	33.22	14.76
9	37.74	10.18	45.69	13.44
10	33.56	16.43	40.22	20.23
11	39.72	15.42	35.84	12.84
12	40.03	16.87	37.96	16.90
13	45.85	19.82	40.64	17.04
14	30.25	10.90	47.39	18.32
15	32.04	9.02	35.65	9.85
16	35.10	8.65	40.73	11.95
17	40.97	9.74	41.29	10.37
18	41.48	21.66	38.08	18.89
19	53.37	12.96	42.83	9.69
20	35.57	13.69	40.86	14.89
21	42.38	11.35	36.37	10.45
22	32.89	10.70	32.02	9.55
23	42.61	14.69	44.90	16.06
24	33.49	17.35	30.03	16.17
25	34.65	16.17	45.69	20.12
26	35.43	10.32	42.79	11.91
27	46.08	7.60	47.94	6.85

*R1, R2 represent repetitions.

Table 6.21 Experimental results of surface micro-geometry, PIR_{max} (Phase-III)

Trial No.	Percent Improvement in R_{max} (PIR_{max})		S/N Ratio (dB)
	Y_{R1}	Y_{R2}	
1	43.75	42.98	32.74
2	47.14	48.03	33.55
3	55.99	52.19	34.65
4	58.88	59.05	35.41
5	62.80	65.02	36.11
6	62.05	61.83	35.84
7	75.54	75.74	37.58
8	52.30	55.57	34.63
9	73.02	70.58	37.12
10	51.05	49.69	34.04
11	61.19	64.17	35.93
12	57.85	55.48	35.06
13	56.78	58.07	35.18
14	63.98	61.35	35.93
15	71.85	72.37	37.16
16	75.35	70.67	37.25
17	76.24	74.89	37.57
18	47.79	50.40	33.81
19	75.72	77.38	37.68
20	61.51	63.56	35.92
21	73.20	71.28	37.17
22	67.48	70.16	36.75
23	65.52	64.24	36.24
24	48.20	46.14	33.47
25	53.32	55.97	34.74
26	70.87	72.17	37.09
27	83.52	85.71	38.55
	$\overline{T}_{PIR\,max}$ = Overall Mean of PIR_{max}		
	= 62.73 %		=35.83 dB

*R1, R2 represent repetitions.

Experimental Results of Part Macro-geometrical Aspects

The out-of-roundness of workpieces, obtained under various trial conditions and their replications, are reported in Table 6.22. The raw and S/N data of process response characteristic the percent improvement in out-of-roundness (PIOR), derived using the equation 5.3, are given in Table 6.23.

The cylindricity of workpieces, measured under various trial conditions and their replications, are reported in Table 6.24. The raw and S/N data of process response characteristic the percent improvement in cylindricity (PICyl), derived using the equation 5.4, are given in Table 6.25.

Experimental Results of Material Removal Aspects

The diameter of workpieces, used in various trial conditions and their replications, are reported in Table 6.26. The raw and S/N data of process response characteristic the diametral increase rate (DIR), derived using the equation 5.7, are given in Table 6.27.

Table 6.22 Out-of-roundness (OR) of workpieces (Phase-III)

Trial No.	R1		R2	
	OR (μm) before ECH	OR (μm) after ECH	OR (μm) before ECH	OR (μm) after ECH
1	45.85	32.09	49.70	33.72
2	50.90	32.12	59.83	36.91
3	63.75	36.78	52.83	32.44
4	70.40	55.40	47.50	36.65
5	78.65	45.43	102.70	65.72
6	89.10	40.17	65.50	31.42
7	49.63	27.20	64.53	35.10
8	74.55	44.85	40.77	26.39
9	54.47	45.80	49.70	40.90
10	57.07	38.40	55.85	35.40
11	63.85	42.50	62.13	38.63
12	76.05	44.56	57.47	35.73
13	66.10	47.80	54.90	41.70
14	71.63	37.88	70.90	37.51
15	53.40	33.90	62.30	37.20
16	40.80	23.01	58.90	35.61
17	50.95	27.27	56.07	30.84
18	53.97	45.20	39.37	31.90
19	96.07	64.30	90.43	63.03
20	39.85	31.80	63.03	50.75
21	61.73	35.12	45.83	27.94
22	50.00	38.60	48.80	37.00
23	48.80	22.70	77.03	32.25
24	44.40	35.40	75.00	58.20
25	49.23	31.41	76.83	46.20
26	58.67	31.01	80.70	39.81
27	69.23	26.60	66.53	28.60

*R1, R2 represent repetitions.

Table 6.23 Experimental results of part macro-geometry, PIOR (Phase-III)

Trial No.	Percent Improvement in OR (PIOR)		S/N Ratio (dB)
	Y_{R1}	Y_{R2}	
1	30.01	32.14	29.83
2	36.90	38.31	31.50
3	42.31	38.59	32.11
4	21.31	22.84	26.86
5	42.23	36.01	31.77
6	54.91	52.04	34.55
7	45.20	45.61	33.14
8	39.85	35.26	31.44
9	15.91	17.71	24.47
10	32.71	36.62	30.76
11	33.44	37.82	30.99
12	41.41	37.83	31.93
13	27.69	24.04	28.19
14	47.12	47.10	33.46
15	36.52	40.29	31.66
16	43.61	39.54	32.35
17	46.48	45.00	33.20
18	16.24	18.97	24.84
19	33.07	30.30	29.99
20	20.20	19.49	25.95
21	43.11	39.04	32.24
22	22.80	24.18	27.41
23	53.48	58.14	34.91
24	20.27	22.40	26.55
25	36.21	39.87	31.57
26	47.14	50.67	33.77
27	61.58	57.01	35.44
	$\overline{T}_{PIOR}$ = Overall Mean of PIOR		
	= 36.64 %		= 30.77 dB

*R1, R2 represent repetitions.

Table 6.24 Cylindricity (Cyl) of workpieces (Phase-III)

Trial No.	R1		R2	
	Cyl (μm) before ECH	Cyl (μm) after ECH	Cyl (μm) before ECH	Cyl (μm) after ECH
1	24.00	14.64	52.10	30.33
2	23.50	11.05	30.10	13.60
3	38.90	17.50	35.90	17.17
4	43.50	24.93	30.60	18.45
5	87.30	47.05	64.20	36.84
6	43.20	10.68	58.20	16.56
7	38.10	15.71	27.40	11.15
8	20.40	10.04	29.80	15.84
9	30.60	24.27	26.30	20.25
10	21.30	12.14	38.00	20.10
11	111.70	62.03	30.70	15.91
12	22.30	10.41	31.00	15.32
13	14.20	9.16	68.70	46.88
14	19.40	6.45	19.30	7.04
15	25.50	13.39	47.50	23.10
16	28.70	12.72	57.20	24.37
17	31.80	11.44	27.80	8.92
18	64.40	50.80	49.60	37.37
19	37.50	21.38	37.60	20.91
20	29.10	21.46	22.10	16.50
21	21.20	9.53	58.60	28.28
22	42.90	30.18	30.50	20.91
23	82.20	23.41	41.30	10.91
24	99.30	67.18	34.40	21.97
25	20.80	11.01	19.50	9.39
26	52.10	20.17	35.80	12.22
27	25.80	5.40	35.30	8.78

*R1, R2 represent repetitions.

Table 6.25 Experimental results of part macro-geometry, PICyl (Phase-III)

Trial No.	Percent Improvement in Cyl (PICyl)		S/N Ratio (dB)
	Y_{R1}	Y_{R2}	
1	39.01	41.79	32.11
2	52.97	54.80	34.63
3	55.01	52.17	34.57
4	42.70	39.69	32.28
5	46.10	42.62	32.92
6	75.29	71.55	37.31
7	58.76	59.29	35.42
8	50.80	46.84	33.75
9	20.69	23.02	26.75
10	43.02	47.10	33.05
11	44.47	48.17	33.29
12	53.33	50.58	34.30
13	35.49	31.76	30.49
14	66.75	63.52	36.27
15	47.47	51.38	33.86
16	55.69	57.40	35.05
17	64.02	67.90	36.37
18	21.12	24.66	27.11
19	42.99	44.39	32.80
20	26.26	25.33	28.23
21	55.05	51.75	34.54
22	29.64	31.43	29.69
23	71.52	73.58	37.21
24	32.35	36.12	30.65
25	47.07	51.83	33.85
26	61.28	65.87	36.05
27	79.05	75.12	37.73
	$\overline{T}_{PICyl}$ = Overall Mean of PICyl		
	= 49.03 %		= 33.34dB

*R1, R2 represent repetitions.

Table 6.26 Diameter (D) of workpieces (Phase-III)

Trial No.	R1		R2	
	D (mm) before ECH	D (mm) after ECH	D (mm) before ECH	D (mm) after ECH
1	59.898	59.982	59.758	59.809
2	59.934	60.001	60.074	60.154
3	59.974	60.026	59.820	59.879
4	60.059	60.155	59.743	59.807
5	60.009	60.101	59.740	59.822
6	60.006	60.078	59.922	59.972
7	60.036	60.114	59.934	59.997
8	59.956	60.012	59.807	59.869
9	59.959	60.054	60.018	60.104
10	59.767	59.829	59.917	59.980
11	59.878	59.957	59.937	60.011
12	59.838	59.902	59.738	59.807
13	59.821	59.871	59.988	60.067
14	59.899	60.000	59.855	59.972
15	59.850	59.975	59.909	60.061
16	59.900	60.026	59.865	59.990
17	59.928	60.108	59.744	59.904
18	59.703	59.753	59.993	60.078
19	59.920	60.128	59.877	60.079
20	59.831	59.859	59.908	59.959
21	59.946	60.249	60.003	60.277
22	59.871	60.011	59.905	60.080
23	59.747	59.964	59.855	60.106
24	60.027	60.186	59.793	59.953
25	60.036	60.159	59.855	59.951
26	59.983	60.235	59.892	60.116
27	59.943	60.225	59.880	60.169

*R1, R2 represent repetitions.

Table 6.27 Experimental results of diametral increase rate (DIR) (Phase-III)

Trial No.	Diametral Increase Rate (DIR) (μm/min)		S/N Ratio (dB)
	Y_{R1}	Y_{R2}	
1	16.76	10.17	21.80
2	13.26	15.86	23.16
3	10.45	11.84	20.89
4	19.19	12.83	23.57
5	18.43	16.40	24.77
6	14.42	10.03	21.32
7	15.45	12.71	22.85
8	11.37	12.35	21.46
9	19.02	17.20	25.13
10	12.31	12.65	21.92
11	15.74	14.83	23.67
12	12.84	13.61	22.42
13	10.17	15.83	21.66
14	20.10	23.50	26.69
15	25.05	30.38	28.73
16	25.05	25.01	27.97
17	35.94	32.15	30.60
18	10.17	16.93	21.82
19	41.64	40.49	32.27
20	5.55	10.35	16.80
21	60.55	54.95	35.20
22	28.11	35.00	29.83
23	43.27	50.15	33.32
24	31.85	32.11	30.10
25	24.52	19.19	26.60
26	50.40	44.82	33.51
27	56.47	57.75	35.13
	$\overline{T}_{DIR}$ = Overall Mean of DIR		
	= 24.02 (μm/min)		= 26.04 dB

*R1, R2 represent repetitions.

6.3.2.2 Stage-II and III studies

Stage-II and III studies were conducted using the special metallographic techniques and procedure described in Chapter-V.

Stage-III Group-II: Microhardness examination

In order to identify the microhardness alterations, if any, due to the process application, five work samples processed under different trial conditions were selected as shown in Table 6.28. An unprocessed work sample was also included in the study.

Table 6.28 Work samples and their trial conditions used for microhardness examination

Work Sample Designation	Trial Condition
32	$C_3EC_3SR_1F_2T_1SOP_1G_3$
49	$C_1EC_3SR_1F_3T_3SOP_2G_2$
50	$C_3EC_1SR_2F_1T_3SOP_1G_3$
34	$C_3EC_3SR_2F_3T_2SOP_2G_1$
9	$C_2EC_1SR_2F_3T_1SOP_3G_1$
R	Without ECH

Vickers microhardness readings were taken using a 100g load at various successive incremental points from the machined surface. Microhardness readings of the work samples are enumerated in Table 6.29 through 6.34.

Table 6.29 Microhardness values of work sample 32

Distance from	HV (Vickers Hardness)			
Machined Surface	R1	R2	R3	Average HV
0.03	245.0	240.0	285.0	256.7
0.07	228.0	311.0	264.0	267.7
0.14	240.0	245.0	272.0	252.3
0.21	264.0	269.0	259.0	264.0
0.28	254.0	228.0	297.0	259.7
0.35	309.0	328.5	274.0	303.8
0.42	274.0	259.0	297.0	276.7
0.49	247.0	228.0	253.0	242.7
0.56	253.0	280.0	309.0	280.7
0.63	228.0	363.0	263.0	284.7
0.70	333.0	269.0	274.0	292.0
0.77	272.0	315.5	240.0	275.8

*R1, R2, R3 represent readings

Table 6.30 Microhardness values of work sample 49

Distance from	HV (Vickers Hardness)			
Machined Surface	R1	R2	R3	Average HV
0.03	228.0	245.0	254.0	242.3
0.07	213.0	280.0	285.0	259.3
0.14	254.0	303.0	216.5	257.8
0.21	254.0	228.0	306.0	262.7
0.28	401.0	274.0	253.0	309.3
0.35	274.0	245.0	309.0	276.0
0.42	259.0	253.0	280.0	264.0
0.49	254.0	315.5	259.0	276.2
0.56	237.0	240.0	228.0	235.0
0.63	237.0	285.0	264.0	262.0
0.70	291.0	274.0	303.0	289.3
0.77	285.0	243.0	292.0	273.3

*R1, R2, R3 represent readings

Table 6.31 Microhardness values of work sample 50

Distance from Machined Surface	HV (Vickers Hardness)			
	R1	R2	R3	Average HV
0.03	315.5	322.0	322.0	319.8
0.07	315.5	309.0	322.0	315.5
0.14	291.0	373.0	280.0	314.7
0.21	363.0	415.0	259.0	345.7
0.28	309.0	259.0	366.0	311.3
0.35	357.0	366.0	306.0	343.0
0.42	279.0	328.5	297.0	301.5
0.49	303.0	272.0	280.0	285.0
0.56	328.5	333.0	216.5	292.7
0.63	224.0	297.0	357.0	292.7
0.70	302.0	401.0	269.0	324.0
0.77	358.5	401.0	374.0	377.8

*R1, R2, R3 represent readings

Table 6.32 Microhardness values of work sample 34

Distance from Machined Surface	HV (Vickers Hardness)			
	R1	R2	R3	Average HV
0.03	401.0	333.0	343.5	359.2
0.07	309.0	309.0	306.0	308.0
0.14	336.0	272.0	328.5	312.2
0.21	374.5	328.5	274.0	325.7
0.28	216.5	280.0	322.0	272.8
0.35	280.0	302.0	269.0	283.7
0.42	401.0	259.0	240.0	300.0
0.49	291.0	237.0	336.0	288.0
0.56	228.0	315.5	259.0	267.5
0.63	328.5	292.0	383.0	334.5
0.70	259.0	366.0	309.0	311.3
0.77	297.0	401.0	264.0	320.7

*R1, R2, R3 represent readings

Table 6.33 Microhardness values of work sample 9

Distance from Machined Surface	HV (Vickers Hardness)			
	R1	R2	R3	Average HV
0.03	614.0	259.0	245.0	372.7
0.07	336.0	264.0	309.0	303.0
0.14	280.0	291.0	264.0	278.3
0.21	291.0	254.0	322.0	289.0
0.28	240.0	285.0	259.0	261.3
0.35	254.0	264.0	264.0	260.7
0.42	216.0	274.0	303.0	264.3
0.49	297.0	285.0	343.5	308.5
0.56	297.0	291.0	351.0	313.0
0.63	467.0	259.0	292.0	339.3
0.70	297.0	302.0	216.0	271.7
0.77	322.0	383.0	259.0	321.3

*R1, R2, R3 represent readings

Table 6.34 Microhardness values of work sample R

Distance from Machined Surface	HV (Vickers Hardness)			
	R1	R2	R3	Average HV
0.03	264.00	264.0	285.0	271.0
0.07	309.0	254.0	232.5	265.2
0.14	420.0	303.0	237.0	320.0
0.21	224.5	291.0	213.0	242.8
0.28	285.0	292.0	259.0	278.7
0.35	280.0	254.0	303.0	279.0
0.42	343.5	401.0	274.0	339.5
0.49	259.0	303.0	245.0	269.0
0.56	274.0	224.5	216.5	238.3
0.63	224.5	276.5	280.0	260.3
0.7	291.0	202.5	297.0	263.5
0.77	221.0	322.0	259.0	267.3

*R1, R2, R3 represent readings

Chapter-VII

ANALYSIS AND DISCUSSION OF RESULTS

Results of experimental studies presented in Chapter-VI have been analyzed and discussed in this chapter. The analysis has made use of graphical representations and various statistical analysis tools to draw relevant conclusions viz-à-viz the objective of concerned investigations. The analysis of Phase-II and III experimental studies has been presented in this chapter while the discussions on phase-IV studies have been included in their respective sections. Prediction of optimal values of various individual process performance characteristics within the selected experimental domain has also been done in this chapter.

7.1 PHASE-II EXPERIMENTAL STUDIES

These studies were conducted to investigate the influence of processing time on the various process performance characteristics of ECH, covering the surface micro-geometrical aspects, part macro-geometrical aspects and material removal aspects. In order to study the effect of the processing time on different process performance characteristics, statistical analysis using ANOVA, F-test, Fisher LSD test, Duncan's multiple range test and regression analysis was performed. There were several objectives of the statistical analysis, such as:

(1) To test for significance of processing time for the performance characteristic concerned,

(2) To test for significance of contrasts,

(3) To obtain a best fit model describing the time dependence behaviour of the performance characteristics,

(4) To select an appropriate processing time for the Phase-III experimentation.

7.1.1 Effects on Percent Improvement in R_a

The results of the studies on the effect of processing time on the percent improvement in R_a (PIR_a) are given in Table 6.7. The experiments were conducted as per the procedure described in Section 6.3.

To perform one-way ANOVA, an effect model was set-up:

$$Y_{ij} = \mu + \tau_i + \varepsilon_{ij}, \quad i = 1, 2, 3, 4 \text{ and } j = 1, 2, 3.$$

Where Y_{ij} is the ijth observation of PIR_a; μ is the overall mean; τ_i is the ith treatment effect and ε_{ij} is the error term. The output from the ANOVA (Dubey and Shan, 1997) is given in Table 7.1.

Table 7.1 ANOVA results for percent improvement in R_a data

Source	SS	D.F.	MS	F	P-value
Processing time	2367.52	3	789.17	117.27*	5.96255E-7
Error	53.84	8	6.73		
Total	2421.36	11			

*Significant at 95 percent confidence level.

In order to determine whether the processing time influences the PIR_a, F-test was performed to see if the mean of PIR_a for processing time levels 'μ_i' are equal. The decision is based on a comparison of the computed F value with the tabulated F value for a given alpha with the appropriate degrees of freedom. An alpha of 0.05 was chosen for this experiment (for other experiments, as well). An F-value of 117.27 indicates that the processing time main effect is significant and there is only a chance of less than 0.0001% that this could have been due to error.

Duncan's multiple range test was now appropriate to judge the contrasts. The change of PIR_a between the successive processing time levels were tested for their significance.

Table 7.2 gives the results the Duncan's multiple range test on incremental PIR_a values observed with processing time.

Table 7.2 Results of Duncan's multiple range test (PIR_a) (Phase-II)

Processing Time (min)	Mean Percent Improvement in R_a	Incremental PIR_a	Duncan's multiple range test results
1.5	53.7	-	-
3.0	80.2	26.45	Significant
4.5	86.3	6.14	Significant
6.0	89.3	2.97	Not significant

The standard error of each average is $S_{\overline{Yi.}} = \sqrt{\frac{MS_E}{n}} = 1.50$. Thus, the least significant range $R_2 = r_{0.05}(2, 8)\ S_{\overline{Yi.}} = 3.26 \times 1.50 = 4.88$.

Polynomial regression between the processing time levels including the beginning of processing (PT=0.00) and their corresponding mean PIR_a was performed using the statistical software Origin 6.1 to obtain a best fit trend of PIR_a with processing time. The results are shown in Table 7.3. The values of 'Prob>|t|' less than 0.05 for both the linear and quadratic coefficients of regression indicate that these terms are significant. The quadratic model F-value of 92.53393 implies the model is significant. There is only 1.069% chance that a 'Model F-value' this large could occur due to noise. A high value of 'R-squared' indicates that about 98.931 percent of variability in PIR_a data is explained by the processing time.

The pattern of variation of PIR_a with the processing time is shown in Fig. 7.1. The ANOVA results indicated that the processing time main effect is highly significant for percent improvement in R_a. Duncan's multiple range test results indicated that the significant increments in PIR_a could be achieved upto a processing time of 4.5 min. Fisher LSD test also led to the same conclusions.

Table 7.3 Polynomial Regression for PIR_a

$PIR_a = A + B_1*(PT) + B_2*(PT)^2$

Parameter	Value	Error	t-Value	Prob>|t|
A	2.2668	5.13995	0.43969	0.70311
B_1	37.291	4.05912	9.18427	0.01165
B_2	-3.8684	0.64873	-5.96034	0.02701

R-Square (COD)	Adj. R-Square	Root-MSE (SD)	N
0.98931	0.97862	5.4615	5

ANOVA Table:

Item	Degrees of Freedom	Sum of Squares	Mean Square	F-statistic	Prob>F
Model	2	5520.204	2760.102	92.53393	0.01069
Error	2	59.656	29.828		
Total	4	5579.86			

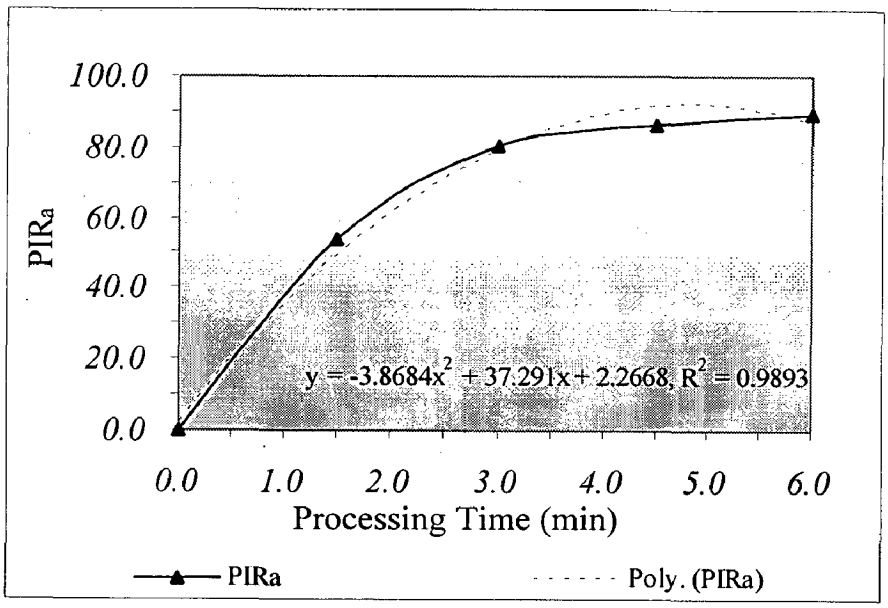

Fig. 7.1 Effect of processing time on percent improvement in R_a

Polynomial regression results show that the pattern of percent improvement in surface roughness value R_a with the processing time in ECH can be approximated by a quadratic relationship in the selected experimental region as given by equation 7.1.

$$PIR_a = 2.2668 + 37.291(PT) - 3.8684(PT)^2 \quad (7.1)$$

From the trend plot of Fig. 7.1 it can be seen that a processing time of 5 min is appropriate for investigating the effects of other variables in ECH process considering the most dominating machining criteria, i.e. the percent improvement in R_a.

It is clear from Fig. 7.1 that the percent improvement in R_a value increases as the processing time increases. Major improvement occurs in the first few minutes of ECH operation and the successive increments decrease as the processing time increases. This behaviour of PIR_a can be explained by considering the effect of processing time on the depth of existing micro- as well as the macro-geometrical error in the surface profile as shown in Fig. 7.2. In ECH, passivating metal oxide film is formed due to the electro-chemical action.

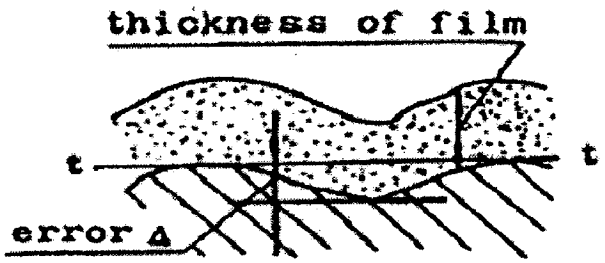

Fig. 7.2 Passivating metal oxide film covering a geometrical error

The action of honing sticks removes the resistive metal oxide film from the higher spots, thus making them more receptive for electrochemical attack. The lower areas still remaining covered with resulting metal oxide film have weaker electrolytic action. As a result, the error depth Δ goes on diminishing (and hence the thickness of resistive film also decreases accordingly) as the processing time increases. The resistivity of the covering metal oxide film, besides other factors, is also dependent upon the thickness. Therefore, the successively decreasing resistive power of the covering metal oxide film due to the

planishing effect of ECH, results in a diminishing pattern of improvement in R_a with the processing time.

7.1.2. Effects on Percent Improvement in R_{max}

Experimental trial results of Phase-II experimentation on the percent improvement in R_{max}, are presented in Table 6.9. The experimentation was carried out as per the method described in Section 6.3.

An analysis similar to PIR_a was performed to analyze the experimental findings on PIR_{max} due to the variation of the processing time. Table 7.4 shows the ANOVA results for PIR_{max}.

Table 7.4 ANOVA results for percent improvement in R_{max} data

Source	SS	D.F.	MS	F	P-value
Processing time	2757.50	3	919.17	216.51*	5.35459E-8
Error	33.96	8	4.25		
Total	2791.46	11			

*Significant at 95 percent confidence level.

The model F-value of 216.51 indicates that the processing time main effect is significant and there is only a chance of less than 0.0001% that this could have been due to error.

The Results of Duncan's multiple range test applied to evaluate the significance of incremental PIR_{max} values observed with processing time are illustrated in Table 7.5.

Table 7.5 Results of Duncan's multiple range test (PIR_{max}) (Phase-II)

Processing Time (min)	Mean Percent Improvement in R_{max}	Incremental PIR_{max}	Duncan's multiple range test results
1.5	48.9	-	-
3.0	80.8	31.91	Significant
4.5	85.0	4.10	Significant
6.0	85.3	0.39	Not significant

The standard error of each average is $S_{\overline{Yi.}} = \sqrt{\frac{MS_E}{n}} = 1.19$. Thus, the least significant range $R_2 = r_{0.05}(2, 8)\ S_{\overline{Yi.}} = 3.26 \times 1.19 = 3.878$.

Similar to PIR_a results, a quadratic model given by equation 7.2 was found best fitting the PIR_{max} data.

$$PIR_{max} = 0.8344 + 37.571(PT) - 3.9653(PT)^2 \qquad (7.2)$$

Polynomial regression analysis between the processing time levels and corresponding PIR_{max} means performed using the statistical software Origin 6.1 is given in Table 7.6. The linear and quadratic coefficients of regression are significant at a significance level of 0.00662 and 0.01499 respectively. The model F-value of 157.6714 implies that the model is significant. There is only a 0.63% chance that a 'Model F-value' this large could occur due to noise. The model is capable of explaining about 99.35 percent of variability in PIR_{max} data. The variation of PIR_{max} with the processing time is shown in Fig. 7.3. The ANOVA results indicate that the processing time main effect is highly significant for percent improvement in R_{max}. Duncan's multiple range test results indicate that the significant increments in PIR_{max} could be achieved upto a processing time of 4.5 min. Fisher LSD test also led to the same conclusions.

Table 7.6 Polynomial Regression for PIR_{max}

$PIR_{max} = A + B_1*(PT) + B_2*(PT)^2$

Parameter	Value	Error	t-Value	Prob>|t|
A	0.8344	3.88973	0.21008	0.85307
B_1	37.571	3.0718	12.23079	0.00662
B_2	-3.9653	0.49094	-8.07654	0.01499

R-Square (COD)	Adj. R-Square	Root-MSE (SD)	N
0.9935	0.9874	4.13307	5

ANOVA Table:

Item	Degrees of Freedom	SS	Mean Square	F-statistic	Prob>F
Model	2	5386.77543	2693.38771	157.67139	0.0063
Error	2	34.16457	17.08229		
Total	[illegible]	[illegible]			

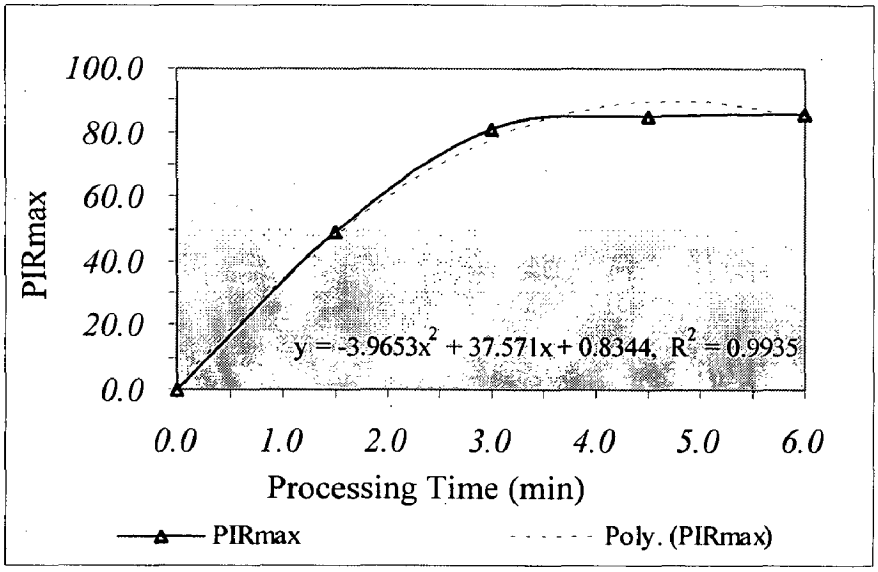

Fig. 7.3 Effect of processing time on percent improvement in R_{max}

Polynomial regression results show that the pattern of percent improvement in surface roughness R_{max} value with the processing time in ECH can be approximated by a quadratic relationship in the selected experimental region. It is clear from the Fig. 7.3 that the percent

improvement in R_{max} value increases as the processing time increases. Major improvement occurs in first few minutes of ECH operation and the successive increments decrease as the processing time increases. The variation of PIR_{max} with processing time followed a pattern similar to that of PIR_a. The effect of diminishing resistive power of metal oxide film, as explained earlier, may be a reason behind this pattern.

7.1.3 Effects on Percent Improvement in Out-of-Roundness

The experimental data for the process macro-geometrical performance characteristic, the percent improvement in out-of-roundness (PIOR) (Table 6.11) was analyzed following an approach similar to that adopted for analyzing the effect of the processing time on the process micro-geometrical aspects, viz. PIR_a and PIR_{max}.

The analysis of variance performed on the phase-II PIOR data reveals that the processing time is equally important in case of percent improvement in out-of-roundness as in the case with percent improvements in surface roughness R_a and R_{max} values. The processing time main effect was found significant at an alpha= 0.05, as illustrated by ANOVA table for PIOR (Table 7.7).

Table 7.7 ANOVA results for percent improvement in OR data

Source	SS	D.F.	MS	F	P-value
Processing time	755.42	3	251.81	33.85*	6.7903E-5
Error	59.52	8	7.44		
Total	814.94	11			

*Significant at 95 percent confidence level.

The model F-value of 33.85 indicate that the processing time main effect is significant and there is only a chance of less than 0.0001% that this could have been due to error.

Duncan's multiple range test applied to test for the significance of incremental PIOR between different levels of the processing time is illustrated in Table 7.8.

Table 7.8 Results of Duncan's multiple range test (PIOR) (Phase-II)

Processing Time (min)	Mean Percent Improvement in OR	Incremental PIOR	Duncan's multiple range test results
1.5	44.2	-	-
3.0	54.2	10.02	Significant
4.5	61.1	6.94	Significant
6.0	65.1	3.94	Not significant

The standard error of each average is $S_{\overline{Yi.}} = \sqrt{\frac{MS_E}{n}} = 1.57$. Thus, the least significant range $R_2 = r_{0.05}(2, 8)\ S_{\overline{Yi.}} = 3.26 \times 1.57 = 5.134$. Duncan's multiple range test results indicate that a processing time of 4.5 min provided the significant increments in PIOR. Same results were drawn from the Fisher LSD test also.

An appropriate quadratic model fitting the PIOR data was derived using the statistical software Origin 6.1 as given in Table 7.9. The pattern of variation of PIOR can be describes as:

$$PIOR = + 3.557 + 25.715(PT) - 2.6515(PT)^2 \quad (7.3)$$

Polynomial regression analysis showed that the linear effect is significant at a 0.0436 significance level while the quadratic coefficient of regression was significant at 0.09616. The model is significant at the alpha of 0.04024.

Table 7.9 Polynomial Regression for PIOR

$PIOR = A + B_1*(PT) + B_2*(PT)^2$

Parameter	Value	Error	t-Value	Prob>|t|
A	3.557	7.03043	0.508	0.66194
B_1	25.715	5.55206	4.63097	0.0436
B_2	-2.6515	0.88734	-2.98736	0.09616

R-Square (COD)	Adj. R-Square	Root-MSE (SD)	N
0.9601	0.91952	7.47025	5

ANOVA Table:

Item	Degrees of Freedom	Sum of Squares	Mean Square	F Statistic	Prob>F
Model	2	2661.85886	1330.92943	23.84983	0.04024
Error	2	111.60914	55.80457		
Total	4	2773.468			

The effect of the processing time on PIOR is shown in Fig.7.4.

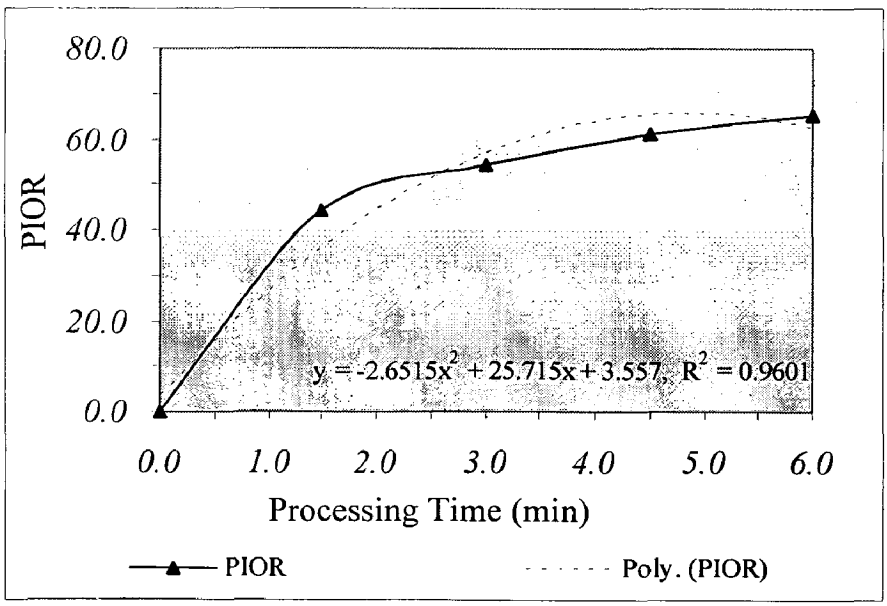

Fig. 7.4 Effect of processing time on percent improvement in out-of-roundness

It can be noticed from Fig. 7.4 that the PIOR increases as the processing time increases. Major improvements are achieved during the first few minutes of the process operation and the successive increments decrease quickly with the increasing processing time. The pattern of improvement in out-of-roundness with processing time is similar to that observed with the process micro-geometrical performance characteristics. As the process cycle proceeds, the out-of-roundness is corrected at faster rate during the initial stages due to the smoothening effect of ECH. However, the effect of diminishing resistive power of metal oxide film reduces the rate of improvement during later stages. Again a processing time of 5 min was found suitable for major improvement in out-of-roundness.

7.1.4 Effects on Percent Improvement in Cylindricity

Experimental trial results of Phase-II experimentation on the percent improvement in cylindricity, are presented in Table 6.13. The analysis of variance of PICyl data illustrated a highly significant effect of the processing time in improving in cylidricity of workpieces as imperative from the model F value of 18.68 (the corresponding P-value= 5.6947E-4) (Table 7.10).

Table 7.10 ANOVA results for percent improvement in cylindricity data

Source	SS	D.F.	MS	F	P-value
Processing time	506.87	3	168.96	18.68	5.6947E-4
Error	72.38	8	9.05		
Total	579.25	11			

*Significant at 95 percent confidence level.

The Results of Duncan's multiple range test applied to evaluate the significance of increments in PICyl between the processing time levels are given in Table 7.11.

Table 7.11 Results of Duncan's multiple range test (PICyl) (Phase-II)

Processing Time (min)	Mean Percent Improvement in Cyl	Incremental PICyl	Duncan's multiple range test results
1.5	58.9	-	-
3.0	66.9	7.93	Significant
4.5	74.6	7.74	Significant
6.0	74.7	0.05	Not significant

The standard error of each average is $S_{\overline{Y}_{i.}} = \sqrt{\frac{MS_E}{n}} = 1.74$. Thus, the least significant range $R_2 = r_{0.05}(2, 8)\ S_{\overline{Y}_{i.}} = 3.26 \times 1.74 = 5.661$.

Polynomial regression analysis shows that a quadratic model, described by equation 7.4, fitted to the PICyl variation with processing time was significant at alpha equal to 0.05953 and the linear and quadratic coefficients of regression were significant at a significance level of 0.05344 and 0.10091 respectively. The lower model F value (18.67) may be due to the presence of too many insignificant terms in the model due to a more complex pattern of percent improvement in cylidricity with processing time.

$$PICyl = 5.1647 + 33.473\ (PT) - 3.7457\ (PT)^2 \qquad (7.4)$$

The variation of PICyl with the processing time is shown in Fig. 7.5. The ANOVA results indicated that the processing time main effect is highly significant for percent improvement in cylindricity. Duncan's multiple range test results indicated that the significant increments in PICyl could be achieved in a processing time of 4.5 min. Fisher LSD test also led to the same conclusions.

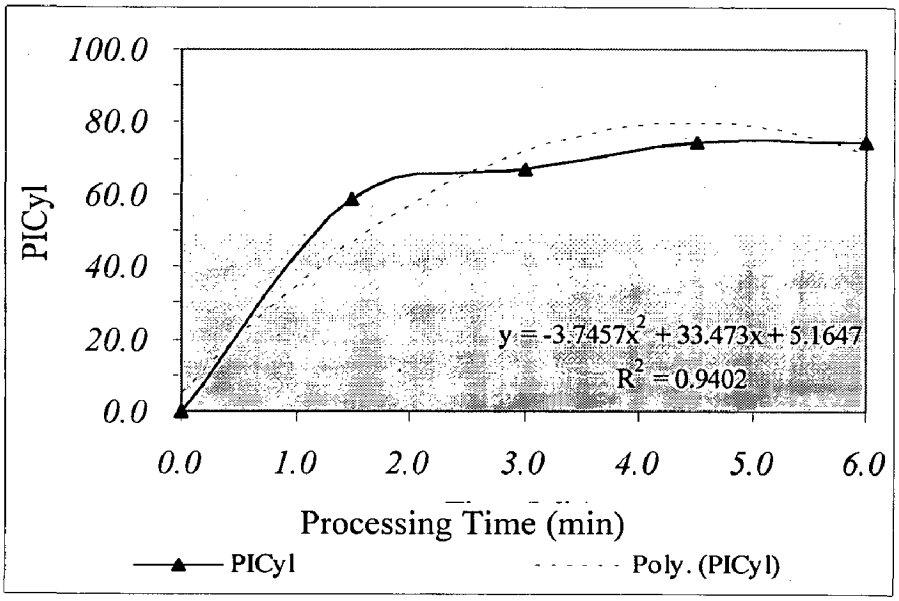

Fig. 7.5 Effect of processing time on percent improvement in cylindricity

Polynomial regression results show that the improvement of cylidricity with the processing time in ECH follows a complex pattern. In the selected experimental region, the percent improvement in cylindricity increases as the processing time increases. Major improvement occurs in the first few minutes of ECH operation and the successive increments decrease rapidly as the processing time increases.

7.1.5 Effects on Percent Improvement in Axis-straightness

Phase-II experimental results on the percent improvement in axis-straightness (PIAS) are given in Table 6.15. The ANOVA results of PIAS data are shown in Table 7.12. The processing time in case of PIAS was not significant at the chosen alpha value of 0.05.

Table 7.12 ANOVA results for percent improvement in axis straightness data

Source	SS	D.F.	MS	F	P-value
Processing time	171.10	3	57.03	2.02	0.18889
Error	225.44	8	28.18		
Total	396.54	11			

As shown in Fig. 7.6, the most of the improvement in axis-straightness is realized in first 1.5 minutes of ECH processing. The further increase in the processing time does not provide any further significant improvement in the axis-straightness. The effects of the processing time on the combined improvements in the out-of-roundness and cylindricity could have resulted in most of the axis-straightness improvements to occur within the short processing time. There is little further improvement in PIAS with increase in the processing time.

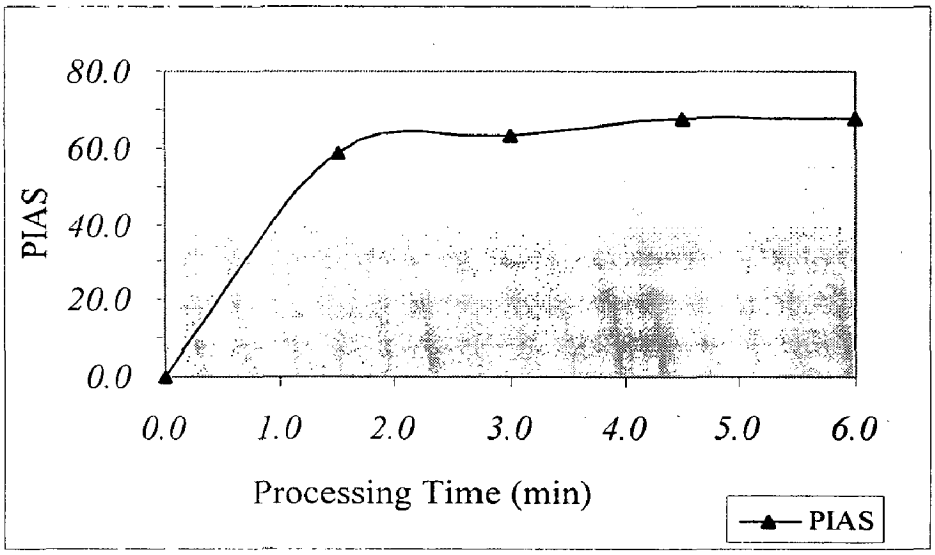

Fig. 7.6 Effect of processing time on percent improvement in AS

The average values of PIAS for different trial conditions are shown in Table 7.13. It can be seen that almost 60 percent improvement in PIAS was realized within a processing time of just 1.5 min.

Table 7.13 Mean PIAS at different processing time levels (Phase-II)

Processing Time (min)	Mean Percent Improvement in AS
1.5	58.5
3.0	63.0
4.5	67.4
6.0	67.7

The improvement in the axis-straightness with the processing time follows a complex pattern as revealed by the fact that the polynomial regression upto a cubic term could not provide a significant model at the chosen significance level of 0.05.

7.1.6 Effects on Diametral Increase Rate

The diametral increase rate reveals the material removal aspects of ECH, which may serve the purpose of stock allowance calculations for a selected processing time required for a desirable improvement in the surface micro-geometry and / or in the part macro-geometry. The processing time trial results on the diametral increase rate are given in Table 6.17. The ANOVA results of DIR data are furnished in Table 7.14. The processing time in case of DIR was not significant at the chosen significance level 0.05, i.e. the mean DIR for all the processing time levels are equal.

Table 7.14 ANOVA results for diametral increase rate data

Source	SS	D.F.	MS	F	P-value
Processing time	359.55	3	119.85	3.37	0.07525
Error	284.61	8	35.58		
Total	644.16	11			

Table 7.15 gives the average DIR values for different processing times.

Table 7.15 Mean DIR at different processing time levels (Phase-II)

Processing Time (min)	Mean DIR (μm/min)
1.5	35.7
3.0	28.9
4.5	26.8
6.0	20.4

The results are plotted in Fig. 7.7.

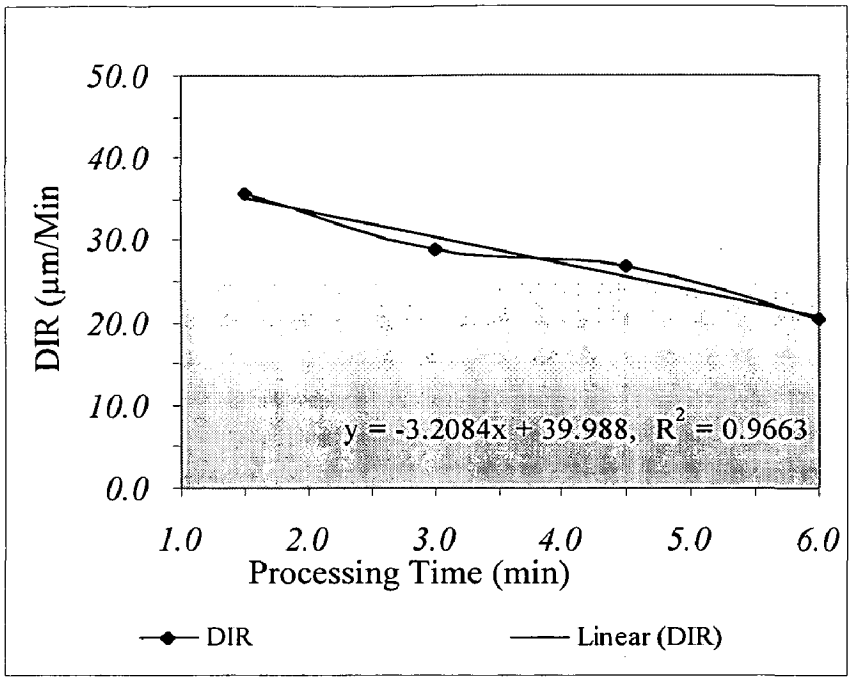

Fig. 7.7 Effect of processing time on diametral increase rate

It can be noticed that the diametral increase rate falls as the processing time increases. But, as revealed from the ANOVA results, the decrease in DIR from 1.5 to 6.0 min of processing is not significant, i.e. DIR is not significantly affected by processing time. An almost constant rate of diametral increase may be due to the use of a constant current mode of power supply. Ebeid and Mahboud (1988) also noted a constant material removal rate irrespective of time upto 5 min in case of a rotating non-expanding cathode during electro-chemical boring of pre-drilled holes. However, they used only electro-chemical process without any mechanical action.

The variation of DIR for the experimental region can be described by a linear equation 7.5:

$$DIR = 39.988 - 3.2084(PT) \quad (7.5)$$

Linear regression analysis results are given in Table 7.16. The model F-value of 56.33252 implies the model is significant. There is only a 1.729 % chance that a 'Model F-

value' this large could occur due to noise. The model is capable of explaining about 96.571 percent of variability in DIR data.

Table 7.16 Linear Regression for DIR

DIR = A + B * (PT)

Parameter	Value	Error	t-Value	Prob>|t|
A	39.988	1.75143	22.80996	0.00192
B	-3.2084	0.42635	-7.5055	0.01729

R-Square (COD)	Adj. R-Square	Root-MSE (SD)	N
0.96571	0.94857	1.43003	4

ANOVA Table:

Item	Degrees of Freedom	Sum of Squares	Mean Square	F Statistic	Prob>F
Model	1	115.2	115.2	56.33252	0.01729
Error	2	4.09	2.045		
Total	3	119.29			

7.2 PHASE-III EXPERIMENTAL STUDIES

The performance of the electro-chemical honing process is influenced by several process parameters. The Ishikawa cause-and-effect analysis (as given in Fig. 5.1) was carried out to identify the various process parameters that can influence the process performance characteristics. The key process input parameters and their ranges were identified through a critical parametric analysis complemented with suitable pilot experiments as discussed in Chapter-V. To make the study more comprehensive, the process performance characteristics were identified from all different aspects of the process performance including the surface micro-geometry, part macro-geometry, surface integrity and material removal aspects. Several facets of the individual performance areas were decided to be examined using both the objective as well as subjective evaluations as given in Chapter-V. Special procedures with high precision instruments as described in Chapter-V were adopted for measuring the responses.

Experimental studies were planned based on the objectives of the study using suitable experimental design and analysis techniques in order to best utilize the time and resources keeping also in view the availability of measuring facilities. The experimentation was done on the developed ECH setup.

The processing time in ECH has a dominating influence on the most of the process performance characteristics as revealed from the analysis of Phase-II experimental studies. Results indicated that a processing time of 5 min is most suitable for observing maximum yields of most of the responses, viz. PIR_a, PIR_{max}, PIOR and PICyl, for the configuration of the selected domain of experimentation. The processing time was not so influential in the case of PIAS and DIR for the altogether different reasons as discussed in Section 7.1.

The Phase-III studies were planned considering most of the main process parameters as given in Table 6.3 for detailed investigations into the ECH process parametric

relationships, work surface characteristics, material removal mechanisms and work surface integrity aspects. Experiments were designed using Taguchi L_{27} OA (Table 6.5) for efficiently evaluating the effects of the seven key process parameters, as identified through parametric analysis, namely current intensity, electrolyte concentration, rotary to reciprocating speed ratio, electrolyte flow rate, electrolyte inlet temperature, stick-out pressure and stick grit size and three interactions, viz. current intensity-electrolyte concentration (C-EC), current intensity-speed ratio (C-SR), and electrolyte concentration-speed ratio (EC-SR), on various process performance aspects. Taguchi experimental designs are equally effective in case of continuous as well as discrete process input parameters. A saturated experiment design was used as suggested by Phadke (1989) to extract the maximum information with least possible experimentation and obtain a better reliability of conclusions drawn by pooling the insignificant effects.

Phase-III results were analyzed in several stages using ANOM for raw data, ANOM for S/N data, ANOVA for raw data, ANOVA for S/N data, Tukey's method, the Kruskal-Wallis Test and MVRA as discussed in Chapter-VI. There were several objectives of the statistical analysis, including:

1. To identify the significant parameters and quantify their effects on various process performance characteristics,
2. To judge the contrasts,
3. To estimate the confidence limits for various mean response values.
4. To select optimal levels of the process parameters for each individual process response characteristics,
5. To estimate optimal value of each individual response obtainable within the experimental zone and establish their confidence interval.

This section deals with the analysis and discussions of stage-I studies of the Phase-III experimentation. Results of stage- II and III studies have been presented in the following sections. The main effects i.e. the effects of process input parameters on the process performance characteristics when they change from one level to another are calculated and plotted as the response curves. These curves show the average values of the process performance characteristics and their average S/N values vs levels of the process input parameters. The average mean response in terms of raw data and S/N data of the process performance characteristics and the associated pooled ANOVA tables are also included. The response curves aid to visualize the parametric effects on the selected process response characteristics. The pooled ANOVA has been performed on the raw data and S/N data to identify the significant process input parameters and to quantify their effects on the response characteristics. The control limits of the mean responses help in a better interpretation of results and selection of optimal levels of process input parameters for various responses.

7.2.1 Percent Improvement in Ra

The average values of percent improvement in R_a (PIR_a) raw data and the corresponding S/N data for each parameter at levels 1, 2, and 3 calculated from Table 6.19 (Chapter-VI) are given in Tables 7.17 and 7.18 respectively. The main effects of the process input parameters are also given in these Tables. The pooled ANOVA results of PIR_a raw data and S/N data are presented in Tables 7.19 and 7.20 respectively. The effect of the process input parameters on percent improvement in R_a are shown in the Fig. 7.8 as response plots.

The analysis of the main effects vis-à-vis 95 percent control limits of PIR_a means indicates that the current intensity, electrolyte concentration, electrolyte inlet temperature, stick-out pressure and stick grit size are having considerable influence as compared to SR and F on the PIR_a. A significance level of 0.05 was selected for this experiment. A similar conclusion can be drawn from the pooled ANOVA for PIR_a as indicated by the significant F ratios of different process input parameters and interactions. The effects of two interactions, (C-EC) and (C-SR) are also significant. The average PIR_a and S/N ratios for C-EC and C-SR interactions at different combinations of respective parameter levels are also given in Tables 7.21 and 7.22 respectively.

The percent contribution of each process input parameter and interaction calculated as per the standard procedure (Roy, 1990) (Table 7.19 and 7.20) indicate that the current intensity, electrolyte concentration, stick-out pressure, stick grit-size and the (C-EC) interaction are the major players affecting PIR_a significantly. Noticeably, the S/N data analyses also fully substantiate the results of standard analyses.

Table 7.17 Average and Main Effects – PIR_a Raw Data (Phase-III)

Process Input Parameter	Average Values, PIR_a (%)			Main Effects, PIR_a (%)	
	L1	L2	L3	L2-L1	L3-L2
C	70.90	71.80	77.12	0.90	5.32
EC	70.15	71.25	78.41	1.10	7.17
SR	73.29	72.50	74.03	-0.79	1.53
F	73.28	73.20	73.34	-0.08	0.14
T	71.90	73.30	74.61	1.40	1.31
SOP	70.49	73.61	75.71	3.11	2.10
G	75.05	75.78	68.99	0.74	-6.80
C-EC	71.99	73.84	73.99	1.84	0.15
C-SR	73.11	72.60	74.11	-0.51	1.51
EC-SR	72.84	73.32	73.66	0.48	0.34

L1, L2 and L3 represent average values of raw data of response of corresponding parameters at levels 1, 2 and 3 respectively. L2-L1 is the average main effect when the corresponding parameter changes from level 1 to level 2. L3-L2 is the average main effect when the corresponding parameter changes from level 2 to level 3.

* 95 % Confidence Limit (CI_1) = ± 0.93

C: Current Intensity, EC: Electrolyte Concentration, SR: Speed Ratio, F: Electrolyte Flow Rate, T: Electrolyte Inlet Temperature, SOP: Stick-out Pressure, G: Grit Size.

Table 7.18 Average and Main Effects – PIR_a S/N Data (Phase-III)

Process Input Parameter	S/N Average Values, PIR_a (dB)			Main Effects, PIR_a (dB)	
	L1	L2	L3	L2-L1	L3-L2
C	36.98	37.09	37.71	0.12	0.62
EC	36.88	37.04	37.86	0.16	0.82
SR	37.25	37.18	37.35	-0.07	0.17
F	37.25	37.26	37.27	0.01	0.01
T	37.11	37.26	37.41	0.15	0.15
SOP	36.93	37.30	37.55	0.37	0.25
G	37.47	37.55	36.76	0.08	-0.79
C-EC	37.10	37.33	37.35	0.23	0.02
C-SR	37.23	37.18	37.37	-0.06	0.19
EC-SR	37.19	37.28	37.31	0.08	0.04

L1, L2 and L3 represent average values of S/N data of response of corresponding parameters at levels 1, 2 and 3 respectively. L2-L1 is the average main effect when the corresponding parameter changes from level 1 to level 2. L3-L2 is the average main effect when the corresponding parameter changes from level 2 to level 3.

* 95 % Confidence Limit (CI_1) = ± 0.15

C: Current Intensity, EC: Electrolyte Concentration, SR: Speed Ratio, F: Electrolyte Flow Rate, T: Electrolyte Inlet Temperature, SOP: Stick-out Pressure, G: Grit Size.

Table 7.21 Average Effects of C-EC Interaction - PIR_a Raw & S/N Data (Phase-III)

	Average Values, PIR_a (%)			S/N Average Values, PIR_a (dB)		
	C_1	C_2	C_3	C_1	C_2	C_3
EC_1	65.22	67.69	77.55	36.28	36.59	37.77
EC_2	70.00	70.95	72.79	36.89	37.01	37.22
EC_3	77.47	76.76	81.01	37.76	37.68	38.15
*95 % Confidence Limit (CI_1) for average values-Raw data = ± 1.61						
*95 % Confidence Limit (CI_1) for average values-S/N data = ± 0.25						

Table 7.22 Average Effects of C-SR Interaction – PIR_a Raw & S/N Data (Phase-III)

	Average Values, PIR_a (%)			S/N Average Values, PIR_a (dB)		
	C_1	C_2	C_3	C_1	C_2	C_3
SR_1	70.59	70.79	78.49	36.91	36.95	37.88
SR_2	68.77	73.67	75.05	36.73	37.33	37.49
SR_3	73.32	70.94	77.82	37.29	37.01	37.76
*95 % Confidence Limit (CI_1) for average values-Raw data = ± 1.61						
*95 % Confidence Limit (CI_1) for average values-S/N data = ± 0.25						

7.2.1.1 Effect of current intensity

A peculiar noticeable behavior of ECH is an increase in PIR_a with increasing current intensities. An increase in current intensity results in a substantial improvement in surface roughness of work. The increase in current intensity increases the current density in the inter-electrode gap and this helps in accelerating the anodic dissolution of the work material. An increase in current density also leads to a corresponding increase in the rate of metal ion production at the anode. The mechanical action of honing sticks removes the passivating metal oxide micro-film formed due to electrolytic action from the higher spots or tight areas thus making them more receptive for preferential electrolytic attack. The lower areas still covered with the protective metal oxide film will have weaker electrolytic action. This phenomenon of differential dissolution is more pronounced at the higher current intensities. As observed by Bhattacharyya and Munda (2003) a highly reactive chemical attack also occurs due to high current density in electro-chemical micromachining. However, such

mechanism is electrolyte dependent and for neutral salts like sodium chloride and sodium nitrate, this phenomenon is less likely. The combined influence of increased metal ion production at anode and accelerating preferential electrolytic dissolution with reactive chemical attacks at higher current intensity results in a pronounced improvement in the surface finish due to the accelerated converging mode of the process wherein the micro-geometrical errors are smoothed out very rapidly. As can be seen from Fig. 7.8a the PIR_a is considerably higher at the 3rd level of the current intensity.

Fasil (2004) also reported that an increased current intensity due to increased voltage across the gap has a significant influence on the resulting surface roughness values. However, he conducted the experiments at comparatively much smaller current intensities. The phenomena governed by viscous layer theory (Cole and Hopenfeld 1963), theory of anodic smoothing (Fitz-Gerald and McGeough 1970) as applied to ECM may also aid to the process mechanism in achieving higher PIR_a at increased current intensities.

The phenomenon of viscous or boundary layer theory is work material and electrolyte related, in which a special boundary layer is formed on work surface as a result of one or more slow rate determining processes such as hydration, complexing or precipitation of metal ion. The interfacial tension of electrolyte with boundary layer produces a smooth contour to the boundary layer and hence, to the anode work surface to produce a mirror-smooth shiny surface. However, the disadvantages of viscous layer, i.e. large long-range unevenness and low material removal rate are well taken care of by the action of honing sticks in ECH.

7.2.1.2 Effect of electrolyte concentration

Fig. 7.8b gives the relationship between the electrolyte concentration and the PIR_a. It can be noticed that an increase in electrolyte concentration increases the PIR_a. This can be attributed to the simultaneous effects on three different aspects. An increase in the electrical conductivity of electrolyte at the increased electrolyte concentration leads to an increased electrolytic action at higher peaks of the surface profile exposed due to the action of honing sticks. It has been reported by Guoqiang et al (1986) that different electrolytes have different physical nature and protective ability of metal oxide film. Therefore, at the same time, a change in the electrolyte concentration may affect the protective ability and physical nature of the metal oxide film. The net effect is that the differential electrolytic dissolution is more pronounced at higher electrolyte concentration. It is noticeable from the ANOVA tables that the electrolyte concentration has the highest contribution in PIR_a of the work surface. A considerable influence of electrolyte concentration on resulting surface roughness values was also noted by Fasil (2004) in the case of sodium nitrate electrolyte.

An interactive nature of current intensity and electrolyte concentration is revealed in Fig. 7.9a and 7.9b. EC_3 appears to be better for achieving a higher PIR_a at all the three levels of the current intensity. The C-EC interaction can be attributed to the combined influence of the current intensity and the electrolyte concentration resulting in a significant contribution to the differential dissolution in addition to the individual effects of the interactive parameters due to the various reasons mentioned earlier.

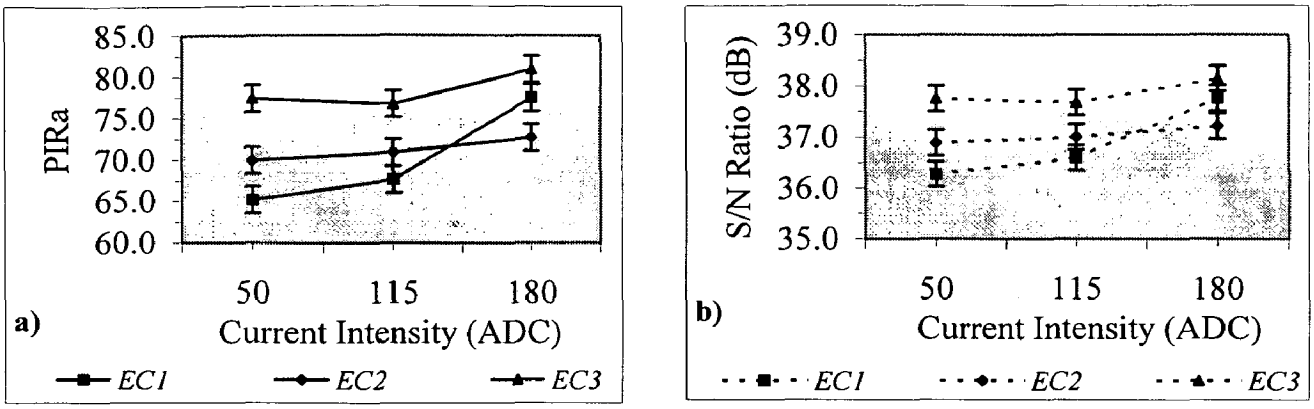

Fig. 7.9 Relation between current intensity and percent improvement in R_a and S/N ratio at different electrolyte concentration levels

7.2.1.3 Effect of rotary to reciprocating speed ratio

The independent effect of speed ratio was not found significant on the percent improvement in R_a. A similar observation on the effect of rotational speed on the resulting surface roughness values in ECH was also reported by Fasil (2004). His experiments were at comparatively very low rotational speeds with a smaller constant speed ratio. However, better micro-geometrical improvements dictate a proper combination of current intensity and rotary to reciprocating speed ratio. This fact is revealed by the ANOVA results, indicating a significant contribution of the current intensity-speed ratio interaction on PIR_a. This fact is also noticeable in Fig. 7.10. The $C_3SR_1$and C_3SR_3 combinations provide higher response values. The C-SR helps deciding the selective electrolytic dissolution of the work material. The findings are in line with those of Guoqiang et al (1986) who pointed out that for better results a good coordination mechanical abrading and electrolytic dissolution is necessitated in ECH.

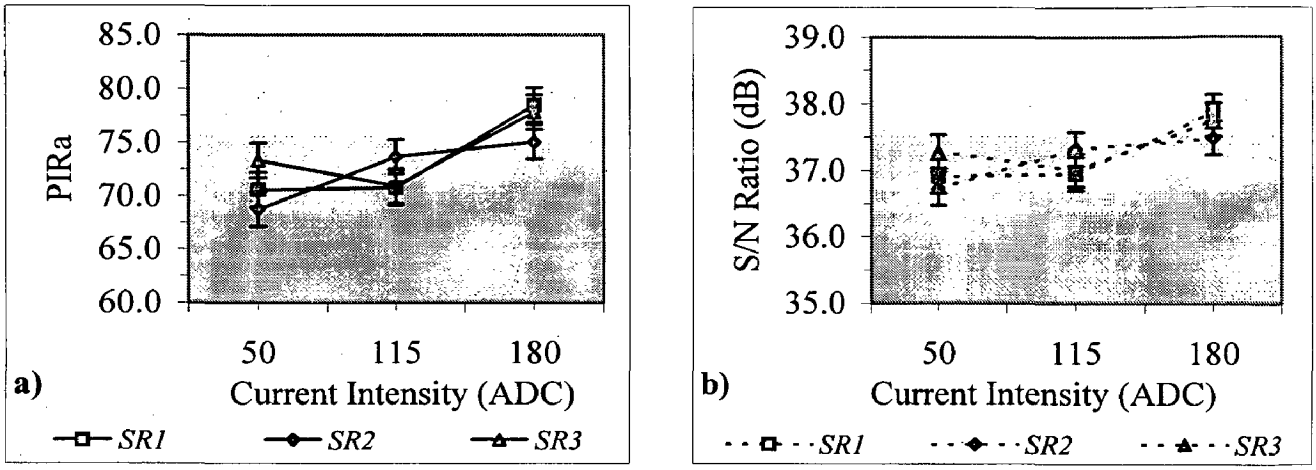

Fig. 7.10 Relation between current intensity and percent improvement in R_a and S/N ratio at different speed ratio levels

7.2.1.4 Effect of electrolyte flow rate

In contrast with the electrochemical machining, the influence of electrolyte flow rate on the percent improvement in R_a is not found to be significant in the present case. This result can be attributed to the unique tool design in which dual mode of electrolyte supply to the IEG is realized resulting in a much uniform distribution of electrolyte. Besides, the cleansing action of the honing sticks in the ECH makes the electrolyte flow rates less consequential in the process.

7.2.1.5 Effect of electrolyte inlet temperature

An effect similar to that of electrolyte concentration was observed when the electrolyte inlet temperature was increased (Fig. 7.8e). Increased percent improvement in R_a was observed at higher electrolyte inlet temperatures. This is due to the fact that the electrolyte conductivity increases with increase in the electrolyte temperature. Also, the change in the electrolyte temperature is likely to modify the nature of metal oxide. As revealed from the percentage contribution (Tables 7.19 and 7.20), the effect of temperature is, however, not so predominant in this case.

7.2.1.6 Effect of stick-out pressure

Fig. 7.8f presents the variation of the percent improvement in R_a with various stick-out pressures. The action of honing stick in ECH can be thought of as a mechanical factor to remove from the higher spots the passivating metal oxide microfilm formed due to electrolytic action. The effectiveness of this depends on the stick-out pressure and stick grit size. An increase in stick-out pressure within the range employed in the present study provided increasingly effective removal of the film leading to better improvements in the surface roughness values.

7.2.1.7 Effect of stick grit size

It can also be noticed from the main effect plot for stick grit-size (Fig. 7.8g) that in contrast to the conventional honing, very fine stick grits provide a lesser PIR_a. The coarser grits for the ECH process in the present study were found to be more effective as compared to fine grits, indicating that a proper selection of the grit-size of honing sticks is necessitated. Coarse grit can provide an effective scrubbing action of metal oxide film. Nurai et al. (1967) also noticed the predominant role of stick grit-size on the resulting surface roughness of the ECHed surface.

ECH can be considered to be an interaction process of controlled electrolytic dissolution and selective mechanical abrading, the efficiency of which in correcting micro and macro-geometrical errors depends highly on the proper coordination of these two actions. The nature of oxide film both in terms of physical characteristics and electrical properties plays a vital role. The current intensity, electrolyte concentration, stick-out pressure and stick grit-size are the major players significantly affecting the surface roughness improvement. If an optimum coordination of EC and mechanical process is achieved, ECH can provide an unmatched surface quality. ECH can be developed as a precision finish machining process for the critical components of tribological relevance.

7.2.1.8 Multi variable regression analysis

The multi variate linear regression was performed using the statistical software Origin 6.1. The MVRA results of PIR_a data are given in Table 7.23. The following linear regression model for PIR_a has been evolved considering the most significant process parameters:

$$PIR_a = 53.87853 + 0.04784\ C + 0.08266\ EC + 0.06794\ T + 0.26089\ SOP - 0.008\ G \quad (7.6)$$

Prob>F for the model is <0.0001, showing that the model can be used to predict the responses in ECH. The value of PIRa predicted at the optimal parameter setting §7.2.1.9, is 85.45%. This is in close agreement with the estimated optimal value of the response.

Table 7.23 MVRA: PIR_a versus C, EC, T, SOP and G

The regression equation is

$PIR_a = 53.87853 + 0.04784\ C + 0.08266\ EC + 0.06794\ T + 0.26089\ SOP - 0.008\ G$

Predictor	Coef	SE Coef	T	P
Constant	53.87853	4.08979	13.17392	<0.0001
C	0.04784	0.01347	3.55116	0.00189
EC	0.08266	0.01751	4.71987	1.16431E-4
T	0.06794	0.04378	1.55193	0.13562
SOP	0.26089	0.08756	2.9795	0.00715
G	-0.008	0.00202	-3.95497	7.23492E-4

R-Square (COD)	Adj. R-Square	Root-MSE (SD)
0.74642	0.68605	3.71491

ANOVA Table:

Item	Degrees of Freedom	Sum of Squares	Mean Square	F Statistic	Prob>F
Model	5	853.09044	170.61809	12.36311	<0.0001
Error	21	289.8121	13.80058		
Total	26	1142.90254			

No evidence of lack of fit ($P \geq 0.1$).

7.2.1.9 Selection of optimal levels

It is revealed from the pooled ANOVA results of the raw data and S/N ratio data of PIR_a that the process input parameters that have significant effect on both the mean PIR_a and variation are the current intensity, electrolyte concentration, electrolyte inlet temperature, stick-out pressure and stick grit-size. The current intensity-electrolyte concentration and current intensity-speed ratio interactions also affect the performance characteristic significantly.

The percentage contribution of each input parameter and interactions (Table 7.19 and 7.20) indicate that the most significant parameters and interactions influencing the average and S/N ratio of PIR_a (in rank order) are the electrolyte concentration, followed by grit-size, current intensity, stick-out pressure, the C-EC interaction, the C-SR interaction and electrolyte inlet temperature.

The trend of variation of the response corresponding to the significant input parameters (as given in Fig. 7.8) indicates that level 3 of the parameters current intensity (C_3), electrolyte concentration (EC_3), electrolyte inlet temperature (T_3) and stick-out pressure (SOP_3) yield the highest mean response as well as the highest average S/N ratio of PIR_a. The stick grit-size at level 2 has provided the maximum average PIR_a and S/N ratio.

The interaction plot of current intensity and electrolyte concentration (Fig. 7.9) also suggests that C_3-EC_3 combination is more effective in achieving the highest mean as well as the highest average S/N value of PIR_a.

The influence of another significant interaction of the current intensity and rotary to reciprocating speed ratio on PIR_a as given in Fig. 7.10 reveals that C_3-SR_1 combination is the best for achieving the highest response in both the cases.

The S/N average values of PIR_a (Tables 7.18, 7.21, 7.22 and 6.19) are given in Table 7.26.

Table 7.26 Average S/N values of PIR_a at optimal level of process parameters (with interactions) (Phase-III)

Optimum Level of Significant Process Parameter	S/N Ratio (dB)
C_3EC_3	38.15
C_3SR_1	37.88
3rd Level of Electrolyte Inlet Temperature (T_3)	37.41
3rd Level of Stick-out Pressure (SOP_3)	37.55
2nd Level of Grit Size (G_2)	37.55
Overall Mean of S/N PIR_a ($\overline{T}_{S/N\ PIRa}$)	37.26
3rd Level of Current Intensity (C_3)	37.71

The predicted optimal value of S/N PIR_a ($u_{S/N\ PIRa}$) is:

$$u_{S/N\ PIRa} = C_3EC_3 + C_3SR_1 + T_3 + SOP_3 + G_2 - 4\,\overline{T}_{S/N\ PIRa} - (C_3 - \overline{T}_{S/N\ PIRa})$$

$$= 39.04 \text{ dB}$$

The following values were used in Eq. 6.9a and 6.9b to obtain 95% confidence interval for the mean of the population and two confirmation experiments (CI_{pop} & CI_{CE}): N = 27, f_e (error D.F.) = (26-14) = 12, v_e (error variance) = 0.67 (Modified Table 7.20), n_{eff} = N / (1+ D.F. associated in the estimate of mean response) = 1.8, R = 2, $F_{0.05}$ (1,12) = 4.7472.

$CI_{pop} = \pm 1.33$

$CI_{CE} = \pm 1.84$

The 95% confidence intervals (CI_{pop} & CI_{CE}) of the predicted optimal S/N PIR_a are:

CI_{pop} : $37.71 < u_{S/NPIRa}$ (dB) < 40.38

CI_{CE} : $37.21 < u_{S/NPIRa}$ (dB) < 40.88

7.2.2 Percent Improvement in R_{max}

The experimental results, average and main effects on raw data, average and main effects on S/N data, pooled ANOVA on raw data and pooled ANOVA on S/N data for percent improvement in R_{max} (PIR_{max}) are presented in Tables 6.21, 7.27 through 7.30 respectively. An analysis similar to that conducted for the PIR_a, reveals that the current intensity, electrolyte concentration, electrolyte inlet temperature, stick-out pressure, stick grit size, current intensity-electrolyte concentration (C-EC) interaction and the current intensity-speed ratio (C-SR) interaction are significant at 0.05 significance level in both the cases of the standard and S/N analysis of the PIR_{max}. The average PIR_{max} and S/N ratios for C-EC and C-SR interactions at different combinations of respective parameters levels are given in Tables 7.31 and 7.32 respectively. The effect of the process input parameters on PIR_{max} have been plotted as response curves in Fig. 7.11.

It can be seen from the pooled ANOVA results that all the significant parameters and interactions are having quite high contributions in both the raw and S/N PIR_{max} as indicated by the percent contribution columns. Noticeably, the S/N data analyses also fully substantiate the results of standard analyses.

Table 7.29 Pooled ANOVA– PIR_{max} Raw Data (Phase-III)

Source	SS	DF	MS	F ratio	% Contribution
C	580.41	2	290.21	46.97*	9.46
EC	794.42	2	397.21	64.29*	13.02
SR	13.44	(2)	Pooled	-	-
F	14.20	(2)	Pooled	-	-
T	850.55	2	425.27	68.83*	13.96
SOP	517.43	2	258.71	41.87*	8.41
G	1686.28	2	843.14	136.47*	27.87
C-EC	1021.38	4	255.35	41.33*	16.59
C-SR	373.71	4	93.43	15.12*	5.81
EC-SR	89.17	(4)	Pooled	-	-
Model	5790.03	18	321.67	52.06*	95.12
e(pooled)	216.25	35	6.18		4.88
Total	6006.28	53			100.00

The Model F ratio of 52.06 implies that Model is significant at 99.5% confidence level.

* Significant at 95% confidence level.

SS: Sum of Square, DF: Degree of Freedom, MS: Mean Square, C: Current Intensity, EC: Electrolyte Concentration, SR: Speed Ratio, F: Electrolyte Flow Rate, T: Electrolyte Inlet Temperature, SOP: Stick-out Pressure, G: Grit Size.

Table 7.30 Pooled ANOVA– PIR_{max} S/N Data (Phase-III)

Source	SS	DF	MS	F ratio	% Contribution
C	5.92	2	2.96	14.50*	9.12
EC	7.86	2	3.93	19.25*	12.33
SR	0.22	(2)	Pooled	-	-
F	0.09	(2)	Pooled	-	-
T	8.05	2	4.03	19.71*	12.64
SOP	5.14	2	2.57	12.60*	7.83
G	16.29	2	8.14	39.88*	26.26
C-EC	11.61	4	2.90	14.22*	17.86
C-SR	3.94	4	0.99	4.83*	5.17
EC-SR	1.33	(4)	Pooled	-	-
Model	58.82	18	3.27	16.00*	91.22
e(pooled)	1.63	8	0.20		8.78
Total	60.46	26			100.00

The Model F ratio of 16.00 implies that Model is significant at 99.5% confidence level.

* Significant at 95% confidence level.

SS: Sum of Square, DF: Degree of Freedom, MS: Mean Square, C: Current Intensity, EC: Electrolyte Concentration, SR: Speed Ratio, F: Electrolyte Flow Rate, T: Electrolyte Inlet Temperature, SOP: Stick-out Pressure, G: Grit Size.

Table 7.31 Average Effects of C-EC Interaction -PIR_{max} Raw and S/N Data (Phase-III)

	Average Values, PIR_{max} (%)			S/N Average Values, PIR_{max} (dB)		
	C_1	C_2	C_3	C_1	C_2	C_3
EC_1	48.35	56.57	70.44	33.65	35.01	36.92
EC_2	61.61	64.07	60.29	35.79	36.09	35.49
EC_3	67.13	65.89	70.26	36.44	36.21	36.89
*95 % Confidence Limit (CI_1) for average values-Raw data = ± 2.06						
*95 % Confidence Limit (CI_1) for average values-S/N data = ± 0.60						

Table 7.32 Average Effects of C-SR Interaction - PIR_{max} Raw and S/N Data (Phase-III)

	Average Values, PIR_{max} (%)			S/N Average Values, PIR_{max} (dB)		
	C_1	C_2	C_3	C_1	C_2	C_3
SR_1	59.32	60.27	66.67	35.24	35.49	36.39
SR_2	55.14	66.97	66.31	34.76	36.48	36.51
SR_3	62.61	59.29	68.01	35.87	35.34	36.40
*95 % Confidence Limit (CI_1) for average values-Raw data = ± 2.06						
*95 % Confidence Limit (CI_1) for average values-S/N data = ± 0.60						

7.2.2.1 Effect of current intensity

The current intensity has a pronounced influence on the percent improvement in R_{max} value both independently and in interaction with other process parameters viz electrolyte concentration and rotary to reciprocating speed ratio. It can be noticed that PIR_{max} increases, as in case with PIR_a, with increasing current intensities (Fig. 7.11a). The improved differential dissolution because of the increased current intensity, increased rate of metal ion production at anode and action of honing sticks and highly reactive chemical attacks, and phenomena related to viscous layer theory, theory of anodic smoothing as described earlier may be the various mechanisms operating in ECH to provide a converging mode of the process operation resulting in the larger PIR_{max} at increased current intensity.

7.2.2.2 Effect of electrolyte concentration

Fig. 7.11b gives the relationship between the electrolyte concentration and the percent improvement in R_{max}. The PIR_{max} increases with the increase of the electrolyte concentration. The increased differential dissolution, due to the simultaneous actions of increased electrolyte conductivity; changing resistive power and physical nature of the resulting metal oxide microfilm and the action of honing sticks explain the increased PIR_{max} at higher electrolyte concentrations.

Besides the independent effect the role of interactive effect of electrolyte concentration with current intensity is seen in Fig. 7.12. EC3 appears consequential for achieving a higher PIR_{max} at all the three levels of current intensity.

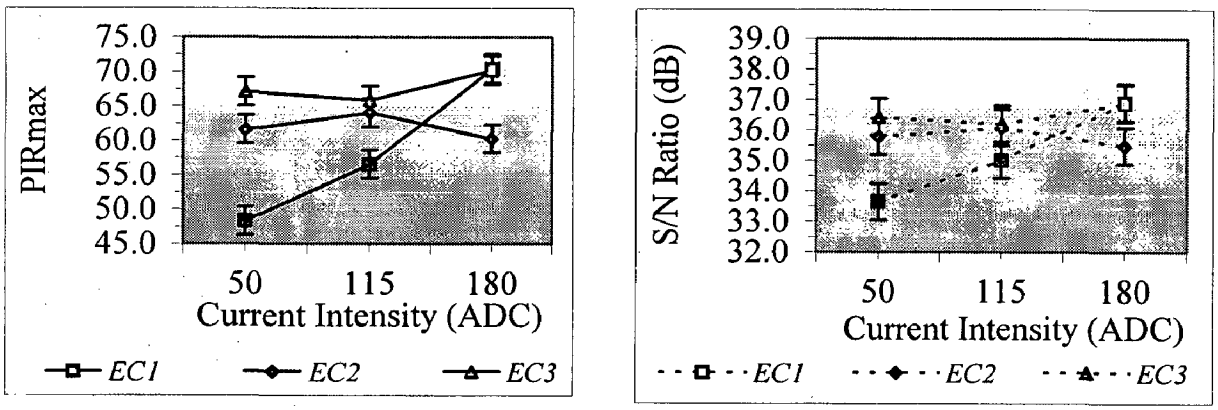

Fig. 7.12 Relation between current intensity and percent improvement in R_{max} and S/N ratio at different electrolyte concentration levels

7.2.2.3 Effect of rotary to reciprocating speed ratio

The independent effect of speed ratio on PIR_{max} is not found significant. However, the importance of a proper combination of current intensity and rotary to reciprocating speed ratio for better PIR_{max} values is revealed in Fig. 7.13. The ANOVA results indicate a significant contribution of the current intensity-speed ratio interaction on PIR_{max}. The C_3SR_3 and C_3SR_2 combinations provide higher response values for raw data and S/N ratio data

respectively. The current intensity- speed ratio interaction (C-SR) helps deciding the selective electrolytic dissolution of the work material.

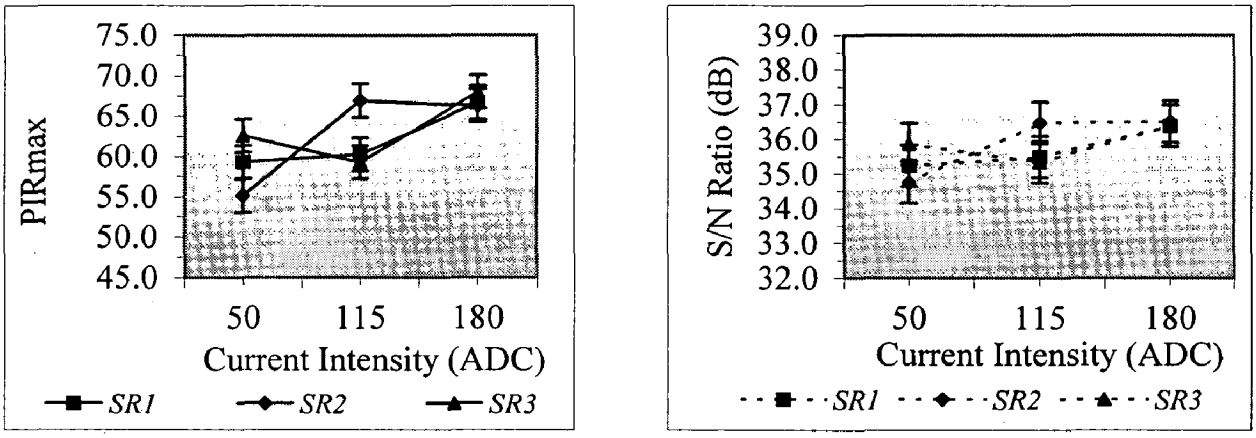

Fig. 7.13 Relation between current intensity and percent improvement in R_{max} and S/N ratio at different speed ratio levels

7.2.2.4 Effect of electrolyte flow rate

As in the case of PIR_a results, the electrolyte flow rate main effect on the percent improvement in R_{max} is not found to be significant at the chosen level of significance 0.05. Tool design incorporating dual mode of electrolyte supply to the IEG and the cleansing action of the honing sticks may be responsible for a less influential effect of electrolyte flow rates in the process as discussed earlier.

7.2.2.5 Effect of electrolyte inlet temperature

Fig.7.11e gives the response plot of electrolyte inlet temperature on the percent improvement in R_{max}. PIR_{max} increases with an increase in the electrolyte inlet temperature. The improved differential dissolution mechanism as in the case with PIR_a resulting due to the improved electrolyte conductivity and possibly modified nature of metal oxide microfilm may be the factor responsible for providing higher PIR_{max} at higher temperature. The

contribution of electrolyte inlet temperature is comparatively more on PIR_{max} than that on PIR_a as revealed from the percentage contribution columns of respective ANOVA results.

7.2.2.6 Effect of stick-out pressure

Fig. 7.11f presents the variation of the percent improvement in R_{max} with various stick-out pressures. Greater PIR_{max} is realized at higher stick-out pressure levels. This can be explained to be resulting from better scrubbing action of honing sticks at higher stick-out pressure removing the passivating metal oxide microfilm formed due to electrolytic action from the higher spots or tight areas. The largest stick-out pressure used in the present study apparently provided highly efficient removal of the film thus higher improvements in surface roughness R_{max} values as well as R_a values were realized.

7.2.2.7 Effect of stick grit-size

The impact of stick grit size on PIR_{max} is found to be more pronounced as compared to PIR_a. It can be seen from the main effect plot for stick grit-size (Fig. 7.11g) that very fine grits provide a smaller PIR_{max}. The coarser grits in the present study were found more effective as compared to fine grits, indicating that a proper selection of grit-size is thus necessitated.

The results of PIR_{max} are quite similar to that of PIR_a. It is interesting to note that the same parameters and interactions are found significant for PIR_a also. However, as observed in the pooled ANOVA tables for raw data as well as the S/N data, the contributions of stick grit size and interactive terms have increased while the independent percentage contributions of the current intensity and electrolyte concentration have decreased slightly, as compared to PIR_a results. This indicates an increased importance of interactions and grit size for R_{max}. It is to point out here that surface roughness R_a values are mean results of the departures y on the profile from the mean line determined on several consecutive sampling lengths L, while the

R_{max} is the maximum peak-to-valley height of the surface micro irregularities within the sampling length. Accordingly, surface roughness R_{max} feature resembles a macro character and has a larger amount of surface irregularity depth associated with it.

7.2.2.8 Multi variable regression analysis

The multi variable regression analysis (MVRA) was performed using the statistical software Origin 6.1. The MVRA results of PIR_{max} data are given in Table 7.33. The following linear regression model for PIR_{max} has been evolved considering the most significant process parameters:

$$PIR_{max} = 37.81053 + 0.06134\ C + 0.09306\ EC + 0.24292\ T + 0.37639\ SOP - 0.01515\ G \quad (7.7)$$

Prob>F for the model is <0.0001, showing that the model can be used to predict the responses in ECH. The predicted optimal result for PIR_{max} is 81.81%. This is in close agreement with the estimated optimal value of the response §7.2.2.10.

Table 7.33 MVRA: PIR_{max} versus C, EC, T, SOP and G

The regression equation is:

PIR_{max} = 37.81053 + 0.06134 C + 0.09306 EC + 0.24292 T + 0.37639 SOP - 0.01515 G

Predictor	Coef	SE Coef	T	P
Constant	37.81053	6.97048	5.42438	<0.0001
C	0.06134	0.02296	2.67175	0.01428
EC	0.09306	0.02985	3.11773	0.00521
T	0.24292	0.07462	3.25547	0.00378
SOP	0.37639	0.14924	2.5221	0.01981
G	-0.01515	0.00345	-4.39114	2.55013E-4

R-Square (COD)	Adj. R-Square	Root-MSE (SD)
0.7166	0.64912	6.33156

ANOVA Table:

Item	D.F.	SS	MS	F Statistic	Prob>F
Model	5	2128.68964	425.73793	10.61992	<0.0001
Error	21	841.86076	40.08861		
Total	26	2970.5504			

No evidence of lack of fit ($P \geq 0.1$).

7.2.2.9 Selection of optimal levels

It is revealed from the pooled ANOVA results of the raw data and S/N data of PIR_{max} that the process input parameters that have significant effect on both the mean PIR_{max} and variation are the current intensity, electrolyte concentration, electrolyte inlet temperature, stick-out pressure and stick grit-size. The current intensity-electrolyte concentration and current intensity-speed ratio interactions also affect the performance characteristic significantly in both the cases.

The percentage contribution of each input parameter and interactions (Table 7.29 and 7.30) indicate that the most influential parameters and interactions as regards the average and S/N ratio PIR_{max}, in decreasing order of their influence, are the grit-size, the C-EC

interaction, electrolyte inlet temperature, electrolyte concentration, current intensity, stick-out pressure, and the C-SR interaction.

The trend of variation of the response corresponding to the significant input parameters (as given in Fig. 7.11) indicates that level 3 of the parameters current intensity (C_3), electrolyte concentration (EC_3), electrolyte inlet temperature (T_3) and stick-out pressure (SOP_3) yield the highest mean response as well as the highest average S/N ratio of PIR_{max}. The stick grit-size at level 2 provided the maximum average PIR_{max} and S/N ratio.

The analysis of interaction plot of current intensity and electrolyte concentration (Fig. 7.12), keeping in view the control limits for level means, suggests that C_3-EC_1 and C_3-EC_3 are equally effective in achieving the highest mean as well as the highest average S/N value of PIR_{max}. Since, the independent influence of the electrolyte concentration is highest at EC_3 and it is being equally more effective at each level of the current intensity as clear from Fig. 7.12, C_3-EC_3 is selected.

The influence of another significant interaction of the current intensity and rotary to reciprocating speed ratio on PIR_{max}, as given in Fig. 7.13, reveals that C_3-SR_3 is the best for achieving the highest response value when raw data is considered while C_3-SR_2 is better in yielding the highest S/N ratio. However, if the control limits are considered these two combinations are equally effective in providing highest PIR_{max} values. Therefore, keeping in view the S/N value C_3-SR_2 is selected.

As, the effect of electrolyte flow rate is found to be insignificant on PIR_{max} and S/N ratio, any suitable level of electrolyte flow rate can be selected conveniently as the optimal response is only calculated from the significant factors (Ross, 1988).

Based on the above analysis, the optimal levels of the control parameters (in this case all the selected parameters and interactions are significant in standard as well as S/N analysis) considering the interactions are given in Table 7.34.

Table 7.34 Optimal level of process parameters for mean PIR_{max} and S/N ratio (with interactions) (Phase-III)

Process Input Parameters		Optimal Levels
Current Intensity (ADC)#	C_3	180
Electrolyte Concentration (g/L)#	EC_3	200
Speed Ratio #	SR_2	150
Electrolyte Flow Rate (lpm)*	F_2	20
Electrolyte Inlet Temperature (°C)	T_3	50
Stick-out Pressure (kPa)	SOP_3	30
Grit Size	G_2	600

** Not significant. Therefore, selected conveniently.*
 # Interactions C-EC and C- SR are significant.

7.2.2.10 Estimation of optimal value of performance characteristic

The optimal values of PIR_{max} and S/N PIR_{max} alongwith their respective confidence intervals have been predicted. The optimal value of the process performance characteristics is predicted considering the effects of the significant parameters and interactions only (Ross, 1988).

Percent Improvement in PIR_{max}

The average values of PIR_{max} (Tables 7.27, 7.31, 7.32 and 6.21) are given in Table 7.35.

Table 7.35 Average values of PIR_{max} at optimal level of process input parameters (with interactions) (Phase-III)

Optimum Level of Significant Process Parameter	PIR_{max} (%)
C_3EC_3	70.26
C_3SR_2	66.31
3rd Level of Electrolyte Inlet Temperature (T_3)	67.52
3rd Level of Stick-out Pressure (SOP_3)	66.76
2nd Level of Grit Size (G_2)	66.76
Overall Mean of PIR_{max} ($\overline{T}_{PIR\max}$)	62.73
3rd Level of Current Intensity (C_3)	67.00

The predicted optimal value of PIR_{max} (u_{PIRmax}) is:

$$u_{PIRmax} = C_3EC_3 + C_3SR_2 + T_3 + SOP_3 + G_2 - 4\ \overline{T}_{PIR\max} - (C_3 - \overline{T}_{PIR\max})$$

$$= 82.42\ \%$$

The 95% confidence interval for the mean of the population and two confirmation experiments (CI_{pop} & CI_{CE}) have been calculated with the following substitutions in Eq. 6.9a and 6.9b:

N = 27 x 2 = 54, f_e (error DF) = (53-14) = 39, v_e (error variance) = 5.54 (recalculated from Table 7.29).

n_{eff} = N / (1+ D.F. associated in the estimate of mean response) = 3.60, R = 2,

$F_{0.05}$ (1, 39) = 4.09341

$CI_{pop} = \pm 2.51$

$CI_{CE} = \pm 4.20$

The 95% confidence intervals (CI_{pop} & CI_{CE}) of the predicted optimal PIR_{max} are:

CI_{pop}: $79.90 < u_{PIRmax}(\%) < 84.93$

CI_{CE}: $78.21 < u_{PIRmax}(\%) < 86.62$

The S/N average values of PIR_{max} (Tables 7.28, 7.31, 7.32 and 6.21) are given in Table 7.36.

Table 7.36 Average S/N values of PIR_{max} at optimal level of process parameters (with interactions) (Phase-III)

Optimum Level of Significant Process Parameter	S/N Ratio (dB)
C_3EC_3	36.89
C_3SR_2	36.51
3rd Level of Electrolyte Inlet Temperature (T_3)	36.48
3rd Level of Stick-out Pressure (SOP_3)	36.39
2nd Level of Grit Size (G_2)	36.36
Overall Mean of S/N PIR_{max} ($\overline{T}_{S/N\ PIR\max}$)	35.83
3rd Level of Current Intensity (C_3)	36.43

The predicted optimal value of S/N PIRmax (u_{PIRmax}) is:

$$u_{S/N\ PIRmax} = C_3EC_3 + C_3SR_2 + T_3 + SOP_3 + G_2 - 4\,\overline{T}_{S/N\ PIR\max} - (C_3 - \overline{T}_{S/N\ PIR\max})$$

$$= 38.70 \text{ dB}$$

The 95% confidence interval for the mean of the population and two confirmation experiments (CI_{pop} & CI_{CE}) have been calculated using equations 6.9a and 6.9b by substituting the following values:

N = 27 = 27, f_e (error D.F.) = (26-14) = 12, v_e (error variance) = 1.29 (modified Table 7.30).

n_{eff} = N / (1+ D.F. associated in the estimate of mean response) = 1.8, R = 2,

$F_{0.05}$ (1,12) = 4.7472

$CI_{pop} = \pm$ 1.84

$CI_{CE} = \pm$ 2.54

The 95% confidence intervals (CI_{pop} & CI_{CE}) of the predicted optimal S/N PIR_{max} are:

CI_{pop}: $36.86 < u_{S/N\ PIRmax}$ (dB) < 40.54

CI_{CE}: $36.16 < u_{S/N\ PIRmax}$ (dB) < 41.24

7.2.3. Percent Improvement in Out-of-Roundness

The experimental results of the part micro-geometrical process performance, the percentage improvement in out-of-roundness (PIOR) (Table 6.23) were analyzed for the average values and main effects of the process input parameters and interactions. The results are given in Tables 7.37 and 7.38 for PIOR raw data and S/N data respectively. The 95% confidence interval limits for the average raw and S/N ratio for the parameter levels have been calculated using the equation 6.7 for a better interpretation of results. The effect of the individual process input parameters on PIOR have been plotted as response curves in Fig. 7.14. The analysis of variance was performed on the PIOR raw data and S/N data to judge the significance of the independent process parameters and their influence on PIOR. The results are presented in Tables 7.39 and 7.40. The pooling of all insignificant factors was done with the error term to achieve a better confidence in the results.

The pooled ANOVA results of raw and S/N PIOR indicate that the rotary to reciprocating speed ratio, stick-out pressure, stick grit size, current intensity-electrolyte concentration interaction and electrolyte concentration-speed ratio interaction are significant at a 0.05 significance level. The average PIOR and S/N ratios for C-EC and EC-SR interactions at different combinations of the respective parameters are given in Tables 7.41 and 7.42 respectively.

Independent influences of the electrochemical based parameters are found to be not significant at the chosen alpha = 0.05. All the mechanical parameters, current intensity-electrolyte concentration interaction and electrolyte concentration-speed ratio interaction assume a greater significance in case of percentage improvement in out-of-roundness. Further, the combined effect of all the mechanical parameters and the effect of interactive terms considered together are equally important for PIOR as revealed from the analysis of

percent contribution columns of the ANOVA tables. The dominance of the mechanical parameters and interactions may be due to the more widely spaced nature of the macro-geometrical errors in the surface profile.

Table 7.37 Average and Main Effects – PIOR Raw Data (Phase-III)

Process Parameter	Average Values, PIOR (%)			Main Effects, PIOR (%)	
	L1	L2	L3	L2-L1	L3-L2
C	35.95	36.25	37.72	0.29	1.47
EC	34.63	36.30	38.99	1.67	2.69
SR	32.65	40.81	36.45	8.16	-4.36
F	39.23	36.69	34.00	-2.54	-2.69
T	37.35	34.08	38.49	-3.27	4.41
SOP	30.83	38.81	40.27	7.99	1.46
G	35.12	43.83	30.96	8.71	-12.87
C-EC	37.86	37.95	34.11	0.09	-3.83
C-SR	37.08	35.62	37.21	-1.46	1.59
EC-SR	37.56	32.75	39.61	-4.80	6.86

L1, L2 and L3 represent average values of raw data of response of corresponding parameters at levels 1, 2 and 3 respectively. L2-L1 is the average main effect when the corresponding parameter changes from level 1 to level 2. L3-L2 is the average main effect when the corresponding parameter changes from level 2 to level 3.

* 95 % Confidence Limit (CI_1) = ± 2.51

C: Current Intensity, EC: Electrolyte Concentration, SR: Speed Ratio, F: Electrolyte Flow, T: Electrolyte Inlet Temperature, SOP: Stick-out Pressure, G: Grit Size.

Table 7.38 Average and Main Effects – PIOR S/N Data (Phase-III)

Process Parameter	S/N Average Values, PIOR (dB)			Main Effects, PIOR (dB)	
	L1	L2	L3	L2-L1	L3-L2
C	30.63	30.82	30.87	0.19	0.05
EC	30.59	30.60	31.14	0.01	0.54
SR	30.01	31.89	30.42	1.88	-1.47
F	31.37	30.80	30.15	-0.58	-0.65
T	30.95	30.10	31.27	-0.85	1.17
SOP	29.27	31.30	31.75	2.02	0.45
G	30.50	32.54	29.28	2.04	-3.26
C-EC	31.12	31.08	30.12	-0.05	-0.96
C-SR	30.81	30.69	30.82	-0.13	0.14
EC-SR	30.96	29.66	31.70	-1.30	2.04

L1, L2 and L3 represent average values of S/N data of response of corresponding parameters at levels 1, 2 and 3 respectively. L2-L1 is the average main effect when the corresponding parameter changes from level 1 to level 2. L3-L2 is the average main effect when the corresponding parameter changes from level 2 to level 3.

* 95 % Confidence Limit (CI_1) = ± 0.72

C: Current Intensity, EC: Electrolyte Concentration, SR: Speed Ratio, F: Electrolyte Flow, T: Electrolyte Inlet Temperature, SOP: Stick-out Pressure, G: Grit Size.

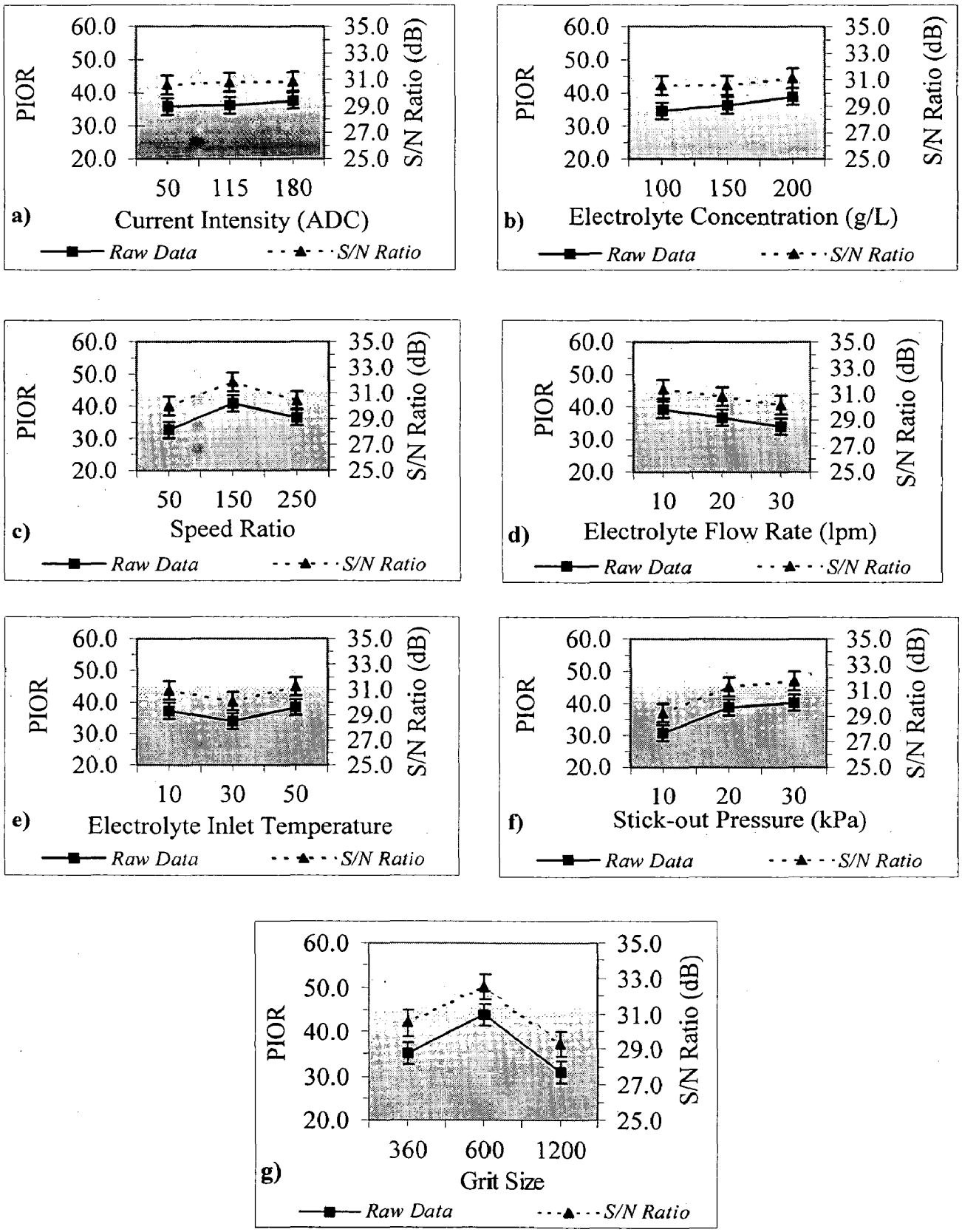

Fig. 7.14 Effects of process parameters on percent improvement in out-of roundness (PIOR) and its S/N ratio (Main Effects)

Table 7.39 Pooled ANOVA– PIOR Raw Data (Phase-III)

Source	SS	DF	MS	F ratio	% Contribution
C	32.27	(2)	Pooled	-	-
EC	174.54	(2)	Pooled	-	-
SR	600.27	2	300.14	10.80*	7.63
F	245.85	(2)	Pooled	-	-
T	188.71	(2)	Pooled	-	-
SOP	930.99	2	465.50	16.76*	12.26
G	1552.75	2	776.38	27.95*	20.96
C-EC	1032.29	4	258.07	9.29*	12.90
C-SR	294.72	(4)	Pooled	-	-
EC-SR	1942.86	4	485.71	17.48*	25.65
Model	6059.16	14	432.80	15.58*	79.39
e(pooled)	1083.44	39	27.78		20.61
Total	7142.61	53			100.00

The Model F ratio of 15.58 implies that Model is significant at 99.5% confidence level.

* Significant at 95% confidence level.

SS: Sum of Square, DF: Degree of Freedom, MS: Mean Square, C: Current Intensity, EC: Electrolyte Concentration, SR: Speed Ratio, F: Electrolyte Flow Rate, T: Electrolyte Inlet Temperature, SOP: Stick-out Pressure, G: Grit Size.

Table 7.40 Pooled ANOVA– PIOR S/N Data (Phase-III)

Source	SS	DF	MS	F ratio	% Contribution
C	0.28	(2)	Pooled	-	-
EC	1.78	(2)	Pooled	-	-
SR	17.52	2	8.76	4.44*	5.59
F	6.76	(2)	Pooled	-	-
T	6.61	(2)	Pooled	-	-
SOP	31.27	2	15.63	7.93*	11.25
G	48.79	2	24.39	12.37*	18.46
C-EC	37.91	4	9.48	4.81*	12.36
C-SR	8.24	(4)	Pooled	-	-
EC-SR	83.81	4	20.95	10.62*	31.25
Model	219.31	14	15.66	7.94*	78.90
e (pooled)	23.67	12	1.97		21.10
Total	242.97	26			100.00

The Model F ratio of 7.94 implies that Model is significant at 99.5% confidence level.

* Significant at 95% confidence level.

SS: Sum of Square, DF: Degree of Freedom, MS: Mean Square, C: Current Intensity, EC: Electrolyte Concentration, SR: Speed Ratio, F: Electrolyte Flow Rate, T: Electrolyte Inlet Temperature, SOP: Stick-out Pressure, G: Grit Size.

Table 7.41 Average Effects of C-EC Interaction – PIOR Raw and S/N Data (Phase-III)

	Average Values, PIOR (%)			S/N Average Values, PIOR (dB)		
	C_1	C_2	C_3	C_1	C_2	C_3
EC_1	36.38	36.64	30.87	31.15	31.22	29.39
EC_2	38.22	37.12	33.54	31.06	31.10	29.62
EC_3	33.26	34.97	48.75	29.69	30.13	33.60
*95 % Confidence Limit (CI_1) for average values-Raw data = ± 4.35						
*95 % Confidence Limit (CI_1) for average values-S/N data = ± 1.25						

Table 7.42 Average Effects of EC-SR Interaction – PIOR Raw & S/N Data (Phase-III)

	Average Values, PIOR (%)			S/N Average Values, PIOR (dB)		
	EC_1	EC_2	EC_3	EC_1	EC_2	EC_3
SR_1	32.47	23.81	41.67	30.19	27.49	32.35
SR_2	31.03	47.34	44.07	29.48	33.38	32.81
SR_3	40.38	37.74	31.24	32.09	30.92	28.25
*95 % Confidence Limit (CI_1) for average values-Raw data = ± 4.35						
*95 % Confidence Limit (CI_1) for average values-S/N data = ± 1.25						

7.2.3.1 Effect of current intensity

It can be seen from Fig. 7.14a that the percentage improvement in out-of-roundness increases as the current intensity increases. However, the independent effect was found quite insignificant. But the combined influence of the current intensity with electrolyte concentration was quite significant as reflected by the F ratio and a considerable percentage contribution of the C-EC interactive term in the pooled ANOVA of raw as well as S/N PIOR. Fig. 7.15 explains the effect of current intensity at different electrolyte concentration levels. An analysis keeping in view the control limits for the interaction level averages shows that C_3-EC_3 combination provides a significantly higher mean and S/N PIOR. However, statistically there is no difference between other combinations. The phenomenon of the improved differential dissolution as discussed earlier in case of surface micro-geometry is a mechanism explaining the higher PIOR at increased current intensity and electrolyte concentration.

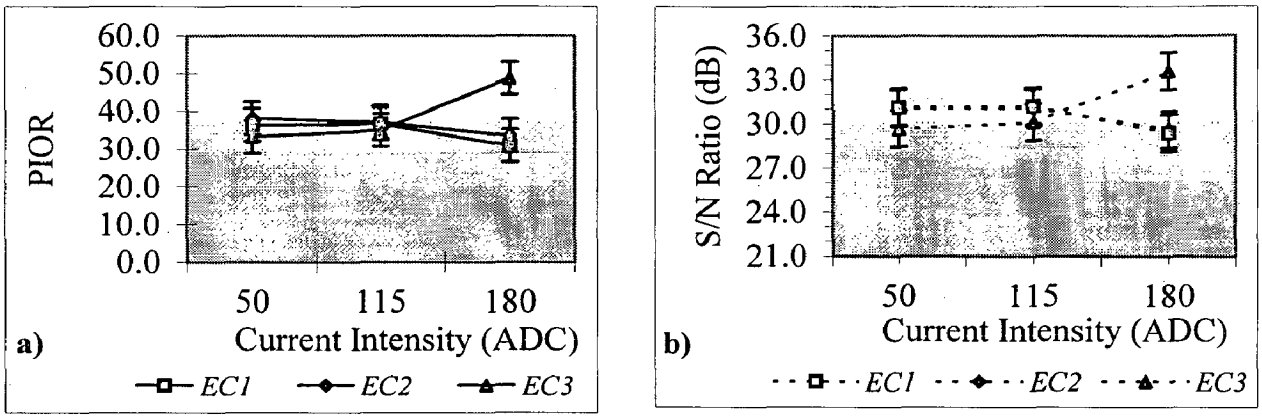

Fig. 7.15 Relation between current intensity and percent improvement in OR and S/N ratio at different electrolyte concentration levels

7.2.3.2 Effect of electrolyte concentration

Fig. 7.14b gives the relationship between the electrolyte concentration and the percent improvement in OR. Similar to the effect of current intensity, the independent influence of the electrolyte concentration was not reflected as significant at the alpha value of 0.05. But its major influence on PIOR was revealed in terms of pronounced C-EC and EC-SR interactions. The interactive effects of the electrolyte concentration with the current intensity and rotary to reciprocating speed ratio are illustrated in Fig. 7.15 and Fig. 7.16 respectively. As apparent from Fig. 7.16, a proper combination of the electrolyte concentration and speed ratio is necessary in order to get better results on PIOR. The 3rd level of the electrolyte concentration provided better PIOR with SR_2 and SR_3. The level 2 of the rotary to reciprocating speed ratio is also suitable with EC_2. The EC-SR interaction helps deciding the selective electrolytic dissolution of the work material due to the various reasons mentioned earlier. Guoqiang et al (1986) also pointed out that for better results a good coordination mechanical abrading and electrolytic dissolution is necessitated in ECH.

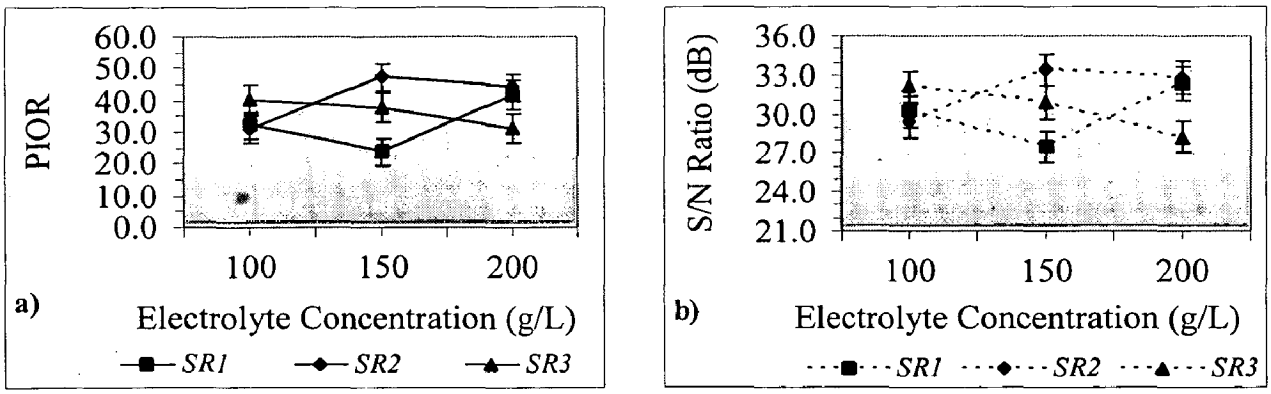

Fig. 7.16 Relation between electrolyte concentration and percent improvement in OR and S/N ratio at different speed ratio levels

7.2.3.3 Effect of rotary to reciprocating speed ratio

The rotary to reciprocating speed ratio plays an important role in case of macro-geometrical surface characteristics like out-of-roundness by the much pronounced influence of both the individual effect of the speed ratio and its interaction with the electrolyte concentration. Better OR values need a proper rotary to reciprocating speed ratio for a particular setting of the other parameters. This fact is revealed in the response plot given in Fig. 7.14c. Level 2 of the rotary to reciprocating speed seems to be better. Almost similar observation can be made from Fig. 7.16. Noticeably, SR_2 provides better response values with the levels 2 and 3 of the electrolyte concentration. Remarkably the independent effect of the speed ratio was found not significant in case of the micro-geometrical properties. But the circumferential nature of spread of the out-of roundness necessitates a suitable level of the speed ratio to be used for better PIOR results. This indicates that the rotary to reciprocating speed ratio assumes a greater relevance in case of process macro-geometrical performance characteristics.

7.2.3.4 Effect of electrolyte flow rate

Similar to the results of the process micro-geometrical performance characteristics, the electrolyte flow rate main effect on the percent improvement in OR was not significant at the chosen level of significance 0.05. Tool design combining the two distinct modes of electrolyte supply to the IEG and the cleansing action of the honing sticks may be responsible for a less influential effect of electrolyte flow rates in the process as discussed earlier.

7.2.3.5 Effect of electrolyte inlet temperature

The effect of the electrolyte inlet temperature on the percent improvement in out-of-roundness was also found to be not significant as with the case of independent effect of the electrolyte concentration. It appears that the impact of change of the electrolyte inlet temperature is not so influential on the differential dissolution to achieve significant changes in PIOR, a macro-geometrical process performance characteristic. Even in the case of PIRa, although the electrolyte inlet temperature was found significant but the percentage contribution was quite low (Tables 7.19 and 7.20).

7.2.3.6 Effect of stick-out pressure

Fig. 7.14f illustrates the variation of the percent improvement in OR as the stick-out pressure varies. The PIOR increases with increase in the stick-out-pressure due primarily to more efficient scrubbing of metal oxide micro-film from the higher spots or tight areas of the surface profile leading to an increased differential dissolution at higher levels of SOP. The results are similar to those achieved in the case of process micro-geometrical performance characteristics.

7.2.3.7 Effect of stick grit-size

A dominating influence of the stick grit size was reflected on the percent improvement in out-of-roundness as on the PIR_a and PIR_{max}. It is apparent from the main effect plot for stick grit-size (Fig. 7.14g) that the coarser grits are more effective as compared to fine grits for achieving higher PIOR values, indicating that a proper selection of grit-size is necessitated. Similar observation was made after the analysis of PIR_a and PIR_{max} data. Coarse grit can provide an effective scrubbing action of metal oxide film. Particularly, the level 2^{nd} provided significantly better results as compared to other levels of the stick grit size

It appears from the discussions that the mechanical parameters and interactions assume an equally important significance in case the process macro-geometrical performance characteristics. Further, the independent contributions from the electro-chemical parameters are decreased considerably as compared to that of process micro-geometrical performance characteristics. It is to mention that decreased contributions (as compared to PIR_a) of independent effects of electrolytic parameters were also noticed in case of PIR_{max}. R_{max} is a micro-geometrical surface characteristic but quite resembles a macro feature of the surface.

The capability of the process in correcting the form deviations in roundness is reflected from the out-of-roundness values of the workpieces, taken before and after ECH application. Remarkably, ECH can rectify a work surface having considerable initial form deviations in roundness (ISO Tolerance Grade 11) to within ISO Tolerance Grade 7/8.

7.2.3.8 Selection of optimal levels

It is revealed from the pooled ANOVA results of the raw data and S/N data of PIOR that the process input parameters and interactions that have significant effect of both the mean and S/N PIOR are the rotary to reciprocating speed ratio, stick-out pressure, stick grit-size, current intensity-electrolyte concentration and electrolyte concentration-speed ratio interactions. The percentage contribution of each input parameter and interactions

Table 7.45 Average S/N values of PIOR at optimal level of process parameters (with interactions) (Phase-III)

Optimum Level of Significant Process Parameter	S/N Ratio (dB)
C_3EC_3	33.60
EC_3SR_2	32.81
3rd Level of Stick-out Pressure (SOP_3)	31.75
2nd Level of Grit Size (G_2)	32.54
Overall Mean of S/N PIOR ($\overline{T}_{S/N\ PIOR}$)	30.77

The predicted optimal value of S/N PIOR ($u_{S/N\ PIOR}$) and corresponding 95% confidence intervals are:

$u_{S/N\ PIOR} = C_3EC_3 + EC_3SR_2 + SOP_3 + G_2 - 3\ \overline{T}_{S/N\ PIOR}$

$= 38.37$ dB

$CI_{pop} = \pm 2.55$, (CI_{pop} : $35.82 < u_{S/NPIOR}$ (dB) < 40.92)

$CI_{CE} = \pm 3.64$, (CI_{CE} : $34.73 < u_{S/NPIOR}$ (dB) < 42.02)

[calculated with N = 27, f_e (error D.F.) = (26-12) = 14, v_e (error variance) = 2.94 (modified Table 7.40), n_{eff} = N / (1+ D.F. associated in the estimate of mean response) = 2.08, R = 2, $F_{0.05}(1,14) = 4.6001$]

7.2.4 Percent Improvement in Cylindricity

The experimental trial results for the percentage improvement in cylindricity (PICyl) (given in Table 6.25) were analyzed and the average and main effects of the process input parameters and interactions for PICyl raw data and S/N data has been presented in Tables 7.46 and 7.47 respectively. The 95% confidence interval limits for the average raw and S/N effects are also given in the respective tables for better interpretation of results. PICyl response plots for the process input parameters are shown in Fig. 7.17. The pooled ANOVA results are illustrated in Tables 7.48 and 7.49. The average effects of the interactions are given in Tables 7.50 through 7.52.

The analysis of variance results of PICyl raw and S/N data are identical to PIOR results except for the more predominating influence of the interactive terms. In this case all the three selected interactions, viz current intensity-electrolyte concentration, current intensity-speed ratio and electrolyte concentration-speed ratio become significant in addition to the significant effects of the rotary to reciprocating speed ratio, stick-out pressure and stick grit size at 0.05 significance level. Independent influences of the electrochemical parameters again turned insignificant at the chosen alpha value of 0.05 as with the case of PIOR. The dominance of the mechanical parameters and interactions may be due to the more widely spaced nature of the macro-geometrical errors in the surface profile.

Table 7.46 Average and Main Effects – PICyl Raw Data (Phase-III)

Process Parameter	Average Values, PICyl (%)			Main Effects, PICyl (%)	
	L1	L2	L3	L2-L1	L3-L2
C	48.50	48.55	50.03	0.04	1.49
EC	46.01	49.39	51.69	3.38	2.30
SR	44.39	54.04	48.65	9.65	-5.40
F	52.19	50.31	44.59	-1.88	-5.72
T	48.98	48.01	50.09	-0.98	2.09
SOP	40.85	51.88	54.36	11.03	2.48
G	45.16	59.02	42.91	13.86	-16.11
C-EC	50.93	51.09	45.06	0.16	-6.03
C-SR	50.53	46.78	49.78	-3.75	3.00
EC-SR	49.87	44.52	52.70	-5.35	8.19

L1, L2 and L3 represent average values of raw data of response of corresponding parameters at levels 1, 2 and 3 respectively. L2-L1 is the average main effect when the corresponding parameter changes from level 1 to level 2. L3-L2 is the average main effect when the corresponding parameter changes from level 2 to level 3.

* 95 % Confidence Limit (CI_1) = ± 2.64

C: Current Intensity, EC: Electrolyte Concentration, SR: Speed Ratio, F: Electrolyte Flow Rate, T: Electrolyte Inlet Temperature, SOP: Stick-out Pressure, G: Grit Size.

Table 7.47 Average and Main Effects – PICyl S/N Data (Phase-III)

Process Parameter	S/N Average Values, PICyl (dB)			Main Effects, PICyl (dB)	
	L1	L2	L3	L2-L1	L3-L2
C	33.30	33.31	33.42	0.01	0.11
EC	33.06	33.41	33.57	0.35	0.16
SR	32.75	34.30	32.98	1.55	-1.32
F	33.83	33.62	32.59	-0.21	-1.03
T	33.30	33.20	33.54	-0.10	0.34
SOP	31.74	33.78	34.50	2.04	0.72
G	32.69	35.14	32.20	2.45	-2.94
C-EC	33.72	33.74	32.57	0.02	-1.18
C-SR	33.62	33.10	33.31	-0.53	0.22
EC-SR	33.44	32.36	34.23	-1.08	1.87

L1, L2 and L3 represent average values of S/N data of response of corresponding parameters at levels 1, 2 and 3 respectively. L2-L1 is the average main effect when the corresponding parameter changes from level 1 to level 2. L3-L2 is the average main effect when the corresponding parameter changes from level 2 to level 3.

* 95 % Confidence Limit (CI_1) = ± 0.78

C: Current Intensity, EC: Electrolyte Concentration, SR: Speed Ratio, F: Electrolyte Flow Rate, T: Electrolyte Inlet Temperature, SOP: Stick-out Pressure, G: Grit Size.

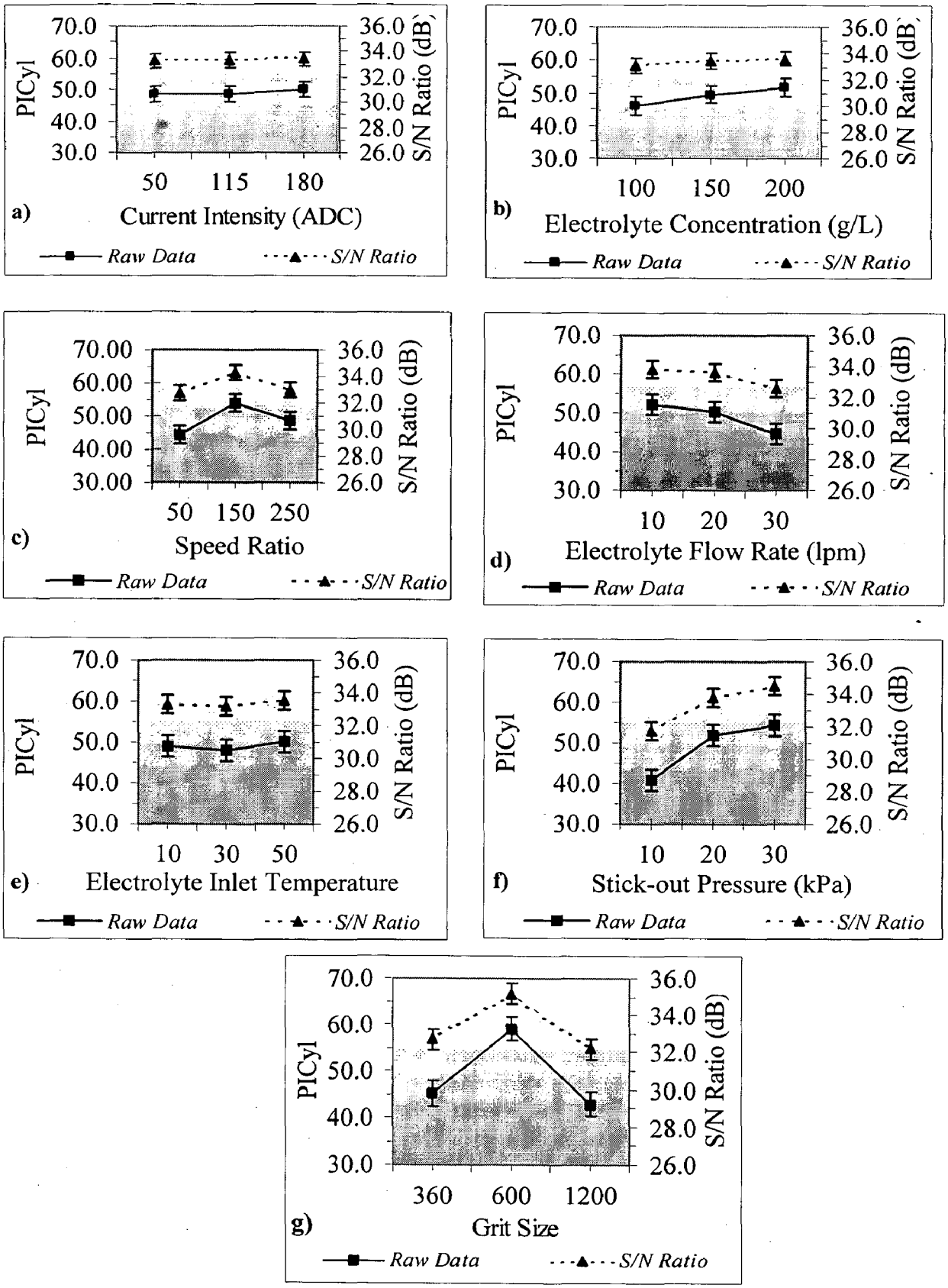

Fig. 7.17 Effects of process parameters on percent improvement in cylindricity (PICyl) and its S/N ratio (Main Effects)

Table 7.48 Pooled ANOVA– PICyl Raw Data (Phase-III)

Source	SS	DF	MS	F ratio	% Contribution
C	27.34	(2)	Pooled	-	-
EC	293.68	(2)	Pooled	-	-
SR	842.51	2	421.26	13.87*	6.56
F	563.94	(2)	Pooled	-	-
T	39.19	(2)	Pooled	-	-
SOP	1862.05	2	931.03	30.65*	15.11
G	2741.47	2	1370.74	45.12*	22.49
C-EC	1675.47	4	418.87	13.79*	13.04
C-SR	933.79	4	233.45	7.68*	6.81
EC-SR	2802.24	4	700.56	23.06*	22.49
Model	10857.54	18	603.20	19.86*	86.49
e(pooled)	1063.29	35	30.38		13.51
Total	11920.83	53			100.00

The Model F ratio of 19.86 implies that Model is significant at 99.5% confidence level.

* Significant at 95% confidence level.

SS: Sum of Square, DF: Degree of Freedom, MS: Mean Square, C: Current Intensity, EC: Electrolyte Concentration, SR: Speed Ratio, F: Electrolyte Flow Rate, T: Electrolyte Inlet Temperature, SOP: Stick-out Pressure, G: Grit Size.

Table 7.49 Pooled ANOVA– PICyl S/N Data (Phase-III)

Source	SS	DF	MS	F ratio	% Contribution
C	0.07	(2)	Pooled	-	-
EC	1.21	(2)	Pooled	-	-
SR	12.63	2	6.32	5.21*	4.46
F	7.86	(2)	Pooled	-	-
T	0.55	(2)	Pooled	-	-
SOP	36.95	2	18.47	15.25*	15.09
G	44.71	2	22.36	18.45*	18.49
C-EC	35.88	4	8.97	7.40*	13.56
C-SR	16.38	4	4.09	3.38*	5.04
EC-SR	72.52	4	18.13	14.97*	29.58
Model	219.08	18	12.17	10.05*	86.23
e (pooled)	8.48	8	1.21		13.77
Total	228.77	26			100.00

The Model F ratio of 10.05 implies that Model is significant at 99.5% confidence level.

* Significant at 95% confidence level.

SS: Sum of Square, DF: Degree of Freedom, MS: Mean Square, C: Current Intensity, EC: Electrolyte Concentration, SR: Speed Ratio, F: Electrolyte Flow Rate, T: Electrolyte Inlet Temperature, SOP: Stick-out Pressure, G: Grit Size.

Table 7.50 Average Effects of C-EC Interaction – PICyl Raw & S/N Data (Phase-III)

	Average Values, PICyl (%)			S/N Average Values, PICyl (dB)		
	C_1	C_2	C_3	C_1	C_2	C_3
EC_1	49.29	47.78	40.96	33.77	33.55	31.86
EC_2	52.99	49.40	45.77	34.17	33.54	32.52
EC_3	43.23	48.47	63.37	31.97	32.84	35.88
*95 % Confidence Limit (CI1) for average values-Raw data = ± 4.57						
*95 % Confidence Limit (CI1) for average values-S/N data = ± 1.36						

Table 7.51 Average Effects of C-SR Interaction – PICyl Raw & S/N Data (Phase-III)

	Average Values, PICyl (%)			S/N Average Values, PICyl (dB)		
	C_1	C_2	C_3	C_1	C_2	C_3
SR_1	46.87	45.08	41.22	33.27	32.86	32.11
SR_2	49.02	59.14	53.97	33.77	35.31	33.83
SR_3	49.62	41.42	54.91	32.88	31.76	34.31
*95 % Confidence Limit (CI1) for average values-Raw data = ± 4.57						
*95 % Confidence Limit (CI1) for average values-S/N data = ± 1.36						

Table 7.52 Average Effects of EC-SR Interaction – PICyl Raw & S/N Data (Phase-III)

	Average Values, PICyl (%)			S/N Average Values, PICyl (dB)		
	EC_1	EC_2	EC_3	EC_1	EC_2	EC_3
SR_1	43.05	35.12	55.01	32.66	30.82	34.77
SR_2	42.00	60.68	59.45	32.05	35.47	35.39
SR_3	52.98	52.36	40.61	34.47	33.94	30.53
*95 % Confidence Limit (CI1) for average values-Raw data = ± 4.57						
*95 % Confidence Limit (CI1) for average values-S/N data = ± 1.36						

7.2.4.1 Effect of current intensity

The independent effect of the current intensity on percent improvement in cylindricity raw as well as S/N response was not found significant as also observed on PIOR. But the interactive influences of the current intensity with electrolyte concentration and rotary to reciprocating speed ratio were quite significant as reflected by the F ratio and a considerable percentage contribution of the C-EC and EC-SR interactive terms in the pooled ANOVA of raw as well as S/N PICyl. The relationship of the current intensity and raw PICyl and S/N

PICyl at different electrolyte concentration levels is shown in Fig. 7.18a and 7.18b respectively. Similar to the results of PIOR, C_3-EC_3 provided significantly higher PICyl values. The influence of current intensity-speed ratio interaction on percent improvement in cylindricity is expressed in Fig. 7.19. The 2nd and 3rd levels of the speed ratio appear to be better particularly at level 3 of current intensity. The combined influence of higher current intensity and electrolyte concentration leading to improved differential dissolution and uniform selective dissolution with the proper combination of current intensity and speed ratio may be responsible for better PICyl. Noticeably the cylindricity, part macro-geometrical characteristic, is measured covering the whole cylinder. This signifies the importance of a suitable speed ratio to be employed viz-a-viz the electrolytic dissolution to achieve better PICyl.

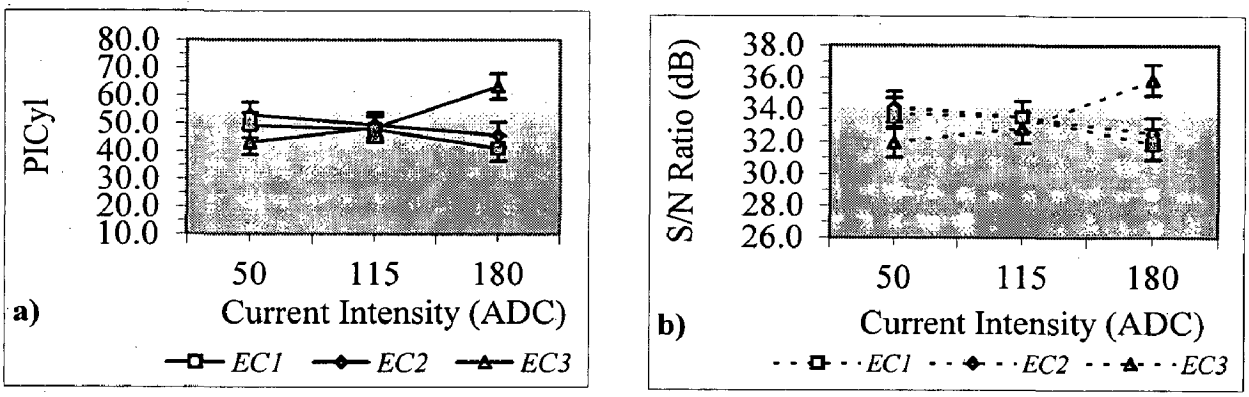

Fig. 7.18 Relation between current intensity and percent improvement in cylindricity and S/N ratio at different electrolyte concentration levels

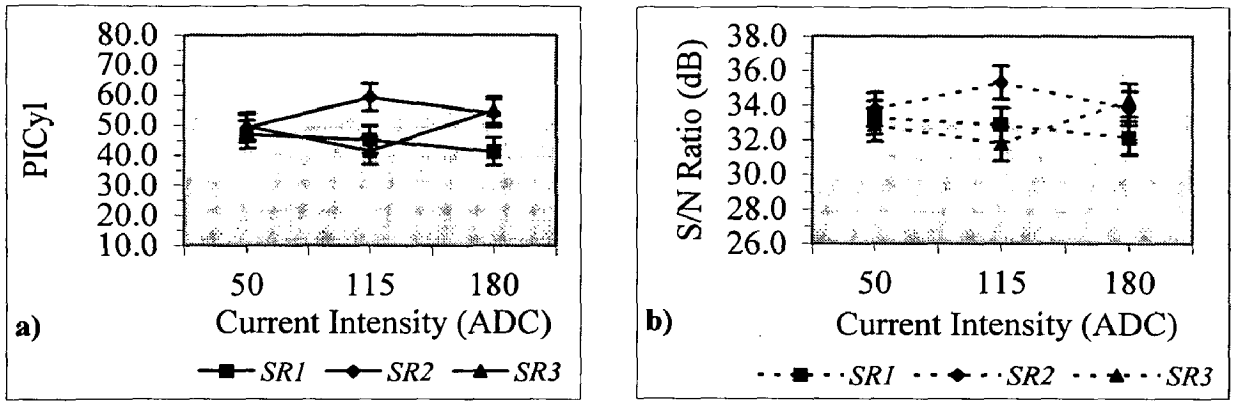

Fig. 7.19 Relation between current intensity and percent improvement in cylindricity and S/N ratio at different speed ratio levels

7.2.4.2 Effect of electrolyte concentration

Fig. 7.17b gives the relationship between the electrolyte concentration and the percent improvement in cylindricity. Similar to the effect of current intensity, the independent influence of the electrolyte concentration was not found as significant at the alpha value of 0.05. But its major influence on PICyl was revealed in terms of significant C-EC and EC-SR interactions. The interactive effects of the electrolyte concentration with the current intensity and rotary to reciprocating speed ratio are illustrated in Fig. 7.18 and 7.20 respectively. These plots highlight the fact that a proper combination of the current intensity, electrolyte concentration and speed ratio is necessary in order to get better results on the process macro-geometrical performance characteristic like PICyl. The 3rd level of the electrolyte concentration with level 3 of the current intensity and level 2 of rotary to reciprocating speed ratio provided better PICyl results. As noted earlier, an effective influence achieved on the selective differential dissolution of the cylindrical surface due to the suitable C-EC-SR combination may have yielded the better PICyl values at C_3-EC_3-SR_2. The interactive nature of the ECH process is clearly highlighted in this case.

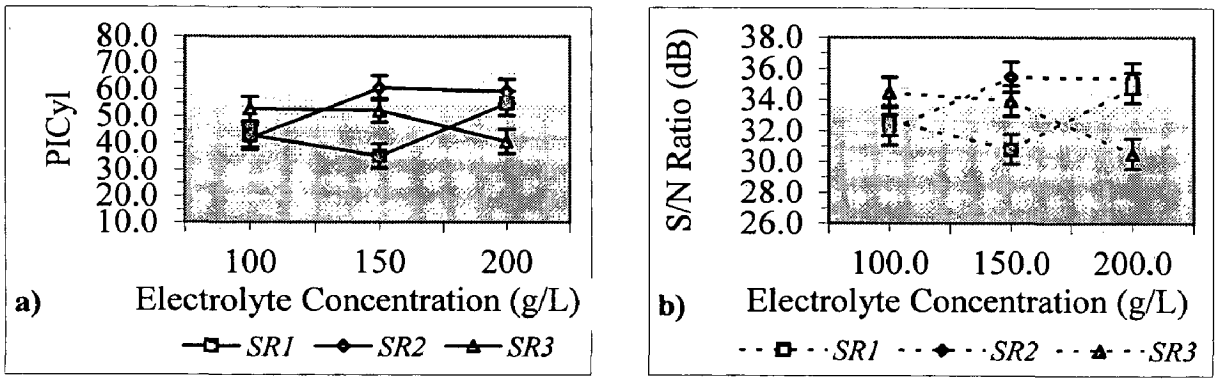

Fig. 7.20 Relation between electrolyte concentration and percent improvement in cylindricity and S/N ratio at different speed ratio levels

7.2.4.3 Effect of rotary to reciprocating speed ratio

The important role of the rotary to reciprocating speed ratio noted for correcting the out-of-roundness error is still more pronounced for PICyl. Besides the individual main effect of the speed ratio, its interactions with current intensity and electrolyte concentration were also found significant as discussed earlier. Better resulting cylindricity requires a proper rotary to reciprocating speed ratio for a particular setting of the other parameters. This fact is revealed in the response plot given in Fig. 7.17c. Level 2 of the rotary to reciprocating speed seems to be better. SR_2 also provided better interaction effects with C_3 and EC_3. Remarkably the independent effect of the speed ratio was found not significant in case of the micro-geometrical characteristics. But the wider spacing of macro-geometrical characteristics requires a suitable level of the speed ratio to be used to achieve a good coordination of the mechanical abrasion and electrolytic dissolution for providing their effective correction. A similar observation was noted in case of PIOR also.

7.2.4.4 Effect of electrolyte flow rate

Similar to the results of the process micro-geometrical performance characteristics and PIOR, the electrolyte flow rate main effect on the percent improvement in cylindricity was also found to be not significant at the chosen level of significance 0.05.

7.2.4.5 Effect of electrolyte inlet temperature

The effect of the electrolyte inlet temperature on the percent improvement in cylindricity was also found to be not significant. Similar was the case with PIOR.

7.2.4.6 Effect of stick-out pressure

Fig. 7.17f illustrates the variation of the percent improvement in cylindicity with various stick-out pressures. The PICyl increases with increase in the stick-out-pressure. An efficient scrubbing of metal oxide micro-film from the higher spots or tight areas of the surface profile leading to an increased differential dissolution at higher levels of SOP as discussed earlier could have resulted in higher PICyl. A similar influence of stick-out pressure was also noticed for process micro-geometrical performance characteristics.

7.2.4.7 Effect of stick grit-size

A dominating influence of the stick grit size was noticed on the percent improvement in cylindricity as also noted with out-of-roundness as well as with PIR_a and PIR_{max}. The main effect plot for stick grit-size on the PICyl raw and S/N data is given in Fig. 7.17g. The coarser grits are more effective as compared to fine grits for achieving higher PICyl values, emphasizing a proper selection of grit-size in the process. G_2 provided significantly higher PICyl results. Similar observation was made after the analysis of PIR_a, PIR_{max} and PIOR data.

Thus it is to be noted that for macro-geometrical error correction in ECH, there is increased contributions of mechanical parameters and interactions, and lesser independent contributions of electrolytic parameters, it is necessary to select proper speed ratio, stick-out pressure and stick grit size, and use appropriate C-EC-SR combination.

ECH can also rectify considerable initial form deviations in cylindricity, as revealed from the cylindricity values of the workpieces taken before and after ECH application. The initial form deviations in cylindricity even of the order of ISO Tolerance Grade 11 were rectified to within ISO Tolerance Grade 4-7.

7.2.4.8 Selection of optimal levels

The process input parameters and interactions that have significant effect on both the raw and S/N PICyl are the rotary to reciprocating speed ratio, stick-out pressure, stick grit-size, current intensity-electrolyte concentration, current intensity-speed ratio, and electrolyte concentration-speed ratio interactions. The percentage contribution of each input parameter and interactions as given in ANOVA tables reveal that the most influential parameters and interactions in decreasing order of their influence are the EC-SR interaction, grit-size, stick-out-pressure, C-EC interaction, C-SR interaction, and speed ratio.

The response plots for the significant process input parameters (Fig. 7.17) indicate that level 2 of the speed ratio (SR_2) and stick grit size (G_2) and level 3 of the stick-out pressure (SOP_3) yield the highest mean response as well as the highest average S/N ratio of PICyl. The analysis of the interaction plots of current intensity-electrolyte concentration (Fig. 7.18), current intensity-speed ratio interaction (Fig. 7.18) and electrolyte concentration-speed ratio (Fig. 7.20) suggests that the combined effects of C_3-EC_3, C_3-SR_2 and EC_3-SR_2 provide the highest mean and S/N values of PICyl. Any suitable level of electrolyte flow rate can be selected as the effects of electrolyte flow rate and electrolyte inlet temperature were found to

be not significant on PICyl and S/N ratio. The optimal levels of the control parameters for PICyl are given in Table 7.53.

Table 7.53 Optimal level of process parameters for mean PICyl and S/N ratio (Phase-III)

Process Input Parameters	Optimal Levels	
Current Intensity (ADC)#	C_3	180
Electrolyte Concentration (g/L)#	EC_3	200
Speed Ratio #	SR_2	150
Electrolyte Flow Rate (lpm)*	F_2	20
Electrolyte Inlet Temperature (°C)*	T_2	30
Stick-out Pressure (kPa)	SOP_3	30
Grit Size	G_2	600

** Not significant. Therefore, selected conveniently.*
 # Interactions C- EC, C- SR and EC- SR are significant.

7.2.4.9 Estimation of optimal values of performance characteristic

Percent improvement in cylindricity

The predicted optimal value of PICyl [derived from Table 7.54] and corresponding 95% confidence intervals are given below:

Table 7.54 Average values of PICyl at optimal level of process parameters (with interactions) (Phase-III)

Optimum Level of Significant Process Parameter	PICyl (%)
C_3EC_3	63.37
C_3SR_2	53.97
EC_3SR_2	59.45
3rd Level of Stick-out Pressure (SOP_3)	54.36
2nd Level of Grit Size (G_2)	59.02
Overall Mean of PICyl ($\overline{T}_{PICyl}$)	49.03
2nd Level of Speed Ratio (SR_2)	54.04

$u_{PICyl} = C_3EC_3 + C_3SR_2 + EC_3SR_2 + SOP_3 + G_2 - 4\,\overline{T}_{PICyl} - (SR_2 - \overline{T}_{PICyl})$

$= 89.04\ \%$

$CI_{pop} = \pm 8.16$, (CI_{pop}: $80.88 < u_{PICyl}(\%) < 97.21$)

$CI_{CE} = \pm 13.13$, (CI_{CE}: $75.91 < u_{PICyl}(\%) < 100$)

[N = 27 x 2 = 54, f_e (error D.F.) = (53-16) = 37, v_e (error variance) = 51.51 (recalculated from Table 7.48), n_{eff} = N / (1+ D.F. associated in the estimate of mean response) = 3.18, R = 2, $F_{0.05}$ (1, 37) = 4.110 in Eq. 6.9a and 6.9b]

The predicted optimal value of S/N PICyl ($u_{S/N\ PICyl}$) with corresponding 95% confidence intervals can be obtained using Table 7.55:

Table 7.55 Average S/N values of PICyl at optimal level of process parameters (with interactions) (Phase-III)

Optimum Level of Significant Process Parameter	S/N Ratio (dB)
C_3EC_3	35.88
C_3SR_2	33.83
EC_3SR_2	35.39
3rd Level of Stick-out Pressure (SOP_3)	34.50
2nd Level of Grit Size (G_2)	35.14
Overall Mean of S/N PICyl ($\overline{T}_{S/N\ PICyl}$)	33.34
2nd Level of Speed Ratio (SR_2)	34.30

$u_{S/N\ PICyl} = C_3EC_3 + C_3SR_2 + EC_3SR_2 + SOP_3 + G_2 - 4\,\overline{T}_{S/N\ PICyl} - (SR_2 - \overline{T}_{S/N\ PICyl})$

$= 40.41$ dB

$CI_{pop} = \pm 2.64$, (CI_{pop}: $37.77 < u_{S/NPICyl}(dB) < 43.05$)

$CI_{CE} = \pm 3.54$, (CI_{CE} : $36.87 < u_{S/NPICyl}(dB) < 43.95$)

[N = 27, f_e (error D.F.) = (26-16) = 10, v_e (error variance) = 2.23 (modified Table 7.49), n_{eff} = N / (1+ D.F. associated in the estimate of mean response) = 1.59, R = 2, $F_{0.05}$ (1, 10) = 4.9646]

7.2.5 Diametral Increase Rate

The experimental results for the material removal process performance characteristic the dimetral increase rate (DIR) are given in Table 6.27. The method of analysis as used for other process performance characteristics was adopted for DIR also. Tables 7.56 and 7.57 give the average and main effects of the process input parameters and interactions for DIR raw data and S/N data respectively. Raw and S/N DIR response plots for the process input parameters are presented in Fig. 7.21. The pooled ANOVA results are illustrated in Tables 7.58 and 7.59.

The analysis of variance indicates a dominating influence of the current intensity for the diametral increase rate raw as well as S/N results. The process input parameters having significant effects on both the raw and S/N DIR at a significance level 0.05 are the current intensity, electrolyte concentration, stick-out pressure and stick grit-size. The rotary to reciprocating speed ratio, electrolyte flow rate, current intensity-speed ratio interaction and electrolyte concentration-speed ratio interaction significantly influenced the mean DIR (the raw data response), but could influence the variation around mean DIR at a lower confidence level (alpha equal to 0.10) except the speed ratio which was found insignificant for S/N DIR. The average DIR and S/N ratios for significant interactions are produced in Tables 7.60 and 7.61 respectively.

Table 7.56 Average and Main Effects – DIR Raw Data (Phase-III)

Process Parameter	Average Values, DIR (μm/min)			Main Effects, DIR (μm/min)	
	L1	L2	L3	L2-L1	L3-L2
C	14.32	19.57	38.18	5.25	18.61
EC	20.77	24.27	27.03	3.50	2.76
SR	20.95	24.14	26.98	3.19	2.84
F	21.58	27.69	22.79	6.11	-4.90
T	22.86	25.49	23.72	2.63	-1.77
SOP	19.00	25.07	27.99	6.06	2.93
G	28.22	27.34	16.51	-0.88	-10.82
C-EC	25.02	24.35	22.70	-0.67	-1.65
C-SR	25.66	24.11	22.30	-1.55	-1.81
EC-SR	26.34	19.88	25.85	-6.46	5.97

L1, L2 and L3 represent average values of raw data of response of corresponding parameters at levels 1, 2 and 3 respectively. L2-L1 is the average main effect when the corresponding parameter changes from level 1 to level 2. L3-L2 is the average main effect when the corresponding parameter changes from level 2 to level 3.

* 95 % Confidence Limit (CI_1) = ± 1.79

C: Current Intensity, EC: Electrolyte Concentration, SR: Speed Ratio, F: Electrolyte Flow Rate, T: Electrolyte Inlet Temperature, SOP: Stick-out Pressure, G: Grit Size.

Table7.57 Average and Main Effects – DIR S/N Data (Phase-III)

Process Parameter	S/N Average Values, DIR (dB)			Main Effects, DIR (dB)	
	L1	L2	L3	L2-L1	L3-L2
C	22.77	25.05	30.30	2.28	5.25
EC	24.24	26.67	27.23	2.43	0.56
SR	25.38	26.00	26.75	0.61	0.75
F	24.82	27.58	25.73	2.76	-1.86
T	25.20	27.20	25.73	2.00	-1.48
SOP	24.43	26.25	27.45	1.83	1.19
G	27.85	26.97	23.32	-0.88	-3.65
C-EC	26.54	25.96	25.64	-0.58	-0.32
C-SR	26.36	26.25	25.53	-0.11	-0.72
EC-SR	26.92	24.55	26.66	-2.37	2.11

L1, L2 and L3 represent average values of S/N data of response of corresponding parameters at levels 1, 2 and 3 respectively. L2-L1 is the average main effect when the corresponding parameter changes from level 1 to level 2. L3-L2 is the average main effect when the corresponding parameter changes from level 2 to level 3.

* 95 % Confidence Limit (CI_1) = ± 1.62

C: Current Intensity, EC: Electrolyte Concentration, SR: Speed Ratio, F: Electrolyte Flow Rate, T: Electrolyte Inlet Temperature, SOP: Stick-out Pressure, G: Grit Size.

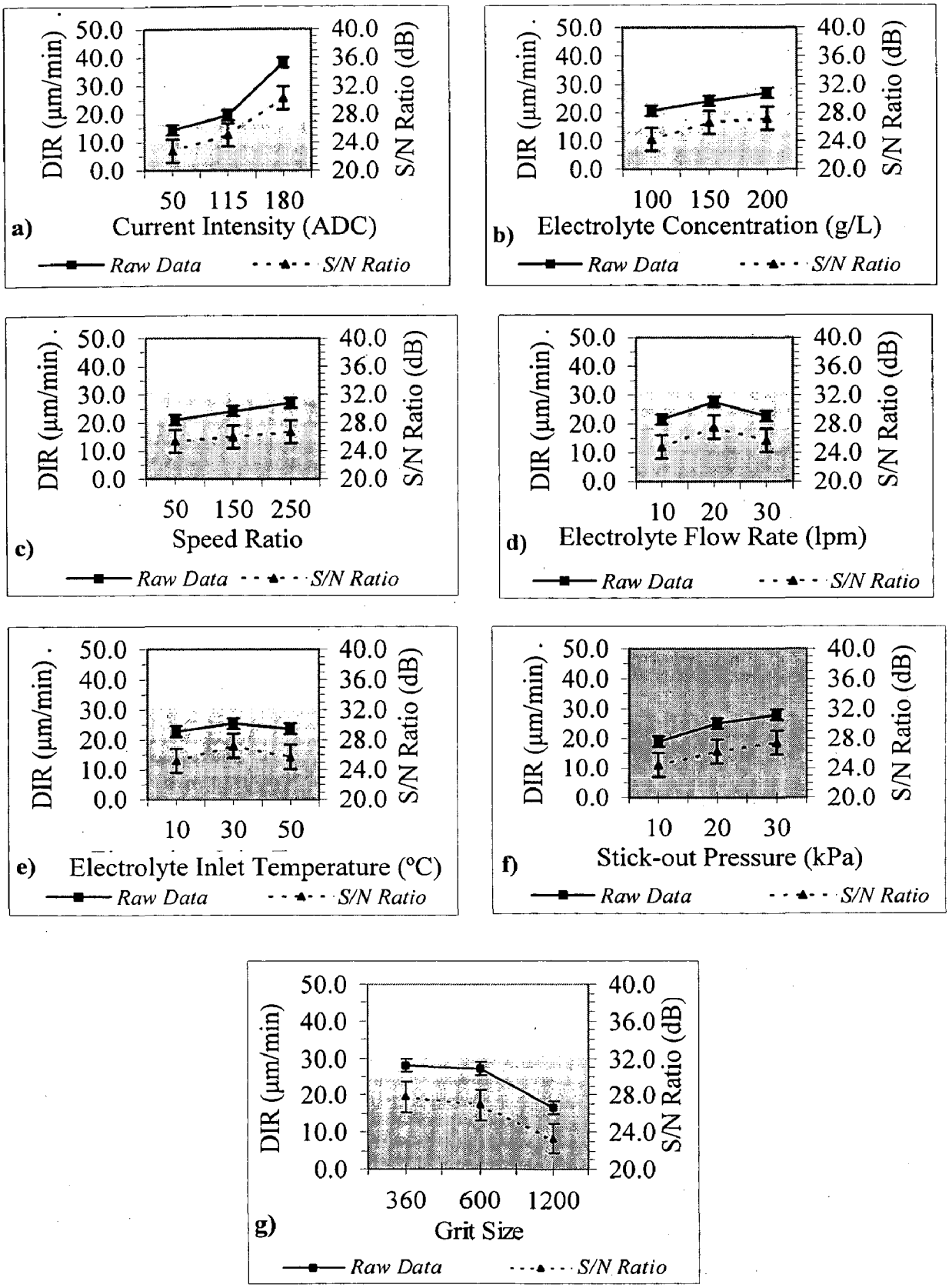

Fig. 7.21 Effects of process parameters on diametral increase rate (DIR) and its S/N ratio (Main Effects)

Table 7.58 Pooled ANOVA– DIR Raw Data (Phase-III)

Source	SS	DF	MS	F ratio	% Contribution
C	5657.29	2	2828.64	203.08*	49.66
EC	354.07	2	177.04	12.71*	2.88
SR	327.53	2	163.76	11.76*	2.64
F	377.21	2	188.61	13.54*	3.08
T	64.82	(2)	-	-	-
SOP	756.62	2	378.31	27.16*	6.43
G	1528.88	2	764.44	54.88*	13.24
C-EC	158.34	(4)	-	-	-
C-SR	898.53	4	224.63	16.13*	7.43
EC-SR	976.96	4	244.24	17.53*	8.13
Model	10877.08	20	543.85	39.04*	93.49
e(pooled)	459.66	33	13.93		6.51
Total	11336.74	53			100.00

The Model F ratio of 39.04 implies that Model is significant at 99.5% confidence level.

* Significant at 95% confidence level.

SS: Sum of Square, DF: Degree of Freedom, MS: Mean Square, C: Current Intensity, EC:- Electrolyte Concentration, SR: Speed Ratio, F: Electrolyte Flow Rate, T: Electrolyte Inlet Temperature, SOP: Stick-out Pressure, G: Grit Size.

Table 7.59 Pooled ANOVA– DIR S/N Data (Phase-III)

Source	SS	DF	MS	F ratio	% Contribution
C	268.55	2	134.28	30.35*	39.93
EC	45.53	2	22.76	5.15*	5.64
SR	8.41	(2)	-	-	-
F	35.58	2	17.79	4.02#	4.11
T	19.31	(2)	-	-	-
SOP	41.58	2	20.79	4.70*	5.03
G	103.92	2	51.96	11.74*	14.62
C-EC	7.68	(4)	-	-	-
C-SR	59.03	4	14.76	3.34#	6.36
EC-SR	60.82	4	15.21	3.44#	6.63
Model	615.01	18	34.17	7.72*	82.31
e(pooled)	35.39	8	4.42		17.69
Total	650.40	26			100.00

The Model F ratio of 7.72 implies that Model is significant at 99.5% confidence level.

*Significant at 95% confidence level.

Significant at 90% confidence level.

SS: Sum of Square, DF: Degree of Freedom, MS: Mean Square, C: Current Intensity, EC: Electrolyte Concentration, SR: Speed Ratio, F: Electrolyte Flow Rate, T: Electrolyte Inlet Temperature, SOP: Stick-out Pressure, G: Grit Size.

Table 7.60 Average Effects of C-SR Interaction – DIR Raw and S/N Data (Phase-III)

	Average Values, DIR (μm/min)			S/N Average Values, DIR (dB)		
	C_1	C_2	C_3	C_1	C_2	C_3
SR_1	14.52	16.84	31.49	22.74	23.85	29.56
SR_2	14.61	23.71	34.09	23.13	26.99	27.87
SR_3	13.83	18.16	48.95	22.45	24.32	33.48
*95 % Confidence Limit (CI_1) for average values-Raw data = ± 3.10						
*95 % Confidence Limit (CI_1) for average values-S/N data = ± 2.80						

Table 7.61 Average Effects of EC-SR Interaction – DIR Raw and S/N Data (Phase-III)

	Average Values, DIR (μm/min)			S/N Average Values, DIR (dB)		
	EC_1	EC_2	EC_3	EC_1	EC_2	EC_3
SR_1	22.34	20.19	20.32	25.33	25.02	25.80
SR_2	12.60	28.64	31.17	21.21	28.26	28.52
SR_3	27.38	23.97	29.59	26.17	26.72	27.36
*95 % Confidence Limit (CI_1) for average values-Raw data = ± 3.10						
*95 % Confidence Limit (CI_1) for average values-S/N data = ± 2.80						

7.2.5.1 Effect of current intensity

A peculiar noticeable behavior of ECH is a simultaneous improvement of surface micro as well as macro-geometrical profile and the diametral increase rate with increasing current intensities. The current intensity has the most dominating influence on both the raw and S/N DIR as revealed in the percentage contribution columns in ANOVA Tables. An increase in current intensity results in a substantial increase in the diametral increase rate as shown in the response curve Fig. 7.20a. The material removal seems to be Faradic in nature wherein the electrochemical dissolution follows the Faraday's law of electrolysis that is the amount of material removed is proportional to the time and the intensity of current flow between the cathode tool and anode workpiece. The increase in current intensity increases the current density in inter-electrode gap (IEG) and this helps in accelerating the anodic dissolution of the work material. Bhattacharyya and Munda (2003) observed that highly reactive chemical attacks also occur at high current density in electro-chemical

micromachining, depending upon the type of electrolyte. The influence of the increased electrolytic dissolution coupled with the accelerated differential dissolution due to the action of the honing sticks and associated phenomena of viscous layer theory (Cole and Hopenfeld, 1963) and theory of anodic smoothing (Fitz-Gerald and McGeough, 1970) as discussed earlier, lead to simultaneous improvements in diametral increase rate and surface micro and macro-profiles at increased current intensities in electro-chemical honing. However, the effect of current intensity is more dominating for DIR. As can be seen from Fig. 7.21a the DIR is considerably higher at the 3rd level of the current intensity. Besides its large independent effect, the current intensity also influences DIR interactively with the rotary to reciprocating speed ratio (Fig. 7.22). The C_3-SR_3 achieved a significantly higher diametral increase rate. The reasons are obvious.

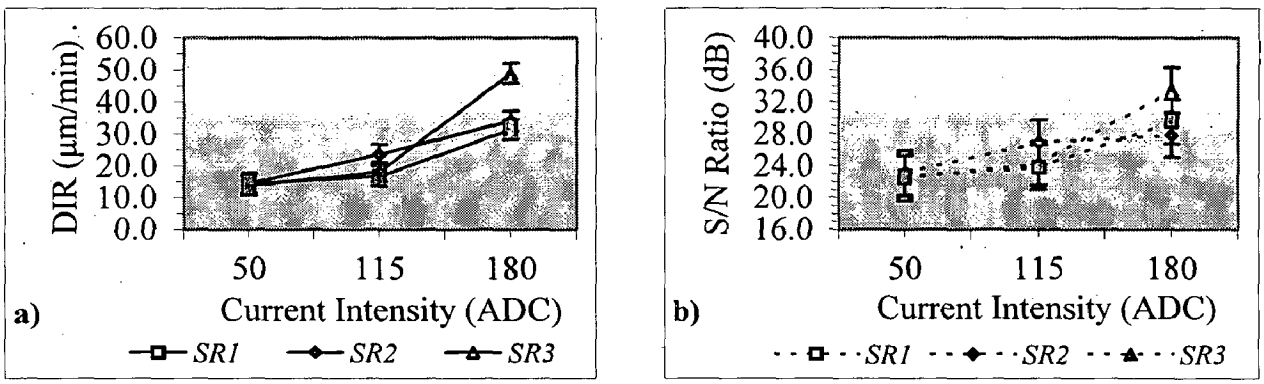

Fig. 7.22 Relation between current intensity and diametral increase rate and S/N ratio at different speed ratio levels

7.2.5.2 Effect of electrolyte concentration

Fig. 7.21b gives the relationship between the electrolyte concentration and the diametral increase rate. Diametral increase rate improves with higher electrolyte concentration. This can be attributed to increase in the electrical conductivity of electrolyte at the increased electrolyte concentration leading to an increased electrolytic action at higher peaks of the surface profile exposed due to the action of honing sticks resulting in a higher diametral increase rate. The contribution of electrolyte concentration on DIR is, although significant, however quite low as compared to its effect on the surface profile corrections. The changed physical nature and the protective ability of the resulting metal oxide microfilm as discussed earlier can be considered to be underlying reasons for this.

An interactive nature of electrolyte concentration and speed ratio for DIR is revealed in Fig. 7.23a and 7.23b. SR_3 appears to be better for achieving a higher diametral increase rate particularly at levels 2 and 3 of the electrolyte concentration. Noticeably, level 2nd of the speed ratio was found suitable for most of the cases of the process micro and macro performance characteristics.

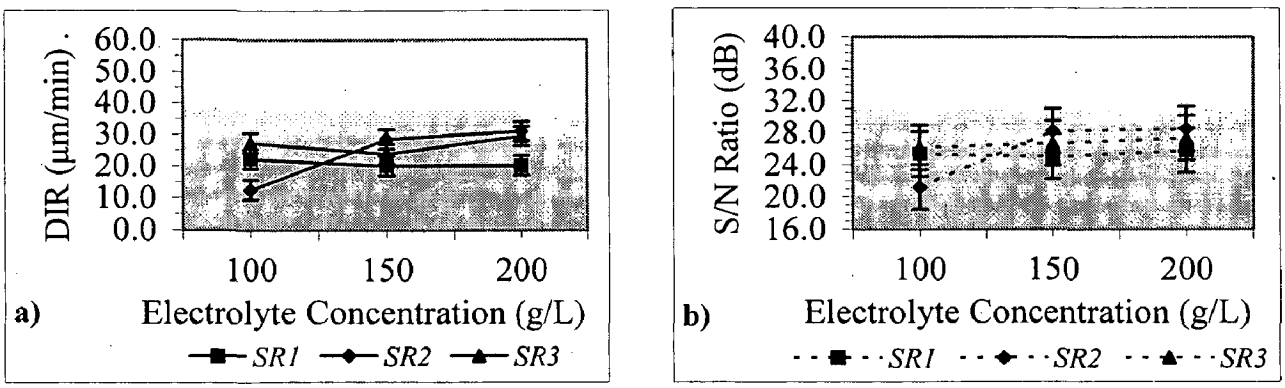

Fig. 7.23 Relation between electrolyte concentration and diametral increase rate and S/N ratio at different speed ratio levels

7.2.5.3 Effect of rotary to reciprocating speed ratio

The rotary to reciprocating speed ratio was found significant for mean diametral increase rate. However, its effect on S/N ratio was not so influential. Besides the individual main effect of the speed ratio, its interactions with current intensity and electrolyte concentration were also significant as discussed earlier. The variation of diametral increase rate with the speed ratio is presented in Fig. 7.21c. DIR improves with increase in the speed ratio. The action of the honing sticks in ECH removes the passivating metal oxide film from the higher spots and tight areas, thus exposing the fresh metal for electrolytic and reactive chemical attacks. This action occurs at faster rate at higher speed ratio leading to a faster diametral increase rate. Level 3 of the rotary to reciprocating speed appears to be better.

7.2.5.4 Effect of electrolyte flow rate

The effect of electrolyte flow rate on diametral increase rate was found significant on diametral increase rate at 0.05 significant level based on F test. However, it did not influence the S/N ratio significantly at the chosen alpha. Further, considering the percentage contribution the effect is not significant enough as the contributions less than five percent are generally not considered significant (Roy, 1990). The cleansing action of the honing sticks along with the better flow characteristics in the IEG achieved due to dual supply mode of electrolyte led to less influential electrolyte flow rate effects in the process as described earlier.

7.2.5.5 Effect of electrolyte inlet temperature

The effect of the electrolyte inlet temperature on the diametral increase rate was found to be not significant.

7.2.5.6 Effect of stick-out pressure

Fig. 7.21f illustrates the variation of diametral increase rate with various stick-out pressures. The DIR increases with increase in the stick-out pressure. An efficient scrubbing of metal oxide micro-film from the higher spots or tight areas of the surface profile at higher levels of SOP as discussed earlier can be considered to have resulted in higher DIR. A similar effect of stick-out pressure on process micro-geometrical as well as macro-geometrical performance characteristics was also noticed.

7.2.5.7 Effect of stick grit size

A dominating influence of the stick grit size was also noticed on the diametral increase rate. The main effect plot for stick grit-size on the DIR raw and S/N data is illustrated in Fig. 7.21g. The coarser grits are more effective as compared to fine grits for achieving higher DIR and accordingly the level1 (G_1) provided the maximum DIR response.

7.2.5.8 Selection of optimal levels

The pooled ANOVA results reveal that the process input parameters having significant effects on both the raw and S/N DIR at a significance level 0.05 are the current intensity, electrolyte concentration, stick-out pressure and stick grit-size. The rotary to reciprocating speed ratio, electrolyte flow rate, current intensity-speed ratio interaction and electrolyte concentration-speed ratio interaction significantly influence the mean DIR (the raw data response), but influence the variation around mean DIR at a lower confidence level (alpha equal to 0.10) except the speed ratio which was found insignificant for S/N DIR. The trend of variation of the response for the significant process input parameters (as given Fig. 7.21) indicates that level 3 of the parameters current intensity, electrolyte concentration, and stick-out pressure and level 1 of grit size yield the highest mean response as well as the highest average S/N ratio of DIR. 3rd level of the rotary to reciprocating speed ratio and level

2 of electrolyte flow rate also provide higher mean DIR. The examination of the interaction plots of current intensity-speed ratio (Fig. 7.22) and electrolyte concentration-speed ratio (Fig. 7.23) suggests that the combined effects of C_3-SR_3 and EC_3-SR_3 provide the highest mean value of DIR. The level of electrolyte inlet temperature can be selected conveniently as the effect of electrolyte inlet temperature was found to be not significant on DIR and S/N ratio. Tables 7.62 and 7.63 illustrate the optimal levels of the process parameters for mean DIR and S/N DIR respectively.

Table 7.62 Optimal level of process parameters for mean DIR (with interaction) (Phase-III)

Process Input Parameters	Optimal Levels	
Current Intensity (ADC)#	C_3	180
Electrolyte Concentration (g/L)#	EC_3	200
Speed Ratio #	SR_3	250
Electrolyte Flow Rate (lpm)	F_2	20
Electrolyte Inlet Temperature (°C)*	T_2	30
Stick-out Pressure (kPa)	SOP_3	30
Grit Size	G_1	360

** Not significant. Therefore, selected conveniently.*
 # Interactions C-SR and E -SR are significant.

Table 7.63 Optimal level of process parameters for S/N DIR (Phase-III)

Process Input Parameters	Optimal Levels	
Current Intensity (ADC)	C_3	180
Electrolyte Concentration (g/L)	EC_3	200
Speed Ratio*	SR_3	250
Electrolyte Flow Rate (lpm)*	F_2	20
Electrolyte Inlet Temperature (°C)*	T_2	30
Stick-out Pressure (kPa)	SOP_3	30
Grit Size	G_1	360

** Not significant. Therefore, selected conveniently. .*

7.2.5.9 Estimation of optimal value of performance characteristic

The optimal value of DIR and S/N ratio are estimated at the selected levels of significant parameters and interactions.

Diametral increase rate

The average values of DIR (from Tables 7.56, 7.60, 7.61 and 6.27) are given in Table 7.64.

Table 7.64 Average values of DIR at optimal level of process input parameters (with interactions) (Phase-III)

Optimum Level of Significant Process Parameter	DIR (μm/min)
C_3SR_3	48.95
EC_3SR_3	29.59
2nd Level of Electrolyte Flow Rate (F_3)	27.69
3rd Level of Stick-out Pressure (SOP_3)	27.99
1st Level of Grit Size (G_1)	28.22
Overall Mean of DIR ($\overline{T}_{DIR}$)	24.02
3rd Level of Speed Ratio (SR_3)	26.98

The predicted optimal value of DIR (u_{DIR}) is:

$$u_{DIR} = C_3SR_3 + EC_3SR_3 + F_3 + SOP_3 + G_1 - 4\,\overline{T}_{DIR} - (SR_3 - \overline{T}_{DIR})$$

$$= 63.39\ (\mu m / min)$$

The 95% confidence interval for the mean of the population and two confirmation experiments (CI_{pop} & CI_{CE}) have been calculated using equations 6.9a and 6.9b by substituting the following values:

N = 27 x 2 = 54, f_e (error D.F.) = (53-14) = 39, v_e (error variance) = 174.32 (modified Table 7.58).

n_{eff} = N / (1+ D.F. associated in the estimate of mean response) = 3.6, R = 2,

$F_{0.05}$ (1, 39) = 4.09341

$CI_{pop} = \pm 14.08$

$CI_{CE} = \pm 23.56$

The 95% confidence intervals (CI_{pop} & CI_{CE}) of the predicted optimal DIR are:

CI_{pop}: $49.31 < u_{DIR}\,(\mu m / min) < 77.47$

CI_{CE}: $39.84 < u_{DIR}\,(\mu m / min) < 86.95$

The S/N average values of DIR (Tables 7.57 and 6.27) are given in Table 7.65

Table 7.65 Average S/N values of DIR at optimal level of process parameters (Phase-III)

Optimum Level of Significant Process Parameter	S/N Ratio (dB)
C_3SR_3#	33.48
EC_3SR_3#	27.36
2nd Level of Electrolyte Flow Rate (F_2)#	27.58
3rd Level of Stick-out Pressure (SOP_3)	27.99
1st Level of Grit Size (G_1)	27.85
Overall Mean of DIR ($\overline{T}_{S/N\,DIR}$)	26.04
# Significant at 0.10 alpha value	

The predicted optimal value of S/N DIR ($u_{SN\,DIR}$) is:

$$u_{S/N\,DIR} = C_3SR_3 + EC_3SR_3 + F_3 + SOP_3 + G_1 - 4\,\overline{T}_{S/N\,DIR}$$

$$= 39.53 \text{ dB}$$

The following values were used in Eq. 6.9a and 6.9b to obtain 95% CI_{pop} & CI_{CE} for optimal mean S/N DIR:

N = 27, f_e (error D.F.) = (26-14) = 12, v_e (error variance) = 29.12 (Modified Table 7.59).

n_{eff} = N / (1+ D.F. associated in the estimate of mean response) = 1.80, R = 2,

$F_{0.05}\,(1, 12) = 4.7472$

$CI_{pop} = \pm 8.76$

$CI_{CE} = \pm 12.08$

The 95% confidence intervals (CI_{pop} & CI_{CE}) of the predicted optimal S/N DIR are:

CI_{pop}: $30.77 < u_{S/N\,DIR}\,(dB) < 48.30$

CI_{CE}: $27.45 < u_{S/N\,DIR}\,(dB) < 51.61$

7.3 PHASE-IV CONFIRMATION EXPERIMENTS

This phase of experimentation was conducted to validate various optimal results of experimental optimization studies and also to verify the findings of analytical studies. Two confirmation experiments have been performed for each of the process performance characteristic at the optimal settings of the process parameters and the average values have been compared statistically with their corresponding predicted values. In case, an optimal settings correspond to an experimental trial condition of the concerned experiment then no confirmation experiment were conducted and the predicted mean has been compared with the result of that trial. The average values of the performance characteristic obtained through the confirmation experiments must be within the 95% confidence interval CI_{CE} of the respective process performance characteristic. However, the average value of the process performance characteristic obtained from the confirmation experiments may or may not lie within 95% CI_{POP} (Ross, 1988). The results of 2 confirmation experiments conducted to validate the predicted optimal values of various process performance characteristics examined in Phase-III Stage-I studies are reported in Table 7.66. Since the confirmation experiment values of the various process performance characteristics lie within the respective 95% confidence intervals of confirmation experiments, the results of Phase-III Stage-I studies are validated.

Veeco

Mag: 10.4 X
Mode: VSI

Surface Statistics:
Ra: 4.39 um
Rq: 5.48 um
Rz: 23.12 um
Rt: 31.61 um

Set-up Parameters:
Size: 368 X 240
Sampling: 1.61 um

Processed Options:
Terms Removed:
Tilt
Filtering:
None

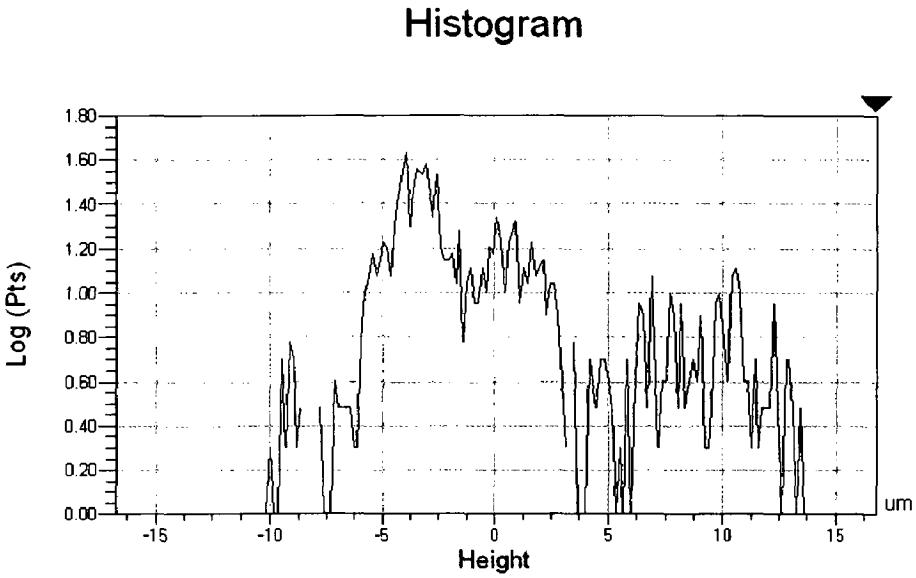

7.24c) Filtered Histogram (Trial Condition-R: Prior to ECH)

Veeco

Mag: 10.4 X
Mode: VSI

Statistics:
tp1: 0.0 %
tp2: 100.0 %
Htp: 31.61 um

Mr1: 23.83 %
Mr2: 95.28 %
RK: 8855.54 nm
Rpk: 11577.02 nm
Rvk: 5146.77 nm
V1: 1.38 um
V2: 121.58 nm

Ra: 4.39 um
Rq: 5.48 um
Rz: 23.12 um

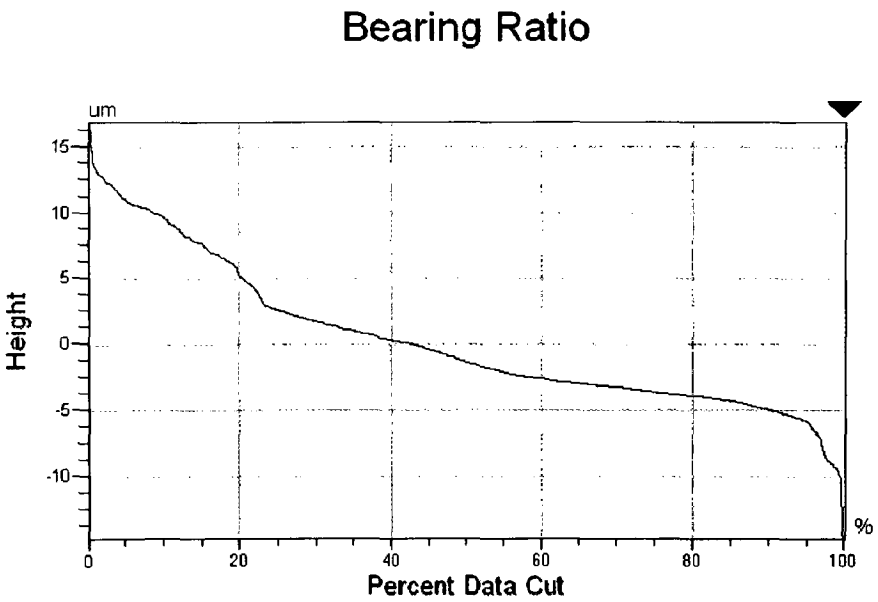

7.24d) Bearing Ratio (Trial Condition-R: Prior to ECH)

7.3 PHASE-IV CONFIRMATION EXPERIMENTS

This phase of experimentation was conducted to validate various optimal results of experimental optimization studies and also to verify the findings of analytical studies. Two confirmation experiments have been performed for each of the process performance characteristic at the optimal settings of the process parameters and the average values have been compared statistically with their corresponding predicted values. In case, an optimal settings correspond to an experimental trial condition of the concerned experiment then no confirmation experiment were conducted and the predicted mean has been compared with the result of that trial. The average values of the performance characteristic obtained through the confirmation experiments must be within the 95% confidence interval CI_{CE} of the respective process performance characteristic. However, the average value of the process performance characteristic obtained from the confirmation experiments may or may not lie within 95% CI_{POP} (Ross, 1988). The results of 2 confirmation experiments conducted to validate the predicted optimal values of various process performance characteristics examined in Phase-III Stage-I studies are reported in Table 7.66. Since the confirmation experiment values of the various process performance characteristics lie within the respective 95% confidence intervals of confirmation experiments, the results of Phase-III Stage-I studies are validated.

Table 7.66 Confirmation experiment results (Phase-III)

Process Performance Characteristic	Optimal Level of Process Parameters	Predicted Optimal Value	95% Confidence Intervals	Actual Value
PIRa	C3, EC3, SR1, F2*, T3, SOP3, G2	88.68 %	CI_{pop}: $82.61 < u_{PIRa}(\%) < 94.75$ CI_{CE}: $78.53 < u_{PIRa}(\%) < 98.83$	87.89%
S/N PIRa	C3, EC3, SR1, F2*, T3, SOP3, G2	39.04dB	CI_{pop}: $37.71 < u_{S/NPIRa}(dB) < 40.38$ CI_{CE}: $37.21 < u_{S/NPIRa}(dB) < 40.88$	38.88dB
PIRmax	C3, EC3, SR2, F2*, T3, SOP3, G2	82.42 %	CI_{pop}: $79.90 < u_{PIRmax}(\%) < 84.93$ CI_{CE}: $78.21 < u_{PIRmax}(\%) < 86.62$	85.36%
S/N PIRmax	C3, EC3, SR2, F2*, T3, SOP3, G2	38.70 dB	CI_{pop}: $36.86 < u_{S/NPIRmax}(dB) < 40.54$ CI_{CE}: $36.16 < u_{S/NPIRmax}(dB) < 41.24$	38.62dB
PIOR	C3, EC3, SR2, F2*, T2*, SOP3, G2	67.00%	CI_{pop}: $60.65 < u_{PIOR}(\%) < 73.35$ CI_{CE}: $55.86 < u_{PIOR}(\%) < 78.14$	63.29%
S/N PIOR	C3, EC3, SR2, F2*, T2*, SOP3, G2	38.37 dB	CI_{pop}: $35.82 < u_{S/NPIOR}(dB) < 40.92$ CI_{CE}: $34.73 < u_{S/NPIOR}(dB) < 42.02$	36.02dB
PICyl	C3, EC3, SR2, F2*, T2*, SOP3, G2	89.04%	CI_{pop}: $80.88 < u_{PICyl}(\%) < 97.21$ CI_{CE}: $75.91 < u_{PICyl}(\%) < 100$	83.07%
S/N PICyl	C3, EC3, SR2, F2*, T2*, SOP3, G2	40.41dB	CI_{pop}: $37.77 < u_{S/NPICyl}(dB) < 43.05$ CI_{CE}: $36.87 < u_{S/NPICyl}(dB) < 43.95$	38.39dB
DIR	C3, EC3, SR3, F2, T2*, SOP3, G1	63.39 (μm/min)	CI_{pop}: $49.31 < u_{DIR}(\mu m/min) < 77.47$ CI_{CE}: $39.84 < u_{DIR}(\mu m/min) < 86.95$	66.04 (μm/min)
S/N DIR	C3, EC3, SR3*, F2*, T2*, SOP3, G1	39.53 dB	CI_{pop}: $30.77 < u_{S/NDIR}(dB) < 48.30$ CI_{CE}: $27.45 < u_{S/NDIR}(dB) < 51.61$	36.39dB

** Not Significant, therefore selected conveniently.*

7.4 PHASE-III STAGE-II STUDIES

These studies have been conducted for the purpose of detailed examination of the work surface characteristics. Different work samples were analyzed using the micrographs of the work surface taken from the optical profiler (Wyko NT 1100) interfaced with Vision® 32 software and scanning electron microscope as described in Sections 5.4.1.3 and 5.4.1.4.

Surface Characterization

The optical and scanning electron micrographs of the raw work surface (before ECH) obtained from precision lathe boring operation are given in Fig. 7.24. Fig. 7.24a gives the standard display (SD) a color-coded topographical map of the raw work surface and the 3D interactive display (3DIP) of the same is illustrated in Fig. 7.24b. The distribution of individual surface height values is shown as filtered histogram in Fig. 7.24c. A curve containing all of the amplitude information of the work surface, called the bearing ratio or material ratio curve is presented in Fig. 7.24d. The bearing ratio curve shows how the bearing ratio, the ratio of the area of a surface intercepted by a plane parallel to the mean plane of the surface profile to the total evolution area, varies with level. 2D analysis and 3D rendering of the work surface data are included as Fig. 7.24e and 7.24f respectively. SEM photographs of the raw work sample taken at 100X, 500X, 1kX, 2kX and 5kX are shown in Fig. 7.24g. The similar micrographs for work samples processed under different ECH trial conditions are presented in Fig. 7.25 through 7.30.

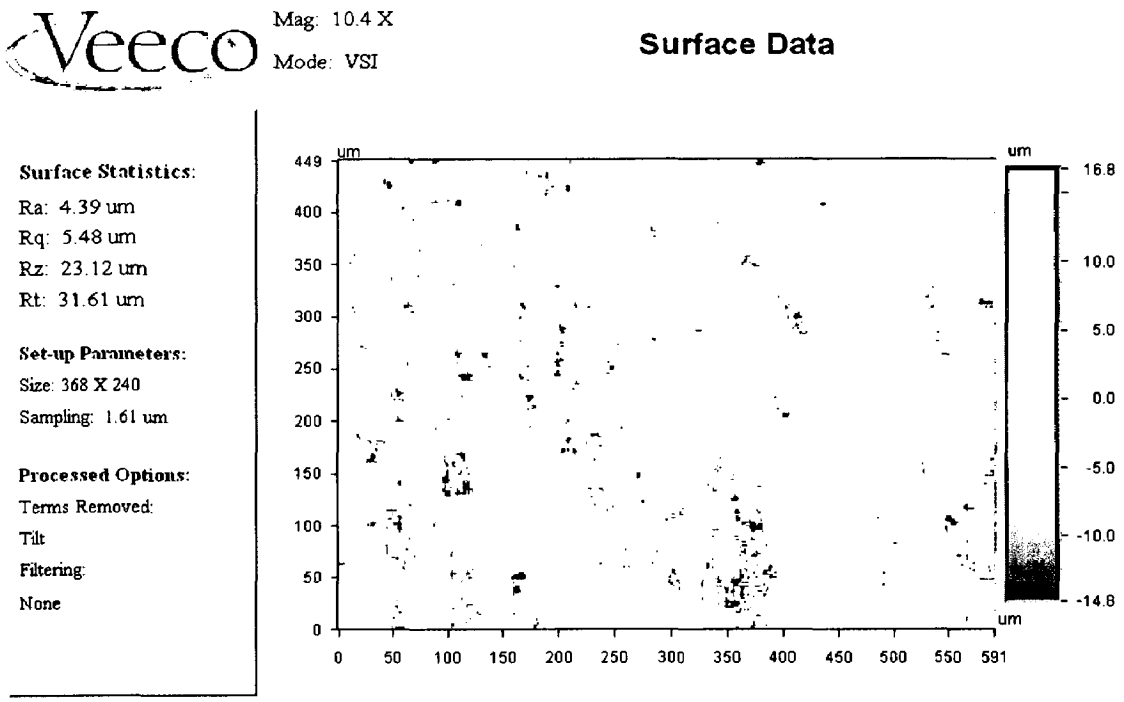

7.24a) Standard Display (Trial Condition- R: Prior to ECH)

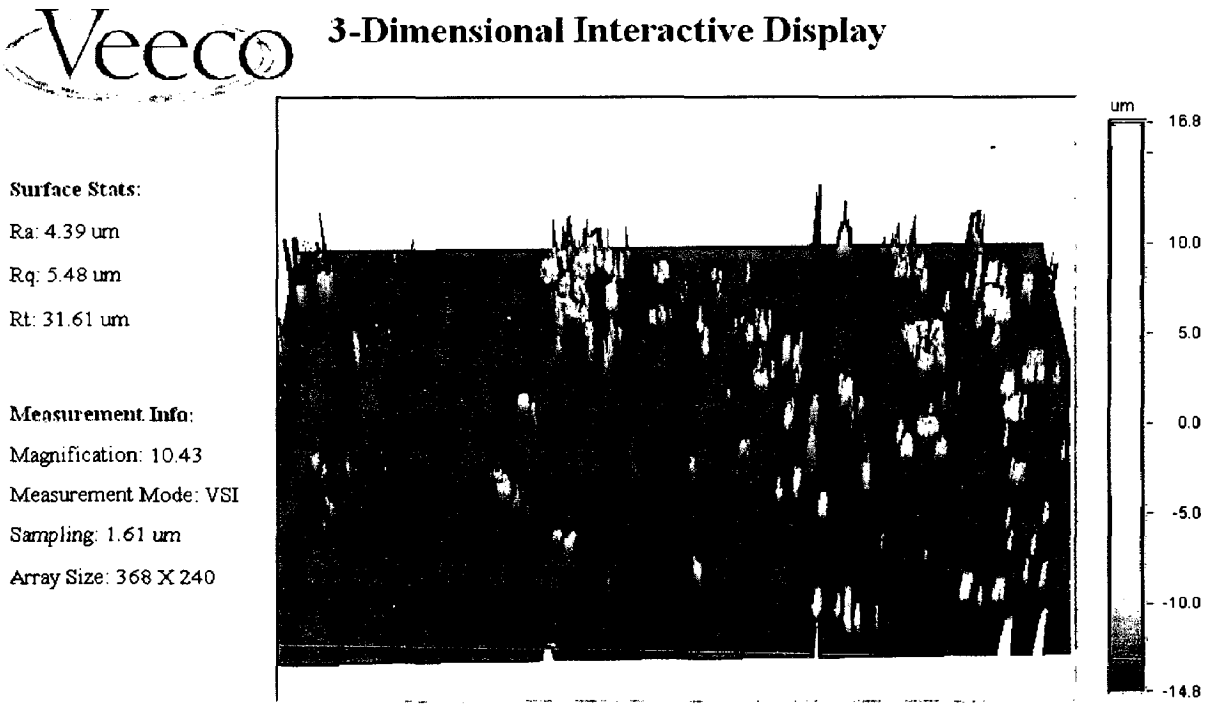

7.24b) 3D Interactive Plot (Trial Condition-R: Prior to ECH)

Veeco

Mag: 10.4 X
Mode: VSI

Surface Statistics:
Ra: 4.39 um
Rq: 5.48 um
Rz: 23.12 um
Rt: 31.61 um

Set-up Parameters:
Size: 368 X 240
Sampling: 1.61 um

Processed Options:
Terms Removed:
Tilt
Filtering:
None

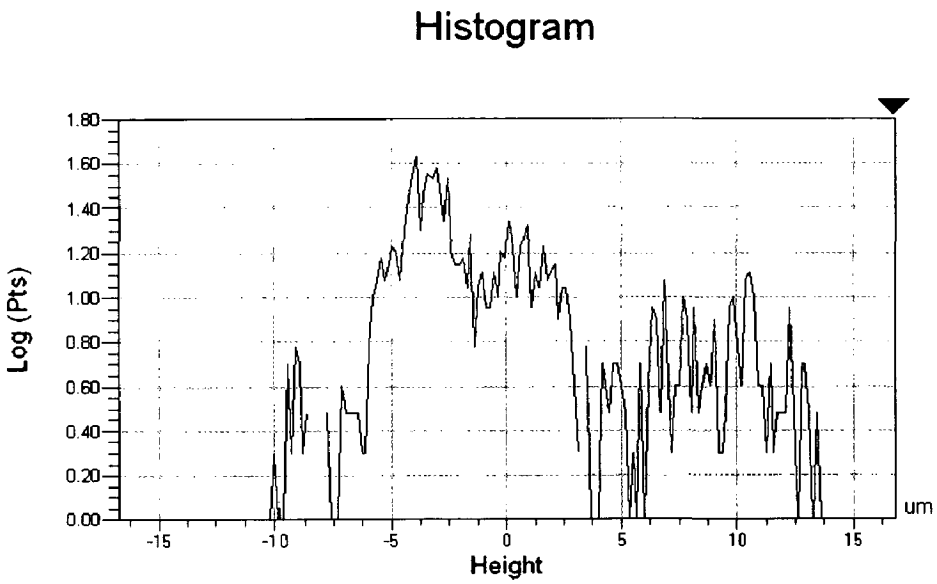

7.24c) Filtered Histogram (Trial Condition-R: Prior to ECH)

Veeco

Mag: 10.4 X
Mode: VSI

Statistics:
tp1: 0.0 %
tp2: 100.0 %
Htp: 31.61 um

Mr1: 23.83 %
Mr2: 95.28 %
RK: 8855.54 nm
Rpk: 11577.02 nm
Rvk: 5146.77 nm
V1: 1.38 um
V2: 121.58 nm

Ra: 4.39 um
Rq: 5.48 um
Rz: 23.12 um

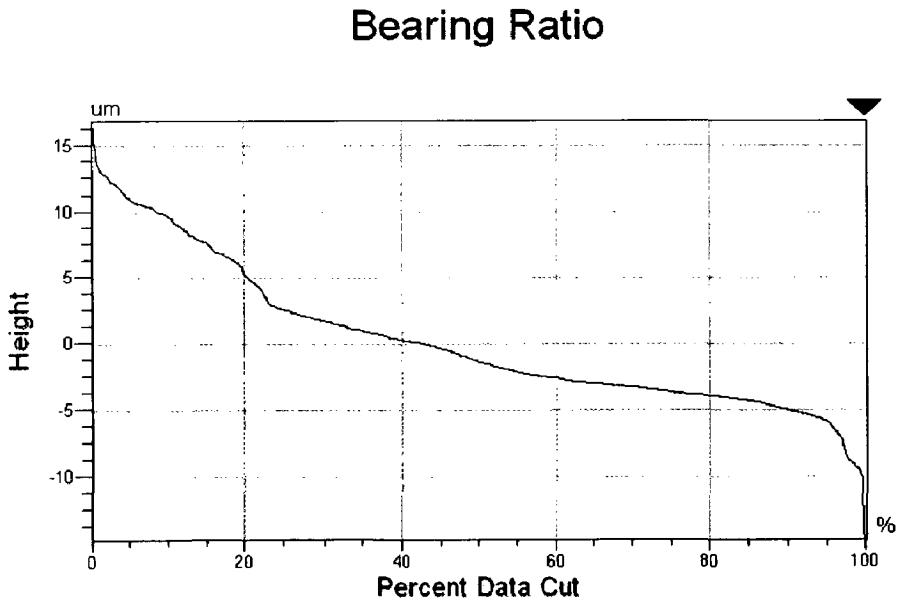

7.24d) Bearing Ratio (Trial Condition-R: Prior to ECH)

Veeco

Mag: 10.4 X

Mode: VSI

3D Plot

Surface Statistics:

Ra: 4.39 um

Rq: 5.48 um

Rz: 23.12 um

Rt: 31.61 um

Set-up Parameters:

Size: 368 X 240

Sampling: 1.61 um

Processed Options:

Terms Removed:

Tilt

Filtering:

None

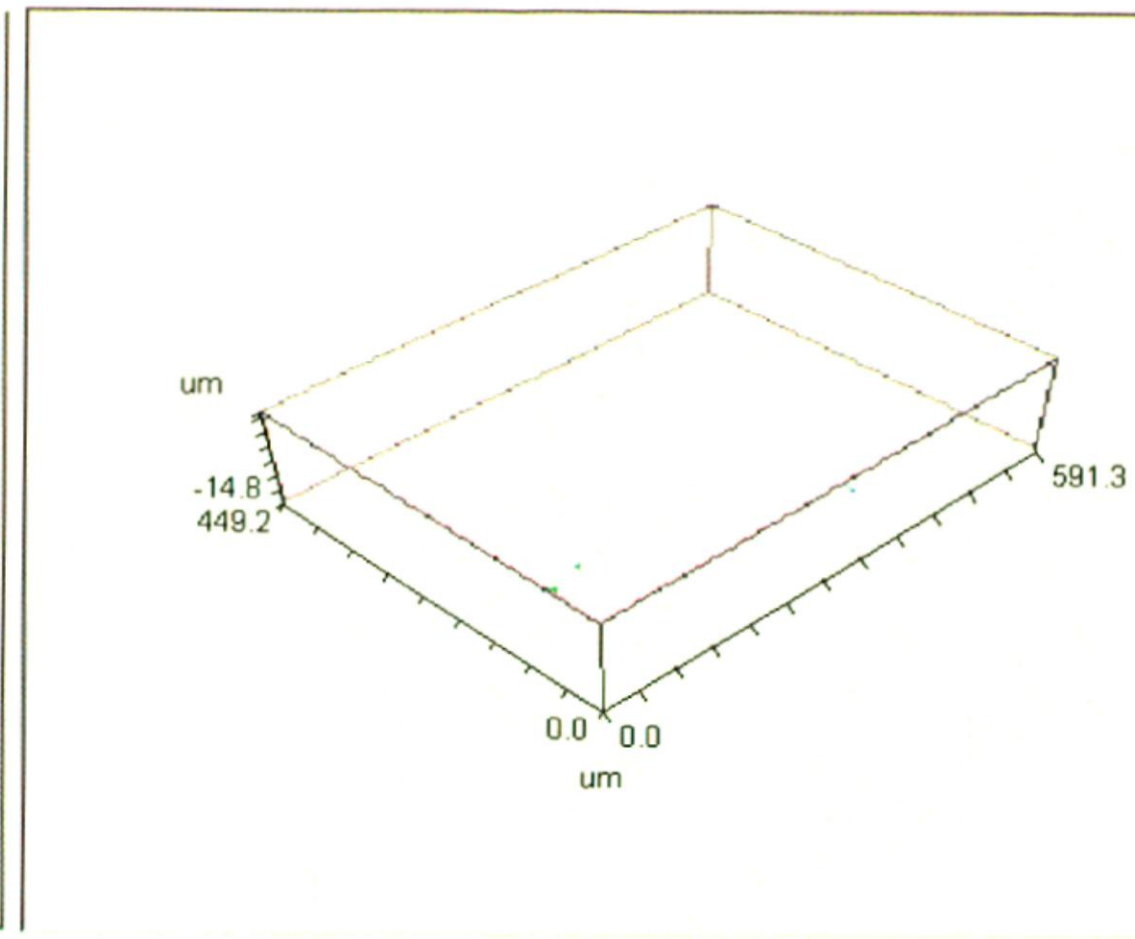

7.24e) 3D Plot (Trial Condition-R: Prior to ECH)

Veeco

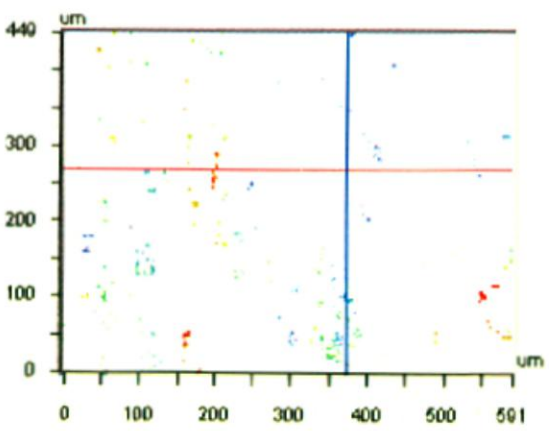

X	370.54	-	-	um
Y	268.78	-	-	um
Ht	-	-	-	um
Dist			-	um
Angle			-	°

X Profile

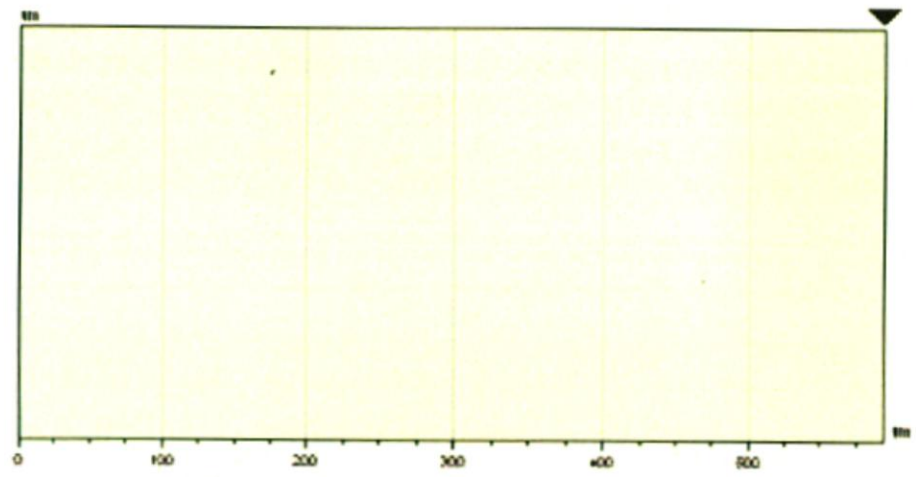

Rq	0.00	um
Ra	0.00	um
Rt	0.00	um
Rp	-1.27	um
Rv	-1.27	um

Angle	0.00	mrad
Curve	0.00	nm
Terms	None	
Avg Ht	-1.27	um
Area	-749.55	um2

Y Profile

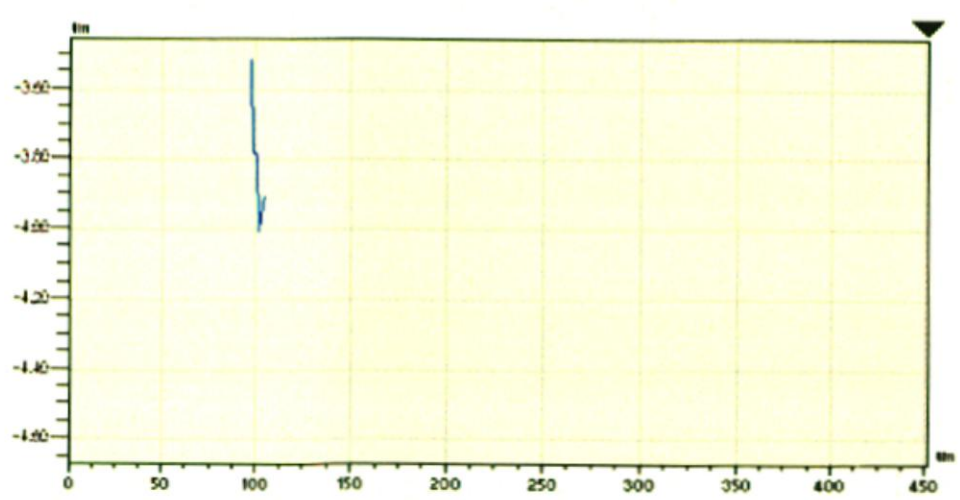

Rq	0.37	um
Ra	0.31	um
Rt	1.11	um
Rp	-3.51	um
Rv	-4.62	um

Angle	0.00	mrad
Curve	0.00	nm
Terms	None	
Avg Ht	-4.01	um
Area	-1801.35	um2

7.24f) 2D Plot (Trial Condition-R: Prior to ECH)

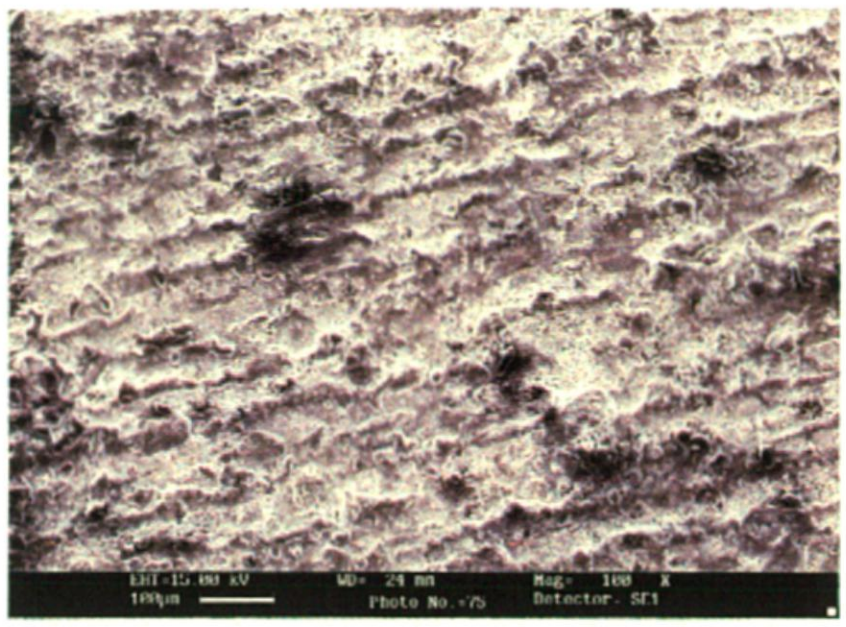

i) 100X

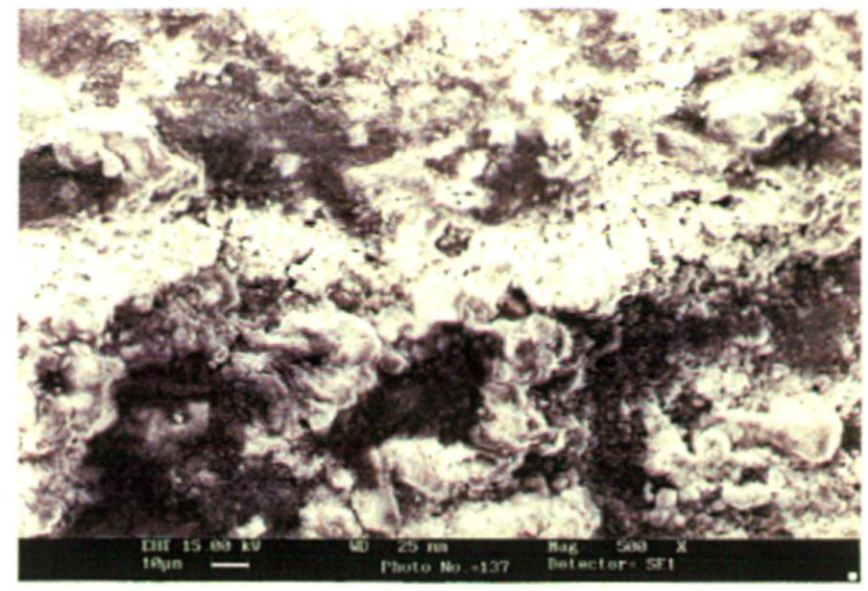

ii) 500X

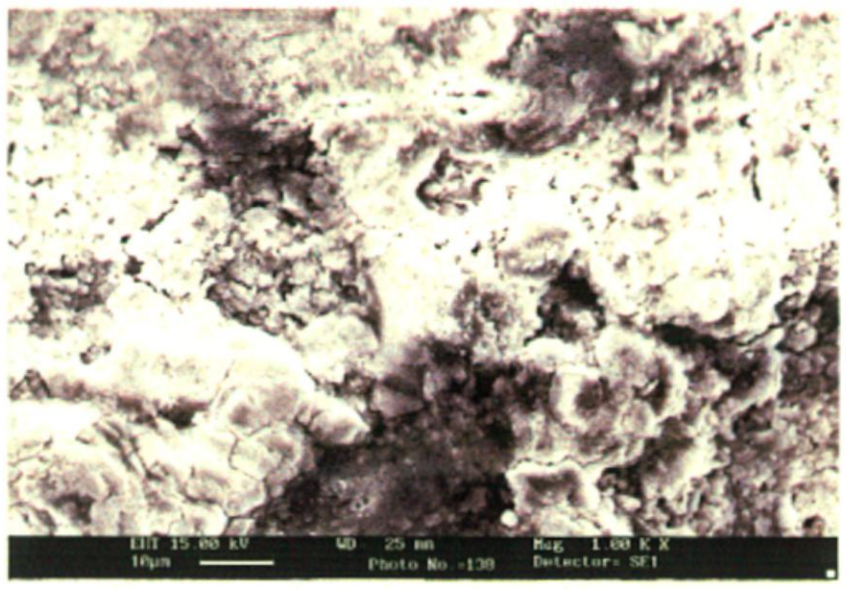

iii) 1 kX,

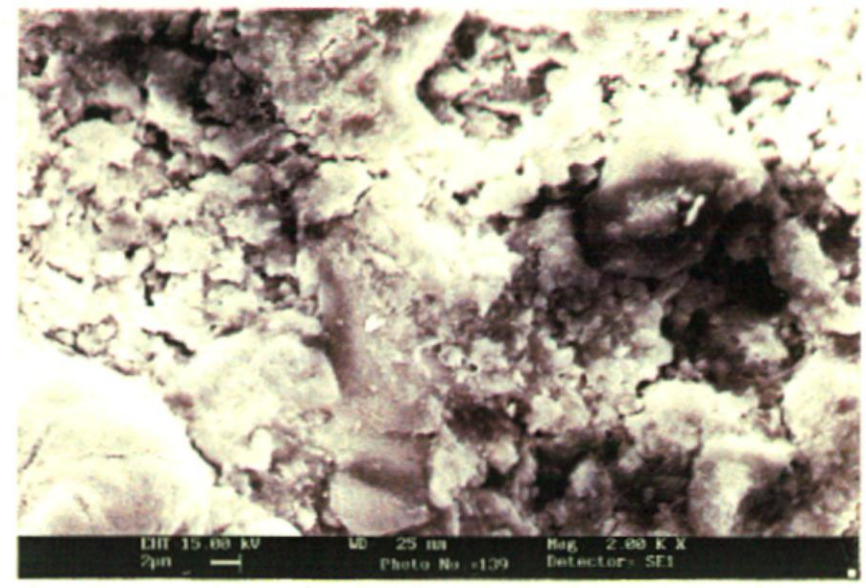

iv) 2 kX

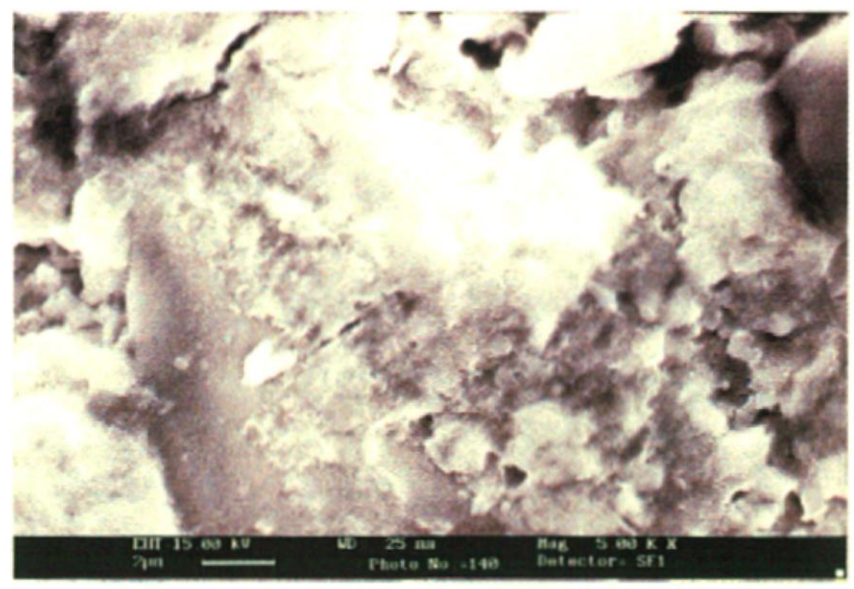

v) 5 kX

7.24g) SEM Photographs (Trial Condition-R: Prior to ECH) (Scale 0.25)

Fig. 7.24 Characteristics of the work-surface prior to ECH
(Raw workpiece obtained from precision lathe boring operation)

Veeco

Mag: 10.4 X

Mode: VSI

Surface Data

Surface Statistics:

Ra: 458.45 nm

Rq: 578.88 nm

Rz: 3.99 um

Rt: 5.85 um

Set-up Parameters:

Size: 368 X 240

Sampling: 1.61 um

Processed Options:

Terms Removed:

Tilt

Filtering:

None

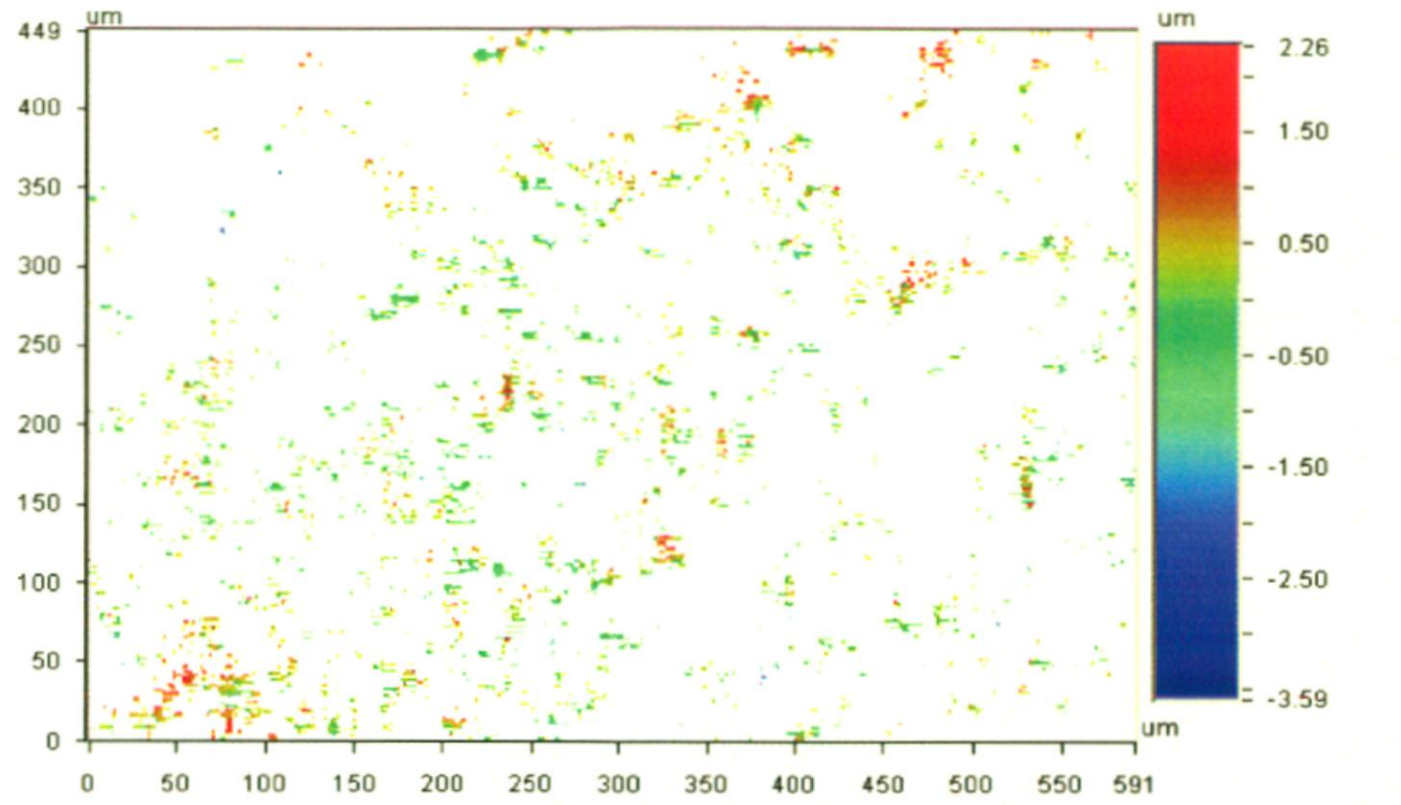

7.25a) Standard Display (ECH Trial Condition-T26: $C_3EC_3SR_2F_3T_2SOP_2G_1$)

Veeco

3-Dimensional Interactive Display

Surface Stats:

Ra: 458.45 nm

Rq: 578.88 nm

Rt: 5.85 um

Measurement Info:

Magnification: 10.43

Measurement Mode: VSI

Sampling: 1.61 um

Array Size: 368 X 240

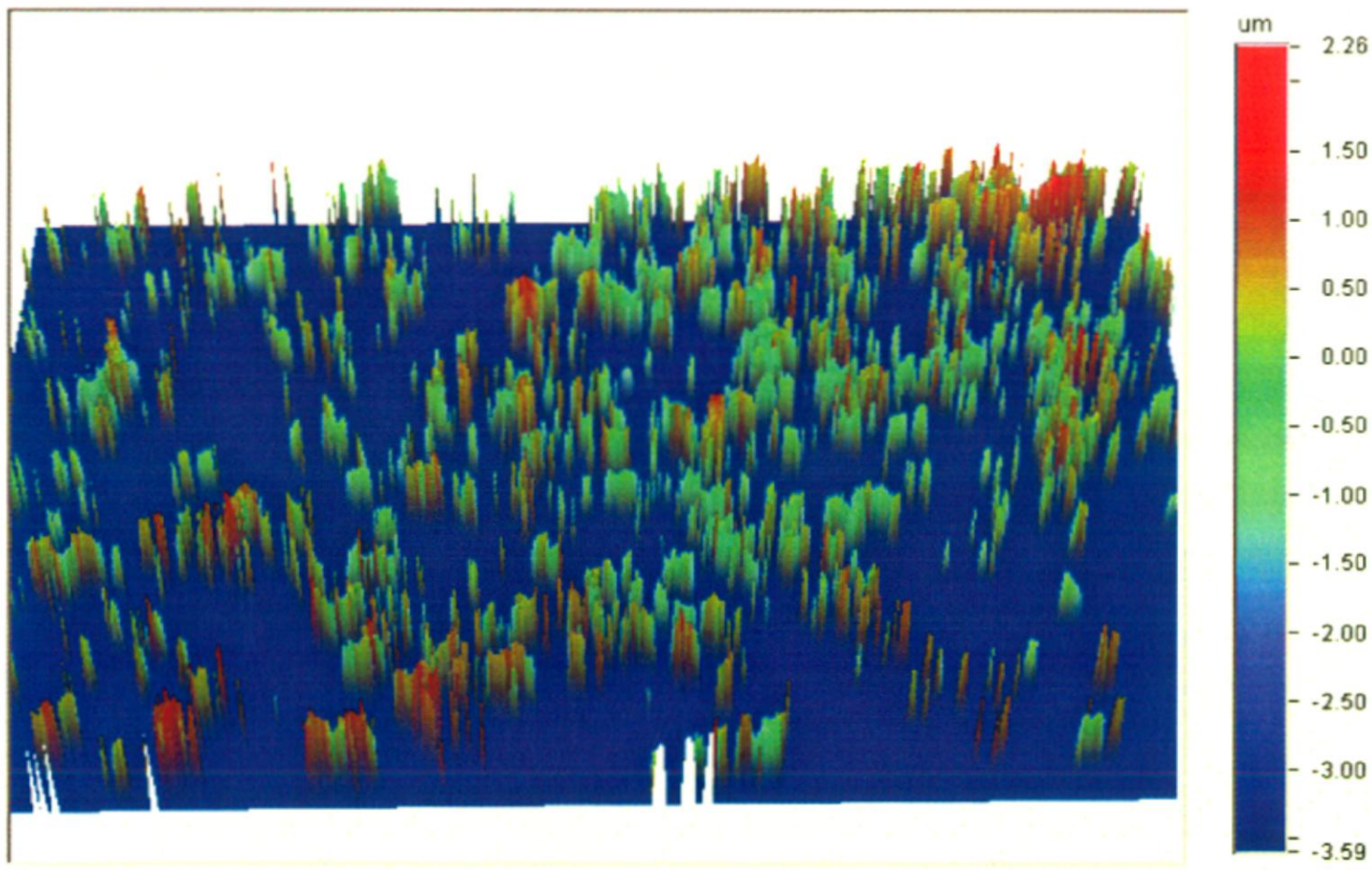

7.25b) 3D Interactive Plot (ECH Trial Condition-T26: $C_3EC_3SR_2F_3T_2SOP_2G_1$)

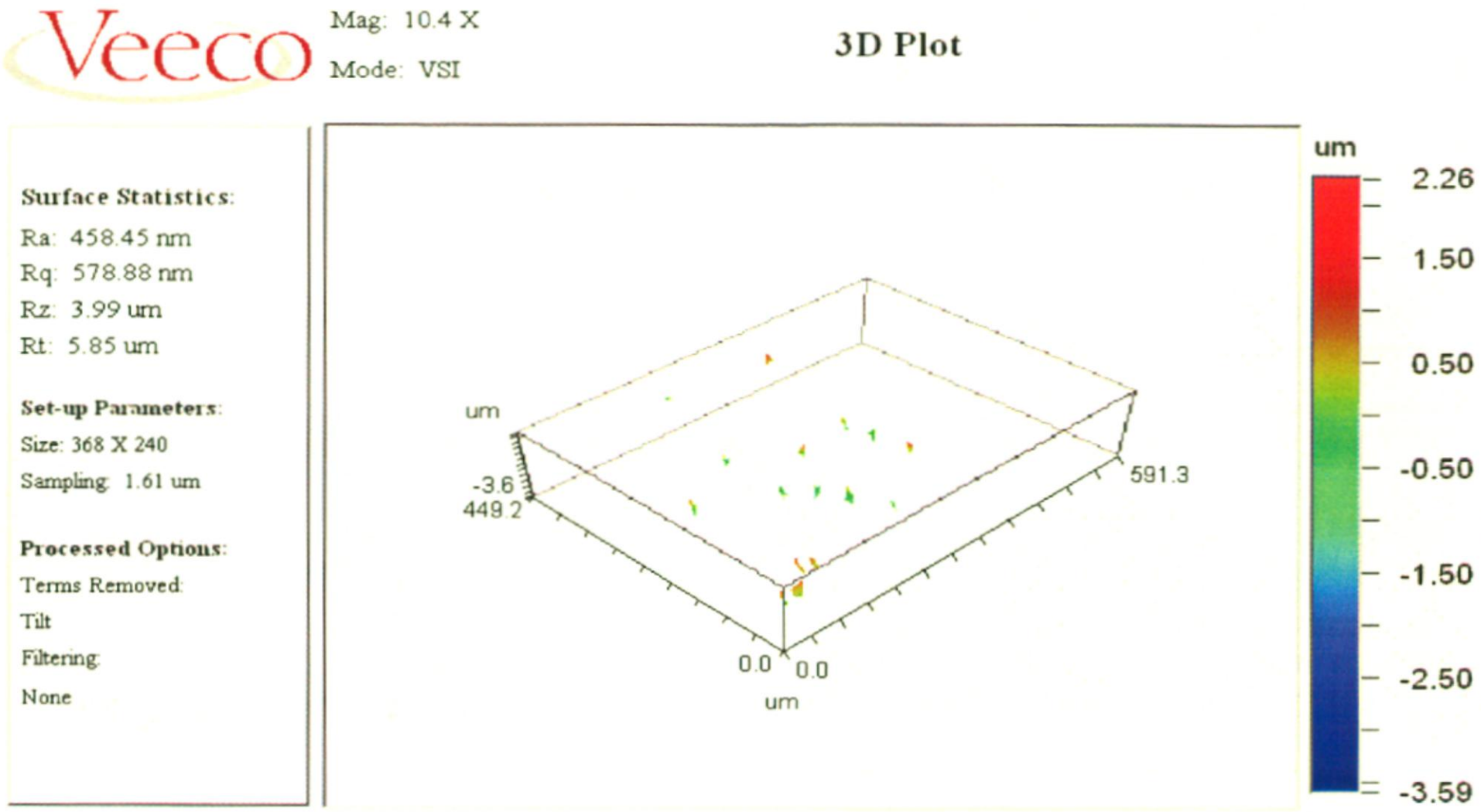

7.25e) 3D Plot ((ECH Trial Condition-T26: $C_3EC_3SR_2F_3T_2SOP_2G_1$)

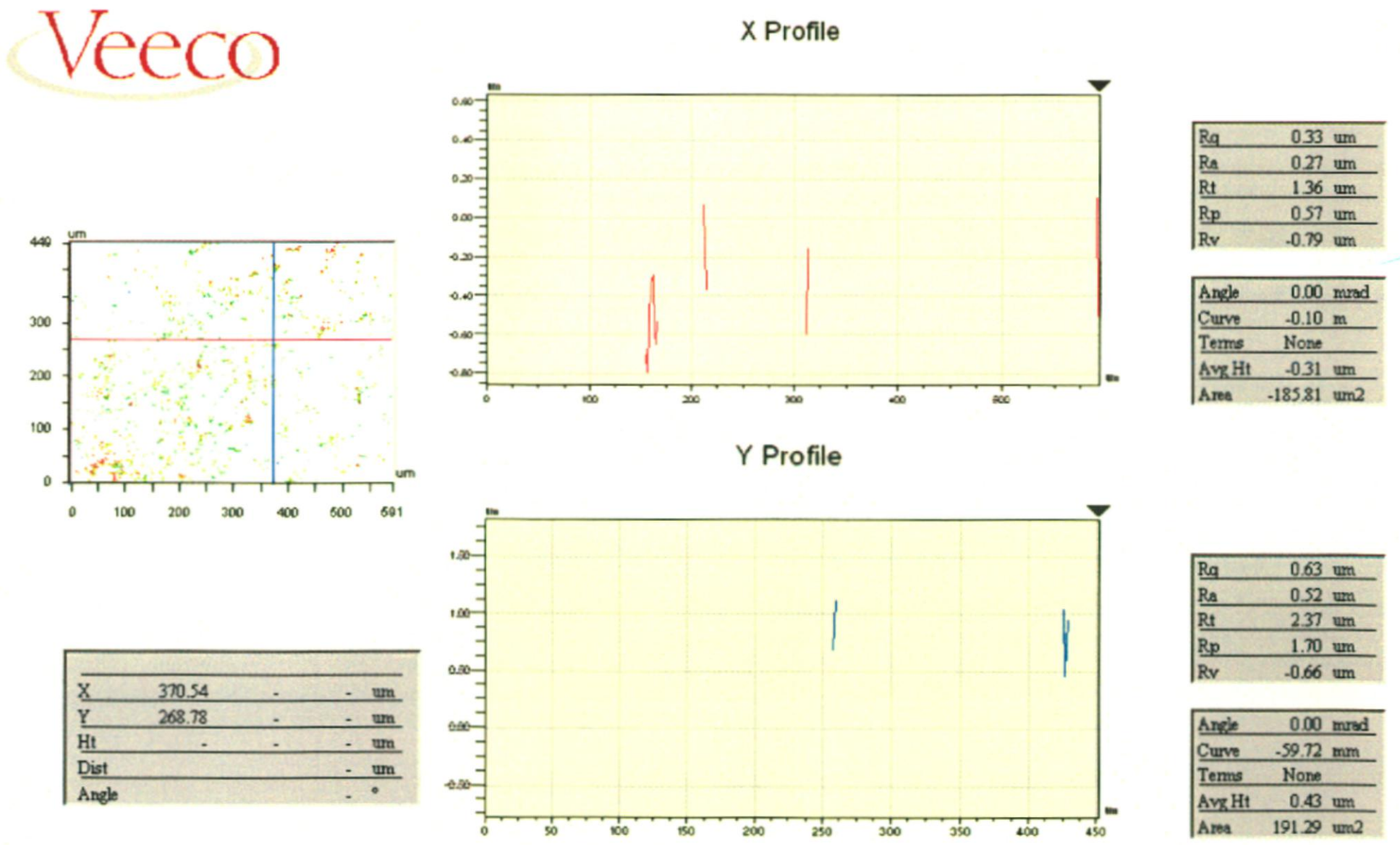

7.25f) 2D Plot (ECH Trial Condition-T26: $C_3EC_3SR_2F_3T_2SOP_2G_1$)

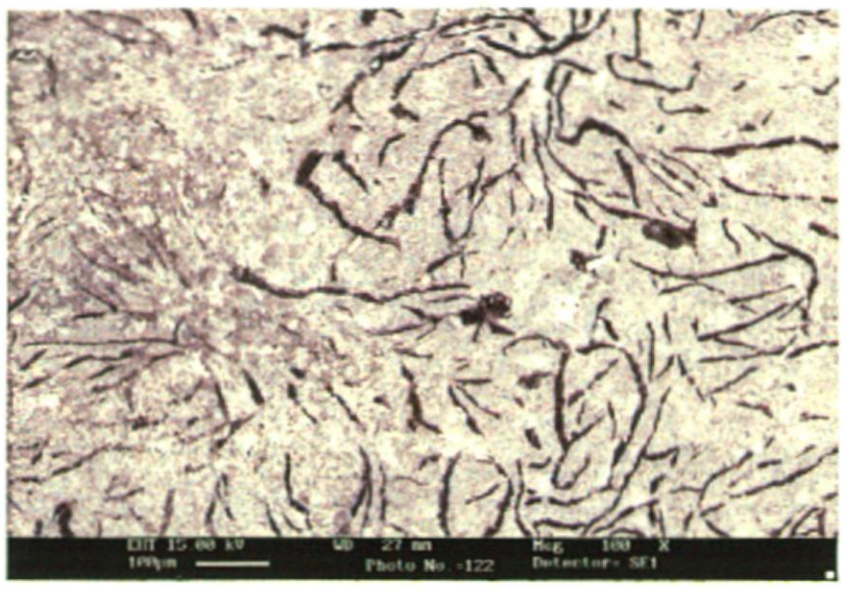

i) 100X

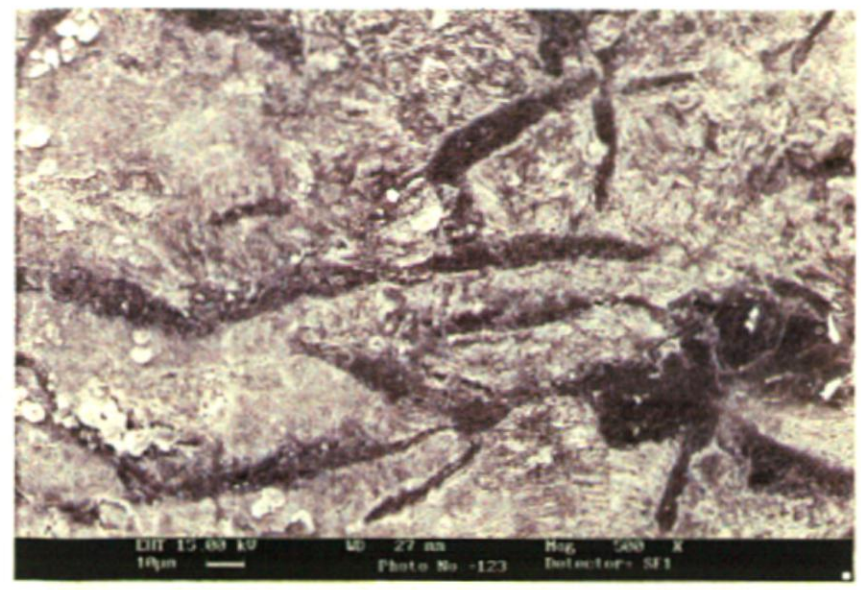

ii) 500X

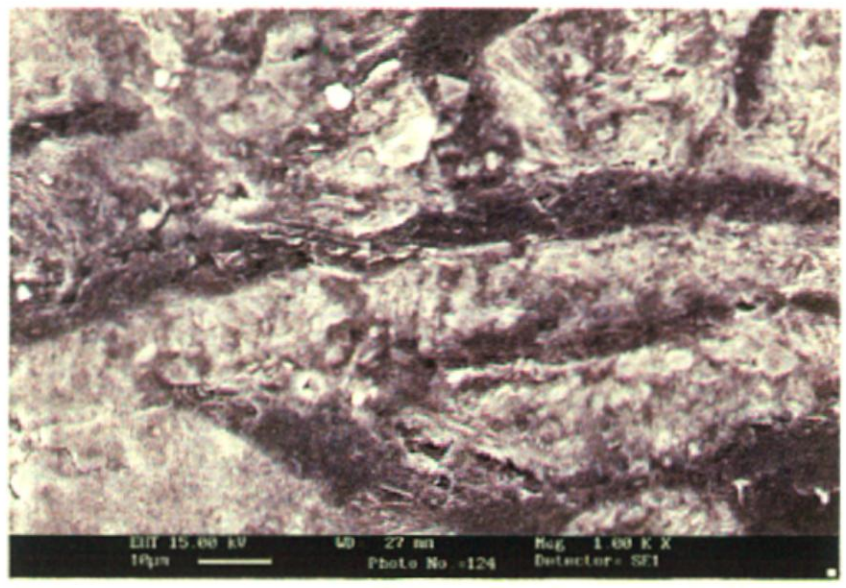

iii) 1 kX

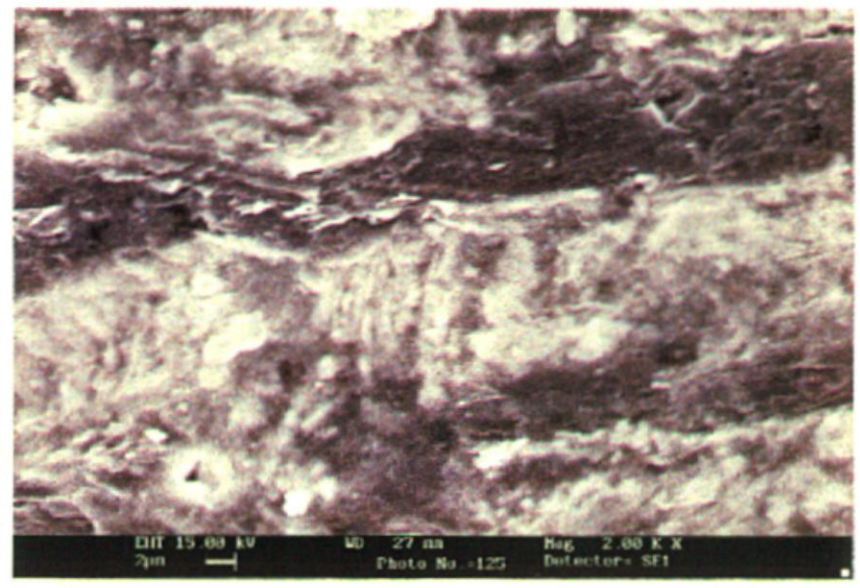

iv) 2 kX

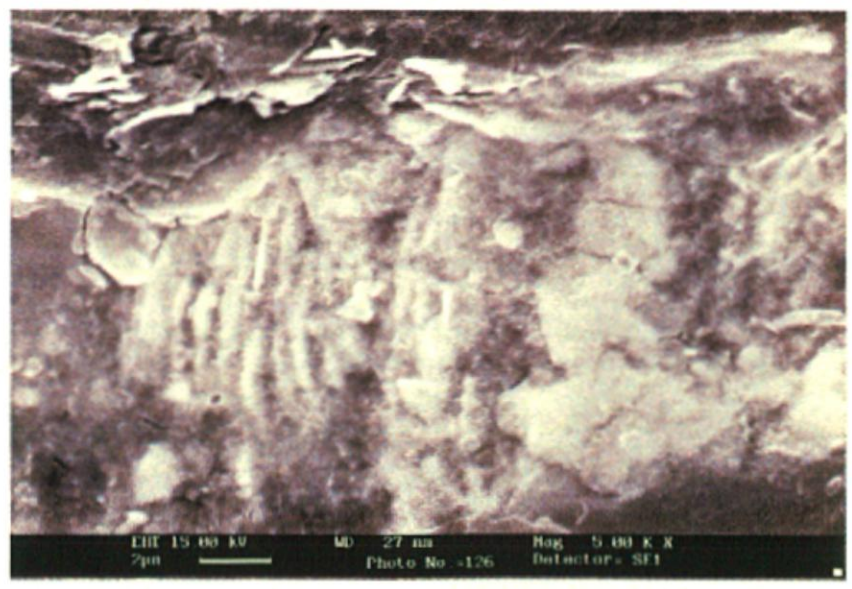

v) 5 kX

7.25g) SEM Photographs (ECH Trial Condition-T26: $C_3EC_3SR_2F_3T_2SOP_2G_1$)

(Scale 0.25)

Fig. 7.25 Characteristics of ECHed work-surface

(ECH Trial Condition: $C_3EC_3SR_2F_3T_2SOP_2G_1$)

The raw worksurface obtained from lathe boring operation is having a highly non-uniform and scattered surface profile while a typically ECH processed worksurface is characterized by concentrated uniform ideal near zero surface roughness pattern as clear from the respective filtered histogram plots. Besides the improvement in average surface roughness value, the uniformity as well as the spread of the roughness profile has much improved as a result of electro-chemical honing. As seen in the bearing ratio curves, almost 30% of the surface roughness data of the raw work sample is lying beyond ± 5um while the 90% surface roughness data in ECHed surface is contained within ± 1um. The most common use of engineering surfaces is to provide a bearing surface to a moving mating component resulting in wear. The ECHed surface can provide a better bearing area and consequently much better wear properties to the processed components. The bearing ratio parameter, t_p is commonly used to simulate the effect of wear on the surface and control the bearing surfaces (ASM Handbook, 1994).

Bearing ratio, t_p is a control parameter for surfaces requiring lubrication. It can be seen that ECH produces plateau honed surfaces, as due to process action the surface profile peaks are removed and the material line (top line of remaining profile) descends, the bearing surface area increases and large valleys are created to retain lubrication for low friction. Parameter Rk, which is derived using the bearing ratio curve, is commonly used to evaluate the plateau honed surfaces (ASM Handbook, 1994). Rk (core roughness depth) is that part of the surface, that after initial running in period, will carry the load and influence the resulting life and performance of the component. The reduced peak height (Rpk) is the top portion of the surface that will wear away in the running-in period and an associated percent length of the top portion of the surface profile (Mr1) will be removed. Similarly, reduced valley depth (Rvk) is the lowest part of the surface that functions to retain lubricant during its working life. A parameter associated to Rvk is Mr2 (percent length of the bottom part of the profile).

ECHed work surface has a much improved R_a, R_t and Rk values as compared to a raw worksurface. Thus, the ECH processed surfaces are characterized with a low frictional wear, improved fatigue endurance properties and better load bearing capability. A comparison of the Rpk and Mr1 parameters indicates that a large portion of the raw worksurface profile is highly susceptible to a fast wear. Almost 12μm of the peak height (25% profile length) of the raw worksurface is likely to wear away during initial running-in period as compared to much lower values (Rpk = 599 nm and Mr1=10%) for the ECHed surface. At the same time, an ECHed surface has better lubricant retention capability as revealed from Mr2 value. The profile portion susceptible to rapid wear has further consequences of aggravated wear rate as these micro-particles get entrapped in the valleys and reduce effective lubrication. Thus, a cumulative effect with an exponential increase rate of wear with time is produced which may result into destructive consequences for critical components. As can be seen from the 2D plots that the preferred y pattern in raw worksurface is crossed during electro-chemical honing process and the surface processed by ECH is characterized with a cross-hatch pattern providing an enhanced lubricant retaining capabilities. Therefore, the ECHed components are expected to have much better tribological properties during service. An analysis of the SD and 3DIP indicates that the much wider spread of surface roughness of raw worksurface (in the range of ± 20um) has reduced to a narrow spread of typical ±2um after electro-chemical honing. An effective removal of the surface profile peaks by electro-chemical honing can also be seen from the 3D plots of the work surfaces.

A representative SEM micrograph of severely deformed cold worked surface of the raw work sample (after the precision lathe boring) is shown in Fig. 7.24g. The surface contains a lot of torn material loosely attached to the surface. Several surface defects such as laps, pits can also be clearly seen. The effective planishing effect of electro-chemical honing

process is revealed by the scanning electron micrographs of the ECH processed work surface in Fig. 7.25g. The process is capable of removing all the traces of loosely held material as well as the surface defects and can correct the severely cold worked surface profile. In addition, no indication of any significant adverse impact of the process on the worksurface is evident in SEM photographs. The ECH finished components, therefore, are expected to have better service performance due to much improved tribological properties.

Another noticeable influential impact of the stick-out pressure and stick grit size on surface micro profile characteristics is revealed in Fig. 7.26 to 7.28. The work samples have been processed with otherwise constant trial condition except the increasing levels of SR, F, T, SOP and G. If the effect of electrolyte flow rate and electrolyte inlet temperature is ignored the influential parameters are SR, SOP and G. Fig. 7.26 gives typical surface profile and scanning electron micrograph of the worksurface processed with level 1 of rotary to reciprocating speed ratio, stick-out pressure and stick grit size ($SR_1SOP_1G_1$). The surface micrographs for the worksurfaces processed with $SR_2SOP_2G_2$ and $SR_3SOP_3G_3$ are shown in Fig. 7.27 and 7.28 respectively. The most influential impact of proper grit size selection is clearly seen in the bearing ratio curves. The final Rk and Rpk as well as surface roughness uniformity deteriorated with the use of very fine grit-size sticks (G3). The trials performed with G_1 and G_2 produced almost similar results with regard to surface microprofile. The results are poor for the trial performed with G_3, even this trial was performed at the highest levels of speed ratio and stick-out pressure. The uniformity decreased from almost 80% within ± 1μm for T-1 and T-2 to almost 50% surface roughness data lying within ± 1μm for T-3 (trial with G_3). Similar results are revealed in filtered histogram by the deceasing log points. The standard displays and 3DIP show that T-1 and T-2 results are quite similar while in T-3 considerable spots are in the range of ± 5μm. The influence of stick-out pressure and

stick grit size on the surface character is seen in SEM photographs. The SOP_2G_2 combination in Fig. 7.27e provided a much better surface condition.

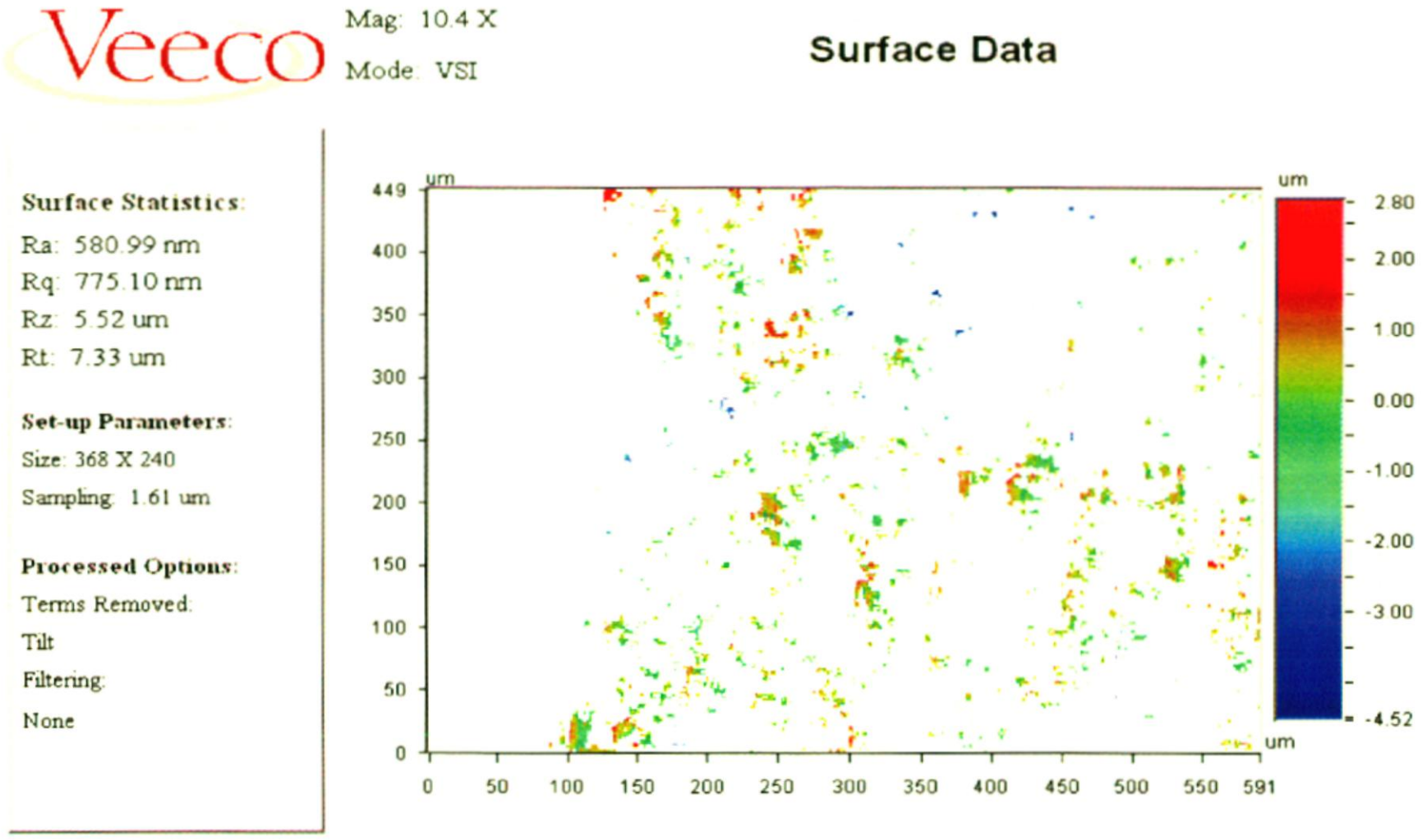

7.26a) Standard Display (ECH Trial Condition-T1: $C_1EC_1SR_1F_1T_1SOP_1G_1$)

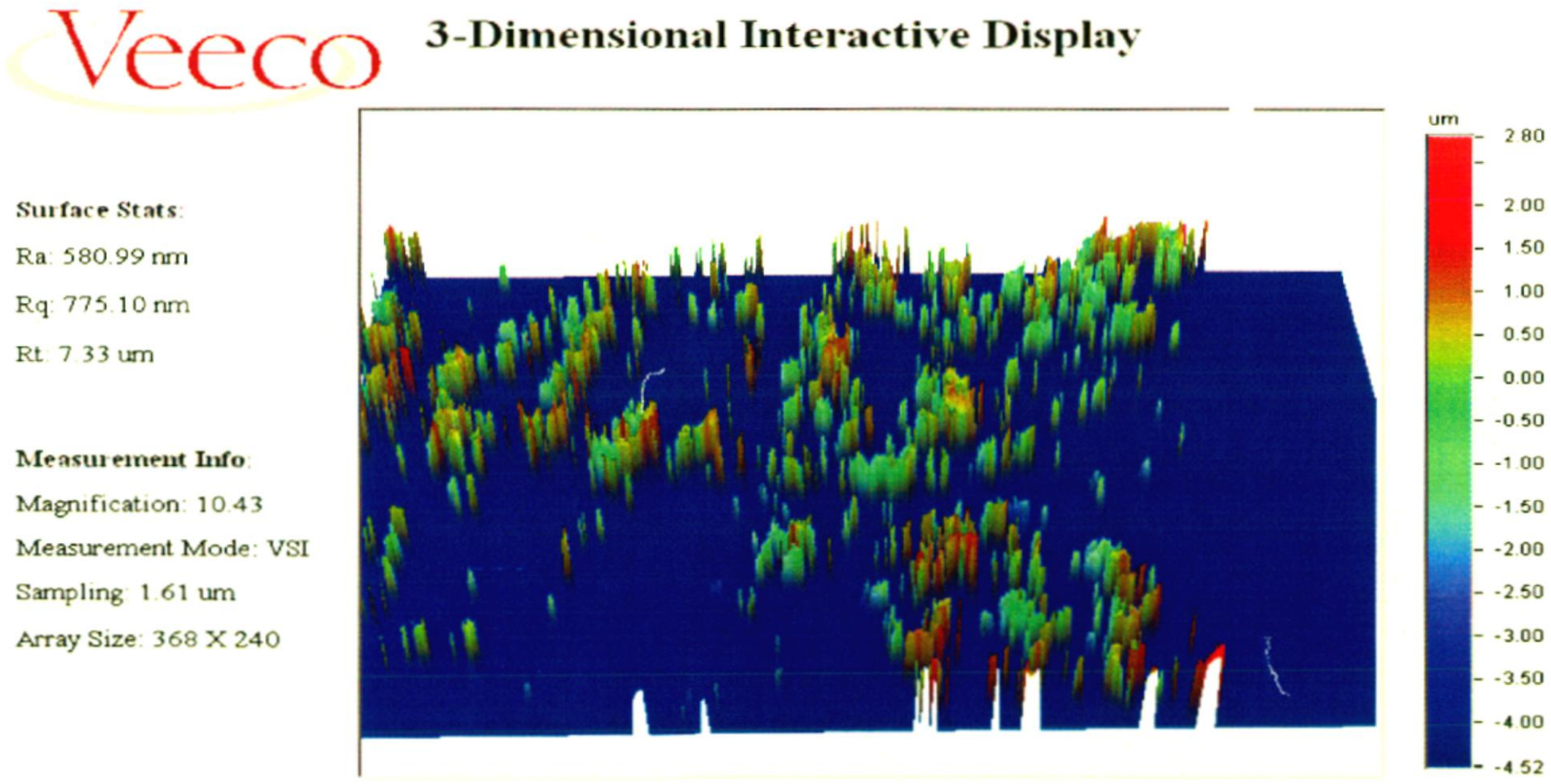

7.26b) 3D Interactive Plot (ECH Trial Condition-T1: $C_1EC_1SR_1F_1T_1SOP_1G_1$)

Veeco

Mag: 10.4 X

Mode: VSI

Surface Data

Surface Statistics:

Ra: 683.60 nm

Rq: 1.03 um

Rz: 6.26 um

Rt: 10.70 um

Set-up Parameters:

Size: 368 X 240

Sampling: 1.61 um

Processed Options:

Terms Removed:

Tilt

Filtering:

None

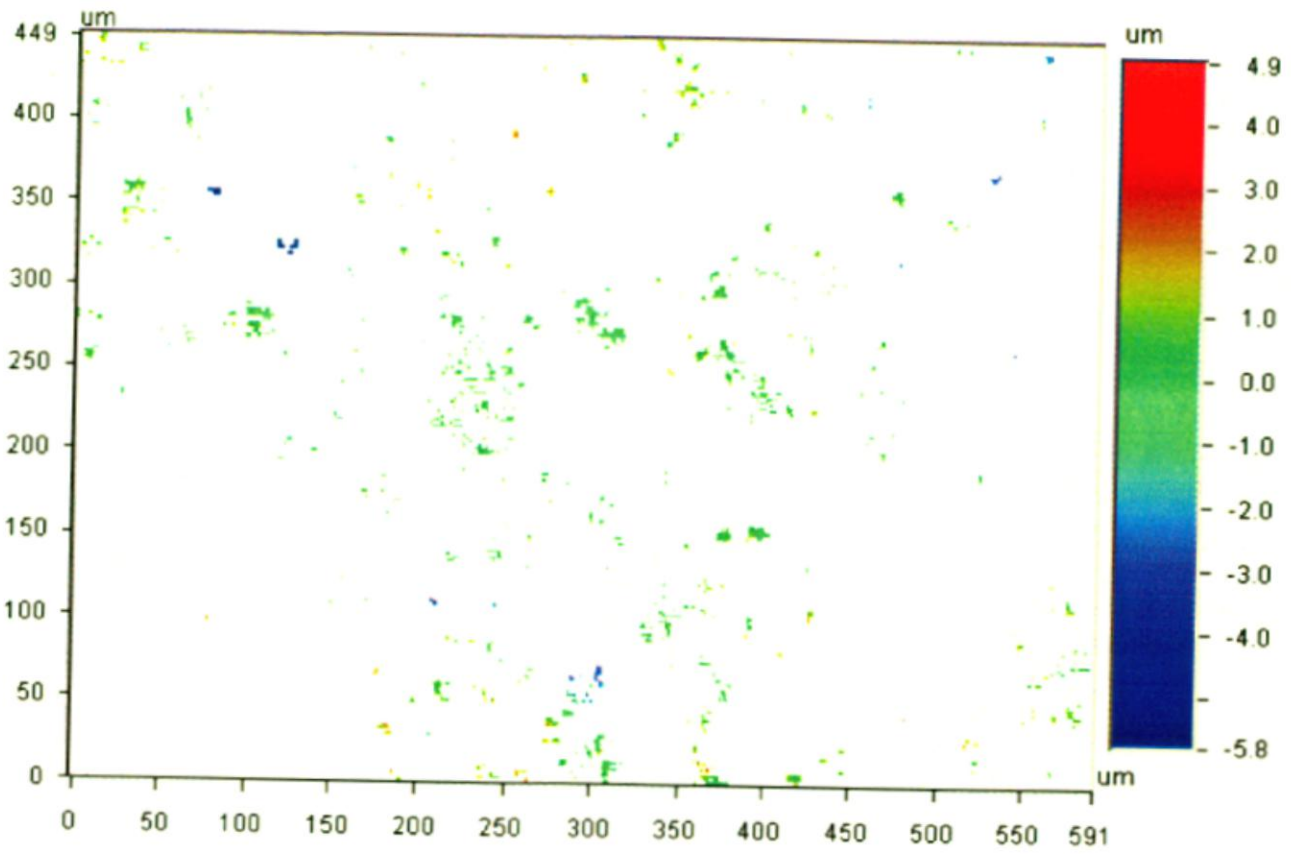

7.27a) Standard Display (ECH Trial Condition-T2: $C_1EC_1SR_2F_2T_2SOP_2G_2$)

Veeco

3-Dimensional Interactive Display

Surface Stats:

Ra: 683.60 nm

Rq: 1.03 um

Rt: 10.70 um

Measurement Info:

Magnification: 10.43

Measurement Mode: VSI

Sampling: 1.61 um

Array Size: 368 X 240

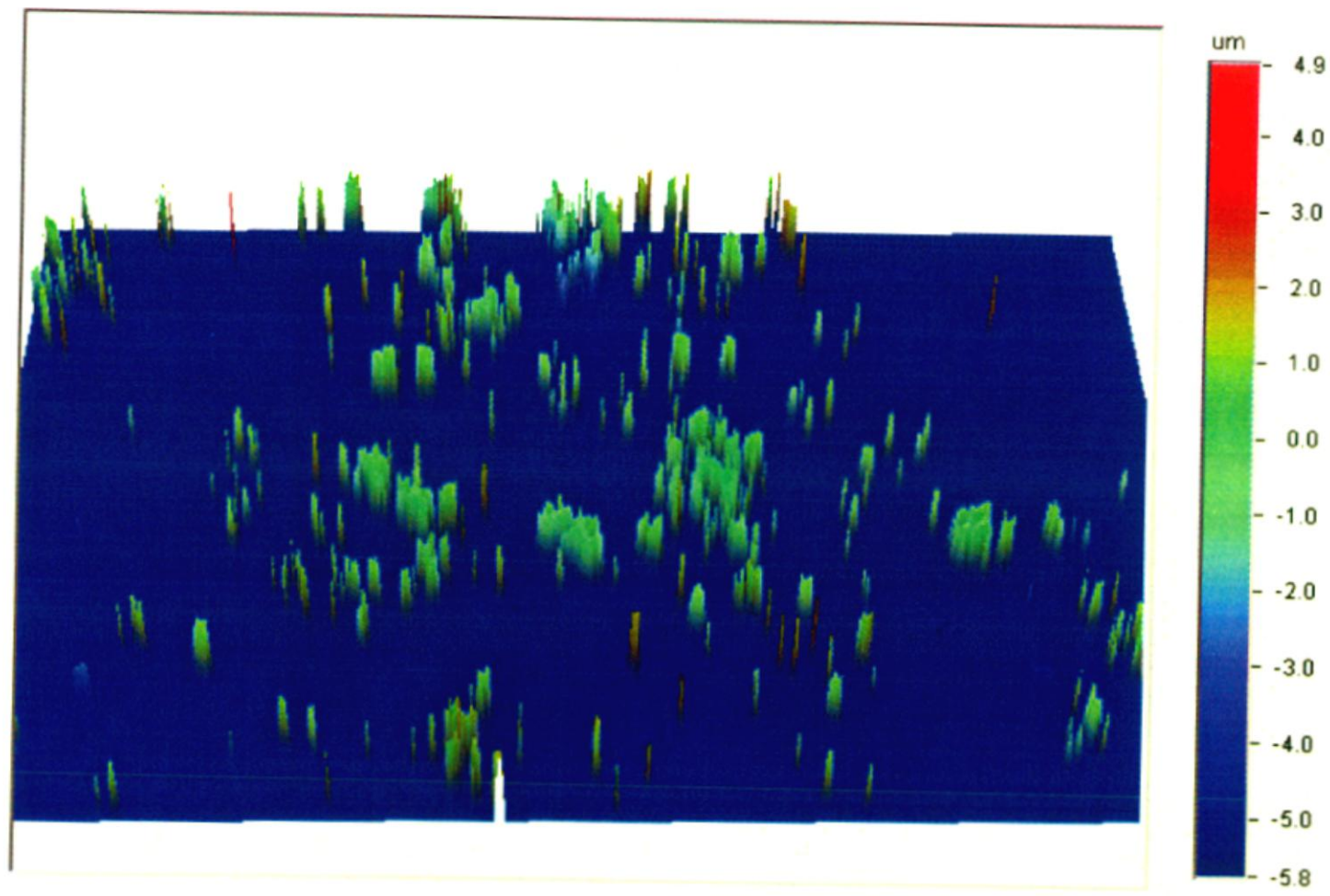

7.27b) 3D Interactive Plot (ECH Trial Condition-T2: $C_1EC_1SR_2F_2T_2SOP_2G_2$)

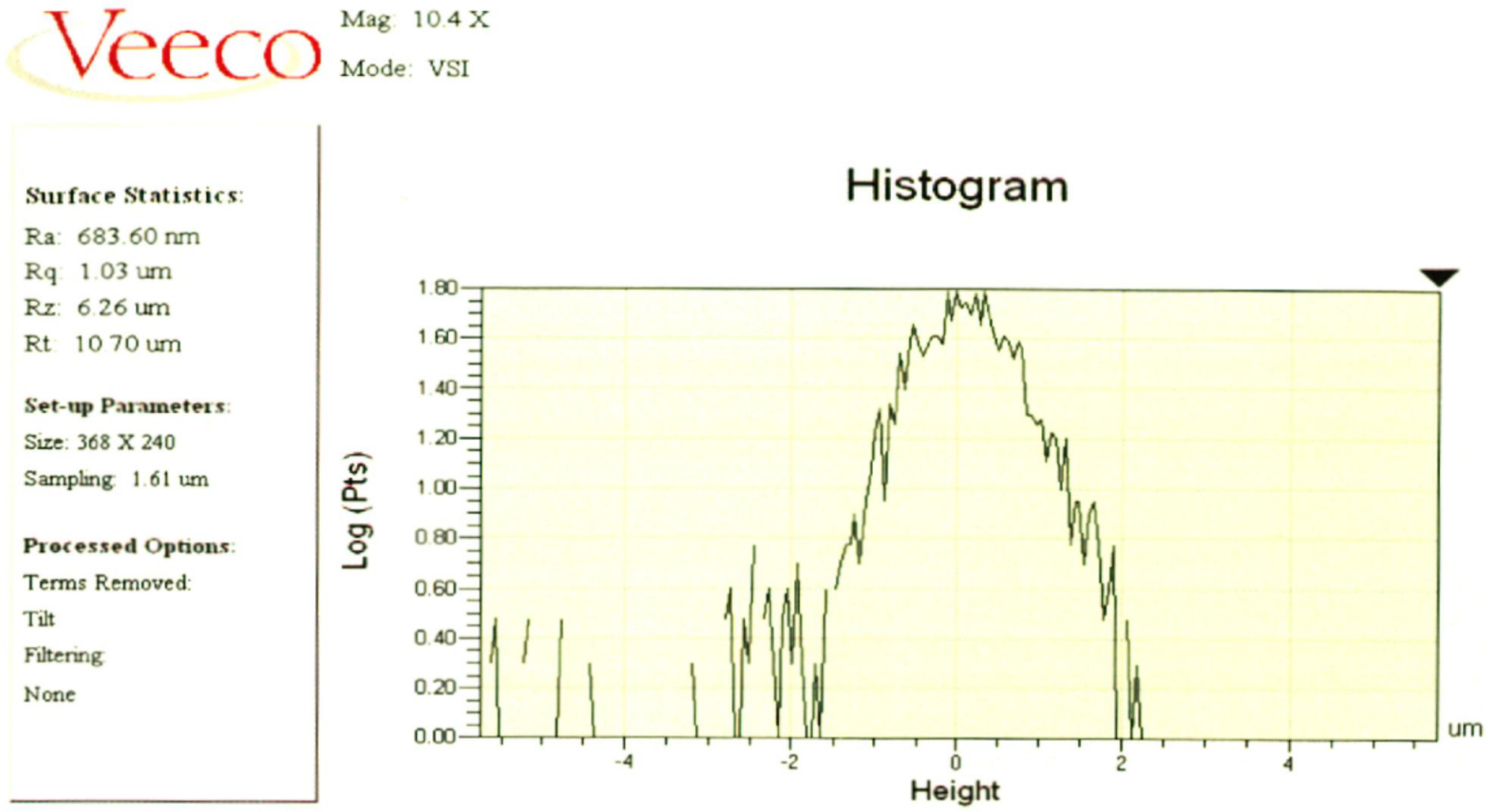

7.27c) Filtered Histogram (ECH Trial Condition-T2: $C_1EC_1SR_2F_2T_2SOP_2G_2$)

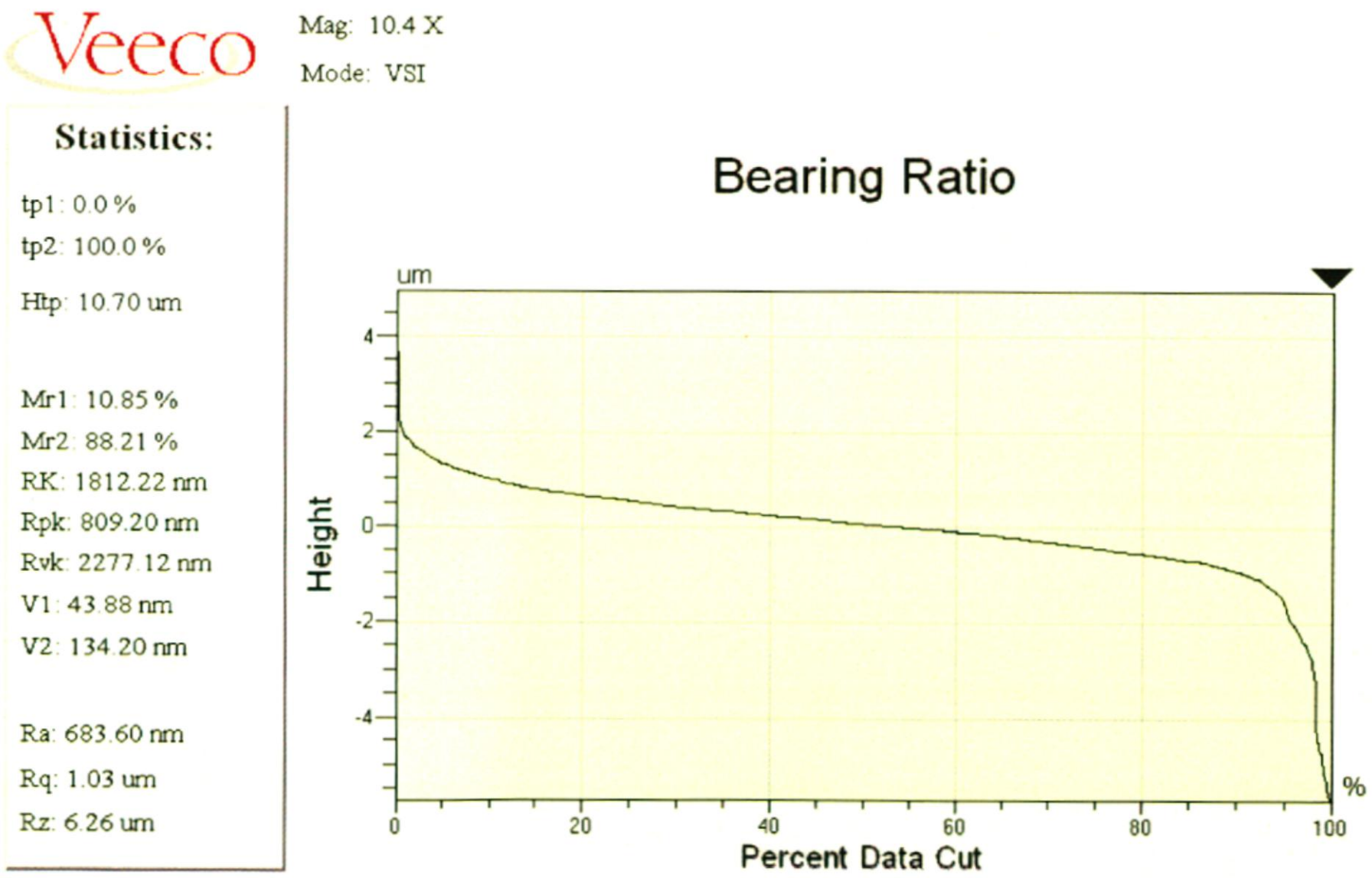

7.27d) Bearing Ratio (ECH Trial Condition-T2: $C_1EC_1SR_2F_2T_2SOP_2G_2$)

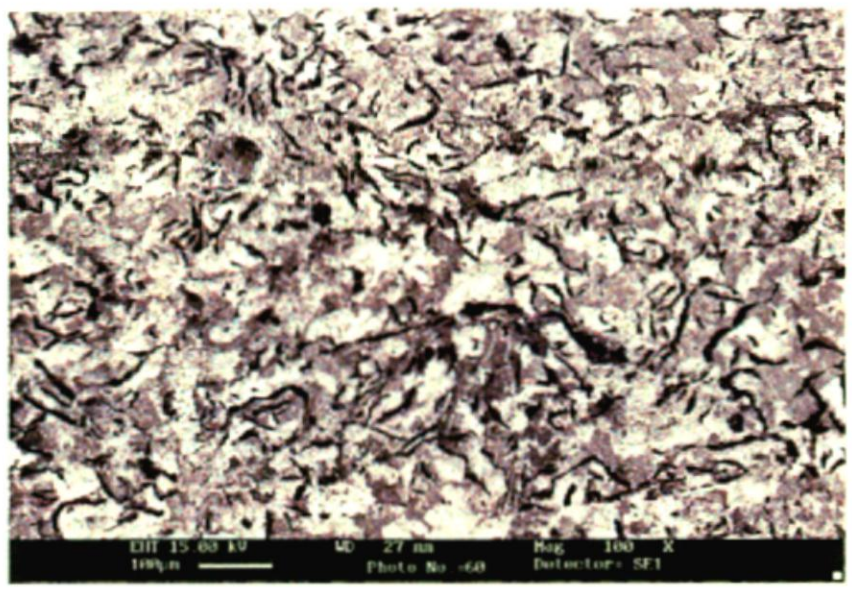

i) 100X

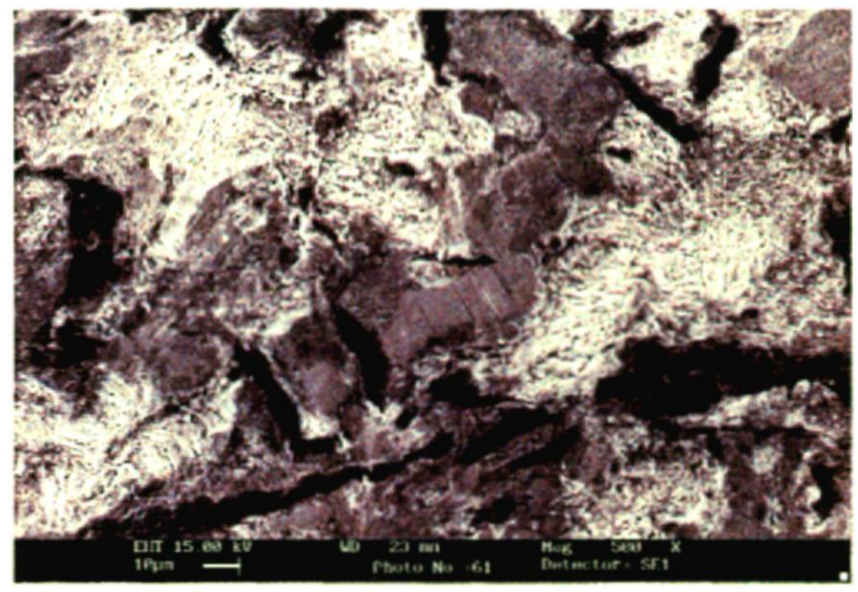

ii) 500X

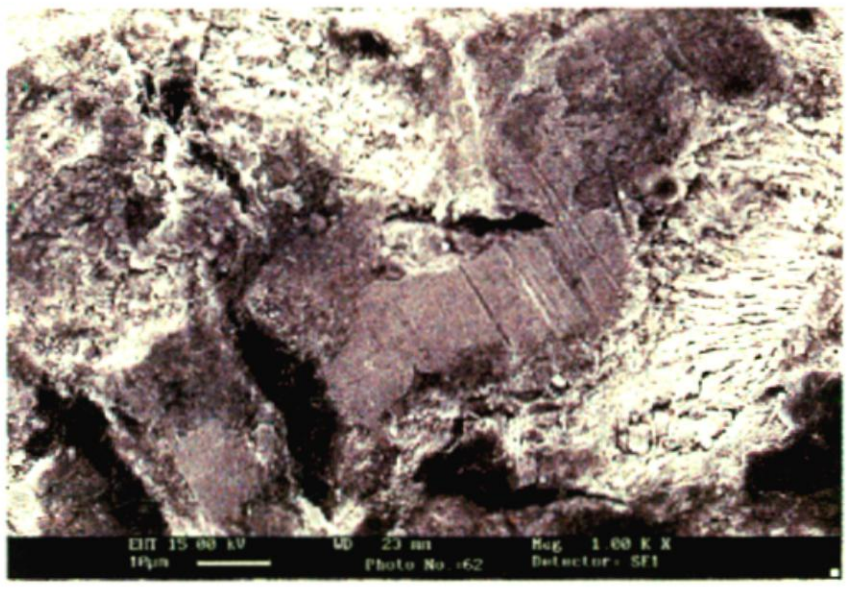

iii) 1 kX

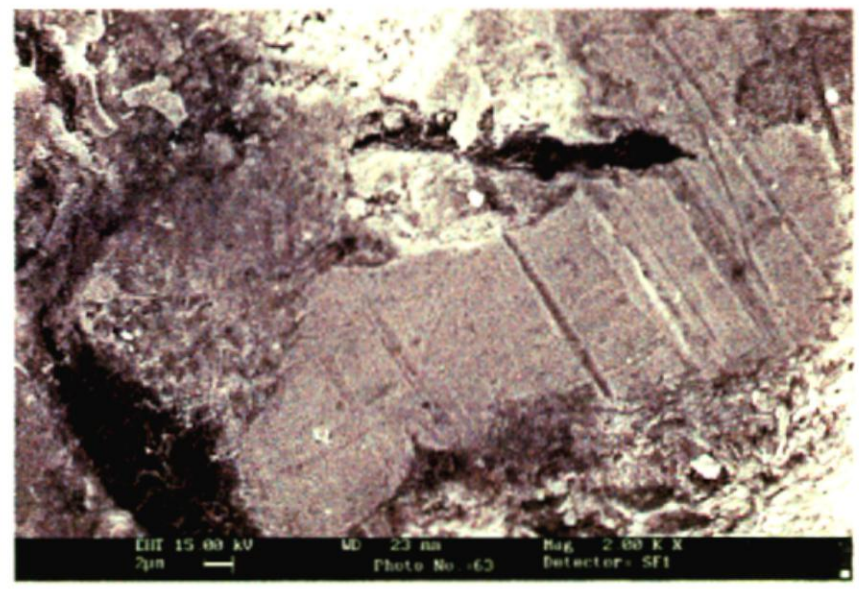

iv) 2 kX

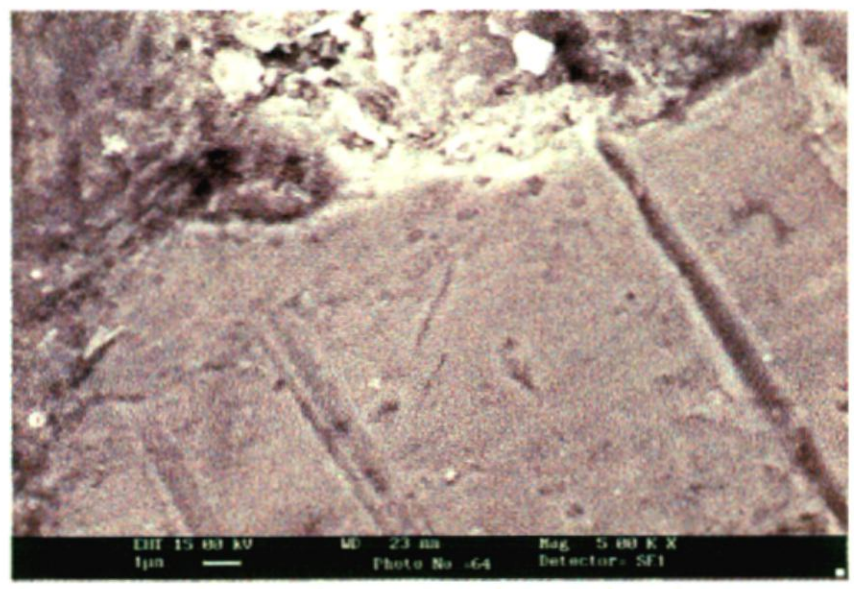

v) 5 kX

7.27e) SEM Photographs (ECH Trial Condition-T2: $C_1EC_1SR_2F_2T_2SOP_2G_2$)

(Scale 0.25)

Fig. 7.27 Characteristics of ECHed work surface

(ECH Trial Condition: $C_1EC_1SR_2F_2T_2SOP_2G_2$)

Veeco

Mag: 10.4 X

Mode: VSI

Surface Data

Surface Statistics:

Ra: 1.12 um

Rq: 1.42 um

Rz: 7.19 um

Rt: 9.49 um

Set-up Parameters:

Size: 368 X 240

Sampling: 1.61 um

Processed Options:

Terms Removed:

Tilt

Filtering:

None

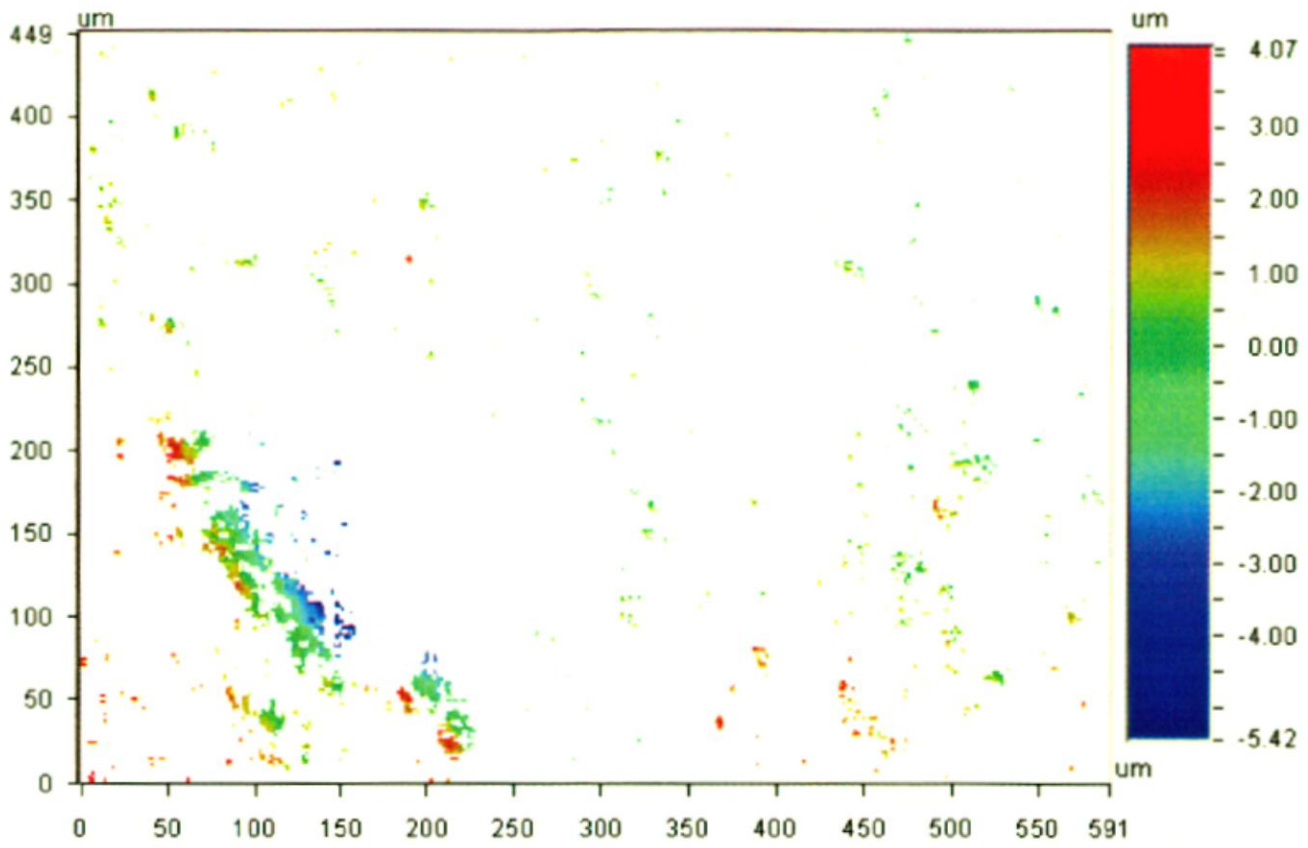

7.28a) Standard Display (ECH Trial Condition-T3: $C_1EC_1SR_3F_3T_3SOP_3G_3$)

Veeco

3-Dimensional Interactive Display

Surface Stats:

Ra: 1.12 um

Rq: 1.42 um

Rt: 9.49 um

Measurement Info:

Magnification: 10.43

Measurement Mode: VSI

Sampling: 1.61 um

Array Size: 368 X 240

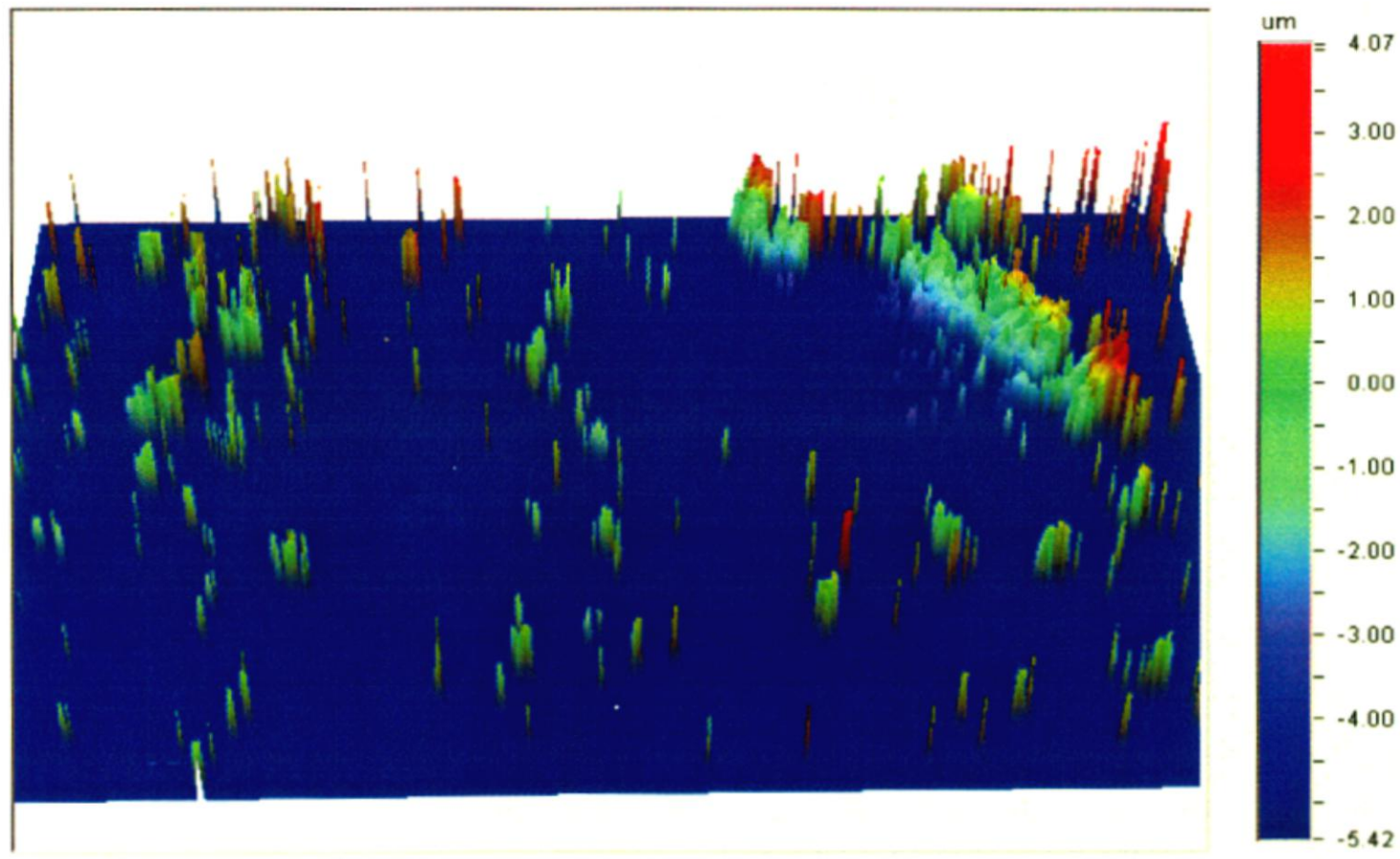

7.28b) 3D Interactive Plot (ECH Trial Condition-T3: $C_1EC_1SR_3F_3T_3SOP_3G_3$)

Mag: 10.4 X
Mode: VSI

Surface Statistics:

Ra: 1.12 um
Rq: 1.42 um
Rz: 7.19 um
Rt: 9.49 um

Set-up Parameters:

Size: 368 X 240
Sampling: 1.61 um

Processed Options:

Terms Removed:
Tilt
Filtering:
None

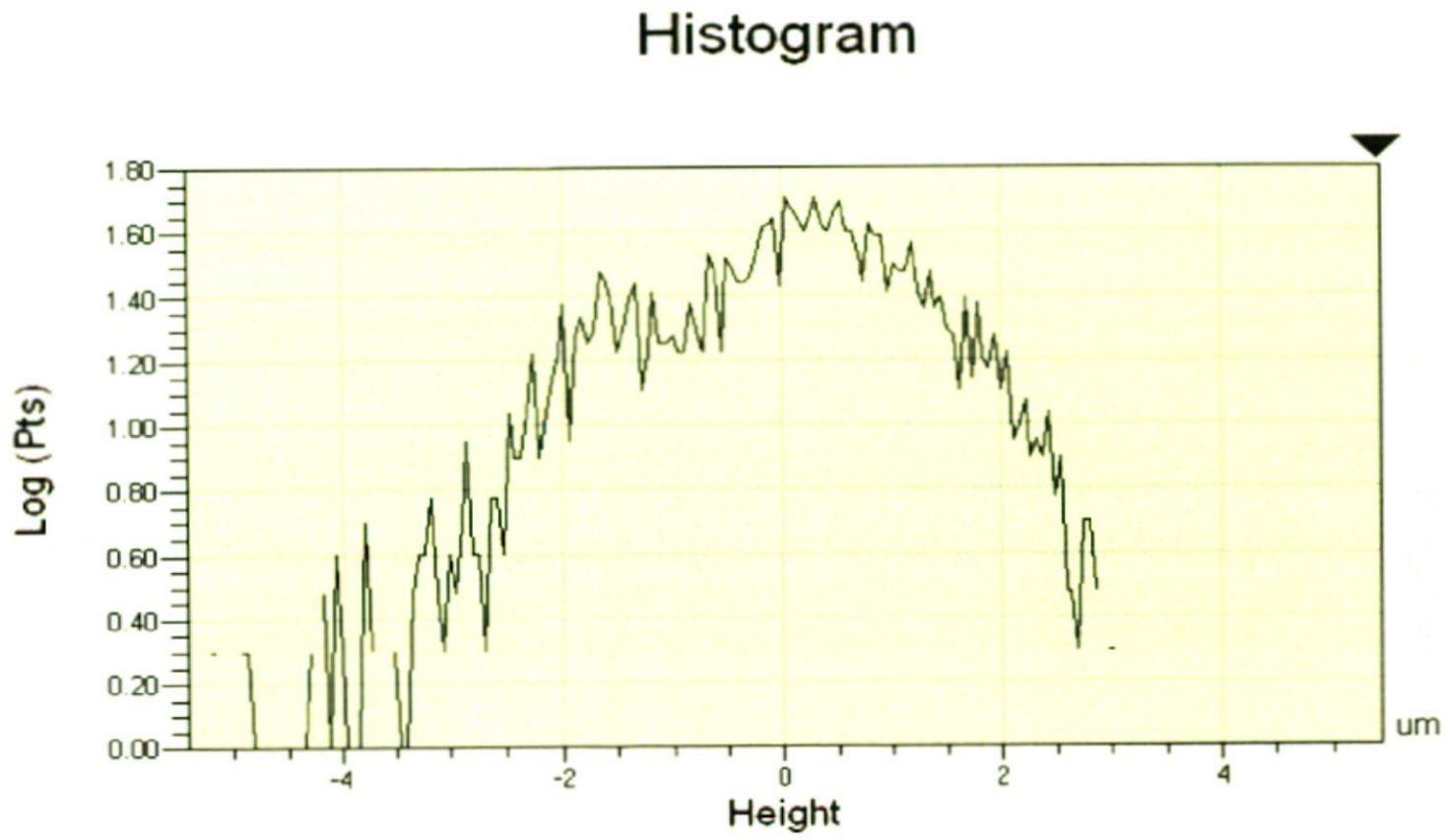

7.28c) Filtered Histogram (ECH Trial Condition-T3: $C_1EC_1SR_3F_3T_3SOP_3G_3$)

Mag: 10.4 X
Mode: VSI

Statistics:

tp1: 0.0 %
tp2: 100.0 %
Htp: 9.49 um

Mr1: 8.59 %
Mr2: 83.62 %
RK: 3300.34 nm
Rpk: 985.13 nm
Rvk: 1618.41 nm
V1: 42.30 nm
V2: 132.51 nm

Ra: 1.12 um
Rq: 1.42 um
Rz: 7.19 um

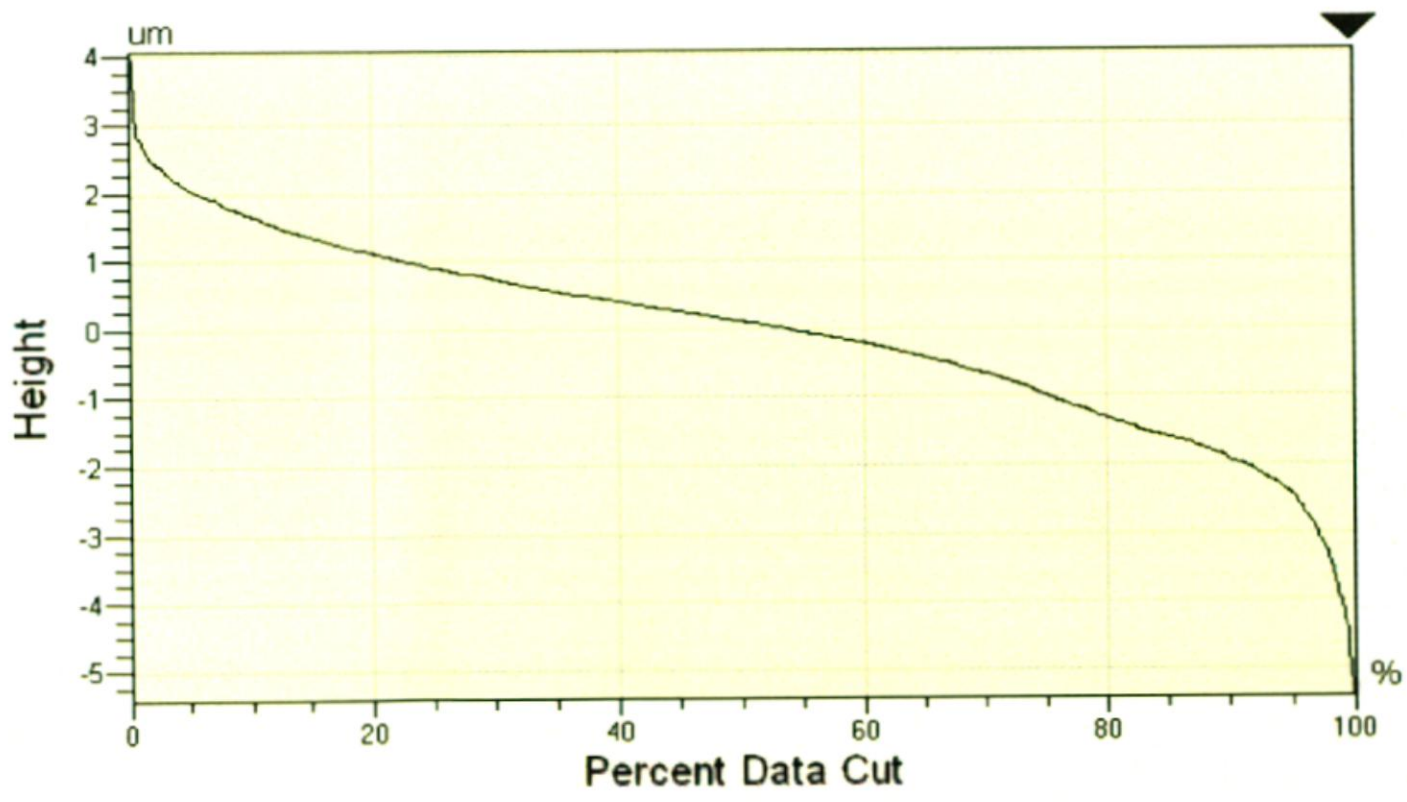

7.28d) Bearing Ratio (ECH Trial Condition-T3: $C_1EC_1SR_3F_3T_3SOP_3G_3$)

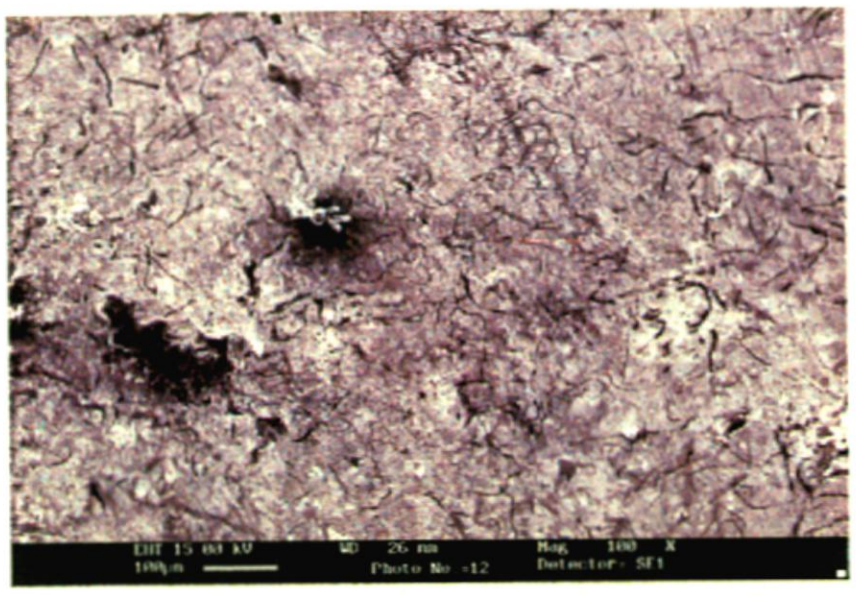

i) 100X

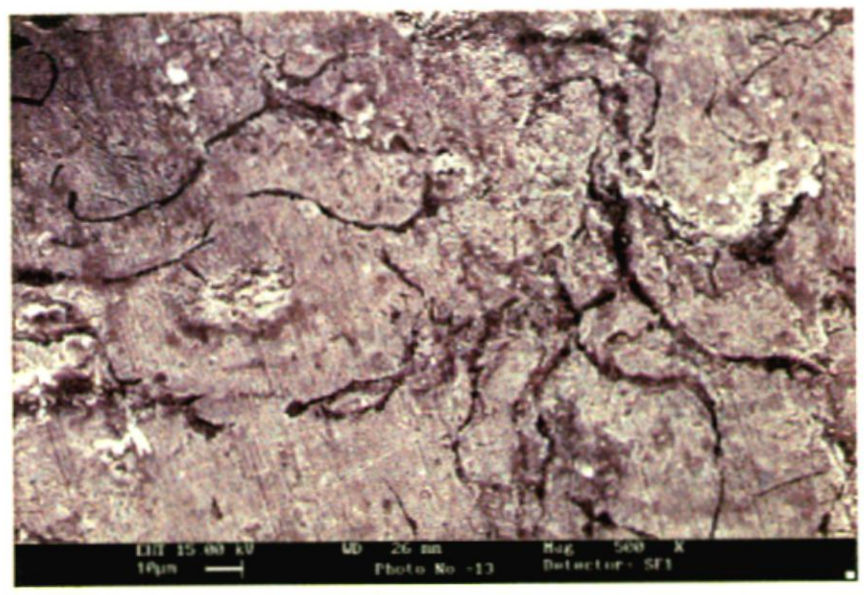

ii) 500X

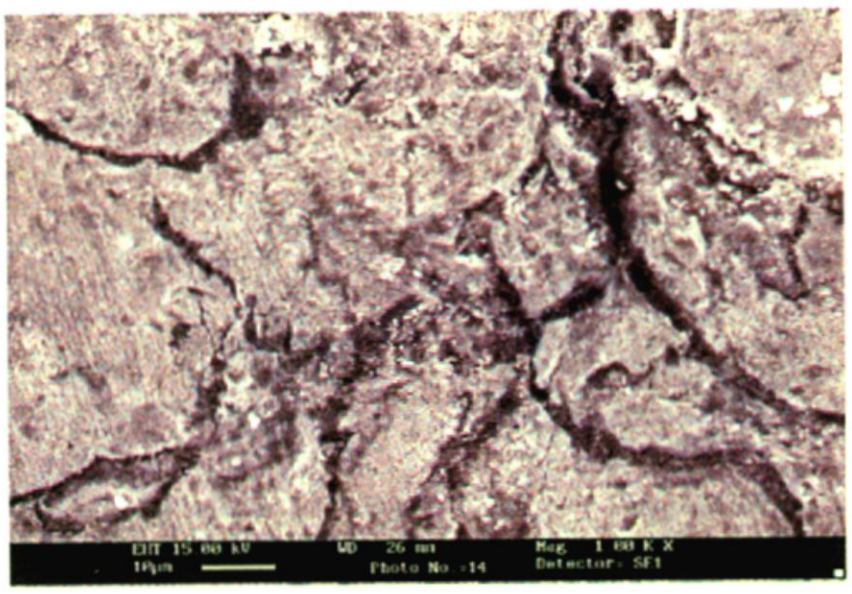

iii) 1 kX

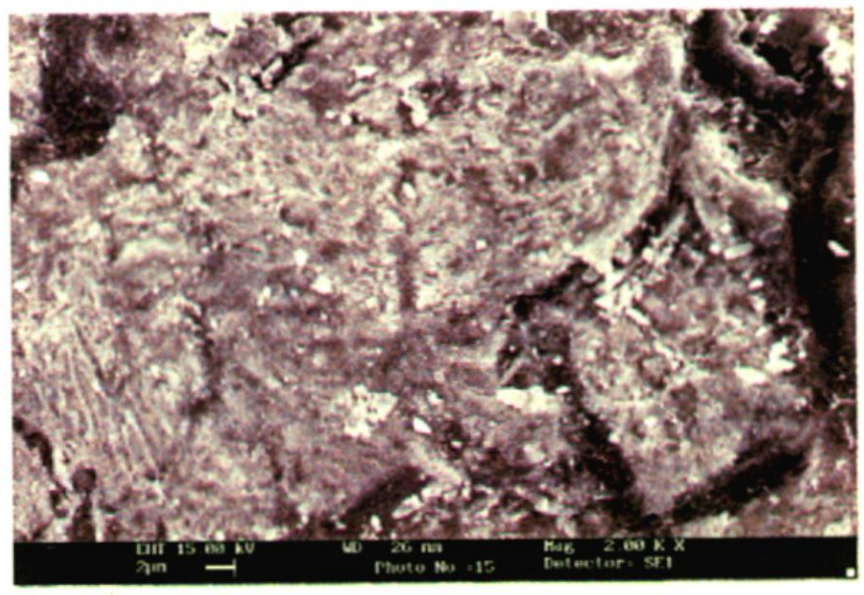

iv) 2 kX

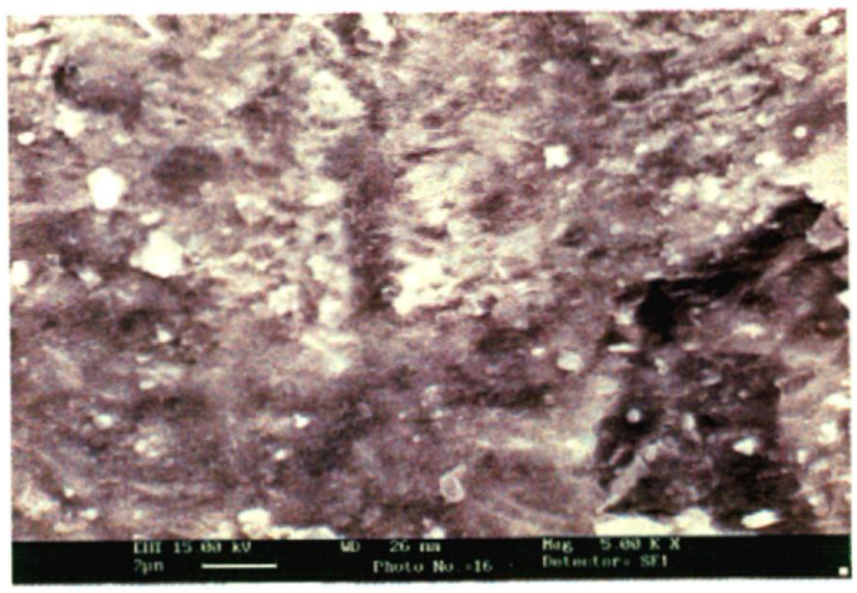

v) 5 kX

7.28e) SEM Photographs (ECH Trial Condition-T3: $C_1EC_1SR_3F_3T_3SOP_3G_3$)

(Scale 0.25)

Fig. 7.28 Characteristics of ECHed worksurface

(ECH Trial Condition: $C_1EC_1SR_3F_3T_3SOP_3G_3$)

The importance of proper coordination of electrolytic dissolution and mechanical abrading in ECH for better surface character can be traced by comparing the results of T-3 (Fig. 7.28) and T-14 (Fig. 7.29). Both the trials have been performed at the 3rd level of the stick grit size. Ignoring the effect of electrolyte flow rate and electrolyte inlet temperature (found quite less influential as revealed in Phase-III Stage-I studies), T-3 is characterized by a lower electrolytic dissolution (C_1EC_1) part accompanied with a higher mechanical abrading (SR_3SOP_3) as compared to T-14 (performed at $C_2EC_2SR_2SOP_2$). The surface characteristics with T-3 are much better than that of T-14. The final R_a, Rk, Rpk and Rvk as well as surface roughness uniformity of the work surface deteriorated with T-14 as compared to T-3 as can be seen from the respective micrographs. The uniformity decreased from almost 50% within ± 1μm for T-3 to almost only 30% surface roughness data lying within ± 1μm for T-14 (Fig. 7.27e and 7.28e). However, the surface profile results are still far superior to the raw work surface. The processed surface microprofile improved drastically in T-27 (Fig. 7.30) as compared to T-3 and T-14. A receptive surface free from any micro defect with highly uniform fine finished surface profiles is obtained.

It can be concluded that the electrochemical dissolution and mechanical action must be synchronized in electro-chemical honing process for better surface micro characteristics. Noticeably, an interactive nature of ECH process was also emphasized based on the findings of the Phase-III Stage-I studies.

Veeco

Mag: 10.4 X

Mode: VSI

Surface Data

Surface Statistics:

Ra: 2.39 um

Rq: 3.16 um

Rz: 18.98 um

Rt: 33.49 um

Set-up Parameters:

Size: 368 X 240

Sampling: 1.61 um

Processed Options:

Terms Removed:

Tilt

Filtering:

None

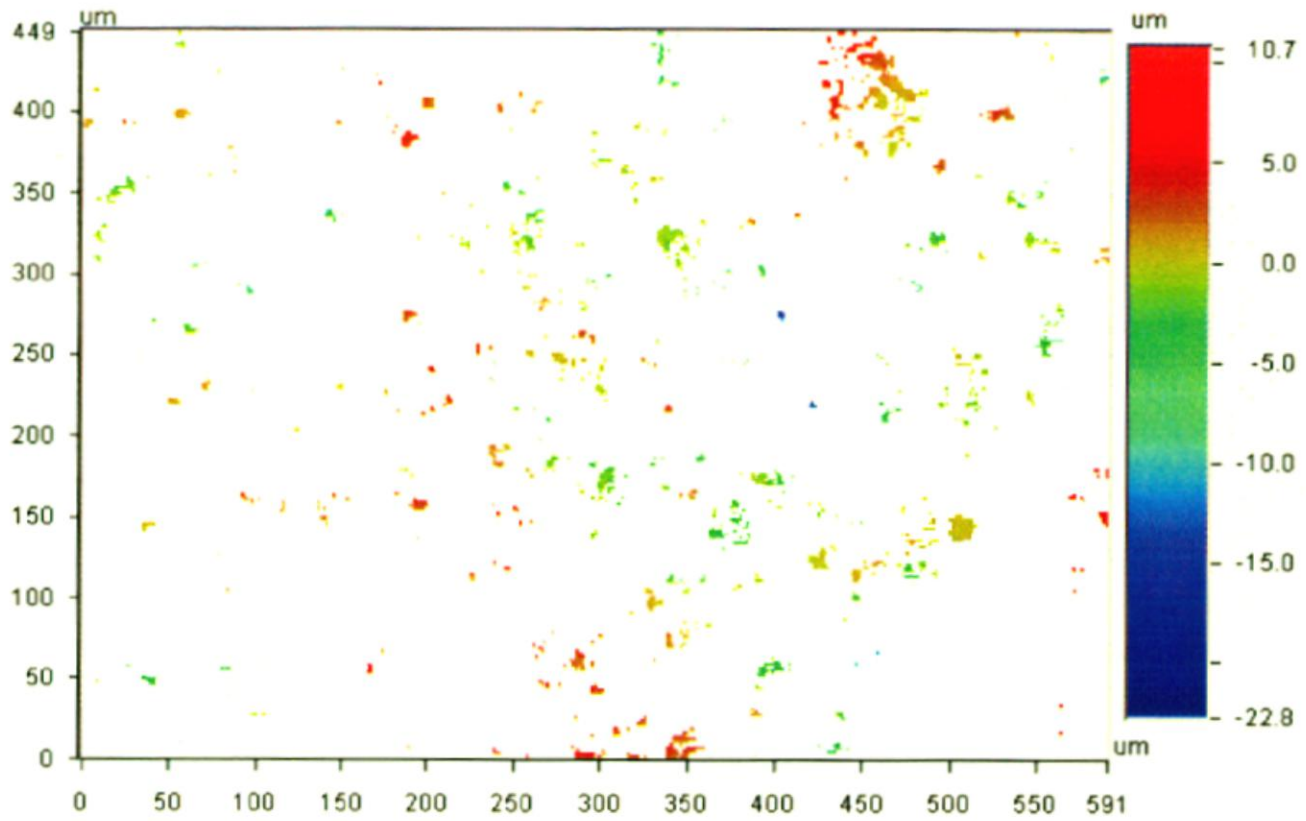

7.29a) Standard Display (ECH Trial Condition-T14: $C_2EC_2SR_2F_1T_2SOP_2G_3$)

Veeco

3-Dimensional Interactive Display

Surface Stats:

Ra: 2.39 um

Rq: 3.16 um

Rt: 33.49 um

Measurement Info:

Magnification: 10.43

Measurement Mode: VSI

Sampling: 1.61 um

Array Size: 368 X 240

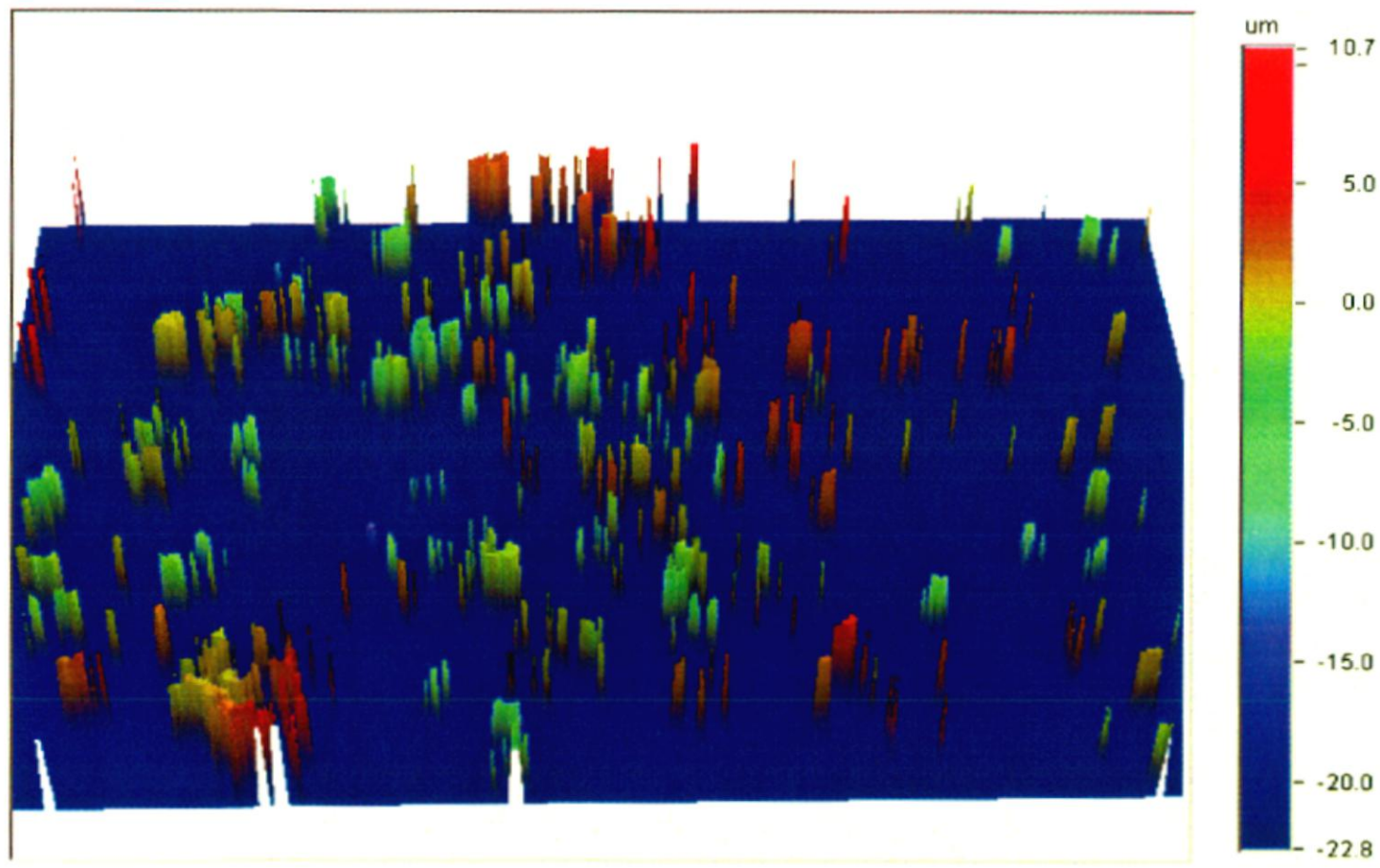

7.29b) 3D Interactive Plot (ECH Trial Condition- T14: $C_2EC_2SR_2F_1T_2SOP_2G_3$)

Veeco

Mag: 10.4 X

Mode: VSI

Surface Statistics:

Ra: 2.39 um

Rq: 3.16 um

Rz: 18.98 um

Rt: 33.49 um

Set-up Parameters:

Size: 368 X 240

Sampling: 1.61 um

Processed Options:

Terms Removed:

Tilt

Filtering:

None

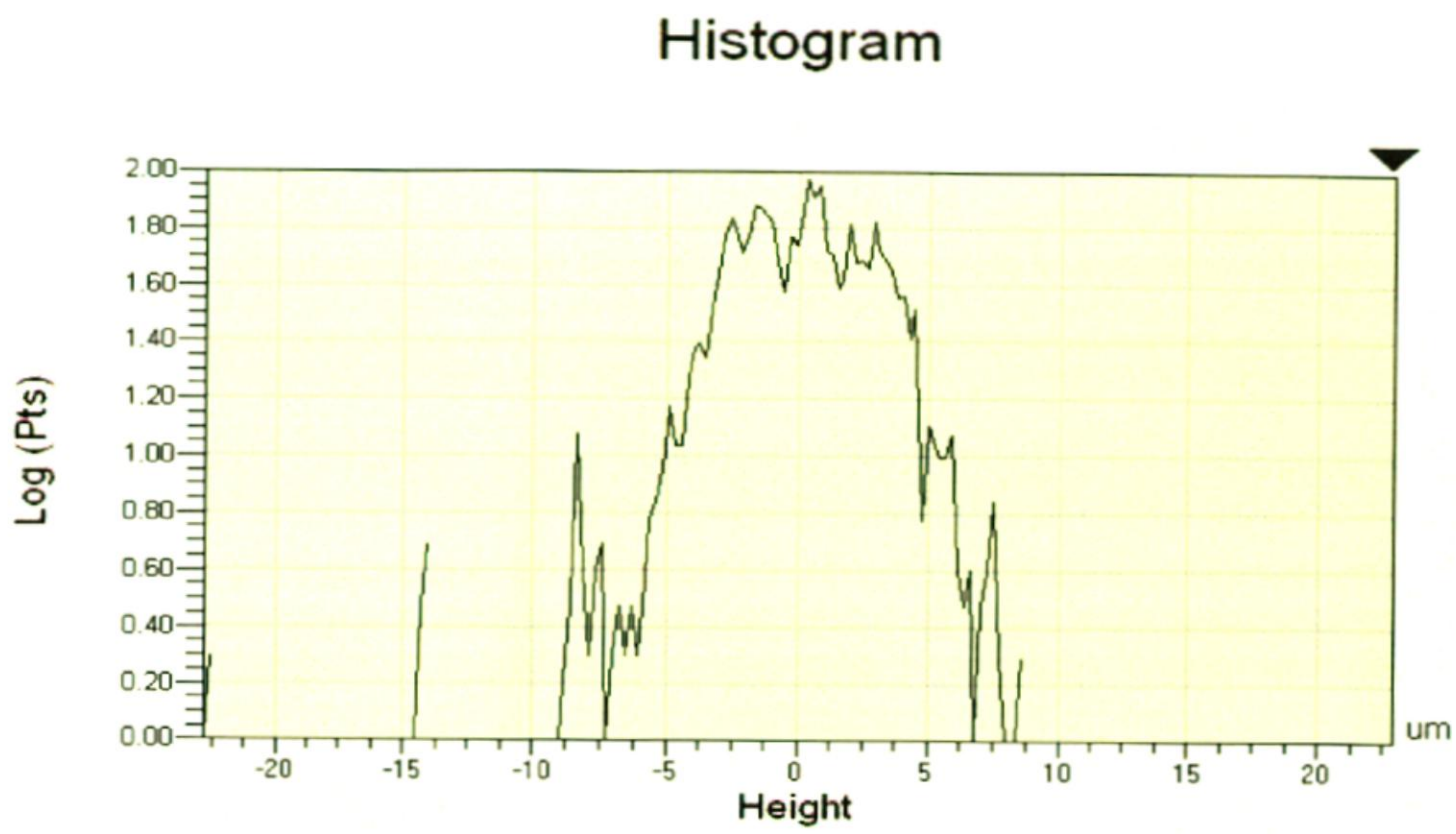

7.29c) Filtered Histogram (ECH Trial Condition- T14: $C_2EC_2SR_2F_1T_2SOP_2G_3$)

Veeco

Mag: 10.4 X

Mode: VSI

Statistics:

tp1: 0.0 %

tp2: 100.0 %

Htp: 33.49 um

Mr1: 9.21 %

Mr2: 92.47 %

RK: 7589.04 nm

Rpk: 2519.16 nm

Rvk: 5229.81 nm

V1: 115.95 nm

V2: 196.90 nm

Ra: 2.39 um

Rq: 3.16 um

Rz: 18.98 um

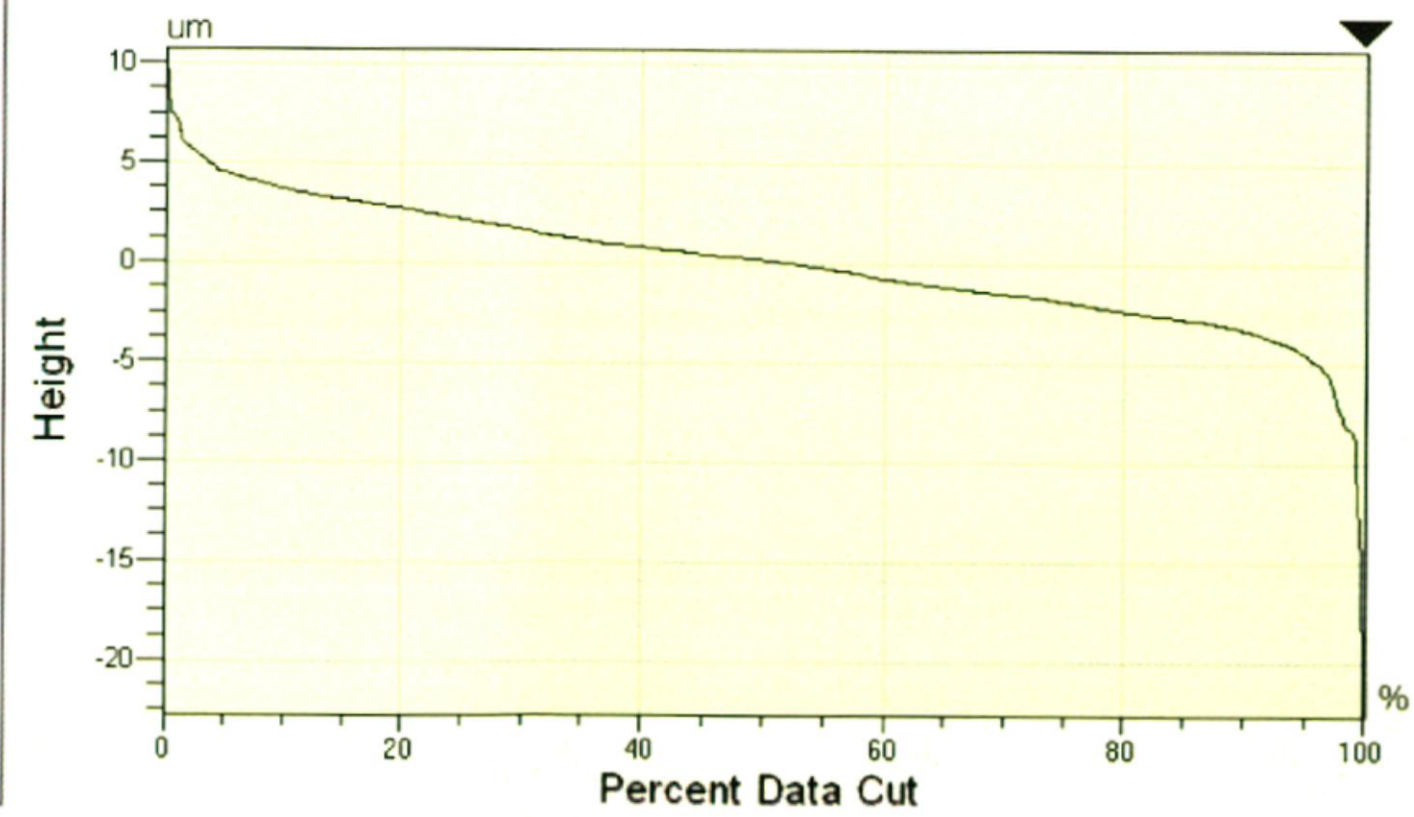

7.29d) Bearing Ratio (ECH Trial Condition- T14: $C_2EC_2SR_2F_1T_2SOP_2G_3$)

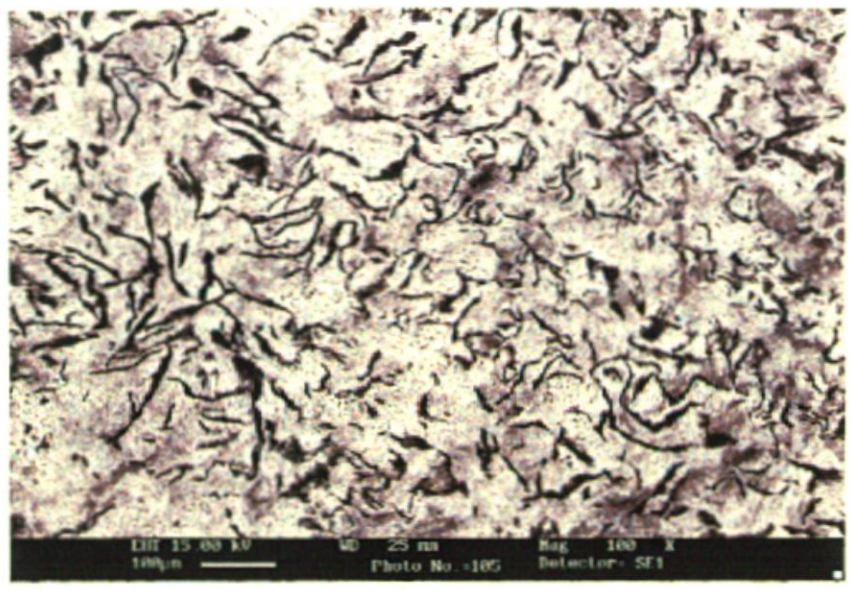

i) 100X

ii) 500X

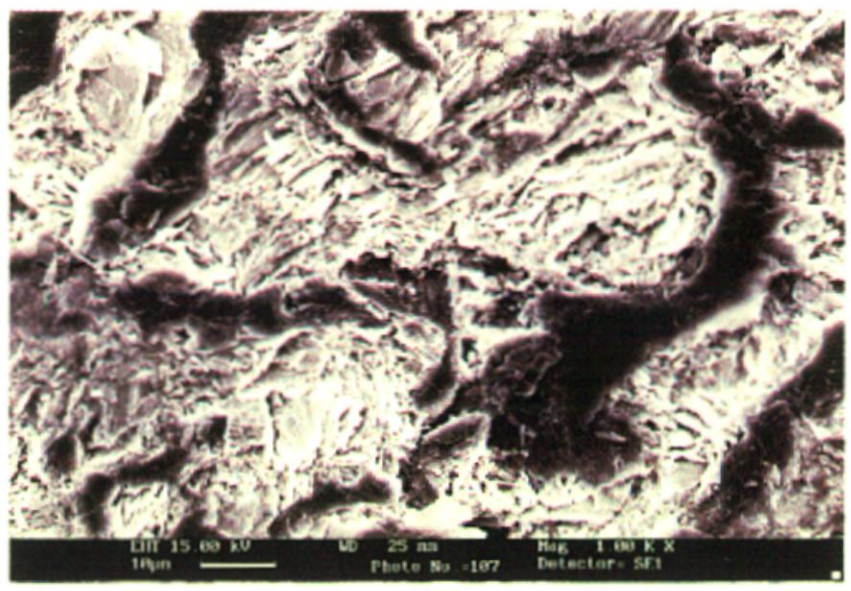

iii) 1 kX

iv) 2 kX

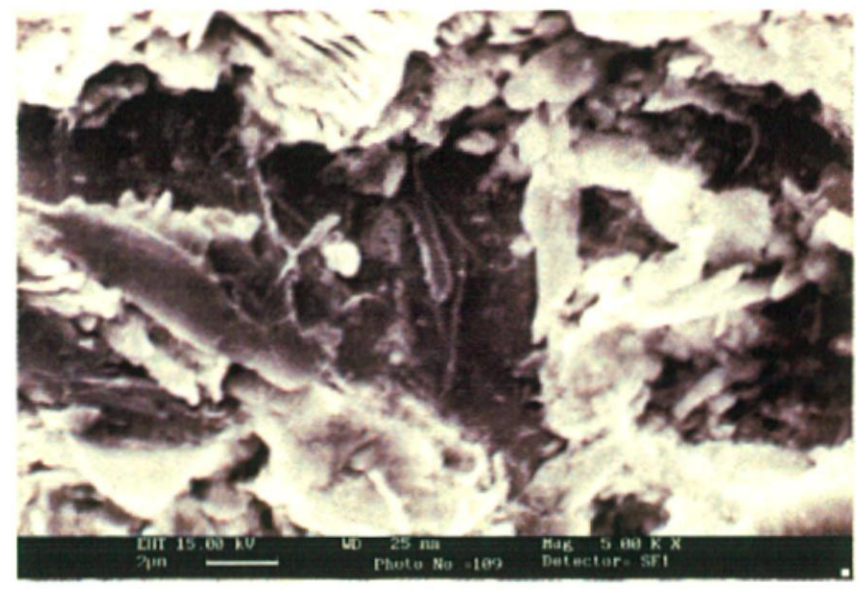

v) 5 kX

7.29e) SEM Photographs (ECH Trial Condition- T14: $C_2EC_2SR_2F_1T_2SOP_2G_3$)

(Scale 0.25)

Fig. 7.29 Characteristics of ECHed worksurface

(ECH Trial Condition: $C_2EC_2SR_2F_1T_2SOP_2G_3$)

Veeco

Mag: 10.4 X

Mode: VSI

Surface Data

Surface Statistics:

Ra: 505.15 nm

Rq: 667.50 nm

Rz: 6.41 um

Rt: 9.92 um

Set-up Parameters:

Size: 368 X 240

Sampling: 1.61 um

Processed Options:

Terms Removed:

Tilt

Filtering:

None

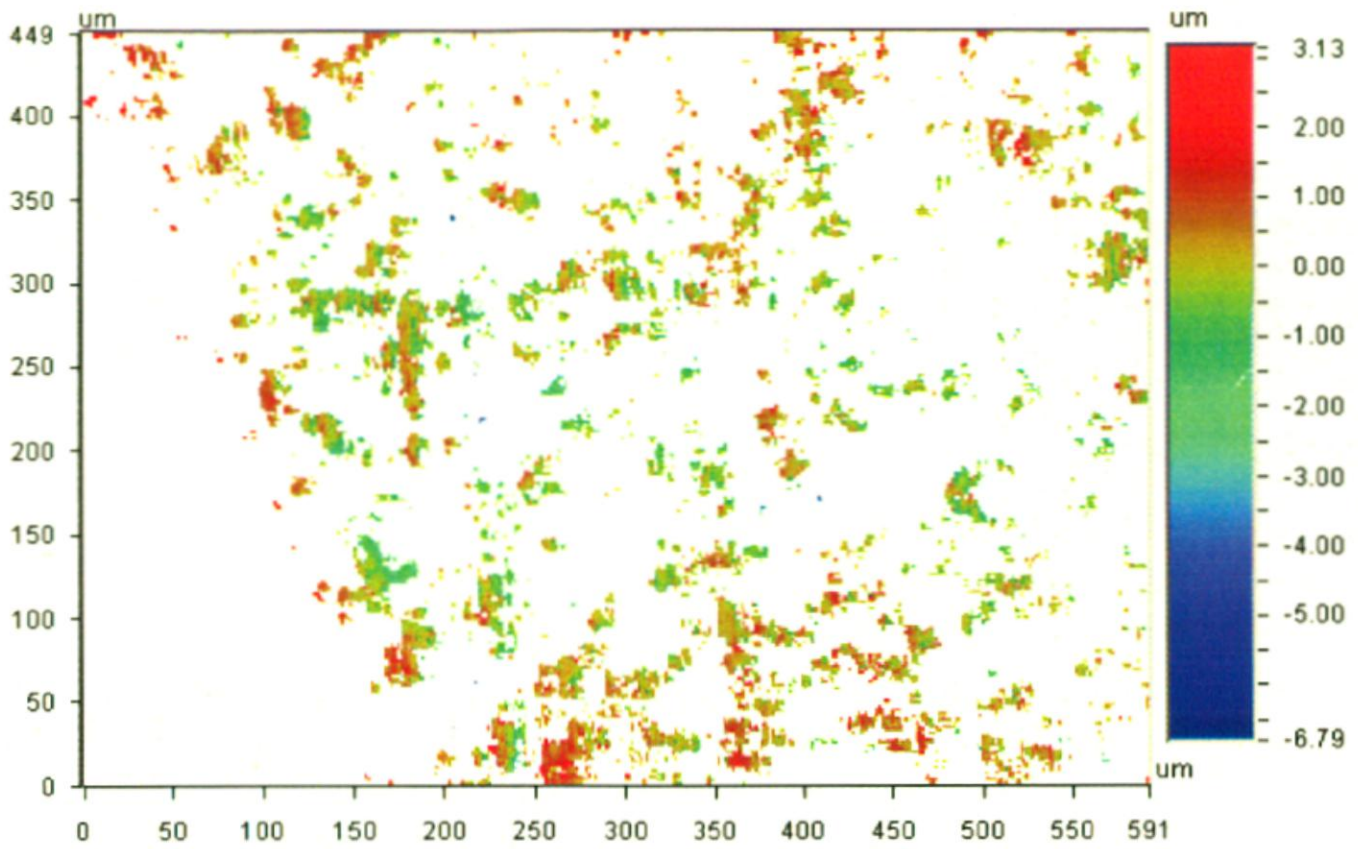

7.30a) Standard Display (ECH Trial Condition-T27: $C_3EC_3SR_3F_1T_3SOP_3G_2$)

Veeco

3-Dimensional Interactive Display

Surface Stats:

Ra: 505.15 nm

Rq: 667.50 nm

Rt: 9.92 um

Measurement Info:

Magnification: 10.43

Measurement Mode: VSI

Sampling: 1.61 um

Array Size: 368 X 240

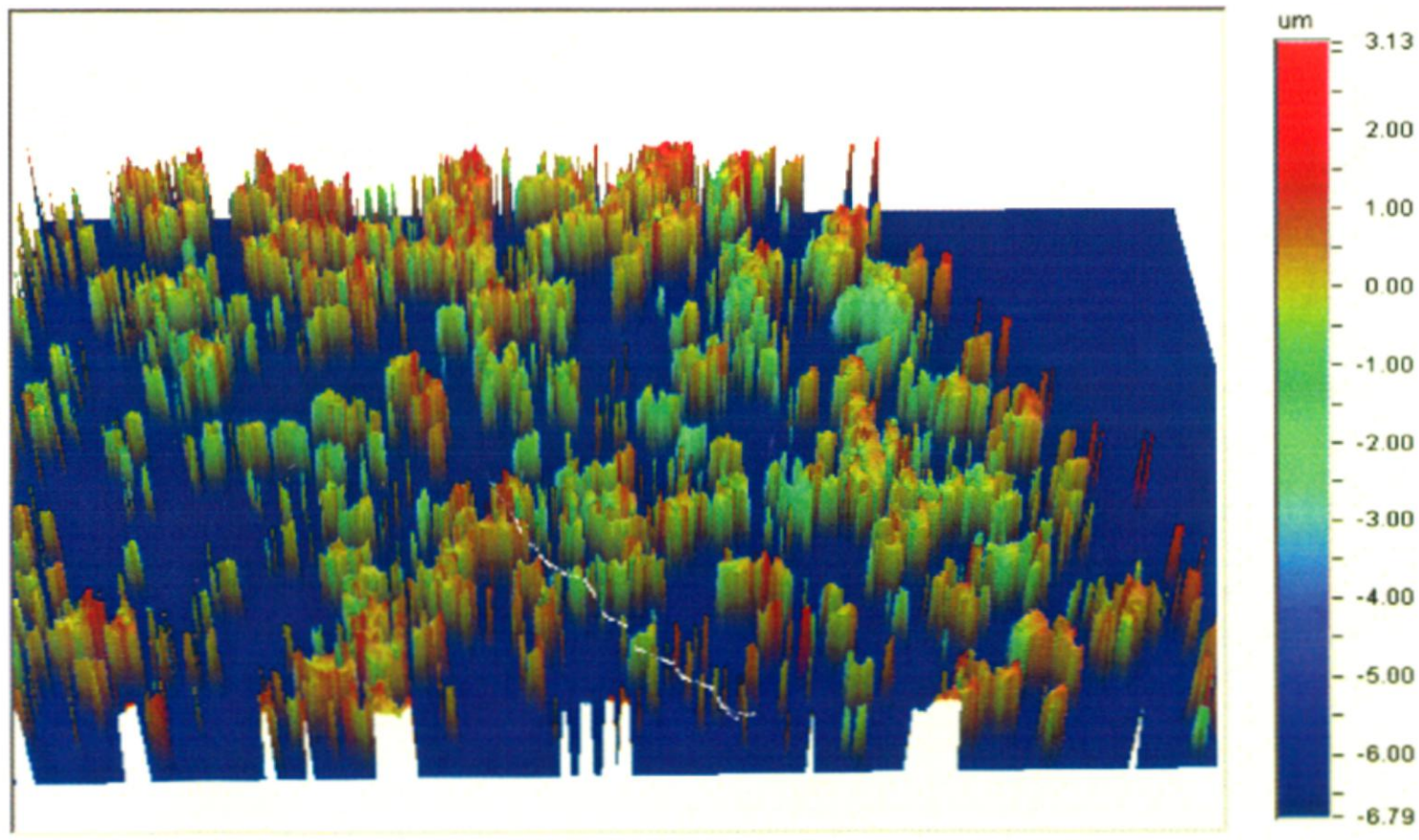

7.30b) 3D Interactive Plot (ECH Trial Condition-T27: $C_3EC_3SR_3F_1T_3SOP_3G_2$)

Veeco

Mag: 10.4 X

Mode: VSI

Surface Statistics:

Ra: 505.15 nm

Rq: 667.50 nm

Rz: 6.41 um

Rt: 9.92 um

Set-up Parameters:

Size: 368 X 240

Sampling: 1.61 um

Processed Options:

Terms Removed:

Tilt

Filtering:

None

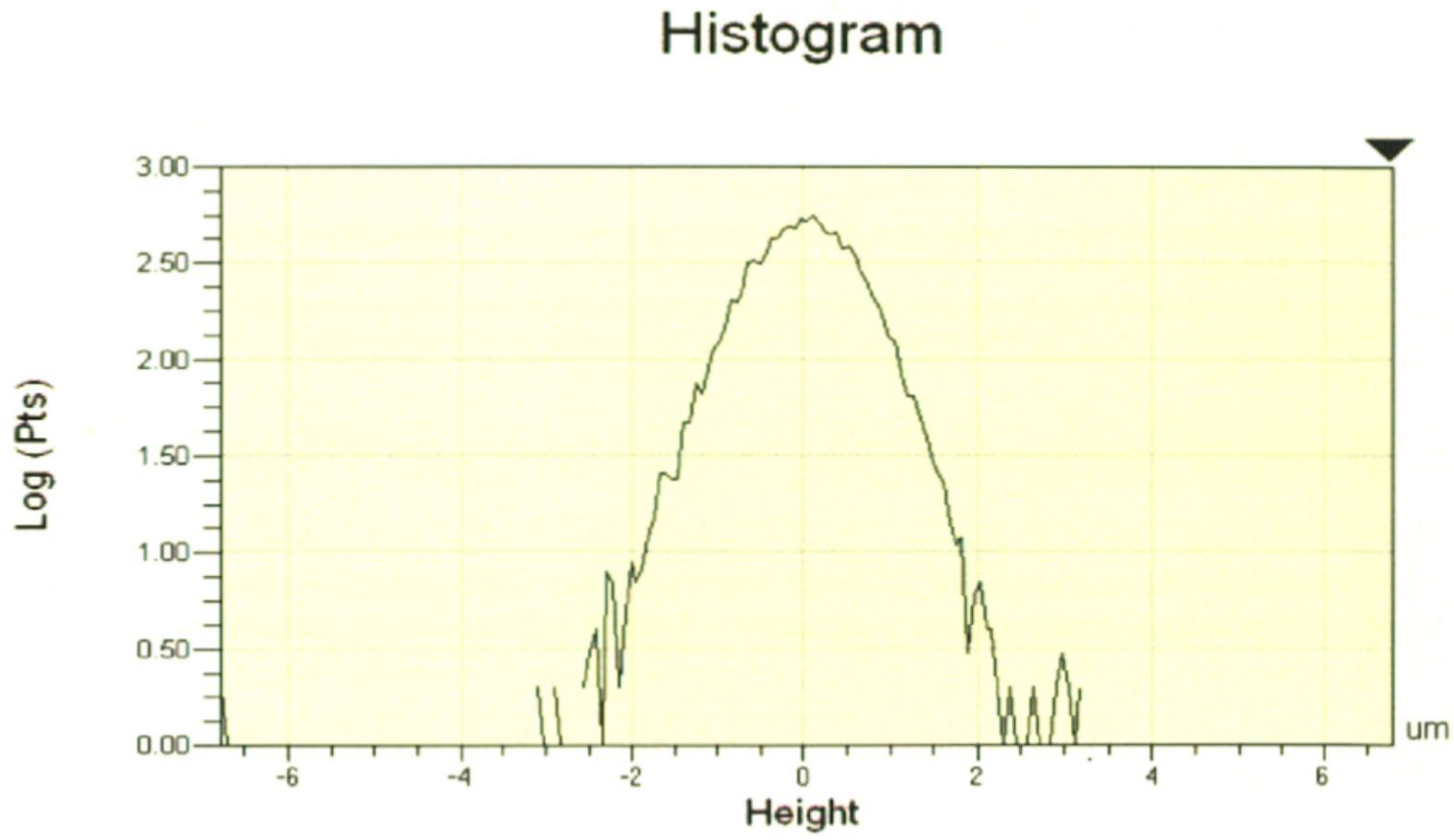

7.30c) Filtered Histogram (ECH Trial Condition-T27: $C_3EC_3SR_3F_1T_3SOP_3G_2$)

Veeco

Mag: 10.4 X

Mode: VSI

Statistics:

tp1: 0.0 %

tp2: 100.0 %

Htp: 9.92 um

Mr1: 9.47 %

Mr2: 89.35 %

RK: 1580.65 nm

Rpk: 675.17 nm

Rvk: 805.20 nm

V1: 31.96 nm

V2: 42.86 nm

Ra: 505.15 nm

Rq: 667.50 nm

Rz: 6.41 um

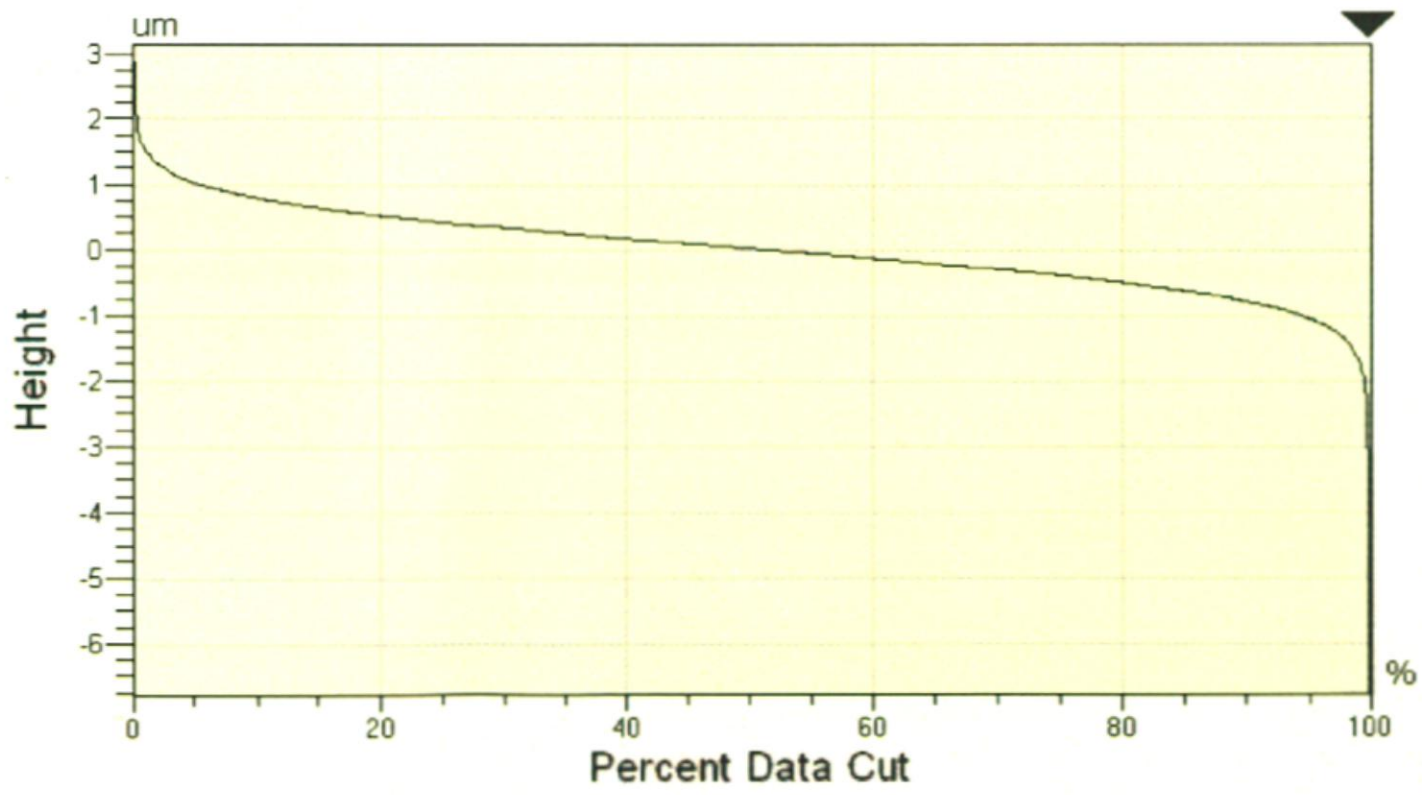

7.30d) Bearing Ratio (ECH Trial Condition-T27: $C_3EC_3SR_3F_1T_3SOP_3G_2$)

Veeco

Mag: 10.4 X

Mode: VSI

3D Plot

Surface Statistics:

Ra: 505.15 nm

Rq: 667.50 nm

Rz: 6.41 um

Rt: 9.92 um

Set-up Parameters:

Size: 368 X 240

Sampling: 1.61 um

Processed Options:

Terms Removed

Tilt

Filtering

None

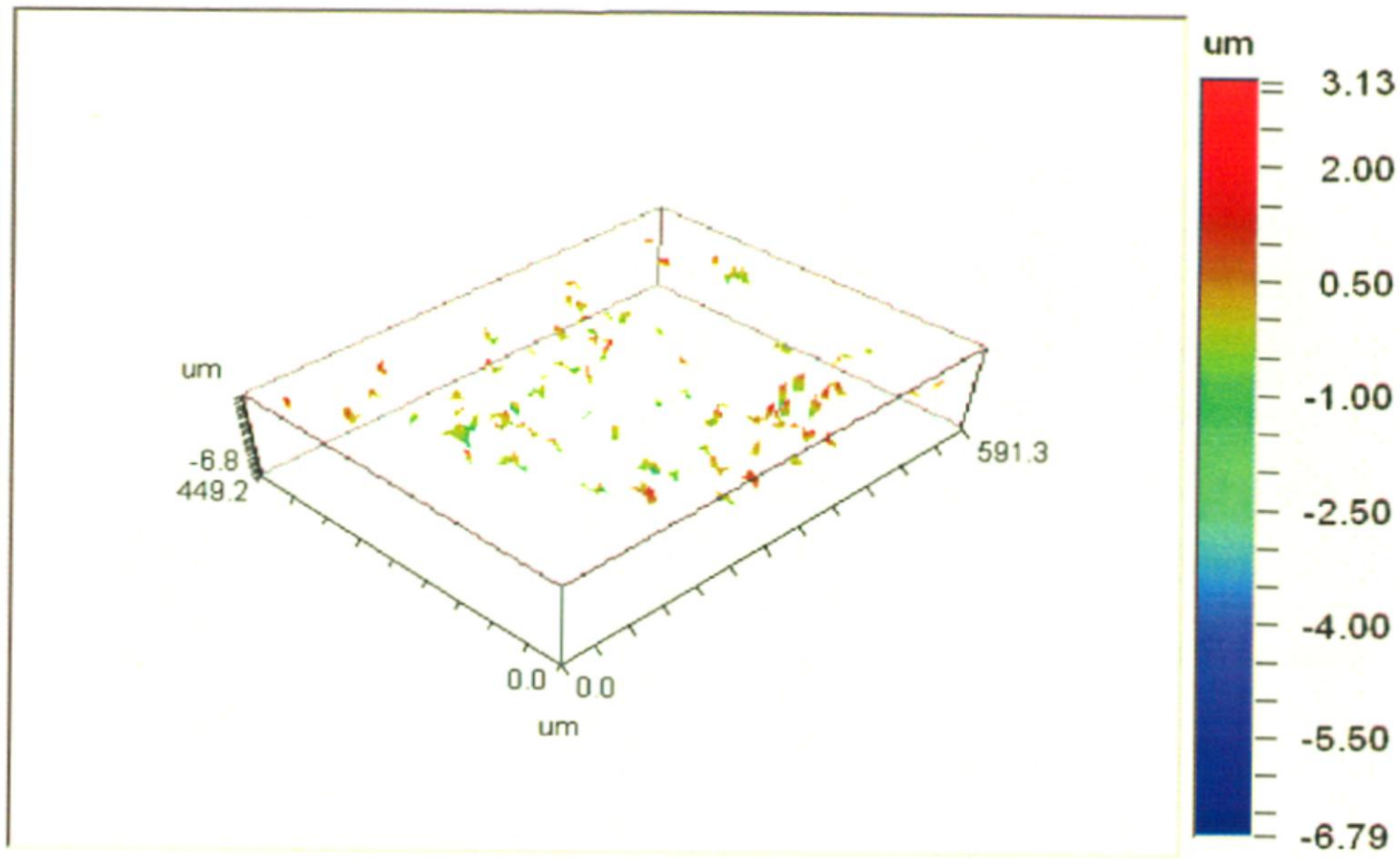

7.30e) 3D Plot (ECH Trial Condition-T27: $C_3EC_3SR_3F_1T_3SOP_3G_2$)

Veeco

X Profile

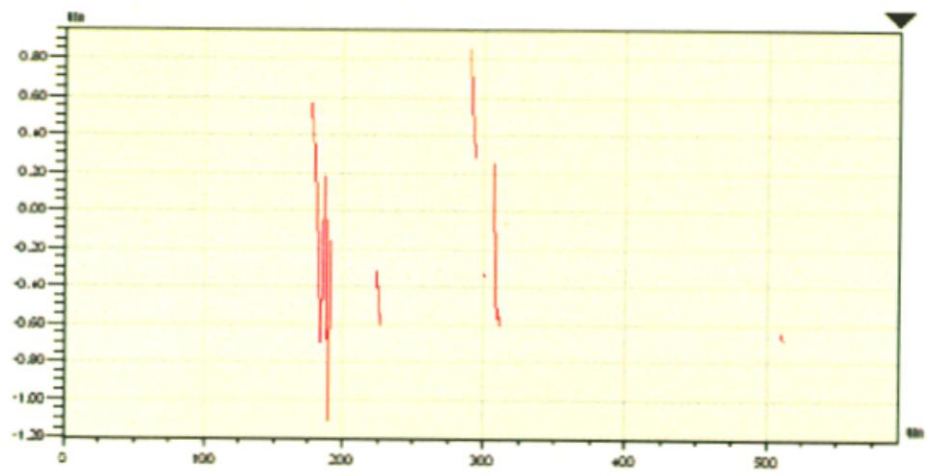

Rq	0.49	um		
Ra	0.41	um		
Rt	1.96	um		
Rp	0.86	um		
Rv	-1.11	um		

Angle	0.00	mrad
Curve	-34.10	mm
Terms	None	
Avg Ht	-0.18	um
Area	-105.98	um2

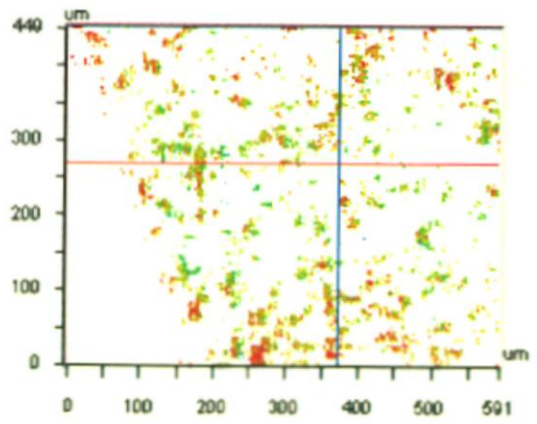

Y Profile

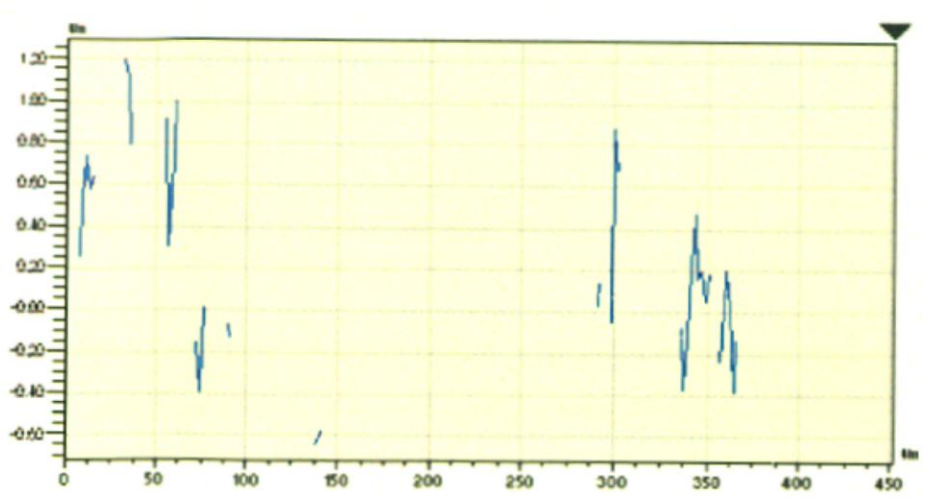

X	370.54	-	-	um
Y	268.78	-	-	um
Ht	-	-	-	um
Dist			-	um
Angle			-	°

Rq	0.46	um
Ra	0.37	um
Rt	1.83	um
Rp	1.20	um
Rv	-0.63	um

Angle	0.00	mrad
Curve	28.25	mm
Terms	None	
Avg Ht	0.21	um
Area	96.49	um2

7.30f) 2D Plot (ECH Trial Condition-T27: $C_3EC_3SR_3F_1T_3SOP_3G_2$)

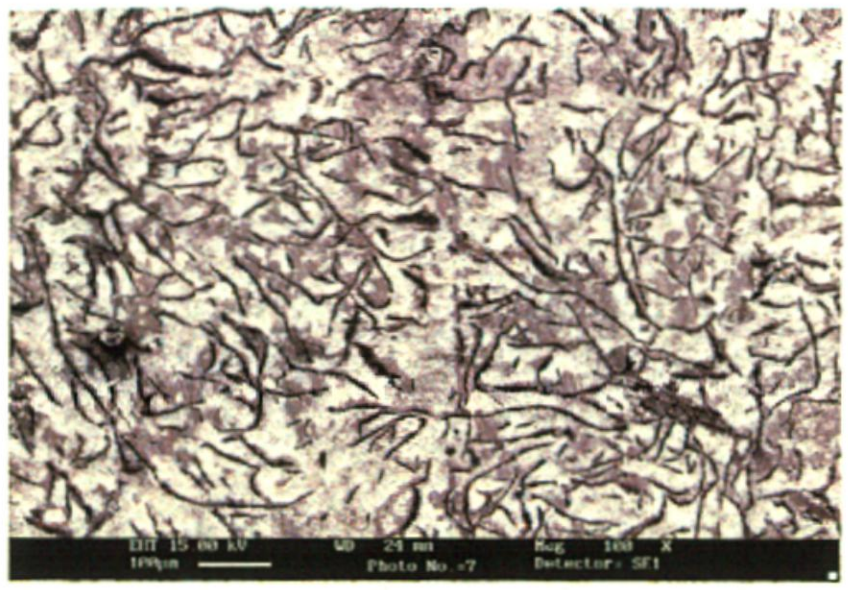

i) 100X

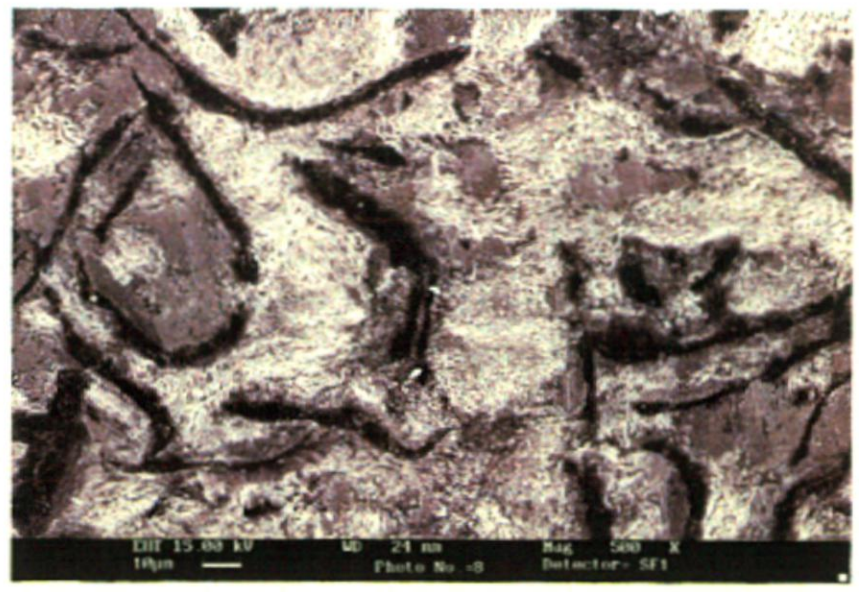

ii) 500X

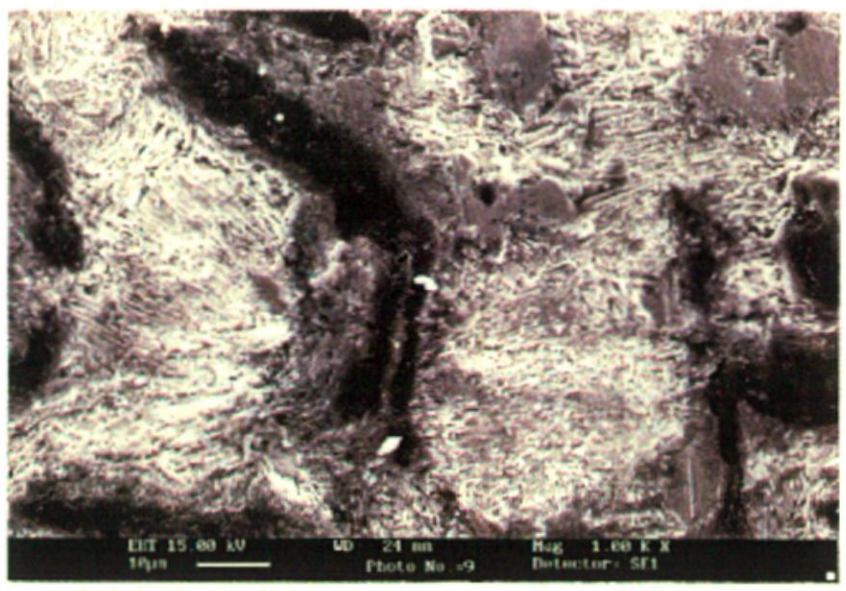

iii) 1 kX

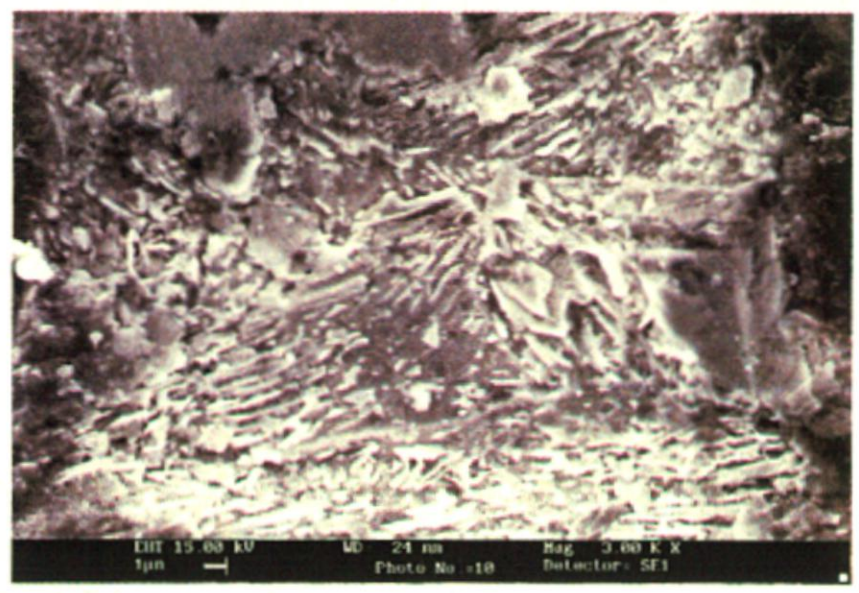

iv) 2 kX

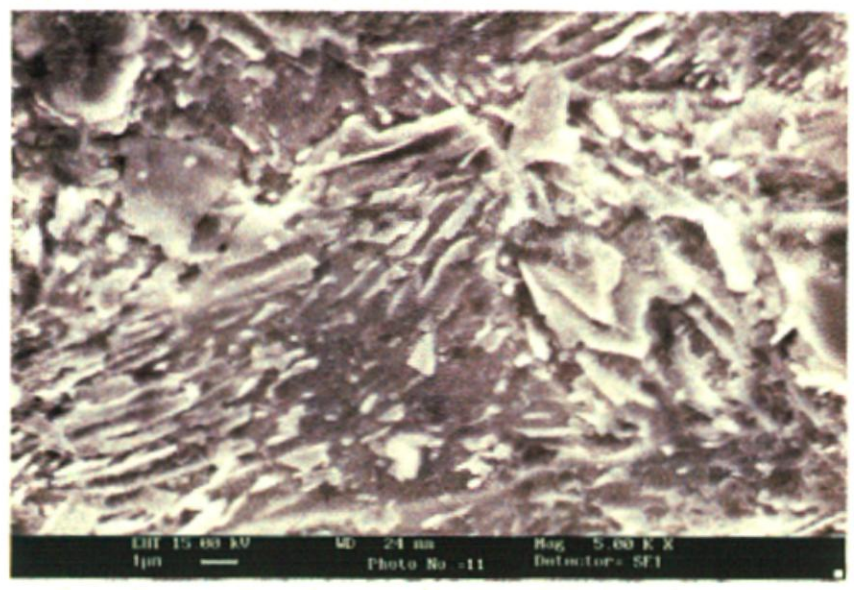

v) 5 kX

7.30g) SEM Photographs (ECH Trial Condition-T27: $C_3EC_3SR_3F_1T_3SOP_3G_2$)

(Scale 0.25)

Fig. 7.30 Characteristics of ECHed worksurface

(ECH Trial Condition: $C_3EC_3SR_3F_1T_3SOP_3G_2$)

7.5 PHASE-III STAGE-III STUDIES

This phase of studies are related to the surface integrity aspects of the work surfaces processed by electro-chemical honing process. Three major aspects of probable sub-surface alterations were examined using the special metallographic techniques discussed in Section 5.4.3. Work sample were selected covering the entire machining domain representing the various trial conditions involved during experimentation including a sample obtained from the precision lathe boring operation prior to ECH. Processing conditions of the various work samples examined for the microstructural changes and microhardness alterations are given in Table 6.28.

7.5.1 Microstructural Examination

In order to identify any sub-surface microstructural changes that could have been resulted due to the ECH processing of the work surface, five work samples processed under different trial conditions were selected as shown in Table 6.28. The microstructure of an unprocessed work sample has already been discussed in Chapter- V. The microstructure of five ECH processed work sample was examined using the special metallographic technique and procedure described in section 5.4.3.1. Fig. 7.31 to 7.35 give the microstructure photographs of the work sample cross section taken with the help of ZEISS Axiovert 200 MAT Inverted Optical Microscope (interfaced with imaging software ZEISS AxioVision Release 4.1, Germany) and LEO VP 435 scanning electron microscope at different magnifications.

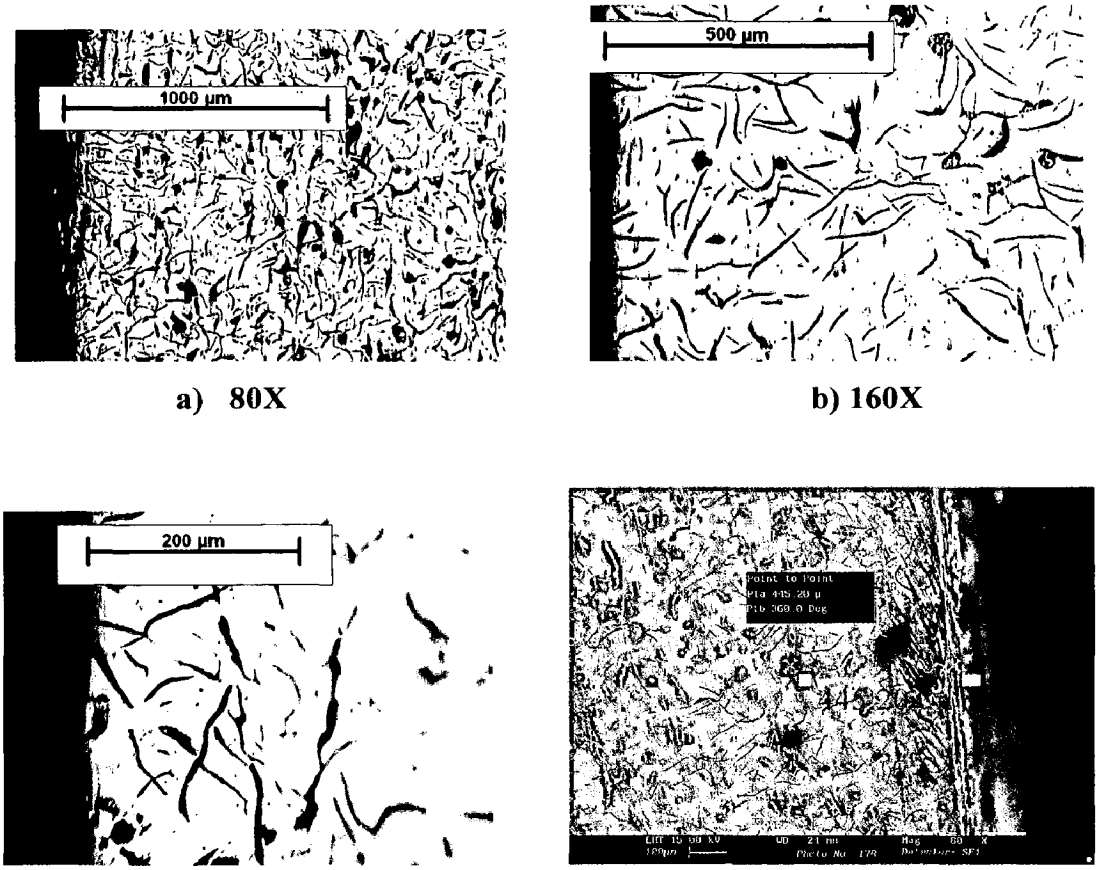

a) 80X b) 160X

c) 320X d) 80X

Fig. 7.32 Microstructure of the work material (Work sample: 49, Machining condition: $C_1EC_3SR_1F_3T_3SOP_2G_2$), a) 80X, scale 0.5, b) 160X, scale 0.5, c) 320 X, scale 0.5, d) SEM micrograph 80X, scale 0.25

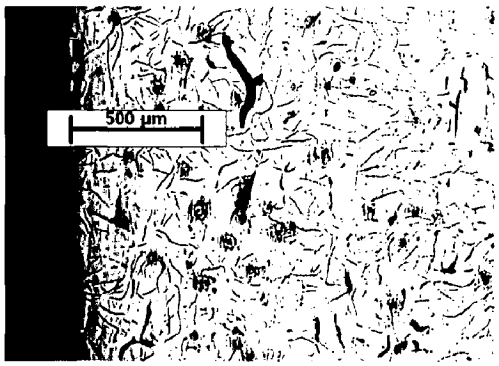

a) 80X

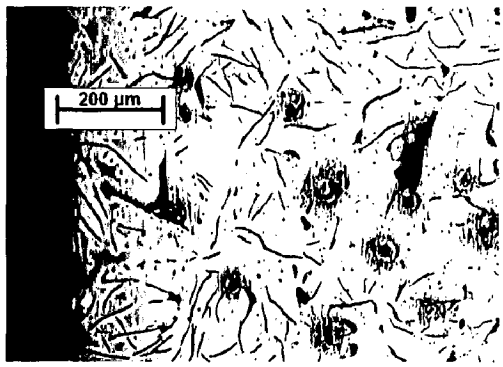

b) 160X

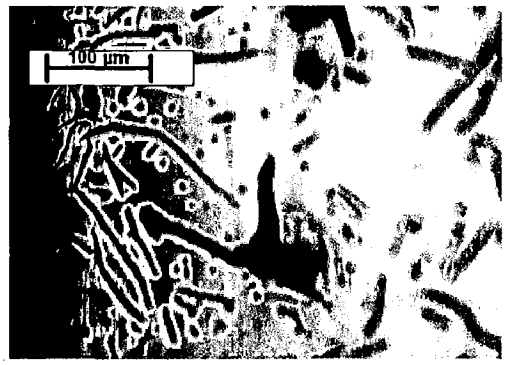

C) 320X

Fig. 7.33 Microstructure of the work material (Work sample: 50, Machining condition: $C_3EC_1SR_2F_1T_3SOP_1G_3$) (Scale 0.5)

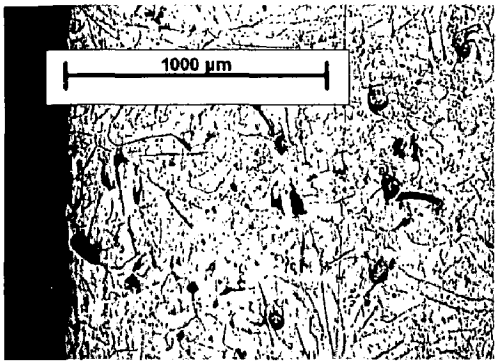

a) 80X

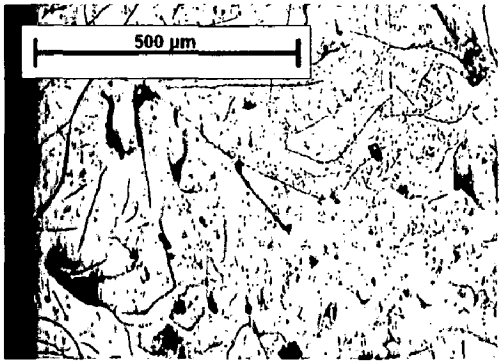

b) 160X

c) 320X

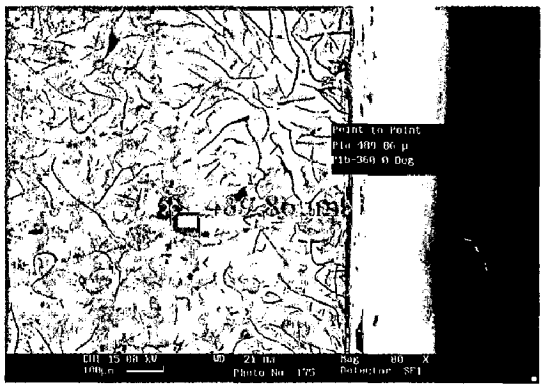

d) 80X

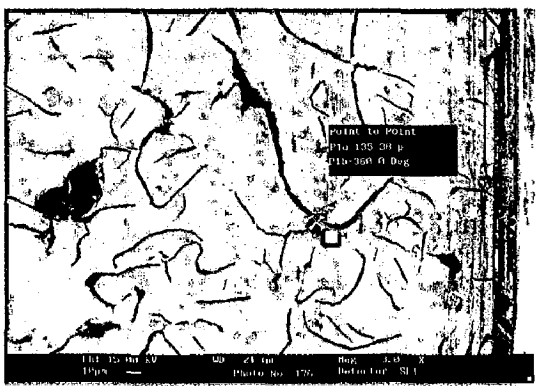

e) 320X

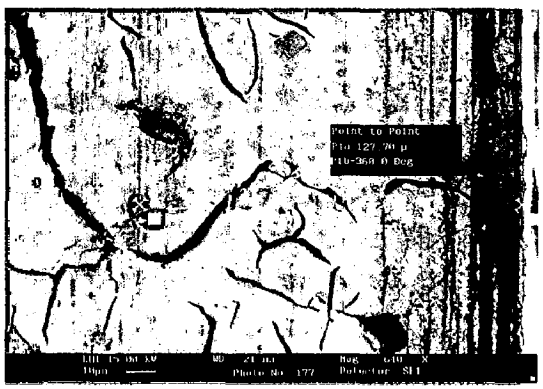

f) 640X

Fig. 7.34 Microstructure of the work material (Work sample: 34, Machining condition: $C_3EC_3SR_2F_3T_2SOP_2G_1$), a) 80X, scale 0.5, b) 160X, scale 0.5, c) 320X, scale 0.5, d) SEM micrograph 80X, scale 0.25, e) SEM micrograph 320X, scale 0.25, f) SEM micrograph 640X, scale 0.25

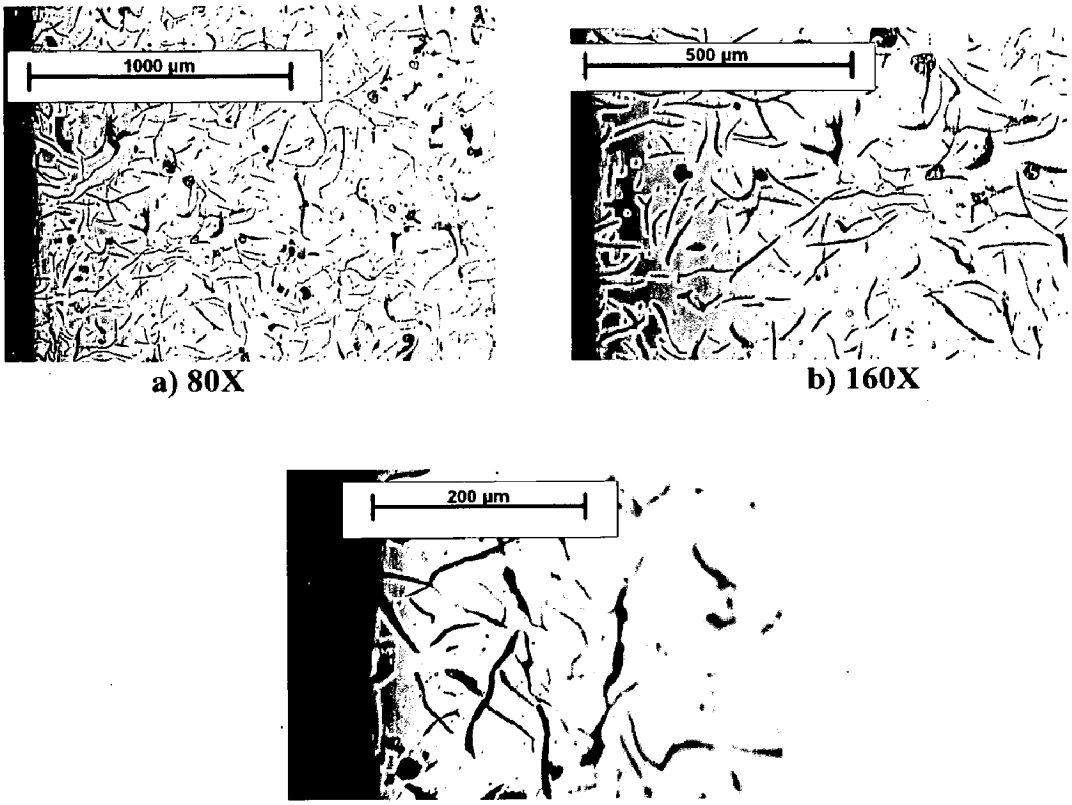

Fig. 7.35 Microstructure of the work material (Work sample: 9, Machining condition: $C_2EC_1SR_2F_3T_1SOP_3G_1$) (Scale 0.5)

The optical micrographs reveal that the microstructure of work material consists of a gray cast iron matrix having ferrite with graphite flakes dispersed through out (ASTM A48). The form of graphite can be categorized as 'Type A' flake graphite-random orientation (ASTM A247). The microstructure photographs of various work samples were taken in the vicinity of the processed work surface in order to identify the microstructural alterations, if any, which might occur in ECH.

From a close scrutiny of the microstructure photographs it can be concluded that electro-chemical honing process does not affect the work material microstructure. There are no indications of any microstructural alterations in the probable altered material zone such as microcracks, selective etching, IGA, micro defects such as inclusions and crevice-like defects, plastic deformations, metallurgical transformations including phase change. Thus, ECH can be an ideal choice for improving the surface integrity (and consequently the service life) of critical components of the tribological significance.

7.5.2 Microhardness Examination

The results of microhardness readings taken at the successively increasing distances from the processed work surface for the various work samples are reported in Chapter-VI (Tables 6.29 through 6.34). Three Vickers microhardness values were taken using 100g load at each successive incremental point from the machined surface with an automatic LEITZ Microhardness tester HMV-2.

The average of the microhardness values in probable altered material zone (PAMZ) was compared with the average of microhardness values taken at considerable distance from the edge to identify any significant changes due to application of ECH. Based on the discussions in Chapter-V, two different probable altered material zones (PAMZ), one involving the gentle machining conditions (extending upto 75μm depth from the machined

surface) and the other involving abusive machining conditions (which can extend to upto 500μm depth from the machined surface) were considered for the purpose of analysis. Material beyond 500μm depth was considered as the parent metal as it is very unlikely to be affected by the process. Results have been analyzed in the following steps:

i) Microhardness data were examined graphically using the average value plots to visualize the variation of microhardness value and identify the trend (if any) as a function of distance from the machined surface [Fig. 7.36-7.41].

ii) Statistical analysis using standard "one-way ANOVA", F-ratio and Tukey's test was performed to identify any significant changes resulted due to process application, assuming the PAMZ and the parent material are independent normally distributed populations with two different treatments: affected and unaffected by ECH respectively. Tukey's method is an excellent data snooping technique for comparing pairs of treatment means (Montgomery, 2004).

iii) The microhardness values recorded in PAMZ and base material were further analyzed using a powerful nonparametric alternative to the analysis of variance and F test, the rank transformation and the Kruskal-Wallis test, which is less likely to be distorted by nonnormality and unusual observations (Montgomery, 2004).

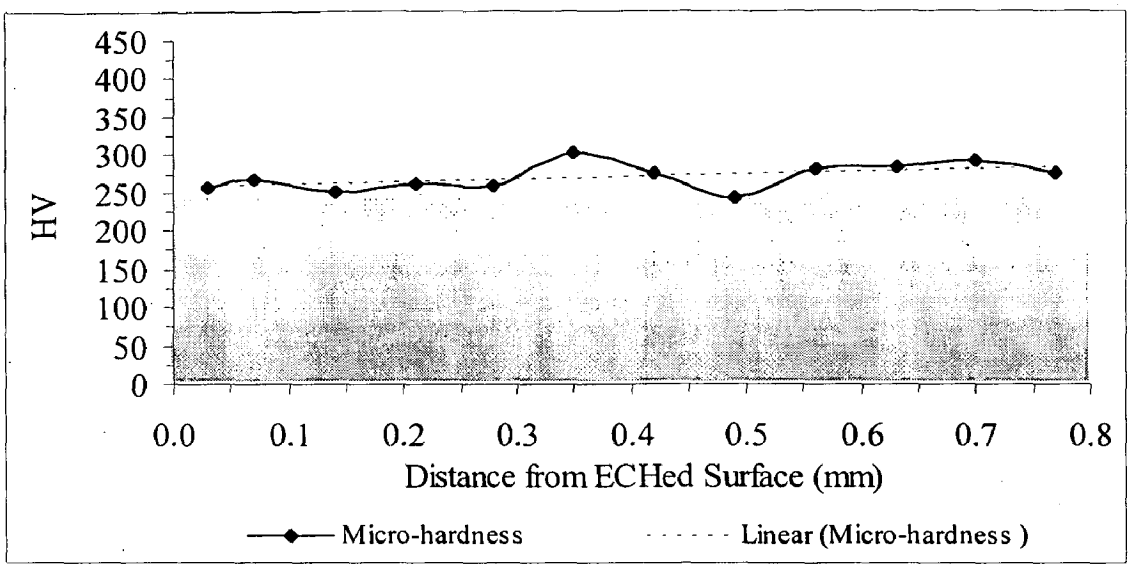

Fig. 7.36 Microhardness variation as a function of distance from the machined surface (Work sample: 32, Machining condition: $C_3EC_3SR_1F_2T_1SOP_1G_3$)

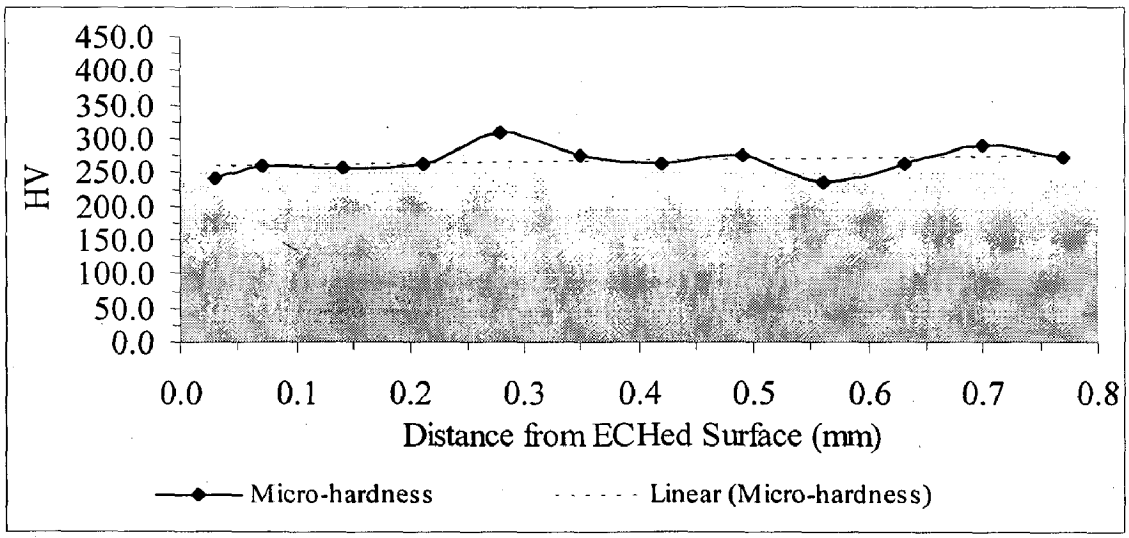

Fig. 7.37 Microhardness variation as a function of distance from the machined surface (Work sample: 49, Machining condition: $C_1EC_3SR_1F_3T_3SOP_2G_2$)

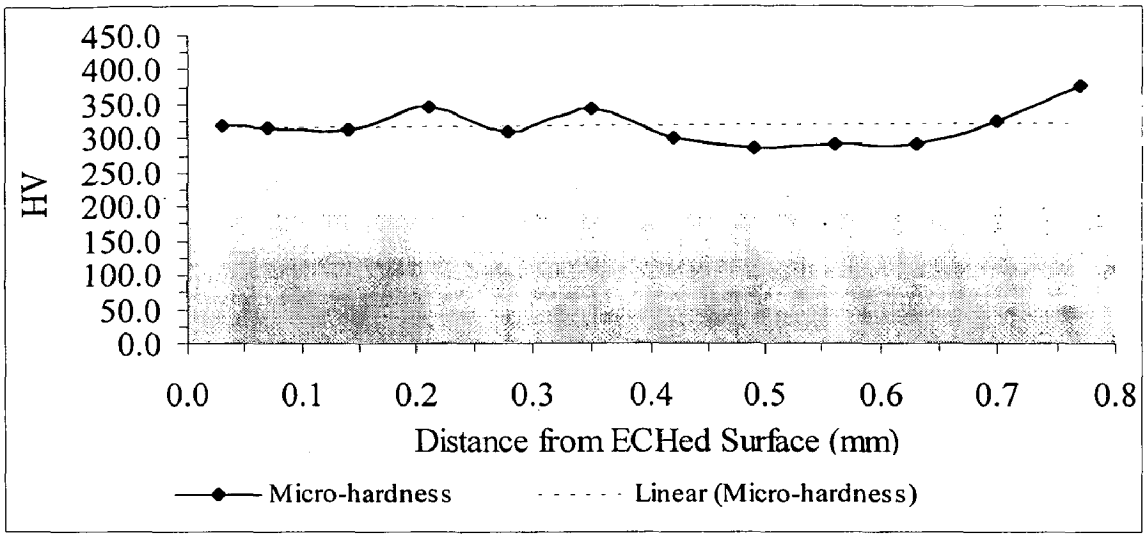

Fig. 7.38 Microhardness variation as a function of distance from the machined surface (Work sample: 50, Machining condition: $C_3EC_1SR_2F_1T_3SOP_1G_3$)

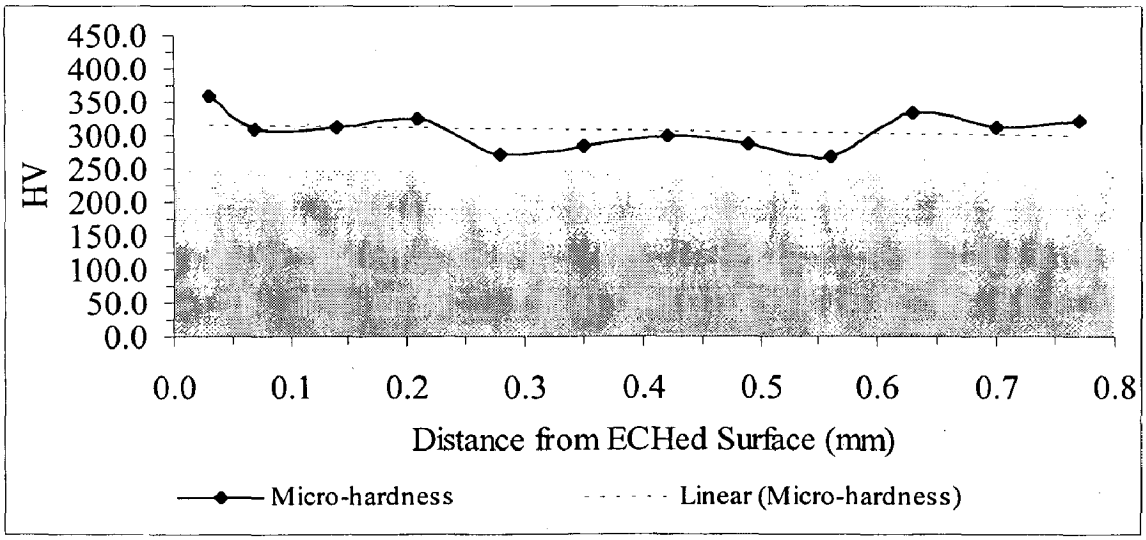

Fig. 7.39 Microhardness variation as a function of distance from the machined surface (Work sample: 34, Machining condition: $C_3EC_3SR_2F_3T_2SOP_2G_1$)

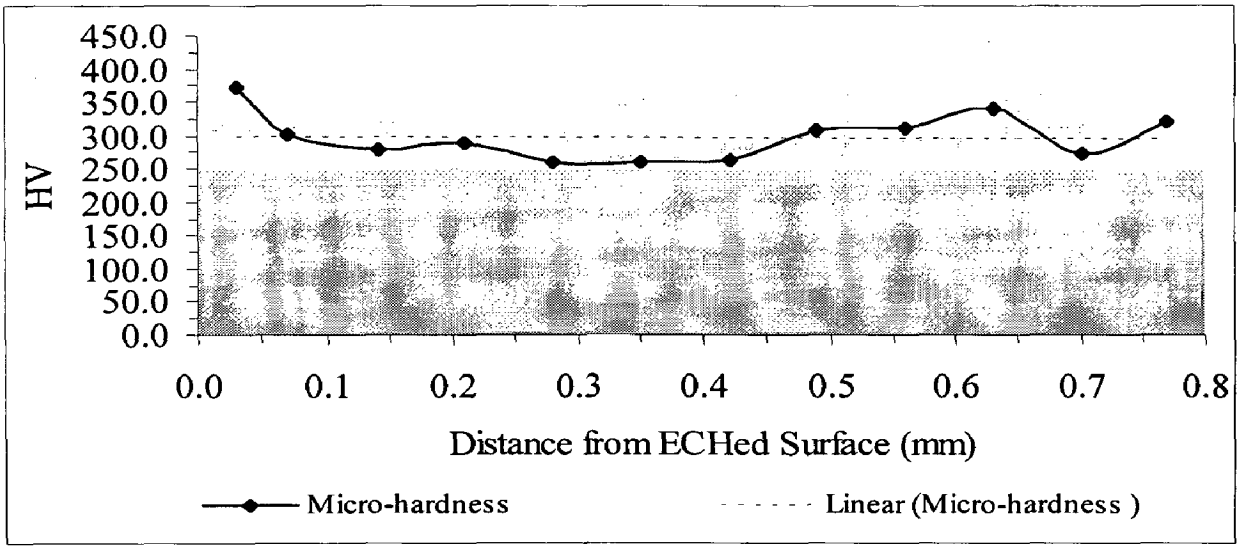

Fig. 7.40 Microhardness variation as a function of distance from the machined surface (Work sample: 9, Machining condition: $C_2EC_1SR_2F_3T_1SOP_3G_1$)

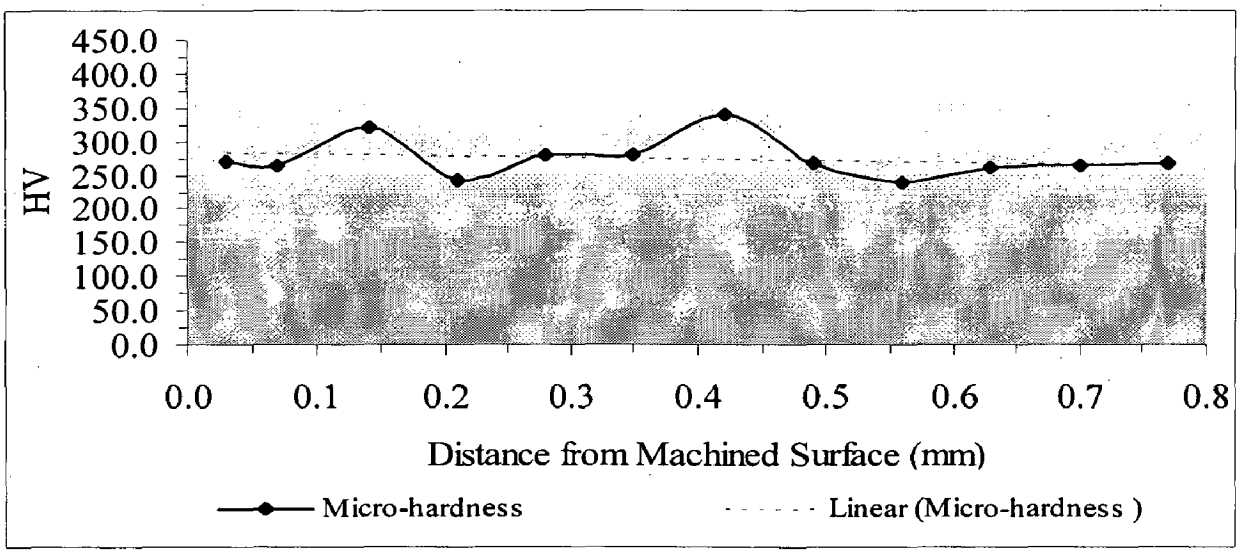

Fig 7.41 Microhardness variation as a function of distance from the machined surface (Work sample: R, Machining condition: before ECH)

A close scrutiny of the pattern of microhardness variation of different work samples with the distance from the machined surface reveals that no dominant overall trend of variation is present in the microhardness values as the functions of depths from the machined surface except the natural random variations due the work material properties. The presence of the randomly oriented soft phases of graphite flakes in the ferritic matrix of the gray cast iron material, as evident in the microstructural examinations of work samples, may be the reason for such random variations in microhardness values.

Another noticeable feature is that the microhardness values of the work samples in the PAMZs are contained within the range of random variations observed in the microhardness values except slightly higher near surface microhardness value associated with the trial conditions of work samples 34 and 9. An effect similar to that obtained with work samples 34 and 9 was observed by Bellows and Tishler (Machining Data Handbook, 1980) in case of electro-chemical machining followed by glass bead peening. They also noticed that with electro-chemical process without glass bead peening, the microhardness values in the vicinity of work surface could decrease.

As evident, the effect of ECH process on the microhardness alterations does not extend beyond a very narrow region near the processed surface (<75μm). Accordingly, there are no evidences of abusive machining conditions and therefore, within the range of the machining conditions employed, ECH process can be categorized as a gentle machining process.

The average microhardness values in PAMZ (<75μm depth from the machined surface) and base material (>500μm depth from the machined surface) are plotted in Fig. 7.42. It is seen that the average microhardness values in PAMZ for work samples 32, 49 and 50 are lower as compared to the base material while the trial conditions of work samples 34 and 9 resulted in a higher average microhardness value in PAMZ than that of their base

material. There is no appreciable difference observed in raw work sample. An analysis of the trial conditions involved with the processing of different work samples shows that the variation in the electrolytic conditions seems to be less influential for the quantum of change in microhardness values. For example, an opposite microhardness alteration results were achieved for work samples 32 and 34 while both the samples were processed with the same levels of the current intensity (C_3) and electrolyte concentration (EC_3). Therefore, the overall influence of the electrolytic conditions of the various trials can be assumed similar. The mechanical conditions of the trials of different work samples, however, are different in the sense that they involved different rotary to reciprocating speed ratio and stick-out pressure combinations. The difference between the average microhardness values in PAMZ and base material for different SR-SOP combinations is plotted in Fig. 7.43a. The difference of surface microhardness (30μm depth) and base material for different SR-SOP combinations is also given in Fig. 7.43b. Both the figures show an identical pattern of SR-SOP influence on microhardness values in PAMZ. It can be seen that an effect similar to ECM followed by glass bead peening is observed with the increasing levels of speed ratio and stick-out pressure in ECH. An improved surface microhardness values as well as average microhardness value in PAMZ are achieved with the increased levels of either of the speed ratio or the stick-out pressure. The effect of speed ratio seems, however, more pronounced. The processed components can be expected to have higher fatigue strength when subjected to dynamic loading. Statistical analysis using standard "one-way ANOVA", F-ratio and Tukey's test and K-W tests (conducted using rank transformation of the data) was performed for the microhardness data recorded in PAMZ (< 75μm depths) and base material (>500μm depths) to test for the significance of the microhardness alterations viz-a-viz random variations due to the microstructural composition of the work material. The ANOVA results for various work samples are given in Tables 7.67 to 7.72.

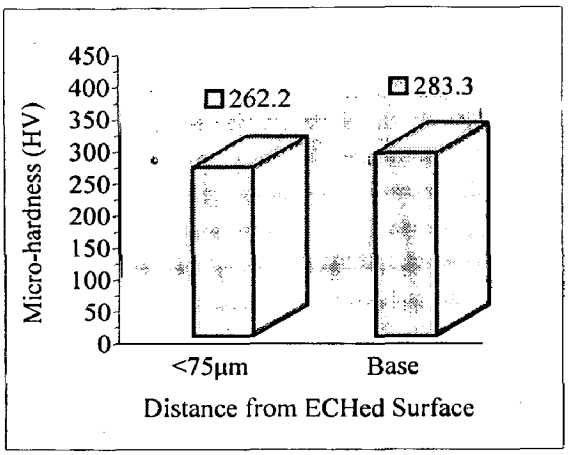

a) Work sample: 32

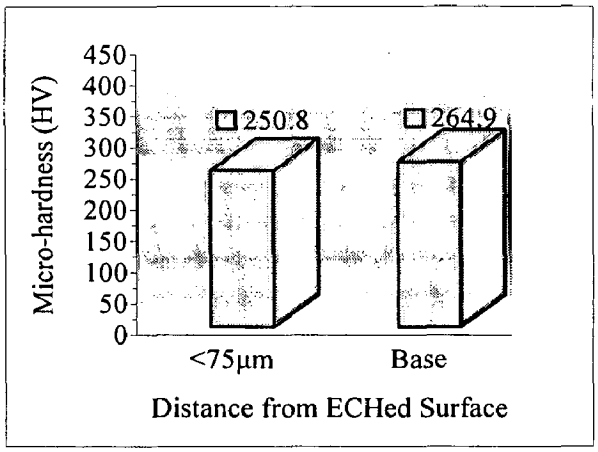

b) Work sample: 49

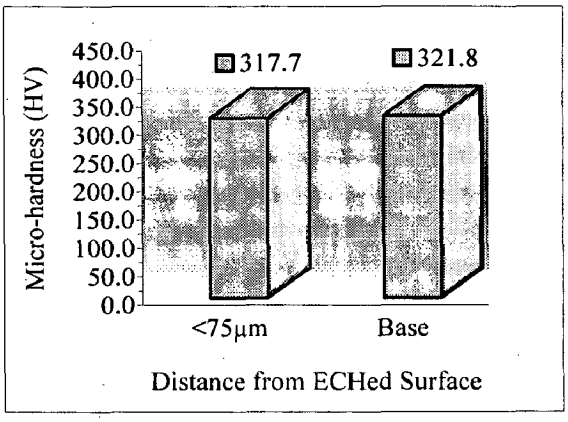

c) Work sample: 50

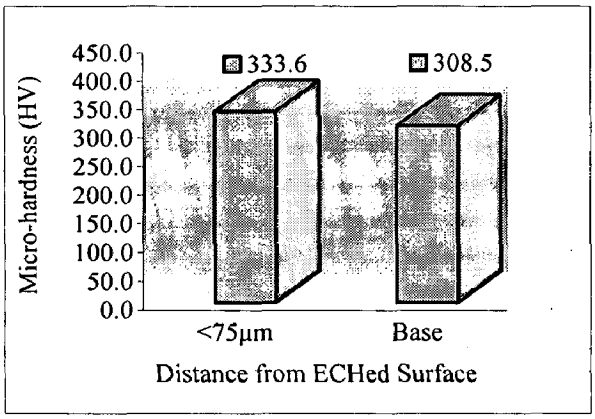

d) Work sample: 34

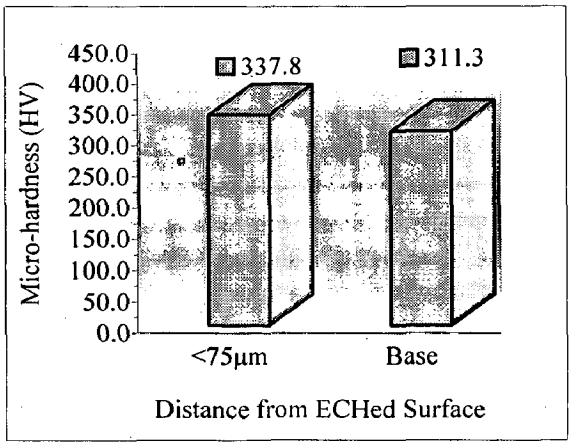

e) Work sample: 9

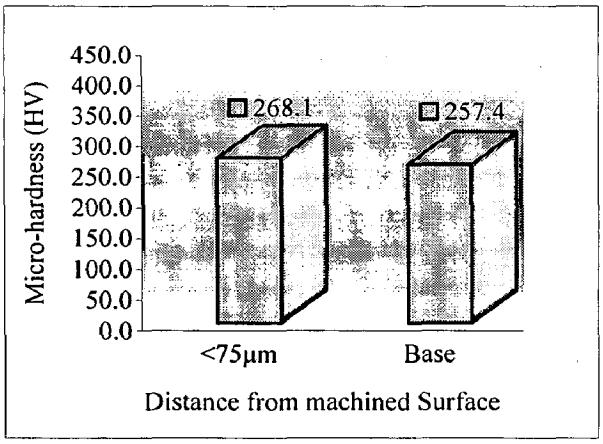

f) Work sample: R

Fig. 7.42 Average microhardness values in PAMZ and base material of different work samples

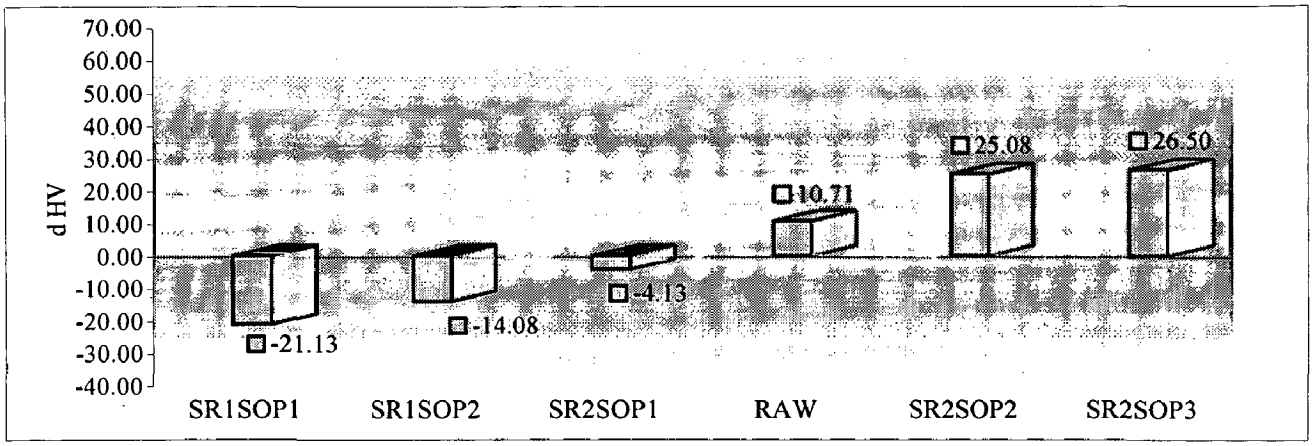

a) Average microhardness value in PAMZ as compared to base material

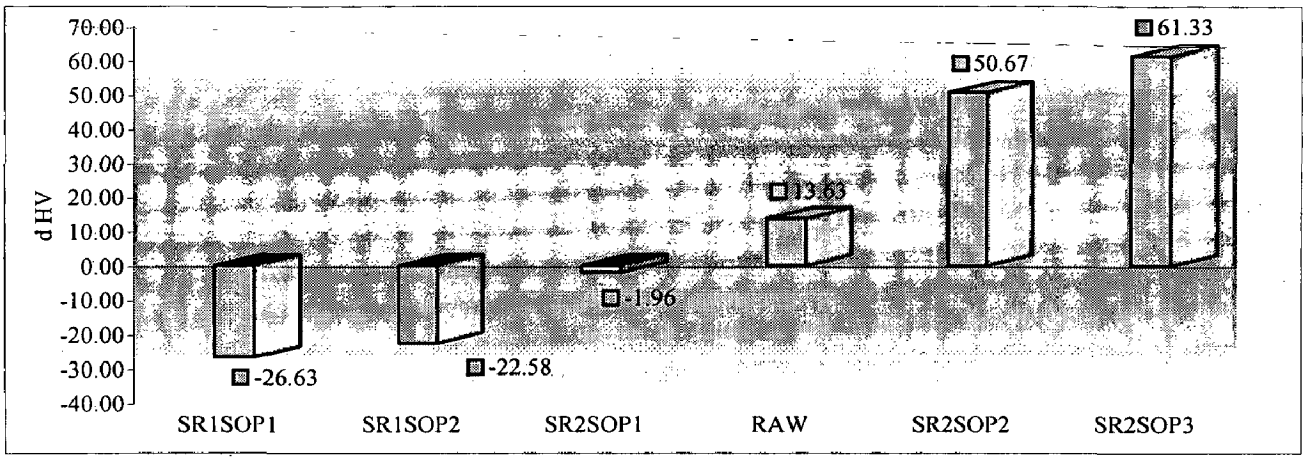

b) Average surface microhardness value (at 30μm) as compared to base material

Fig. 7.43 Difference between the average microhardness values in PAMZ and base material for different SR-SOP combinations

Table 7.67 ANOVA results for work sample 32

Source	SS	D.F.	MS	F	P-value
Location	215.93	1.00	215.93	0.15308	0.70077
Error	22564.99	16.00	1410.31		
Total	22780.92	17.00	22780.92		

Table 7.68 ANOVA results for work sample 49

Source	SS	D.F.	MS	F	P-value
Location	1009.83	1.00	1009.83	1.4155	0.25152
Error	11414.59	16.00	713.41		
Total	12424.42	17.00			

Table 7.69 ANOVA results for work sample 50

Source	SS	D.F.	MS	F	P-value
Location	68.06	1.00	68.06	0.02555	0.87499
Error	42615.06	16.00	2663.44		
Total	42683.13	17.00			

Table 7.70 ANOVA results for work sample 34

Source	SS	D.F.	MS	F	P-value
Location	2516.69	1.00	2516.69	1.05299	0.32008
Error	38240.71	16.00	2390.04		
Total	40757.40	17.00			

Table 7.71 ANOVA results for work sample 9

Source	SS	D.F.	MS	F	P-value
Location	2809.00	1.00	2809.00	0.31148	0.5845
Error	144293.50	16.00	9018.34		
Total	147102.50	17.00			

Table 7.72 ANOVA results for work sample R

Source	SS	D.F.	MS	F	P-value
Location	458.67	1.00	458.67	0.37331	0.54979
Error	19658.77	16.00	1228.67		
Total	20117.44	17.00			

In order to determine whether the mean microhardness value in the two locations i.e. PAMZ and base material are equal, F-test was performed. The decision was based on a comparison of the computed F value to a tabulated F value for a given alpha with the appropriate degrees of freedom. Alternatively, P-value could be used for decision-making. The P-value is defined as the smallest level of significance that would lead to rejection of the null hypothesis H_o: $\mu_1 = \mu_2$ (Montgomery, 2004). ANOVA results indicate that the average microhardness values in PMAZ and base material of work samples 32, 49, 50, 34, 9 and R are different at a significance level of 0.70077, 0.25152, 0.87499, 0.32008, 0.5845 and 0.54979 respectively. The lower confidence levels could have been due to the variation in microhardness data because of non-uniform microstructure of the work material. Tables 7.73 and 7.74 summarize the results of Tukey's method and K-W tests performed for PAMZ and base material microhardness data for various work samples. To perform K-W test the microhardness data of PAMZ and base material was transformed into ranks. The K-W test shows that the results of work samples 49 and 34 are significant at about 88% and 75.6% confidence levels respectively.

Table 7.73 Results of Tukey's method for microhardeness data

Work Sample No.	Critical Value of Tukey's Statistic ($T_{0.10}$) [alpha = 0.10]	Observed Difference of Average Microhardness in PAMZ and Base	Difference of Surface Microhardness and Base
32	32.80	(-) 21.13	(-) 26.63
49	23.33	(-) 14.08	(-) 22.58
50	45.07	(-) 04.13	(-) 01.96
34	42.69	(+) 25.08	(+) 50.67
9	82.93	(+) 26.50	(+) 61.33
R	30.61	(+) 10.71	(+) 13.63

Table 7.74 Results of K-W test for microhardeness data

Work Sample No.	K-W Statistic (H) [alpha=0.05]
32	0.05
49	2.56
50	0.32
34	1.38
9	0.01
R	0.32

Based on the above analysis it can be concluded that:

1. Effects similar to that 'electrochemical machining followed by shot peening with glass beads' on the surface and sub-surface microhardness values can be simultaneously realized in electro-chemical honing. Higher rotary to reciprocating speed ratios and stick-out pressures provide considerably higher surface as well as sub-surface microhardness values. The parts processed by ECH are expected to have better fatigue resistance during service.
2. Results indicate that the effect of ECH processing on microhardness alterations are confined to within a narrow near-surface depths which are normally noticed for manufacturing processes when operated with gentle touch. Accordingly ECH can be categorized as a gentle machining process at least within the domain of present experimentation studies.
3. The sub-surface microhardness changes were found significant at lower confidence levels in the present case due to the inherent variation in the microhardness values because of the non-uniform microstructural matrix of the work material. The results may, however, be verified for a homogeneous work material.

7.5.3 Residual Stress Evaluation

The residual stress test samples corresponding to the trial conditions of the work samples 32, 34, 9 and R used in microhardness examination, were subjected to X-ray diffraction (XRD) analysis to identify any change in surface residual stresses that might have occurred as a result of ECH application. Diffraction patterns were obtained on Bruker AXS D-8 Advance Diffractometer with CuK_α radiation and nickel filter at 30 mA and 40 kV. The specimens were scanned with a scanning speed of 1.5 kcps in 2θ range of 10 to 110° @ 2°/min goniometer rotation and the intensities were recorded. For the intensity peaks and corresponding values of 2θ, the interplanar spacing 'd' is calculated using the Bragg's law.

$$2d \sin\theta = n\lambda \tag{7.8}$$

where, λ is the wave length of CuK_α radiation used for the diffraction and is taken as 1.54 Å for estimating the 'd' values. Diffractometer being interfaced with Bruker DIFFRAC^{plus} X-Ray diffraction software provided 'd' values directly on the diffraction pattern. The X-ray diffraction patterns for the various work samples are given in Fig. 7.44 to 7.47.

Areas of various diffraction peaks were calculated using Origin 6.1 software. Assuming the intensity of the most prominent peak as 100%, the relative intensities were calculated for all the peaks, which were finally used for identification of the phases corresponding to prominent peaks with the help of inorganic ASTM X-ray diffraction data cards. Results show that in all the work samples, major peaks correspond to the various structures of Iron Carbide (Fe-C) as also revealed in the microstructural examination. The following relationship was employed for the calculation of residual stresses (Cullity and Stock, 2001; Zulfiqar et al, 2005):

$$\sigma_R = -\frac{E}{2(1+\nu)}\cot\theta_o \times \frac{\partial 2\theta}{\partial \sin^2\psi} \tag{7.9}$$

where, σ_R is the calculated surface residual stress, E the Young's modulus, ν the Poisson's ratio, θ_o the standard Bragg's angle, 2θ the diffract angle, and ψ the angle between the sample normal and diffraction plane normal. Partial derivatives were taken because all but the variables of interest are held fixed during the differentiation. Taking the values of E and ν for ASTM 35 gray CI as 100 GPa, and 0.28 respectively, change in compressive residual stresses for different work sample are given in Fig. 7.48. The value of the surface residual stress appears to be related to the speed ratio and stick-out pressure. Since the purpose of this analysis was to assess the change in surface residual stresses (if any) due to the influence of the ECH process, the state of raw work surface was taken as referencing condition. The distribution of stress inside the material is quite complex and depends on several factors which are not easy to control e.g. the matrix of gray cast iron, as seen in microstructural studies, is not well defined and uniquely oriented as the material itself is a form of mechanical mixture. This makes extremely difficult to determining precisely the stress distribution inside the material. Even though, there are clear indications of increased surface compressive residual stresses with higher speed ratio-stick-out pressure combinations in ECH. Effects similar to gentle ECM with glass bead peening are seen. Noticeably, the similar effects of speed ratio-stick-out pressure were observed on surface microhardness. Therefore, the ECHed components can be expected to provide a better fatigue endurance.

Based on the results of various studies conducted, ECH can be thought of an ideal choice for improving the surface quality including surface texture as well as the surface integrity of critical components resulting in increased service life and better service performance.

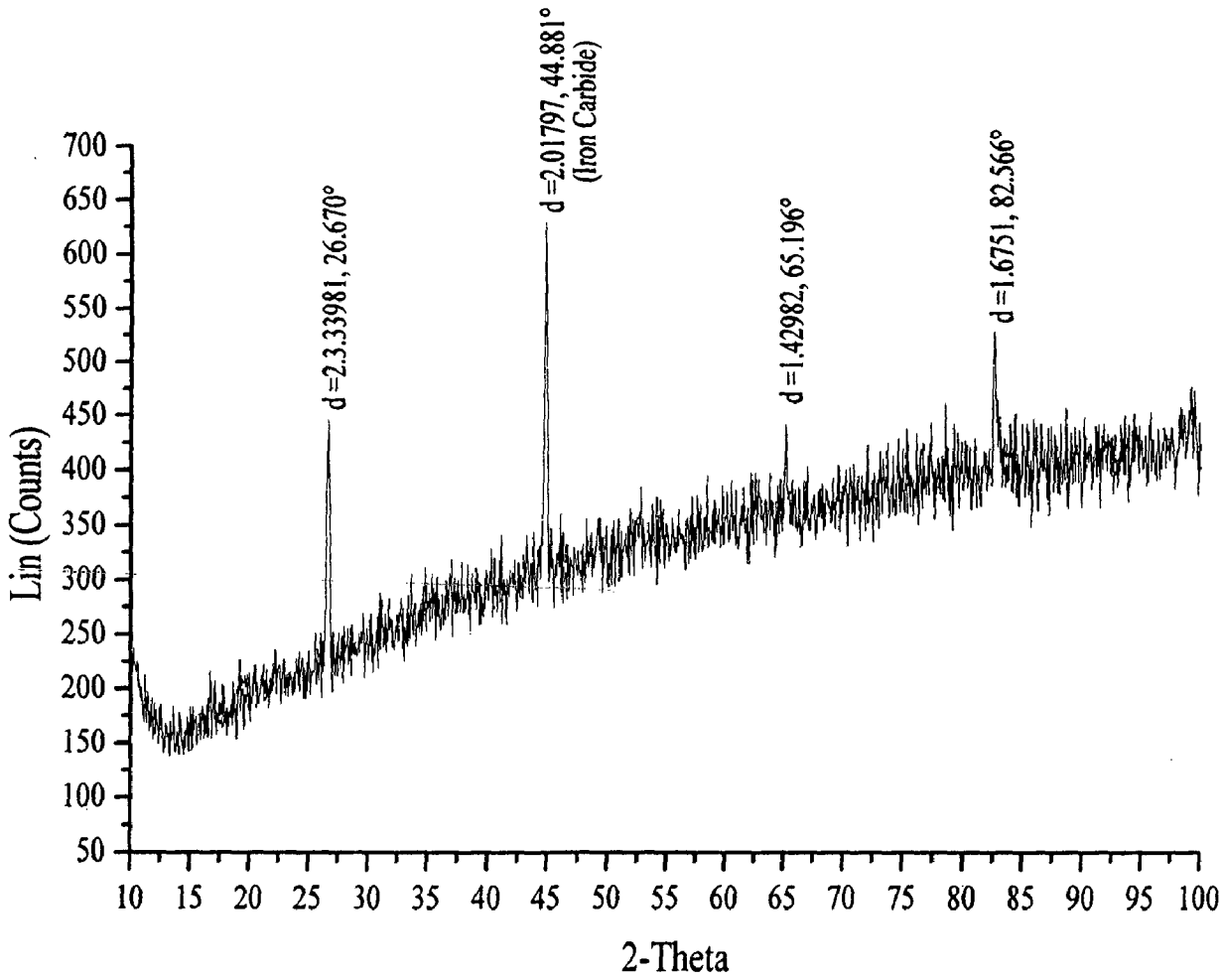

Fig. 7.44 X-ray diffraction pattern of ECHed work sample "32" (Machining condition: $C_3EC_3SR_1F_2T_1SOP_1G_3$)

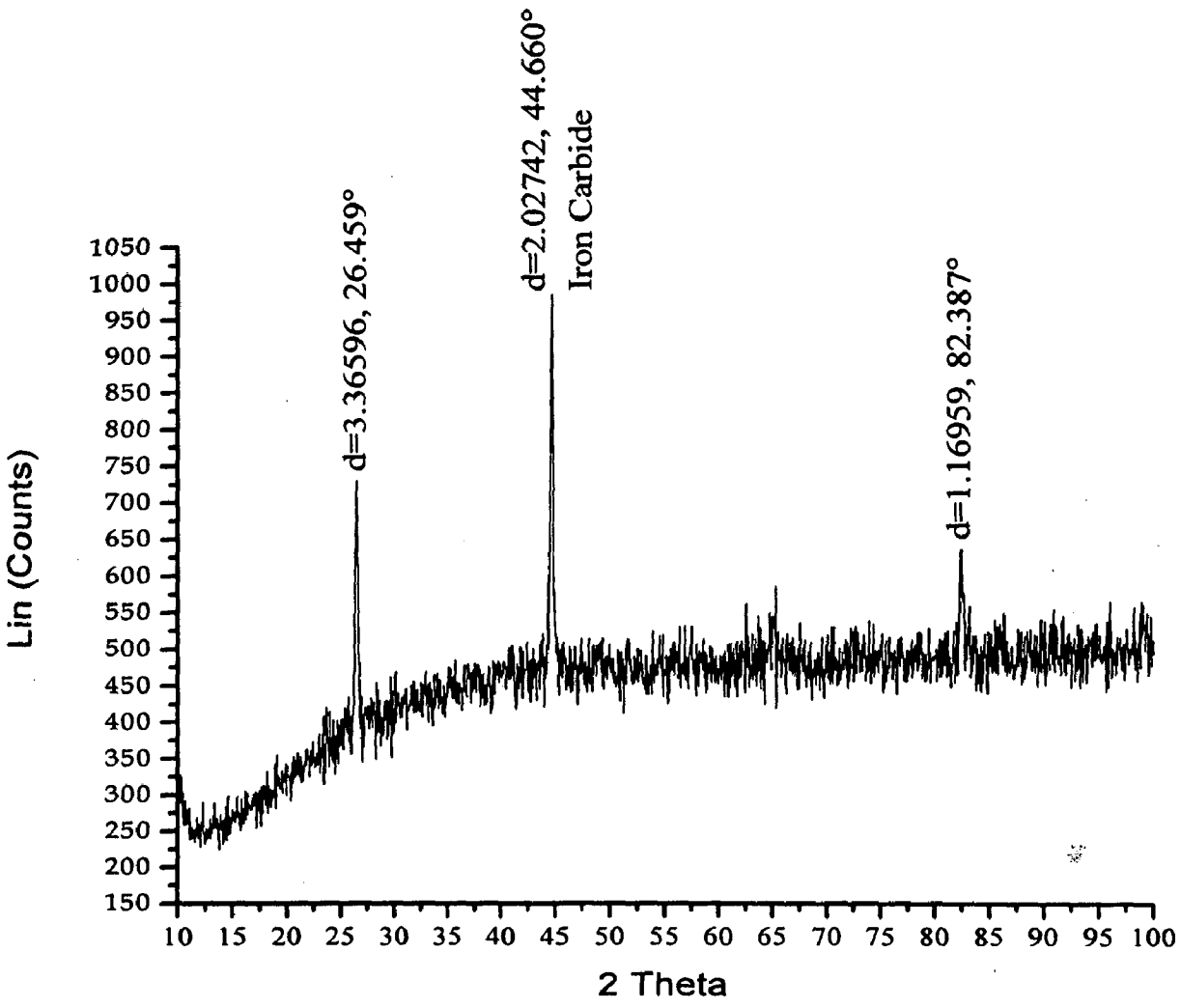

Fig. 7.45 X-ray diffraction pattern of ECHed work sample "34" (Machining condition: $C_3EC_3SR_2F_3T_2SOP_2G_1$)

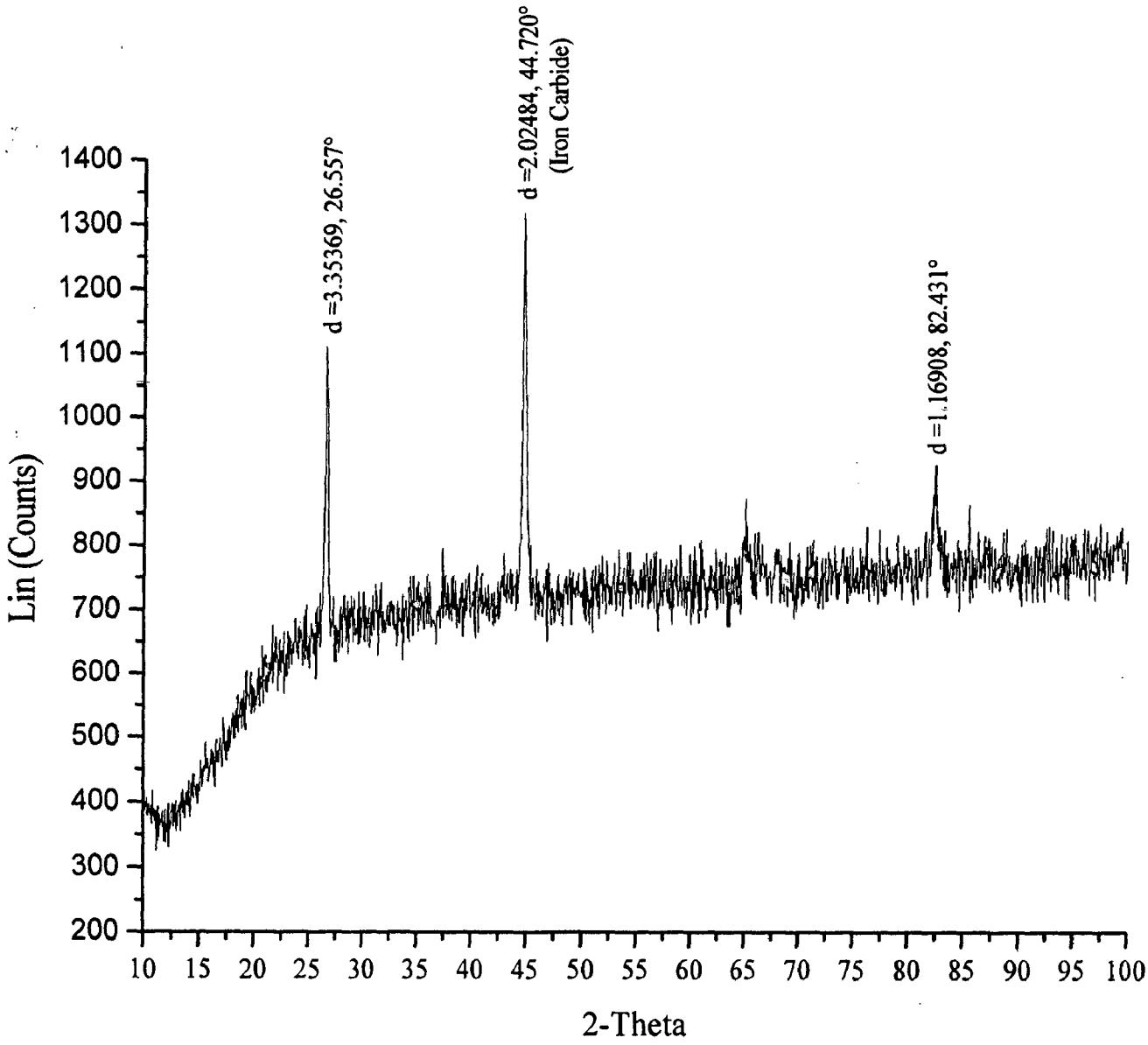

Fig. 7.46 X-ray diffraction pattern of ECHed work sample "9" (Machining condition: $C_2EC_1SR_2F_3T_1SOP_3G_1$)

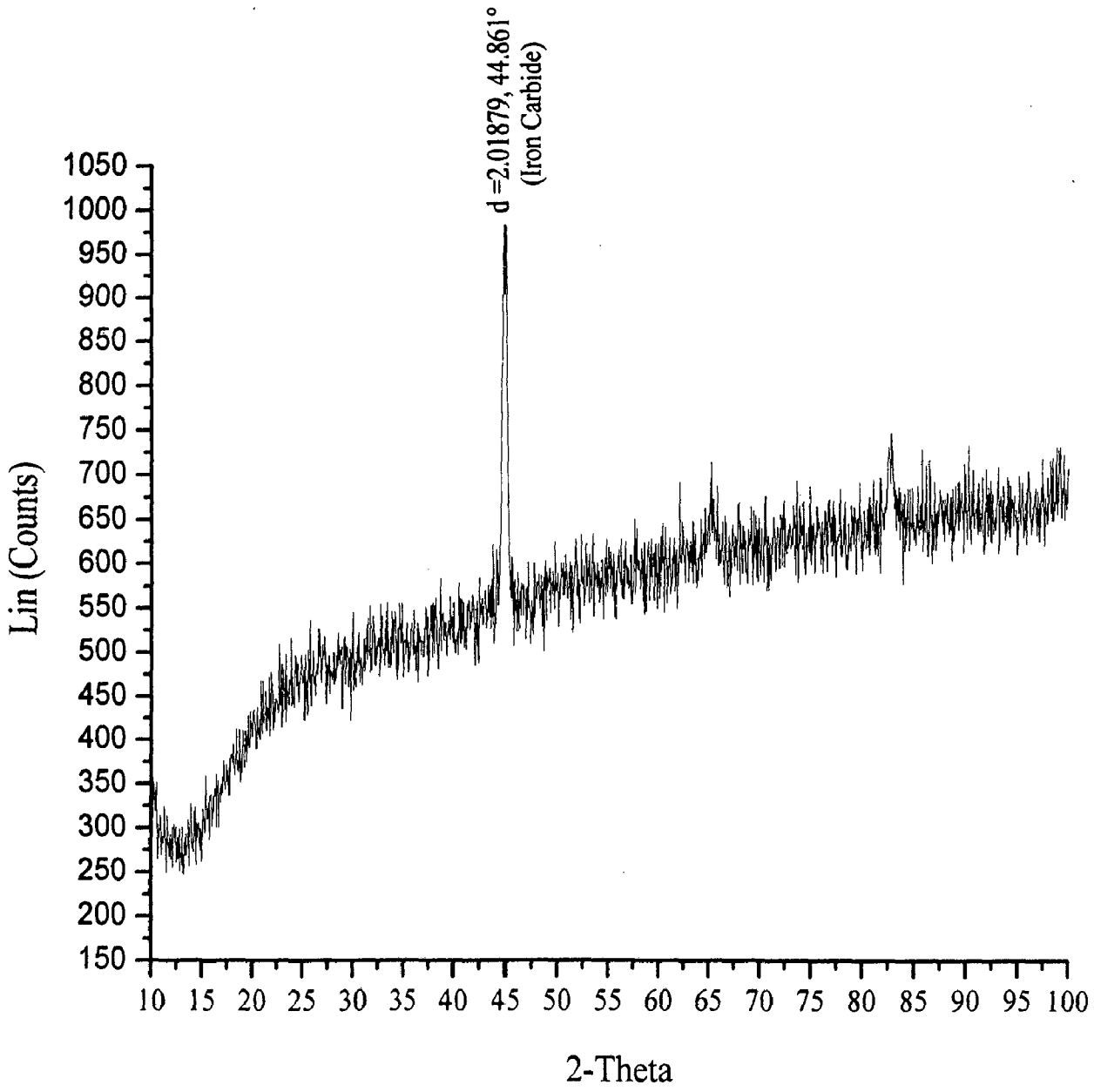

Fig. 7.47 X-ray diffraction pattern of work sample "R"
(Machining condition: before ECH)

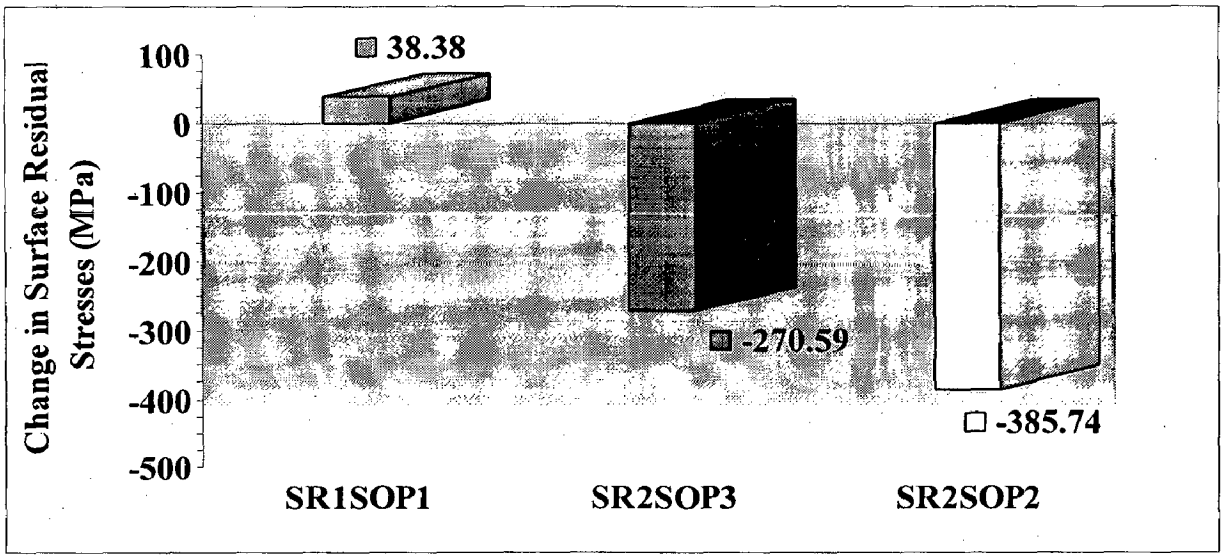

Fig. 7.48 Residual stress change in the work surface processed with different trial conditions (Negative sign indicates compressive stress)

Chapter-VIII
MULTI-PERFORMANCE MODELING AND OPTIMIZATION STUDIES

Taguchi design is proved to be an efficient tool to produce high quality products at low cost. The objective of Taguchi robust design is to determine the optimal parameter settings and making the process performance insensitive to various sources of variations. This approach can economically satisfy the need of problem solving and design optimization. The Taguchi technique allows the process optimization with minimum number of experiments without any need for process model development. Thus, by this method, it is possible to reduce the time and cost of experimental investigations and thus enhance the performance. Most of the investigations on Taguchi application are on the optimization of a single performance characteristic (Ross, 1988), as the original technique was designed to optimize a single response. The optimization ECH process, using Taguchi methodology, concerning individual performance characteristics has been carried out in Chapter-VII. As noticed that a single setting of process parameters may be optimal for one performance characteristic but the same setting may yield poor results for other performance characteristic. A need, therefore, arises to obtain one single optimal setting of the process input parameters so that the product or process can achieve an optimal or near optimal results for different performance criteria.

Process modeling and multi-response optimization have become vital for utilizing the full potential of the manufacturing processes to meet the challenges of stringent requirements on surface quality, tolerances and production rates demanded by the manufacturing community in globally competitive scenario.

Many heuristic methodologies were evolved to solve the multi-performance optimization problems. Lind et al. (1960), Floros and Chinnan (1998) used the graphical approach for multi-performance optimization in which a region is examined for the overlapping response contours and a condition is identified which is reasonably good for all the responses. This method, however, is not very useful when the performance characteristics are more than three. In Dual response surface technique (Myers and Carter, 1975) a primary response function is optimized restricting second function to desirable values. Several modifications have been suggested to the original Taguchi design for solving multi-response optimization problems. The desirability function (DF) approach, developed by Harrington, involves the transformation of each estimated response variable into a desirability value and finally combining them into a single function to provide the overall desirability of the multiple performance characteristics (Harrington, 1965; Derringer and Suich, 1980). The method is basically a trade-off between the various performance characteristics. Khuri and Conlon (1981) proposed a Generalized Distance Approach (GDA) in which the deviations from the ideal optimum measured as distance function are minimized to get favorable compromise conditions for all the responses. This method is advantageous in that both the correlations among the responses as well as their individual variances are considered. Byrne and Taguchi (1987) presented a case where the performance characteristics were independently optimized using Taguchi approach and then the results were compared subjectively to select the best levels in terms of performance characteristics of interest. Logothetis and Haigh (1988) used multiple regression and linear programming for multi-response optimization considering five responses by Taguchi Method. The objective function was optimized sequentially considering one of the responses as primary while ignoring the possible correlations among the responses. Shiau (1990) used weighted S/N ratios for representing the overall performance of a process. Phadke (1989) presented a

case of product with multiple characteristics with a weight assigned to each quality characteristic from practical experience. Elsayed and Chen (1993) presented a model using loss function to determine the optimal settings of process parameters of a production process for products having multiple characteristics. Pignatiello (1993) used squared deviation from the target and variance to form an expected loss function for optimizing multiple responses. A procedure involving three simultaneous functions, the weighted loss function, desirability function and distance function was presented by Layne (1995). Tong and Su (1997) proposed multi-response optimization with Taguchi method by fuzzy multiple attribute decision making using multi-response S/N ratio determined through the integration of the quality loss for all the responses. Antony (2000) introduced principal component analysis (PCA) for the multi-response optimization of submerged arc welding parameters. In PCA, a smaller set of uncorrelated principal component variables are derived through transformation of a set of correlated response variables (Johnson, 1998). Also, when the chosen principal component with only less variation can be explained by total variation, the multi-performance index is not evident enough to replace multi-response (Jeyapaul et al., 2005).

The methodology of Taguchi's quality loss function, in association with other tools, has proved to be an efficient optimization tool for multiple process performance characteristics. The method has been employed in the recent past for the optimization of several processes such as V-Process casting (Barua et.al., 1997), gas tungsten arc welding (Tarng and Yang, 1998), face milling (Lin, 2002), magnetic-field assisted abrasive flow machining (Singh et.al., 2002) and hot turning (Tosun and Ozler, 2004).

In the recent years, the use of Artificial Intelligence techniques (e.g. neural networks, genetic algorithms and fuzzy logic) for process modeling and multi-performance characteristic optimization is also gaining attraction. Wang and Chou (2005) used a neural-Taguchi-based quasi time optimization control strategy for chemical-mechanical polishing

process (CMP) by combining neural networks and Taguchi experimental method. The CMP process was modeled for weighted S/N performance characteristics using the neural network with cascade steepest descendant learning algorithm. Cook et.al (2000) developed an integrated NN-GA technique for process parameter optimization of the particle-board manufacturing process. Petterson et.al. (2003) modeled the burden layer thickness in a blast furnace as a function of potential process variables using neural networks with simultaneous training of weights and connections using evolutionary algorithm. A part of neural net was trained using GA and nearly optimized values provided by GA were used as inputs to the rest linear least square nodes, thus facilitating a rapid convergence. The hybrid NN-GA approach has evolved considerable interest in areas like alloy design, polymer processing, welding, metal machining (both traditional as well as non-traditional) (Chakraborti, 2004). The hybrid neural network (NN) and genetic algorithm (GA) has been used for the modeling and multi-performance optimization of various advanced manufacturing processes such as electric discharge machining process (Wang et.al., 2003), Abrasive Water Jet Cutting (Srinivasu et.al., 2004) and electro-jet drilling process (Sen and Shan, 2006).

The use of Fuzzy Logic in combination with NN and GA has also started gaining momentum in solving many multi-objective optimization problems. A multiple adaptive neuro-fuzzy inference system (MANFIS), an extension of a single output neuro-fuzzy inference system (ANFIS), was used to model the response surface of a chemical process and the resulting multiple objective decision making problem was optimized by a genetic algorithm (Cheng et.al., 2002). Ostermark (2000) proposed a hybrid genetic fuzzy neural network (GFNN) for solving the multigroup classification problems. A key feature of this approach is the genetic adaptation of membership functions to new data, i.e. learning is reflected in the shape of the membership functions using evolutionary techniques combined with the fuzzy neural computations. In other instances, a Fuzzy logic based Taguchi method

was used by Lu and Antony (2002) for a multi-response optimization case study and Sen (2005) for multi-performance optimization of EJD process.

In the present investigation, the multi-performance modeling and optimization of electro-chemical honing (ECH) process has been performed utilizing the three most effective approaches used in the recent years. Applications of the 'Utility based Taguchi Approach', 'Taguchi-NN-GA Multi-Performance Optimization Control Strategy' and 'Fuzzy-Taguchi Inference Application' for multi-performance optimization of ECH process have been discussed in this chapter.

8.1 UTILITY BASED TAGUCHI APPROACH TO MULTI-PERFORMANCE OPTIMIZATION

The whole concept of the modern quality control and improvement programs revolves around the 'customer satisfaction' (ISO 9001:2000). The utility of a particular product's feature measures its usefulness for the product's functional requirements. There may be several features (attributes) of relevance for the utility of a particular product though with varying importance in the eyes of evaluator (customer). Due to the stringent functional requirements imposed on the critical components now a days, a lot of emphasis is required to be placed on the overall utility of the products that are produced by a manufacturing process. Therefore, it is vital to optimize the manufacturing process in a way that maximizes the overall utility of the product. The overall utility of a product is the sum of utilities of each of its quality characteristics.

If x_i is the measure of effectiveness of a process performance characteristic i (contributing to the i^{th} attribute of the product) and there are n performance characteristics evaluating the outcome, then overall utility function can be expressed as (Derek, 1982):

$$U(x_1, x_2, ..., x_n) = f\,[U_1(x_1), U_2(x_2), ..., U_n(x_n)] \tag{8.1}$$

If the function is assumed linear, then the overall utility can be estimated as:

$$U(x_1, x_2, ..., x_n) = \sum_{i=1}^{n} W_i U(x_i) \tag{8.2}$$

where W_i is the weightage assigned to the i^{th} performance characteristic such that the sum of weightages for all the n process performance characteristics is equal to 1.

The multi-performance optimization of the process maximizing the overall utility in-turn provides the enhanced functional value for the product. The utility values of different process performance characteristics are determined on the basis of a preference scale constructed for each performance characteristic. These scales are weighted to obtain an

overall utility value of the multiple performance characteristics. The weighing is done to satisfy the test of indifference on the various performance characteristics. A logarithmic preference scale is desirable (Gupta and Murthy, 1980). The minimum acceptable value for each performance characteristic is set out at 0 preference number and the best available performance is assigned a preference number of 9. For a logarithmic scale the preference number (P_i) is given by (Gupta and Murthy, 1980):

$$P_i = A \log \left(\frac{x_i}{x_i'} \right) \tag{8.3}$$

where x_i are the values of performance characteristic i, x_i' is the minimum acceptable value of i^{th} performance characteristic and A is a constant. At the optimum value (x_i^*) of the i^{th} performance characteristic, $P_i = 9$. Therefore,

$$A = \frac{9}{\log \frac{x_i^*}{x_i'}} \tag{8.4}$$

The next step is to assign weights or relative importance to various performance characteristics considered for optimization. This assignment is subjective and based on experience. Moreover, it depends on the end use of the product or it may depend on the customers' preference. The weightages should be assigned such that the following condition holds:

$$\sum_{i=1}^{n} W_i = 1 \tag{8.5}$$

The overall utility can be calculated as:

$$U_j = \sum_{i=1}^{n} W_i P_i \tag{8.6}$$

where j is the product index.

8.1.1 Algorithm of 'Utility based Taguchi Approach' for Multi-Performance Optimization

Steps involved in the 'Utility based Taguchi approach' algorithm for the multi-response optimization are given below:

1. Using Taguchi experimental design and analysis, find optimal value for each selected process performance characteristic.
2. Based on the optimal value and minimum acceptable level, construct a preference scale for each performance characteristic. (Eqs. 8.3 and 8.4).
3. Assign weightages (W_i) based on the experience and customer preference, satisfying equation 8.5.
4. Find overall utility values for various experimental trials considering all the performance characteristics involved in multi-performance optimization.
5. Use these values as raw responses of the experimental trial conditions of selected experimental matrix. If the trials are repeated, find S/N ratios (HB type), as the utility is a higher-the-better type characteristic.
6. Analyze the results as per the procedure suggested by Taguchi §6.2.4).
7. Find the optimal settings of the process parameters for mean and S/N utility based on the analysis in step 6.
8. Predict the optimal values of different performance characteristics by using the optimal levels of the significant parameters determined in step 7.
9. Verify the optimal results by conducting confirmation experiments.

8.1.2 Multi-Performance Optimization of ECH Process using Utility Based Taguchi Approach

It was observed in Chapter VII that the optimal settings of process input parameters for different performance characteristics were conflicting in nature. For example, stick grit size level 2 (G_2) provided the maximum PICyl and PIOR values while G_1 was found suitable for achieving the highest diametral increase rate. In the case of process micro-geometrical performance characteristic viz. PIR_a and PIR_{max}, the same two levels of the grit-size were indifferent for optimal values.

The following five different multi-performance cases of electro-chemical honing process have been modeled and optimized using "Utility based Taguchi Approach":

1. Model 1: Percent Improvements in Surface Roughness R_a and Out-of-Roundness (PIR_a-PIOR)
2. Model 2: Percent Improvements in Surface Roughness R_a and Cylindricity (PIR_a-PICyl)
3. Model 3: Percent Improvement in Surface Roughness R_a and Diametral Increase Rate (PIR_a-DIR)
4. Model 4: Percent Improvements in Surface Roughness R_a, Out-of-Roundness and Diametral Increase Rate (PIR_a-PIOR-DIR)
5. Model 5: Percent Improvements in Surface Roughness R_a, Cylindricity and Diametral Increase Rate (PIR_a-PICyl-DIR).

Being the most dominant machining criterion, the PIR_a has been included in all the models. The optimal results of individual process performance characteristics as determined in Phase-III Stage-I studies are summarized in Table 8.1.

Table 8.1 Optimal results of ECH process performance characteristics (Phase-III)

Process Performance Characteristic	Optimal Settings of Process Parameters	Process Parameters Significant at 95% Confidence Level	Predicted Optimal Value of Performance Characteristic (x_i^*)	Minimum acceptable Value of Performance Characteristic ($x_i^'$)
PIR_a	C_3 EC_3 SR_1 F_2 T_3 SOP_3 G_2	C^*, EC^*, SR^*, T, SOP, G	88.68 %	60.00 %
PIOR	C_3 EC_3 SR_2 F_2 T_2 SOP_3 G_2	$C^{\#}$, $EC^{\#}$, $SR^{\#}$, SOP, G	67.00 %	15.00 %
PICyl	C_3 EC_3 SR_2 F_2 T_2 SOP_3 G_2	$C^{\$}$, $EC^{\$}$, $SR^{\$}$, SOP, G	89.04 %	20.00 %
DIR	C_3 EC_3 SR_3 F_2 T_2 SOP_3 G_1	$C^{\&}$, $EC^{\&}$, $SR^{\&}$, F SOP, G	63.39 (μm/min)	5.00 (μm/min)

** Interactions C-EC and C- SR are significant.*
 # Interactions C-EC and EC-SR are significant.
$ Interactions C-EC, C-SR and EC-SR are significant.
& Interactions C-SR and E -SR are significant.
Insignificant parameters are set at economic levels.
C: Current Intensity, EC: Electrolyte Concentration, SR: Speed Ratio, F: Electrolyte Flow Rate, T: Electrolyte Inlet Temperature, SOP: Stick-out Pressure, G: Grit Size.

The experimental trial results of Phase-III studies for PIR_a, PIOR, PICyl and DIR are given in Tables 6.19, 6.23, 6.25 and 6.27 respectively in Chapter-VI. Since all the process performance characteristics are higher-the-better type, the minimum acceptable value of the respective performance characteristic has been decided based on minimum of the experimental trial results.

A preference scale, as given in Table 8.2, has been constructed for each process performance characteristic using the values shown in Table 8.1 and equations 8.3 and 8.4.

Table 8.2 Preference scales for ECH process performance characteristics (Raw Data-Phase-III)

Process Performance Characteristic	Preference Scale
Percent Improvement in R_a (PIR_a)	$P_{PIRa} = 53.04 \log (x_i / 60)$
Percent Improvement in Out-of-Roundness (PIOR)	$P_{PIOR} = 13.85 \log (x_i / 15)$
Percent Improvement in Cylindricity (PICyl)	$P_{PICyl} = 13.88 \log (x_i / 20)$
Diametral Increase Rate (DIR)	$P_{DIR} = 8.16 \log (x_i / 5)$

CASE-I: TWO PERFORMANCE CHARACTERISTICS

8.1.3 Model 1: PIR_a-PIOR

The overall utility values calculated considering together the PIR_a and PIOR for different trial conditions of Phase-III experimental studies are recorded in Table 8.3. The utility values have been determined assigning equal weightages to both the process performance characteristics in equation 8.6 (i.e. $W_{PIRa} = W_{PIOR} = 0.5$), on the assumption that both the performance characteristics are equally important. The $(S/N\ ratio)_{HB}$ for different trial conditions are also calculated in Table 8.3 as the utility value is higher-the-better type characteristic.

The overall mean and S/N utility data for PIR_a-PIOR have been analyzed using analysis of means (ANOM) and analysis of variances (ANOVA) based on the approach described in Section 6.2.4 of Chapter VI. The ANOM results are given in Tables 8.4 and 8.5 respectively for raw and S/N utility and the response plots are shown in Fig. 8.1. The pooled ANOVA results are given in Tables 8.6 and 8.7. The ANOVA results indicate that the electrolyte concentration (EC), stick-out pressure (SOP) and stick grit-size (G) and electrolyte concentration-speed ratio (EC-SR) interaction influence both the mean and S/N utility significantly at an alpha of 0.05. While the current intensity(C), interactions C-EC and C-SR affect only the mean (raw) utility. The average utility and S/N ratios for interactions C-EC, C-SR and EC-SR are produced in Tables 8.8, 8.9 and 8.10 respectively. The respective interaction plots are illustrated in Fig. 8.2.

Table 8.3 Utility values (PIR_a-PIOR)

Trial No.	Utility Values (UTILS)		S/N Ratio (dB)
	Y_{R1}	Y_{R2}	
1	2.14	2.87	7.69
2	3.67	4.05	11.70
3	4.71	4.13	12.85
4	2.66	2.66	8.51
5	4.80	3.81	12.51
6	6.09	6.28	15.82
7	7.16	6.62	16.74
8	5.65	4.15	13.49
9	3.33	3.48	10.64
10	2.76	3.44	9.66
11	4.52	5.05	13.56
12	4.42	4.09	12.55
13	3.56	2.89	10.03
14	4.85	5.12	13.94
15	5.10	5.79	14.67
16	6.81	6.03	16.10
17	6.43	6.85	16.43
18	1.90	2.63	6.76
19	6.20	5.79	15.54
20	2.72	2.47	8.25
21	6.27	6.32	15.98
22	4.36	4.43	12.86
23	6.03	6.66	16.02
24	1.92	2.48	6.65
25	4.75	5.72	14.27
26	6.72	7.40	16.95
27	8.42	8.53	18.56
	$\bar{T}_{UTIL}$ = Overall Mean of UTIL		
	= 4.77		= 12.92 dB

*R1, R2 represent repetitions.

Table 8.4 Average and Main Effects (Utility: PIR_a-PIOR: Raw Data)

Process Input Parameter	Average Utility (UTILS)			Main Effects (UTILS)	
	L1	L2	L3	L2-L1	L3-L2
C	4.35	4.57	5.40	0.22	0.83
EC	4.20	4.42	5.70	0.22	1.28
SR	4.49	5.05	4.77	0.56	-0.28
F	4.97	4.78	4.57	-0.19	-0.20
T	4.64	4.54	5.14	-0.10	0.60
SOP	3.82	5.00	5.49	1.18	0.49
G	4.96	5.76	3.60	0.81	-2.17
C-EC	4.68	4.97	4.67	0.29	-0.30
C-SR	4.75	4.63	4.93	-0.11	0.30
EC-SR	4.74	4.40	5.17	-0.34	0.76

L1, L2 and L3 represent average values of raw data of response of corresponding parameters at levels 1, 2 and 3 respectively. L2-L1 is the average main effect when the corresponding parameter changes from level 1 to level 2. L3-L2 is the average main effect when the corresponding parameter changes from level 2 to level 3.
* 95 % Confidence Limit (CI_1) = ± 0.30
C: Current Intensity, EC: Electrolyte Concentration, SR: Speed Ratio, F: Electrolyte Flow Rate, T: Electrolyte Inlet Temperature, SOP: Stick-out Pressure, G: Grit Size.

Table 8.5 Average and Main Effects (Utility: PIR_a-PIOR: S/N Data)

Process Input Parameter	Average S/N Utility (dB)			Main Effects (dB)	
	L1	L2	L3	L2-L1	L3-L2
C	12.22	12.63	13.90	0.42	1.26
EC	11.98	12.33	14.44	0.36	2.10
SR	12.38	13.65	12.72	1.27	-0.93
F	13.25	13.10	12.40	-0.15	-0.70
T	12.62	12.51	13.62	-0.12	1.11
SOP	11.00	13.38	14.37	2.38	0.99
G	13.44	14.82	10.49	1.38	-4.34
C-EC	12.65	13.24	12.86	0.59	-0.38
C-SR	12.57	12.72	13.46	0.16	0.73
EC-SR	12.68	12.15	13.92	-0.53	1.78

L1, L2 and L3 represent average values of S/N data of response of corresponding parameters at levels 1, 2 and 3 respectively. L2-L1 is the average main effect when the corresponding parameter changes from level 1 to level 2. L3-L2 is the average main effect when the corresponding parameter changes from level 2 to level 3.
* 95 % Confidence Limit (CI_1) = ± 1.47
C: Current Intensity, EC: Electrolyte Concentration, SR: Speed Ratio, F: Electrolyte Flow Rate, T: Electrolyte Inlet Temperature, SOP: Stick-out Pressure, G: Grit Size.

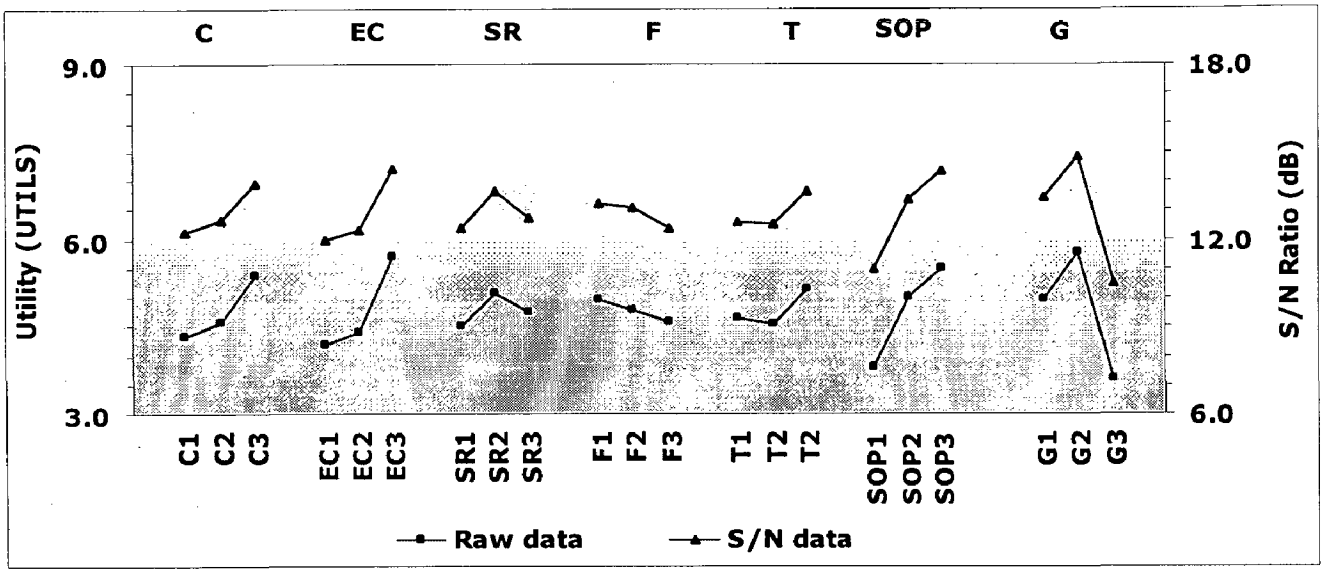

Fig. 8.1 Effects of process parameters on Utility: PIR_a-PIOR and S/N ratio (Main Effects)

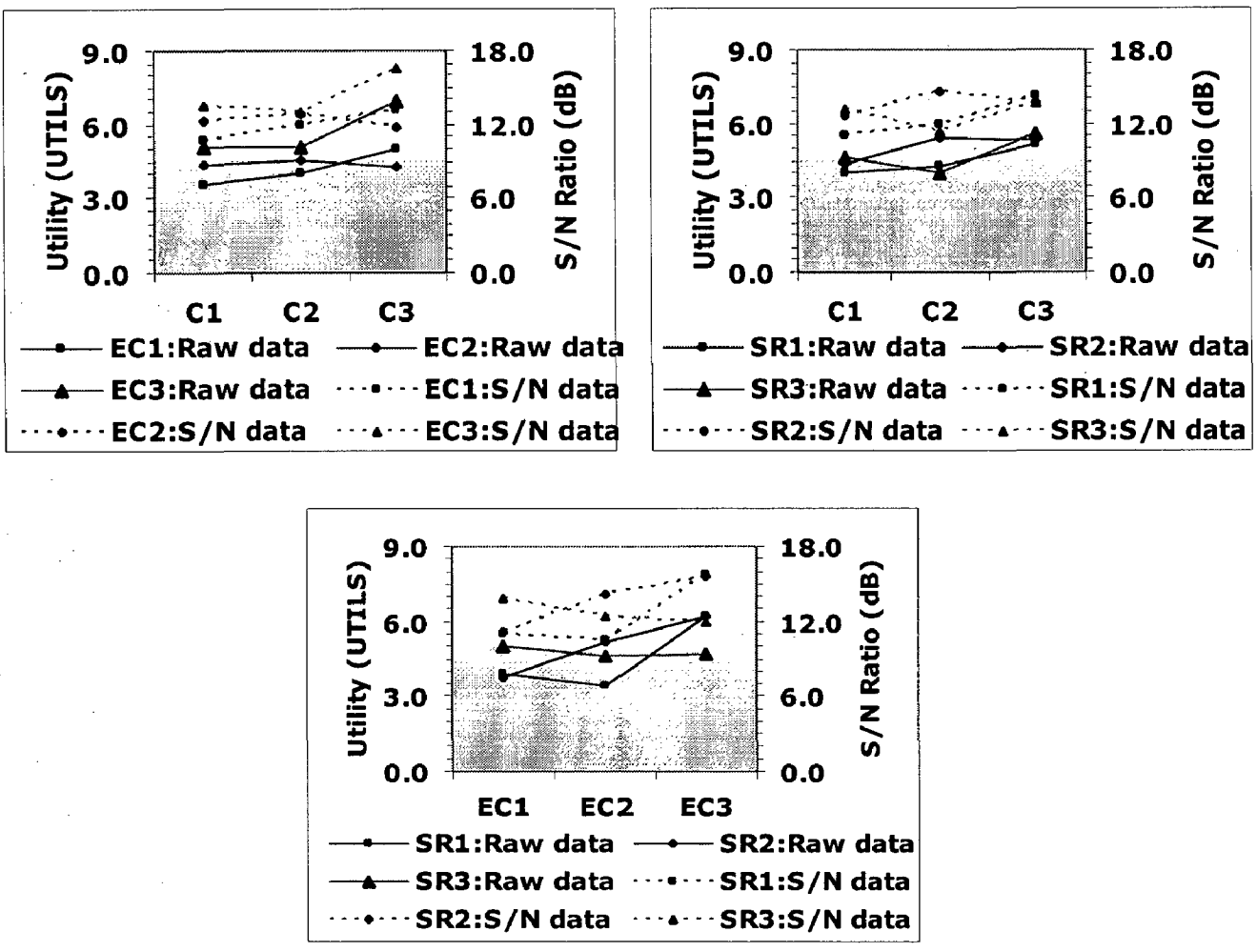

Fig. 8.2 Interaction plots (Utility: PIR_a-PIOR)

Table 8.6 Pooled ANOVA (Utility: PIR_a-PIOR: Raw Data)

Source	SS	DF	MS	F ratio	% Contribution
C	11.08	2	5.54	14.02*	6.68
EC	23.60	2	11.80	29.85*	14.80
SR	2.84	(2)	Pooled	-	-
F	1.40	(2)	Pooled	-	-
T	3.75	(2)	Pooled	-	-
SOP	26.70	2	13.35	33.76*	16.81
G	43.24	2	21.62	54.69*	27.55
C-EC	8.42	4	2.10	5.32*	4.44
C-SR	6.60	4	1.65	4.17*	3.26
EC-SR	21.39	4	5.35	13.53*	12.86
Model	141.03	20	7.05	17.84*	86.40
e(pooled)	13.05	33	0.40		13.60
Total	154.07	53			100.00

The Model F ratio of 17.84 implies that Model is significant at 99.5% confidence level.

* Significant at 95% confidence level.

SS: Sum of Square, DF: Degree of Freedom, MS: Mean Square, C: Current Intensity, EC: Electrolyte Concentration, SR: Speed Ratio, F: Electrolyte Flow Rate, T: Electrolyte Inlet Temperature, SOP: Stick-out Pressure, G: Grit Size.

Table 8.7 Pooled ANOVA (Utility: PIR_a-PIOR: S/N Data)

Source	SS	DF	MS	F ratio	% Contribution
C	13.77	(2)	Pooled	-	-
EC	31.83	2	15.92	3.68*	7.78
SR	7.80	(2)	Pooled	-	-
F	3.71	(2)	Pooled	-	-
T	6.66	(2)	Pooled	-	-
SOP	53.80	2	26.90	6.21*	15.16
G	88.29	2	44.15	10.20*	26.74
C-EC	18.61	(4)	Pooled	-	-
C-SR	18.71	(4)	Pooled	-	-
EC-SR	54.62	4	13.65	3.15*	12.53
Model	228.54	10	22.85	5.28*	62.20
e(pooled)	69.27	16	4.33		37.80
Total	297.81	26			100.00

The Model F ratio of 5.28 implies that Model is significant at 99.5% confidence level.

* Significant at 95% confidence level.

SS: Sum of Square, DF: Degree of Freedom, MS: Mean Square, C: Current Intensity, EC: Electrolyte Concentration, SR: Speed Ratio, F: Electrolyte Flow Rate, T: Electrolyte Inlet Temperature, SOP: Stick-out Pressure, G: Grit Size.

Table 8.8 Average Effects of C-EC Interaction (Utility: PIR_a-PIOR: Raw & S/N Data)

	Average Values, Utility (UTILS)			S/N Average Values, Utility (dB)		
	C_1	C_2	C_3	C_1	C_2	C_3
EC_1	3.59	4.05	4.96	10.75	11.92	13.26
EC_2	4.39	4.55	4.32	12.28	12.88	11.84
EC_3	5.06	5.11	6.92	13.62	13.10	16.59

*95 % Confidence Limit (CI_1) for average values-Raw data = ± 0.52

*95 % Confidence Limit (CI_1) for average values-S/N data = ± 2.55

Table 8.9 Average Effects of C-SR Interaction (Utility: PIR_a-PIOR: Raw & S/N Data)

	Average Values, Utility (UTILS)			S/N Average Values, Utility (dB)		
	C_1	C_2	C_3	C_1	C_2	C_3
SR_1	4.02	4.25	5.21	10.98	11.93	14.22
SR_2	4.35	5.47	5.33	12.57	14.64	13.74
SR_3	4.67	3.99	5.66	13.10	11.33	13.73

*95 % Confidence Limit (CI_1) for average values-Raw data = ± 0.52

*95 % Confidence Limit (CI_1) for average values-S/N data = ± 2.55

Table 8.10 Average Effects of EC-SR Interaction (Utility: PIR_a-PIOR: Raw & S/N Data)

	Average Values, Utility (UTILS)			S/N Average Values, Utility (dB)		
	EC_1	EC_2	EC_3	EC_1	EC_2	EC_3
SR_1	3.87	3.43	6.18	10.97	10.47	15.70
SR_2	3.75	5.21	6.20	11.17	14.16	15.62
SR_3	4.99	4.61	4.71	13.79	12.38	11.99

*95 % Confidence Limit (CI_1) for average values-Raw data = ± 0.52

*95 % Confidence Limit (CI_1) for average values-S/N data = ± 2.55

8.1.3.1 Selection of Optimal Levels

The response plots for the significant input parameters (Fig. 8.1) indicate that level 3 of current intensity (C_3); electrolyte concentration (EC_3); stick-out pressure (SOP_3); and stick grit-size at level 2 (G_2) provide the maximum utility. Analyses of interaction plots for significant interactions (Fig. 8.2) reveal that the combinations C_3-EC_3, C_3-SR_2 and EC_3-SR_2 yield the highest mean PIR_a-PIOR utility.

Similarly considering the significant parameters for S/N utility, 3rd level of the electrolyte concentration (EC_3), stick-out pressure (SOP_3) and 2nd level of stick grit-size (G_2) correspond to the highest S/N utility (Fig. 8.1). The EC-SR interaction plot (Fig. 8.2) suggests that combinations EC_3-SR_2 and EC_3-SR_1 result in best S/N utility value. The insignificant parameters can be kept at economic levels as the optimal response is calculated only from the significant factors.

Based on the above analysis, the optimal levels of the process input parameters for mean and S/N utility optimizing the PIR_a-PIOR are given in Tables 8.11 and 8.12 respectively.

Table 8.11 Optimal level of process parameters for mean utility: PIR_a-PIOR

Process Input Parameters	Optimal Levels	
Current Intensity (ADC)#	C_3	180
Electrolyte Concentration (g/L)#	EC_3	200
Speed Ratio #	SR_2	150
Electrolyte Flow Rate (lpm)*	F_1	10
Electrolyte Inlet Temperature (°C)*	T_3	50
Stick-out Pressure (kPa)	SOP_3	30
Grit Size	G_2	600

** Not significant. Therefore, selected conveniently.*
 # Interactions C-EC, C-SR and EC-SR are significant.

Table 8.12 Optimal level of process parameters for S/N utility: PIR_a-PIOR

Process Input Parameters		Optimal Levels
Current Intensity (ADC)*	C_3	180
Electrolyte Concentration (g/L)#	EC_3	200
Speed Ratio #	SR_2	150
Electrolyte Flow Rate (lpm)*	F_1	10
Electrolyte Inlet Temperature (°C)*	T_3	50
Stick-out Pressure (kPa)	SOP_3	30
Grit Size	G_2	600

** Not significant. Therefore, selected conveniently.*
 # Interactions EC- SR is significant.

8.1.3.2 Estimation of Optimal Values of Performance Characteristics

a) Percent Improvement in R_a

The optimal values of PIR_a and S/N ratio are estimated at the selected levels of significant parameters and interactions. The average values of PIR_a (Tables 7.17, 7.21, 7.22 and 6.19) are reproduced in Table 8.13.

Table 8.13 Average values of PIR_a at optimal level of process input parameters

Optimum Level of Significant Process Parameter	PIR_a (%)
C_3EC_3	81.01
C_3SR_2	75.05
EC_3SR_2	77.87
3rd Level of Stick-out Pressure (SOP_3)	75.71
2nd Level of Grit Size (G_2)	75.78
Overall Mean of PIR_a ($\bar{T}_{PIRa}$)	73.27
3rd Level of Current Intensity (C_3)	77.12
3rd Level of Electrolyte Concentration (EC_3)	78.41

The predicted optimal value of PIR_a (u_{PIRa}) is:

$$u_{PIRa} = C_3EC_3 + C_3SR_2 + C_3SR_2 + SOP_3 + G_2 - 4\,\bar{T}_{PIRa} - (C_3 + EC_3 - 2*\bar{T}_{PIRa})$$

$$= 83.35\ \%$$

The 95% confidence interval for optimal mean of the population and two confirmation experiments (CI_{pop} and CI_{CE}) have been calculated using equations 6.9a and 6.9b by substituting the following values:

N = 27 x 2 = 54, f_e (error D.F.) = (53-16) = 37, v_e (error variance) = 35.57 (modified Table 7.19).

n_{eff} = N / (1+ D.F. associated in the estimate of mean response) = 3.176, R = 2,

$F_{0.05}$ (1, 37) = 4.110

$CI_{pop} = \pm 6.78$

$CI_{CE} = \pm 10.91$

The 95% confidence intervals (CI_{pop} & CI_{CE}) of the predicted optimal PIR_a are:

CI_{pop} : $76.57 < u_{PIRa}(\%) < 90.13$

CI_{CE} : $72.43 < u_{PIRa}(\%) < 94.26$

The S/N PIR_a average values (Tables 7.18, 7.21, 7.22 and 6.19) are given in Table 8.14.

Table 8.14 Average S/N values of PIR_a at optimal level of process parameters

Optimum Level of Significant Process Parameter	S/N Ratio (dB)
EC_3SR_2	37.80
3rd Level of Stick-out Pressure (SOP_3)	37.55
2nd Level of Grit Size (G_2)	37.55
Overall Mean of S/N PIR_a ($\bar{T}_{S/NPIRa}$)	37.26

The predicted optimal value of S/N PIR_a (u_{PIRa}) is:

$$u_{S/NPIRa} = EC_3SR_2 + SOP_3 + G_2 - 2\,\bar{T}_{S/NPIRa}$$

$$= 38.38 \text{ dB}$$

The following values were used in Eq. 6.9a and 6.9b to obtain 95% CI_{pop} & CI_{CE} for optimal mean S/N PIR_a:

N = 27, f_e (error D.F.) = (26-8) = 18, v_e (error variance) = 0.59 (modified Table 7.20).

n_{eff} = N / (1+ D.F. associated in the estimate of mean response) = 3, R = 2,

$F_{0.05}$ (1, 18) = 4.4193

$CI_{pop} = \pm 0.93$

$CI_{CE} = \pm 1.47$

The 95% confidence intervals (CI_{pop} & CI_{CE}) of the predicted optimal S/N PIR_a are:

CI_{pop} : $37.45 < u_{S/NPIRa}$ (dB) < 39.31

CI_{CE} : $36.91 < u_{S/NPIRa}$ (dB) < 39.85

b) Percent Improvement in Out-of-roundness

The average values of mean PIOR (Tables 7.37, 7.41, 7.42 and 6.23) are produced in Table 8.15.

Table 8.15 Average values of PIOR at optimal level of process input parameters

Optimum Level of Significant Process Parameter	PIOR (%)
C_3EC_3	48.75
EC_3SR_2	41.52
EC_3SR_2	44.07
3rd Level of Stick-out Pressure (SOP_3)	40.27
2nd Level of Grit Size (G_2)	43.83
Overall Mean of PIOR ($\bar{T}_{PIOR}$)	36.64
3rd Level of Current Intensity (C_3)	37.72
3rd Level of Electrolyte Concentration (EC_3)	38.99

The predicted optimal value of PIOR (u_{PIOR}) is:

$$u_{PIOR} = C_3EC_3 + C_3SR_2 + EC_3SR_2 + SOP_3 + G_2 - 4\bar{T}_{PIOR} - (C_3 + EC_3 - 2\bar{T}_{PIOR})$$

$$= 68.45\ \%$$

The 95% CI_{pop} and CI_{CE} for optimal mean PIOR have been calculated with the following values of the terms in Eq. 6.9a and 6.9b:

N = 27 x 2 = 54, f_e (error D.F.) = (53-16) = 37, v_e (error variance) = 37.54 (recalculated from Table 7.39).

n_{eff} = N / (1+ D.F. associated in the estimate of mean response) = 3.18, R = 2,

$F_{0.05}$ (1, 37) = 4.110

$CI_{pop} = \pm 6.97$

$CI_{CE} = \pm 11.21$

The 95% confidence intervals (CI_{pop} & CI_{CE}) of the predicted optimal PIOR are:

CI_{pop} : $61.48 < u_{PIOR}(\%) < 75.42$

CI_{CE} : $57.24 < u_{PIOR}(\%) < 79.66$

The S/N PIOR average values (Tables 7.38, 7.41, 7.42 and 6.23) are given in Table 8.16.

Table 8.16 Average S/N values of PIOR at optimal level of process parameters.

Optimum Level of Significant Process Parameter	S/N Ratio (dB)
EC_3SR_2	32.81
3rd Stick-out Pressure (SOP_3)	31.75
2nd Grit Size (G_2)	32.54
Overall Mean of S/N PIOR ($\bar{T}_{S/NPIOR}$)	30.77

The predicted optimal value of S/N PIOR ($u_{S/NPIOR}$) is:

$$u_{S/NPIOR} = EC_3SR_2 + SOP_3 + G_2 - 2\bar{T}_{S/NPIOR}$$

$$= 35.55 \text{ dB}$$

The values used to calculate 95% confidence interval for optimal mean S/N PIOR are:

N = 27, f_e (error DF) = (26-8) = 18, v_e (error variance) = 4.39 (recalculated from Table 7.40).

n_{eff} = N / (1+ DF associated in the estimate of mean response) = 3, R = 2,

$F_{0.05}$ (1, 18) = 4.4.139

$CI_{pop} = \pm 2.54$

$CI_{CE} = \pm 4.02$

The 95% confidence intervals (CI_{pop} & CI_{CE}) of the predicted optimal S/N PIOR are:

CI_{pop} : $33.01 < u_{S/NPIOR}$ (dB) < 38.09

CI_{CE} : $31.53 < u_{S/NPIOR}$ (dB) < 39.57

8.1.4 Model 2: PIR_a-PICyl

The overall utility values and corresponding S/N ratios for PIR_a (Tables 6.19) and PICyl (Table 6.25) considered together are given in Table 8.17 using the respective preference scales with equal weightages.

The ANOM and ANOVA results for mean utility and S/N utility are reported in Tables 8.18 to 8.24 and the response plots are shown in Fig. 8.3 and 8.4. Based on the analysis it is seen that the process parameters current intensity (C), electrolyte concentration (EC), stick-out pressure (SOP), stickgrit-size (G) and the interactions C-EC, C-SR and EC-SR significantly affect the mean utility at 0.05 alpha while EC, SOP, G and EC-SR are significant for S/N utility.

Table 8.17 Utility values (PIR_a-PICyl)

Trial No.	Utility Values (UTILS)		S/N Ratio (dB)
	Y_{R1}	Y_{R2}	
1	2.07	2.80	7.42
2	3.90	4.27	12.19
3	4.64	4.18	12.85
4	3.89	3.46	11.27
5	4.20	3.46	11.55
6	6.18	6.38	15.96
7	7.09	6.55	16.65
8	5.52	4.14	13.41
9	3.25	3.41	10.44
10	2.72	3.33	9.49
11	4.51	4.92	13.45
12	4.32	4.10	12.48
13	3.45	2.87	9.87
14	5.04	5.16	14.15
15	5.03	5.66	14.51
16	6.69	6.29	16.23
17	6.54	7.23	16.73
18	1.82	2.56	6.44
19	6.13	6.08	15.71
20	2.65	2.39	8.00
21	6.14	6.31	15.88
22	4.29	4.35	12.71
23	6.05	6.52	15.94
24	2.47	3.06	8.68
25	4.68	5.65	14.15
26	6.65	7.33	16.86
27	8.31	8.50	18.49
	$\overline{T}_{UTIL}$ = Overall Mean of UTIL		
	= 4.80		= 13.02 dB

*R1, R2 represent repetitions.

Table 8.18 Average and Main Effects (Utility: PIR_a - PICyl: Raw Data)

Process Input Parameter	Average Values, Utility (UTILS)			Main Effects, Utility (UTILS)	
	L1	L2	L3	L2-L1	L3-L2
C	4.41	4.57	5.42	0.16	0.85
EC	4.19	4.53	5.68	0.34	1.15
SR	4.58	5.03	4.80	0.45	-0.23
F	4.95	4.89	4.55	-0.06	-0.34
T	4.59	4.75	5.06	0.16	0.31
SOP	3.81	5.00	5.58	1.19	0.58
G	4.85	5.80	3.74	0.95	-2.06
C-EC	4.72	5.03	4.65	0.31	-0.38
C-SR	4.86	4.61	4.93	-0.26	0.33
EC-SR	4.74	4.48	5.18	-0.27	0.70

L1, L2 and L3 represent average values of raw data of response of corresponding parameters at levels 1, 2 and 3 respectively. L2-L1 is the average main effect when the corresponding parameter changes from level 1 to level 2. L3-L2 is the average main effect when the corresponding parameter changes from level 2 to level 3.
* 95 % Confidence Limit (CI_1) = ± 0.26
C: Current Intensity, EC: Electrolyte Concentration, SR: Speed Ratio, F: Electrolyte Flow Rate, T: Electrolyte Inlet Temperature, SOP: Stick-out Pressure, G: Grit Size.

Table 8.19 Average and Main Effects (Utility: PIR_a-PICyl: S/N Data)

Process Input Parameter	S/N Average Values, Utility (dB)			Main Effects, Utility (dB)	
	L1	L2	L3	L2-L1	L3-L2
C	12.42	12.59	14.05	0.18	1.45
EC	11.94	12.74	14.38	0.80	1.64
SR	12.61	13.59	12.86	0.97	-0.73
F	13.21	13.40	12.45	0.20	-0.95
T	12.50	13.11	13.44	0.61	0.33
SOP	11.03	13.37	14.65	2.34	1.28
G	13.23	14.89	10.94	1.66	-3.96
C-EC	12.76	13.41	12.88	0.65	-0.53
C-SR	12.91	12.72	13.43	-0.19	0.71
EC-SR	12.69	12.37	14.00	-0.32	1.62

L1, L2 and L3 represent average values of S/N data of response of corresponding parameters at levels 1, 2 and 3 respectively. L2-L1 is the average main effect when the corresponding parameter changes from level 1 to level 2. L3-L2 is the average main effect when the corresponding parameter changes from level 2 to level 3.
* 95 % Confidence Limit (CI_1) = ± 1.41
C: Current Intensity, EC: Electrolyte Concentration, SR: Speed Ratio, F: Electrolyte Flow Rate, T: Electrolyte Inlet Temperature, SOP: Stick-out Pressure, G: Grit Size.

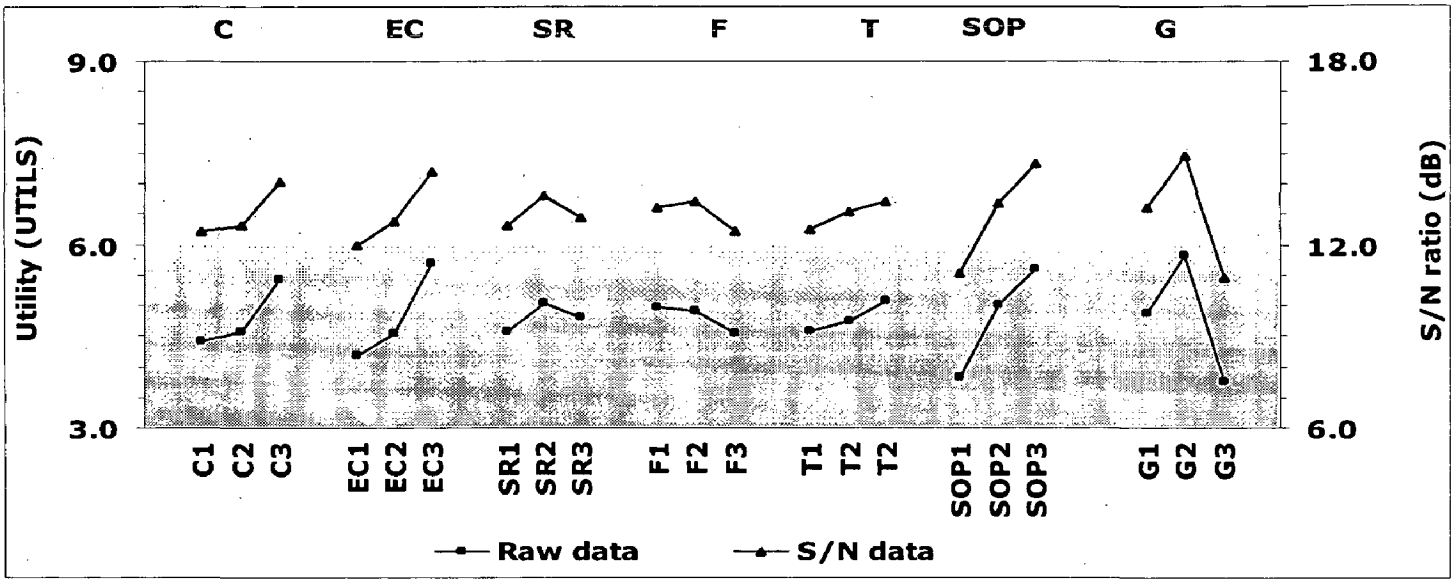

Fig. 8.3 Effects of process parameters on Utility: PIR_a-PICyl and S/N ratio (Main Effects)

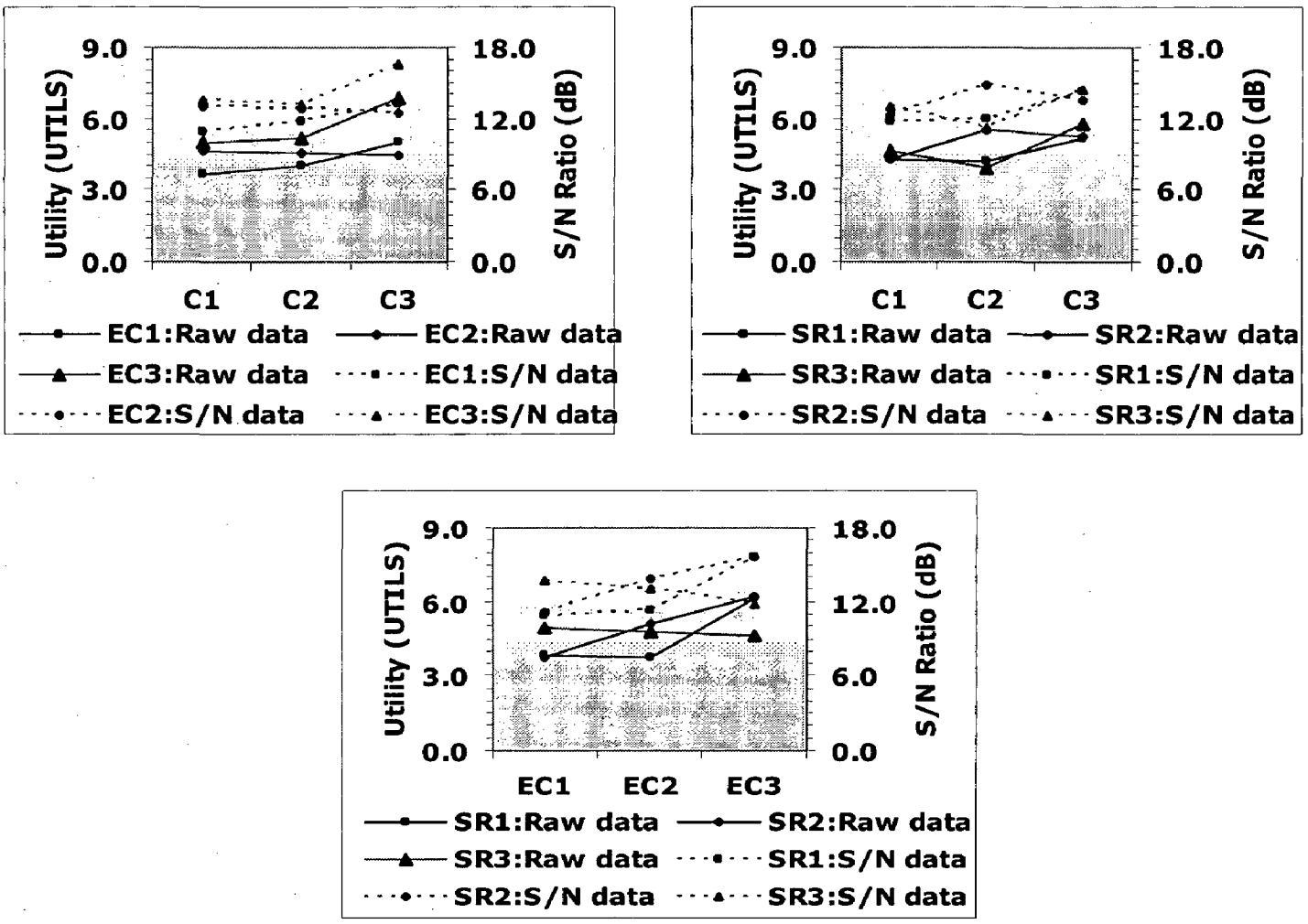

Fig. 8.4 Interaction plots (Utility: PIR_a-PICyl)

Table 8.20 Pooled ANOVA (Utility: PIR_a-PICyl: Raw Data)

Source	SS	DF	MS	F ratio	% Contribution
C	10.61	2	5.31	17.79*	6.85
EC	21.86	2	10.93	36.65*	14.55
SR	1.82	(2)	Pooled	-	-
F	1.67	(2)	Pooled	-	-
T	2.11	(2)	Pooled	-	-
SOP	29.47	2	14.74	49.41*	19.76
G	38.31	2	19.16	64.24*	25.81
C-EC	7.54	4	1.88	6.32*	4.34
C-SR	9.37	4	2.34	7.85*	5.59
EC-SR	19.15	4	4.79	16.05*	12.29
Model	136.31	20	6.82	22.86*	89.19
e(pooled)	9.84	33	0.30		10.81
Total	146.15	53			100.00

The Model F ratio of 22.86 implies that Model is significant at 99.5% confidence level.

* Significant at 95% confidence level.

SS: Sum of Square, DF: Degree of Freedom, MS: Mean Square, C: Current Intensity, EC: Electrolyte Concentration, SR: Speed Ratio, F: Electrolyte Flow Rate, T: Electrolyte Inlet Temperature, SOP: Stick-out Pressure, G: Grit Size.

Table 8.21 Pooled ANOVA (Utility: PIR_a-PICyl: S/N Data)

Source	SS	DF	MS	F ratio	% Contribution
C	14.41	(2)	Pooled	-	-
EC	27.79	2	13.90	3.49*	7.25
SR	4.61	(2)	Pooled	-	-
F	4.52	(2)	Pooled	-	-
T	4.08	(2)	Pooled	-	-
SOP	60.61	2	30.30	7.62*	19.24
G	70.99	2	35.50	8.92*	23.03
C-EC	15.00	(4)	Pooled	-	-
C-SR	21.03	(4)	Pooled	-	-
EC-SR	50.69	4	12.67	3.19*	12.71
Model	210.08	10	21.01	5.28*	62.22
e(pooled)	63.65	16	3.98		37.78
Total	273.73	26			100.00

The Model F ratio of 5.28 implies that Model is significant at 99.5% confidence level.

* Significant at 95% confidence level.

SS: Sum of Square, DF: Degree of Freedom, MS: Mean Square, C: Current Intensity, EC: Electrolyte Concentration, SR: Speed Ratio, F: Electrolyte Flow Rate, T: Electrolyte Inlet Temperature, SOP: Stick-out Pressure, G: Grit Size.

Table 8.22 Average Effects of C-EC Interaction (Utility: PIR_a-PICyl: Raw & S/N Data)

	Average Values, Utility (UTILS)			S/N Average Values, Utility (dB)		
	C_1	C_2	C_3	C_1	C_2	C_3
EC_1	3.64	3.99	4.95	10.82	11.81	13.20
EC_2	4.60	4.53	4.46	12.92	12.84	12.44
EC_3	4.99	5.19	6.85	13.50	13.13	16.50

*95 % Confidence Limit (CI_1) for average values-Raw data = ± 0.45

*95 % Confidence Limit (CI_1) for average values-S/N data = ± 2.44

Table 8.23 Average Effects of C-SR Interaction (Utility: PIR_a-PICyl: Raw & S/N Data)

	Average Values, Utility (UTILS)			S/N Average Values, Utility (dB)		
	C_1	C_2	C_3	C_1	C_2	C_3
SR_1	4.31	4.22	5.20	11.78	11.87	14.19
SR_2	4.25	5.57	5.26	12.38	14.77	13.60
SR_3	4.67	3.92	5.80	13.08	11.14	14.35

*95 % Confidence Limit (CI_1) for average values-Raw data = ± 0.45

*95 % Confidence Limit (CI_1) for average values-S/N data = ± 2.44

Table 8.24 Average Effects of EC-SR Interaction (Utility: PIR_a-PICyl: Raw & S/N Data)

	Average Values, Utility (UTILS)			S/N Average Values, Utility (dB)		
	EC_1	EC_2	EC_3	EC_1	EC_2	EC_3
SR_1	3.86	3.72	6.16	10.88	11.29	15.68
SR_2	3.77	5.07	6.24	11.21	13.88	15.67
SR_3	4.95	4.80	4.64	13.73	13.05	11.79

*95 % Confidence Limit (CI_1) for average values-Raw data = ± 0.45

*95 % Confidence Limit (CI_1) for average values-S/N data = ± 2.44

8.1.4.1 Selection of Optimal Levels

Based on the analysis, the optimal levels of the process input parameters for mean and S/N PIRa-PICyl utility are given in Tables 8.25 and 8.26 respectively.

Table 8.25 Optimal level of process parameters for mean utility: PIR_a-PICyl

Process Input Parameters		Optimal Levels
Current Intensity (ADC)#	C_3	180
Electrolyte Concentration (g/L)#	EC_3	200
Speed Ratio #	SR_2	150
Electrolyte Flow Rate (lpm)*	F_1	10
Electrolyte Inlet Temperature (°C)*	T_3	50
Stick-out Pressure (kPa)	SOP_3	30
Grit Size	G_2	600

** Not significant. Therefore, selected conveniently.*
 # Interactions C-EC, C-SR and EC-SR are significant.

Table 8.26 Optimal level of process parameters for S/N utility: PIR_a-PICyl

Process Input Parameters		Optimal Levels
Current Intensity (ADC)*	C_3	180
Electrolyte Concentration (g/L)#	EC_3	200
Speed Ratio #	SR_2	150
Electrolyte Flow Rate (lpm)*	F_1	10
Electrolyte Inlet Temperature (°C)*	T_3	50
Stick-out Pressure (kPa)	SOP_3	30
Grit Size	G_2	600

** Not significant. Therefore, selected conveniently.*
 # Interactions EC-SR is significant.

8.1.4.2 Estimation of Optimal Values of Performance Characteristics

a) Percent Improvement in R_a

The optimal results for PIR_a and S/N PIR_a are the same as determined for Utility PIR_a-PIOR §8.1.3.2.

b) Percent Improvement in Cylindricity

The average values of PICyl and S/N PICyl (Tables 7.46, 7.47, 7.50, 7.51, 7.52 and 6.25) for the optimal levels of the process parameters and interactions are produced in Table 8.27 and 8.28 respectively.

Table 8.27 Average values of PICyl at optimal level of process input parameters

Optimum Level of Significant Process Parameter	PICyl (%)
C_3EC_3	63.37
EC_3SR_2	53.97
EC_3SR_2	59.45
3rd Level of Stick-out Pressure (SOP_3)	54.36
2nd Level of Grit Size (G_2)	59.02
Overall Mean of PICyl ($\overline{T}_{PICyl}$)	49.03
3rd Level of Current Intensity (C_3)	50.03
3rd Level of Electrolyte Concentration (EC_3)	51.69

Table 8.28 Average S/N values of PICyl at optimal level of process parameters

Optimum Level of Significant Process Parameter	S/N Ratio (dB)
EC_3SR_2	35.39
3rd Stick-out Pressure (SOP_3)	34.50
2nd Grit Size (G_2)	35.14
Overall Mean of S/N PICyl ($\overline{T}_{S/NPICyl}$)	33.34

The predicted optimal value of PICyl (u_{PICyl}) is:

$$u_{PICyl} = C_3EC_3 + C_3SR_2 + EC_3SR_2 + SOP_3 + G_2 - 4\,\bar{T}_{PICyl} - (C_3 + EC_3 - 2\,\bar{T}_{PICyl})$$

$$= 90.39\ \%$$

The 95% confidence interval for the mean of the population and two confirmation experiments (CI_{pop} & CI_{CE}) have been calculated with the following substitutions in Eq. 6.9a and 6.9b:

N = 27 x 2 = 54, f_e (error D.F.) = (53-16) = 37, v_e (error variance) = 51.51(recalculated from Table 7.48).

n_{eff} = N / (1+ D.F. associated in the estimate of mean response) = 3.18, R = 2,

$F_{0.05}$ (1, 37) = 4.110

$Cl_{pop} = \pm 8.16$

$Cl_{CE} = \pm 13.13$

The 95% confidence intervals (CI_{pop} & CI_{CE}) of the predicted optimal PICyl are:

CI_{pop} : $82.23 < u_{PICyl}(\%) < 98.56$

CI_{CE} : $77.26 < u_{PICyl}(\%) < 100.00$

The predicted optimal value of S/N PICyl ($u_{S/N\ PICyl}$) is:

$$u_{S/N\ PICyl} = EC_3SR_2 + SOP_3 + G_2 - 2\,\bar{T}_{S/NPICyl}$$

$$= 38.35\ dB$$

The 95% confidence interval for the mean of the population and two confirmation experiments (CI_{pop} & CI_{CE}) have been calculated using equations 6.9a and 6.9b by substituting the following values:

N = 27, f_e (error D.F.) = (26-8) = 18, v_e (error variance) = 4.14 (recalculated from Table 7.49).

n_{eff} = N / (1+ DF associated in the estimate of mean response) = 3, R = 2,

$F_{0.05}$ (1,18) = 4.4139

$CI_{pop} = \pm 2.47$

$CI_{CE} = \pm 3.90$

The 95% confidence intervals (CI_{pop} & CI_{CE}) of the predicted optimal S/N PICyl are:

CI_{pop} : $35.88 < u_{S/NPICyl}$ (dB) < 40.82

CI_{CE} : $34.45 < u_{S/NPICyl}$ (dB) < 42.25

8.1.5 Model 3: PIR_a-DIR

The composite utility values alongwith S/N ratios for combined optimization of PIR_a and diametral increase rate are given in Table 8.29. The utility values have been calculated from Tables 6.19 and 6.27 using the preference scale of PIR_a and DIR from Table 8.2. ECH is a micro-finishing process and PIR_a assumes a dominating significance as compared to DIR. Therefore, PIR_a and DIR have been assigned the weightages of 0.8 and 0.2 respectively.

Based on the ANOM and ANOVA results, as illustrated in Tables 8.30 to 8.35, it can be concluded that the process parameters and interactions C, EC, T, SOP, G, C-EC and C-SR all significantly affect the mean utility at 0.05 alpha while only C, EC, SOP, G are significant for S/N utility.

Table 8.29 Utility values (PIR_a-DIR)

Trial No.	Utility Values (UTILS)		S/N Ratio (dB)
	Y_{R1}	Y_{R2}	
1	0.94	1.42	0.91
2	2.23	2.79	7.83
3	3.06	2.67	9.09
4	3.53	2.90	10.02
5	3.62	2.73	9.78
6	4.25	4.56	12.86
7	6.94	5.90	16.07
8	4.92	3.16	11.51
9	5.99	5.65	15.29
10	1.30	1.86	3.57
11	4.18	4.41	12.65
12	2.85	2.80	9.01
13	3.25	3.17	10.13
14	3.23	3.78	10.82
15	5.02	5.79	14.59
16	6.90	6.12	16.23
17	6.25	7.00	16.38
18	3.16	3.94	10.85
19	7.62	7.37	17.49
20	3.00	3.21	9.82
21	6.71	7.20	16.84
22	6.19	6.16	15.82
23	5.06	5.78	14.62
24	2.94	3.36	9.91
25	4.49	5.40	13.77
26	6.88	7.54	17.13
27	8.39	8.95	18.75
	$\bar{T}_{UTIL}$ = Overall Mean of UTIL		
	= 4.60		= 12.29 dB

*R1, R2 represent repetitions.

Table 8.30 Average and Main Effects (Utility: PIR_a-DIR: Raw Data)

Process Input Parameter	Average Values, Utility (UTILS)			Main Effects, Utility (UTILS)	
	L1	L2	L3	L2-L1	L3-L2
C	3.74	4.17	5.90	0.43	1.74
EC	3.65	4.19	5.98	0.54	1.79
SR	4.53	4.43	4.85	-0.10	0.42
F	4.49	4.72	4.60	0.23	-0.12
T	4.22	4.69	4.89	0.47	0.20
SOP	3.78	4.70	5.32	0.92	0.62
G	5.19	5.29	3.33	0.09	-1.96
C x EC	4.31	4.74	4.76	0.44	0.02
C x SR	4.58	4.44	4.79	-0.13	0.35
EC x SR	4.53	4.52	4.76	-0.01	0.25

L1, L2 and L3 represent average values of raw data of response of corresponding parameters at levels 1, 2 and 3 respectively. L2-L1 is the average main effect when the corresponding parameter changes from level 1 to level 2. L3-L2 is the average main effect when the corresponding parameter changes from level 2 to level 3.

* 95 % Confidence Limit (CI_1) = ± 0.25

C: Current Intensity, EC: Electrolyte Concentration, SR: Speed Ratio, F: Electrolyte Flow Rate, T: Electrolyte Inlet Temperature, SOP: Stick-out Pressure, G: Grit Size.

Table 8.31 Average and Main Effects (Utility: PIR_a - DIR: S/N Data)

Process Input Parameter	S/N Average Values, Utility (dB)			Main Effects, Utility (dB)	
	L1	L2	L3	L2-L1	L3-L2
C	10.37	11.58	14.90	1.21	3.32
EC	9.69	12.06	15.11	2.37	3.05
SR	11.56	12.28	13.02	0.72	0.74
F	11.75	12.54	12.57	0.80	0.02
T	11.57	12.64	12.65	1.06	0.01
SOP	10.56	12.42	13.88	1.86	1.46
G	13.25	13.68	9.93	0.44	-3.75
C x EC	11.37	12.66	12.83	1.29	0.18
C x SR	11.96	11.95	12.94	-0.01	0.98
EC x SR	11.47	12.49	12.90	1.03	0.40

L1, L2 and L3 represent average values of S/N data of response of corresponding parameters at levels 1, 2 and 3 respectively. L2-L1 is the average main effect when the corresponding parameter changes from level 1 to level 2. L3-L2 is the average main effect when the corresponding parameter changes from level 2 to level 3.

* 95 % Confidence Limit (CI_1) = ± 1.77

C: Current Intensity, EC: Electrolyte Concentration, SR: Speed Ratio, F: Electrolyte Flow Rate, T: Electrolyte Inlet Temperature, SOP: Stick-out Pressure, G: Grit Size.

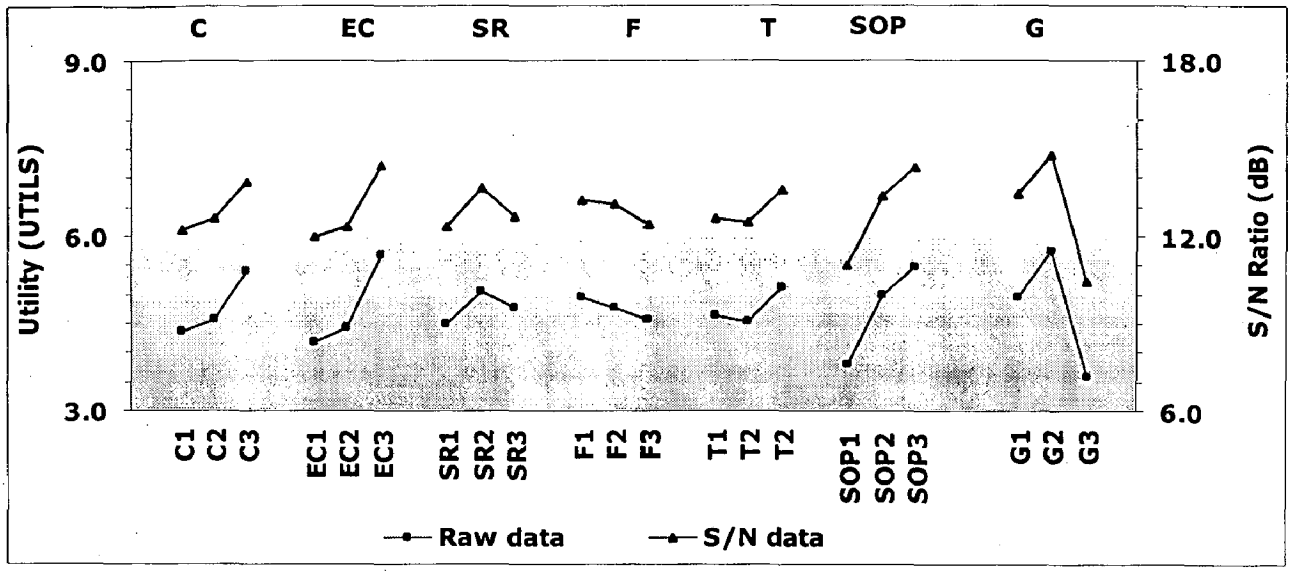

Fig. 8.5 Effect of process parameters on Utility: PIR_a-DIR and S/N ratio (Main Effects)

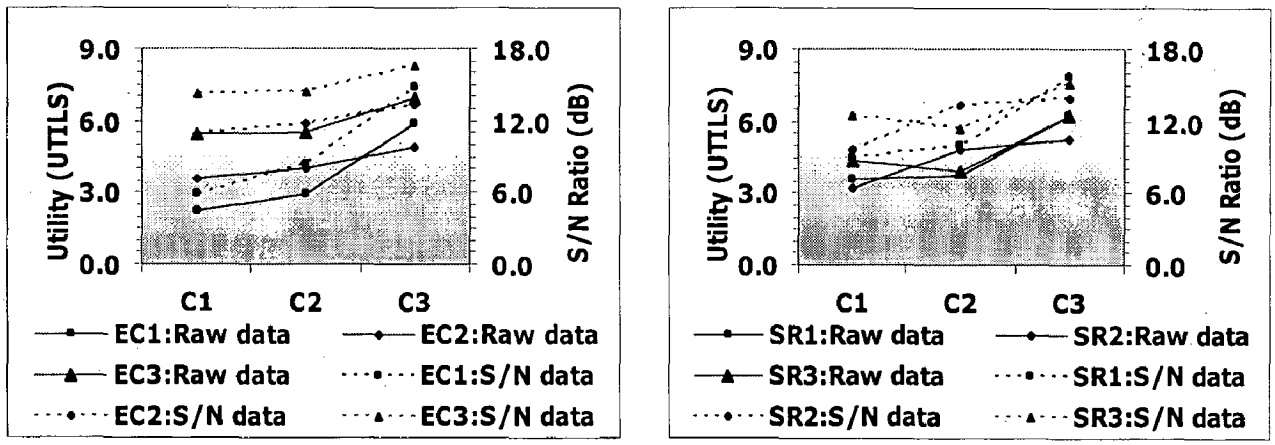

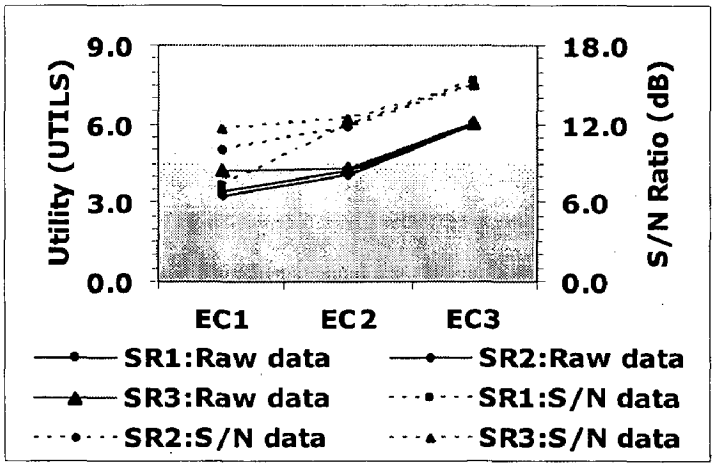

Fig. 8.6 Interaction plots (Utility: PIR_a-DIR)

Table 8.32 Pooled ANOVA (Utility: PIR_a-DIR: Raw Data)

Source	SS	DF	MS	F ratio	% Contribution
C	47.32	2	23.66	85.77*	23.14
EC	53.60	2	26.80	97.15*	26.25
SR	1.74	(2)	Pooled	-	-
F	0.47	(2)	Pooled	-	-
T	4.24	2	2.12	7.69*	1.83
SOP	21.70	2	10.85	39.33*	10.46
G	43.90	2	21.95	79.57*	21.45
C-EC	11.81	4	2.95	10.71*	5.30
C-SR	9.88	4	2.47	8.95*	4.34
EC-SR	1.50	(4)	Pooled	-	-
Model	192.47	18	10.69	38.76*	92.77
e(pooled)	9.66	35	0.28		7.23
Total	202.12	53			100.00

The Model F ratio of 38.76 implies that Model is significant at 99.5% confidence level.
* Significant at 95% confidence level.
SS: Sum of Square, DF: Degree of Freedom, MS: Mean Square, C: Current Intensity, EC: Electrolyte Concentration, SR: Speed Ratio, F: Electrolyte Flow Rate, T: Electrolyte Inlet Temperature, SOP: Stick-out Pressure, G: Grit Size.

Table 8.33 Pooled ANOVA (Utility: PIR_a-DIR: S/N Data)

Source	SS	DF	MS	F ratio	% Contribution
C	99.17	2	49.58	7.73*	18.24
EC	132.84	2	66.42	10.36*	25.35
SR	9.64	(2)	Pooled	-	-
F	3.94	(2)	Pooled	-	-
T	6.89	(2)	Pooled	-	-
SOP	50.07	2	25.03	3.90*	7.87
G	75.91	2	37.96	5.92*	13.33
C-EC	43.13	(4)	Pooled	-	-
C-SR	31.62	(4)	Pooled	-	-
EC-SR	20.22	(4)	Pooled	-	-
Model	357.99	8	44.75	6.98*	64.78
e(pooled)	115.44	18	6.41		35.22
Total	473.43	26			100.00

The Model F ratio of 6.98 implies that Model is significant at 99.5% confidence level.
* Significant at 95% confidence level.
SS: Sum of Square, DF: Degree of Freedom, MS: Mean Square, C: Current Intensity, EC: Electrolyte Concentration, SR: Speed Ratio, F: Electrolyte Flow Rate, T: Electrolyte Inlet Temperature, SOP: Stick-out Pressure, G: Grit Size.

Table 8.34 Average Effects of C-EC Interaction (Utility: PIR_a-DIR: Raw & S/N Data)

	Average Values, Utility (UTILS)			S/N Average Values, Utility (dB)		
	C_1	C_2	C_3	C_1	C_2	C_3
EC_1	2.19	2.90	5.85	5.94	8.41	14.71
EC_2	3.60	4.04	4.92	10.89	11.85	13.45
EC_3	5.43	5.56	6.94	14.29	14.48	16.55

*95 % Confidence Limit (CI_1) for average values-Raw data = ± 0.44

*95 % Confidence Limit (CI_1) for average values-S/N data = ± 3.07

Table 8.35 Average Effects of C-SR Interaction (Utility: PIR_a-DIR: Raw & S/N Data)

	Average Values, Utility (UTILS)			S/N Average Values, Utility (dB)		
	C_1	C_2	C_3	C_1	C_2	C_3
SR_1	3.61	3.77	6.21	9.00	9.98	15.69
SR_2	3.24	4.81	5.24	9.71	13.28	13.86
SR_3	4.36	3.93	6.26	12.41	11.48	15.16

*95 % Confidence Limit (CI_1) for average values-Raw data = ± 0.44

*95 % Confidence Limit (CI_1) for average values-S/N data = ± 3.07

8.1.5.1 Selection of Optimal Levels

An analysis of the response plot for overall utility of PIR_a-DIR (Fig. 8.5 and 8.6) indicates the optimal levels of the significant parameters for mean and S/N utility as given in Tables 8.36 and 8.37 respectively.

Table 8.36 Optimal level of process parameters for mean utility: PIR_a-DIR

Process Input Parameters	Optimal Levels	
Current Intensity (ADC)#	C_3	180
Electrolyte Concentration (g/L)#	EC_3	200
Speed Ratio #	SR_3	250
Electrolyte Flow Rate (lpm)*	F_1	10
Electrolyte Inlet Temperature (°C)	T_3	50
Stick-out Pressure (kPa)	SOP_3	30
Grit Size	G_2	600

** Not significant. Therefore, selected conveniently.*

 # Interactions C-EC, and C-SR are significant.

Table 8.37 Optimal level of process parameters for S/N utility: PIR_a-DIR

Process Input Parameters	Optimal Levels	
Current Intensity (ADC)	C_3	180
Electrolyte Concentration (g/L)	EC_3	200
Speed Ratio *	SR_3	250
Electrolyte Flow Rate (lpm)*	F_1	10
Electrolyte Inlet Temperature (°C)*	T_3	50
Stick-out Pressure (kPa)	SOP_3	30
Grit Size	G_2	600

** Not significant. Therefore, selected conveniently.*

8.1.5.2 Estimation of Optimal Performance Characteristic Values

a) Percent Improvement in R_a

Tables 8.38 and 8.39 show the average values of PIR_a and S/N PIR_a at the optimal levels of respective significant parameters and interactions already obtained and given in Tables 7.17, 7.18, 7.21, 7.22 and 6.19.

Table 8.38 Average values of PIR_a at optimal level of process input parameters

Optimum Level of Significant Process Parameter	PIR_a (%)
C_3EC_3	81.01
C_3SR_3	77.82
3rd Level of Electrolyte Inlet Temperature (T_3)	74.61
3rd Level of Stick-out Pressure (SOP_3)	75.71
2nd Level of Grit Size (G_2)	75.78
Overall Mean of PIR_a ($\bar{T}_{PIRa}$)	73.27
3rd Level of Current Intensity (C_3)	77.12

The predicted optimal value of PIR_a (u_{PIRa}) and corresponding 95% confidence intervals are calculated as given below:

$$u_{PIRa} = C_3EC_3 + C_3SR_3 + T_3 + SOP_3 + G_2 - 4\,\bar{T}_{PIRa} - (C_3 - \bar{T}_{PIRa})$$

$$= 88.01\ \%$$

$CI_{pop} = \pm 6.07$, i.e. CI_{pop}: $81.94 < u_{PIRa}(\%) < 94.07$

$CI_{CE} = \pm 10.15$, i.e. CI_{CE}: $77.85 < u_{PIRa}(\%) < 98.16$

The following values were used in Eq. 6.9a and 6.9b:

N = 27 x 2 = 54, f_e (error DF) = (53-14) = 39, v_e (error variance) = 32.39 (modified Table 7.19), $n_{eff} = 3.6$, R = 2, $F_{0.05}(1, 39) = 4.09341$

Table 8.39 Average S/N values of PIR_a at optimal level of process parameters

Optimum Level of Significant Process Parameter	S/N Ratio (dB)
C_3	37.71
EC_3	37.86
3rd Stick-out Pressure (SOP_3)	37.55
2nd Grit Size (G_2)	37.55
Overall Mean of S/N PIR_a ($\bar{T}_{S/NPIRa}$)	37.26

The predicted optimal value of S/N PIR_a ($\mu_{S/NPIRa}$) and corresponding 95% confidence interval are:

$$u_{S/N\ PIRa} = C_3 + EC_3 + SOP_3 + G_2 - 3\,\bar{T}_{S/NPIRa} = 38.89\ dB$$

$CI_{pop} = \pm 0.49$, (CI_{pop} : $38.40 < u_{S/NPIRa}$ (dB) < 39.38)

$CI_{CE} = \pm 0.78$, (CI_{CE} : $38.11 < u_{S/NPIRa}$ (dB) < 39.67)

[calculated with N = 27, f_e = (26-8) = 18, $v_e = 0.17$ (modified Table 7.20), $n_{eff} = 3$, R = 2, $F_{0.05}(1,18) = 4.4139$]

b) Diametral Increase Rate

The predicted optimal value of DIR (u_{DIR}) [derived from Table 8.40] and corresponding 95% confidence intervals are given below:

$u_{DIR} = C_3EC_3 + C_3SR_3 + T_3 + SOP_3 + G_2 - 4\overline{T}_{DIR} - (C_3 - \overline{T}_{DIR}) = 59.95$ (μm/min)

$CI_{pop} = \pm 15.20$, (CI_{pop} : $44.74 < u_{DIR}$ (μm/min) < 75.15)

$CI_{CE} = \pm 25.44$, (CI_{CE} : $34.50 < u_{DIR}$ (μm/min) < 85.39)

[$N = 27 \times 2 = 54$, $f_e = (53-14) = 39$, $v_e = 203.32$ (recalculated from Table 7.58), $n_{eff} = 3.60$, $R = 2$, $F_{0.05}(1, 39) = 4.09341$ in Eq. 6.9a and 6.9b]

Table 8.40 Average values of DIR at optimal level of process input parameters

Optimum Level of Significant Process Parameter	DIR (μm/min)
C_3EC_3	42.19
C_3SR_3	48.95
3rd Level of Electrolyte Inlet Temperature (T_3)	23.72
3rd Level of Stick-out Pressure (SOP_3)	27.99
2nd Level of Grit Size (G_2)	27.34
Overall Mean of DIR ($\overline{T}_{DIR}$)	24.02
3rd Level of Current Intensity (C_3)	38.18

The predicted optimal value of S/N DIR ($u_{S/NDIR}$) with corresponding 95% confidence intervals can be obtained using Table 8.41:

Table 8.41 Average S/N values of DIR at optimal level of process parameters

Optimum Level of Significant Process Parameter	S/N Ratio (dB)
C_3	30.30
EC_3	27.23
3rd Stick-out Pressure (SOP_3)	27.45
2nd Grit Size (G_2)	26.97
Overall Mean of S/N DIR ($\overline{T}_{S/NDIR}$)	26.04

$u_{S/N\,DIR} = C_3 + EC_3 + SOP_3 + G_2 - 3\,\overline{T}_{S/NDIR} = 33.82$ dB

$CI_{pop} = \pm 3.95$, (CI_{pop} : $29.87 < u_{S/NDIR}$ (dB) < 37.77)

$CI_{CE} = \pm 6.24$, (CI_{CE} : $27.57 < u_{S/NDIR}$ (dB) < 40.06)

[N = 27, f_e= (26-8) = 18, v_e= 10.60 (modified Table 7.59), n_{eff} = 3, R = 2, $F_{0.05}$ (1,18) = 4.4139]

CASE-II: THREE PERFORMANCE CHARACTERISTICS

8.1.6 Model 4: PIR_a-PIOR-DIR

The composite raw and S/N utility values for combined optimization of PIR_a, PIOR and DIR are given in Table 8.42. Phase-III experimental trial results(Tables 6.19, 6.23 and 6.27) were transformed into the composite utility values using respective preference scales and assigning 0.4, 0.4, 0.2 weights respectively. The ANOM results are given in Tables 8.43-44 and 8.47-48 and the response plots are shown in Fig. 8.7 and 8.8. The ANOVA results (Tables 8.45-46) show that C, EC, SOP, G, C-SR and EC-SR significantly influence both the mean and S/N utility.

Table 8.42 Utility values (PIRa-PIOR-DIR)

Trial No.	Utility Values (UTILS)		S/N Ratio (dB)
	Y_{R1}	Y_{R2}	
1	2.57	2.80	8.55
2	3.63	4.06	11.65
3	4.29	3.91	12.23
4	3.08	2.80	9.34
5	4.76	3.89	12.59
6	5.62	5.52	14.92
7	6.53	5.96	15.88
8	5.10	3.96	12.91
9	3.61	3.66	11.21
10	2.85	3.41	9.80
11	4.43	4.81	13.27
12	4.20	3.98	12.23
13	3.35	3.13	10.20
14	4.86	5.19	14.01
15	5.22	5.91	14.86
16	6.59	5.96	15.92
17	6.54	6.80	16.48
18	2.02	2.97	7.47
19	6.46	6.12	15.96
20	2.25	2.49	7.46
21	6.78	6.75	16.61
22	4.72	4.92	13.65
23	6.35	6.96	16.44
24	2.85	3.30	9.69
25	4.93	5.53	14.32
26	7.01	7.48	17.19
27	8.45	8.56	18.59
	$\bar{T}_{UTIL}$ = Overall Mean of UTIL		
	= 4.81		= 13.09 dB

Table 8.43 Average and Main Effects (Utility: PIR_a -PIOR-DIR: Raw Data)

Process Input Parameter	Average Values, Utility (UTILS)			Main Effects, Utility (UTILS)	
	L1	L2	L3	L2-L1	L3-L2
C	4.21	4.57	5.66	0.36	1.09
EC	4.21	4.58	5.65	0.37	1.07
SR	4.54	5.03	4.87	0.49	-0.17
F	4.87	4.94	4.63	0.06	-0.31
T	4.64	4.71	5.08	0.07	0.37
SOP	3.93	5.01	5.50	1.09	0.48
G	5.10	5.68	3.66	0.57	-2.02
C-EC	4.78	4.96	4.69	0.18	-0.27
C-SR	4.82	4.72	4.90	-0.11	0.18
EC-SR	4.86	4.40	5.17	-0.46	0.77

L1, L2 and L3 represent average values of raw data of response of corresponding parameters at levels 1, 2 and 3 respectively. L2-L1 is the average main effect when the corresponding parameter changes from level 1 to level 2. L3-L2 is the average main effect when the corresponding parameter changes from level 2 to level 3.
* 95 % Confidence Limit (CI_1) = ± 0.29
C: Current Intensity, EC: Electrolyte Concentration, SR: Speed Ratio, F: Electrolyte Flow Rate, T: Electrolyte Inlet Temperature, SOP: Stick-out Pressure, G: Grit Size.

Table 8.44 Average and Main Effects (Utility: PIR_a-PIOR-DIR: S/N Data)

Process Input Parameter	S/N Average Values, Utility (dB)			Main Effects, Utility (dB)	
	L1	L2	L3	L2-L1	L3-L2
C	12.14	12.69	14.44	0.55	1.74
EC	11.97	12.86	14.44	0.88	1.59
SR	12.62	13.56	13.09	0.93	-0.47
F	13.14	13.41	12.72	0.27	-0.69
T	12.74	13.02	13.51	0.28	0.48
SOP	11.42	13.46	14.39	2.05	0.93
G	13.76	14.71	10.81	0.94	-3.90
C-EC	12.98	13.28	13.01	0.30	-0.27
C-SR	12.88	12.98	13.41	0.10	0.43
EC-SR	13.05	12.27	13.95	-0.79	1.68

L1, L2 and L3 represent average values of S/N data of response of corresponding parameters at levels 1, 2 and 3 respectively. L2-L1 is the average main effect when the corresponding parameter changes from level 1 to level 2. L3-L2 is the average main effect when the corresponding parameter changes from level 2 to level 3.
* 95 % Confidence Limit (CI_1) = ± 0.98
C: Current Intensity, EC: Electrolyte Concentration, SR: Speed Ratio, F: Electrolyte Flow Rate, T: Electrolyte Inlet Temperature, SOP: Stick-out Pressure, G: Grit Size.

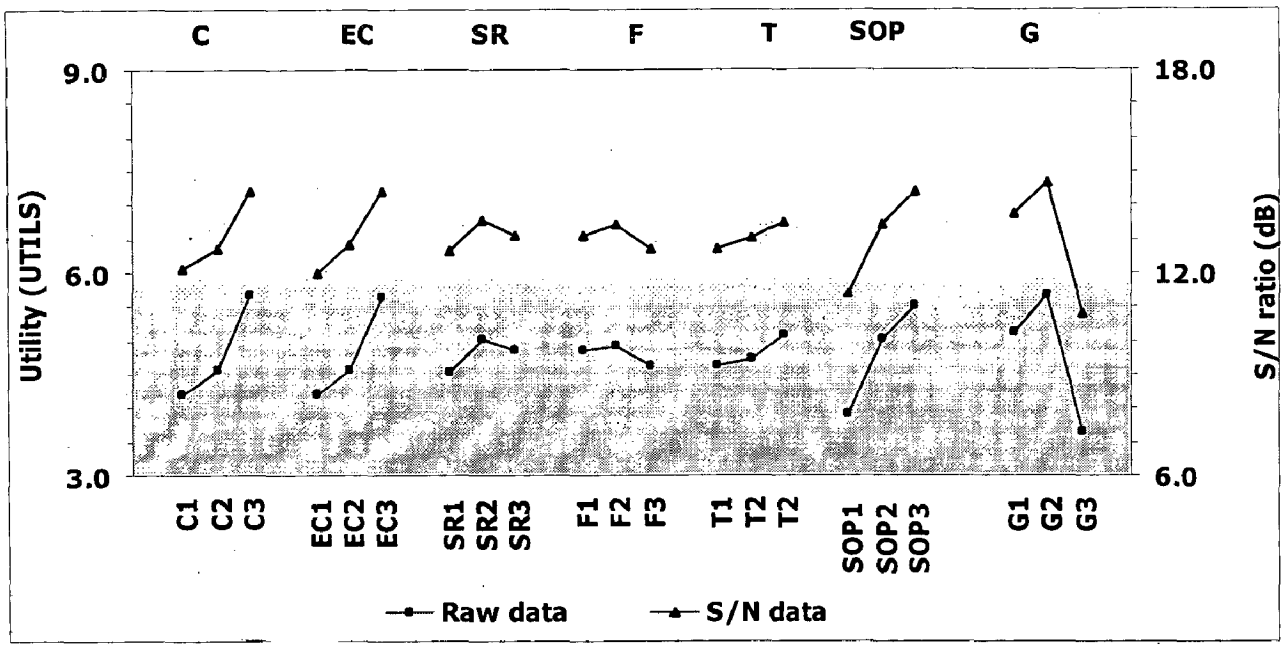

Fig. 8.7 Effects of process parameters on Utility: PIR_a-PIOR-DIR and S/N ratio (Main Effects)

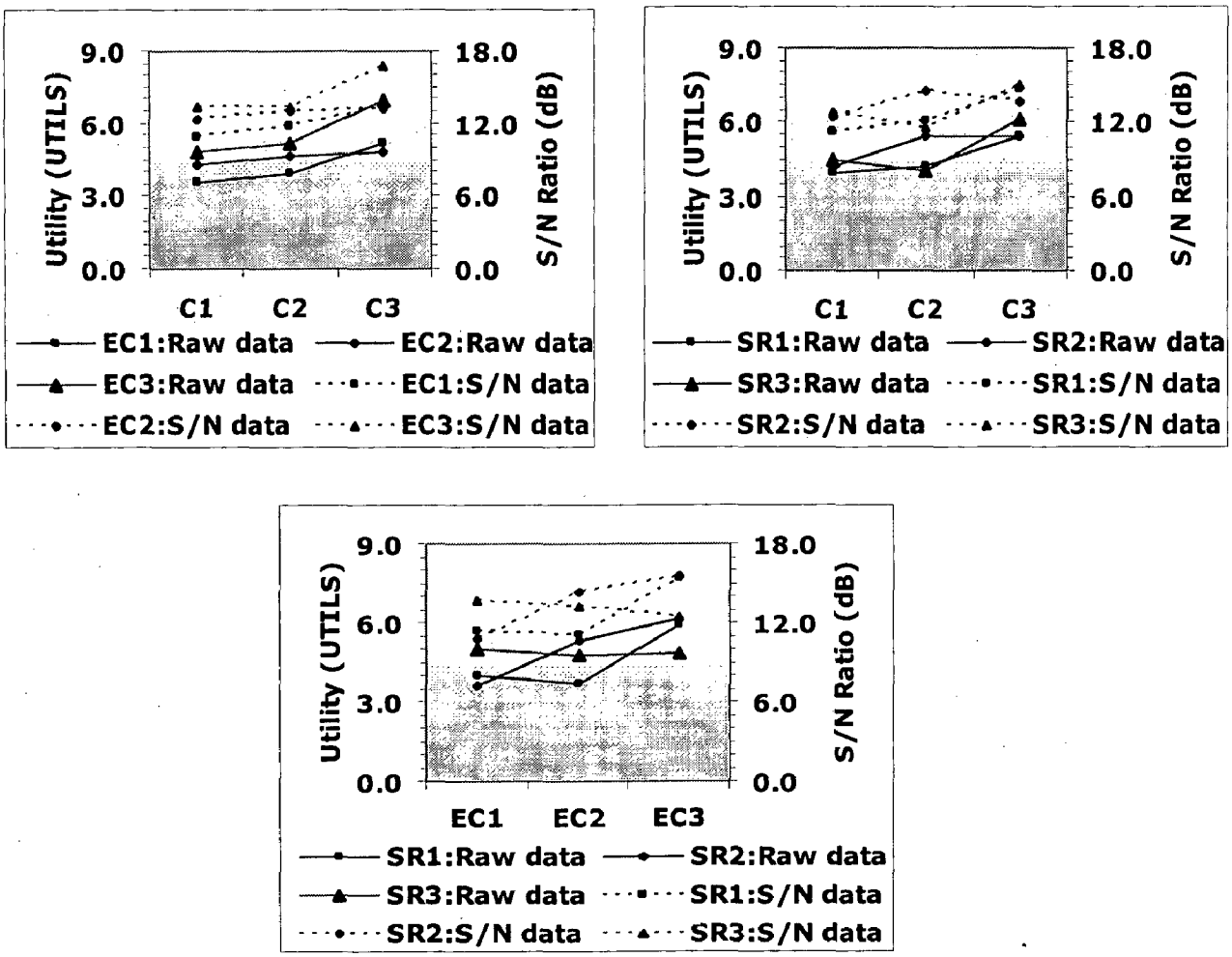

Fig. 8.8 Interaction plots (Utility: PIR_a-PIOR-DIR)

Table 8.45 Pooled ANOVA (Utility: PIR_a-PIOR-DIR: Raw Data)

Source	SS	DF	MS	F ratio	% Contribution
C	20.64	2	10.32	27.47*	14.00
EC	20.04	2	10.02	26.67*	13.58
SR	2.28	(2)	Pooled	-	-
F	0.97	(2)	Pooled	-	-
T	1.98	(2)	Pooled	-	-
SOP	23.38	2	11.69	31.12*	15.93
G	39.16	2	19.58	52.11*	27.03
C-EC	5.29	(4)	Pooled	-	-
C-SR	7.19	4	1.80	4.78*	4.00
EC-SR	17.77	4	4.44	11.82*	11.45
Model	128.19	16	8.01	21.32*	85.98
e(pooled)	13.90	37	0.38		14.02
Total	142.09	53			100.00

The Model F ratio of 21.32 implies that Model is significant at 99.5% confidence level.

* Significant at 95% confidence level.

SS: Sum of Square, DF: Degree of Freedom, MS: Mean Square, C: Current Intensity, EC: Electrolyte Concentration, SR: Speed Ratio, F: Electrolyte Flow Rate, T: Electrolyte Inlet Temperature, SOP: Stick-out Pressure, G: Grit Size.

Table 8.46 Pooled ANOVA (Utility: PIR_a-PIOR-DIR: S/N Data)

Source	SS	DF	MS	F ratio	% Contribution
C	25.80	2	12.90	7.44*	8.88
EC	28.18	2	14.09	8.13*	9.83
SR	3.92	(2)	Pooled	-	-
F	2.18	(2)	Pooled	-	-
T	2.67	(2)	Pooled	-	-
SOP	41.76	2	20.88	12.05*	15.23
G	74.52	2	37.26	21.49*	28.26
C-EC	8.56	(4)	Pooled	-	-
C-SR	18.93	4	4.73	2.73*	4.77
EC-SR	44.90	4	11.23	6.48*	15.10
Model	234.10	16	14.63	8.44*	82.07
e(pooled)	17.34	10	1.73		17.93
Total	251.44	26			100.00

The Model F ratio of 8.44 implies that Model is significant at 99.5% confidence level.

* Significant at 95% confidence level.

SS: Sum of Square, DF: Degree of Freedom, MS: Mean Square, C: Current Intensity, EC: Electrolyte Concentration, SR: Speed Ratio, F: Electrolyte Flow Rate, T: Electrolyte Inlet Temperature, SOP: Stick-out Pressure, G: Grit Size.

Table 8.47 Average Effects of C-SR Interaction (Utility: PIR_a-PIOR-DIR: Raw & S/N Data)

	Average Values, Utility (UTILS)			S/N Average Values, Utility (dB)		
	C_1	C_2	C_3	C_1	C_2	C_3
SR_1	3.96	4.21	5.45	11.26	11.97	14.65
SR_2	4.23	5.44	5.42	12.39	14.59	13.70
SR_3	4.44	4.05	6.12	12.79	11.52	14.96

*95 % Confidence Limit (CI_1) for average values-Raw data = ± 0.51

*95 % Confidence Limit (CI_1) for average values-S/N data = ± 1.69

Table 8.48 Average Effects of EC-SR Interaction (Utility: PIR_a-PIOR-DIR: Raw & S/N Data)

	Average Values, Utility (UTILS)			S/N Average Values, Utility (dB)		
	EC_1	EC_2	EC_3	EC_1	EC_2	EC_3
SR_1	4.03	3.67	5.92	11.44	11.06	15.38
SR_2	3.61	5.34	6.15	10.80	14.35	15.53
SR_3	4.99	4.74	4.88	13.69	13.16	12.42

*95 % Confidence Limit (CI_1) for average values-Raw data = ± 0.51

*95 % Confidence Limit (CI_1) for average values-S/N data = ± 1.69

8.1.6.1 Prediction of Optimal Values of Performance Characteristics

The optimal levels of the process input parameters for mean and S/N utility of Model: PIR_a-PIOR-DIR are as given in Tables 8.49.

Table 8.49 Optimal level of process parameters for Utility: PIR_a-PIOR-DIR

Process Input Parameters	Optimal Levels	
Current Intensity (ADC)#	C_3	180
Electrolyte Concentration (g/L)#	EC_3	200
Speed Ratio #	SR_2	150
Electrolyte Flow Rate (lpm)*	F_1	10
Electrolyte Inlet Temperature (°C)*	T_3	50
Stick-out Pressure (kPa)	SOP_3	30
Grit Size	G_2	600

** Not significant. Therefore, selected conveniently.*

 # Interactions C- SR, and EC-SR are significant.

Tables 8.50-55 represent the values of the process performance characteristics at the selected optimal level of the process parameters maximizing the overall utility of combined responses.

Table 8.50 Average PIR_a at optimal level of process input parameters

Optimum Level of Significant Process Parameter	PIR_a (%)
C_3SR_2	75.05
EC_3SR_2	77.87
3rd Level of Stick-out Pressure (SOP_3)	75.71
2nd Level of Grit Size (G_2)	75.78
Overall Mean of PIR_a ($\bar{T}_{PIRa}$)	73.27

Table 8.51 Average S/N PIR_a at optimal level of process parameters

Optimum Level of Significant Process Parameter	S/N Ratio (dB)
C_3SR_2	37.49
EC_3SR_2	37.80
3rd Level of Stick-out Pressure (SOP_3)	37.55
2nd Level of Grit Size (G_2)	37.55
Overall Mean of S/N PIR_a ($\bar{T}_{S/NPIRa}$)	37.26

Table 8.52 Average PIOR at optimal level of process input parameters

Optimum Level of Significant Process Parameter	PIOR (%)
C_3SR_2	41.52
EC_3SR_2	44.07
3rd Level of Stick-out Pressure (SOP_3)	40.27
2nd Level of Grit Size (G_2)	43.83
Overall Mean of PIOR ($\bar{T}_{PIOR}$)	36.64

Table 8.53 Average S/NPIOR optimal level of process parameters

Optimum Level of Significant Process Parameter	S/N Ratio (dB)
C_3SR_2	31.54
EC_3SR_2	32.81
3rd Level of Stick-out Pressure (SOP_3)	31.75
2nd Level of Grit Size (G_2)	32.54
Overall Mean of S/N PIOR ($\bar{T}_{S/NPIOR}$)	30.77

Table 8.54 Average DIR at optimal level of process input parameters

Optimum Level of Significant Process Parameter	DIR (μm/min)
C_3SR_2	34.09
EC_3SR_2	31.17
3rd Level of Stick-out Pressure (SOP_3)	27.99
2nd Level of Grit Size (G_2)	27.34
Overall Mean of DIR ($\overline{T}_{DIR}$)	24.02

Table 8.55 Average S/N DIR at optimal level of process parameters

Optimum Level of Significant Process Parameter	S/N Ratio (dB)
C_3SR_2	27.87
EC_3SR_2	28.52
3rd Level of Stick-out Pressure (SOP_3)	27.45
2nd Level of Grit Size (G_2)	26.97
Overall Mean of S/N DIR ($\overline{T}_{S/NDIR}$)	26.04

The optimal values and corresponding 95% confidence intervals for population mean and mean of two confirmation experiments for the various performance characteristics are calculated below:

$\mathbf{u_{PIRa}} = C_3SR_2 + EC_3SR_2 + SOP_3 + G_2 - 3\ \overline{T}_{PIRa} = 84.60\ \%$

$CI_{pop} = \pm\ 6.01$, (CI_{pop}: $78.59 < u_{PIRa}(\%) < 90.61$)

$CI_{CE} = \pm\ 10.54$, (CI_{CE}: $74.06 < u_{PIRa}(\%) < 95.14$)

[$N = 27 \times 2 = 54$, $f_e = (53\text{-}12) = 41$, $v_e = 36.75$ (modified Table 7.19), $n_{eff} = 4.15$, $R = 2$, $F_{0.05}(1, 41) = 4.08062$]

$\mathbf{u_{S/N\ PIRa}} = C_3SR_2 + EC_3SR_2 + SOP_3 + G_2 - 3\ \overline{T}_{S/NPIRa} = 38.60$ dB

$CI_{pop} = \pm\ 1.24$, (CI_{pop} : $37.36 < u_{S/NPIRa}$ (dB) < 39.85)

$CI_{CE} = \pm\ 1.78$, (CI_{CE} : $36.83 < u_{S/NPIRa}$ (dB) < 40.38)

[$N = 27$, $f_e = (26\text{-}12) = 14$, $v_e = 0.70$ (modified Table 7.20), $n_{eff} = 2.08$, $R = 2$,

$F_{0.05}(1, 14) = 4.6001$]

$\mathbf{u_{PIOR}} = C_3SR_2 + EC_3SR_2 + SOP_3 + G_2 - 3\overline{T}_{PIOR} = 59.77\ \%$

$CI_{pop} = \pm 7.62$, (CI_{pop}: $52.16 < u_{PIOR}(\%) < 67.39$)

$CI_{CE} = \pm 13.36$, (CI_{CE}: $46.41 < u_{PIOR}(\%) < 73.14$)

[N = 27 x 2 = 54, $f_e = (53\text{-}12) = 41$, $v_e = 59.06$ (recalculated from Table 7.39),

$n_{eff} = 4.15$, R = 2, $F_{0.05}(1, 41) = 4.08062$]

$\mathbf{u_{S/N\ PIOR}} = C_3SR_2 + EC_3SR_2 + SOP_3 + G_2 - 3\ \overline{T}_{S/NPIOR} = 36.32$ dB

$CI_{pop} = \pm 3.35$, (CI_{pop}: $32.97 < u_{S/NPIOR}(dB) < 39.67$)

$CI_{CE} = \pm 4.78$, (CI_{CE}: $31.54 < u_{S/N\ PIOR}(dB) < 41.10$)

[N = 27, $f_e = (26\text{-}12) = 14$, $v_e = 5.06$ (recalculated from Table 7.40), $n_{eff} = 2.08$, R = 2,

$F_{0.05}(1, 14) = 4.6001$]

$\mathbf{u_{DIR}} = C_3SR_2 + EC_3SR_2 + SOP_3 + G_2 - 3\ \overline{T}_{DIR} = 48.53$ (μm/min)

$Cl_{pop} = \pm 13.11$, (CI_{pop}: $35.41 < u_{DIR}(\mu m/min) < 61.64$)

$Cl_{CE} = \pm 23.00$, (CI_{CE}: $25.52 < u_{DIR}(\mu m/min) < 71.53$)

[N = 27 x 2 = 54, $f_e = (53\text{-}12) = 41$, $v_e = 175.02$ (recalculated from Table 7.58),

$n_{eff} = 4.15$, R = 2, $F_{0.05}(1, 41) = 4.08062$]

$\mathbf{u_{S/N\ DIR}} = C_3SR_2 + EC_3SR_2 + SOP_3 + G_2 - 3\ \overline{T}_{S/NDIR} = 32.68$ dB

$CI_{pop} = \pm 7.80$, (CI_{pop}: $24.88 < u_{S/NDIR}(dB) < 40.49$)

$CI_{CE} = \pm 11.14$, (CI_{CE}: $21.54 < u_{S/NDIR}(dB) < 43.83$)

[N = 27, $f_e = (26\text{-}12) = 14$, $v_e = 27.50$ (modified Table 7.59), $n_{eff} = 2.08$, R = 2,

$F_{0.05}(1, 14) = 4.6001$]

8.1.7 Model 5: PIR_a-PICyl-DIR

The overall raw utility values and S/N utility, ANOM and ANOVA for raw and S/N data and corresponding response plots for combined three ECH performance characteristics namely PIR_a, PICyl and DIR are presented in Table 8.56-62 and Fig. 8.9-10. Preferences assigned to PIR_a, PICyl and DIR are 0.4, 0.4 and 0.2 respectively. Results indicate that C, EC, G, C-SR and EC-SR are significant for both the mean and S/N utility.

Table 8.56 Utility values (PIR_a-PICyl-DIR)

Trial No.	Utility Values (UTILS)		S/N Ratio (dB)
	Y_{R1}	Y_{R2}	
1	2.51	2.74	8.36
2	3.81	4.24	12.05
3	4.23	3.95	12.22
4	4.07	3.44	11.40
5	4.29	3.61	11.83
6	5.70	5.60	15.04
7	6.47	5.90	15.80
8	5.00	3.95	12.84
9	3.55	3.60	11.06
10	2.82	3.33	9.66
11	4.42	4.71	13.18
12	4.12	3.99	12.16
13	3.26	3.11	10.06
14	5.02	5.22	14.18
15	5.17	5.81	14.74
16	6.49	6.17	16.02
17	6.63	7.10	16.72
18	1.96	2.91	7.24
19	6.41	6.35	16.09
20	2.19	2.43	7.24
21	6.68	6.74	16.54
22	4.66	4.86	13.54
23	6.37	6.85	16.38
24	3.29	3.76	10.88
25	4.87	5.47	14.23
26	6.96	7.42	17.12
27	8.37	8.53	18.54
	T_{UTIL} = Overall Mean of UTIL = 4.84		= 13.15 dB

*R1, R2 represent repetitions.

Table 8.57 Average and Main Effects (Utility: PIR_a -PICyl-DIR: Raw Data)

Process Input Parameter	Average Values, Utility (UTILS)			Main Effects, Utility (UTILS)	
	L1	L2	L3	L2-L1	L3-L2
C	4.26	4.57	5.68	0.31	1.11
EC	4.20	4.67	5.63	0.47	0.96
SR	4.61	5.01	4.89	0.41	-0.12
F	4.86	5.03	4.61	0.17	-0.42
T	4.60	4.88	5.02	0.28	0.14
SOP	3.92	5.02	5.57	1.10	0.56
G	5.02	5.71	3.77	0.69	-1.94
C-EC	4.81	5.01	4.68	0.20	-0.33
C-SR	4.91	4.69	4.90	-0.22	0.21
EC-SR	4.86	4.46	5.18	-0.40	0.72

L1, L2 and L3 represent average values of raw data of response of corresponding parameters at levels 1, 2 and 3 respectively. L2-L1 is the average main effect when the corresponding parameter changes from level 1 to level 2. L3-L2 is the average main effect when the corresponding parameter changes from level 2 to level 3.

* 95 % Confidence Limit (CI_l) = ± 0.28

C: Current Intensity, EC: Electrolyte Concentration, SR: Speed Ratio, F: Electrolyte Flow Rate, T: Electrolyte Inlet Temperature, SOP: Stick-out Pressure, G: Grit Size.

Table 8.58 Average and Main Effects (Utility: PIR_a-PICyl-DIR: S/N Data)

Process Input Parameter	S/N Average Values, Utility (dB)			Main Effects, Utility (dB)	
	L1	L2	L3	L2-L1	L3-L2
C	12.29	12.66	14.51	0.37	1.85
EC	11.94	13.12	14.40	1.17	1.28
SR	12.80	13.51	13.16	0.71	-0.35
F	13.10	13.64	12.71	0.54	-0.93
T	12.65	13.44	13.37	0.79	-0.08
SOP	11.39	13.46	14.60	2.07	1.14
G	13.60	14.76	11.10	1.16	-3.66
C-EC	13.05	13.40	13.00	0.35	-0.40
C-SR	13.11	12.95	13.39	-0.16	0.44
EC-SR	13.04	12.42	14.00	-0.63	1.58

L1, L2 and L3 represent average values of S/N data of response of corresponding parameters at levels 1, 2 and 3 respectively. L2-L1 is the average main effect when the corresponding parameter changes from level 1 to level 2. L3-L2 is the average main effect when the corresponding parameter changes from level 2 to level 3.

* 95 % Confidence Limit (CI_l) = ± 0.96

C: Current Intensity, EC: Electrolyte Concentration, SR: Speed Ratio, F: Electrolyte Flow Rate, T: Electrolyte Inlet Temperature, SOP: Stick-out Pressure, G: Grit Size.

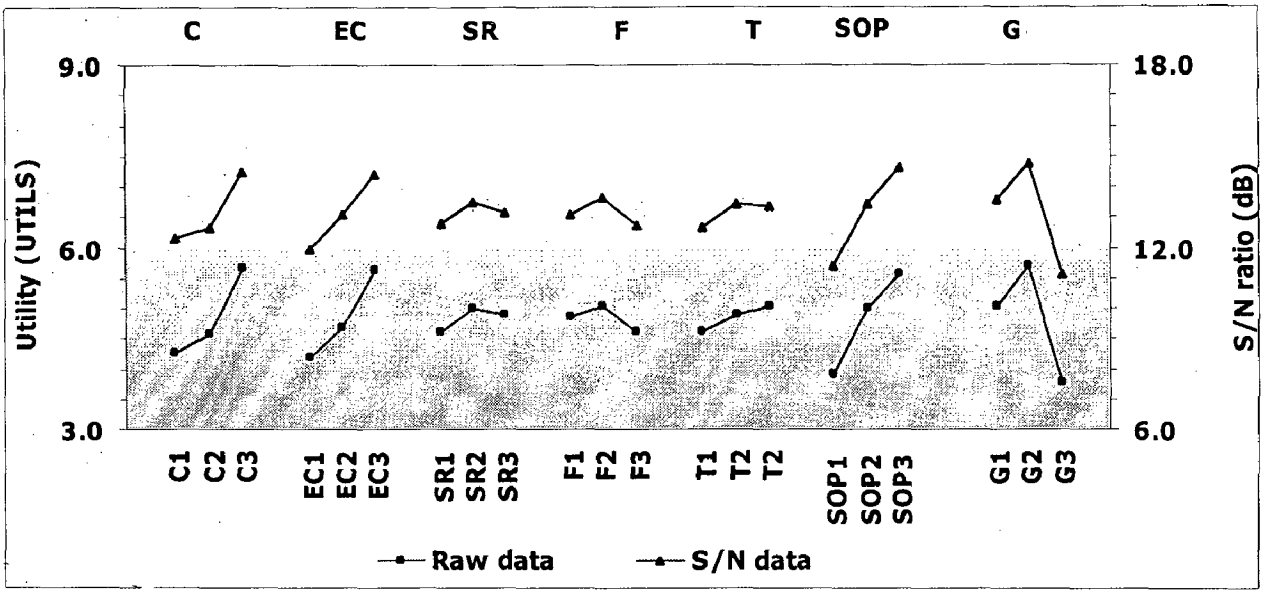

Fig. 8.9 Effects of process parameters on Utility: PIR_a-PICyl-DIR and S/N Ratio (Main Effects)

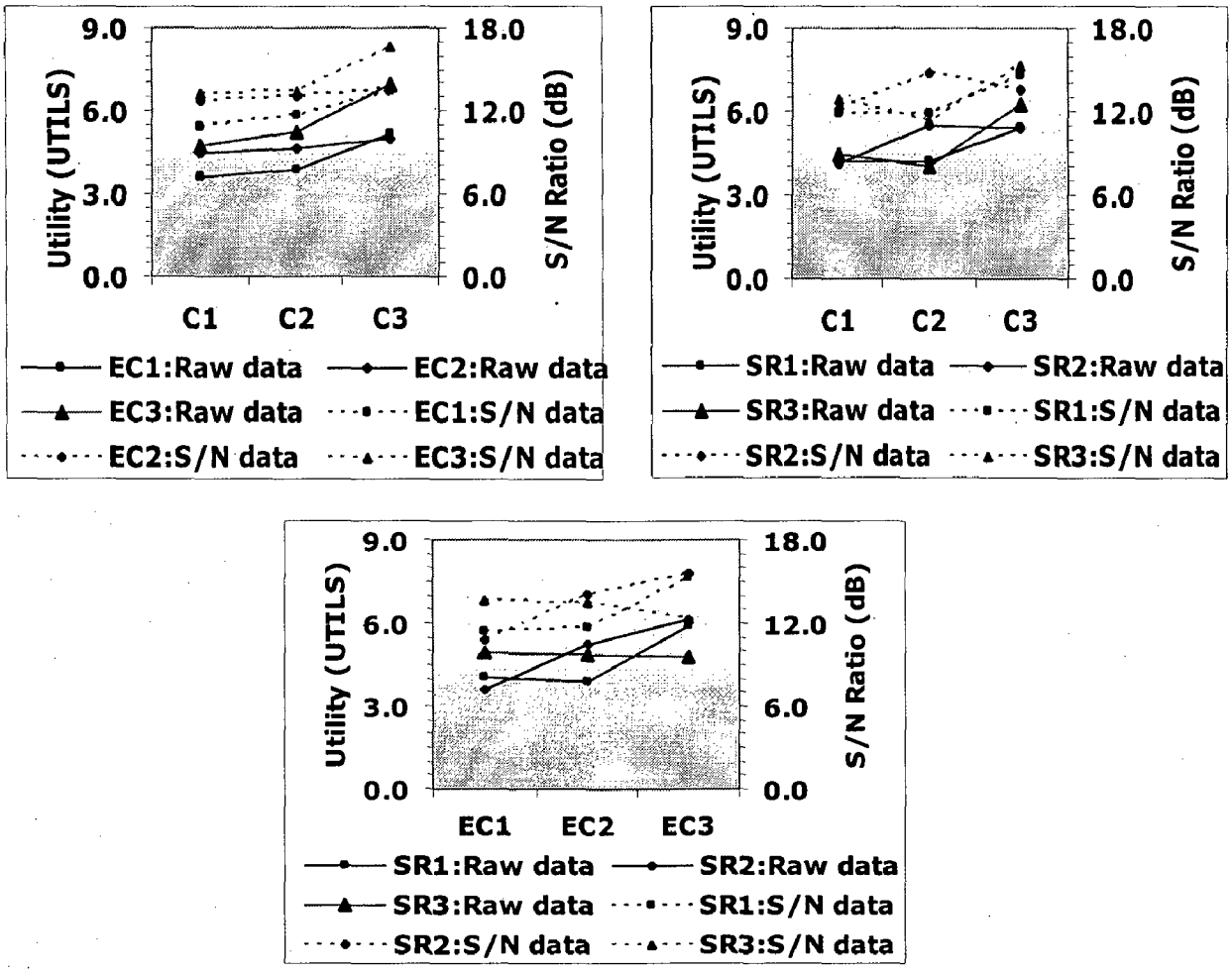

Fig. 8.10 Interaction plots (Utility: PIR_a-PICyl-DIR and S/N Ratio)

Table 8.59 Pooled ANOVA (Utility: PIR_a-PICyl-DIR: Raw Data)

Source	SS	DF	MS	F ratio	% Contribution
C	20.06	2	10.03	29.59*	14.10
EC	19.08	2	9.54	28.14*	13.39
SR	1.55	(2)	Pooled	-	-
F	1.60	(2)	Pooled	-	-
T	1.62	(2)	Pooled	-	-
SOP	25.47	2	12.74	37.58*	18.04
G	34.74	2	17.37	51.25*	24.79
C-EC	4.87	(4)	Pooled	-	-
C-SR	9.72	4	2.43	7.17*	6.09
EC-SR	15.83	4	3.96	11.68*	10.53
Model	124.91	16	7.81	23.03*	86.93
e(pooled)	12.54	37	0.34		13.07
Total	137.45	53			100.00

The Model F ratio of 23.03 implies that Model is significant at 99.5% confidence level.

* Significant at 95% confidence level.

SS: Sum of Square, DF: Degree of Freedom, MS: Mean Square, C: Current Intensity, EC: Electrolyte Concentration, SR: Speed Ratio, F: Electrolyte Flow Rate, T: Electrolyte Inlet Temperature, SOP: Stick-out Pressure, G: Grit Size.

Table 8.60 Pooled ANOVA (Utility: PIR_a-PICyl-DIR: S/N Data)

Source	SS	DF	MS	F ratio	% Contribution
C	25.41	2	12.70	7.52*	9.03
EC	27.07	2	13.54	8.02*	9.71
SR	2.27	(2)	Pooled	-	-
F	3.92	(2)	Pooled	-	-
T	3.43	(2)	Pooled	-	-
SOP	47.60	2	23.80	14.10*	18.13
G	63.01	2	31.50	18.66*	24.45
C-EC	7.26	(4)	Pooled	-	-
C-SR	22.60	4	5.65	3.35*	6.50
EC-SR	41.36	4	10.34	6.13*	14.19
Model	227.05	16	14.19	8.41*	82.01
e(pooled)	16.88	10	1.69		17.99
Total	243.93	26			100.00

The Model F ratio of 8.41 implies that Model is significant at 99.5% confidence level.

* Significant at 95% confidence level.

SS: Sum of Square, DF: Degree of Freedom, MS: Mean Square, C: Current Intensity, EC: Electrolyte Concentration, SR: Speed Ratio, F: Electrolyte Flow Rate, T: Electrolyte Inlet Temperature, SOP: Stick-out Pressure, G: Grit Size.

Table 8.61 Average Effects of C-SR Interaction (Utility: PIR_a-PICyl-DIR: Raw & S/N Data)

	Average Values, Utility (UTILS)			S/N Average Values, Utility (dB)		
	C_1	C_2	C_3	C_1	C_2	C_3
SR_1	4.19	4.20	5.44	11.85	11.91	14.62
SR_2	4.15	5.52	5.37	12.24	14.69	13.58
SR_3	4.44	3.99	6.23	12.78	11.38	15.32

*95 % Confidence Limit (CI_1) for average values-Raw data = ± 0.48

*95 % Confidence Limit (CI_1) for average values-S/N data = ± 1.67

Table 8.62 Average Effects of EC-SR Interaction (Utility: PIR_a-PICyl-DIR: Raw & S/N Data)

	Average Values, Utility (UTILS)			S/N Average Values, Utility (dB)		
	EC_1	EC_2	EC_3	EC_1	EC_2	EC_3
SR_1	4.02	3.90	5.90	11.37	11.67	15.35
SR_2	3.63	5.23	6.18	10.82	14.13	15.56
SR_3	4.95	4.89	4.82	13.64	13.55	12.28

*95 % Confidence Limit (CI_1) for average values-Raw data = ± 0.48

*95 % Confidence Limit (CI_1) for average values-S/N data = ± 1.67

8.1.7.1 Prediction of Optimal Values of Performance Characteristics

The analysis reveals the optimal levels of the process input parameters for mean and S/N utility of Model: PIR_a-PICyl-DIR as given in Tables 8.63.

Table 8.63 Optimal level of process parameters for Utility: PIR_a-PICyl-DIR

Process Input Parameters	Optimal Levels	
Current Intensity (ADC)#	C_3	180
Electrolyte Concentration (g/L)#	EC_3	200
Speed Ratio #	SR_2	150
Electrolyte Flow Rate (lpm)*	F_1	10
Electrolyte Inlet Temperature (°C)*	T_3	50
Stick-out Pressure (kPa)	SOP_3	30
Grit Size	G_2	600

** Not significant. Therefore, selected conveniently.*

 # Interactions C-SR, and EC-SR are significant.

Since the optimal levels of the process parameters are the same as in combined optimization of PIR_a, PIOR and DIR, the same optimal predicted results for PIR_a and DIR are applicable in this case also. The average values of PICyl and S/N PICyl for the selected optimal parameter levels are shown in Tables 8.64 and 8.65 respectively.

Table 8.64 Average PICyl at optimal level of process input parameters

Optimum Level of Significant Process Parameter	PICyl(%)
C_3SR_2	53.97
EC_3SR_2	59.45
3rd Level of Stick-out Pressure (SOP_3)	54.36
2nd Level of Grit Size (G_2)	59.02
Overall Mean of PIOR ($\bar{T}_{PICyl}$)	49.03

Table 8.65 Average S/N PICyl at optimal level of process parameters

Optimum Level of Significant Process Parameter	S/N Ratio (dB)
C_3SR_2	33.83
EC_3SR_2	35.39
3rd Level of Stick-out Pressure (SOP_3)	34.50
2nd Level of Grit Size (G_2)	35.14
Overall Mean of S/N PICyl ($\bar{T}_{S/NPICyl}$)	33.34

The optimal values of PICyl (u_{PICyl}) and S/N PICyl ($u_{S/NPICyl}$) alongwith the respective 95% CI_{pop} & CI_{CE} can be calculated as shown below:

$\mathbf{u_{PICyl}} = C_3SR_2 + EC_3SR_2 + SOP_3 + G_2 - 3\bar{T}_{PICyl} = 79.72\ \%$

$CI_{pop} = \pm 9.26$, (CI_{pop}: $70.45 < u_{PICyl}(\%) < 88.98$)

$CI_{CE} = \pm 16.25$, (CI_{CE} : $63.47 < u_{PICyl}(\%) < 95.97$)

[$N = 27 \times 2 = 54$, $f_e = (53\text{-}12) = 41$, $v_e = 87.35$ (recalculated from Table 7.48),

$n_{eff} = 4.15$, $R = 2$, $F_{0.05}(1,41) = 4.08062$]

$\mathbf{u_{S/N\ PICyl}} = C_3SR_2 + EC_3SR_2 + SOP_3 + G_2 - 3\ \bar{T}_{S/NPICyl} = 38.83$ dB

[$N = 27$, $f_e = (26\text{-}12) = 14$, $v_e = 4.16$ (recalculated from Table 7.49), $n_{eff} = 2.08$, $R = 2$,

$F_{0.05}(1,14) = 4.6001$]

$CI_{pop} = \pm 3.03$, (CI_{pop}: $35.80 < u_{S/NPICyl}$ (dB) < 41.87)

$CI_{CE} = \pm 4.33$, (CI_{CE}: $34.50 < u_{S/NPICyl}$ (dB) < 43.17)

8.1.8 Confirmation Experiments

In order to validate the optimal results of various process performance characteristics of ECH obtained through developed 'Utility based Taguchi Approach Models' for multi-performance optimization, two confirmation experiments were performed for each of the process performance characteristic at the optimal settings of the process parameters and the average values have been compared statistically with their corresponding predicted values. The average values of the performance characteristic obtained through the confirmation experiments must be within the 95% confidence interval CI_{CE} of the respective process performance characteristic. However, the average value of the process performance characteristic obtained from the confirmation experiments may or may not lie within 95% CI_{POP}. With a varying significance of different process input parameters, the optimal level for various 'Utility based Taguchi Approach multi-performance optimization Models' correspond to a single setting, $C_3EC_3SR_2F_1T_3SOP_3G_2$. The results of the confirmation experiments are given in Table 8.66. Since confirmation experiment mean values for the various process performance characteristics lie within their respective 95% CI_{CE}, 'Utility based Taguchi Approach Models for Multi-Performance Optimization of ECH' are, therefore, validated.

Table 8.66 Confirmation experiment results
(Utility based Taguchi Approach Multi Performance Optimization Models)

Utility based Taguchi Approach Models	Process Performance Characteristic	Predicted Optimal Values	95% Confidence Interval (CI_{CE})	Actual CE Values
Model 1: PIR_a-PIOR	PIR_a	83.35 %	$72.43 < u_{PIRa}(\%) < 94.26$	85.36%
	S/N PIR_a	38.38 dB	$36.91 < u_{S/NPIRa}$ (dB)< 39.85	38.62dB
	PIOR	68.45 %	$57.24 < u_{PIOR}(\%) < 79.66$	63.29%
	S/N PIOR	35.55 dB	$31.53 < u_{S/NPIOR}$ (dB)< 39.57	36.02dB
Model 2: PIR_a-PICyl	PIR_a	83.35 %	$72.43 < u_{PIRa}(\%) < 94.26$	85.36%
	S/N PIR_a	38.38 dB	$36.91 < u_{S/NPIRa}$ (dB)< 39.85	38.62dB
	PICyl	90.39 %	$77.26 < u_{PICyl}(\%) < 100$	83.07%
	S/N PICyl	38.35 dB	$34.45 < u_{S/NPICyl}$ (dB)< 42.25	38.39dB
Model 3: PIR_a-DIR	PIR_a	88.01 %	$77.85 < u_{PIRa}(\%) < 98.16$	85.36%
	S/N PIR_a	38.89 dB	$38.11 < u_{S/NPIRa}$ (dB)< 39.67	38.62dB
	DIR	59.95 (μm/min)	$34.50 < u_{DIR}$ (μm/min) < 85.39	54.17 (μm/min)
	S/N DIR	33.82 dB	$27.57 < u_{S/NDIR}$ (dB) < 40.06	34.66dB
Model 4: PIR_a-PIOR-DIR	PIR_a	84.60 %	$74.06 < u_{PIRa}(\%) < 95.14$	85.36%
	S/N PIR_a	38.60 dB	$36.83 < u_{S/NPIRa}$ (dB)< 40.38	38.62dB
	PIOR	59.77 %	$46.41 < u_{PIOR}(\%) < 73.14$	63.29%
	S/N PIOR	36.32 dB	$31.54 < u_{S/NPIOR}$ (dB)< 41.10	36.02dB
	DIR	48.53 (μm/min)	$25.52 < u_{DIR}$ (μm/min) < 71.53	54.17 (μm/min)
	S/N DIR	32.68 dB	$21.54 < u_{S/NDIR}$ (dB) < 43.83	34.66dB
Model 5: PIR_a-PICyl-DIR	PIR_a	84.60 %	$74.06 < u_{PIRa}(\%) < 95.14$	85.36%
	S/N PIR_a	38.60 dB	$36.83 < u_{S/NPIRa}$ (dB)< 40.38	38.62dB
	PICyl	79.72 %	$63.47 < u_{PICyl}(\%) < 95.97$	83.07%
	S/N PICyl	38.83 dB	$34.50 < u_{S/NPICyl}$ (dB)< 43.17	38.39dB
	DIR	48.53 (μm/min)	$25.52 < u_{DIR}$ (μm/min) < 71.53	54.17 (μm/min)
	S/N DIR	32.68 dB	$21.54 < u_{S/NDIR}$ (dB) < 43.83	34.66dB

8.2. TAGUCHI-NN-GA MULTI-PERFORMANCE OPTIMIZATION CONTROL STRATEGY

The effect of increasing international competition in business is relentless pressure on manufacturing organizations to lower product costs and increase product quality. For the manufacturing organization, these pressures translate into a continuous effort to reduce process variability and maintain a stable manufacturing operation optimizing several process performance characteristics as per the demand. The methodology of Taguchi's quality loss function has proved to be an efficient tool to produce high quality products at low cost. The loss function is usually transformed in one of the three most commonly used signal-to-noise ratios (S/N ratio) § 6.2.4.2. A high value of S/N ratio implies that the signal is much higher than the random effect of the noise factors irrespective of the category of the process performance characteristics. This property can serve as a tool in case of single performance characteristic optimization. But in the case of multi-response optimization an overall evaluation of the S/N ratio is required, as a higher value of S/N ratio for one performance characteristic may correspond to a lower one in case of another.

In the modern era of soft computing and automation the use of artificial intelligence techniques like artificial neural network (also referred to as NN) is finding ever increasing applications to model and control the engineering processes. NN is a computational mechanism that is able to "acquire, represent, and compute a mapping from multivariate space of information to another, given a set of data representing that mapping" (Garrett, 1994). NN is capable of learning from training examples and ending meaningful solutions without the need to specify the relationship among variables. It can capture nonlinear and complex interactions among variables in a system (Goh and Kulhawy, 2003). Genetic algorithms are computerized search and optimization algorithms based on the mechanics of natural genetics and natural selection (Rajasekaran and Pai, 2003). Genetic algorithms work

with a set of individuals, representing possible solutions of the task. The selection principle is applied by using a criterion, giving an evaluation for the individual with respect to the desired solution. The best-suited individuals create the next generation. GAs can perform parallel and global search, optimization and generalization, but as GAs are computational tools, they need a single figure of merit as a fitness function to perform optimization (Goldberg, 1989; Deb, 1999; Deb 2001). The multi-performance optimization can be done either using an aggregating function like desirability function to transform the multi-objective problem as a single objective to be optimized using GAs or the multi-responses can also be optimized simultaneously using some criteria like Pareto optimality.

The combination of Taguchi loss function, NN and GA can provide an effective platform for the multi-performance optimization and control of complex manufacturing processes such as ECH, involving several correlated process variables. The proposed strategy is comprised of three stages. First, a neural network model is developed to predict the S/N ratios of various process performance characteristics obtained through Taguchi experiment design and analysis on the basis of process input parameters and trial conditions. Next, the multi-performance outputs from the NN are converted into the desirability values based on respective preference scales. Finally the optimal solution can be obtained in two different ways: either the desirability values of various performance characteristics are unified using the desirability function or modified desirability function (Derringer and Suich, 1980) to provide a single fitness function for GA in the final stage to obtain the nearest optimal values of the performance characteristics and corresponding parameter settings; or using directly the desirability values of multiple responses to obtain a set of Pareto-optimal solutions by GA.

8.2.1 Artificial Neural Networks (ANN)

An *Artificial Neural Network (ANN)* is a computational tool having AI origins. A neural network is a massively parallel distributed processor made up of simple processing units, which has a natural propensity for storing experiential knowledge and making it available for use (Hykin, 2003). An NN, in general, is a highly interconnected network of processing elements called neurons in an architecture inspired by the brain. Neural networks exhibit characteristics such as mapping capability or pattern association, generalization, robustness, fault tolerance and parallel and high speed information processing (Rajasekaran and Pai, 2003). NN are used for a wide range of applications covering character recognition, speech recognition, mapping from spelling to sound, motor control, data training and many more areas of applications. Though NN architectures have been broadly classified as single layer feed forward networks, multiplayer feed forward networks, and recurrent networks, over the years several other NN architectures have evolved. During the last two decades, NN algorithms have been rapidly developed for universal function approximator (Cardaliaguet and Euvrand, 1992; Chapman and Crossland, 1995; Hornik et al., 1989, 1990; Schueremans and Van Gemert, 2005).

Although Multilayer Feedforward (MLFF) networks with backpropagation learning are much discussed and most popular (Rajasekaran and Pai, 2003), another neural network-radial basis function neural network (RBF NN) is increasingly getting attraction recently (Chen and Chen, 1995; Haykin, 2003; Li, 1996; Mai-Duy and Tran-Cong, 2003; Park and Sandberg, 1993; Warnes et al., 1998; Zuo and Fan, 2006; Zhang Yun-Xin and TanYong-Ji, 2006). Deng (2006) used RBF NN for structural analysis for implicit performance function. Another application of RBF NN was reported by Verma et al. (2006) for gas turbine condition monitoring and fault isolation. The RBF NN showed significant noise reduction and when combined with the Genetic Fuzzy System led to a diagnostic system that was

highly robust to the presence of noise in data. A RBF NN and GA based model was constructed by Han et al. (2005) for plasma etching process control. GA-RBFNN provided much improved predictions of etch responses as compared to statistical regression models. A similar finding was also reported by Kim and Park (2004) when plasma etch process was modeled using RBF NN. In another instance, a Taguchi-tuned RBF network was found highly effective for high precision motion control (Tan and Tang, 2001). West et al. (1999) demonstrated that the radial basis function network was superior to three control models recently proposed for complex manufacturing processes: multivariate Shewhart, multivariate exponentially weighted moving average statistic, and a feed forward neural network with logistic units trained by back-propagation (often called a back-propagation neural network).

The reason is that the training of a RBF network can be essentially faster than the methods used to train Multilayer Perceptron networks (Moody and Darken, 1989). The BPNN does not yield the approximating capabilities of RBF networks. Therefore the theory of RBF neural networks is still the subject of extensive ongoing researches (Orr, 1999). Li (1996) proved that any multivariate function and all its existing derivatives can be simultaneously approximated by a radial basis function network, where the assumptions on the functions are relatively mild. Hussain et al. (2002) applied radial basis function and polynomial metamodels (i.e. response surface metamodel) to approximate the input-output functions and compared their effectiveness qualitatively and quantitatively and concluded that radial function metamodels provide a better fit than the polynomial metamodels. One remarkable feature of RBF networks is described as follows (Bishop, 1995): "RBF networks possess the property of best approximation. An approximation scheme has this property if, in the set of approximating functions (i.e. the set of functions corresponding to all possible choices of the adjustable parameters) there is one function which has minimum

approximating error for any given function to be approximated. This property is not shared by MLPs".

The present study, therefore, utilized the Radial Basis Function Networks (RBF NN) to model the non-linear functional relationships between the process input parameters and the Taguchi loss function (S/N ratios) of multiple process performance characteristics of ECH. The experimental results were also modeled using multilayer feedforward networks with backpropagation training based on standard steepest descent gradient approach as well as Levenberg-Marquardt (LMBP) algorithm which is an effective accelerated learning backpropagation algorithm. In the following sections, a brief introduction of standard BPNN, LMBP NN and RBF NN, is presented. Detailed treatments are given in (Haykin, 2003; Rajasekaran and Pai, 2001; Cichocki and Unbehauen, 1996; Ham and Kostanic, 2002).

8.2.1.1 Back Propagation Neural Network (BPNN)

The *multilayer feedforwad neural networks* commonly referred to as *multilayer perceptrons* (MLPs) (Fig. 8.11) consist of an input layer (a set of sensory nodes), one or more hidden layers of computation nodes, and an output layer of computation nodes. A popular algorithm used to train the MLP NN is the error backpropagation algorithm or error-correction learning rule (or simply backpropagation) which is based on the steepest descent gradient approach applied to the minimization of an energy function representing the instantaneous error. For the learning phase, an input pattern is applied to the network, and its effect propagates through the network layer-by-layer, while keeping the synaptic weights of the network fixed, until an output is produced. The output pattern is compared with the desired output and the error signal generated is then propagated backward against the synaptic connections and synaptic weights are adjusted in accordance with an error

correction rule to make the actual response of the network move closer to the desired response (Haykin, 2003).

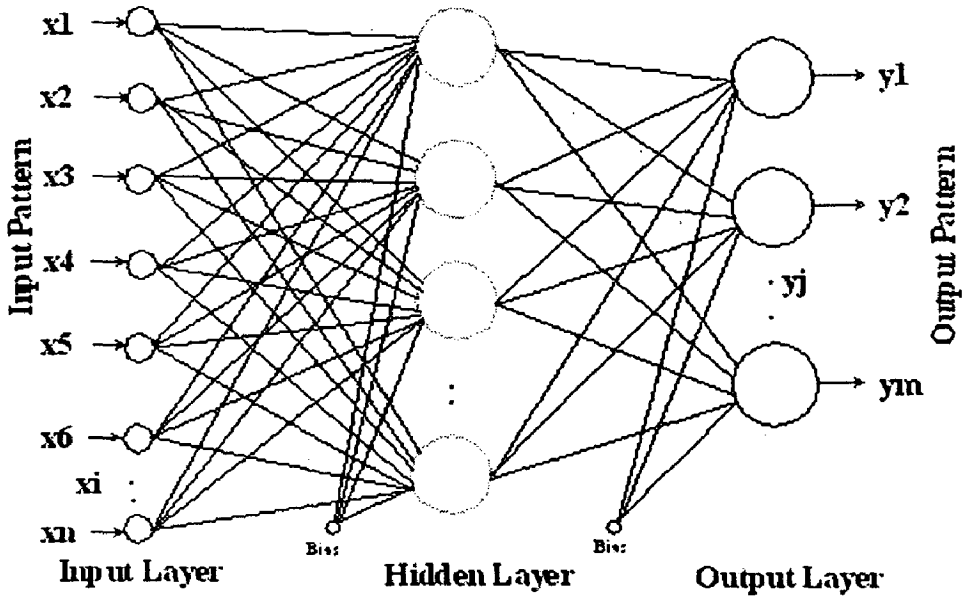

Fig. 8.11 Architecture of a three-layer MLP NN

The neurons (i) in the input layer distribute the input signals x_i to neurons in the hidden layer. Each neuron (j) in the hidden layer sums up its input signals x_i after weighing them with the strength of the respective connections w_{ij} to produce its output y_j as:

$$y_j = f\left(\sum w_{ji} x_i\right) \tag{8.7}$$

where, f is a nonlinear activation function. Assuming the use of a tansigmoidal function, the output is given as:

$$y_j = f(\upsilon) = \tanh(\upsilon) \tag{8.8}$$

where, υ is the induced local field (i.e. the weighted sum of all synaptic inputs plus the bias). Using the steepest descent gradient approach, the learning rule for a network weight in any layer is obtained by minimizing an energy function representing the mean instantaneous sum

of squared error (Eq) by comparing the desired (d_{qj}) and actual (y_{qj}) network outputs for the (q^{th}) input pattern.

$$Eq = \frac{1}{2}\sum_{j=1}^{n}(d_{qj} - yqj)^2 \qquad (8.9)$$

where, n is the total number of output nodes. The learning rule for the network weight in any layer is given as:

$$\Delta w_{ji} = \mu \delta_j x_i \qquad (8.10)$$

where, $\mu \geq 0$ is the learning rate parameter which influences the rate of convergence. For a too large learning rate, the search path will oscillate and converge more slowly, while convergence time increases significantly if μ is too small. $\delta_j = -\frac{\partial Eq}{\partial \upsilon_j}$, commonly referred to as local error or delta, depends on whether neuron is an output neuron or a hidden neuron.

For output neurons: $\delta_j = \frac{\partial f}{\partial \upsilon_j}(y_{dj} - y_j)$ (8.11)

For hidden neurons: $\delta_j = \frac{\partial f}{\partial \upsilon_j}(\sum_r w_{kj}\delta r)$ (8.12)

where, y_{dj} is the desired output for neuron j. During the training process, the desired outputs of the hidden neurons are not known. The difference between the desired and actual outputs of a hidden neuron is, therefore, estimated by the weighted sum of the δ_r terms already obtained for neurons r connected to the output of j.

A momentum term α is added to delta rule (8.10) to improve the convergence and smooth out the descent path by avoiding the instability due to extreme changes in the gradients resulting from local anomalies (Pham and Karaboga, 2000).

$$\Delta w_{ji}(k+1) = \mu \delta_j x_i + \alpha \Delta w_{ji}(k) \qquad (8.13)$$

where, subscript k indicates the evaluation of appropriate matrices at $w = w(k)$.

8.2.1.2 Levenberg-Marquardt (LMBP) Algorithm

The Levenberg-Marquardt backpropagation (LMBP) algorithm represents a simplified version of Newton's Method, a well established numerical optimization technique with quadratic speed of convergence, applied for training the MLP networks. The LM algorithm for updating the network weights is given as (Ham and Kostanic, 2002):

$$w(k+1) = w(k) - \left[J_k^T J_k + \mu_k I \right]^{-1} J_k^T e_k \tag{8.14}$$

where, $J \in \Re^{PxN}$ is the Jacobian Matrix, $I \in \Re^{NxN}$ is the identity matrix, parameter μ(mu) is the small number, w and e represent the weight and error vectors respectively, subscript k indicates the evaluation of appropriate matrices at $w = w(k)$, P is defined as the total number of training pairs multiplied by the number of output neurons.

LM algorithm represents a transition between the steepest gradient descent method and Newton's method. For a small value of mu, LM algorithm approximates the Newton's method:

$$\begin{aligned} w(k+1) &= w(k) - H_k^{-1} g_k \\ &\approx w(k) - \left[J_k^T J_k \right] J^T{}_k e_k \end{aligned} \tag{8.15}$$

where, $H_k^{-1} \in \Re^{NxN}$ is the inverse of Hessian matrix and $g = \frac{\delta E(w)}{\delta w}$ is the gradient of energy function. As the value of mu is increased, it approaches the steepest gradient descent algorithm for weight updating:

$$\begin{aligned} w(k+1) &= w(k) - \alpha_k \, g_k \\ &\approx w(k) - \frac{1}{\mu_k} J_k^T e_k \end{aligned} \tag{8.16}$$

8.2.1.3 Radial Basis Function Neural Networks (RBF NN)

The architecture of the radial basis function neural network (Fig. 8.12) involves three layers: an input layer, a single hidden layer of nonlinear processing neurons, and an output layer. The input layer consists of source nodes (sensory units) connecting network to its environment. All hidden units simultaneously receive the n-dimensional real-valued input vector x. The second only hidden layer in the network applies a nonlinear transformation of the input space to the hidden space using hidden neurons (processing units) performing a radial basis function. The output layer computes the RBF NN response (output to the activation pattern applied to the input layer) as a linear weighted sum of the hidden layer outputs (radial basis functions).

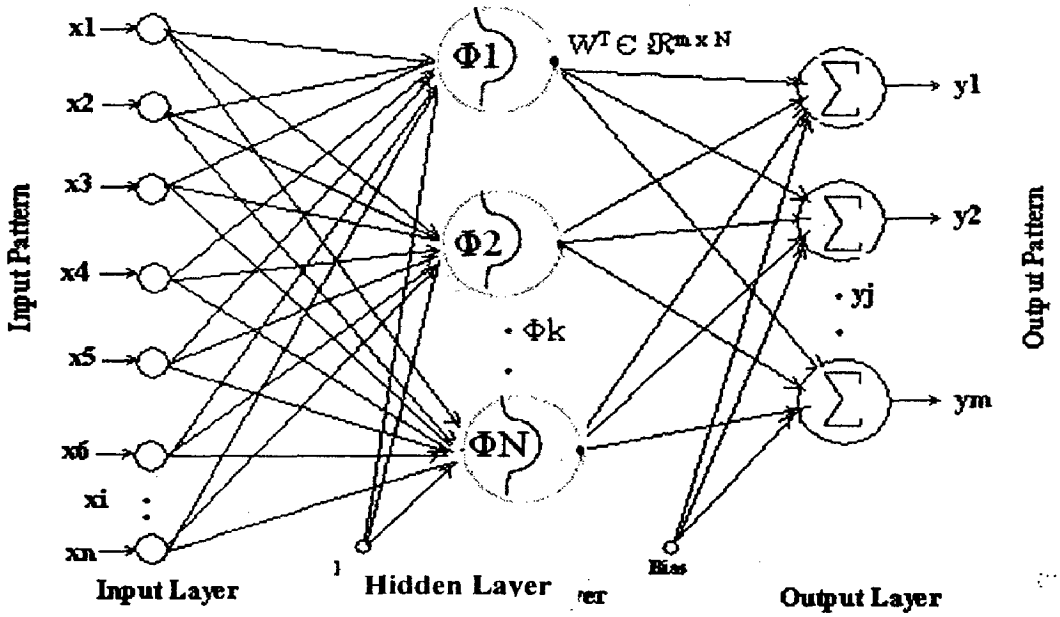

Fig. 8.12 The RBF NN architecture
: a radial basis function neural network consisting of a single hidden layer of locally tuned nonlinear RBF units which are fully interconnected to an output layer of linear units.

There is no interaction of the neurons in the output layer and, therefore, an RBF NN having more than one output can be considered as superposition of several single-output networks sharing a common hidden layer (Ham and Kostanic, 2002). In most of the applications the hidden space is of high dimensionality mainly because of two reasons. The

higher the dimension of the hidden space the more accurate is input-output mapping approximation by the network (Haykin, 2003). A pattern-recognition problem cast in a high-dimensional space is more likely to be linearly separable than in low-dimensional space (Cover, 1965). This also provides a justification for the rationale of a nonlinear transformation followed by a linear transformation in RBFNN, which essentially means that RBF NN can be trained using least-squares algorithms, making them very attractive for complex process modeling and control applications.

An RBF is a multidimensional function which depends on the Euclidean distance between the input vector x and RBF center c. Generally, the radial functions employed in the RBFN can be any function that decreases (or increases) monotonically with distance from a central point. There are a number of possible functions that meet this criterion including the Gaussian, multiquadratic, thin plate splines and inverse multiquadratic functions. The most popular and widely used is the Gaussian function, G(x), which has a peak at the center c and decreases monotonically. The Gaussian function provides better smoothing and interpolation properties (West et al., 1999; Ham and Kostanic, 2002). Therefore, a Gaussian RBF was employed as activation function in the present study.

All hidden units simultaneously receive the n-dimensional real-valued input vector x (in the present study n represents the number of input process parameters i.e. n =7). Each hidden unit output (RBF) Φ_k (x) (k = 1,. . . , N) is obtained by calculating the "closeness" of the input x to an n-dimensional parameter vector, where k is associated with the k^{th} hidden unit, N is the number of radial basis functions, i.e. the number of hidden units, and $N \leq Q$, Q is the number of input training pairs.

The output of a k^{th}-hidden neuron is a nonlinear function of the Euclidean distance between its associated center and the input to the network. The response characteristics of the k^{th} Gaussian hidden RBF are given as:

$$G_k(x, c_k) = \varphi_k(r) = \exp\left(-\frac{\|x - c_k\|^2}{\sigma^2_k}\right) \qquad \forall k = 1, 2, \ldots, N \qquad (8.17)$$

where, $\varphi_k(r)$ is called radial basis function, $r = \|x - c_k\|$ denotes the Euclidean distance $= \sqrt{(x - c_k)(x - c_k)} = \sqrt{\sum_{i=1}^{n}(x_i - c_i k)^2}$; and c_k is the centroid or centers of the radial basis function that are defined points to perform an adequate sampling of the input vector space, and the parameter σ is commonly referred to as the SPREAD parameter to control the 'width' of the RBF. The widths determine the radii of the areas around the centers, in which the activations from the pattern units are significant. The output of the RBF NN, y_j is a weighted linear combination of the N Gaussian radial basis functions:

$$y_j(x) = \sum_{k=1}^{N} w_{jk} \exp\left(-\frac{\|x - c_k\|^2}{\sigma^2_k}\right) + w_{jo} \qquad \forall j = 1, 2, \ldots, m \qquad (8.18)$$

where yj is the calculated value for each of the m output neurons, w_{j0} is the bias term associated with yj, and w_{jk} are elements of the weight vector W. The RBF network is frequently referred to as a local network because the output y_j is calculated from only those radial basis functions whose centers, c_k, are close to the input vector X. It is this property that enables the RBFNN to learn the bounded decision regions of complex process control applications (West et al., 1999).

There are three sets of RBF NN parameters, the position of RBF centers (centroids) of the hidden layer, the receptive field widths (SPREAD of RBF), and the output layer weights. Finding the centers, spread and weights of the hidden nodes constitutes the training of an RBF network. The position of the centers and spread of RBFs are critical for the optimal performance of an RBF network.

Three different learning strategies for designing an RBF NN depending upon the approach adopted to specify the RBF centers (Haykin, 2003) are: the fixed centers selected

at random, self-organized selection of centers using commonly employed " k-means clustering algorithm", supervised selection of centers and strict interpolation with regularization.

In the simplest approach called the batch training algorithm or training with fixed RBF centers, a fixed number of input vectors are selected randomly as RBF centers and the spread parameter is commonly set using heuristic procedures. For a Gaussian RBF (Ham and Kostanic, 2002):

$$\sigma = \frac{d_{max}}{\sqrt{K}} \tag{8.19}$$

where d_{max} is the maximum Euclidean distance between the K selected centers.

The RBF NN output for a training input vector q is given as:

$$y(q) = \sum_{k=1}^{N} w_{jk}\, \varphi(x(q), ck) + w_{jo} \qquad q = 1, 2, \ldots, Q \tag{8.20a}$$

$$\text{or } O = \varphi\, W \tag{8.20b}$$

After determining the centers and spread of RBFs, weight setting in output can be determined in a deterministic way to minimize the mean squared error E between the actual and desired network outputs in single-shot process using pseudo-inverse matrices:

$$E = \frac{1}{2}\sum_{q=1}^{Q}(T - O)^2 \tag{8.21}$$

and the resulting weight (W) matrix between the pattern and output layers is simply expressed as:

$$W = (\varphi^T \varphi)^{-1} \varphi^T T = \varphi^+ T \tag{8.22}$$

where O and T represent the output matrix of the pattern layer and target matrix, respectively and φ^+ denotes the pseudoinverse of nonlinear mapping matrix φ (Han et al., 2005). The closed-form solution provided from (8.22) makes the training of RBF NN very fast as compared to BPNN and even counterpropagation networks. Another important point is that

8.2.2 Desirability Function

Desirability function approach is employed to convert the multi-performance problem effectively into a single response problem (Derringer and Suich, 1980; Montgomery, 2004). The NN output in terms of multi-performance characteristics is converted into the desirability function to provide a fitness function for GA to obtain optimal/nearest setting of process input parameters. The approach involves a zero to one scale mapping of predicted response values y_i to convert them into the desirability values d_i of the individual performance characteristics, i.e.

$$0 \le d_i \le 1 \tag{8.23}$$

Zero desirability indicates that the predicted response value is completely undesirable. As d_i increases, the desirability of the particular response value is higher. For performance variable y_i having both the upper and lower bounds, Derringer and Suich (1980) suggested a two-sided transformation:

$$d_i = \begin{cases} \left(\dfrac{y_i - L_i}{T_i - L_i}\right)^r & L_i \le y_i \le T_i \\ \left(\dfrac{U_i - y_i}{U_i - T_i}\right)^r & T_i \le y_i \le U_i \\ 0 & y_i \le L_i \text{ or } y_i \ge T_i \end{cases} \tag{8.24}$$

where L_i, U_i, T_i and y_i are the lower limit, upper limit, target and actual value of the performance characteristic respectively.

For maximizing y_i, a one-sided transformation can be used:

$$d_i = \begin{cases} 0 & y_i \le L_i \\ \left(\dfrac{y_i - L_i}{y_{i\max} - L_i}\right) & L_i \le y_i \le y_{i\max} \\ 1 & y_i \ge y_{i\max} \end{cases} \tag{8.25}$$

where $y_{i\max}$ is the highest value of response y_i.

The individual desirability values of the multiple performance characteristics are combined using the geometric mean to obtain an overall assessment of the composite desirability of the combined responses, defined as the desirability function D $(0 \le D \le 1)$:

$$D = (d_1 \times d_2 \times \ldots\ldots \times d_n)^{1/n} \tag{8.26}$$

Kros and Mastrangelo (2001) suggested a modified desirability method using a weighted composite desirability approach:

$$D = \left(d_1^{w_1} d_2^{w_2} d_3^{w_3} \ldots\ldots d_n^{w_i}\right)^{1/\sum w_i} \tag{8.27}$$

where w_i is defined as a response weight. This approach offers flexibility to the user in deciding the preferences of the various performance characteristics. However, the use of modified desirability function approach is quite subjective and sensitive to the relative preference assigned to the responses in deriving the composite function.

8.2.3 Non-dominating Pareto Optimal Solutions

An alternative approach to solve the multi-performance optimization problem is of non-dominated sorting genetic algorithm (NSGA) for finding the multiple Pareto-optimal solutions [Goldberg, 1989; Srinivas and Deb, 1994]. The Pareto-optimal solutions are a set of solutions, which are superior to the rest of the solutions in the search space considering all the objectives (performances) but are inferior to other solutions in the space for one or more objectives. The knowledge of many Pareto-optimal solutions can be very useful for the

process user in deciding the optimal machining strategies, particularly when the current setting has changed and a new solution is required to be implemented.

Let k objective functions are to be minimized:

$$\underset{x \in \Re^n}{\text{Min}} \; f(x) = (d_1(x), d_2(x) \ldots . d_k(x))^T \tag{8.28}$$

where, $f(x)$ is an imaginary function of the multiple functions $d_i(x)$ (in our case the multi-response output of NN converted into the desirability values. A vector q is said to dominate vector p if (Andrew Popov Hamburg, 2005):

$$\forall i \in (1, 2 \ldots k) : di(q) \leq di(p) \text{ and } \exists j \in (1, 2 \ldots k) : dj(q) < dj(p) \tag{8.29}$$

thus for at least one fitness function value of q is less than that of p.

Pareto optimality is defined as (Andrew Popov Hamburg, 2005): a vector $x \in S$ is a Pareto-optimal solution if and only if there is no vector $y \in S$, for which $f(y) = (d_1(y), d_2(y) \ldots d_k(y))$ dominates $f(x) = (d_1(x), d_2(x) \ldots d_k(x))$

A set of non-dominated Pareto-optimal solutions forms a Pareto surface.

8.2.4 Genetic Algorithms

Traditional methods of optimization have limitations in the case of multi-variable problem having more than one optimal solution or involving multi-performance optimization. Genetic Algorithms (GAs), a part of the group of meta-heuristic methods called as Evolutionary Algorithms (EA), are finding ever-increasing applications in recent years to solve such complex optimization problems. GAs possess several advantageous features, making them more popular and effective over traditional techniques, such as: they work with a set of solutions (population) instead of a single solution, thus more likely to produce global optimal solution as well as a number of optimal solutions independent of initial solution, can work with continuous as well as discrete objective functions, they are

probabilistic in nature, can be parallelized, can handle any nature of constraints, can produce a set of Pareto-optimal solutions for user flexibility.

GAs are direct, parallel, stochastic methods for global search and optimization, which imitates the evolution of the living beings and mimic the Darwinian theory of survival of the fittest principle of the nature to make a search process (Andrey Popov Hamburg, 2005). Idea of Evolutionary Algorithms (EA) was introduced in 1960 by I. Rechenberg in his work on evolutionary strategies. The evolutionary algorithms model natural evolution process using the three main principles of the natural evolution: reproduction, natural selection and diversity of the species, maintained by the differences of each generation with the previous. Prof. Holland of University of Michigan envisaged the concept of genetic algorithms in his seminal work (Holland, 1975) and thereafter a number of contributions were made to this field (Goldberg, 1989; Davis, 1991; Michalewicz, 1992; Deb, 1999; Deb, 2001; Rajasekaran and Pai, 2003, Andrew Popov Hamburg, 2005).

Genetic algorithms need design space to be converted into genetic space by coding of unknown variables x_i's in contrast to traditional optimization methods. The working advantage with coded variable space is that coding discretizes the search space even though the function is continuous. In GAs, chromosomes (individuals) represent set of genes, which code the independent variables. Every chromosome represents a solution of the given problem and a set of different chromosomes (individuals) forms a generation. By means of evolutionary operations, like selection, recombination and mutation an offspring population is created. Genes could be Boolean, integers, floating point or string variables, as well as any combination of these. On the other hand, individual and vector of variables can be used for chromosomes.

Binary coding of variables, where the sub-genes code powers of 2, the search space is discretized and solution accuracy depends upon the string length used to code the variable.

Drawback of this coding is the non-linear transformation from one space to another making the possible values which are close to one-another in one space to have a big difference in the other. This phenomenon is known as Hamming cliffs. While in real coded GAs, real values of the variables are used and every gene, representing a real valued variable is divided into sub-genes, coding different powers of 10. Every sub-gene can be modified independently from the others. Further, real-coded GAs can work directly with continuous as well as mixed representation of the variables. Therefore, real coding was adopted for this work.

Genetic Algorithms work with a population of individuals (a set of different chromosomes consisting of independent variables coded as strings for binary or values for real coded) created at random, which evolve by means of selection and other operators like crossover and mutation. Each individual is evaluated with respect to its adaptation (fitness) to the desired fitness function. The selection chooses the best gene combinations (individuals), which through crossover and mutation should drive to better solutions in the next population. GAs are usually suitable for maximization problems. However, minimization problems can easily be solved using suitable transformations.

One of the most often used schemes of GAs (Andrew Popov Hamburg, 2005) is shown on Fig. 8.13.

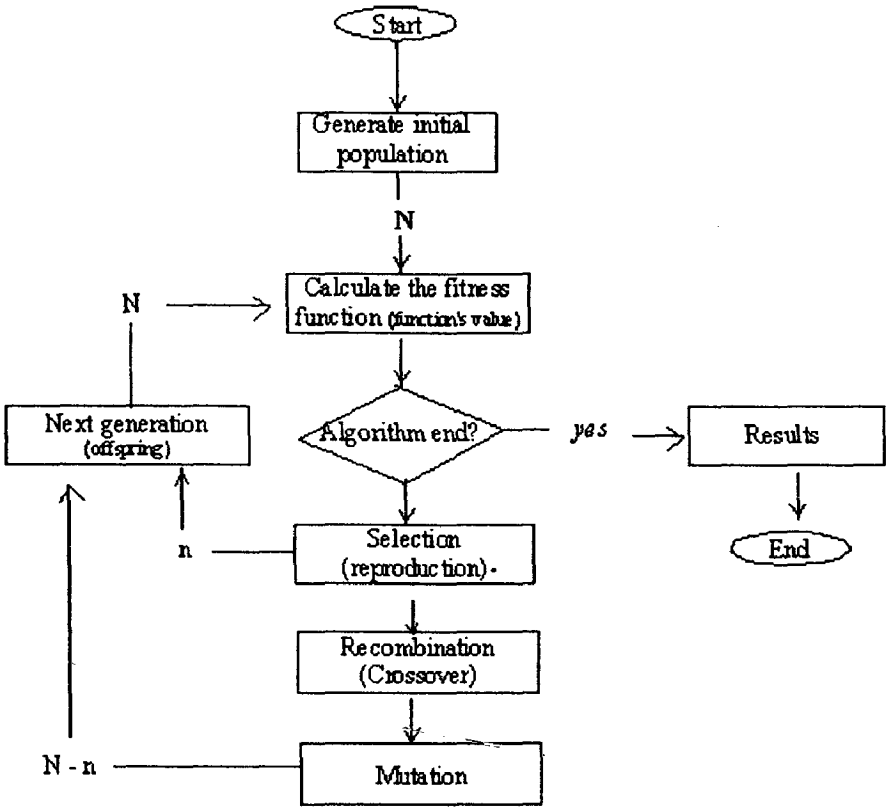

Fig. 8.13 General scheme of GAs

1. Generate initial population: in most of the algorithms the first generation is randomly created. For the easier computational procedure, all populations have the same number (N) of individuals. Maximum population is usually kept 5-30 times the number of independent variables (Deb, 2001).

2. Calculate the values of the fitness function to be optimized.

3. Check for termination of algorithm – based on different criteria such as if the fitness function value of the best individual is within defined range around a set value, maximum number of iterations (normally kept 100-500, it is the most widely used stopping criterion and hence used for the present study), stall generation if within initially set number of generations there is no improvement of fitness function value of the best individual.

4. Selection – the selection operator is also called the reproduction operator. According to Darwin's evolution theory of survival of the fittest, the best one should survive and create new offspring. The emphasis is to select the above average good solutions and eliminate the

bad solutions. Make multiple copies of them in probabilistic manner keeping the population size constant. From amongst all individuals in the current population best ones are selected to continue and produce offspring population by means of crossover and mutation. At this stage elitism could be used – the best n individuals are directly transferred to the next generation. The elitism can very rapidly increase the performance of GA as it prevents losing the best found solutions and thus guarantees that the value of the optimization function cannot get worsened. The various methods of selecting chromosomes of parents to crossover are: Roulette-wheel selection (proportionate reproductive operator), Boltzmann selection, Tournament selection, Rank selection, and Steady state selection. Being simpler to implement, Roulette-wheel selection is commonly used. It works with proportional to fitness function selection. The probability (P) of a chromosome to be selected is the proportion of fitness function value of the chromosome to the sum of fitness function values of all populations in a generation. In order to avoid the possibility of local optimal solutions which could be obtained due to the domination of certain individuals, a rank selection or a Gauss selection can be employed. In rank selection, the individuals are assigned a rank based on the fitness function value and roulette wheel is used with P defined as (Andrew Popov Hamburg, 2005):

$$P = \beta.(1-\beta)^{(\text{rank}-1)} \tag{8.28}$$

where β is user defined adjustable parameter. In Gauss selection, individuals are sorted according to their fitness function value and a random number generated with Gaussian distribution is used.

5. Crossover – it is a recombination operator by which the individuals chosen by selection recombine with each other and new individuals are created. The aim of the crossover operator is to get offspring individuals that inherit the best possible combination of the characteristics of their parents. In crossover, a pair of two individuals is selected from the

mating pool at random, then a cross-site is randomly selected along the string length and the position values are exchanged between two individuals. Cross over can be single or multi-point. In conventional (scattered) crossover, a bit mask is used. This can be used with all types of genes. Solution space becomes evolutionary and mutation is used to find optimal solution. Another crossover called blending (intermediate) crossover where a function of a random number between 0 to 1 and a user defined exploration coefficient α is used (Andrew Popov Hamburg, 2005). The crossover operation is mainly responsible for new individuals. Crossover rate, termed as probability of crossover, denoting the number of pairs to be crossed to the total fixed population, typically ranges from 0.5-1 (Rajasekaran and Pai, 2001).

6. Mutation – by means of random change of the value of a gene with a low mutation rate. The chromosome selection as well as the selection of genes is random. Mutation is done to preserve diversity in the population and hence ensure that even if none of the individuals contain the necessary gene value for the extremum, it is still possible to reach the extremum. The mutation rate denoting the number of individuals to be mutated (rounded to an integer number) is usually kept low (typically about 0.001 to 0.5) to avoid degeneration of GA into random walk (Rajasekaran and Pai, 2003).

7. New generation – the elite individuals chosen from the selection are combined with those who passed the crossover and mutation, and form the next generation.

In non-dominated sorting genetic algorithm (NSGA) for finding the multiple Pareto-optimal solutions, the individuals in a population are successively sorted for different Pareto-surfaces and assigned a rank. Then the roulette wheel selection is employed in the above mentioned GA algorithm. NSGA provides fastest selection and better convergence (Andrew Popov Hamburg, 2005).

8.2.5 Taguchi-NN-GA Multi-Performance Optimization Algorithm

Taguchi-NN-DF-GA optimization control strategy applied to multi-performance optimization of ECH is comprised of the following steps:

1. Use the Taguchi methodology to design and conduct the experiments,
2. Use the Taguchi loss function approach (S/N ratio analysis) to obtain the optimal value for each of the multiple performance characteristics to be optimized,
3. Use an appropriate RBF NN structure to model the relationship between the ECH process parameters and multiple responses,
4. Set the process free parameters such as goal and spread of radial basis function and simulate the network,
5. Find an input vector with the greatest error and add a RADBAS neuron with weights equal to that vector,
6. Redesign the PURELIN layer weights to minimize error.
7. If the performance $\leq$ goal then step 8 else step 5,
8. Fine-tune the resulting parameters. If yes then step 4 else 9,
9. Compute the desirability values d_i's of each response trained by NN. If single objective optimal solution is desired, then step 10 else for NSGA step 12,
10. Compute the geometric mean of the desirability values to find the composite desirability function or use the process knowledge to obtain a weighted composite function based on the preferences assigned to multiple performance characteristics. The composite fitness function will act as the fitness function to GA,
11. Use the desirability values d_i's of each response trained by NN as the multi-objectives to be maximized using NSGA,
12. Initialize GA parameters. Choose population size N, crossover, mutation and other parameters. Choose a maximum allowable generation number t_{max}, and set $t=0$,

13. Generate initial feasible random population,
14. Evaluate the fitness of each individual in the population,
15. Perform GA operations, including selection, crossover, and mutation. This creates a new set of parameters, which possibly is better than the previous generation. This completes one generation.
16. Set t = t + 1. If $t > t_{max}$ or other termination criteria is satisfied, then the process is terminated. Otherwise process is repeated from step 12.

The flowchart of the Taguchi-NN-DF-GA algorithm is given in Appendix D.

8.2.6 Optimization of ECH using Taguchi-NN-DF-GA Multi-Performance Optimization Control Strategy

Six different cases considering two, three and even four ECH performance characteristics have been modeled and optimized using the approach: PIR_a-PIOR; PIR_a-PICyl; PIR_a-DIR; PIR_a-PIOR-DIR; PIR_a-PICyl-DIR; and PIR_a-PIOR-PICyl-DIR. The input layer of neural networks consisted of seven neurons representing the seven process input parameters and the output layer contained two, three or four neurons depending upon the case to represent the process performance characteristics. 75% of the experimental database was utilized to train the network and 25% for testing the model. The database used in the network spans the permissible range of process input parameters (Chapter-VI, Phase-III Stage-I studies). Programs were developed in MATLAB 7.0.1 using RBF NN, and three layered BPNN trained separately with GDM and LM methods.

The MATLAB function NEWRB was used to design the RBF NN. NEWRB adds neurons to the hidden layer of a radial basis network until it meets the specified mean squared error goal. NEWRB creates a two-layer network. The first layer has RADBAS neurons (with commonly used Gaussian transfer function), and calculates its weighted inputs

with DIST, and its net input with NETPROD. The second layer has PURELIN neurons, calculates its weighted input with DOTPROD and its net inputs with NETSUM. Both layers have biases.

RBF networks with different mean squared error goals were simulated and it was found that with a goal of 1E-03, RBF NN worked well for all the cases considered. Next, the networks were simulated with different spreads of radial basis functions to find a best value of spread parameter for each of the cases of multi-performance modeling. The RBF NN results for the different models are given in Fig. 8.14 to 8.19. Figures depict the pattern of variation of sum of square training error and maximum percentage testing error of various performance characteristics with respect to the spread parameter. It is observed that that in all the cases RBF NN mapped the complex input-output relations of the process very well for a wide range of spread parameter. The RBF Networks with the SPREADS yielding good overall results (Table 8.67) were selected to model different cases of multi-response optimization. The modeling results are given in Tables 8.68 to 8.73. The results predicted by RBF networks are in good close agreement with the experimental results.

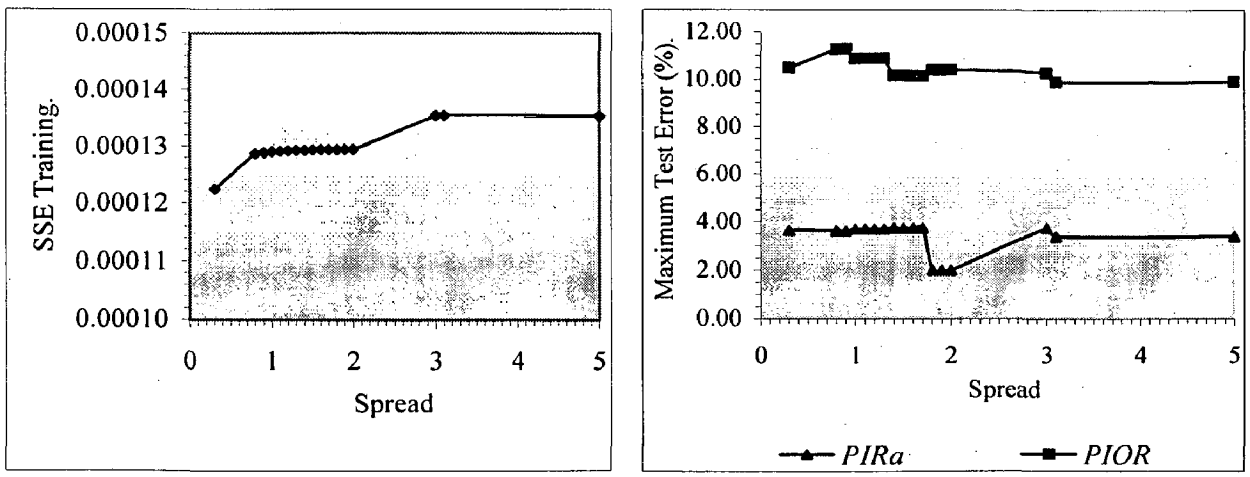

a) b)

Fig. 8.14 SSE training and maximum test error with different spreads of RBF (Model: PIR_a-PIOR)

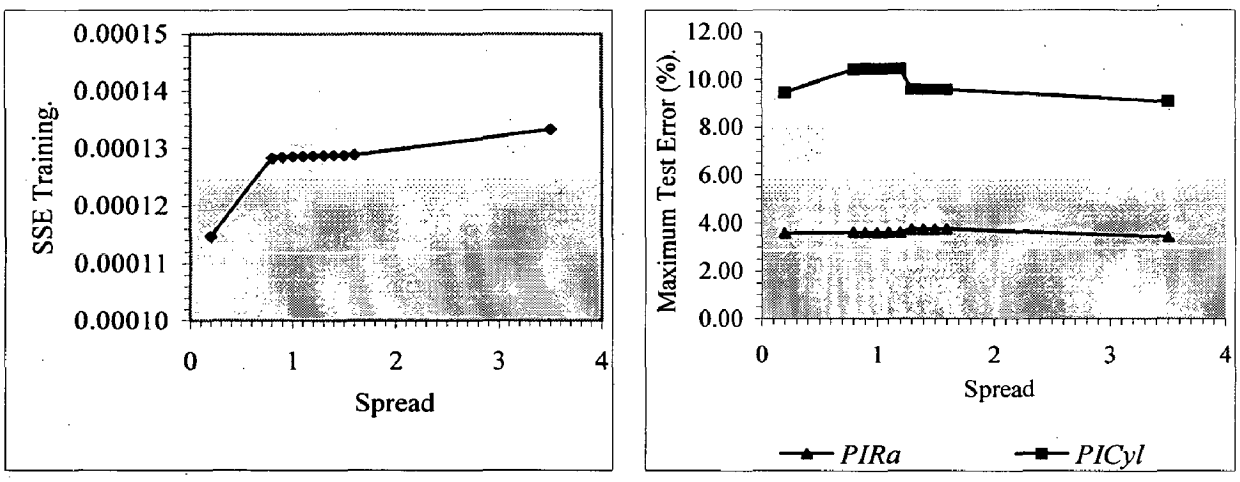

a) b)

Fig. 8.15 SSE training and maximum test error with different spreads of RBF (Model: PIR_a-PICyl)

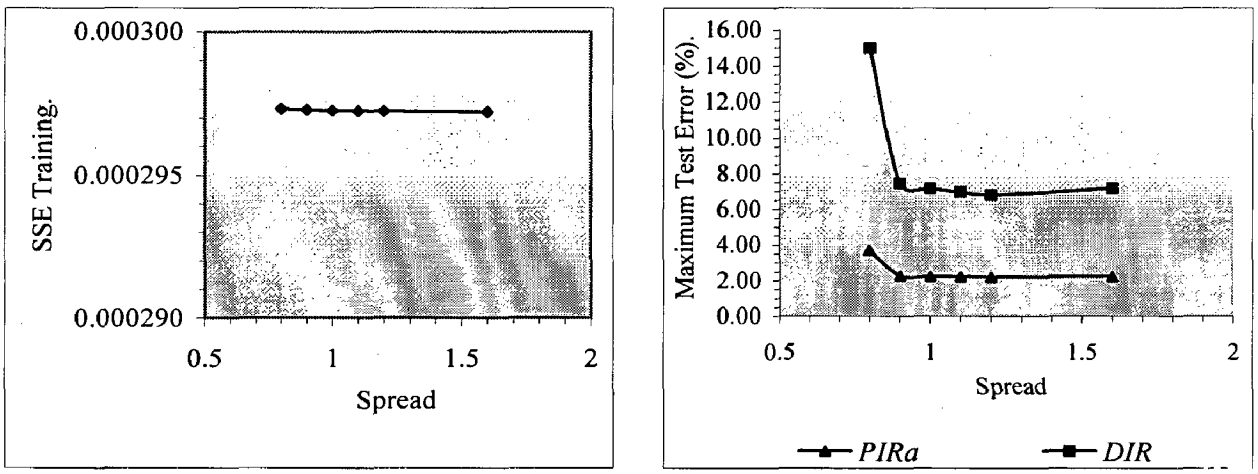

a) b)

Fig. 8.16 SSE training and maximum test error with different spreads of RBF (Model: PIR_a-DIR)

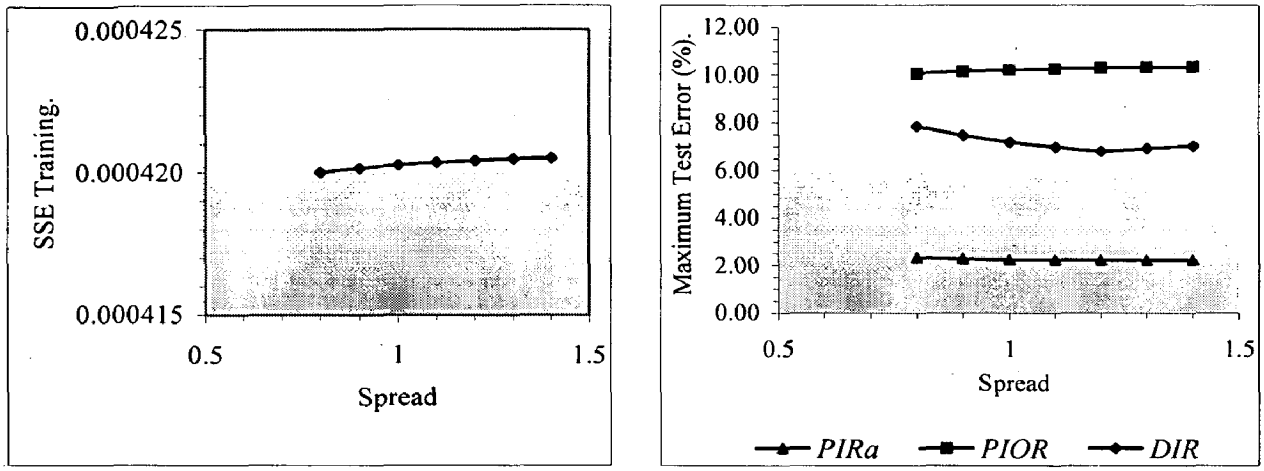

a) b)

Fig. 8.17 SSE training and maximum test error with different spreads of RBF (Model: PIR_a-PIOR-DIR)

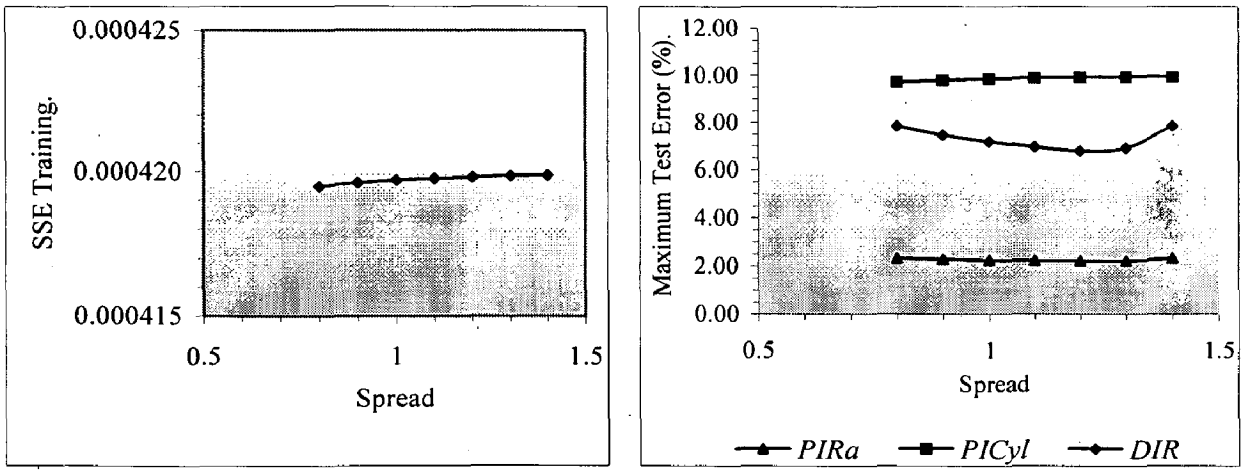

a) b)

Fig. 8.18 SSE training and maximum test error with different spreads of RBF (Model: PIR_a-PICyl-DIR)

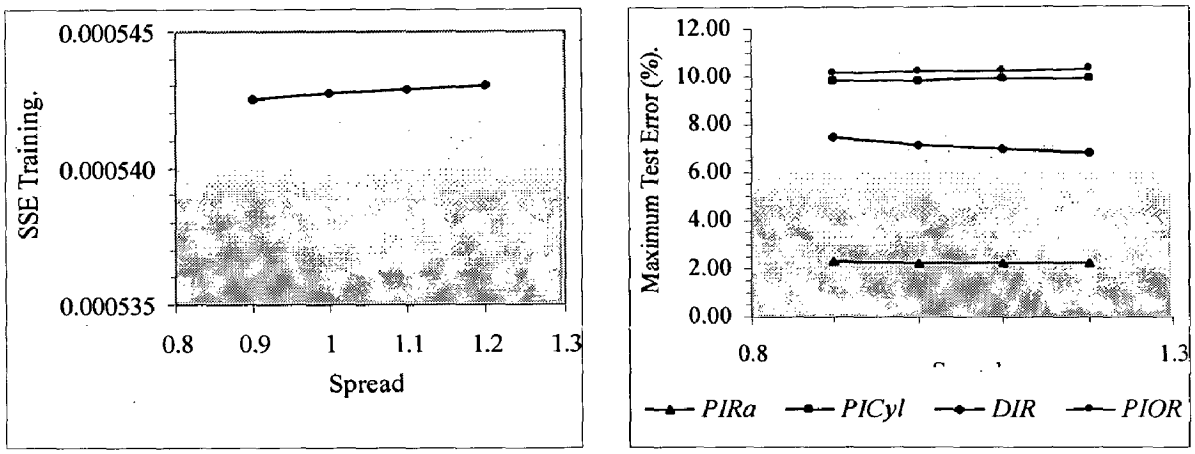

a) b)

Fig. 8.19 SSE training and maximum test error with different spreads of RBF (Model: PIR_a-PIOR-PICyl-DIR)

Table 8.67 Selected RBF NN for different Models (Goal= 1E-03)

Sl.No.	Model	RBF SPREAD
1	PIR_a-PIOR	3.1
2	PIR_a-PICyl	3.5
3	PIR_a-DIR	1.2
4	PIR_a-PIOR-DIR	0.8
5	PIR_a-PICyl-DIR	0.8
6	PIR_a-PIOR-PICyl-DIR	0.9

Some of the multi-performance cases were also modeled using a three-layer BPNN with GDM and LM training approaches. The MATLAB function newff with tansigmoidal neurons in the hidden layer and purelin neurons in output layer was used, with traingdm and traianlm functions for training the BPN and LM networks respectively. Three network architectures adapted were 7-9-2, 7-9-3 and 7-9-4 for the cases of two, three and four responses respectively. The number of neurons in hidden layer was decided by hit and trial method. A random generator is used to initialize the weights. The simulated results for training in case of modeling PIR_a-PICyl using

constant parameters set at 0.9) took about ten thousand iterations to reduce the sum of squared error to 0.0020 (Fig. 8.20), while for the same case LM algorithm (with initial mu =0.001) achieved the SSE of less than 0.0002 in just 2 epochs (Fig. 8.21). The performance of LM network used for multi-performance modeling of PIR_a-PIOR and PIR_a-PIOR-PICyl-DIR are presented in Fig. 8.22 and 8.23 respectively. The results predicted by BPN and LM networks (Tables 8.74 to 8.78) also look fairly close to the experimental results, indicating that these networks can also be utilized for multi-performance modeling of ECH. However, the results obtained with RBF NN even with four responses are much better.

Table 8.68 RBF NN multi-performance modeling results (PIR_a-PIOR)

S. No.	Process Input Parameters							Experimental (S/N Response)		Predicted		% Error	
	C	EC	SR	F	T	SOP	G	PIR_a	PIOR	PIR_a	PIOR	PIR_a	PIOR
1	50	100	150	20	30	20	600	36.39	31.50	37.63	31.63	3.41	0.41
2	50	150	150	30	50	10	360	36.64	31.77	37.62	30.43	2.69	4.19
3	50	200	150	10	10	30	1200	37.16	31.44	36.72	29.07	1.17	7.54
4	115	100	150	30	10	30	360	37.21	30.99	37.63	30.48	1.11	1.64
5	115	200	150	20	50	10	600	38.04	33.20	37.64	31.66	1.06	4.65
6	180	150	150	20	10	30	600	37.37	34.91	37.63	31.67	0.70	9.30
7	180	200	150	30	30	20	360	38.21	33.77	37.62	30.42	1.53	9.91

Table 8.69 RBF NN multi-performance modeling results (PIR_a-PICyl)

S. No.	Process Input Parameters							Experimental (S/N Response)		Predicted		% Error	
	C	EC	SR	F	T	SOP	G	PIR_a	PICyl	PIR_a	PICyl	PIR_a	PICyl
1	50	100	150	20	30	20	600	36.39	34.63	37.64	34.09	3.43	1.54
2	50	150	150	30	50	10	360	36.64	32.92	37.62	32.70	2.68	0.66
3	50	200	150	10	10	30	1200	37.16	33.75	36.74	31.96	1.13	5.30
4	115	100	150	30	10	30	360	37.21	33.29	37.62	32.83	1.08	1.39
5	115	200	150	20	50	10	600	38.04	36.37	37.65	34.11	1.04	6.22
6	180	150	150	20	10	30	600	37.37	37.21	37.63	34.20	0.71	8.08
7	180	200	150	30	30	20	360	38.21	36.05	37.61	32.77	1.56	9.10

Table 8.70 RBF NN multi-performance modeling results (PIR_a-DIR)

S. No.	Process Input Parameters							Experimental (S/N Response)		Predicted		% Error	
	C	EC	SR	F	T	SOP	G	PIR_a	DIR	PIR_a	DIR	PIR_a	DIR
1	50	100	150	20	30	20	600	36.39	23.16	37.068	22.285	1.87	3.77
2	50	150	150	30	50	10	360	36.64	24.77	37.102	23.187	1.26	6.40
3	50	200	150	10	10	30	1200	37.16	21.46	36.325	20.571	2.24	4.14
4	115	100	150	30	10	30	360	37.21	23.67	37.365	25.249	0.41	6.66
5	115	200	150	20	50	10	600	38.04	30.60	37.925	28.88	0.30	5.62
6	180	150	150	20	10	30	600	37.37	33.32	38.18	30.923	2.17	7.19
7	180	200	150	30	30	20	360	38.21	33.51	38.191	31.693	0.04	5.42

Table 8.71 RBF NN multi-performance modeling results (PIRa-PIOR-DIR)

S. No	Process Input Parameters							Experimental (S/N Response)			Predicted			% Error		
	C	EC	SR	F	T	SOP	G	PIR_a	PIOR	DIR	PIR_a	PIOR	DIR	PIR_a	PIOR	DIR
1	50	100	150	20	30	20	600	36.39	31.50	23.16	37.00	31.27	21.66	1.68	0.73	6.46
2	50	150	150	30	50	10	360	36.64	31.77	24.77	37.06	30.88	22.83	1.14	2.81	7.87
3	50	200	150	10	10	30	1200	37.16	31.44	21.46	36.36	28.85	20.83	2.15	8.25	2.95
4	115	100	150	30	10	30	360	37.21	30.99	23.67	37.34	30.89	25.08	0.35	0.31	5.95
5	115	200	150	20	50	10	600	38.04	33.20	30.60	37.96	31.40	29.10	0.21	5.42	4.90
6	180	150	150	20	10	30	600	37.37	34.91	33.32	38.25	31.39	31.41	2.34	10.08	5.72
7	180	200	150	30	30	20	360	38.21	33.77	33.51	38.24	30.96	32.13	0.09	8.32	4.11

Table 8.72 RBF NN multi-performance modeling results (PIR_a-PICyl-DIR)

S. No	Process Input Parameters							Experimental (S/N Response)			Predicted			% Error		
	C	EC	SR	F	T	SOP	G	PIR_a	PICyl	DIR	PIR_a	PICyl	DIR	PIR_a	PICyl	DIR
1	50	100	150	20	30	20	600	36.39	34.63	23.16	37.00	33.80	21.66	1.68	2.39	6.46
2	50	150	150	30	50	10	360	36.64	32.92	24.77	37.06	33.45	22.83	1.14	1.61	7.87
3	50	200	150	10	10	30	1200	37.16	33.75	21.46	36.36	31.91	20.83	2.15	5.45	2.95
4	115	100	150	30	10	30	360	37.21	33.29	23.67	37.34	33.39	25.08	0.35	0.29	5.95
5	115	200	150	20	50	10	600	38.04	36.37	30.60	37.96	33.67	29.10	0.21	7.43	4.90
6	180	150	150	20	10	30	600	37.37	37.21	33.32	38.25	33.59	31.41	2.34	9.72	5.72
7	180	200	150	30	30	20	360	38.21	36.05	33.51	38.24	33.23	32.13	0.09	7.82	4.11

Table 8.73 RBF NN multi-performance modeling results (PIR_a-PIOR-PICyl-DIR)

S. No	Process Input Parameters							Experimental (S/N Response)				Predicted				% Error			
	C	EC	SR	F	T	SOP	G	PIR_a	PIOR	PICyl	DIR	PIR_a	PIOR	PICyl	DIR	PIR_a	PIOR	PICyl	DIR
1	50	100	150	20	30	20	600	36.39	31.50	34.63	23.16	37.02	31.28	33.81	21.83	1.73	0.69	2.35	5.74
2	50	150	150	30	50	10	360	36.64	31.77	32.92	24.77	37.07	30.89	33.47	22.92	1.17	2.77	1.67	7.49
3	50	200	150	10	10	30	1200	37.16	31.44	33.75	21.46	36.35	28.87	31.94	20.75	2.18	8.18	5.37	3.31
4	115	100	150	30	10	30	360	37.21	30.99	33.29	23.67	37.35	30.90	33.40	25.13	0.36	0.30	0.32	6.13
5	115	200	150	20	50	10	600	38.04	33.20	36.37	30.60	37.95	31.38	33.65	29.04	0.24	5.48	7.48	5.09
6	180	150	150	20	10	30	600	37.37	34.91	37.21	33.32	38.23	31.36	33.56	31.28	2.30	10.16	9.80	6.12
7	180	200	150	30	30	20	360	38.21	33.77	36.05	33.51	38.23	30.94	33.20	32.02	0.06	8.38	7.89	4.44

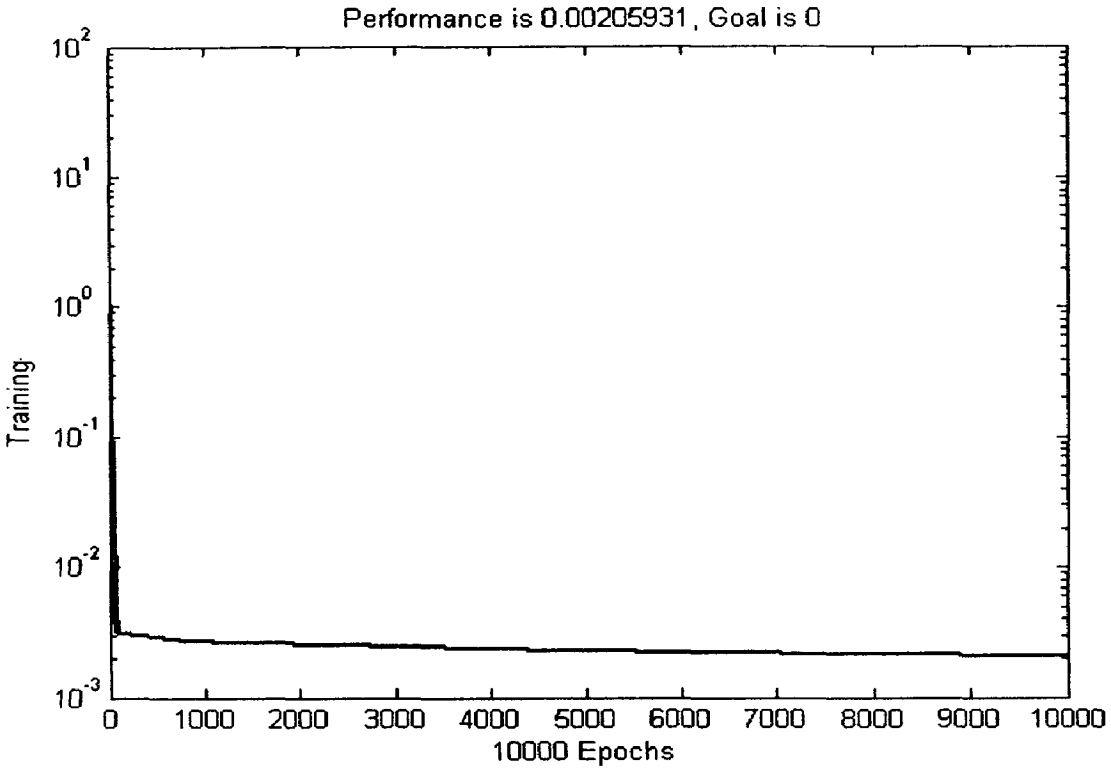

Fig. 8.20 Variation of total error with number of epochs of BPNN (Model: PIR_a-PICyl)

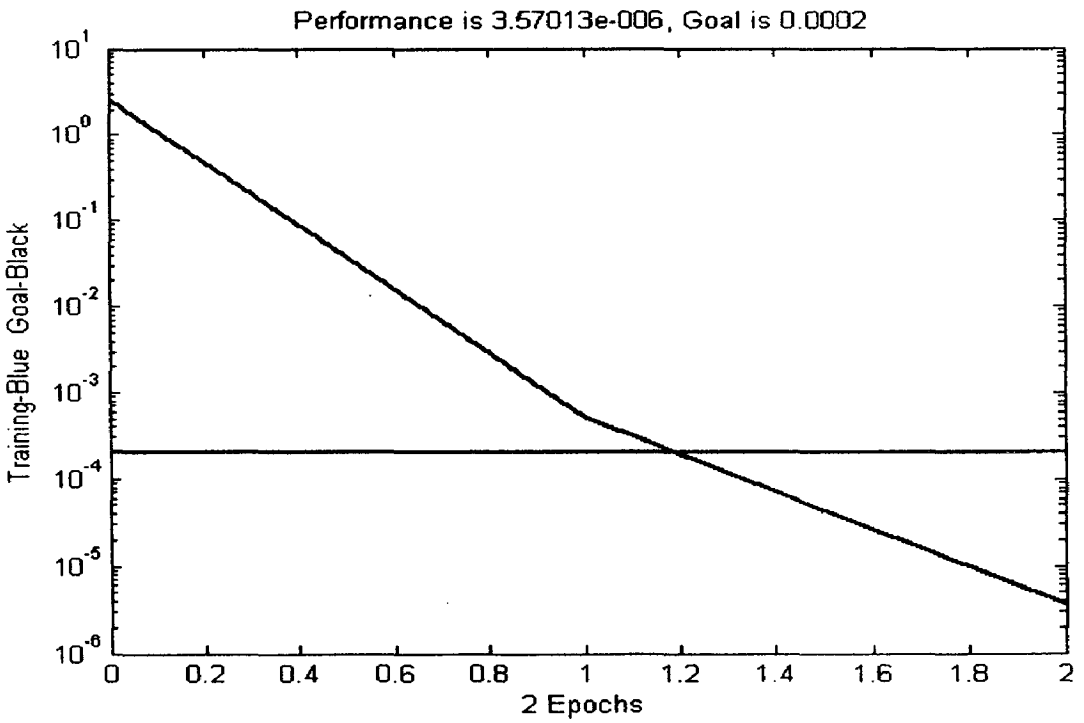

Fig. 8.21 Variation of total error with number of epochs of LM algorithm (Model: PIR_a-PICyl)

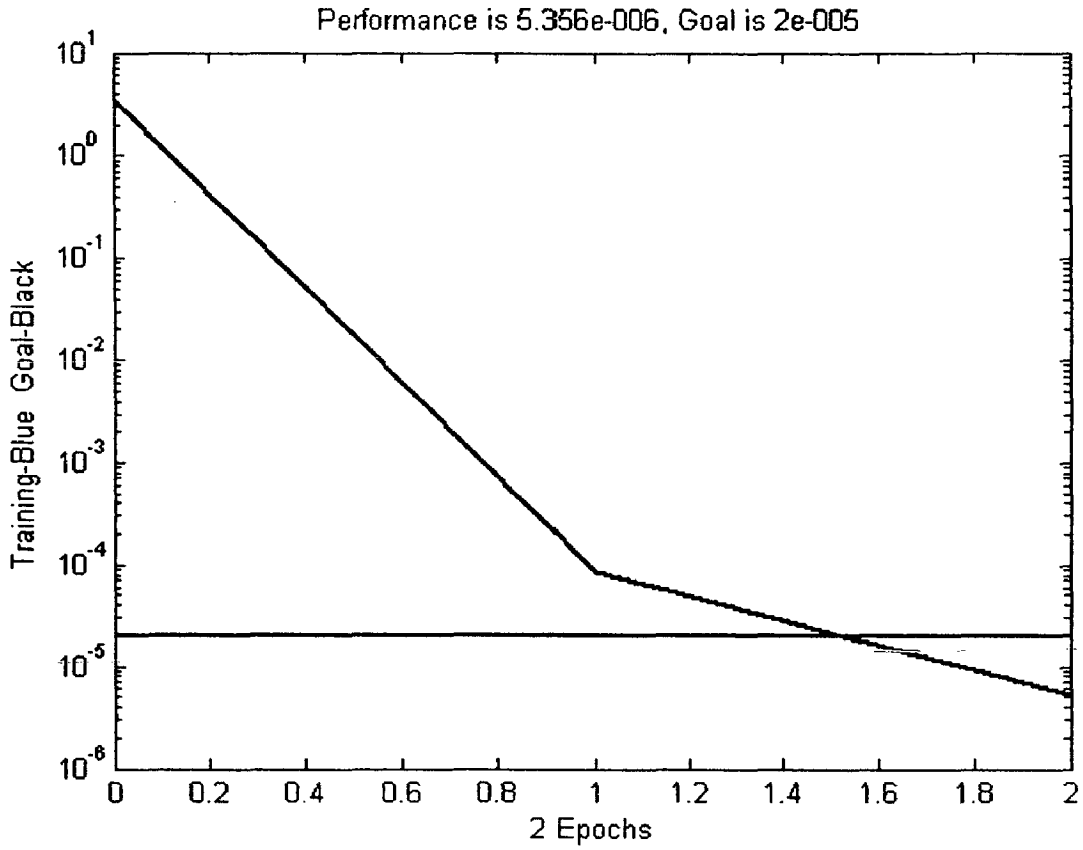

Fig. 8.22 Variation of total error with number of epochs of LM algorithm (Model: PIR_a-PIOR)

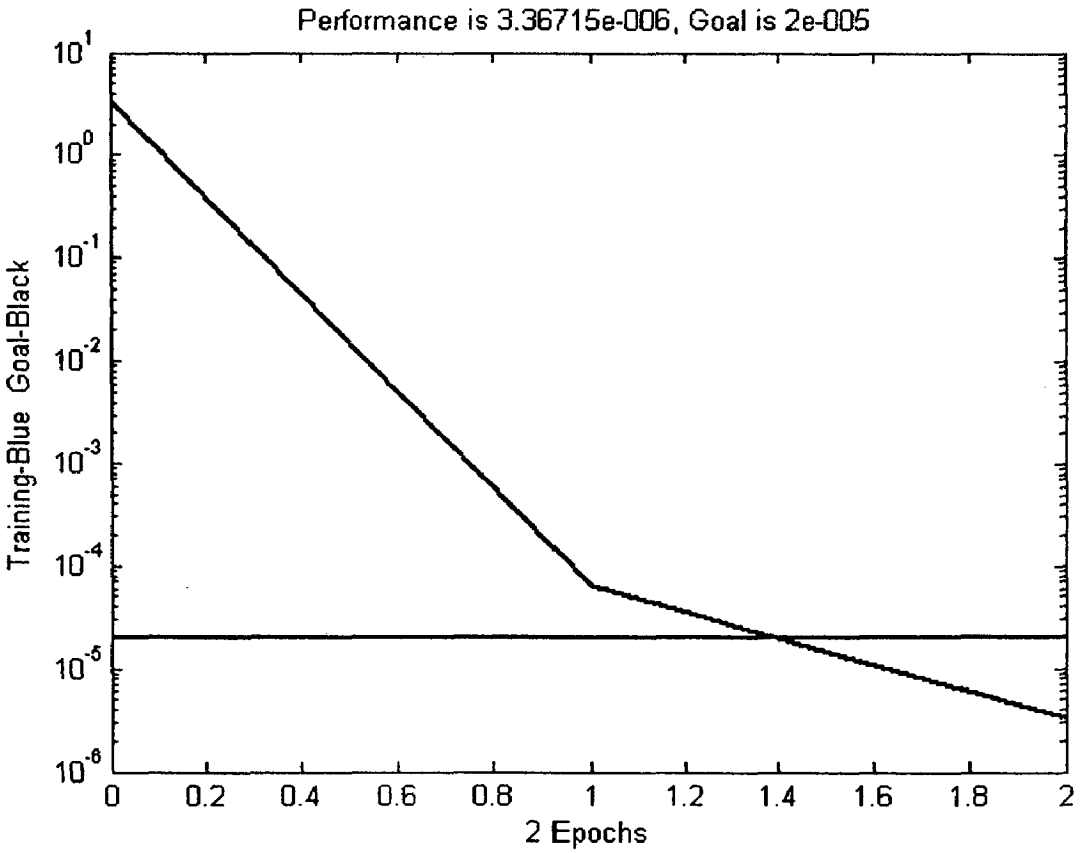

Fig. 8.23 Variation of total error with number of epochs of LM algorithm (Model: PIR_a-PIOR-PICyl-DIR)

Table 8.74 BPN NN multi-performance modeling results (PIR_a-PICyl)

S. No.	Process Input Parameters							Experimental (S/N Response)		Predicted		% Error	
	C	EC	SR	F	T	SOP	G	PIR_a	PICyl	PIR_a	PICyl	PIR_a	PICyl
1	50	100	150	20	30	20	600	36.39	34.63	37.32	33.76	2.56	2.50
2	50	150	150	30	50	10	360	36.64	32.92	37.31	33.44	1.82	1.59
3	50	200	150	10	10	30	1200	37.16	33.75	37.32	33.77	0.44	0.05
4	115	100	150	30	10	30	360	37.21	33.29	37.53	33.54	0.86	0.74
5	115	150	150	10	30	20	1200	36.72	36.27	37.32	33.77	1.62	6.90
6	115	200	150	20	50	10	600	38.04	36.37	37.32	33.72	1.90	7.31
7	180	150	150	20	10	30	600	37.37	37.21	37.32	33.76	0.13	9.26
8	180	200	150	30	30	20	360	38.21	36.05	37.31	33.58	2.33	6.85

Table 8.75 LM algorithm results (PIR_a-PICyl)

S. No.	Process Input Parameters							Experimental (S/N Response)		Predicted		% Error	
	C	EC	SR	F	T	SOP	G	PIR_a	PICyl	PIR_a	PICyl	PIR_a	PICyl
1	50	100	150	20	30	20	600	36.39	34.63	36.19	35.13	0.54	1.45
2	50	150	150	30	50	10	360	36.64	32.92	34.96	33.91	4.58	3.01
3	50	200	150	10	10	30	1200	37.16	33.75	36.95	35.19	0.55	4.27
4	115	100	150	30	10	30	360	37.21	33.29	38.38	35.35	3.14	6.18
5	115	200	150	20	50	10	600	38.04	36.37	36.29	34.23	4.60	5.90
6	180	150	150	20	10	30	600	37.37	37.21	38.88	34.73	4.05	6.66
7	180	200	150	30	30	20	360	38.21	36.05	37.21	33.71	2.62	6.49

Table 8.76 LM algorithm results (PIR_a-PIOR)

S. No.	Process Input Parameters							Experimental (S/N Response)		Predicted		% Error	
	C	EC	SR	F	T	SOP	G	PIR_a	PIOR	PIR_a	PIOR	PIR_a	PIOR
1	50	100	150	20	30	20	600	36.39	31.50	35.27	29.82	3.08	5.32
2	50	150	150	30	50	10	360	36.64	31.77	36.65	31.09	0.02	2.14
3	50	200	150	10	10	30	1200	37.16	31.44	36.56	31.66	1.62	0.70
4	115	100	150	30	10	30	360	37.21	30.99	36.71	31.29	1.36	0.98
5	115	200	150	20	50	10	600	38.04	33.20	36.83	33.70	3.18	1.50
6	180	150	150	20	10	30	600	37.37	34.91	35.92	34.60	3.88	0.90
7	180	200	150	30	30	20	360	38.21	33.77	34.59	32.43	9.46	3.98

Table 8.77 LM algorithm results (PIR_a-PICyl-DIR)

S. No	Process Input Parameters							Experimental (S/N Response)			Predicted			% Error		
	C	EC	SR	F	T	SOP	G	PIR_a	PICyl	DIR	PIR_a	PICyl	DIR	PIR_a	PICyl	DIR
1	50	100	150	20	30	20	600	36.39	34.63	23.16	37.50	35.93	23.56	3.05	3.78	1.74
2	50	150	150	30	50	10	360	36.64	32.92	24.77	37.41	31.32	23.06	2.11	4.87	6.92
3	50	200	150	10	10	30	1200	37.16	33.75	21.46	36.95	36.45	21.50	0.56	8.00	0.18
4	115	100	150	30	10	30	360	37.21	33.29	23.67	37.01	30.62	23.51	0.56	8.04	0.68
5	115	200	150	20	50	10	600	38.04	36.37	30.60	38.21	33.80	32.60	0.43	7.07	6.52
6	180	150	150	20	10	30	600	37.37	37.21	33.32	37.81	33.43	32.06	1.16	10.17	3.77
7	180	200	150	30	30	20	360	38.21	36.05	33.51	38.17	31.85	32.89	0.10	11.66	1.85

Table 8.78 LM algorithm results (PIR_a-PIOR-PICyl-DIR)

S. No	Process Input Parameters							Experimental (S/N Response)				Predicted				% Error			
	C	EC	SR	F	T	SOP	G	PIR_a	PIOR	PICyl	DIR	PIR_a	PIOR	PICyl	DIR	PIR_a	PIOR	PICyl	DIR
1	50	100	150	20	30	20	600	36.39	31.50	34.63	23.16	35.27	28.79	32.64	19.74	3.08	8.59	5.73	14.76
2	50	150	150	30	50	10	360	36.64	31.77	32.92	24.77	36.77	27.67	31.06	25.00	0.35	12.90	5.64	0.92
3	50	200	150	10	10	30	1200	37.16	31.44	33.75	21.46	36.90	27.12	31.66	21.91	0.69	13.74	6.20	2.10
4	115	100	150	30	10	30	360	37.21	30.99	33.29	23.67	36.76	29.65	33.48	25.91	1.22	4.33	0.54	9.46
5	115	200	150	20	50	10	600	38.04	33.20	36.37	30.60	38.68	33.35	35.72	34.67	1.69	0.44	1.79	13.30
6	180	150	150	20	10	30	600	37.37	34.91	37.21	33.32	38.42	31.85	34.95	31.87	2.82	8.76	6.09	4.35
7	180	200	150	30	30	20	360	38.21	33.77	36.05	33.51	38.28	31.71	34.85	36.08	0.20	6.11	3.34	7.68

The developed RBF NN models were used for multi-performance optimization of ECH. After training and validating the networks, multi-performance problems were transformed into single response problem using desirability and modified desirability approaches. The upper and lower limits for PIR_a, PIOR, PICyl and DIR, decided on the basis of experimental results, respectively are U_i: (39.04, 38.37, 40.41, 39.53) dB and L_i: (35.00, 20.00, 25.00, 15.00) dB to scale the responses. Modified desirability functions are based on the same weighing scheme as used in "Utility based Taguchi approach". For Model: PIR_a-PIOR-PICyl-DIR, weightages are 0.40, 0.25, 0.25 and 0.1 respectively. The modified desirability method provides flexibility to the user in assigning preferences to individual performance characteristics in multi-performance optimization problem. Desirability function or modified desirability function, whichever is selected, acts as a single fitness function for GA optimization. For obtaining non-dominated Pareto-optimal solutions, desirability values of the different performance characteristics were directly used as multi-objectives for GA. Optimization was performed using '***Genetic Algorithms for Optimization- Programs for MATLAB*** **®, Version 1.0'** with a standard setting GAopt(-5) with scattered crossover(Andrey Popov Hamburg, 2005). GA programs were integrated with the respective RBF NN programs using desirability/modified desirability approaches. The following GA parameters were specified to get the optimal solutions:

Genetic Algorithm Parameters

Maximum iterations	500
Population size	100
Mutation rate	0.3
Best rate	0.1, for single-objective optimization this is percentage population, which is copied to the next generation without changes (elite coefficient). For multi-objective optimization this is used to define maximum number of Pareto-surface individuals as: Pareto-individuals= Max (3, round(PopSize.BestRate)).
New rate	0.1000, Percentage of newly created individuals in a generation.
TolX	1.0000e-004, precision of variables
pSelect	1 selection parameter (depends on selection, β in case of rank selection.
pRecomb	0, recombination parameter (depends on crossover type, α in case of blending crossover).

The GA performance in 'Taguchi-RBFNN-DF/ Mod.DF-GA multi-performance optimization control strategy' for the six aforementioned problems of ECH is shown in Fig. 8.24-33. In all the cases, a fast improvement in fitness values is achieved during initial generations followed by a smooth fitness during last generations. The desirability of the optimal results is fairly high in all the models. The optimal results for various models with a population size 100 are given in Tables 8.79-88. The accuracy of optimal prediction and consistency of convergence of each model was assessed with five runs and similar optimal results were observed in each case. Further, the models were also run with GA population size of 200 individuals and no appreciable difference was observed. Tables 8.79–88 also include the results with 200 population size. Therefore for a better computational efficiency, a population size of 100 can be adopted without degrading the optimal solutions and thus, used in non-dominated sorting genetic algorithm (NSGA). The set of 10 non-dominated Pareto-optimal solutions obtained for different multi-performance models of ECH are

presented in Tables 8.89-8.93. These solutions can provide flexibility to the user in changed requirements. NSGA performance is shown in Fig. 8.34-39.

As discussed earlier in Chapter-V, PIR_{max} is also equally important as R_{max} has a pronounced bearing on the fatigue endurance performance and fracture strength of the component material. Therefore, as a case study, PIR_{max}-PIOR-PICyl-DIR was also modeled and optimized using Taguchi-RBFNN-GA approach. The RBF NN modeling results, optimal results using desirability function, optimal results with modified desirability approach (with same weightages as used in PIR_a-PIOR-PICyl-DIR) and Pareto-optimal solutions are presented in Tables 8.95-8.98 respectively. GA performance is shown in Fig. 8.40-8.42 respectively. Results are quite similar to that with PIR_a-PIOR-PICyl-DIR. Multi-response optimization using Ra, therefore, simultaneously seems to optimize R_{max} also. It is clear that R_{max} can well be used in place of R_a. Noticeably, a similar parametric condition was found significant in the both cases i.e. PIR_a and PIR_{max} when these performance characteristics were analyzed individually in Chapter-VII.

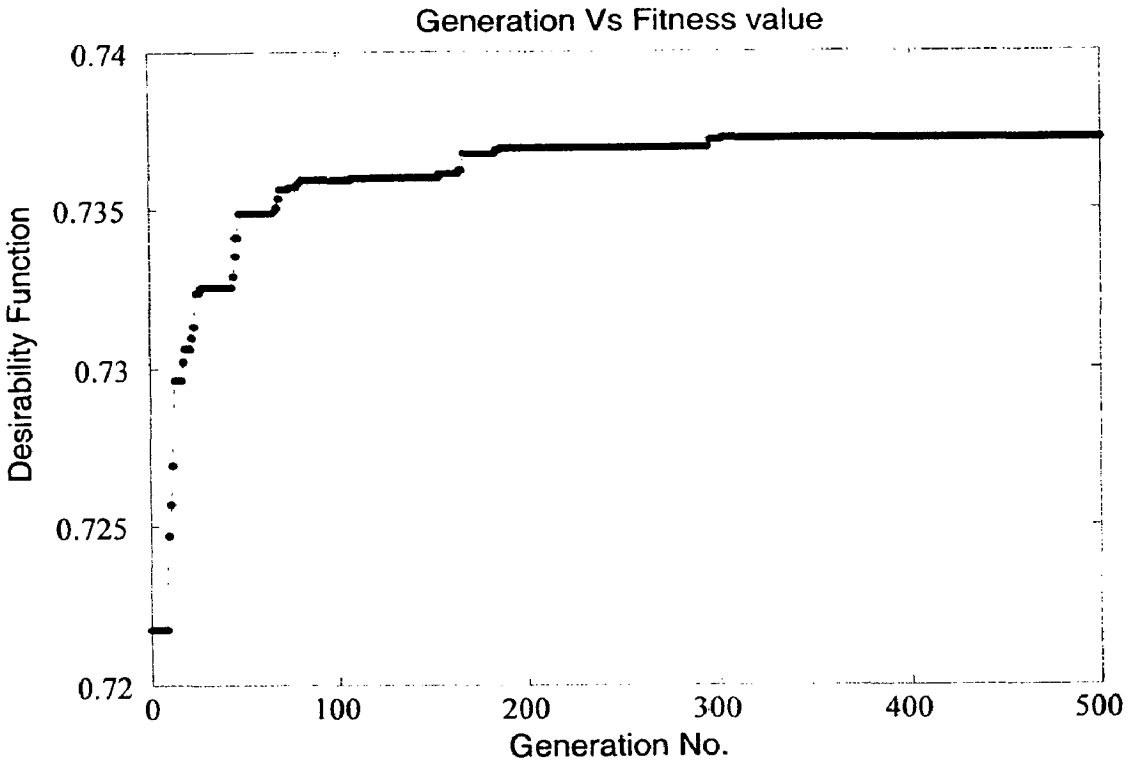

Fig. 8.24 Improvement in maximum fitness of composite desirability with GA generations (DF/mod. DF approach, Model: PIR_a-PIOR)

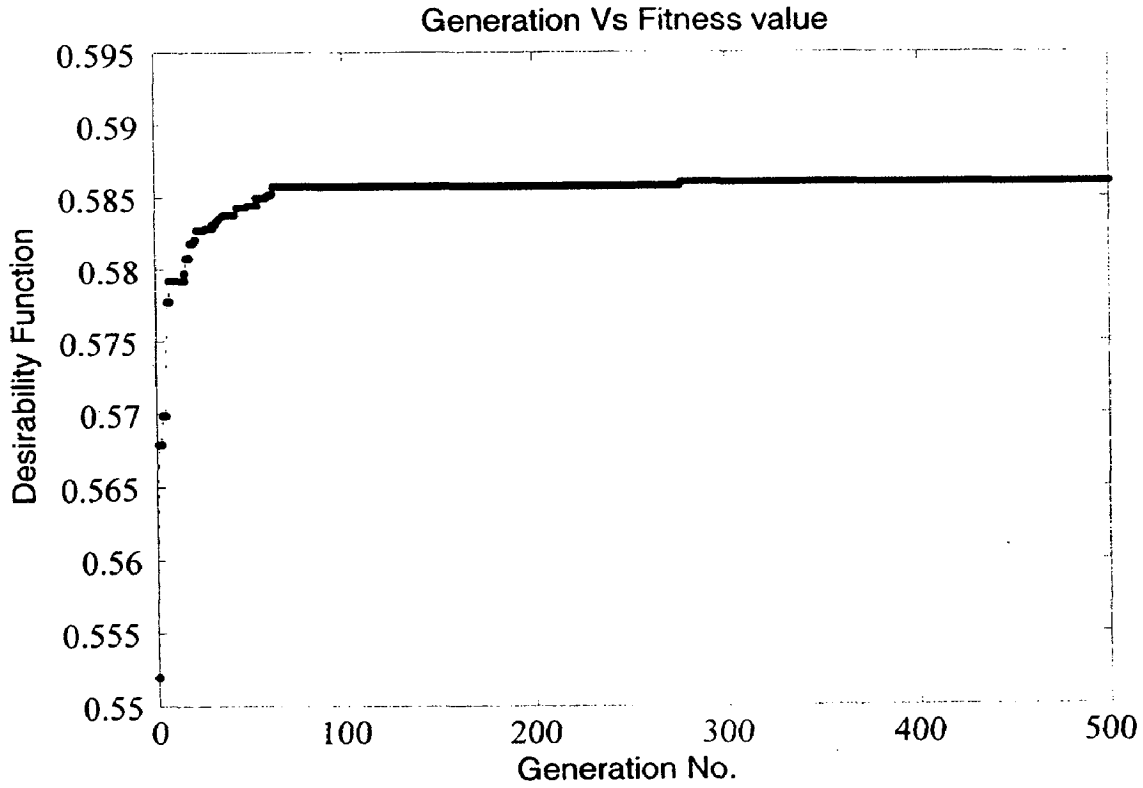

Fig. 8.25 Improvement in maximum fitness of composite desirability with GA generations (DF/mod. DF approach, Model: PIR_a-PICyl)

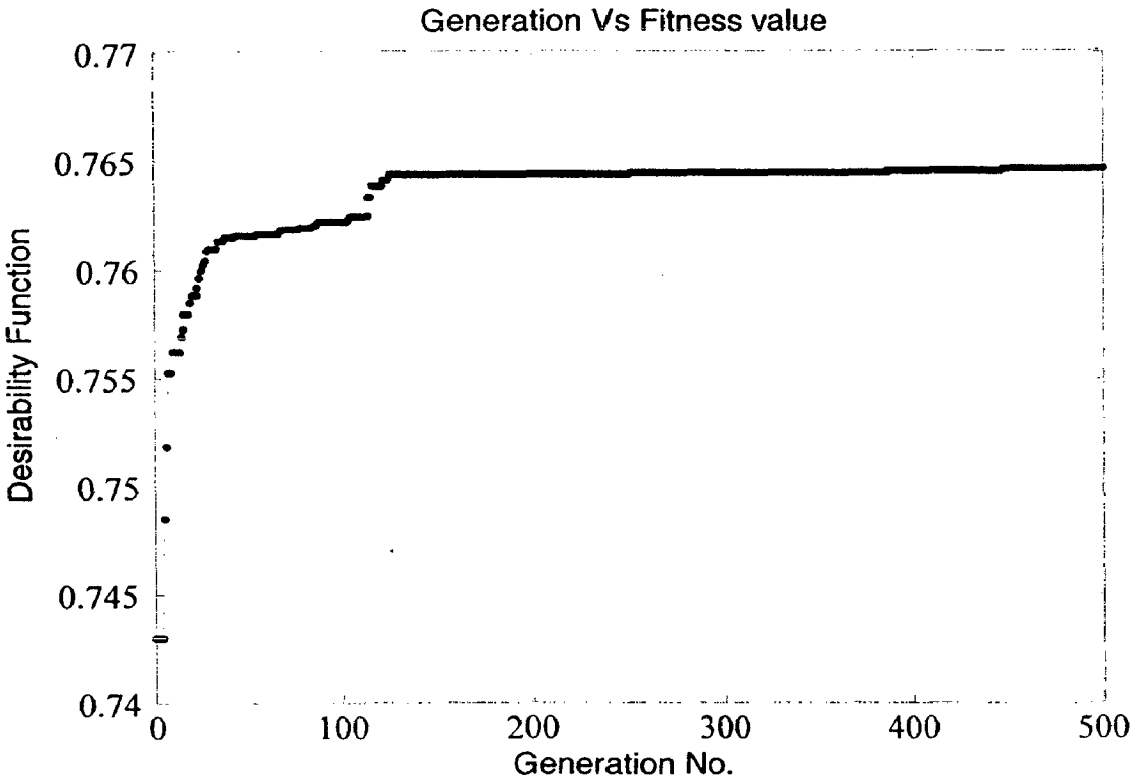

Fig. 8.26 Improvement in maximum fitness of composite desirability with GA generations (DF approach, Model: PIR_a-DIR)

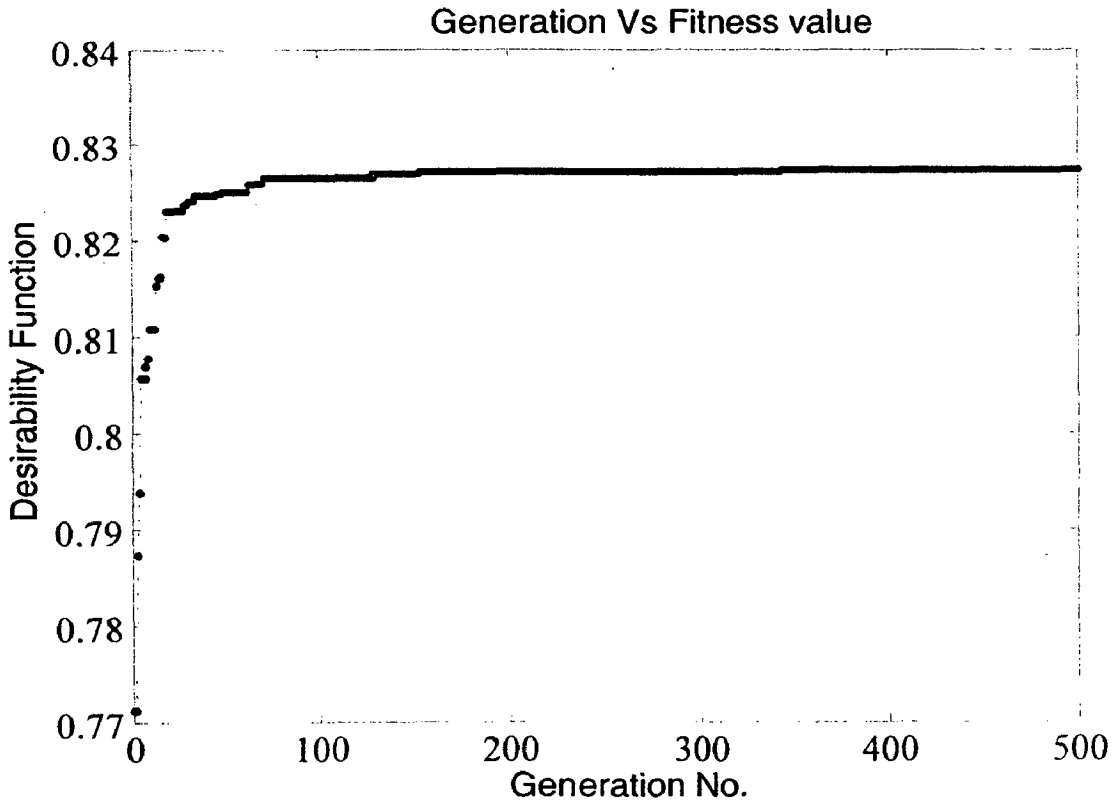

Fig. 8.27 Improvement in maximum fitness of composite desirability with GA generations (mod. DF approach, Model: PIR_a-DIR)

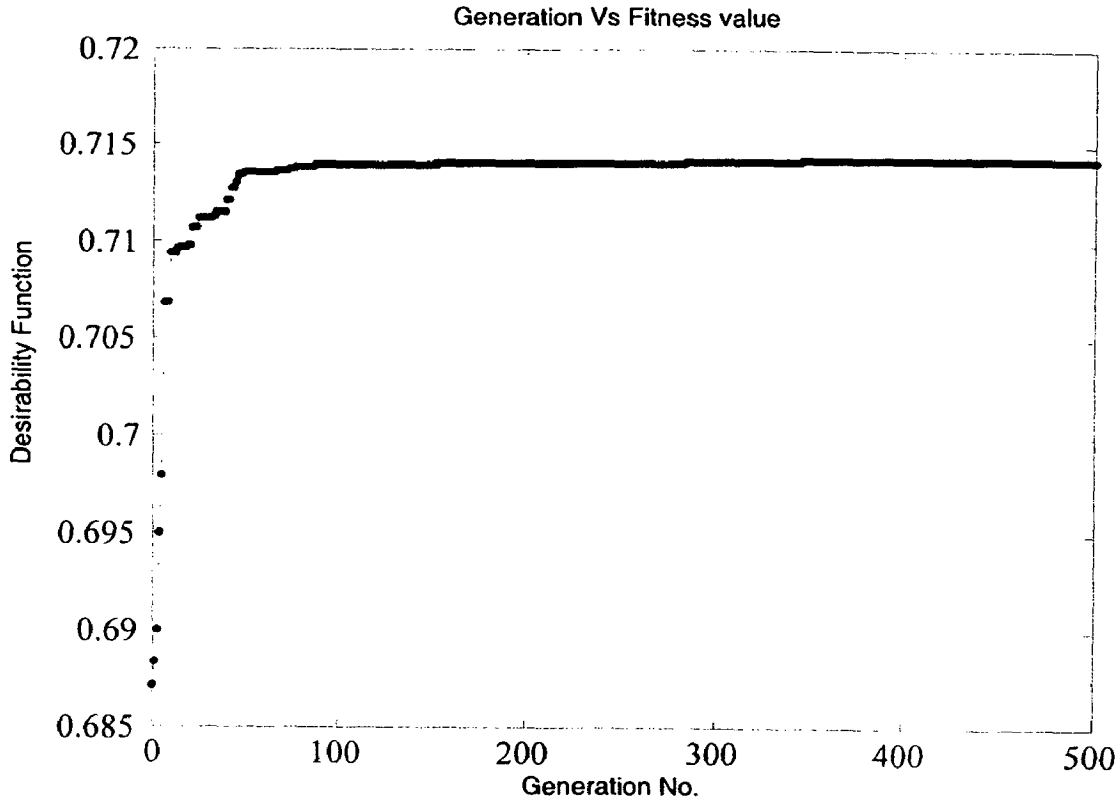

Fig. 8.28 Improvement in maximum fitness of composite desirability with GA generations (DF approach, Model: PIR_a-PIOR-DIR)

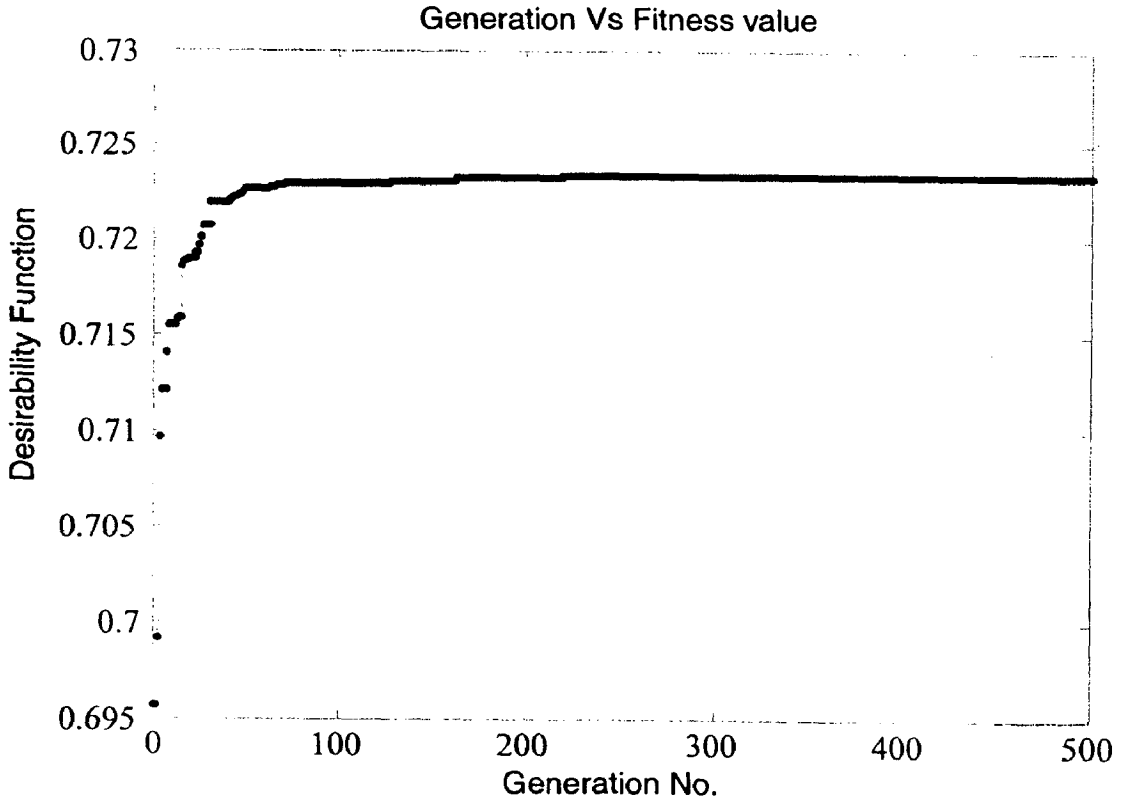

Fig. 8.29 Improvement in maximum fitness of composite desirability with GA generations (mod. DF approach, Model: PIR_a-PIOR-DIR)

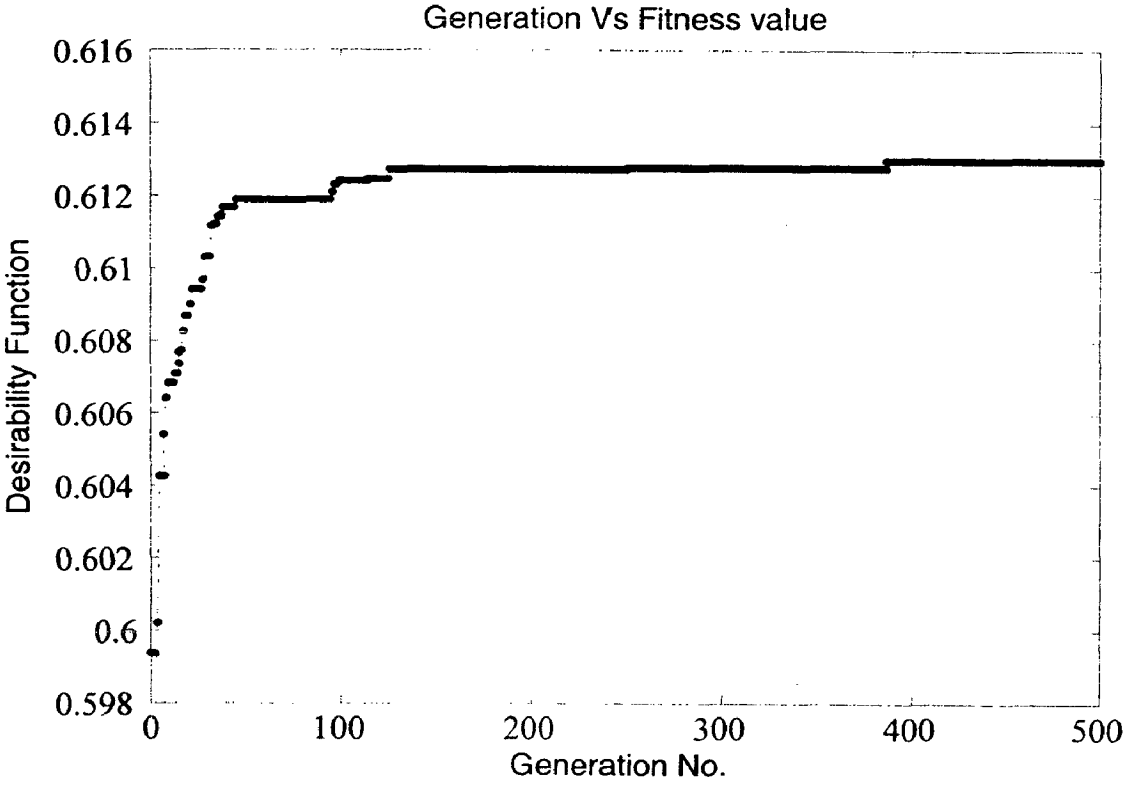

Fig. 8.30 Improvement in maximum fitness of composite desirability with GA generations (DF approach, Model: PIR_a-PICyl-DIR)

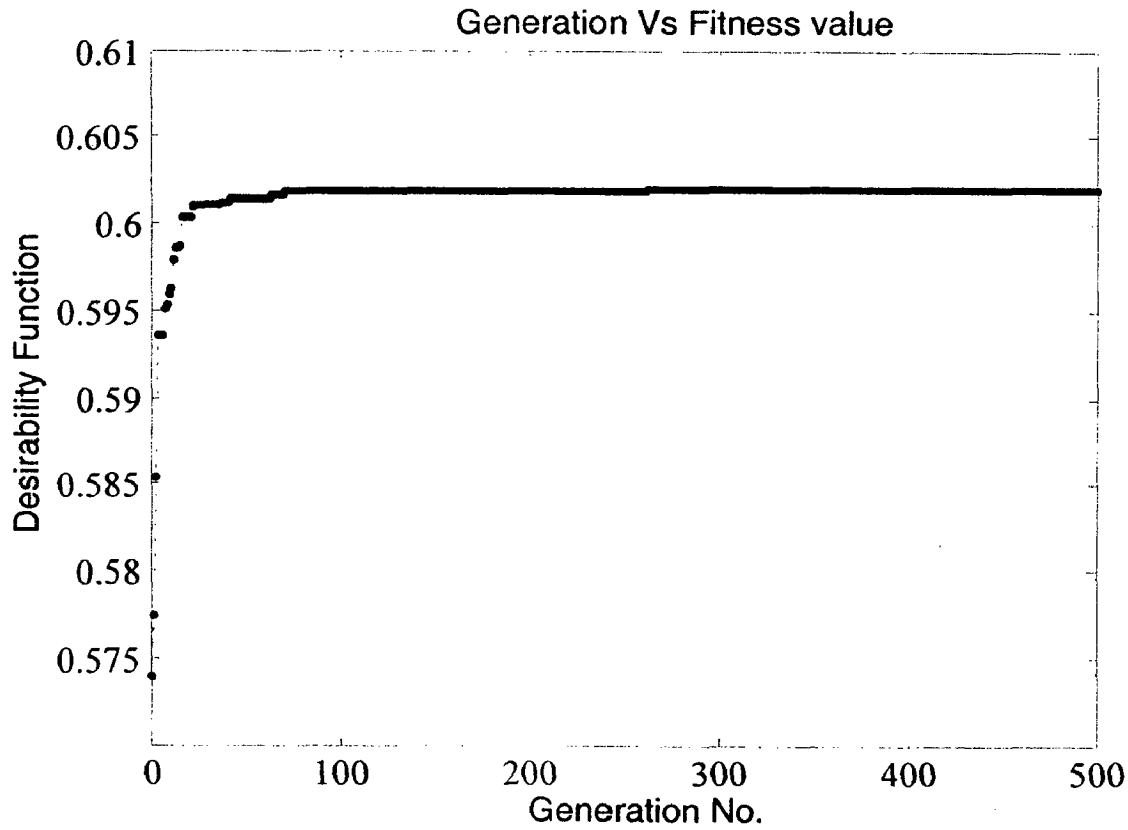

Fig. 8.31 Improvement in maximum fitness of composite desirability with GA generations (mod. DF approach, Model: PIR_a-PICyl-DIR)

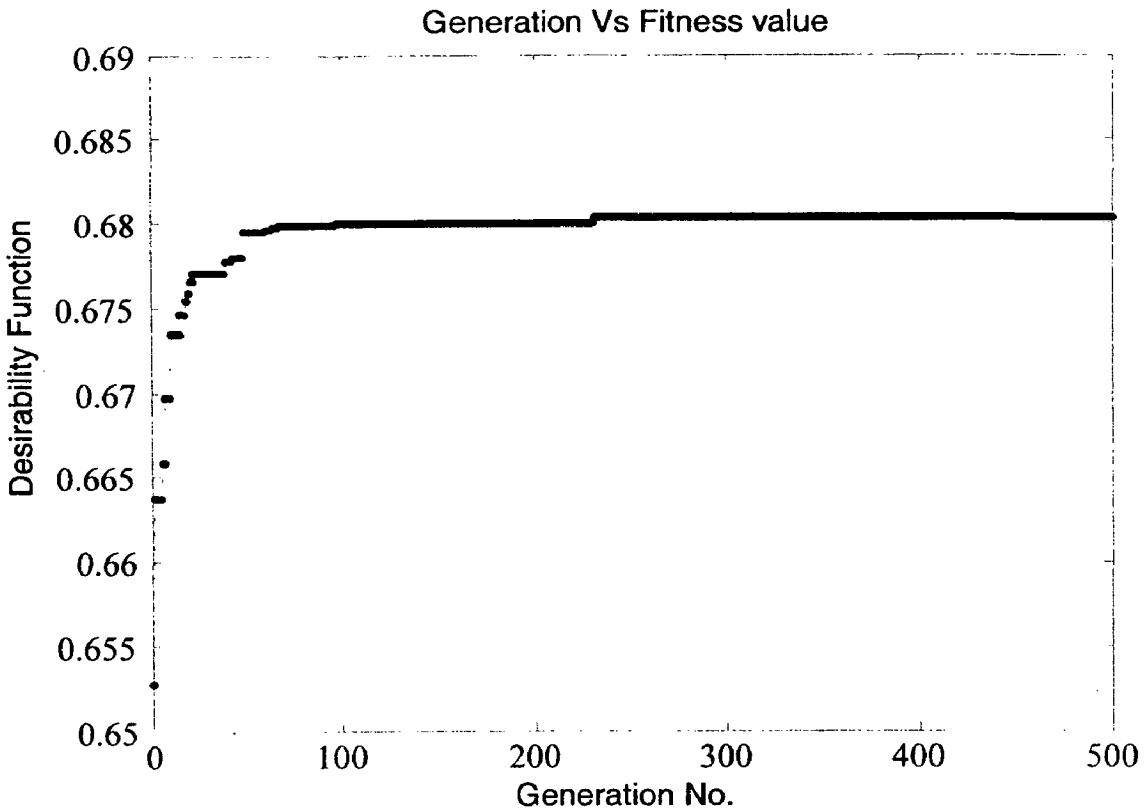

Fig. 8.32 Improvement in maximum fitness of composite desirability with GA generations (DF approach, Model: PIR_a-PIOR-PICyl-DIR)

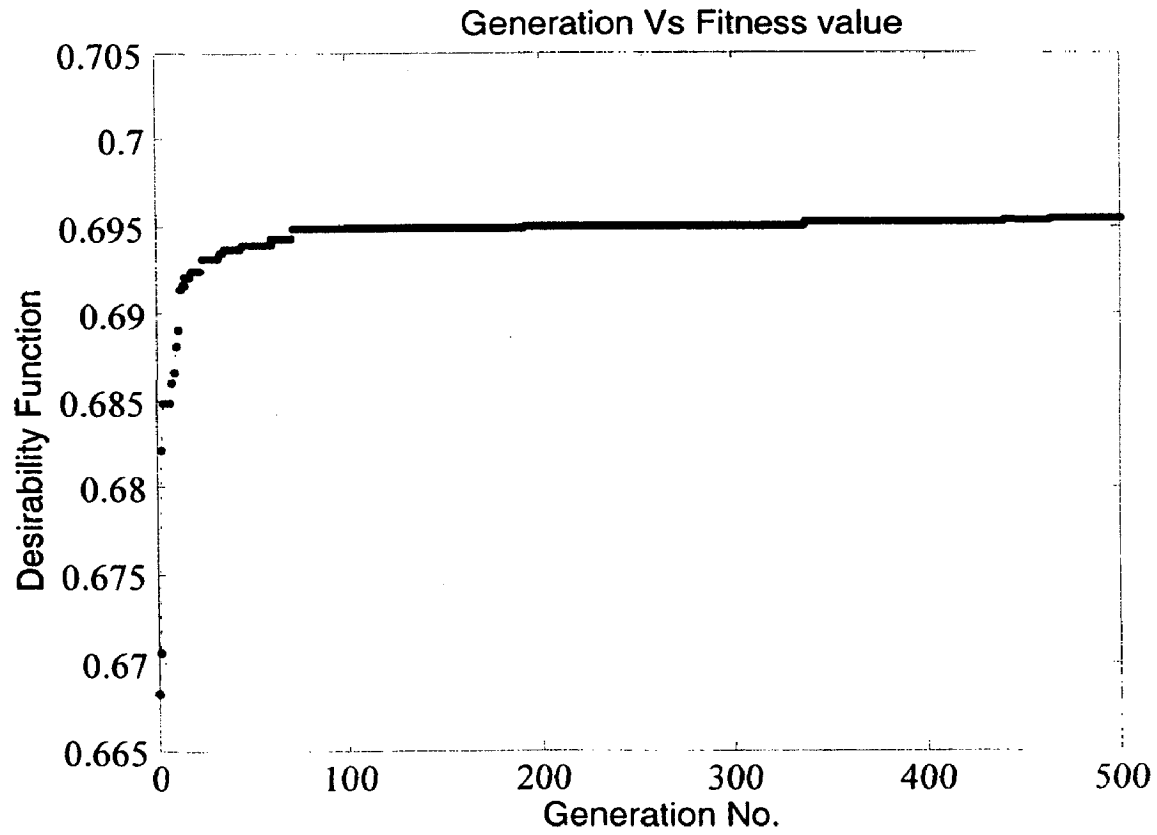

Fig. 8.33 Improvement in maximum fitness of composite desirability with GA generations (mod. DF approach, Model: PIR_a-PIOR-PICyl-DIR)

Table 8.79 Taguchi-RBF NN-DF/Mod.DF-GA Multi-Performance Optimization Results (PIR_a-PIOR)

Pop. Size	Generation No(s).	Optimal Fitness Value (Dnet/Mod Dnet)	Optimal Process Input Parameters							Optimal Performance Characteristics (dB)	
			C	EC	SR	F	T	SOP	G	PIR_a	PIOR
100	295, 298, 299, 302, 318, 375, 500	0.7372	179.97	199.95	249.41	10.80	49.72	29.88	596.07	37.61	31.06
200	432, 500	0.7372	179.84	199.82	249.87	10.04	49.97	29.98	598.61	37.61	31.07

Table 8.80 Taguchi-RBF NN-DF/Mod.DF-GA Multi-Performance Optimization Results (PIR_a-PICyl)

Pop. Size	Generation No(s).	Optimal Fitness Value (Dnet/Mod Dnet)	Optimal Process Input Parameters							Optimal Performance Characteristics (dB)	
			C	EC	SR	F	T	SOP	G	PIR_a	PICyl
100	277, 375, 500	0.5861	179.93	199.91	248.26	18.53	49.94	29.85	603.58	37.59	33.23
200	209, 213, 227, 241, 244, 250, 260, 270, 275, 343, 344, 345, 375, 397, 500	0.5862	179.93	199.99	249.65	10.05	49.99	29.95	601.78	37.60	33.23

Table 8.81 Taguchi-RBF NN-DF-GA Multi-Performance Optimization Results (PIR_a-DIR)

Pop. Size	Generation No(s).	Optimal Fitness Value	Optimal Process Input Parameters							Optimal Performance Characteristics (dB)	
		(Dnet)	C	EC	SR	F	T	SOP	G	PIR_a	DIR
100	448, 457, 468, 487, 500	0.7646	179.99	199.76	249.18	12.52	49.85	29.87	599.65	38.48	33.13
200	155, 250, 375, 500	0.7647	180.00	199.98	247.22	10.56	49.85	29.91	598.55	38.48	33.14

Table 8.82 Taguchi-RBF NN-Mod.DF-GA Multi-Performance Optimization Results (PIR_a-DIR)

Pop. Size	Generation No(s).	Optimal Fitness Value	Optimal Process Input Parameters							Optimal Performance Characteristics (dB)	
		(Mod.Dnet)	C	EC	SR	F	T	SOP	G	PIR_a	DIR
100	346, 375, 500	0.8274	179.99	199.95	245.90	10.42	49.76	29.97	593.98	38.48	33.13
200	217, 250, 375, 500	0.8275	179.94	199.95	249.36	10.03	49.98	29.90	601.42	38.48	33.14

Table 8.83 Taguchi-RBF NN-DF-GA Multi-Performance Optimization Results (PIR_a-PIOR-DIR)

Pop. Size	Generation No(s).	Optimal Fitness Value	Optimal Process Input Parameters							Optimal Performance Characteristics (dB)		
		(Dnet)	C	EC	SR	F	T	SOP	G	PIR_a	PIOR	DIR
100	346, 375, 500	0.7143	179.99	199.95	249.21	10.02	49.78	29.84	596.67	38.55	31.49	33.71
200	180, 250, 325, 341, 375, 500	0.7436	179.90	199.97	249.23	10.04	49.98	29.93	600.53	38.55	31.49	33.71

Table 8.84 Taguchi-RBF NN-Mod.DF-GA Multi-Performance Optimization Results (PIR_a-PIOR-DIR)

Pop. Size	Generation No(s).	Optimal Fitness Value (Mod. Dnet)	Optimal Process Input Parameters							Optimal Performance Characteristics (dB)		
			C	EC	SR	F	T	SOP	G	PIR_a	PIOR	DIR
100	336, 341, 359, 375, 500	0.7234	179.89	199.99	249.30	12.76	49.95	29.98	600.01	38.55	31.49	33.71
200	258, 375, 500	0.7411	179.99	199.77	249.40	10.08	49.94	29.99	600.48	38.55	31.49	33.71

Table 8.85 Taguchi-RBF NN-DF-GA Multi-Performance Optimization Results (PIR_a-PICyl-DIR)

Pop. Size	Generation No(s).	Optimal Fitness Value (Dnet)	Optimal Process Input Parameters							Optimal Performance Characteristics (dB)		
			C	EC	SR	F	T	SOP	G	PIR_a	PICyl	DIR
100	387, 500	0.6130	179.85	199.72	247.03	10.15	49.82	29.84	600.40	38.55	33.60	33.69
200	209, 250, 268, 318, 324, 351, 375, 413, 414, 434 500	0.6130	179.89	199.99	248.38	10.01	49.89	29.99	600.68	38.55	33.60	33.69

Table 8.86 Taguchi-RBF NN-Mod.DF-GA Multi-Performance Optimization Results (PIR_a-PICyl-DIR)

Pop. Size	Generation No(s).	Optimal Fitness Value (Mod.Dnet)	Optimal Process Input Parameters							Optimal Performance Characteristics (dB)		
			C	EC	SR	F	T	SOP	G	PIR_a	PICyl	DIR
100	262, 263, 333, 334, 375, 500	0.6020	179.99	199.23	249.89	10.23	49.77	29.89	596.67	38.55	33.60	33.69
200	227, 250, 375, 438, 440, 447, 448, 464, 483, 500	0.7436	179.96	199.98	249.18	10.00	49.90	29.90	599.74	38.55	33.60	33.71

Table 8.87 Taguchi-RBF NN-DF-GA Multi-Performance Optimization Results (PIR_a-PIOR-PICyl-DIR)

Pop. Size	Generation No(s).	Optimal Fitness Value (Dnet)	Optimal Process Input Parameters							Optimal Performance Characteristics (dB)			
			C	EC	SR	F	T	SOP	G	PIR_a	PIOR	PICyl	DIR
100	232, 250, 375, 500	0.6803	179.97	199.64	247.97	10.51	49.92	30.00	599.87	38.53	31.45	33.56	33.49
200	404, 500	0.6804	179.96	199.96	249.80	14.58	49.94	29.92	598.29	38.53	31.45	33.56	33.50

Table 8.88 Taguchi-RBF NN-Mod.DF-GA Multi-Performance Optimization Results (PIR_a-PIOR-PICyl-DIR)

Pop. Size	Generation No(s).	Optimal Fitness Value	Optimal Process Input Parameters							Optimal Performance Characteristics (dB)			
		(Mod.Dnet)	C	EC	SR	F	T	SOP	G	PIR_a	PIOR	PICyl	DIR
100	465, 500	0.6954	179.93	199.94	249.61	10.04	49.99	30.00	599.73	38.53	31.45	33.56	33.50
200	258, 375, 500	0.6955	179.99	199.93	249.90	13.19	49.94	30.00	599.78	38.53	31.45	33.56	33.50

Table 8.89 Taguchi-RBF NN-NSGA Pareto-Optimal Results (PIR_a-PIOR)

Optimal Fitness Value (di)		Optimal Process Input Parameters							Optimal Performance Characteristics (dB)	
PIRa	PIOR	C	EC	SR	F	T	SOP	G	PIR_a	PIOR
0.869	0.623	178.95	198.68	248.58	11.12	49.46	29.11	588.57	37.61	31.05
0.763	0.624	136.17	182.80	249.21	10.04	36.44	26.70	598.89	37.62	31.15
0.824	0.624	157.91	198.12	248.98	14.08	44.73	27.71	598.89	37.61	31.11
0.792	0.624	147.37	184.22	249.21	10.04	44.73	26.70	598.89	37.62	31.13
0.804	0.624	153.25	191.80	248.98	10.04	36.44	26.77	598.89	37.61	31.13
0.775	0.624	142.40	182.80	248.98	10.04	36.44	26.77	598.89	37.62	31.15
0.815	0.624	157.91	182.80	248.98	13.14	48.89	29.09	598.89	37.61	31.12
0.834	0.624	168.83	182.80	248.98	12.57	44.73	26.77	598.89	37.61	31.11
0.859	0.624	175.73	198.12	248.98	10.04	44.73	29.15	598.89	37.61	31.09
0.844	0.624	174.66	182.80	248.98	10.04	42.53	26.77	598.89	37.61	31.11

Table 8.90 Taguchi-RBF NN-NSGA Pareto-Optimal Results (PIR_a-PCyl)

Optimal Fitness Value (di)		Optimal Process Input Parameters							Optimal Performance Characteristics (dB)	
PIRa	PICyl	C	EC	SR	F	T	SOP	G	PIR_a	PICyl
0.763	0.395	136.25	182.80	249.62	10.36	36.31	26.34	600.77	37.60	33.30
0.871	0.394	179.87	199.21	249.62	10.13	49.75	29.75	600.77	37.60	33.23
0.805	0.395	149.20	194.78	249.62	10.13	45.59	29.75	600.77	37.59	33.30
0.775	0.395	141.09	184.10	249.62	10.31	37.62	27.28	600.77	37.60	33.29
0.783	0.395	141.09	194.78	249.62	10.13	37.62	29.75	600.77	37.59	33.31
0.796	0.395	149.20	184.10	249.62	10.13	45.59	29.75	600.77	37.60	33.28
0.836	0.395	169.26	184.10	249.62	10.31	45.59	29.75	600.77	37.60	33.22
0.862	0.394	175.23	199.21	249.62	16.44	49.75	26.41	600.77	37.60	33.24
0.846	0.395	166.75	199.21	249.62	10.13	49.75	29.75	600.77	37.59	33.27
0.819	0.395	156.82	194.78	249.62	10.88	45.59	24.05	600.77	37.60	33.28

Table 8.91 Taguchi-RBF NN-NSGA Pareto-Optimal Results (PIR_a-DIR)

Optimal Fitness Value (di)		Optimal Process Input Parameters							Optimal Performance Characteristics (dB)	
PIRa	DIR	C	EC	SR	F	T	SOP	G	PIR_a	DIR
0.869	0.671	179.59	199.60	246.48	15.64	47.03	29.58	594.18	38.47	33.05
0.801	0.671	147.01	195.15	249.94	10.10	47.81	25.96	598.91	38.21	30.96
0.776	0.671	141.98	184.14	249.94	11.94	37.83	26.56	598.91	38.11	30.21
0.860	0.671	179.36	193.93	249.94	24.89	40.66	26.56	598.91	38.43	32.77
0.812	0.671	157.01	184.14	249.94	11.94	45.76	26.84	598.91	38.25	31.28
0.765	0.671	136.81	183.54	249.94	10.10	36.36	26.56	598.91	38.07	29.85
0.823	0.671	165.02	185.94	249.94	10.10	36.27	28.45	598.91	38.29	31.64
0.786	0.671	141.98	191.59	249.94	14.88	43.91	26.84	598.91	38.15	30.50
0.851	0.671	172.92	193.93	249.94	10.45	45.76	26.48	598.91	38.40	32.48
0.841	0.671	172.92	184.73	249.94	10.10	40.66	26.56	598.91	38.36	32.17

Table 8.92 Taguchi-RBF NN-NSGA Pareto-Optimal Results (PIR_a-PIOR-DIR)

Optimal Fitness Value (di)			Optimal Process Input Parameters							Optimal Performance Characteristics (dB)		
PIRa	PIOR	DIR	C	EC	SR	F	T	SOP	G	PIR_a	PIOR	DIR
0.513	0.619	0.770	51.12	120.28	240.02	11.36	11.70	10.72	601.52	37.06	31.37	21.94
0.870	0.623	0.757	179.69	198.72	247.63	10.60	48.96	29.58	601.52	38.55	31.49	33.64
0.548	0.620	0.769	58.29	127.74	232.86	24.31	29.32	21.65	601.52	37.20	31.39	23.06
0.584	0.621	0.768	68.67	135.30	247.63	26.35	38.15	29.97	601.52	37.35	31.42	24.21
0.639	0.622	0.766	99.35	131.35	232.86	19.91	29.32	23.91	601.52	37.58	31.44	26.00
0.696	0.623	0.764	123.13	149.13	243.55	23.14	20.91	12.94	601.52	37.82	31.47	27.87
0.733	0.624	0.763	123.13	195.19	243.55	23.14	20.91	13.95	601.52	37.98	31.48	29.09
0.847	0.623	0.758	179.69	198.72	243.55	12.75	13.00	29.01	601.52	38.45	31.48	32.88
0.773	0.624	0.761	147.92	163.13	247.63	17.82	41.18	21.77	601.52	38.14	31.49	30.40
0.801	0.624	0.760	163.95	183.15	242.95	26.35	12.95	14.67	601.52	38.26	31.49	31.36

Table 8.93 Taguchi-RBF NN-NSGA Pareto-Optimal Results (PIR_a-PICyl-DIR)

Optimal Fitness Value (di)			Optimal Process Input Parameters							Optimal Performance Characteristics (dB)		
PIRa	PICyl	DIR	C	EC	SR	F	T	SOP	G	PIR_a	PICyl	DIR
0.872	0.394	0.757	179.92	199.96	248.07	16.07	49.12	29.82	601.65	38.55	33.60	33.69
0.499	0.389	0.770	51.41	103.98	248.07	11.27	10.22	15.90	601.65	37.00	33.87	21.51
0.536	0.391	0.769	57.52	130.74	248.07	23.13	10.22	21.20	601.65	37.15	33.86	22.69
0.598	0.392	0.767	57.52	176.60	238.33	19.34	46.27	26.15	601.65	37.41	33.83	24.69
0.793	0.394	0.760	163.90	173.56	248.07	14.68	10.22	20.22	607.86	38.23	33.68	31.08
0.683	0.394	0.765	102.97	173.00	238.33	26.44	32.28	26.15	601.65	37.77	33.78	27.43
0.721	0.395	0.763	114.10	186.52	221.53	10.08	38.92	27.72	601.65	37.93	33.75	28.69
0.637	0.394	0.767	88.88	167.38	238.33	12.60	15.67	16.67	593.10	37.57	33.81	25.92
0.840	0.394	0.758	179.20	189.86	220.53	11.91	15.67	24.03	607.86	38.42	33.63	32.64
0.763	0.393	0.761	160.27	123.73	248.07	27.40	38.92	21.62	607.86	38.10	33.69	30.10

Table 8.94 Taguchi-RBF NN-NSGA Pareto-Optimal Results (PIR_a-PIOR-PICyl-DIR)

Optimal Fitness Value (di)				Optimal Process Input Parameters							Optimal Performance Characteristics (dB)			
PIRa	PIOR	PICyl	DIR	C	EC	SR	F	T	SOP	G	PIR_a	PIOR	PICyl	DIR
0.5029	0.6187	0.5426	0.2774	50.12	110.25	249.96	12.69	11.32	17.95	598.72	37.03	31.37	33.88	21.81
0.8682	0.6233	0.5233	0.7486	179.46	199.00	243.88	11.65	46.85	27.07	596.84	38.51	31.45	33.56	33.37
0.5693	0.6209	0.5404	0.3613	66.28	128.64	237.61	13.35	34.37	22.78	596.84	37.30	31.41	33.85	23.86
0.5298	0.6197	0.5418	0.3112	58.62	116.81	248.24	10.09	14.29	22.95	596.84	37.14	31.39	33.87	22.63
0.7295	0.6238	0.5328	0.5668	120.77	196.47	243.88	23.04	18.20	25.65	596.84	37.95	31.46	33.72	28.91
0.6303	0.6227	0.5381	0.4386	81.42	172.61	243.88	28.51	21.05	27.07	598.72	37.55	31.44	33.81	25.76
0.7599	0.6238	0.5308	0.6066	146.86	153.15	243.88	11.65	35.72	27.07	596.84	38.07	31.46	33.69	29.88
0.8037	0.6236	0.5277	0.664	163.37	187.65	243.88	14.86	13.38	11.42	596.84	38.25	31.46	33.64	31.29
0.8413	0.6235	0.5252	0.7132	171.84	196.47	243.88	16.30	34.37	13.58	596.84	38.40	31.45	33.60	32.50
0.6715	0.6232	0.5360	0.4918	89.68	187.65	248.24	14.32	40.26	24.02	584.37	37.72	31.45	33.77	27.07

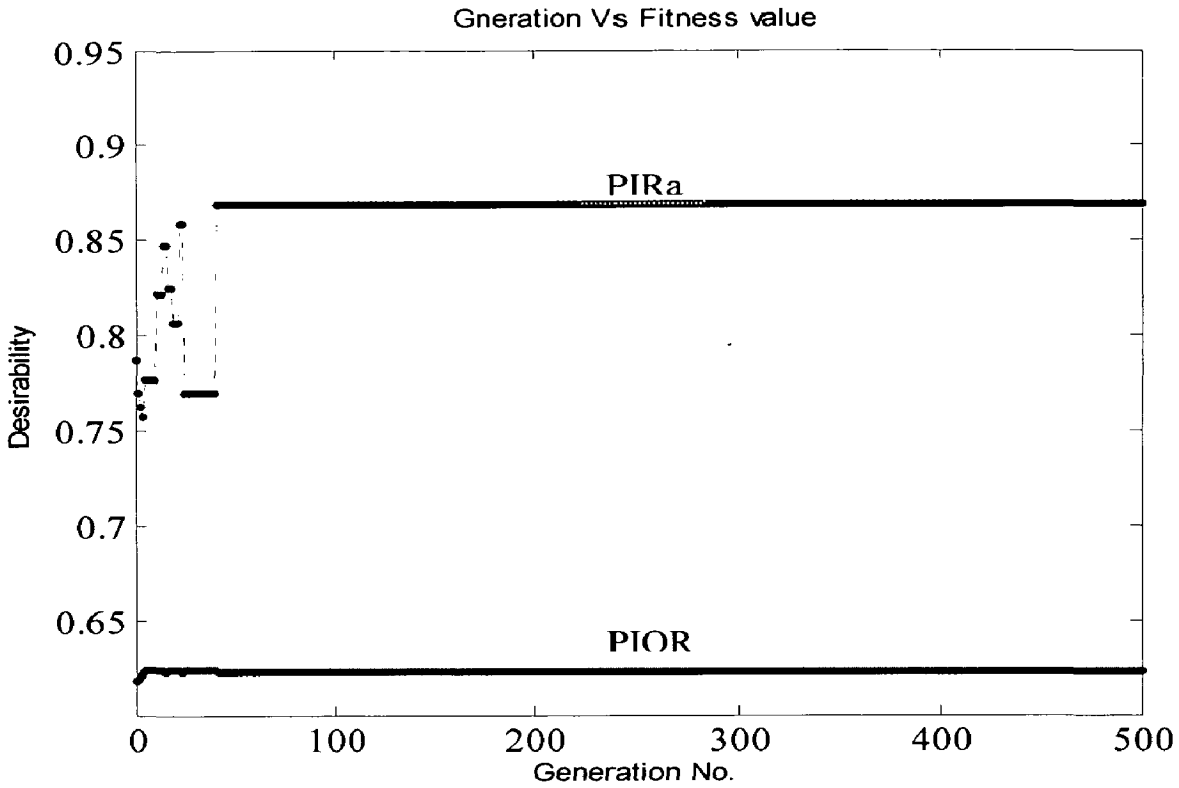

Fig. 8.34 Improvement in maximum fitness of different performance characteristics with NSGA generations (Model: PIR_a-PIOR)

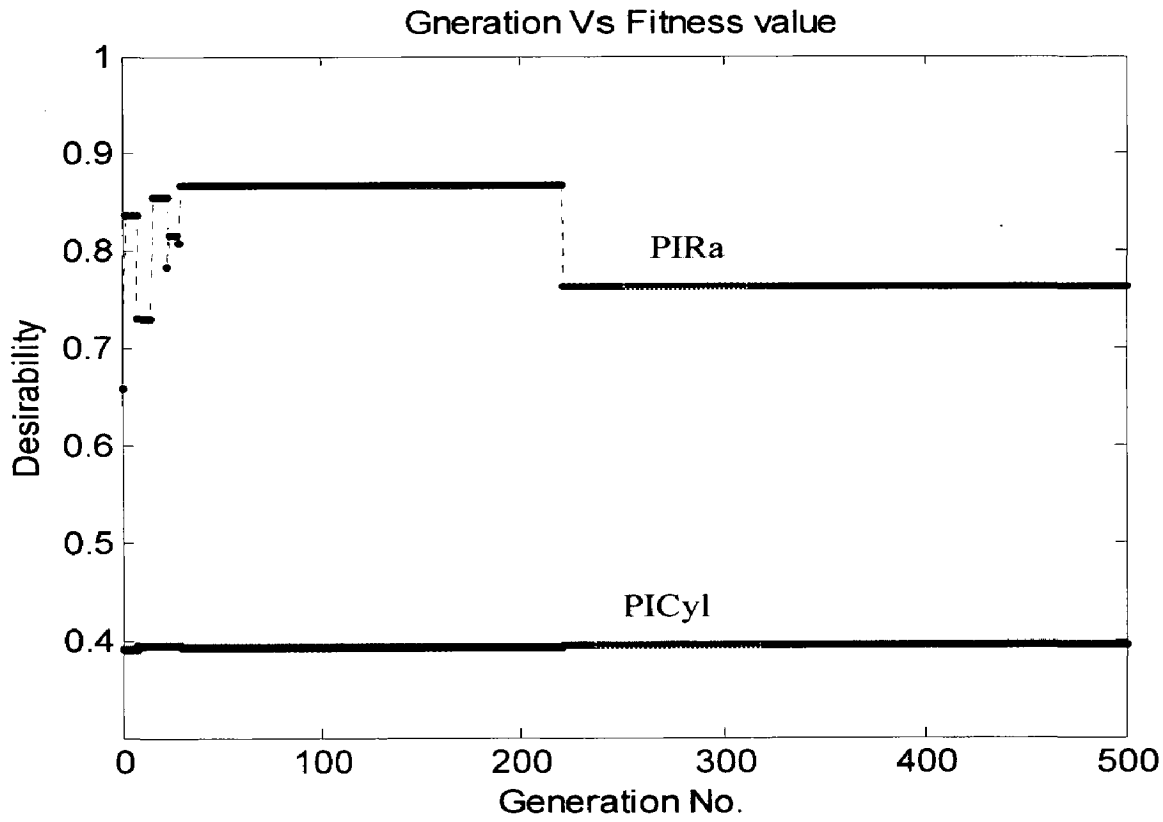

Fig. 8.35 Improvement in maximum fitness of different performance characteristics with NSGA generations (Model: PIR_a-PICyl)

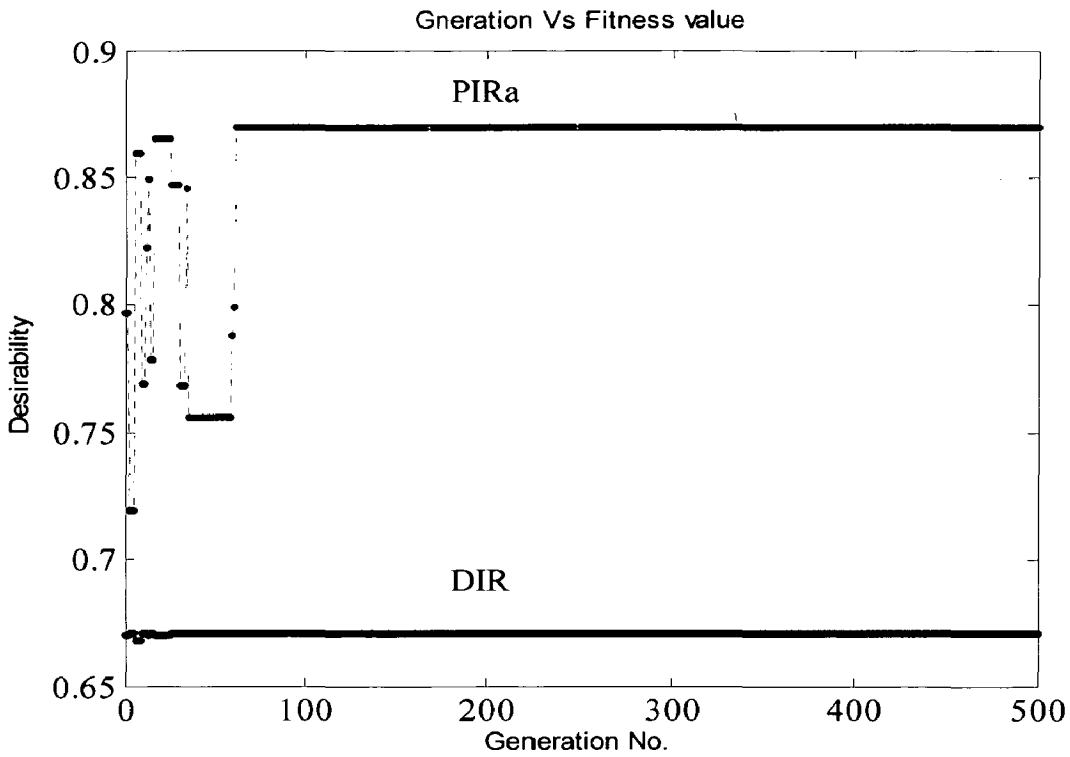

Fig. 8.36 Improvement in maximum fitness of different performance characteristics with NSGA generations (Model: PIR_a-DIR)

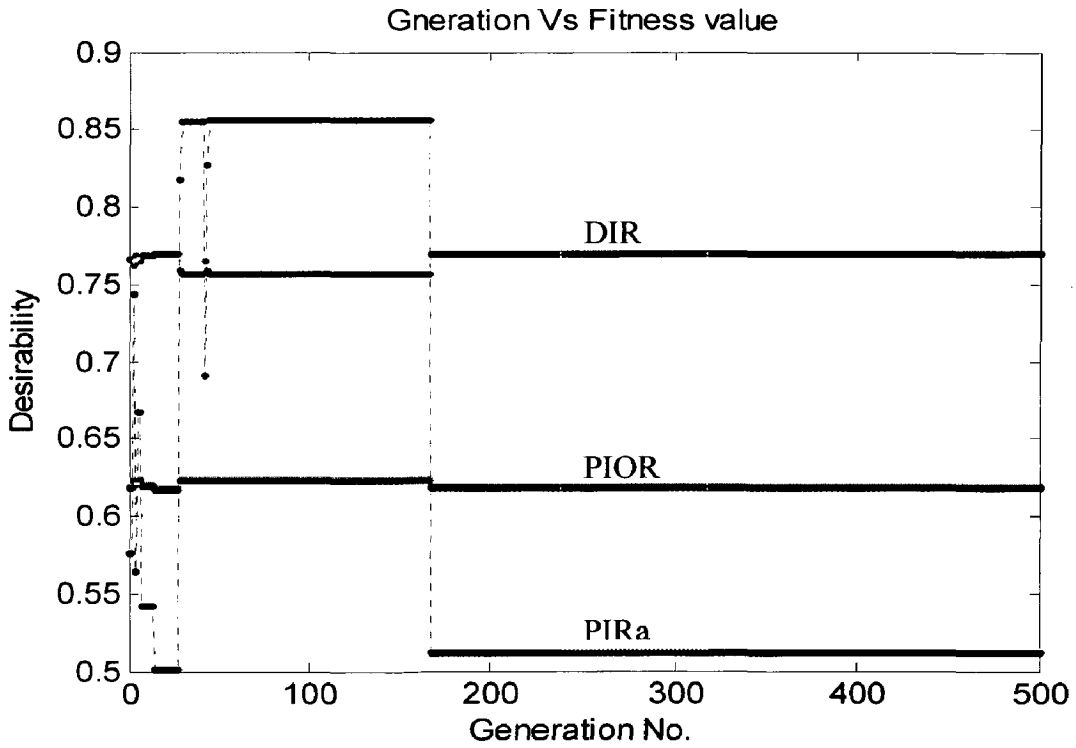

Fig. 8.37 Improvement in maximum fitness of different performance characteristics with NSGA generations (Model: PIR_a-PIOR-DIR)

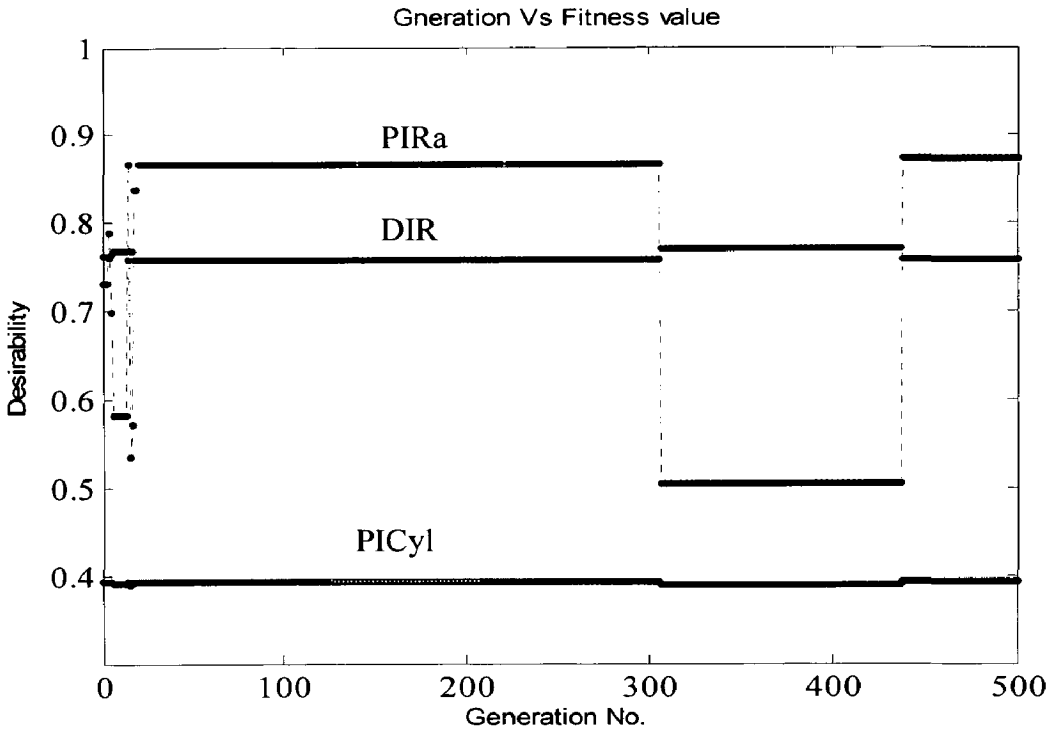

Fig. 8.38 Improvement in maximum fitness of different performance characteristics with NSGA generations (Model: PIR_a-PICyl-DIR)

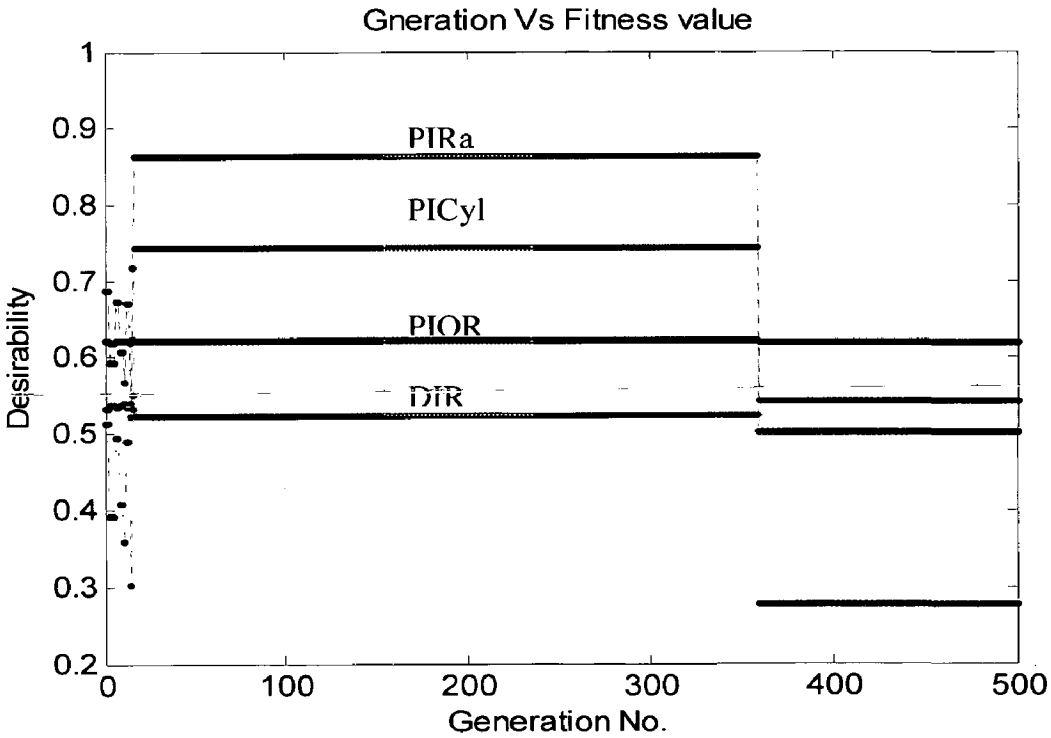

Fig. 8.39 Improvement in maximum fitness of different performance characteristics with NSGA generations (Model: PIR_a-PIOR-PICyl-DIR)

Table 8.95 RBF NN Modeling Results (PIR_{max}-PIOR-PICyl-DIR)

S. No	Process Input Parameters							Experimental (S/N Response)				Predicted				% Error			
	C	EC	SR	F	T	SOP	G	PIR_{max}	PIOR	PICyl	DIR	PIR_{max}	PIOR	PICyl	DIR	PIR_{max}	PIOR	PICyl	DIR
1	50	100	150	20	30	20	600	33.55	31.50	34.63	23.16	35.70	31.28	33.81	21.83	6.41	0.69	2.35	5.74
2	50	150	150	30	50	10	360	36.11	31.77	32.92	24.77	35.70	30.89	33.47	22.92	1.13	2.77	1.67	7.49
3	50	200	150	10	10	30	1200	34.63	31.44	33.75	21.46	34.19	28.87	31.94	20.75	1.27	8.18	5.37	3.31
4	115	100	150	30	10	30	360	35.93	30.99	33.29	23.67	36.13	30.90	33.40	25.13	0.55	0.30	0.32	6.13
5	115	200	150	20	50	10	600	37.57	33.20	36.37	30.60	37.16	31.38	33.65	29.04	1.08	5.48	7.48	5.09
6	180	150	150	20	10	30	600	36.24	34.91	37.21	33.32	37.58	31.36	33.56	31.28	3.71	10.16	9.80	6.12
7	180	200	150	30	30	20	360	37.09	33.77	36.05	33.51	37.50	30.94	33.20	32.02	1.11	8.38	7.89	4.44

Table 8.96 Taguchi-RBF NN-DF-GA Multi-Performance Optimization Results (PIR_{max}-PIOR-PICyl-DIR)

Pop. Size	Generation No(s).	Optimal Fitness Value	Optimal Process Input Parameters							Optimal Performance Characteristics (dB)			
		(Dnet)	C	EC	SR	F	T	SOP	G	PIR_{max}	PIOR	PICyl	DIR
100	500	0.6875	179.93	199.99	249.29	10.10	49.90	29.98	601.35	38.06	31.45	33.56	33.50

Table 8.97 Taguchi-RBF NN-Mod.DF-GA Multi-Performance Optimization Results (PIR_{max}-PIOR-PICyl-DIR)

Pop. Size	Generation No(s).	Optimal Fitness Value	Optimal Process Input Parameters							Optimal Performance Characteristics (dB)			
		(MDnet)	C	EC	SR	F	T	SOP	G	PIR_{max}	PIOR	PICyl	DIR
100	500	0.7071	179.94	200.00	248.03	10.35	49.98	29.98	600.26	38.06	31.45	33.56	33.50

Table 8.98 Taguchi-RBF NN-NSGA Pareto-Optimal Results (PIR_{max}-PIOR-PICyl-DIR)

Optimal Fitness Value (di)				Optimal Process Input Parameters							Optimal Performance Characteristics (dB)			
PIRmax	PIOR	PICyl	DIR	C	EC	SR	F	T	SOP	G	PIR_{max}	PIOR	PICyl	DIR
0.7491	0.6186	0.5426	0.2752	50.79	108.63	248.25	12.23	10.08	10.08	599.39	35.73	31.36	33.88	21.74
0.7663	0.6205	0.5419	0.3246	53.14	143.90	248.25	12.68	15.27	16.76	599.39	35.98	31.40	33.87	22.96
0.7804	0.6213	0.5405	0.3664	68.35	135.22	248.25	12.68	26.71	16.70	599.39	36.19	31.41	33.85	23.99
0.8221	0.6233	0.5361	0.4904	95.28	192.86	248.25	12.68	15.90	15.50	599.39	36.80	31.45	33.77	27.03
0.8715	0.6229	0.5283	0.6406	170.47	142.87	248.25	13.46	15.90	23.01	599.39	37.52	31.44	33.65	30.72
0.7990	0.6224	0.5387	0.4215	84.42	155.74	240.50	27.09	15.27	14.00	599.39	36.47	31.43	33.82	25.34
0.8382	0.6239	0.5342	0.5382	118.86	170.57	237.33	14.40	21.03	29.23	599.39	37.04	31.46	33.74	28.21
0.9089	0.6232	0.5230	0.7533	179.86	199.78	248.25	15.31	49.94	29.23	599.39	38.06	31.45	33.56	33.48
0.8936	0.6235	0.5255	0.7067	170.47	186.98	240.50	27.52	43.29	12.19	599.39	37.84	31.45	33.60	32.34
0.8605	0.6230	0.5300	0.6070	142.57	173.86	248.25	27.52	28.34	16.33	649.42	37.36	31.44	33.68	29.89

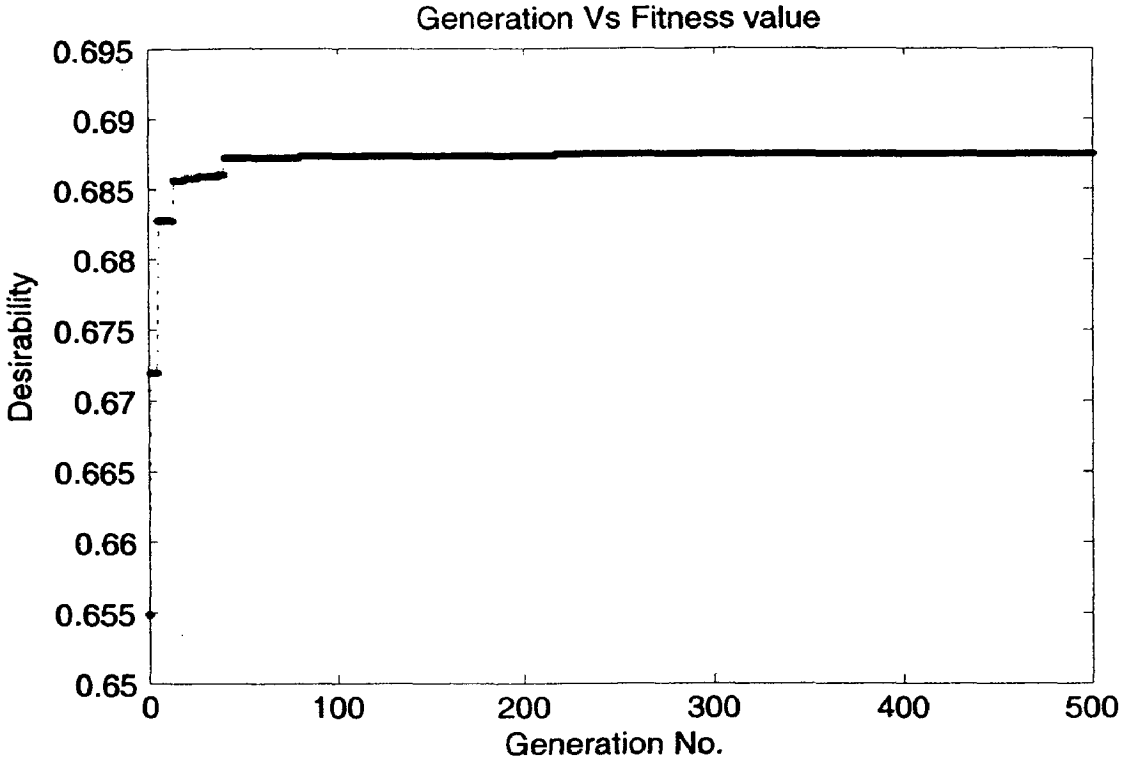

Fig. 8.40 Improvement in maximum fitness of composite desirability with GA generations (DF approach, Model: PIR_{max}-PIOR-PICyl-DIR)

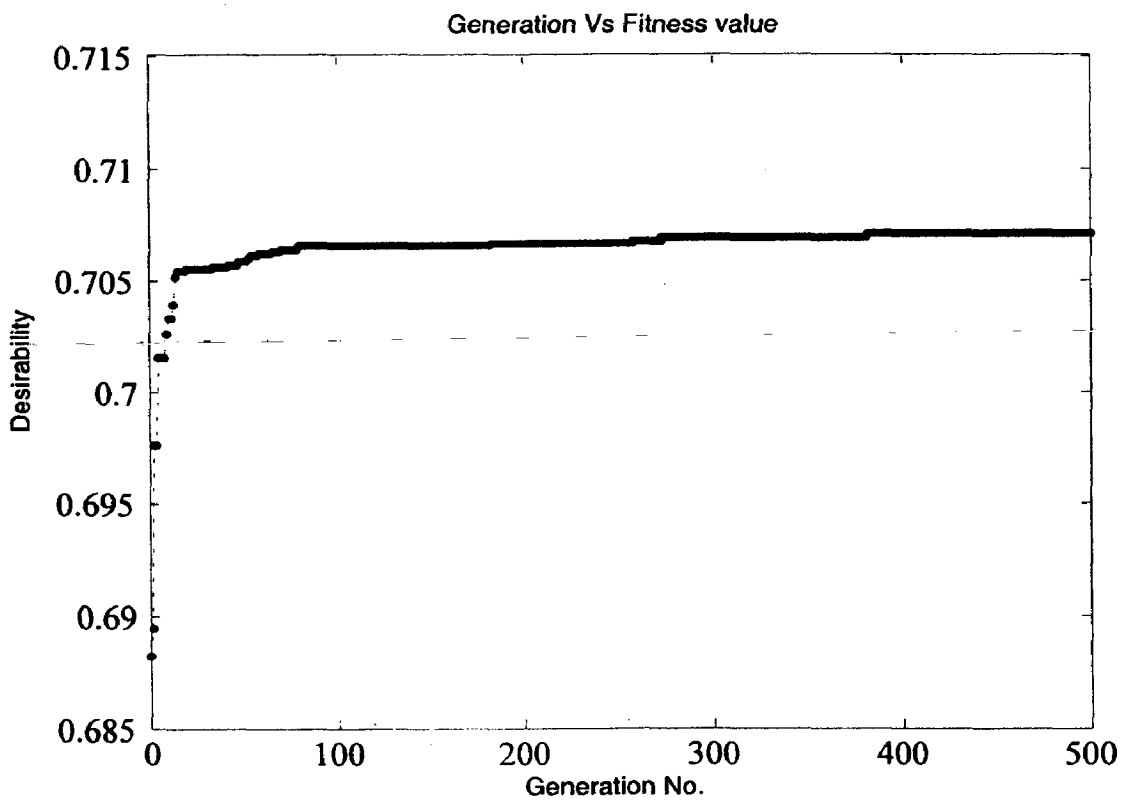

Fig. 8.41 Improvement in maximum fitness of composite desirability with GA generations (Mod.DF approach, Model: PIR_{max}-PIOR-PICyl-DIR)

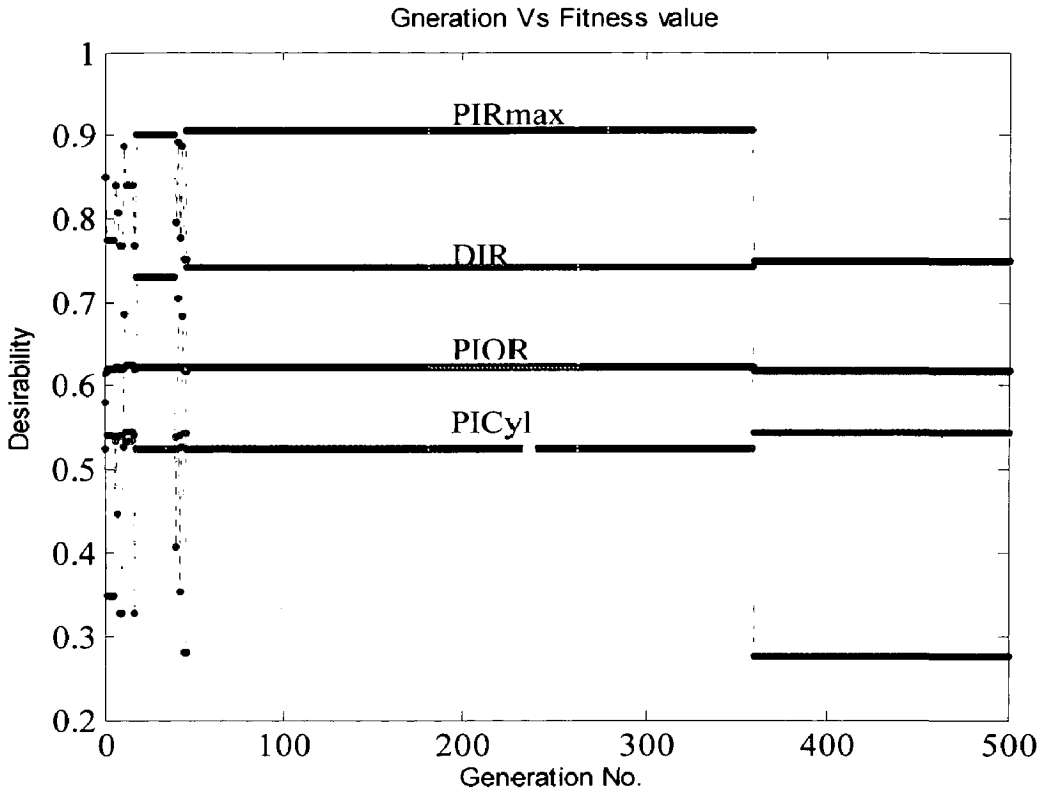

Fig. 8.42 Improvement in maximum fitness of different performance characteristics with NSGA generations (Model: PIR_{max}-PIOR-PICyl-DIR)

8.2.7 Confirmation Experiments

Most of the optimal parameter settings obtained using desirability approaches as well as some of the optimal parameter settings using NSGA approach can be approximately represented by a trial condition with current intensity = 180 ADC; electrolyte concentration = 200g/L; rotary to reciprocating speed ratio = 250; electrolyte flow rate = 10 lpm; electrolyte inlet temperature = 50°C; stick-out pressure = 30 kPa and stick grit-size = 600. The actual experimental results, for multiple process performance characteristics considered for optimization in different multi-performance models are given in Table 8.99. There is a close agreement between the predicted optimal values and their corresponding actual values of the various process performance characteristics. The 'Taguchi-RBF NN-DF-GA Optimization Control Strategy Models for Multi-Performance Optimization of ECH' are, therefore, validated. The actual results are even slightly better, particularly for PIOR and PICyl. This may be due to the influence of the significant interactions. It can be recalled that interaction effects of current intensity, electrolyte concentration and speed ratio were found dominating in case of PIOR and PICyl in phase-III experimental studies. The property of RBFNN that is a multi-output network can be considered as superposition of single output network is clearly reflected in various results. Further, within the range of experimental domain, desirability and modified desirability as well as non-dominating GA produced almost the similar results. NSGA in addition provided a set of optimal solutions suitable for different conditions as well.

Table 8.99 Confirmation experiment results ("Taguchi-RBF NN-GA Multi-Performance Optimization Control Strategy")

Model	Approach	Predicted Optimal Values (dB)				Actual Results (dB)				Difference (%)			
		PIR_a	PIOR	PICyl	DIR	PIR_a	PIOR	PICyl	DIR	PIR_a	PIOR	PICyl	DIR
PIRa-PIOR	DF/Mod.DF	37.61	31.06	-	-	38.83	35.44	-	-	3.16	12.35	-	-
	NSGA	37.61	31.05	-	-	38.83	35.44	-	-	3.16	12.38	-	-
PIRa-PICyl	DF/Mod.DF	37.60	-	33.23	-	38.83	-	37.73	-	3.19	-	11.93	-
	NSGA	37.59	-	33.27	-	38.83	-	37.73	-	3.19	-	11.94	-
PIRa-DIR	DF	38.48	-	-	33.13	38.83	-	-	35.13	0.92	-	-	5.70
	Mod.DF	38.48	-	-	33.13	38.83	-	-	35.13	0.92	-	-	5.69
	NSGA	38.47	-	-	33.05	38.83	-	-	35.13	0.94	-	-	5.93
PIRa-PIOR-DIR	DF	38.55	31.49	-	33.71	38.83	35.44	-	35.13	0.72	11.15	-	4.06
	Mod.DF	38.55	31.49	-	33.70	38.83	35.44	-	35.13	0.72	11.15	-	4.07
	NSGA	38.55	31.49	-	33.64	38.83	35.44	-	35.13	0.74	11.15		4.25
PIRa-PICyl-DIR	DF	38.55	-	33.60	33.69	38.83	-	37.73	35.13	0.73	-	10.94	4.10
	Mod.DF	38.55	-	33.60	33.69	38.83	-	37.73	35.13	0.73	-	10.94	4.10
	NSGA	38.55	-	33.60	33.69	38.83	-	37.73	35.13	0.73	-	10.94	4.10
PIRa-PIOR-PICyl-DIR	DF	38.53	31.45	33.56	33.49	38.83	35.44	37.73	35.13	0.79	11.26	11.05	4.66
	Mod.DF	38.53	31.45	33.56	33.50	38.83	35.44	37.73	35.13	0.79	11.26	11.06	4.66
	NSGA	38.51	31.45	33.56	33.37	38.83	35.44	37.73	35.13	0.84	11.26	11.04	5.03

8.3 FUZZY-TAGUCHI INFERENCE APPLICATION TO ECH

8.3.1 Fuzzy Inference System

The real world problems are quite complex owing to uncertainty. Modeling of ill-defined and uncertain systems based on conventional mathematical tools is either not well suited or sometimes not possible. A fuzzy inference system can model the qualitative aspects of human knowledge and reasoning processes without employing precise quantitative analyses. It is an excellent mathematical tool to handle uncertainty arising due to vagueness. Fuzzy set theory was first propounded by Lofty A. Zadeh (1987) in his seminal paper (Zadeh, 1965) and since then a lot of theoretical developments have taken place in the field. It is the Japanese industries who have much exploited the potential of the technique for the modeling and control of their processes/systems.

A fuzzy set supports a flexible sort of membership of the elements to a set as against a crisp set in which an element either belongs to or does not belong to the set. It can contain elements with many degree of membership (between 0 and 1). Thus a membership function is associated with a fuzzy set that maps every element of the universe of discourse (or the reference set) to the interval [0, 1].

The fuzzy inference system (FIS) uses the "process knowledge" (in the form of fuzzy logic rules and the membership functions) which is often gathered based on the "experimental experience" to approximate the expert perception and judgment in modeling the process input-output relationship involving linguistic variables rather than a complicated dynamic model. The utilization of fuzzy logic rules (fuzzy if-then rules), linguistic variables and approximate reasoning provides a means to incorporate human expert experience in designing the controller (Lin et al., 2001).

Fuzzy inference systems [also known as fuzzy-rule-based systems or fuzzy models or expert system or fuzzy associative memories (FAM), or fuzzy logic controllers (FLC)] is composed of basically five functional blocks (Jang, 1993) (Fig. 8.43):

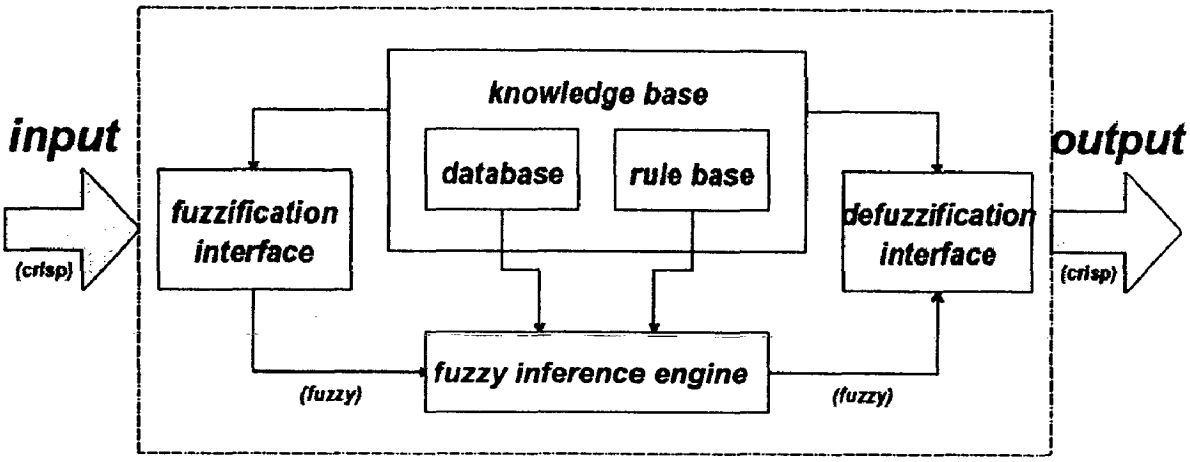

Fig. 8.43 Schematic diagram of the fuzzy inference system

- a **rule base** containing a number of fuzzy if-then rules formulated on the basis of process knowledge. Fuzzy if-then rules or fuzzy conditional statements are expressions of the form IF A THEN B, where A and B are labels of fuzzy sets, e.g. *Rule m*: IF $x_1 = A_{m1}$ and $x_2 = A_{m2}$ and $x_n = A_{mn}$ THEN $y = B_m$, where x_1, ..., x_n are the control variables (inputs), y is the action variable (output), $A_{i1},\ldots,A_{in}$ and B_i (i = 1, ..., m) are linguistic variables in the universe of discourse of x_i and y respectively.
- a **database** defining the membership functions of the fuzzy sets used in the fuzzy rules. Triangular, trapezoidal and bell-shaped (Gaussian) membership functions are commonly used.
- a **fuzzy inference engine** which performs the inference operations on the rules. The operators within the logic rules form the inference engine. Generally, logic rules use AND (maximum value) or OR (minimum value) as connecting operators.

- a **fuzzification interface** which transforms the crisp inputs into degrees of match with linguistic values;
- a **defuzzification interface** which transforms the fuzzy inference results into a crisp output. Centroid (centre of gravity or centre of area), center of sums and mean of maxima methods are commonly employed for defuzzification.

The rule base and the database are jointly referred to as the knowledge base. Two types of FIS are in use: (i) Mamdani-type and (ii) Sugeno type. Mamdani's FIS (used in GA tuned FIS in the present study) involves five steps: (i) fuzzification of input variables, (ii) application of fuzzy operators, (iii) implication from the antecedent to the consequent, (iv) aggregation of the consequents across the rules, and (v) defuzzification (Hayward and Davidson, 2003; Ross, 2004).

It is important to realize that the performance of an *FIS* is largely dependent upon the accuracy of the formulated knowledge base. No standard methods exist for transforming human knowledge or experience into the rule base and database of a fuzzy inference system. There is a need for effective methods for tuning the membership functions and rule base so as to minimize the output error or maximize the performance index.

The application of *GAs* for rule base development, membership function adjustment, and training fuzzy rule-based models to represent specific data has been intensively demonstrated in recent years (Herrera et al., 1995; Nandi and Pratihar, 2004). *GAs* can be used to fine tune the membership distributions of input and output variables and to simultaneously optimize the number of rules in the rule base. Since *GA* is also computationally demanding, the FIS tuning is generally done offline as shown in Fig. 8.44.

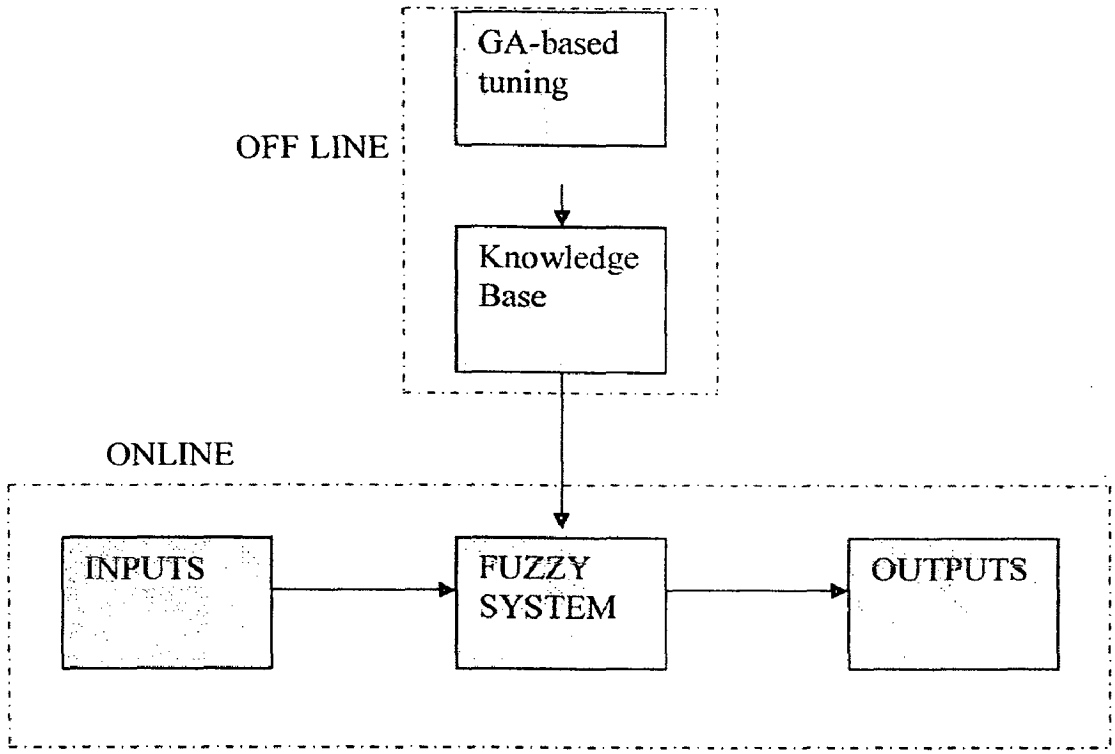

Fig. 8.44 Schematic diagram of a genetic fuzzy system

A limitation of using only expert knowledge is the inability to tune a fuzzy system to give precise outputs for several, possibly contradictory, input combinations. The use of neural network training techniques allows FIS to learn the intricacies inherent in empirical data. The ability to make use of both expert and empirical information greatly enhances the utility of a FIS. An emerging trend is *Adaptive-Network-based Fuzzy Inference System, (ANFIS)*, which can serve as a basis for constructing a set of fuzzy if-then rules with appropriate membership functions to generate the stipulated input-output pairs. ANFIS makes use of a hybrid learning rule to optimize the FIS parameters of a first order Sugeno system. ANFIS architecture for a first-order Sugeno system can be represented as in Fig. 8.45 (Jang, 1993; Hines, 1997).

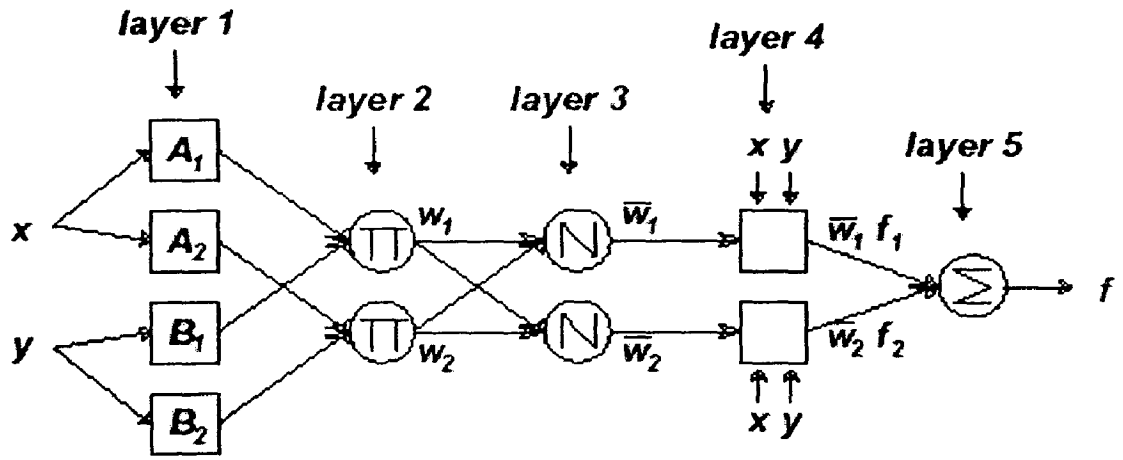

Fig. 8.45 ANFIS architecture of a two-input, two-rule first-order Sugeno model [Jang, 1993]

For simplicity, if we assume that FIS has two inputs x and y and one output z and the rule base consists of two fuzzy if-then rules of Takagi and Sugeno's type:

Rule1: *If* x *is* A_1 *and* y *is* B_1, *then* $f_1 = p_1 x + q_1 y + r_1$

Rule2: *If* x *is* A_2 *and* y *is* B_2, *then* $f_2 = p_2 x + q_2 y + r_2$

where the consequent parameters (p, q, r) of the rules contribute through a first order polynomial. The ANFIS architecture consists of five layers with the output of the node in each respective layer represented by O_i^l, where i is the ith node of layerl.

Layer1: Generate the membership grades

Every node in this layer is a square node with membership function $O_i^1 = \mu_{A_i}(x)$, where Ai is the linguistic label associated with this node function. For a Guassian membership function,

$$O_i^1 = \mu_{A_i}(x) = \exp\left[-\left(\frac{x - c_i}{a_i}\right)^2\right]$$

A universe of discourse (Table 8.100) for the control (input) and action (output/response) variables was decided based on the analysis of available experimental data on the selected performance characteristics (Chapter-VI, Tables 6.19, 6.25, 6.27).

Table 8.100 Universe of discourse of various FIS variables

	Variable	Universe of Discourse	
Control	PIR_a	35.80	38.83
	PICyl	26.75	37.73
	DIR	16.80	35.20
Action	MRPI	0.00	1.00

The control variables were fuzzified using four equally spaced bell-shaped (Gaussian) membership functions selected conventionally (Table 8.101a), while seven equally spaced Gaussian curves were utilized for fuzzification of the action variable (MRPI) for better visibility (Table 8.101b). Linguistic terms used for membership functions are low (L), medium (M), high (H) and very high (VH) for input variables and very low (VL), low (L), low small (LS), medium (M), high small (HS), high (H) and very high (VH) for output variable as given in Table 8.101.

Table 8.101

a) Linguistic variables for the input parameters

Control Variable	Membership Functions (Initial)			
	L	M	H	VH
PIR_a	35.80	36.81	37.82	38.83
PICyl	26.75	30.41	34.07	37.73
DIR	16.80	22.93	29.07	35.20

b) Linguistic variables for the output parameter

Response Variable	Membership Functions						
	VL	L	LS	M	HS	H	VH
MRPI (initial)	0.00	0.17	0.33	0.50	0.67	0.83	1.00

A fuzzy rule base comprising of a total of 64 rules was formulated based on experimental knowledge of the ECH process as given in Table 8.102. In the present problem since there are three input variables each with four membership functions hence total number of rules initially considered were 4^3 i.e. 64. Finally the fuzzy output of all the fuzzy rules for given input values was processed and converted back into a crisp value. For defuzzification, centroid method, being most popular, has been adopted in the present work. A program was written in MATLAB environment for FIS evaluation, which comprised of various steps such as fuzzification, rule strength calculation and defuzzification.

Table 8.102 Initial Rule Base of ECH FIS

S.No.	PIR_a	PICyl	DIR	MRPI
1.	L	L	L	L
2.	L	L	M	LS
3.	L	L	H	LS
4.	L	L	VH	M
5.	L	M	L	LS
6.	L	M	M	LS
7.	L	M	H	LS
8.	L	M	VH	M
9.	L	H	L	M
10.	L	H	M	M
11.	L	H	H	M
12.	L	H	VH	M
13.	L	VH	L	M
14.	L	VH	M	M
15.	L	VH	H	M
16.	L	VH	VH	HS
17.	M	L	L	LS
18.	M	L	M	LS
19.	M	L	H	LS
20.	M	L	VH	M
21.	M	M	L	M
22.	M	M	M	M
23.	M	M	H	M
24.	M	M	VH	M
25.	M	H	L	M
26.	M	H	M	HS
27.	M	H	H	HS
28.	M	H	VH	HS
29.	M	VH	L	HS
30.	M	VH	M	HS

strings of tuning variables are processed with GA operators like reproduction, crossover and mutation etc. Iterations are performed until the stopping criterion is met.

The actual implementation has been done by systematically following the above mentioned steps: parameter selection, fuzzy inference and GA application as shown in flow chart (Fig. 8.47). The optimal GA-tuned membership functions of FIS are given in Fig. 8.48. These membership distributions truly represent the respective variable's behavior and hence, considered for further FIS evaluation and prediction of output.

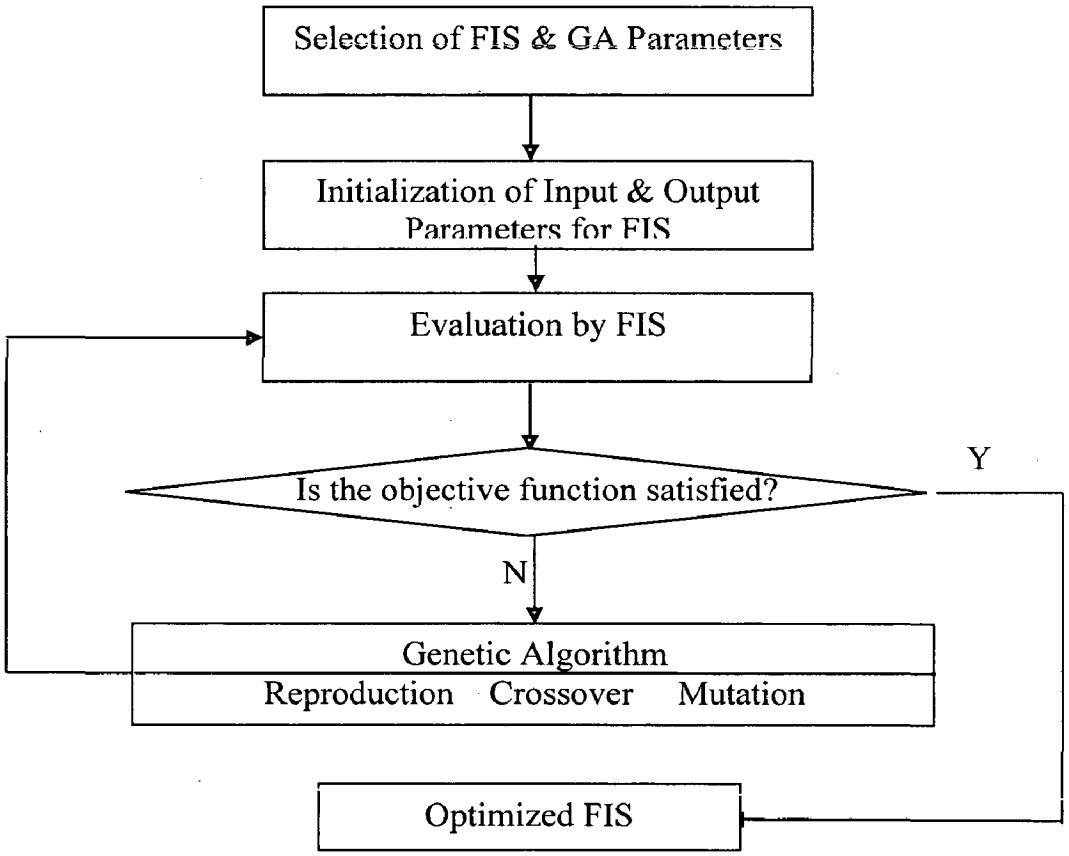

Fig. 8.47 Flow chart for optimization of FIS using GA

Rulebase tuning

For rule-base optimization, a binary string of 64 bits (equal to the number of all possible rules) is generated at random initially and the decision on inclusion of a rule in FIS evaluation depends on whether the bit corresponding to that particular rule is one or zero. Every rule has a matching bit in the binary and a rule is included if the bit is one and discarded if the bit is zero. Out of 64 fuzzy rules only 17 rules were considered after tuning, the rest 47 rules were discarded as given in Table 8.103.

Fitness evaluation

For GA-based optimization, twenty seven sets of input parameter values (obtained from experiments) were given to FIS and outputs from FIS were compared with the actual outputs from the experiments. The average of the absolute error for these twenty seven cases was taken as the fitness function for genetic algorithm. GA was used with different sets of its parameters but there was no significant improvement in the performance of the optimized FIS and hence parameter set of GA was accepted where crossover and mutation probabilities were 0.95 and 0.05 respectively and the population size was 100 strings.

The results of the GA-tuned "Fuzzy Taguchi Multi-Performance Modeling" of ECH for 'PIRa-PICyl-DIR' are given in Table 8.104.

8.3.2.3 ANFIS Modeling of ECH

A three-input-one-output ANFIS modeling of ECH for the present case study was done using a Sugeno System Version 2. The optimized membership functions for the control variables (PIRa, PICyl, DIR) and the output (MRPI) for the 64 rules are given in Fig. 8.49. ANFIS Multi-Performance Modeling results for ECH are also presented in the Table 8.104.

The control surfaces generated by GA tuned FIS and ANFIS for the combined influence of two-control parameters combinations on the action parameter are illustrated in Fig. 8.50 and 8.51 respectively.

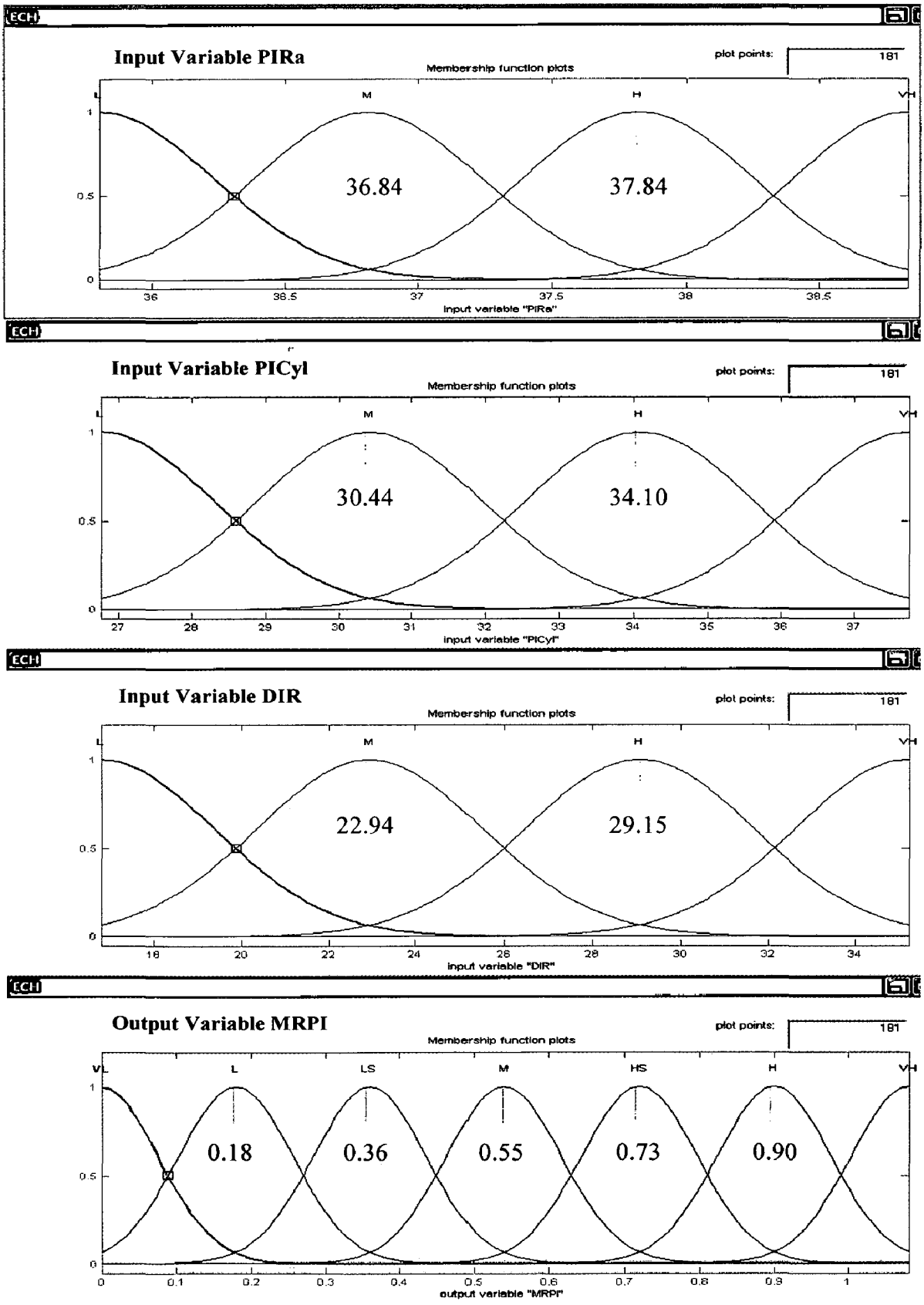

Fig. 8.48 GA tuned membership functions of FIS

Table 8.103 GA optimized rule base of ECH FIS

Sr.No.	PIR_a	PICyl	DIR	MRPI
1.	L	H	M	M
2.	M	H	M	HS
3.	M	VH	M	HS
4.	H	H	M	HS
5.	M	VH	M	HS
6.	M	M	M	M
7.	M	VH	H	H
8.	H	H	H	H
9.	H	VH	H	H
10.	M	L	M	LS
11.	VH	H	VH	VH
12.	M	M	L	M
13.	H	H	VH	H
14.	H	M	H	HS
15.	H	VH	VH	VH
16.	M	H	H	HS
17.	VH	VH	VH	VH

Table 8.104 FIS modeling results (PIR_a- PICyl-DIR)

Trial No.	PIR_a (dB)	PICyl (dB)	DIR (dB)	MRPI(GA tuned FIS)	MRPI(ANFIS)
1	35.80	32.11	21.80	0.564	0.500
2	36.39	34.63	23.16	0.664	0.487
3	36.65	34.57	20.89	0.691	0.605
4	36.70	32.28	23.57	0.644	0.610
5	36.64	32.92	24.77	0.668	0.620
6	37.34	37.31	21.32	0.722	0.695
7	38.24	35.42	22.85	0.734	0.700
8	37.16	33.75	21.46	0.692	0.610
9	37.88	26.75	25.13	0.534	0.485
10	36.00	33.05	21.92	0.586	0.490
11	37.21	33.29	23.67	0.702	0.600
12	36.57	34.30	22.42	0.682	0.595
13	36.77	30.49	21.66	0.549	0.500
14	36.72	36.27	26.69	0.792	0.725
15	37.54	33.86	28.73	0.820	0.745
16	38.09	35.05	27.97	0.858	0.750
17	38.04	36.37	30.60	0.898	0.850
18	36.91	27.11	21.82	0.897	0.405
19	38.39	32.80	32.27	0.851	0.900
20	36.89	28.23	16.80	0.514	0.455
21	38.02	34.54	35.20	0.892	0.800
22	37.86	29.69	29.83	0.701	0.620
23	37.37	37.21	33.32	0.901	0.925
24	36.43	30.65	30.10	0.658	0.650
25	37.40	33.85	26.60	0.796	0.755
26	38.21	36.05	33.51	0.927	0.935
27	38.83	37.73	35.13	0.998	1.000

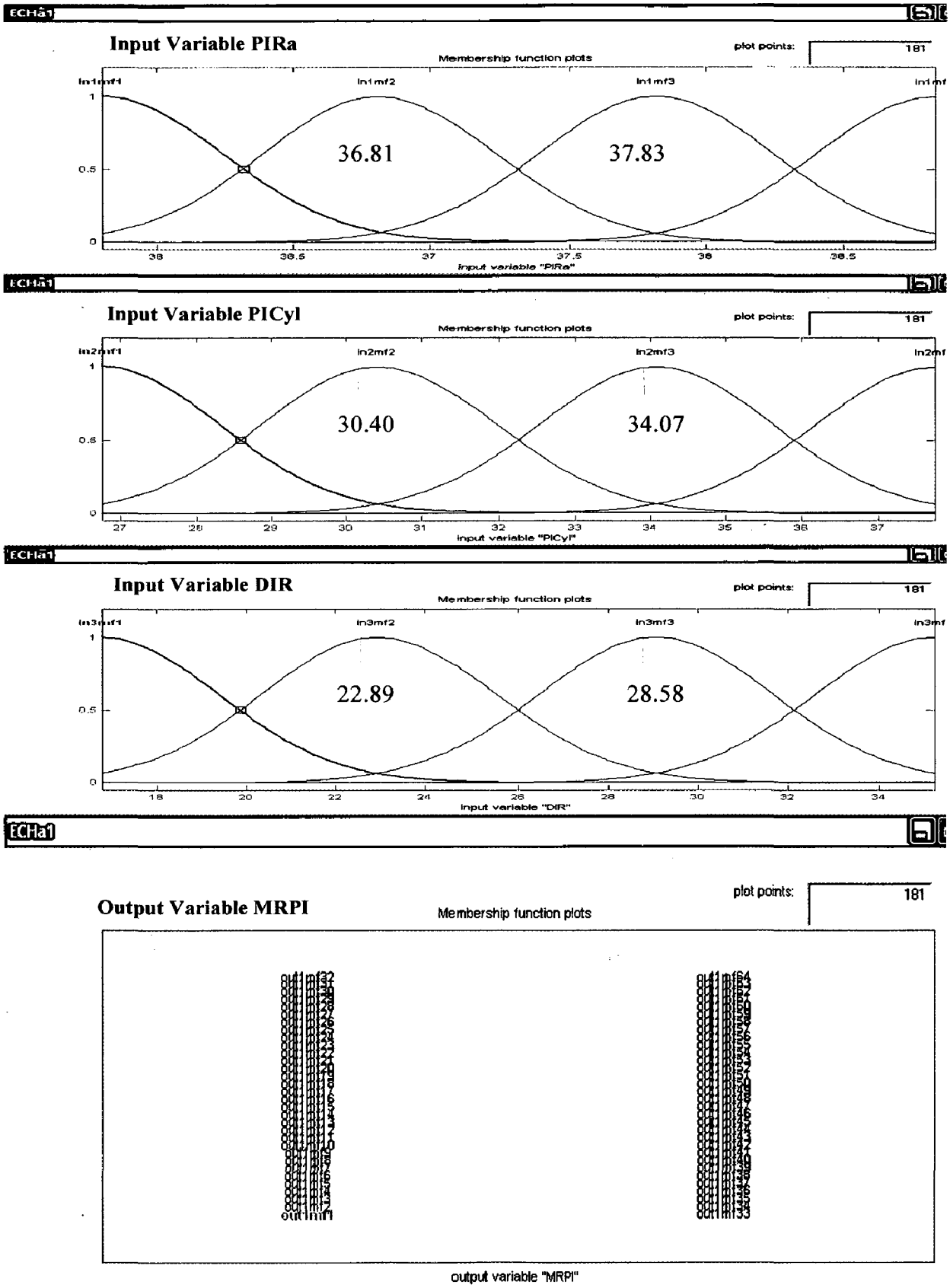

Fig. 8.49 ANFIS membership function plots

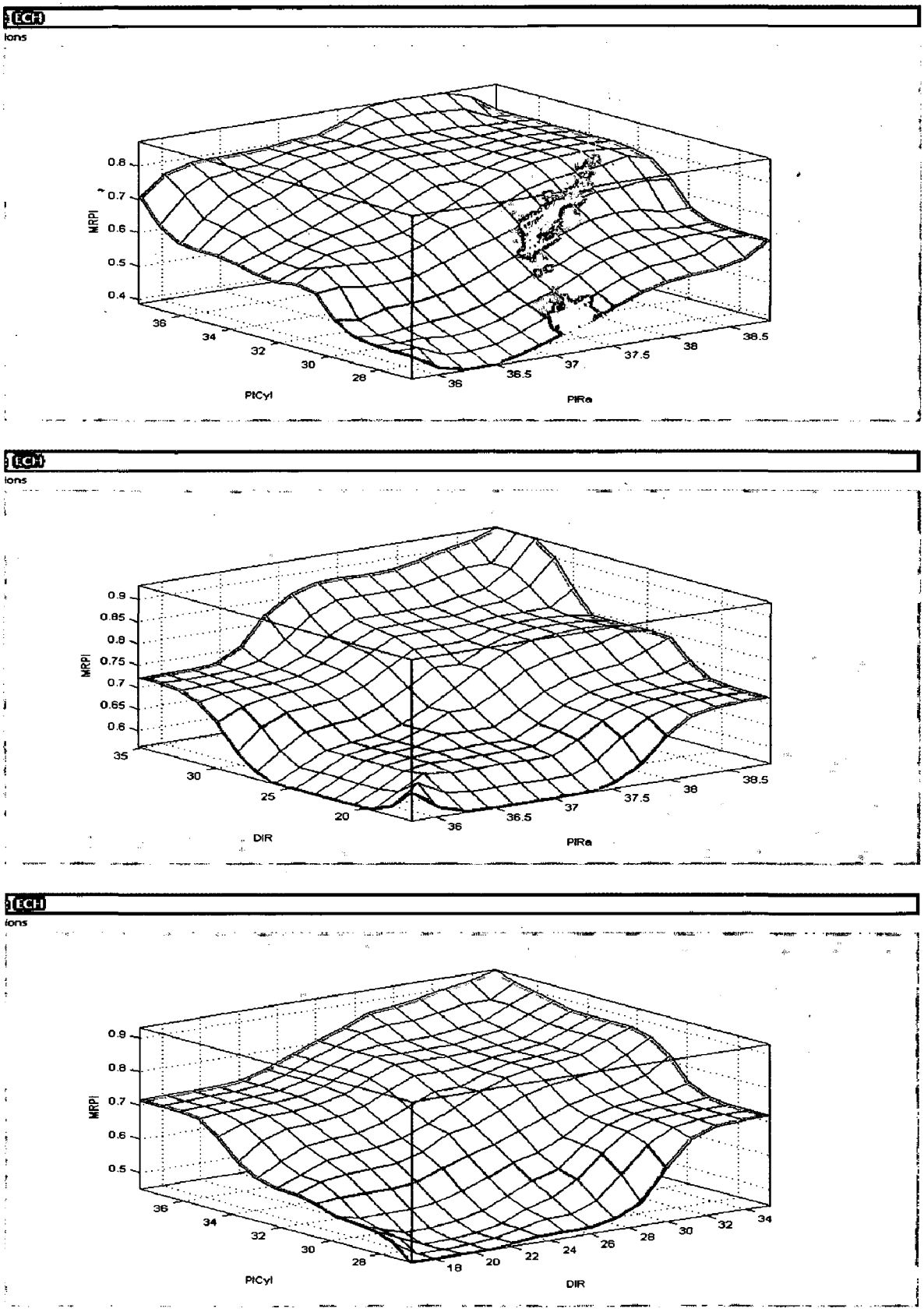

Fig. 8.50 GA tuned FIS control surface plots

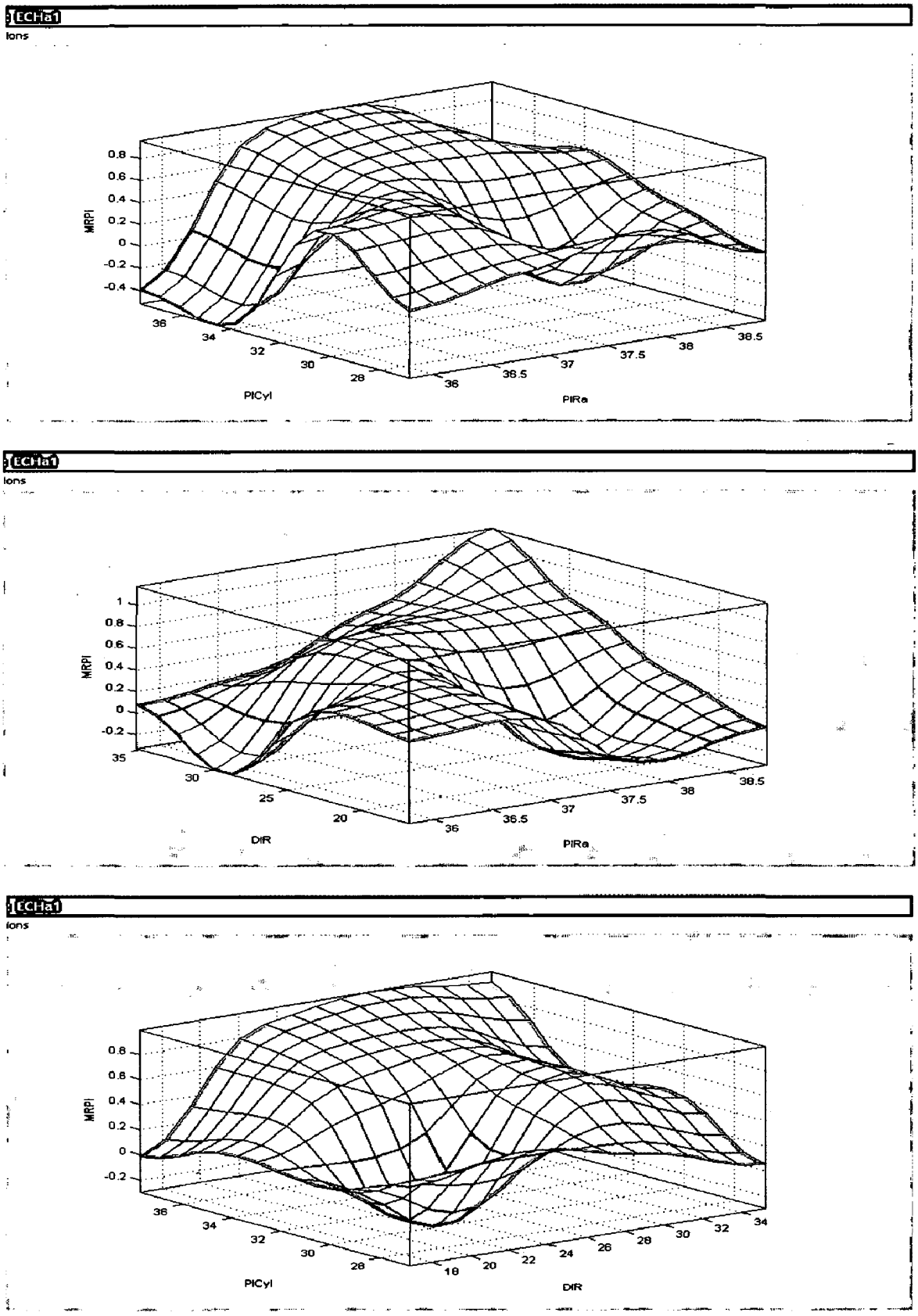

Fig. 8.51 Control surfaces generated by ANFIS

8.3.2.4 Analysis of ECH FIS Results

The GA-tuned FIS and ANFIS multi-performance modeling results for ECH MRPI (Table 8.104) were analyzed using the standard procedure for analysis of means (ANOM), analysis of variances (ANOVA) and F ratio in order to

1. identify the significant parameters and quantify their effects on multi response performance index,
2. select the optimal levels of the process parameters for MRPI,
3. estimate optimal value MRPI obtainable within the experimental region.

The ANOM results are given in Tables 8.105 and 8.106 respectively for GA tuned FIS MRPI and ANFIS MRPI. The response plots are shown in Fig. 8.52. The pooled ANOVA results are given in Tables 8.107 and 8.108. The ANOVA results indicate that the current intensity (A), electrolyte concentration (EC), stick-out pressure (SOP), and stick grit-size (G) and all the three interactive terms, namely the current intensity-electrolyte concentration (C-EC), current intensity-speed ratio (C-SR) and electrolyte concentration-speed ratio (EC-SR) are significant for both the GA tuned FIS MRPI and ANFIS MRPI. The independent effect of speed ratio is also significant for the GA tuned FIS MRPI. The respective interaction plots are illustrated in Fig. 8.53.

An examination of the response and interaction plots for the significant parameters and interactions indicates that the MRPI with both the approaches is highest at the 3rd levels of the current intensity (C_3), electrolyte concentration (EC_3), speed ratio (SR_3) and stick-out pressure (SOP_3) while the stickgrit size level 2 (G2) provides the maximum MRPI. The insignificant parameters the electrolyte flow rate (F) and electrolyte inlet temperature (T) can be selected as appropriate. The predicted optimal value of MRPI is quite high and similar with both the approaches. The predicted optimal MRPI using GA tuned FIS and ANFIS for ECH multi-performance optimization are 1.000 and 0.991, respectively.

Table 8.105 Multi-Response Performance Index: PIR_a-PICyl-DIR
(GA tuned FIS)

Process Input Parameter	Multi-Response Performance Index (MRPI)			
	L1	L2	L3	Max-Min
C	0.657	0.754	0.804	0.147
EC	0.683	0.717	0.815	0.132
SR	0.698	0.751	0.766	0.068
F	0.725	0.748	0.742	0.006
T	0.746	0.734	0.734	0.012
SOP	0.651	0.768	0.795	0.144
G	0.741	0.778	0.697	0.081
C-EC	0.757	0.759	0.698	0.061
C-SR	0.754	0.741	0.721	0.033
EC-SR	0.751	0.704	0.761	0.057
			Mean MRPI= 0.738	

L1, L2 and L3 represent average values of MRPI of corresponding parameters at levels 1, 2 and 3 respectively.
C: Current Intensity, EC: Electrolyte Concentration, SR: Speed Ratio, F: Electrolyte Flow Rate, T: Electrolyte Inlet Temperature, SOP: Stick-out Pressure, G: Grit Size.

Table 8.106 Multi-Response Performance Index: PIR_a-PICyl-DIR
(ANFIS)

Process Input Parameter	Multi-Response Performance Index (MRPI)			
	L1	L2	L3	Max-Min
C	0.590	0.629	0.782	0.192
EC	0.604	0.677	0.721	0.118
SR	0.647	0.690	0.664	0.042
F	0.661	0.683	0.657	0.026
T	0.643	0.682	0.676	0.039
SOP	0.601	0.651	0.749	0.148
G	0.673	0.739	0.589	0.150
C-EC	0.669	0.688	0.644	0.044
C-SR	0.684	0.647	0.671	0.037
EC-SR	0.690	0.611	0.700	0.089
			Mean MRPI= 0.667	

L1, L2 and L3 represent average values of MRPI of corresponding parameters at levels 1, 2 and 3 respectively.
C: Current Intensity, EC: Electrolyte Concentration, SR: Speed Ratio, F: Electrolyte Flow Rate, T: Electrolyte Inlet Temperature, SOP: Stick-out Pressure, G: Grit Size.

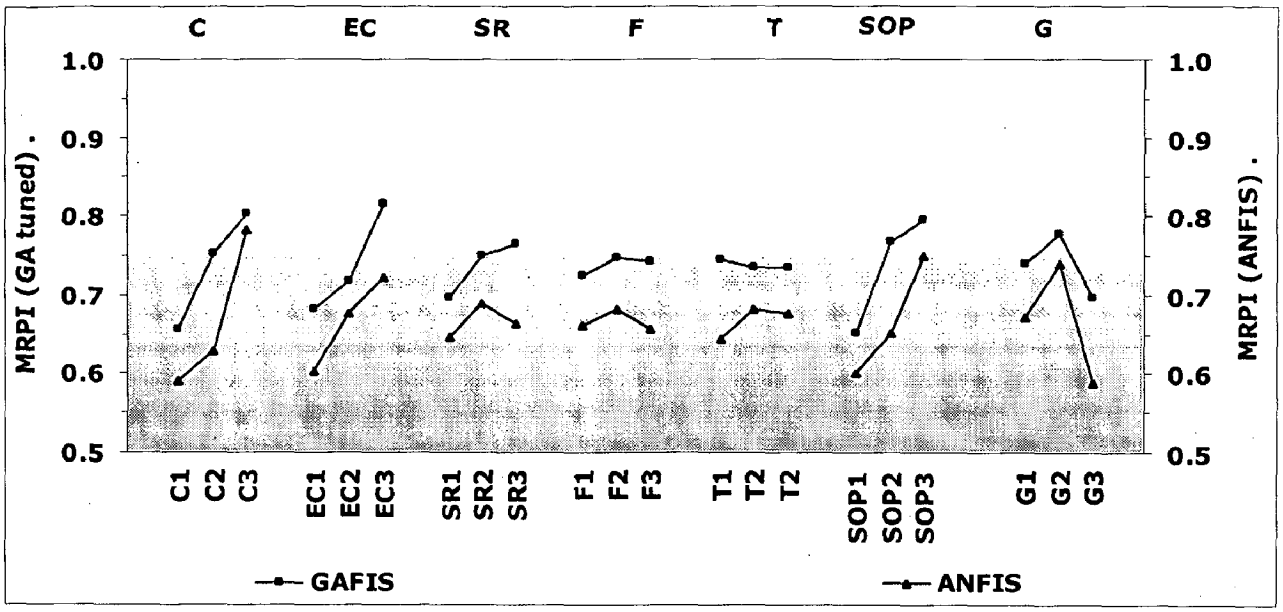

Fig. 8.52 Response plot (GA tuned FIS and ANFIS: PIR_a-PICyl-DIR)

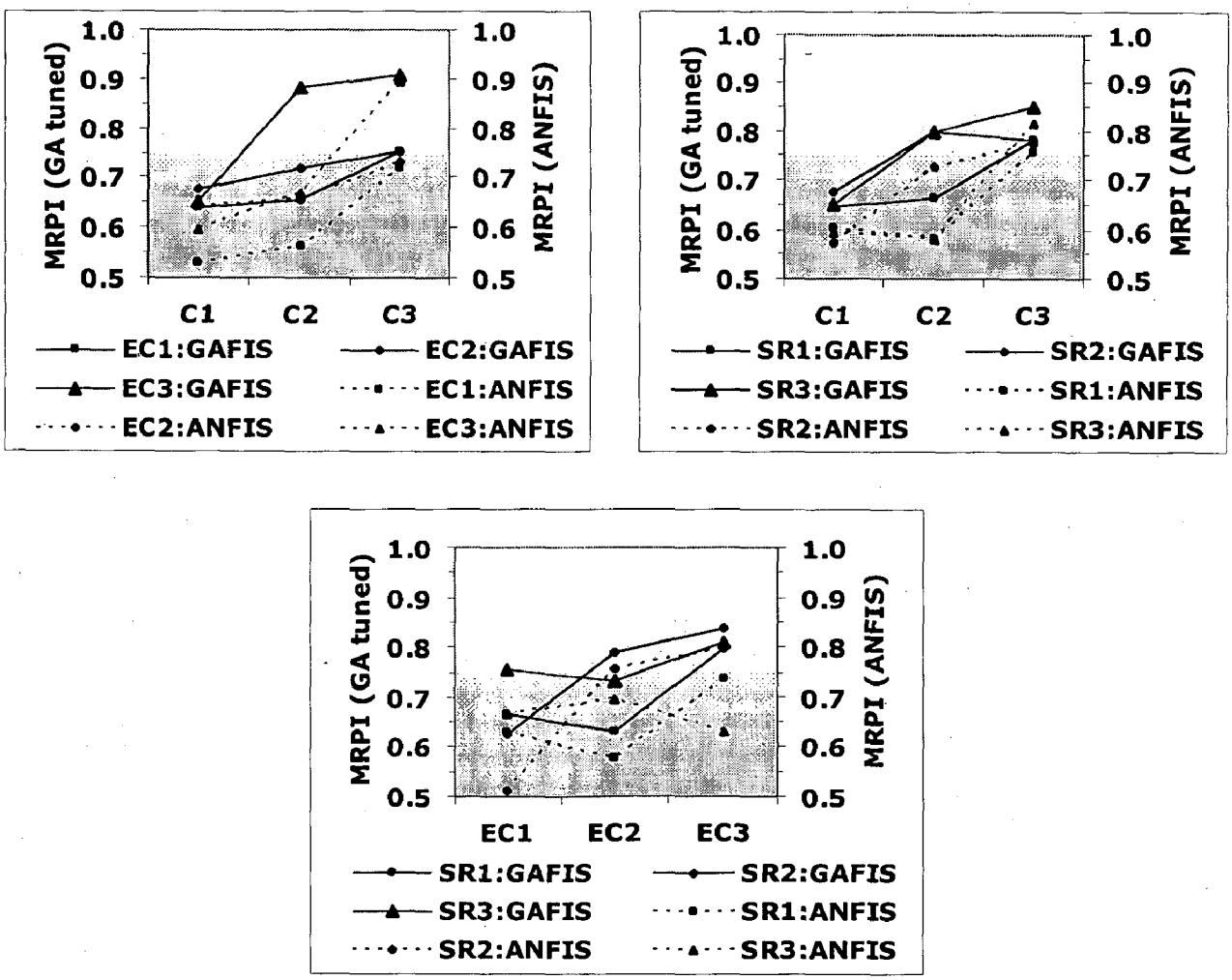

Fig. 8.53 Interaction plots (GA tuned FIS and ANFIS: PIR_a-PICyl-DIR)

Table 8.107 Pooled ANOVA MRPI: PIR_a-PICyl-DIR
(GA tuned FIS)

Source	SS	DF	MS	F ratio	% Contribution
C	0.101	2	0.050	57.83*	21.45
EC	0.084	2	0.042	48.46*	17.91
SR	0.023	2	0.011	13.13*	4.58
F	0.003	(2)	Pooled	-	-
T	0.001	(2)	Pooled	-	-
SOP	0.105	2	0.053	60.37*	22.41
G	0.030	2	0.015	16.99*	6.04
C-EC	0.048	4	0.012	13.82*	9.68
C-SR	0.024	4	0.006	6.81*	4.38
EC-SR	0.043	4	0.011	12.45*	8.64
Model	0.458	22	0.021	23.90*	95.09
e(pooled)	0.003	4	0.001		4.91
Total	0.462	26			100.00

The Model F ratio of 23.90 implies that Model is significant at 99.5% confidence level.
* Significant at 95% confidence level.
SS: Sum of Square, DF: Degree of Freedom, MS: Mean Square, C: Current Intensity, EC: Electrolyte Concentration, SR: Speed Ratio, F: Electrolyte Flow Rate, T: Electrolyte Inlet Temperature, SOP: Stick-out Pressure, G: Grit Size.

Table 8.108 Pooled ANOVA MRPI: PIR_a-PICyl-DIR
(ANFIS)

Source	SS	DF	MS	F ratio	% Contribution
C	0.186	2	0.093	28.61*	26.67
EC	0.063	2	0.032	9.78*	8.48
SR	0.008	(2)	Pooled	-	-
F	0.003	(2)	Pooled	-	-
T	0.008	(2)	Pooled	-	-
SOP	0.103	2	0.051	15.82*	14.31
G	0.101	2	0.051	15.60*	14.11
C-EC	0.035	4	0.009	2.71*	3.29
C-SR	0.041	4	0.010	3.12*	4.10
EC-SR	0.124	4	0.031	9.53*	16.48
Model	0.652	20	0.033	10.05*	87.44
e(pooled)	0.019	6	0.003		12.56
Total	0.672	26			100.00

The Model F ratio of 10.05 implies that Model is significant at 99.5% confidence level.
* Significant at 95% confidence level.
SS: Sum of Square, DF: Degree of Freedom, MS: Mean Square, C: Current Intensity, EC: Electrolyte Concentration, SR: Speed Ratio, F: Electrolyte Flow Rate, T: Electrolyte Inlet Temperature, SOP: Stick-out Pressure, G: Grit Size.

8.3.2.5 Confirmation Experiments

Once the optimal parametric setting is selected, the last step is to verify the improvements of the process performance characteristics using the optimal level of the process parameters. Table 8.109 gives the actual experimental results. It can be seen that the PIRa improved from 61.67% to 87.47%, PICyl improved from 40.40% to 77.09% and DIR increased from 13.47(μm/min) to 57.11(μm/min). The actual MRPI results are also quite similar and in good close agreement with those predicted using GA tuned FIS and ANFIS.

Table 8.109 Confirmation Experiment

	Initial condition		Optimal condition		Experimental	
	GA-FIS	ANFIS	Prediction GA-FIS	Prediction ANFIS	GA-FIS	ANFIS
Parameter	$C_1EC_1SR_1F_1T_1SOP_1G_1$		$C_3EC_3SR_3F_1T_1SOP_3G_2$		$C_3EC_3SR_3F_1T_1SOP_3G_2$	
PIR_a (%)	61.67				87.47	
PICyl (%)	40.40				77.09	
DIR (μm / min)	13.47				57.11	
MRPI	0.564	0.500	1.000	0.991	0.998	1.000
% improvement in MRPI					76.95	100

8.4 A COMPARISON OF "UTILITY BASED TAGUCHI APPROACH", "TAGUCHI-NN-GA MULTI-PERFORMANCE OPTIMIZATION CONTROL STRATEGY" AND "TAGUCHI-FUZZY INFERENCE APPLICATION" APPLIED TO ECH

The multi-performance optimization of electro-chemical honing process was carried out using three different approaches utilized effectively in the recent past for multi-performance modeling and optimization of the manufacturing processes by the researchers. The 'Utility based Taguchi Approach' and 'Taguchi-NN-GA Multi-performance Optimization Control Strategy' methodologies have their own distinguishing features as well as the limitations. 'Utility based Taguchi approach' is based on the experimental analysis and is easier to implement. This approach models the multiple performance characteristics exclusively considering the desired factorial interactions in obtaining the optimal values of process performance characteristics. It is based on the preferences (weights) assigned to the various performance characteristics and thus provides a flexibility to the user. However, it is also sensitive to the subjective preferences assigned to various responses and primarily is an off-line optimization technique. 'Taguchi-NN-GA Multi-Performance Optimization Control Strategy', on the other hand, is an artificial intelligence based approach and can be utilized as an on-line multi-performance optimization and process control. It is flexible enough to utilize different approaches best suiting the current situation. Multi-response optimization can be done by using desirability function without any subjective preference as well as by using a modified desirability function similar to Utility based Taguchi method to provide user flexibility. Even a set of multiple Pareto-optimal solutions using non-dominated sorting genetic algorithms can be obtained suitable for changing process conditions. However, this method does not give any exclusive treatment to factorial interactions and models the input-output relationships with factorial combinations. The optimal results are based on the modeling accuracy of neural network utilized as well as the accuracy of prediction and consistency of convergence of GA. This method is also computationally demanding.

Similarly, being an artificial intelligence based technique; the 'Fuzzy Inference Application' can serve as a reliable tool for process modeling and control. The fuzzy inference system has been much exploited by Japanese industries for process modeling and control. However, the efficiency of an FIS is much dependent on data base (membership function) and rule base formulated on the basis of the process knowledge. To improve the performance of an FIS, recent use of genetic algorithms and neural network adaptation is gaining attention. If properly tuned, the FIS can become a reliable tool for the process modeling and optimization control. In the present application both the GA tuned FIS and ANFIS applied to ECH process for a case provided results similar to that obtained with Taguchi-RBFNN-GA approach.

As the multi-performance modeling and optimization of ECH using 'Utility based Taguchi Approach' and the Taguchi-NN-GA Optimization Control Strategy with modified desirability approaches were performed with the same preferences assigned to multiple responses, these cases have been considered for an objective comparison. The optimal results have been already discussed and validated. Fig. 8.54 illustrates the optimal results with two approaches for different ECH multi-performance optimization models. It is seen that both the approaches provide quite similar optimal values of performance characteristics for various models. The results for the most dominant machining criterion i.e. PIR_a and also for DIR are very closely resembling in both the approaches. Another point to mention is that that the 'Utility based Taguchi Approach' predicted a slightly higher optimal value for part macro-geometrical characteristics i.e. PIOR and PICyl. It is to mention that these performance characteristics were found dominated by the interactive terms of the prospective factors in Chapter-VI. The predicted optimal results are sensitive to the way the interactions are treated.

The experimental results at the optimal parametric conditions predicted using the three approaches are quite close as given in Table 8.110 and Fig. 8.55.

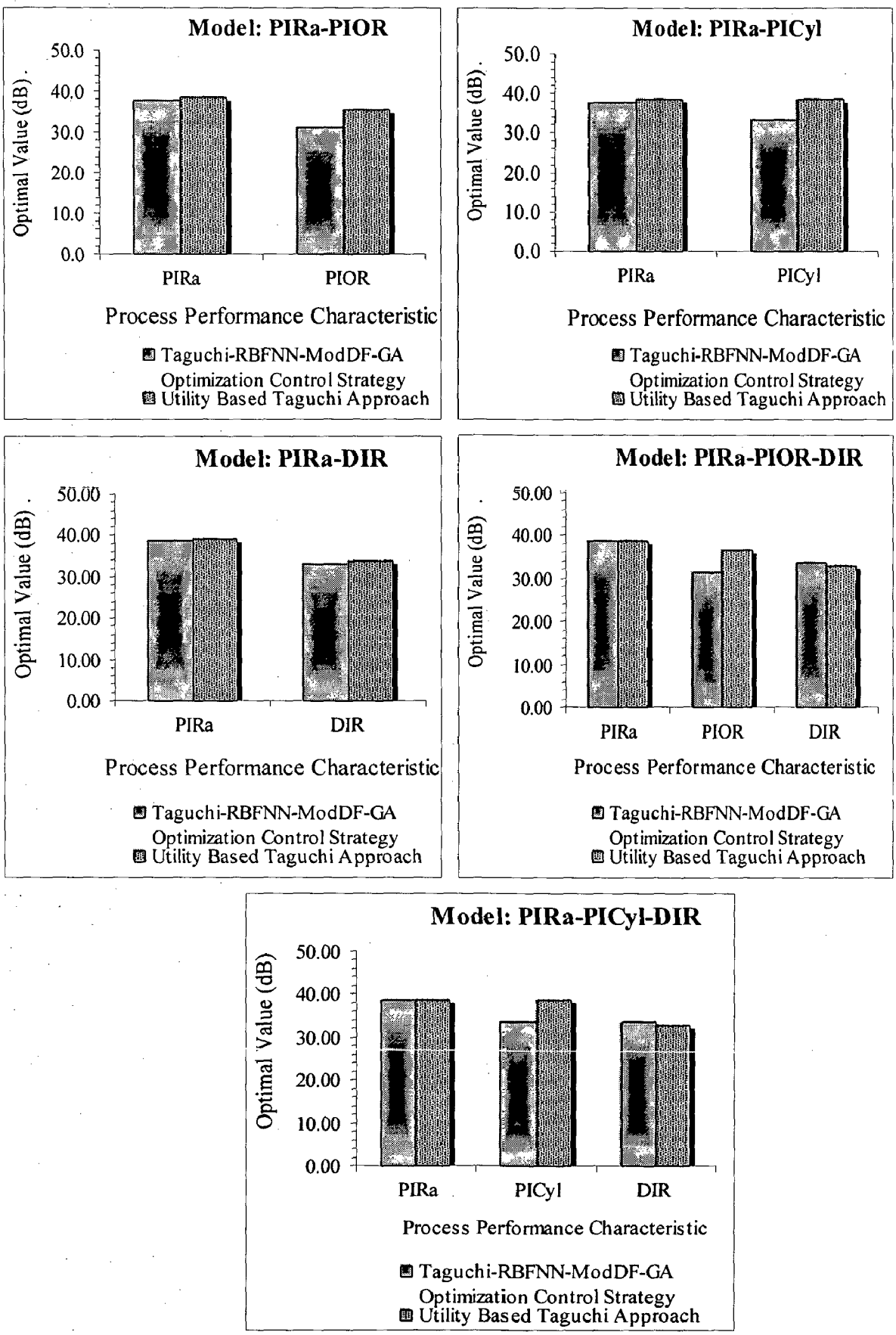

Fig. 8.54 Multi-performance predicted optimal results based on two approaches

Table 8.110 Experimental results ("Utility based Taguchi Approach", "Taguchi-RBF NN-DF-GA Multi-Performance Optimization Control Strategy" and "Fuzzy Inference Application" to ECH)

Approach	Optimal parametric condition	Experimental results (dB)				Difference (%)			
		PIR_a	PIOR	PICyl	DIR	PIR_a	PIOR	PICyl	DIR
Utility based Taguchi approach	$C_3EC_3SR_2\ F_1T_3SOP_3G_2$	38.62	36.02	38.39	34.66				
Taguchi-NN-DF-GA approach	$C_3EC_3SR_3F_1T_3SOP_3G_2$	38.83	35.44	37.73	35.13	0.54	1.61	1.71	1.35
Fuzzy Inference application	$C_3EC_3SR_3F_1T_3SOP_3G_2$	38.83		37.73	35.13	0.54		1.71	1.35

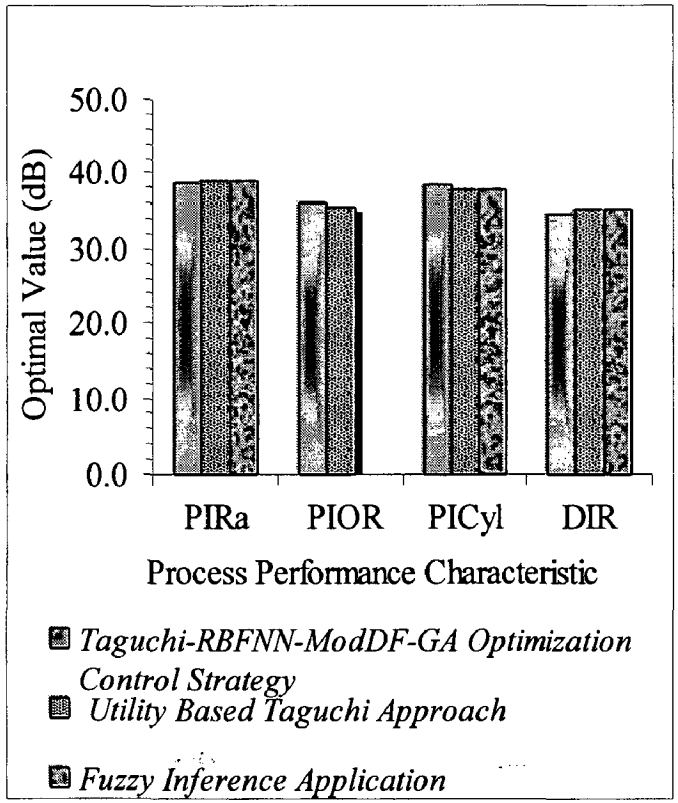

Fig. 8.55 Multi-performance experimental optimal results based on three approaches

Chapter-IX
CONCLUSIONS, GUIDELINES AND SCOPE OF FUTURE RESEARCH

Due to the lack of information available in literature on electro-chemical honing process and non-availability of the ECH equipment it was necessary to indigenously develop a setup and perform experimental studies in order to raise the process knowledge base. Process modeling and multi-response optimization was vital for utilizing the full potential of ECH to meet the challenges of stringent requirements on surface quality, tolerances and production rates demanded by the manufacturing community in globally competitive scenario.

Based on the results of the studies as embodied in the previous chapters, the important findings and main conclusions of this research work are summarized in the present chapter. This chapter also highlights the scope of future research. A brief guidelines formulated on the basis of results from the present research work are also given in this chapter for the benefit of the process user.

9.1 CONCLUSIONS

The following conclusions can be drawn from the results of the present research on the ECH conducted within the selected range of process parameters.

9.1.1 Development of Electro-Chemical Honing Setup

1. An ECH setup with several unique features that provides a precise control over a wide range of process input parameters has been developed indigenously.

9.1.2 Time dependent behaviour of ECH

2. Processing time (PT) in ECH significantly influences the percent improvements in R_a (PIR_a), R_{max} (PIR_{max}), and out-of-roundness (PIOR).

3. Effect of processing time is also significant for percent improvement in cylindricity (PICyl), at a slightly lower significance level.

4. Patterns of variation of PIR_a, PIR_{max}, PIOR and PICyl with PT follow a quadratic trend. Major improvement occurs in the first few minutes of ECH operation and rate of successive improvements diminish.

5. The processing time main effect in case of improvement in axis-straightness (AS) is not significant. AS improves very rapidly and further improvements almost flatten.

6. Diametral increase rate (DIR) remains almost constant with the processing time.

7. The following empirical models for PIR_a, PIR_{max}, PIOR, PICyl and DIR as function of processing time (PT) have been developed that can be utilized by the process user for deciding a suitable time required for a desired performance:

- Percent improvement in surface roughness value R_a

  $PIR_a = 2.2668 + 37.291(PT) - 3.8684(PT)^2$

- Percent improvement in surface roughness value R_{max}

  $PIR_{max} = 0.8344 + 37.571(PT) - 3.9653\ (PT)^2$

- Percent improvement in out-of-roundness

  $PIOR = 3.557 + 25.715\ (PT) - 2.6515\ (PT)^2$

- Percent improvement in cylindricity

  $PICyl = 5.1647 + 33.473\ (PT) - 3.7457\ (PT)^2$

- Diametral increase rate

  $DIR = 39.988 - 3.2084\ (PT)$

8. Significant results in PIR_a, PIR_{max}, PIOR and PICyl can be achieved within a 5 min processing time.

9.1.3 Material Removal Mechanism and Effect of Key Process Parameters on ECH Performance

9. Current intensity, electrolyte concentration, speed ratio, stick-out-pressure and stick grit-size are the major players influencing ECH performance.

10. Electrolyte flow rate is found to be less influential in contrast to that seen in ECM due to the improved electrolytic condition in the inter-electrode gap because of the dual electrolyte supply mode employed in the developed setup and also due to the cleansing action of the honing sticks.

11. The process is highly interactive in nature. A good coordination of the electro-chemical dissolution and selective mechanical abrading is required for better results in ECH performance.

12. The electrolyte has tremendous bearing in electro-chemical honing process. The selection of electrolyte composition and concentration is, therefore, crucial for the process performance. The electrolyte with composition ¾ part NaCl + ¼ part $NaNO_3$ and concentration 200g/L is found better in the present study.

13. A unique behaviour of ECH is the simultaneous improvement in all different process performance characteristics with the increased current intensity.

14. The phenomena of increased differential dissolution, viscous layer theory, anodic smoothing, highly reactive chemical attack (electrolyte dependent) and upto certain extent the conventional honing are some mechanisms operating simultaneously for the impressive behaviour of ECH process.

15. Proper grit-size selection is crucial in the process. In contrast to the conventional machining processes, the coarse grit-sizes due to their effective scrubbing action in ECH provide increased DIR and improved process micro- as well as macro-geometrical performance characteristics simultaneously.

16. For macro-geometrical error correction in ECH, mechanical parameters and interactions assume dominating role with a less influential independent effects of electrolytic parameters.

17. Better macro-geometrical results require suitable speed ratio, stick-out pressure and abrasive grit size owing to their wide-spaced feature.

18. ECH is capable of rectifying considerable initial form deviations in roundness and cylindricity (ISO Tolerance Grade 11) and can finish parts with much improved out-of-roundness and cylindricity tolerance (within the range ISO Tolerance Grade 7/8 and 4/7 respectively).

19. MVRA models developed for PIR_a and PIR_{max} can provide the process user flexibility with the flexibility in deciding potential applications of ECH:

- **Percent improvement in surface roughness value R_a:**

$$PIR_a = 53.87853 + 0.04784\ C + 0.08266\ EC + 0.06794\ T + 0.26089\ SOP - 0.00800\ G$$

- **Percent improvement in surface roughness value R_{max}:**

$$PIR_{max} = 37.81053 + 0.06134\ C + 0.09306\ EC + 0.24292\ T + 0.37639\ SOP - 0.01515\ G$$

20. Optimal results for different performance characteristics are reported and validated through confirmation experiments. The optimal settings of the process input parameters for the various process performance characteristics are:

- **Percent improvements in surface roughness value R_a**

▪ Current intensity (ADC)	:	180
▪ Electrolyte concentration (g/L)	:	200
▪ Rotary to reciprocating speed ratio	:	50
▪ Electrolyte flow rate (lpm)	:	20
▪ Electrolyte inlet temperature (°C)	:	50
▪ Stick-out pressure (kPa)	:	30
▪ Stick grit size	:	600

- **Percent improvements in surface roughness value R_{max}**

  - Current intensity (ADC) : 180
  - Electrolyte concentration (g/L) : 200
  - Rotary to reciprocating speed ratio : 150
  - Electrolyte flow rate (lpm) : 20
  - Electrolyte inlet temperature (°C) : 50
  - Stick-out pressure (kPa) : 30
  - Stick grit size : 600

- **Percent improvements in out-of-roundness and cylindricity**

  - Current intensity (ADC) : 180
  - Electrolyte concentration (g/L) : 200
  - Rotary to reciprocating speed ratio : 150
  - Electrolyte flow rate (lpm) : 20
  - Electrolyte inlet temperature (°C) : 30
  - Stick-out pressure (kPa) : 30
  - Stick grit size : 600

- **Diametral increase rate**

  - Current intensity (ADC) : 180
  - Electrolyte concentration (g/L) : 200
  - Rotary to reciprocating speed ratio : 250
  - Electrolyte flow rate (lpm) : 20
  - Electrolyte inlet temperature (°C) : 30
  - Stick-out pressure (kPa) : 30
  - Stick grit size : 360

9.1.4 Work Surface Characterization Aspects

21. ECH can provide a fine-finished surface with a very narrow spread of surface roughness value.

22. An ideal near-zero surface profile can be produced by ECH.

23. A nano-finished uniform plateau-honed work surface having much better characteristic parameters coupled with very small proportion of profile susceptible to initial rapid wear and a crosshatch lay pattern can be obtained by ECH. The ECHed parts can therefore have excellent bearing and lubricant retaining surface and hence, unexcelled wear and tribological performance.

24. Stick grit-size plays a dynamic role in determining quality of ECHed surface.

25. Proper coordination of electrolytic dissolution and mechanical scrubbing is necessary for obtaining better surface characteristics.

9.1.5 Work Surface Integrity Aspects

26. Process, if properly operated, can have no significant microstructural changes.

27. Effects similar to 'gentle electro-chemical machining followed by shot peening with glass beads' on the surface compressive residual stresses and sub-surface microhardness can be realized in ECH with higher speed ratio and stick-out pressure. The higher speed ratio and stick-out pressure in the present study provided increased surface microhardness and compressive residual stresses. Thus, ECHed components can have unexcelled wear and fatigue endurance properties.

28. ECH can become an ideal choice for improving the surface integrity of critical components resulting in increased service life and better in-service performance.

9.1.6 Multi-Performance Modeling and Optimization of ECH Process

29. Several cases of ECH with multiple performance parameters have been effectively modeled and optimized using both the off-line and AI based three most commonly used recent approaches. Results were validated with actual experiments.

30. Five cases of multiple ECH process performance characteristics were modeled and optimized using the Utility based Taguchi approach. The optimal settings of the process input parameters for simultaneous optimization of process productivity (DIR), surface micro-geometrical aspect (PIR_a) and part macro-geometrical aspect (PIOR as well as PICyl) are:

- Current intensity (ADC) : 180
- Electrolyte concentration (g/L) : 200
- Rotary to reciprocating speed ratio : 150
- Electrolyte flow rate (lpm) : 10
- Electrolyte inlet temperature (°C) : 50
- Stick-out pressure (kPa) : 30
- Stick grit size : 600

31. The combination of Taguchi loss function, NN and GA has been demonstrated to provide an effective platform for an on-line multi-performance modeling, optimization and control of such as ECH and similar complex manufacturing processes involving several correlated processes variables. Radial basis function neural network for multi-performance modeling of ECH even with four ECH responses provided very low approximating error with on-shot training for a wide range of RBF spread parameter. The case studies with backpropagation neural network with GDM and LM learning algorithms have demonstrated that these networks can also be utilized but the approximating capability is poor, particularly with more than three multiple responses.

32. Desirability function approach was employed to convert the multi-performance problem effectively into a single response problem and optimal settings of process input parameters were determined using genetic algorithm for seven different multi-performance optimization cases of ECH. The results were also obtained using the

modified desirability function approach, which incorporates the user's preference for flexibility. The optimal parametric settings for simultaneous optimization of PIR_a (as well as PIR_{max}), PIOR, PICyl and DIR using desirability as well as modified desirability function approaches can be given as:

- Current intensity (ADC) : 180
- Electrolyte concentration (g/L) : 200
- Rotary to reciprocating speed ratio : 250
- Electrolyte flow rate (lpm) : 10
- Electrolyte inlet temperature (°C) : 50
- Stick-out pressure (kPa) : 30
- Stick grit size : 600

33. A Fuzzy Taguchi Inference application to ECH process has been attempted for a multi-performance optimization case. This allows simultaneous consideration and improvement of the performance characteristics related to the process productivity (DIR) and those associated with surface micro-geometry (PIR_a) and part macro-geometry (PICyl). GA and NN tuning was performed to optimize the FIS performance. Both the methods provided same optimal parameter setting as obtained through 'RBFNN-DF-GA multi-performance optimization control strategy'.

34. Optimal results with the different approaches are quite similar and in good close agreement with the experimental values.

35. A set of Pareto- optimal solutions for all the seven multi-performance optimization cases of ECH have been obtained using non-dominated sorting genetic algorithm. These are useful as they can incorporate user flexibility, particularly beneficial when it is necessary to change machining strategies.

9.2 GUIDELINES FOR BETTER ECH RESULTS

1. The SS cathode tool body must be machined accurately and should be of sufficient length to maintain full coverage of the bore during entire stroking.
2. A high rotational as well as translational accuracy and stiffness of tool must be ensured.
3. Length of honing sticks should be not less than half of the bore length.
4. The stroke length of tool should be selected such that the sticks travel almost 1/3 of their length or 20mm out on either end of the bore.
5. The length, initial compression and stiffness of all the springs should be ensured to be precisely same in order to ensure an equal stick-out-pressure on every honing stick.
6. Free float conditions must be ensured to the workpiece.
7. Proper selection of electrolyte composition and concentration depending upon the work material and process performance is crucial.
8. Proper grit size selection is necessitated for good results.
9. The mechanical scrubbing action must be synchronized with electrolytic dissolution for the best overall results.
10. Mechanical scrubbing action of honing stick must be restricted to a minimum, just enough to remove preferentially the protective metal oxide microfilm from the higher spots protruding from the ideal configuration. Mechanical contribution is generally less than 5% or even less than 1% for better surface integrity results.
11. Stick-out-pressure and speed ratio combination has a bearing on the surface character as well as on the resulting surface microhardness and compressive residual stresses. Therefore, process requires a suitable SOP-SR combination to be used for better surface quality results.
12. Macro-geometrical corrections require a suitable speed ratio to be used in the process.

9.3 SCOPE OF FUTURE RESEARCH ON ECH

Further efforts may be directed in the following directions:

1. Sodium chloride and sodium nitrate are the most commonly used electrolytes in ECH and the present investigations utilized a proportion of these two electrolytes found effective in the process for the selected work material. The use of various other electrolytes may be examined possibly for improved results.
2. The use of magnetic field has been demonstrated effective with several hybrid processes such as electro-chemical grinding, abrasive flow machining, abrasive-finishing. The performance of magnetically assisted ECH may be explored.
3. A pulsed DC power supply may be used.
4. Elaborate simulation of the ECH process may be undertaken to achieve a real-time interaction with the user to provide on-line process control.
5. Three dimensional analysis of the ECH process may be carried out using tools like finite element modeling to gain better insight of the process behaviour.
6. The possibilities of the application of the process on external surfaces may be explored to expand the application horizon.

REFERENCES

1. **Adler, Y.P., Markova, E.V., and Granovsky, Y.V. (1975),** *The Design of Experiments to Find Optimal Conditions,* Mir Publishers, Moscow.
2. **Andrey Popov Hamburg (2005),** *Genetic Algorithms for Optimization-Programs for MATLAB* ®, Version 1.0, User Manual.
3. **Antony, J. (2000),** "Multi-Response Optimization in Industrial Experiments using Taguchi Quality Loss Function and Principal Component Analysis", Quality and Reliability Engineering International, Vol. 16, pp.3-8.
4. *ASM Handbook* **(1994),** Vol.5, ASM International, The Materials Information Society, Meterials Park, Ohio.
5. **Banerjee, S., and Nandi, B. N. (1988),** "On Pulsed Current Electrochemical Grinding", 13th AIMTDR Conference, Jadavpur University, pp F-21 -24.
6. **Barkar, T.B. (1990),** Engineering Quality by Design, Marcel Dekker Inc., New York.
7. **Barua, P.B., Kumar, P., and Gaindhar, J.L. (1997),** "Optimal Setting of Process Parameters for Multi-Characteristic Products using Taguchi Design and Utility-Concept- An Approach", Proceedings of the ICAMIE, Feb. 6-8, Vol.2, University of Roorkee, pp 839-842.
8. **Benedict, G.F. (1987),** *Nontraditional Manufacturing Processes*, Marcel Dekker Inc., New York.
9. **Bhattacharyya, B., and Munda, J. (2003),** "Experimental Investigation on the Influence of Electrochemical Machining Parameters on Machining Rate and Accuracy in Micromachining Domain", International Journal of Machine Tools and Manufacture, Vol.43, No.13, pp.1301-1310.

10. **Bishop, C.M. (1995),** *Neural Networks for Pattern Recognition*, Oxford: Clarendon Press.

11. **Bolz, R.W. (1981),** *Production Processes the Productivity Handbook*, 5th Edition, Industrial Press Inc, 200 Madison Avenue, New York.

12. **Box, G.E.P., Hunter, W.G., and Hunter, J.S. (1978),** *Statistics for Experimenters*, Wiley, New York.

13. **Bralla, J.G. (1986),** *Handbook of Product Design for Manufacturing*, McGraw-Hill Book Company.

14. **Budzynski, A.F. (1983),** "Research on Optimization of the Process of Electrochemical Honing", ISEM 7, Birmingham, pp. 355-371.

15. **Budzynski, A.F. (1995),** "Theoretical Analysis and Experimental Investigations of the Possibility of Shaping Rotational Cylinder Surface by using Electrochemical Honing", ISEM XI, pp 567-576.

16. **Byrne, D.M., and Taguchi, S. (1987),** "The Taguchi Approach to Parameter Design", Quality Progress, Vol.20, No.12, December, pp.19-26.

17. **Cardaliaguet, P., and Euvrand, G. (1992),** "Approximation of a Function and Its Derivatives with a Neural Network", Neural Networks 5, pp. 207–220.

18. **Carr, K., and Ferreira, P. (1995),** "Verification of Form Tolerances Part-II: Cylindricity and Straightness of a Median Line", Precision Engineering, 17, pp.144-156.

19. **Chakraborti, N. (2004),** "Genetic Algorithms in Materials Design and Processing", International Materials Reviews, Vol.49, No.3-4, pp. 246-260.

20. **Chapman, O.J.V., and Crossland, A.D. (1995),** *Neural Networks in Probabilistic Structural Mechanics,* In: Sundararajan, C. (Ed.), Probabilistic Structural Mechanics Handbook: Theory and Industrial Application. Chapman & Hall, pp. 317–330.

21. **Chen Chi –Pin, Liu Jian, Wei Guo-Chan, Wan Chao-Bin, and Wan Jian (1981),** "Electro-chemical Honing of Gears: A New Method of Gear Finishing", STCE 30/01/1981, CIRP Annals, pp 103-106.

22. **Chen, T., and Chen, H. (1995),** "Approximation Capability to Functions of Several Variables, Nonlinear Functional and Operators by Radial Basis Function Neural Networks", IEEE Transactions on Neural Networks 32 (6), 904–910.

23. **Cheng, C.B., Cheng, C.J., and Lee, E.S. (2002),** "Neuro-Fuzzy and Genetic Algorithm in Multiple Response Optimization", Computers and Mathematics with Applications, An International Journal, Vol.44, pp. 1503-1514.

24. **Cichocki, A., and Unbehauen, R. (1996),** *Neural Networks for Optimization and Signal Processing*, John Wiley & Sons, New York.

25. **Cole, R.R., and Hopenfeld, H. (1963),** "An Investigation of Electrolytic Jet Polishing at High Current Densities", ASME Transactions, Journal of Engineering for Industry, Series B, 85(4), pp.395.

26. **Cook, D.F., Ragsdale, C.T., and Major, R.L. (2000),** "Combining a Neural Network with a Genetic Algorithm for Process Parameter Optimisation", Engineering Applications of Artificial Intelligence, Vol.13, pp. 391-396.

27. **Cover, T.M. (1965),** "Geometrical and Statistical Properties of Systems of Linear Inequalities with Applications in Pattern Recognition", IEEE Transactions on Electronic Computers, Vol.EC-14, pp. 326-334.

28. **Cullity, B.D., and Stock, S.R. (2001),** "Elements of X-Ray Diffraction", Prentice Hall, 3rd Ed., N.J.

29. **Davis, L. (1991),** *Handbook of Genetic Algorithms*, Van Nostrand, Reinhold, New York.

30. **De Chiffre, L., Lonardo, P., Trumpold, H., Lucca, D.A., Goch, G., Brown, C.A., Raja, J., and Hansen, H.N. (2000),** "Quantitative Characterization of Surface Texture", Annals of CIRP, Vol.49, No.2, pp. 635-652.

31. **Deb, K. (1999),** "An Introduction to Genetic Algorithms", Sadhna, Vol.24, No.4, pp. 293-315.

32. **Deb, K. (2001),** *Multi-Objective Optimization using Evolutionary Algorithms*, John Wiley, Singapore.

33. **DeGarmo, Paul E., Black, J.T., Kosher, and Ronald A. (1997),** *Materials and Processes in Manufacturing*, 8th Ed., Prentice-Hall of India Pvt. Ltd., New Delhi.

34. **Deng, J. (2006)** "Structural Reliability Analysis for Implicit Performance Function using Radial Basis Function Network", International Journal of Solids and Structures 43, 3255–3291.

35. **Derek, W. Bunn (1982),** *Analysis for Optimal Decisions*, John Wiely and Sons, New York.

36. **Derringer, G., and Suich, R. (1980),** "Simultaneous Optimisation of Several Response Variables", Journal of Quality Technology, Volume 12(4), pp 214-218.

37. **Dubey, A.K. (1996),** *Development of the Set-up and Study Process Characteristics of Abrasive Flow Machining*, M.E. Dissertation, University of Roorkee (India).

38. **Dubey, A.K., and Shan, H.S (1997),** "Micromachining by Flow of Abrasives", Proc. 17th All India Manufacturing Technology Design & Research Conference, Jan. 9-11, REC, Warangal, pp. 269-275.

39. **Dubey, A.K., Shan, H.S., and Jain, N.K. (2006a),** "Precision Micro-Finishing by Electro-Chemical Honing", To be Presented in International Conference on Manufacturing Science and Technology, Aug. 28-30, Melaka.

40. **Dubey, A.K., Shan, H.S., and Jain, N.K. (2006b),** "Analysis of Surface Roughness and Out-of-Roundness in Electro-Chemical Honing Process", To be Presented in 1st International and 22nd All India Manufacturing Technology Design & Research Conference (22nd AIMTDR), 21st -23rd December, IIT, Roorkee.

41. **Ebeid, S. J., and Abdel Mahboud, A. M. (1988),** "High Speed Electrochemical Boring", Precision Engg., Volume 10, Issue 2, pp 80-84.

42. **Elsayed, E.A., and Chen, A. (1993),** "Optimal Levels of Process Parameters for Products with Multiple Characteristics", Int. J. Prod. Res., Vol.31, no.5, pp.1117-1132.

43. **Eshelman, R.H. (1963),** "Electrochemical Honing Reports Ready for Production Jobs", Iron Age, pp.124.

44. **Evans, M. (2003),** *Optimisation of Manufacturing Processes*, Maney Publishing, 1 Carlton House Terrace, London.

45. **Fasil, T. (2004),** *Parametric Optimization of Electrochemical Honing*, M. Tech. Dissertation, IIT Roorkee.

46. **Fitz-Gerald, J.M., and McGeough, A. (1970),** "A Model for the Mechanism Controlling Surface Finish in Electrochemical Machining", Proceedings of the Conference on Electrical Methods of Machining, Forming and Coating, London, March 17-19, pp.72-80.

47. **Floros, J.D., and Chinnan, M.S. (1998),** "Computer Graphics-Assisted Optimization for Product and Process Development", Food Technology, Vol.42, No. 72-78.

48. **Garrett, J.H.J. (1994),** "Where and Why Artificial Neural Networks are Applicable in Civil Engineering", Journal of Computing in Civil Engineering, ASCE 8 (2), pp.129–130.

49. **Gerry, Schnitzler (2001),** "What's Happening with Honing", Performance Products, Sunnen Products Co., St. Louis, MO, Manufacturing Engineering, SME.

50. **Goh, A.T.C., and Kulhawy, F.H. (2003),** "Neural Network Approach to Model the Limit State Surface for Reliability Analysis", Canadian Geotechnical Journal 40 (6), pp. 1235–1244.

51. **Goldberg, D.E. (1989),** Genetic Algorithms in Search, Optimisation and Machine Learning, Addison Wesley, New York.

52. **Guoqiang, W., Mianhong, W., and Chiping, C. (1986),** "An Investigation Into the Ability of Correcting Error in ECH", CIRP Annals, Vol 35, No. 1, pp. 125-127.

53. **Guoqiang, W., Wang Zhao-Bing, and Chen Chi-Ping (1987),** "Field Controlled Electro-chemical Honing of Gears", Precision Engg., Volume 9, Issue 4, pp 218-221.

54. **Gupta, V. and Murthy, P.N. (1980),** *An Introduction to Engineering Design Method*, Tata McGraw-Hill, New Delhi.

55. **Hajra Choudhury, S.K., Bose, S.K., and Hajra Choudhury, A.K., (1991),** *Elements of Workshop Technology, Vol. II Machine Tools,* 8th Ed., Media Promoters & Publishers Pvt. Ltd., Mumbai.

56. **Ham, F.M., and Kostanic, I. (2002),** *Principles of Neurocomputing for Science and Engineering*, Tata McGraw-Hill Publishing Company Ltd., New Delhi.

57. **Han, D., Moon, S.B., Park, K., Kim, B., Lee, K. K., and Kim, N. J. (2005),** "Modelling of Plasma Etching Process using Radial Basis Function Network and Genetic Algorithm", Vacuum, 79, pp. 140–147.

58. **Harrington, E. (1965),** "The Desirability Function", Industrial Quality Control, Vol. 21, No. 10, pp. 494-498.

59. **Haykin, S. (2003),** *Neural Networks*, Pearson Education Inc., New Delhi.

60. **Hayward, G., and Davidson, V. (2003)**, "Fuzzy Logic Applications", Analyst (the royal Society of Chemistry Journal), Vol 128, pp. 1304-1306.

61. **HE, F., ZHANG, W., and NEZU, K. (2000)**, "A Precision Machining of Gears (Slow-Scanning Field Controlled Electrochemical Honing)", JSME International Journal Series C, Vol. 43, No.2, pp. 486-491.

62. **Herrera, F., Lozano, M., and Vergedgay, J.L. (1995)**, "Tuning Fuzzy Logic Controller by Genetic Algorithms", International Journal of Approximate Reasoning, Vol. 12, pp. 299-315.

63. **Hines, J.W. (1997)**, *MATLAB supplement to Fuzzy and Neural Approaches in Engineering*, John Wiley & Sons, Inc., New York.

64. **Holland, J.H. (1975)**, *Adaptation of Neural and Artificial Systems*, University of Michigan Press, Ann. Arbor.

65. **Horgan, I.F. (1962)**, "Electrolytic Boost for Honing", American Mach.

66. **Hornik, K., Stinchcombe, M., and White, H. (1989)**, "Multi-Layer Feed-Forward Networks are Universal Approximators', Neural Networks 2, 359–368.

67. **Hornik, K., Stinchcombe, M., and White, H. (1990)**, "Universal Approximation of an Unknown Mapping and its Derivatives using Multi-layer Feed-Forward Networks", Neural Networks 3, 551–560.

68. **Hussain, M.F., Barton, R.R., and Joshi, S.B. (2002)**, "Metamodeling: Radial Basis Functions, Versus Polynomials", European Journal of Operational Research, 138(1), pp. 142-154.

69. **Jain, V.K. (2002)**, *Advanced Machining Processes*, Allied Publishers Pvt Ltd, New Delhi.

70. **Jang, J-S Roger (1993)**, "ANFIS: Adaptive Network-Based Fuzzy Inference System", IEEE Trans. on Systems, Man and Cybernetics, Vol.23, No.3, pp. 665-685.

90. **Lu, D., and Antony, J. (2002),** "Optimization of Multiple Responses using a Fuzzy-Rule Based Inference System", Int. Journal of Prod. Research, Vol.40, No. 7, pp. 1613-1625.

91. *Machining Data Handbook* **(1980),** Vol.2, 3rd Edition, Machinability Data Center, Metcut Research Associates Inc., Cincinnati, Ohio.

92. **Mai-Duy, N., and Tran-Cong, T. (2003),** "Approximation of Function and Its Derivatives using Radial Basis Function Networks", Applied Mathematical Modeling 27 (3), 197–220.

93. **Merchant, M.E. (1962),** "Newer Methods for the Precision Working of Metals-Research and Present Status", Proc. Int. Conf. Production Research (ASME), pp. 93-107.

94. *Metals Handbook* **(1980),** Vol.3, 8th Edition, American Society for Metals, Metals Park, Ohio.

95. **Michalewicz, Z. (1992),** "Genetic Algorithm + Data Structures = Evolution Program", Springer Verlag, Berlin.

96. **Montgomery, Douglas C. (2004),** *Design and Analysis of Experiments*, John Wiley & Sons Inc., New York.

97. **Moody, J., and Darken, C.J. (1989),** "Fast Learning in Networks of Locally Tuned Processing Units", Neural Computation 1, 281-294.

98. **Myres, R.H., and Carter, W.H. (1975),** "Response Surface Techniques for Dual Response Systems", Technometrics, Vol. 15, pp. 301-307.

99. **Nandi, A.K., and Pratihar, D.K. (2004),** "Automatic Design of Fuzzy Logic Controller using a Genetic Algorithm to Predict Power Requirements and Surface Finish in Grinding", Journal of Materials Processing Technology, Vol.148, pp. 288-300.

100. **Nurai, T., et al (1967),** "Study on Electrolytic Honing", J. Mech Lab, 21, Tokyo, pp. 78-86.

101. *Operating Instructions*, Leitz Micro-hardness Tester, Germany.

102. *Operating Instructions*, Universal Measuring Software, UMESS 300, ZEISS Germany.

103. **Orr, M.J.L., (1999),** "Recent Advances in Radial Basis Function Networks", Technical Report, University of Edinburgh.

104. **Ostermark, R. (2000),** "A Hybrid Genetic Fuzzy Neural Network Algorithm Designed for Classification Problems Involving Several Groups", Fuzzy Set and Systems, Vol.114, pp.311-324.

105. **Pandey, P.C., and Shan, H.S. (2005),** *Modern Machining Processes*, Tata McGraw-Hill Publishing Company Limited, New Delhi.

106. **Park, J., and Sandberg, I. (1993),** "Approximation and Radial-Basis-Function Networks", Neural Computation 5, 305–316.

107. **Peterson, F., Hinnela, J., and Saxena, H. (2003),** "Evolutionary Neural Network Modeling of Blast Furnace Burden Distribution", Materials and Manufacturing Processes, Vol.18, No.3, pp. 385-399.

108. **Peterson, R.G. (1985),** *Design and Analysis of Experiments,* Marcel Dekker Inc., New York.

109. **Phadke, M.S. (1989),** *Quality engineering using Robust Design*", Prentice Hall, New Jersey.

110. **Pham, D.T., and Karaboga, D. (2000),** "Intelligent Optimisation Techniques", Springer Verlag London.

111. **Pignatiello (Jr.), J.J. (1993),** "Strategies for Robust Multi-Response Quality Engineering", IIE Trans., Vol.25, No.3, pp.5-15.

112. *Production Technology* **(1980),** HMT Bangalore, Tata McGraw-Hill Publishing Company Ltd.

113. **Rajasekaran, S., and Pai, G.A.V. (2003),** *Neural Networks, Fuzzy Logic, and Genetic Algorithms Synthesis and Applications,* Prentice-Hall of India Pvt. Ltd., New Delhi.

114. **Rajurkar, K.P., Kozak, J., and Wei, B. (1993),** "Study of Pulse Electrochemical Machining Characteristics", CIRP Annals, Vol. 42/1, pp 231-234.

115. **Rajurkar, K.P., Zhu, D., McGeough, J.A., Kozak, J., and De Silva, A. (1999),** "New Developments in Electrochemical Machining", Annals of CIRP, Vol.48, No.2, pp.567-579.

116. **Randlett, E. A. Jr., and Ellis, M. P. (1967),** "Electrochemical Honing", ASTM MR67-648, pp. 1-13.

117. **Randlett, E. A. Jr., and Ellis, M. P. (1968),** "Electrochemical Honing", ASTM MR68-815, 1968, pp- 1-11.

118. **Reed-Hill, Robert E., and Abbaschian, R., (2003),** *Physical Metallurgy Principles*, 3rd Ed, Thomson Asia Pvt. Ltd., Singapore.

119. **Ross, Philip J. (1988),** *Taguchi Techniques for Quality Engineering*, McGraw-Hill Book Company, New York.

120. **Ross, T. (2004),** Fuzzy Logic with Engineering Applications, John Wiley and Sons, New York.

121. **Roy, Ranjit K. (1990),** *A Primer on the Taguchi Method*, Van Nostrand Reinhold, New York.

122. **Schueremans, L., and Van Gemert, D. (2005),** "Benefit of Splines and Neural Networks in Simulation Based Structural Reliability Analysis", Structural Safety 27, 246–261.

123. **Sen, M. (2005),** *Electro Jet Drilling in Some Nickel Base Super Alloys*, Ph.D. Thesis, Indian Institute of Technology, Roorkee.

124. **Sen, M., and Shan, H.S. (2006),** "Optimal Selection of Machining Conditions in the Electro Jet Drilling Process using Hybrid NN-DF-GA Approach", Int. J. of Materials and Manufacturing Processes (Accepted).

125. **Shan, H. S. (2006),** *Advanced Manufacturing Methods*, Tata McGraw-Hill, New Delhi.

126. **Sharma, P.C. (2004),** *A Text Book of Production Technology*", 6th Edition, S. Chand and Company Ltd, New Delhi.

127. **Shiau, G.H. (1990),** "A Study of the Sintering Properties of Iron Ores using the Taguchi's Parameter Design", J. of Chinese Statistical Association, Vol.28, pp. 253-275.

128. **Singh, S., Shan, H.S., and Kumar, P. (2002),** "Parametric Optimization of Magnetic-Field Assisted Abrasive Flow Machining by the Taguchi Method", Quality and Reliability Engineering International, Vol.18, pp. 273-283.

129. **Srinivas, N., and Deb, K. (1994),** "Multi-Objective Function Optimization Using Non-dominated Sorting Genetic Algorithms", Evolutionary Computation, 2(3), 221-248.

130. **Srinivasu, D.S., Ramesh Babu, N., and Srinivasa, Y.G. (2004),** "Neuro-Genetic Approach for Automatic Selection of Process Parameters in Abrasive Water Jet Cutting Considering the Variation in Bore Diameter of Focussing Nozzle", Proceedings 21st AIMTDR, Dec.20-22nd, Vellore, India, pp.887-893.

131. **Srinivasulu Reddy, A., Soni, J.S., Sridhar, T. and Janardhan Reddy, T.A. (1999),** "Evaluation of Surface Finish in EDM Process using Factorial Technique", Quest 99, National Conference, Bangalore.

132. **Taguchi, G. (1987),** *System of Experimental Design*, UNIPUB, Kraus International Publications, New York.

133. **Tan, K.K., and Tang, K.Z. (2001),** "Taguchi-Tuned Radial Basis Function with Application to High Precision Motion Control", Artificial Intelligence in Engineering, 15, pp. 25-36.

134. **Taniguchi, N. (1983),** "Current Status In and Future Trends of Ultraprecision Machining and Ultrafine Materials Processing", Annls. CIRP, Vol. 32, No. 2, pp. 573-582.

135. **Tarng, Y.S., and Yang, W.H. (1998),** "Optimisation of the Weld Bead Geometry in Gas Tungsten Arc Welding by the Taguchi Method", Int. Journal of Advance Manufacturing Technology, Vol.14, pp. 549-554.

136. *Technical Reference Manual*, Wyko NT 1100, VEECO, Elvira Road, Tucson, AZ 85706 USA.

137. **Tong, L.-I., and Su, C.-T. (1997),** "Optimizing Multi-Response Problems in Taguchi Method by Fuzzy Multiple Attribute Decision Making", Quality and Reliability Engineering International, Vol.13, pp.25-34.

138. *Tool and Manufacturing Engineers Handbook* **(1983),** Vol.1, 4th Edition, Society of Manufacturing Engineers, Dearborn, Michigan.

139. **Tosun, N., and Ozler, L. (2004),** "Optimisation for Hot Turning Operations with Multiple Performance Characteristics", Int. Journal of Advance Manufacturing Technology, Vol.23, pp.777-782.

140. **Verma, R., Roy N., and Ranjan Ganguli, R. (2006),** "Gas Turbine Diagnostics Using A Soft Computing Approach", Applied Mathematics and Computation, 172, pp. 1342–1363.

141. **Wang, G.J., and Chou, M. H. (2005),** "A Neural-Taguchi-Based Quasi Time-Optimization Control Strategy for Chemical-Mechanical Polishing Processes", International Journal of Advance Manufacturing Technology, Vol. 26, pp. 759-765.

142. **Wang, K., Gelgele, H.L., Yi, Yuan, Q., and Fang, M. (2003),** "A Hybrid Intelligent Method for Modeling the EDM Process", International Journal of Machine Tools and Manufacture, Vol. 43, pp. 995-999.

143. **Warnes, R.M., Glassey, J., Montague, A.G., and Kara, B. (1998),** "Application of Radial Basis Function and Feedforward Artifcial Neural Networks to the *Escherichia Coli* Fermentation Process", Neurocomputing, 20, pp. 67–82.

144. **West, D.A., Mangiameli, P.M., and Chen, S.K. (1999),** "Control of Complex Manufacturing Processes: A Comparison of SPC Methods with A Radial Basis Function Neural Network", Omega, Int. J. Mgmt. Sci., 27, pp. 349-362.

145. **Wilson, J.F. (1971),** *Practice and Theory of Electrochemical Machining*, Wiley Interscience, New York.

146. **Zadeh, L.A. (1965),** "Fuzzy Sets", Inf. Control, Vol. 8, pp. 338-353.

147. **Zadeh, L.A. (1987),** *Fuzzy Sets and Applications,* John Wiley and Sons, New York.

148. **Zhang, Yun-Xin, and Tan, Yong-Ji (2006),** "Meshless Schemes for Unsteady Navier-Stokes Equations in Vorticity Formulation Using Radial Basis Functions", Journal of Computational and Applied Mathematics 192, 328–338.

149. **Zulfiqar, A.K., Mark, H., Shogo, T., and Ying, W. (2005),** "Ceramic Rolling Elements With Ring Crack Defects- A Residual Stress Approach", Materials Science and Engineering (A), Vol. 404, pp. 221-226.

150. **Zuo, X.Q., and Fan, Y.S. (2006),** "A Chaos Search Immune Algorithm with Its Application to Neuro-Fuzzy controller design", Chaos, Solitons and Fractals, 30, pp. 94–109.

PLANNED PUBLICATIONS

1. **Dubey, A.K., Shan, H.S., Jain, N.K.** Precision micro-finishing by electro-chemical honing. To be presented in *International Conference on Manufacturing Science and Technology*' 2006, Melaka, 28-30 August 2006.
2. **Dubey, A.K., Shan, H.S., Jain N.K.** Analysis of surface roughness and out-of-roundness in electro-chemical honing process. To be presented in *1st International and 22nd AIMTDR*, IIT Roorkee (India), 21-23 December 2006.
3. **Dubey, A.K., Shan, H.S., Jain N.K.** Morphology of ECHed surface. (communicated)
4. **Dubey, A.K., Shan, H.S., Jain, N.K.** Experimental investigations on electro-chemical honing. (communicated)
5. **Dubey, A.K., Shan, H.S., Jain, N.K.** Multi-response optimization of electro-chemical honing process using utility based Taguchi approach. (communicated)
6. **Dubey, A.K., Shan, H.S., Jain, N.K.** Fuzzy logic inference applications to electro-chemical honing. (to be communicated)
7. **Dubey, A.K., Shan, H.S., Jain, N.K.** Multi-performance optimization of ECH using Taguchi-NN-DF-GA approach. (communicated)
8. **Dubey, A.K., Shan, H.S., Jain, N.K.** Multi-objective optimization of ECH using non-dominated sorting genetic algorithms. (to be communicated)
9. **Dubey, A.K., Shan, H.S., Jain, N.K.** State of art of electro-chemical honing process. (to be communicated)

APPENDIX-A

SPECIFICATIONS / TECHNICAL DATA OF SETUP COMPONENTS

- **DC Power Supply**

Make	:	M/s Electrocon Electronics, Roorkee
Output voltage	:	3-30VDC (adjustable in 8 steps, further fine tune 8 steps)
Output current	:	200ADC (adjustable)
Input supply	:	1Φ 220V AC
Wiring	:	Silver impregnated copper wire with Teflon insulation.

- **Digital Voltmeter**

Make	:	M/s Creative Control, Mumbai
Model	:	96x96
Input	:	50VDC
Operating Supply	:	220VAC

- **Digital Ammeter**

Make	:	M/s Creative Control, Mumbai
Model	:	96x96
Input	:	200ADC, 75mVDC
Operating Supply	:	220VAC

- **Main Controller Output Ammeter**

Make	:	M/s Automatic Electric Ltd., Mumbai
Range	:	0-300Ã

- **Slip Ring**

Rating	:	6.5 kW
Type	:	Copper dual slip ring with ceramic insulation

- **Constant Voltage Transformer**

Make	:	M/s Spectrum Power Control, New Delhi
Output	:	220/230V ±1%
Amps	:	8
kVA	:	2

- **Rotary Drive DC Motor with Controller**

Make	:	M/s New Electron
kW	:	1
V	:	220
A	:	4
RPM	:	1500, with forward and backward rotation

- **Digital Tachometer**

Make	:	M/s Systems & Controls, Bangalore
Model	:	HTM 590
Range	:	0-9999 rpm, (0-999.9 meter/min)
Accuracy	:	± 1 rpm

- **Reciprocating Drive Stepper Motors**

Make	:	M/s Srijan Control Drives, Pune
Type	:	DC Stepping Motor Type STM 1101
Torque	:	20 kg-cm
Volt	:	12V
Current	:	Max. 1.5A / phase

Make	:	M/s Srijan Control Drives, Pune
Type	:	DC Stepping Motor Type STM 1100
Torque	:	10 kg-cm
Volt	:	12V
Current	:	Max. 1.5A / phase

- **8501 Microprocessor Training Kit**

Make	:	M/s Vinytics, New Delhi
Model	:	VMC-8501
Interface card	:	Stepper Motor Controller Card, Vinytics
Power supply	:	+12V/5A, PS-V, Vinytics

Table A1 Stepper motor program
(20 kg-cm, 10 kg-cm and 10 kg-cm stepper motor unit-tandom compounded)

- **Main Program:**

2000	3E	201d	d3	203A	cd
2001	80	201E	00	203B	00
2002	d3	201F	cd	203C	21
2003	03	2020	00	203D	3E
2004	06	2021	21	203E	A9
2005	1A	2022	05	203F	d3
2006	3E	2023	c2	2040	00
2007	A9	2024	06	2041	cd
2008	d3	2025	20	2042	00
2009	00	2026	06	2043	21
200A	cd	2027	1A	2044	05
200B	00	2028	3E	2045	c2
200C	21	2029	9A	2046	28
200D	3E	202A	d3	2047	20
200E	65	202B	00	2048	c3
200F	d3	202c	cd	2049	00
2010	00	202d	00	204A	20
2011	cd	202E	21		
2012	00	202F	3E		
2013	21	2030	56		
2014	3E	2031	d3		
2015	56	2032	00		
2016	d3	2033	cd		
2017	00	2034	00		
2018	cd	2035	21		
2019	00	2036	3E		
201A	21	2037	65		
201B	3E	2038	d3		
201C	9A	2039	00		

- **Delay Program:**

2100	11		2104	BC
2101	00		2105	03
2102	OF	10, 15, 25	2106	c9
2103	cd			

APPENDIX-B

SPECIFICATIONS OF MEASURING INSTRUMENTS / EQUIPMENT

- **Workpiece Cleaner**

Make and type	:	Vibronics Ultrasonic Cleaner
Cleaning medium	:	Acetone

- **Surface Roughness Meter**

Make	:	Mahr Federal Inc.
Model	:	Mahr Perthometer 4615

- **Optical Profilometer**

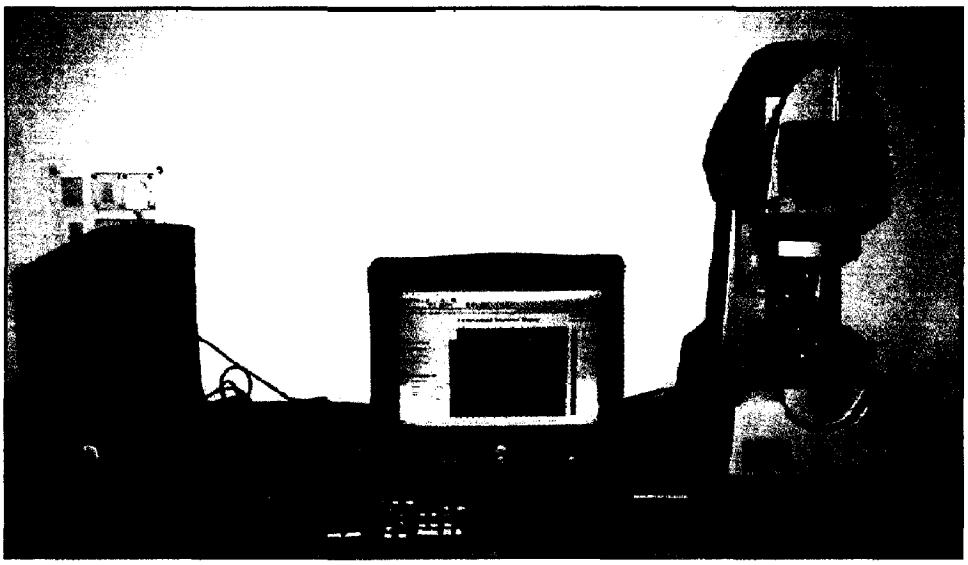

Make	:	VEECO, Elvira Road, Tucson, AZ 85706 USA.
Model	:	Wyko NT 1100 interfaced with Vision® 32 software
Magnification	:	10X
Field of View (FOV) Lenses	:	1.5X
Permissible X and Y displacement	:	4"
Tip and Tilt	:	± 4°
Power input	:	90-260 V, 47-63 Hz

- **3D Co-ordinate Measuring Machine**

Make	:	ZEISS, Germany
Model	:	MOUSER KMZ 201210 interfaced with Universal Measuring Software UMESS 300

- **Scanning Electron Microscope**

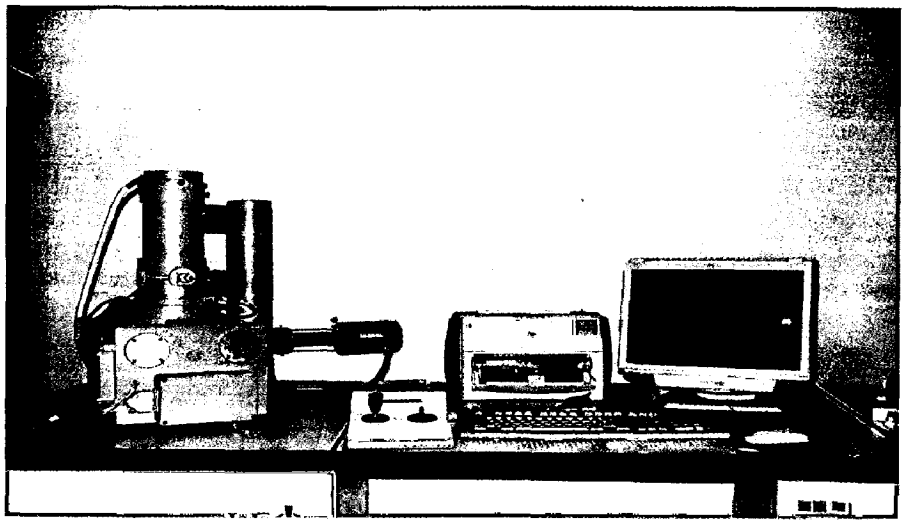

Make	:	LEO
Model	:	435 VP
Resolution	:	4 nm in HV and 6 nm in VP
Acc. voltage	:	Upto 30 kV
Magnification	:	10X to 300000X
Stages	:	X, Y, Z, θ, φ and Eucentric Goniometer
Detection Mode	:	SE and BSD
Image recording	:	Printer and Camera

- **Optical Microscope**

Make	:	ZEISS Axiovert 200 MAT Inverted Optical Microscope interfaced with Imaging Software ZEISS Axio Vision Release 4.1 Germany

- **Micro-hardness Tester**

Make	:	Ernst. Leitz Wetzlar GMBH, Germany
Model:	:	Mini Load-2

- **Hardness Testing Machine**

Make	:	WPM, Germany
Model:	:	HP0250

- **X-Ray Diffractometer**

Make	:	BRUKER
Model	:	AXS D8 Advance
Target	:	Cu, Fe and Mo
Working voltage	:	10-110 kV
Tube current	:	4.0 – 80 mA
Goniometer speed range	:	0° - 150°
Accessories	:	interfaced with Bruker DIFFRAC^{plus} X-Ray diffraction software

- **Digital pH Meter**

Make	:	Toshniwal Inst. Mfg. Pvt. Ltd, Ajmer
Model:	:	CAT. No. CL46

- **Digital Conductivity Meter**

Make	:	Agrawal Electronics, 202, Shivshakti Ind. Estate, LBS Marg, Mumbai
Model:	:	Testronix 15
Conductivity Cell		CD-06

- **Electronic Balance**

Make	:	Sartorius
Model:	:	1518
Least count	:	1 mg

APPENDIX-C

WORK MATERIAL AND ELECTROLYTE PROPERTIES

- **Work Material: Gray Iron (ASTM - A 48)**

Grade	:	ASTM 35 gray cast iron
Microstructure	:	Ferritic / pearlitic matrix with Type A graphite flake distribution (ASTM A247)
Modulus of elasticity (E) (GPa)	:	100-119
Torsional Modulus (GPa)	:	40-48
HB	:	212
Tensile strength (MPa)	:	252
Compressive strength (MPa)	:	855
Torsional shear strength (MPa)	:	334
Density (g/cc)	:	6.95-7.35
Thermal conductivity(W/m-K)	:	46

- **Electrolyte (¾ part NaCl plus ¼ part $NaNO_3$)**

Temperature	Conductivity (mS)			pH		
(°C)	100g/L	150g/L	200g/L	100g/L	150g/L	200g/L
7	57.4	75.4	77.2	7.98	7.88	7.59
10	61.7	80.7	84.5	7.98	7.87	7.57
15	69.3	88.5	96.2	7.92	7.92	7.69
25	80.4	102.5	108.1	8.10	8.12	8.03
30	84.7	108.1	113.5	8.08	8.12	8.03
35	93.1	118.1	128.9	7.98	8.03	8.05
45	104.1	129.7	141.9	7.95	7.97	7.90
50	109.9	132.1	144.6	8.02	7.85	7.70

APPENDIX-D

FLOW CHART: RBFNN-DF/MOD DF-GA , FLOW CHART: RBFNN-NSGA

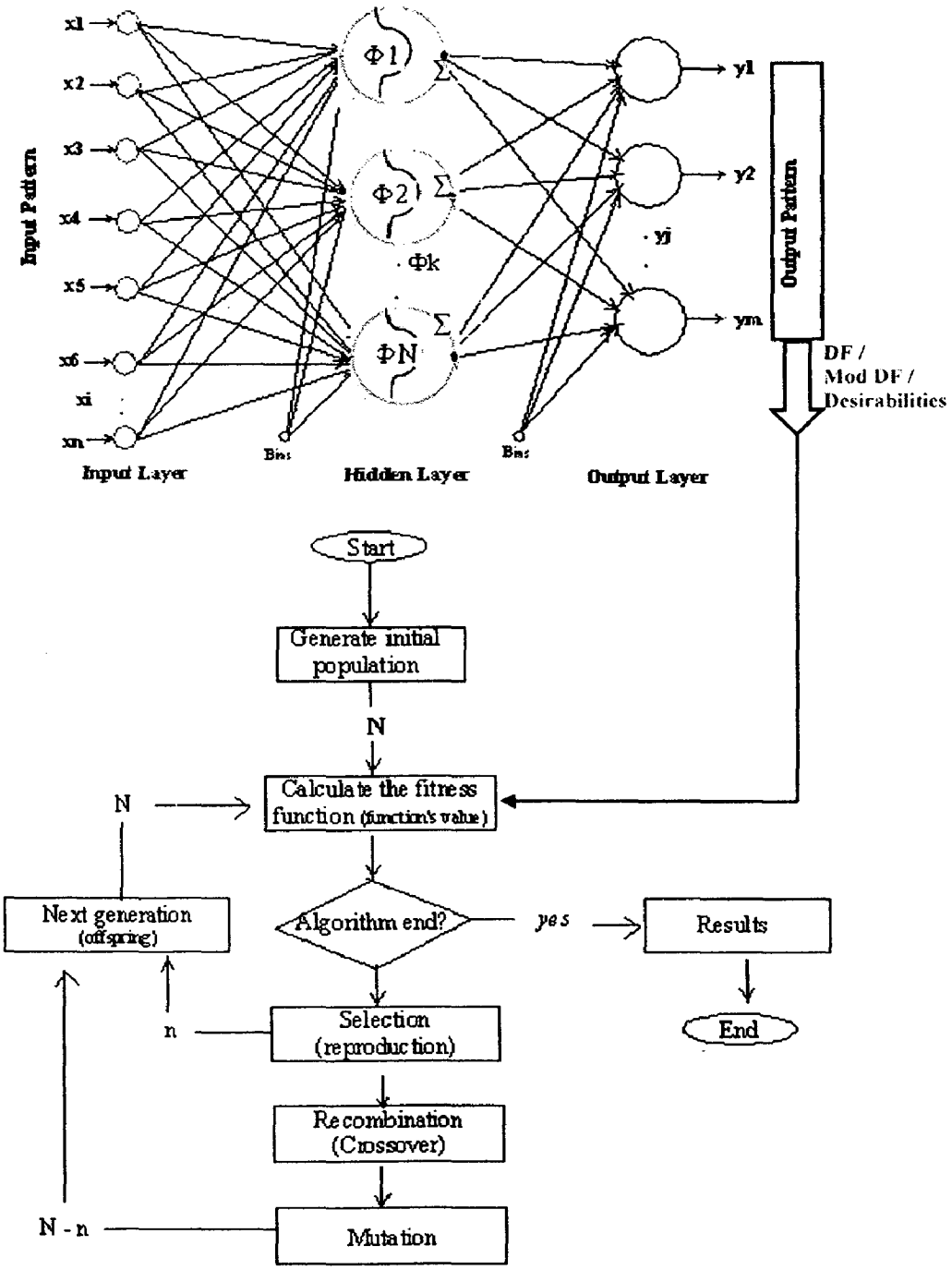

Fig. A.D.2 RBFNN-DF/Mod DF-GA and RBFNN-NSGA flow chart